West Virginia University

DOE Award No. : FE-0001163

Final Report

October 2009 to September 2014

In-Situ MVA of CO_2 Sequestration Using Smart Field Technology

Submitted by:
Petroleum and Natural Gas Engineering Department
West Virginia University Research Corporation
866 Chestnut Ridge Rd.
Morgantown WV 26506-6845

Principal Investigator: Shahab D. Mohaghegh

PREPARED FOR:
UNITED STATES DEPARTMENT OF ENERGY
NATIONAL ENERGY TECHNOLOGY LABORATORY

NOVEMBER 1, 2014
Revised: March 2015

Office of Fossil Energy

Disclaimer

Abstract

Capability of underground carbon dioxide storage to confine and sustain injected CO_2 for a long period of time is the main concern for geologic CO_2 sequestration. If a leakage from a geological CO_2 sequestration site occurs, it is crucial to find the approximate amount and the location of the leak, in a timely manner, in order to implement proper remediation activities.

An overwhelming majority of research and development for storage site monitoring has been concentrated on atmospheric, surface or near surface monitoring of the sequestered CO_2. This study aims to monitor the integrity of CO_2 storage at the reservoir level. This work proposes developing in-situ CO_2 Monitoring and Verification technology based on the implementation of Permanent Down-hole Gauges (PDG) or “Smart Wells” along with Artificial Intelligence and Data Mining (AI&DM). The technology attempts to identify the characteristics of the CO_2 leakage by de-convolving the pressure signals collected from Permanent Down-hole Gauges (PDG).

Citronelle field, a saline aquifer reservoir, located in the U.S. was considered as the basis for this study. A reservoir simulation model for CO_2 sequestration in the Citronelle field was developed and history matched. PDGs were installed, and therefore were considered in the numerical model, at the injection well and an observation well. Upon completion of the history matching process, high frequency pressure data from PDGs were generated using the history matched numerical model using different CO_2 leakage scenarios. Since pressure signal behaviors were too complicated to de-convolute using any existing mathematical formulations, a Machine Learning-based technology was introduced for this purpose. An Intelligent Leakage Detection System (ILDS) was developed as the result of this effort using the machine learning and pattern recognition technologies.

The ILDS is able to detect leakage characteristics in a short period of time (less than a day from its occurrence) demonstrating the capability of the system in quantifying leakage characteristics subject to complex rate behaviors. The performance of ILDS is examined under different conditions such as multiple well leakages, cap rock leakage, availability of an additional monitoring well, presence of pressure drift and noise in the pressure sensor and uncertainty in the reservoir model.

TABLE OF CONTENTS

List of Tables 18
Executive Summary 20
Site Selection 26
Citronelle Field- Saline Aquifer 26
Selection of Reservoir Modeling Software 28
Background Study on Candidate Sites 28
Reservoir Simulation and Modeling 33
ARI Simulation Model 33
Developing Lateral Heterogeneity for the Field (the WVU Model) 45
Numerical Modeling (Permeability Realizations) 53
Geological Model Development 61
WVU Numerical Modeling Based on Porosity Logs 68
Geological Model-Sand layer Development 74
WVU Numerical Model - Initial Results 83
Gridding Sensitivity Analysis 87
Designing Different Injection Scenarios 90
Sensitivity Analysis on Reservoir Simulation Results 93
Sensitivity Analysis 95
Permeability 95
Permeability Ratio 98
Gas Relative Permeability Curves 99
Maximum Residual Gas Saturation 101
Brine Compressibility 102
Brine Density 103
Boundary Condition 105
History Matching of the Reservoir Simulation Model 108
Collecting injection data 108
Collection of Pressure Data (De-noising and averaging) 109
In-Situ CO_2 Behavior Validation - Early Injection Data 111
In-Situ CO_2 Behavior Validation - Entire Injection Data 122
History Matched Model Validation 130
Leakage Modeling 134

Data Preparation for the Intelligent Leak Detection System (ILDS) 148
Leakage in Wells D-9-2 and D-9-10 158
Intelligent Leakage Detection System 160
Processing of High Frequency Data Streams – Data Summarization 160
Preparation of High Frequency Data for Pattern Recognition 164
Neural Network Architecture Design 167
Neural Network Training and Calibration 169
Pattern Recognition Analysis 171
Intelligent Leakage Detection System Development- Heterogeneous Model 177
Pattern Recognition Analysis 177
Neural Net Data Preparation 178
Neural network training, Calibration and Verification 180
Neural Network Validation 183
Neural Network Model Analysis 185
ILDS Enhancement and Evaluation 186
Real-time Intelligent Leakage Detection System (RT-ILDS) 187
Detection Time 193
Testing RT-ILDS for Multiple Geological Realization 196
Detection of Leaks at Different Vertical Locations along the Wells 199
Effect of Gauge Accuracy or Pressure Drift on RT-ILDS Results 205
Use of Well Head Pressure at Injection Well 208
RT-ILDS for Variable CO_2 Leakage Rates 210
Use of Pressure Down-hole Gauge (PDG) in Injection Well 217
Leakage from the Cap-rock 218
Multi-Well Leakage 222
Analysis to Demonstrate the Project Technology's Ability to Support DOE's Goal of Less Than 1% CO2 Leakage over 100 Years 226
Conclusions 227
Appendices 228
Appendix1 229
Appendix 2 232
De-noising of Permanent Down hole Gauge Data using Wavelets 232
Methodology of de-noising using wavelet 235

Perform Wavelet De-noising Using Matlab 237
High Frequency Data Generation 240
De-noising and Data Smoothing 245
Determination of noise distribution and level 250
Adding noise to the simulation data, de-noising and data summarizing 252
Performing Pattern Recognition Analysis 253
Neural Network Architecture Design 253
Neural Network Training and Calibration 254
Neural Network Validation for Noisy data 257
Appendix 3 268
Appendix 4 275
Appendix 5 281
Appendix 6 290
Appendix 7 299
Appendix 8 302
Appendix 9 303
Appendix 10 307
Appendix 11 311
Appendix 12 312
Appendix 13 320
References 321

List of Figures

Figure 1. Location of the Citronelle Dome in the State of Alabama, the United States of America. 21
Figure 2. The location of the well logs and three cross sections for correlating the wells. 22
Figure 3. Quality of the history match of the reservoir simulation model. 22
Figure 4. Modeling the CO_2 leakage from the abandoned wells in the Citronelle Dome. 23
Figure 5. Accuracy of the Intelligent Leakage Detection System (ILDS) in identifying the location of the leakage. 23
Figure 6. . Accuracy of the Intelligent Leakage Detection System (ILDS) in identifying the amount of the leakage. 24
Figure 7. A snapshot of the interface developed for the Intelligent Leakage Detection System (ILDS). 25
Figure 8. Rodessa Oil and Saline Reservoirs (Left) - Tuscaloosa-Eutaw Saline Reservoirs (Right) 29
Figure 9. Map of the 5 spot CO_2 – EOR 30
Figure 10. Gas Relative Permeability (Red) - Oil Relative Permeability (Blue) 34
Figure 11. Water Relative Permeability (Red) - Oil Relative Permeability (Blue) 34
Figure 12. Citronelle Model Structure 35
Figure 13. Gas Saturation around the injection well - Scenario 1 36
Figure 14. Cumulative Gas Rate & Gas rate Standard Condition at the injection period 37
Figure 15. Well Block Pressure at the injection period 37
Figure 16. Cumulative Gas Rate & Gas rate Standard Condition at the monitoring period 38
Figure 17. Well Block Pressure at the monitoring period 38
Figure 18. Gas Saturation around the injection well - Scenario 2 39
Figure 19. Cumulative Gas Rate & Gas rate Standard Condition at the injection period 40
Figure 20. Well Block Pressure at the injection period 40
Figure 21. Cumulative Gas Rate & Gas rate Standard Condition at the monitoring period 41
Figure 22. Well Block Pressure at the monitoring period 41
Figure 23. Gas Saturation around the injection well - Scenario 3 42
Figure 24. Cumulative Gas Rate & Gas rate Standard Condition at the injection period 43
Figure 25. Well Block Pressure at the injection period 43
Figure 26. Cumulative Gas Rate & Gas rate Standard Condition at the monitoring period 44
Figure 27. Well Block Pressure at the monitoring period 44
Figure 28. CO_2 Gas mole fraction at the end of the injection 48
Figure 29. CO_2 Gas mole fraction after 10 years of monitoring 48
Figure 30.The porosity-permeability correlation proposed by ARI 49
Figure 31.The porosity-permeability correlation in different rock types 50
Figure 32. New and revised porosity distribution 54
Figure 33. New and revised permeability distribution 54
Figure 34. CO_2 mole fraction at the end of the injection period in heterogeneous model 55
Figure 35. CO_2 mole fraction at the end of the injection period in homogenous model 55
Figure 36. CO_2 Gas mole fraction after 30 years of monitoring in heterogeneous model 56
Figure 37. CO_2 Gas mole fraction after 30 years of monitoring in homogenous model 56

Figure 38. Change in CO_2 Gas mole fraction over 30 years of monitoring in heterogeneous model 57
Figure 39. Gas Saturation at the end of the injection in heterogeneous model 57
Figure 40. Gas Saturation at the end of the injection in homogenous model 58
Figure 41. Gas saturation after 30 years of monitoring in heterogeneous model 58
Figure 42. Gas Saturation after 30 years of monitoring in homogenous model 59
Figure 43. Change in gas saturation over 30 years of monitoring in heterogeneous model 59
Figure 44. The distribution of CO_2 around the injection well D-9-7 in both heterogeneous and homogenous models. 60
Figure 45. The location of cross section A-A' and B-B' and the wells on them, ARI report[7] 62
Figure 46. The sand layers of injection well D-9-7 and its corresponding well log, the report (SECARB 2010). 63
Figure 47. The location of top five sand layers on the resistivity and SP log based on the geological model, Well D-9-1 65
Figure 48. The location of top five sand layers on the resistivity and SP log based on the geological model, Well D-4-14 66
Figure 49. Porosity Distribution, Realization case number 1. 68
Figure 50. Porosity Distribution, Realization case number 2. 69
Figure 51. Porosity Distribution, Realization case number 3. 69
Figure 52. Porosity Distribution, Realization case number 4. 70
Figure 53. Porosity Distribution, Realization case number 5. 70
Figure 54. Porosity Distribution, Realization case number 6. 71
Figure 55. Porosity Distribution, Realization case number 7. 71
Figure 56. Porosity Distribution, Realization case number 8. 72
Figure 57. Porosity Distribution, Realization case number 9. 72
Figure 58. The distance of CO_2 extension from the injection well D-9-7 in whole nine models 73
Figure 59. Cumulative Gas against Time for all different realization cases 73
Figure 60. The location of cross sections A-A' and B-B' and the wells on them, ARI report 74
Figure 61. The location of cross section A-A', B-B' and C-C' and the wells on them, WVU Model 75
Figure 62. The sand layers of injection well D-9-7 and its corresponding well log, in the SECARB report (SECARB 2010). 76
Figure 63. The sand layers of injection well D-9-7 and its corresponding well log, the WVU Model 77
Figure 64. Sand layers on Cross section A-A', the WVU Model. 78
Figure 65. Sand layers on Cross section B-B', the WVU Model. 78
Figure 66. Sand layers on Cross section C-C', the WVU Model 78
Figure 67. Grid tops in WVU Model 79
Figure 68. Grid Thickness in WVU Model. 79
Figure 69. Geological dip of the reservoir, the WVU Model (left) and the ARI Model (right) 80
Figure 70. The porosity-permeability correlation proposed by ARI 81
Figure 71. Porosity - permeability relation between core and log in D-9-8 82
Figure 72. The porosity-permeability correlation in different rock types 83
Figure 73. Porosity distribution in the WVU Model 84

Figure 74. The extension of CO_2 plume in WVU Model 84
Figure 75. Gas Saturation in the WVU Model 85
Figure 76. The Extension of CO_2 Plume in the ARI New Model 85
Figure 77. Gas Saturation in the ARI New Model 86
Figure 78. The extension of CO_2 Plume in the ARI Old Model 86
Figure 79. Citronelle model with all coarse grid-blocks (case 1) 87
Figure 80. Citronelle model with coarse and fine grid-blocks (case 2) 88
Figure 81. Citronelle model having 4 types of grid-blocks (case 3) 88
Figure 82. CO_2 Saturation at the location of the observation well 89
Figure 83. CO_2 Saturation at the a grid close to the injection well 89
Figure 84. Pressure distribution for the base case 91
Figure 85. Pressure distribution for Run7 (L=4years, G=5E10 ft3) 91
Figure 86. Saturation distribution for the base case 92
Figure 87. Saturation distribution for Run7 (L=4years, G=5E10 ft3) 92
Figure 88. CO_2 Plume extension in the first layer 500 years after injection 93
Figure 89. CO_2 Plume extension in all layers 500 years after injection 94
Figure 90. Pressure behavior in the observation well (base case model) 94
Figure 91. Porosity-permeability cross-plot 96
Figure 92. CO_2 injectivity for different rock types 96
Figure 93. Reservoir pressure in observation well for different rock types 97
Figure 94. Reservoir pressure in observation well for different permeability ratio 98
Figure 95. Different gas relative permeability curves 100
Figure 96. Reservoir pressure in observation well for different gas relative permeability curves 100
Figure 97. Reservoir pressure in observation well for different brine compressibility 102
Figure 98. Reservoir pressure in observation well for different brine densities 103
Figure 99. Different locations for constant pressure boundary (Fetkovich aquifer) – Presence of the aquifer is indicated by the pink line next to the boundary 105
Figure 100. Reservoir pressure in observation well for different boundary conditions 105
Figure 101. CO_2 Injection rate history 108
Figure 102. Original (noisy) and De-noised Pressure data in one day (9/10/2012) 109
Figure 103. Original (noisy) and De-noised Pressure data for the entire interval 109
Figure 104. Daily averaged Pressure data from 2 PDGs 110
Figure 105. The Grid tops of the reservoir Simulation Model 111
Figure 106. Comparison between actual PDG data and simulation results –base case 112
Figure 107. Different rock types based relationship between porosity and permeability 113
Figure 108. Comparison between actual PDG data and simulation results –Modified Permeability 114
Figure 109. Comparison between actual PDG data and simulation results –Modified reference pressure and brine density 115
Figure 110. Comparison between actual PDG data and simulation results –Modified reference pressure and brine density 115
Figure 111. Comparison between actual PDG data and simulation results –modified transmissibility multiplier 116

Figure 112. Relative permeability curves (Right: water relative permeability, Left: gas relative permeability) 117
Figure 113. Comparison between actual PDG data and simulation results –modified gas relative permeability 118
Figure 114. Comparison between actual PDG data and simulation results –modified gas relative permeability-best history matched results with no additional data 119
Figure 115. Comparison between actual PDG data and simulation results –modified gas relative permeability-best history matched results with additional data 120
Figure 116. Comparison between actual PDG data and simulation results –results with lowest mismatch (modified brine compressibility) 121
Figure 117. Location of the injection and observation well in the area of interest 122
Figure 118. CO_2 injection history at Citronelle field 123
Figure 119. Daily pressure data from PDGs @ observation well 124
Figure 120. Model's pressure results and actual history for the base model 125
Figure 121. Porosity-permeability cross plot 126
Figure 122. Model's pressure results and actual history; modified, pressure reference, brine density and permeability 126
Figure 123. Two permeability regions in the reservoir 127
Figure 124. Model's pressure results and actual history; modified permeability in different reservoir regions 128
Figure 125. Increased volume modifier at the east boundary (left) and well cross sections (right) 129
Figure 126. Model's pressure results and actual history; final history match 129
Figure 127. Last three months of injection rate 130
Figure 128. Daily pressure data for last three months of injection 131
Figure 129. Model's pressure result and actual data for prediction and history 131
Figure 130. Pressure behavior in observation well during 500 years post injection (latest history matched model) 132
Figure 131. CO_2 plume extension in the first layer (500 years after injection-latest history matched model) 133
Figure 132. CO_2 plume extension in all the layers (500 years after injection-latest history matched model) 133
Figure 133. Saturation profile in 2-D model 134
Figure 134. Reservoir pressure and leakage rate at min BHP 25000kpa 135
Figure 135. Reservoir pressure and leakage rate at Surface Gas rate 20SM3/day 136
Figure 136. Leakage rate for Cap Rock leakage 136
Figure 137. Location of the injection, observation and 2 leakage wells in the first layer of the Citronelle field 137
Figure 138. Leakage rate at leak2 and pressure profile in observation well (D-9-8) 138
Figure 139.The extension of CO_2 plume in WVU Model 138
Figure 140. Gas Saturation in different layers of the Citronelle aquifer (WVU Model) 139
Figure 141. Location of Wells within 1.0 Mile of the Proposed Injection Site 140
Figure 142. Location of the injection, observation and 4 leakage wells in the first layer of the Citronelle field 141

Figure 143. Pressure behavior of the reservoir during leakage of CO_2 and water.....142
Figure 144. Pressure behavior of the reservoir during leakage of CO_2 with 1 bbl/day water constraint.....143
Figure 145. Maximum leakage rate through one well.....143
Figure 146. Pressure behavior in the observation well (D-9-8) for the leakage rate =175000 scf/day.....144
Figure 147. Pressure behavior in the observation well (D-9-8) for the leakage rate =50000 scf/day.....145
Figure 148. Pressure behavior in the observation well (D-9-8) for the leakage rate = 175,000 scf/day of two wells.....146
Figure 149. Pressure behavior in the observation well (D-9-8) for the leakage rate = 175,000 & 50,000 scf/day in two wells.....146
Figure 150. Pressure behavior in the observation well (D-9-8) for the leakage rate = 175,000 & 50,000 scf/day of 4 wells.....147
Figure 151. Reservoir model with the existing wells in Area of Investigation.....149
Figure 152. Location of the wells that represent leakage rates in Table 1.....150
Figure 153. Pressure behavior in well D-9-8 in the case that no leakage happens.....151
Figure 154. ΔP in well D-9-8 in the case that well D-9-6 leakage rate is 1,830 ft^3/day.....152
Figure 155. ΔP in Injection well in the case that well D-9-6 leakage rate is 1,830 ft^3/day.....153
Figure 156. ΔP in well D-9-8 in the case that well D-9-6 leakage rate is 11,025 ft^3/day.....153
Figure 157. ΔP in well D-9-8 in the case that well D-9-7 leakage rate is 11,025 ft^3/day.....154
Figure 158. ΔP in well D-9-8 in the case that well D-9-6 leakage rate is 42,000 ft^3/day.....154
Figure 159. ΔP in Injection well in the case that well D-9-6 leakage rate is 42,000 ft^3/day.....155
Figure 160. ΔP in well D-9-8 in the case that well D-9-6 leakage rate is 73,500 ft^3/day.....156
Figure 161. ΔP in injection well in the case that well D-9-6 leakage rate is 73,500 ft^3/day.....156
Figure 162. ΔP in well D9-8 in the case that well D-9-2 leakage rate is 42,000 ft^3/day.....158
Figure 163. ΔP in well D9-8 in the case that well D-9-2 leakage rate is 99,750 ft^3/day.....159
Figure 164.CO_2 Plume Extension in the first layer of the Citronelle Field 4 years after the end of injection.....160
Figure 165. ΔP in injection well in the case that well D-9-6 leakage rate is 30000ft3/day.....162
Figure 166. Key performance indicator analysis results for the latitude of the leakage.....164
Figure 167. Key performance indicator analysis results for the longitude of the leakage.....165
Figure 168. Key performance indicator analysis results for the CO_2 leakage rate.....165
Figure 169. Neural network architecture.....167
Figure 170. Neural Network training results for the leakage location(X).....169
Figure 171. Neural Network Calibration results for the leakage location(X).....169
Figure 172. Neural Network training results for the leakage rate.....170
Figure 173. Neural Network calibration results for the leakage rate.....170
Figure 174. Pressure difference when no leakage happens compared to the case that leakage occurs.....171
Figure 175. Pressure difference in Observation well and the corresponding descriptive statistics.....172
Figure 176. Verification results for leakage location(X) - clean data.....173
Figure 177 . Verification results for leakage location(Y) - clean data.....173

Figure 178. Verification results for leakage rate 174
Figure 179. Results for blind runs, leakage rates 175
Figure 180. Neural Network pridiction for Leakage rate(network trained for each well individually) 176
Figure 181. Location of five wells in the CO_2 plume area 177
Figure 182. Reservoir Pressure in the observation Well (D-9-8).....178
Figure 183. Key performance indicator for Leakage location (left) and rate(right).....179
Figure 184. Neural Network architecture.....179
Figure 185. Neural Network training results for the leakage location(X) 180
Figure 186. Neural Network training results for the leakage rate 181
Figure 187. Neural Network Calibration results for the leakage location(X) 182
Figure 188. Neural Network calibration results for the leakage rate.....182
Figure 189: Neural Network Verification results for the leakage rate 183
Figure 190. Results for neural network validation-leakage locations 184
Figure 191: Results for neural network validation-leakage rate 184
Figure 192. Neural Network prediction errors for Leakage location 185
Figure 193. Neural Network prediction errors for Leakage rates 186
Figure 194. Key performance Indicator for the Leakage Location 188
Figure 195. Key performance Indicator for the leakage rate at well D-9-8 189
Figure 196. Neural network results for leakage location 190
Figure 197. Neural network results for leakage rate in well D-9-8.....190
Figure 198. R-ILDS Leakage Location prediction, all blind runs 191
Figure 199. R-ILDS Leakage rate prediction, all blind runs 191
Figure 200. Histogram for the error in neural network's location prediction 192
Figure 201. Neural network prediction errors for Leakage rates in well D-9-8.....192
Figure 202. Distance of possible leakage locations to the observation well.....193
Figure 203. Comparison of pressure signal amplitude when wells leaked with the same rate .194
Figure 204. Detection time for each rate at different locations.....196
Figure 205. Original and new ΔP, at observation well subject to lowering reservoir porosity ...198
Figure 206. CO_2 plume extension in different layers.....200
Figure 207. Transmissibility multiplier for shale layers.....200
Figure 208. Pressure change in observation well when leakage initiated at layer 5.....201
Figure 209. Leakage location prediction; leakage took place at different vertical locations.....203
Figure 210. Leakage rate prediction at well D-9-7 when leakage took place at different vertical locations.....204
Figure 211. Leakage rate prediction at well D-9-8 when leakage took place at different vertical locations.....205
Figure 212. PSD distribution for the sensors 206
Figure 213. Time to report a leak based on different PSD values.....207
Figure 214. R-ILDS prediction for leakage location based on different drift values 207
Figure 215. Different time cycles during and after CO_2 injection.....208
Figure 216. Sustained Casing Pressure 209
Figure 217. Step function CO_2 leakage rate 210
Figure 218. Logarithmic and exponential CO_2 leakage rates.....211

Figure 219. Linear CO_2 leakage rates 211
Figure 220. Neural network results for leakage location 212
Figure 221. Neural network results for leakage rates at well D-9-8 213
Figure 222. Rate function for the blind test of the ILDS. 214
Figure 223. R-ILDS prediction for leakage location (variable rate) 214
Figure 224. R-ILDS prediction for leakage rate in well D-9-8 (variable rate) 215
Figure 225. KPI for CO_2 leakage rate in well D-9-8 216
Figure 226. Relative frequency & cum. probability for the leakage rate at time 162 hr 216
Figure 227. Location of the injection and observation well in the area of interest 217
Figure 228. Pressure signals subject to leakages at well D-9-6 and D-9-8 218
Figure 229. Cap-rock leakage location 219
Figure 230. Pressure behavior in the observation well and CO_2 rate due to cap rock leakage 220
Figure 231. 9 different locations for cap-rock leakages and 3 blind runs 221
Figure 232. Neural network results for two-well leakage 223
Figure 233. R-ILDS predictions for two-well leakages 225
Figure 234. Pressure change in the observation well when leakage rate is 2850 ft^3/day or 1% of the total injected volume. 226
Figure 278 - survey plot showing the location of the proposed injection well, and the proposed observation 231
Figure 235. Wavelet Transform and Inverse Wavelet Transform Flow Chart 234
Figure 236. Original Noisy Signal for Electrical Consumption 234
Figure 237. De-noised Signal Using Wavelets 235
Figure 238. Comparison of Noisy and Simulated Data 236
Figure 239. Screenshot of data reading 237
Figure 240. Application of code to noisy data 238
Figure 241. Screen shot of de-noised data in excel 239
Figure 242. De-noising data comparison 239
Figure 243. Totally fine grid model with heterogeneous permeability 240
Figure 244. 5 different permeability realizations based on the rock conductivity 241
Figure 245. CO_2 Plume extension in different layers of the reservoir 242
Figure 246.CO_2 Plume extension in first layer of the reservoir and location of the wells 242
Figure 247. Pressure data for 2 years (year 2014 to 2016) without any noise 244
Figure 248. Pressure data for 2 years (year 2014 to 2016) after adding the noise and outlier .244
Figure 249. Histogram Pressure data for 2 years (year 2014 to 2016) after adding the noise and outlier 245
Figure 250. Rigorous SURE thresholding method 246
Figure 251.Heuristics SURE thresholding method 246
Figure 252.Fixed form threshold method 247
Figure 253. Soft thresholding (red: noisy data, black: de-noised data) 248
Figure 254. Hard thresholding (red: noisy data, black: de-noised) 248
Figure 255. Reprocessing the de-noised data (red: noisy data, black: de-noised data) 249
Figure 256. Monitoring Well (D-9-8#2) PDG data 250
Figure 257. GRNN results for fitted pressure curve 251
Figure 258. Noise distribution for actual PDG data (6500 records, Normal Distribution) 252

Figure 259. Presure data from simulator(red),added noise(green) and denoised (black) when well D-9-6 leaks with the rate of 30Mcf....253
Figure 260. Neural Network architecture....254
Figure 261. Neural network training results for the leakage location; de-noised pressure data after 3 weeks of leakage....255
Figure 262. Neural network training results for the leakage Rate; de-noised pressure data after 3 weeks of leakage....255
Figure 263. Neural network calibration results for the leakage location Y; de-noised pressure data after 3 weeks of leakage....256
Figure 264. Neural network calibration results for the leakage rate; de-noised pressure data after 3 weeks of leakage....256
Figure 265. Clean (blue) and Noisy (red) high frequency pressure data from observation well257
Figure 266. Noisy and De-noised pressure data using Wavelet threshold method....258
Figure 267. Noisy and De-noised pressure data using GRNN....259
Figure 268. Verification results for leakage location(X)-noisy data....259
Figure 269. Verification results for leakage location(Y)-noisy data....260
Figure 270. Verification results for leakage Rate(Y)-noisy data....260
Figure 365. De-noising pressure data for leakage scenario#1 (red: noisy data, black: de- noised data)....261
Figure 366. De-noising pressure data for scenario 1 during post injection (red: noisy data, black: de-noised data)....261
Figure 367. De-noising pressure data for scenario 2 during post injection (red: noisy data, black: de-noised data)....262
Figure 368. De-noising pressure data for scenario 3 during post injection (red: noisy data, black: de-noised data)....262
Figure 369. De-noising pressure data for scenario 4 during post injection (red: noisy data, black: de-noised data)....263
Figure 370. De-noising pressure data for scenario 5 during post injection (red: noisy data, black: de-noised data)....263
Figure 371. De-noising pressure data for scenario 6 during post injection (red: noisy data, black: de-noised data)....264
Figure 372. De-noising pressure data for scenario 7 during post injection (red: noisy data, black: de-noised data)....264
Figure 373. De-noising pressure data for scenario 8 during post injection (red: noisy data, black: de-noised data)....265
Figure 374. De-noising pressure data for scenario 9 during post injection (red: noisy data, black: de-noised data)....265
Figure 375. De-noising pressure data for scenario 10 during post injection (red: noisy data, black: de-noised data)....266
Figure 376. De-noising pressure data for scenario 11 during post injection (red: noisy data, black: de-noised data)....266
Figure 377:De-noising pressure data for scenario 12 during post injection (red: noisy data, black: de-noised data)....267

Figure 279. Comparison between actual PDG data and simulation results –Modified reservoir boundary (smaller boundary) 268
Figure 280. Comparison between actual PDG data and simulation results –Modified vertical permeability (K_v=.1*k_h) 269
Figure 281. Comparison between actual PDG data and simulation results –Modified brine compressibility (Cbr=1e-6) 269
Figure 282. Comparison between actual PDG data and simulation results –Modified reservoir boundary (with updated reservoir parameters) 270
Figure 283. Comparison between actual PDG data and simulation results –Modified reservoir water relative permeability (with updated reservoir parameters) 270
Figure 284. Comparison between actual PDG data and simulation results –Base Case 271
Figure 285. Comparison between actual PDG data and simulation results –K_{rg} high 271
Figure 286. Comparison between actual PDG data and simulation results –K_{rg} low 272
Figure 287. Comparison between actual PDG data and simulation results –K_v/K_h=.9 272
Figure 288. Comparison between actual PDG data and simulation results –K is half of the base case 273
Figure 289. Comparison between actual PDG data and simulation results –K_{rw} high 273
Figure 290. Comparison between actual PDG data and simulation results –reservoir with smaller boundary 274
Figure 291. Comparison between actual PDG data and simulation results –reservoir with smaller boundary 274
Figure 292. ΔP in well D-9-8 well in the case that well D-9-6 leakage rate is 99750ft^3/day 275
Figure 293. ΔP in well D-9-8 well in the case that well D-9-6 leakage rate is 120750ft^3/day. ...275
Figure 294. ΔP in well D-9-8 and Injection well in the case that well D-9-6 leakage rate is 131250ft3/day. 276
Figure 295. ΔP in well D-9-8 well in the case that well D-9-2 leakage rate is 1830ft^3/day. 276
Figure 296. ΔP in well D-9-8 well in the case that well D-9-2 leakage rate is 5250ft^3/day. 277
Figure 297. ΔP in well D-9-8 well in the case that well D-9-2 leakage rate is 11250ft3/day. 277
Figure 298. ΔP in well D-9-8 and Injection well in the case that well D-9-2 leakage rate is 42000ft^3/day 278
Figure 299. ΔP in well D-9-8 and Injection well in the case that well D-9-2 leakage rate is 73500ft^3/day. 278
Figure 300. ΔP in well D-9-8 and Injection well in the case that well D-9-2 leakage rate is 99750ft3/day. 279
Figure 301. ΔP in well D-9-8 well in the case that well D-9-10 leakage rate is 1830ft3/day. 279
Figure 302. ΔP in well D-9-8 well in the case that well D-9-10 leakage rate is 5250ft3/day. 280
Figure 303. ΔP in well D-9-8 well in the case that well D-9-10 leakage rate is 11025ft^3/day. ...280
Figure 304.Actual Leakage Location(X) - Neural Network training results -1 week after leakage 281
Figure 305. Actual Leakage Location(Y) - Neural Network training results -1 week after leakage 281
Figure 306. Actual Leakage Rate - Neural Network training results -1 week after leakage 282
Figure 307. Errors in Leakage Rate (Neural Network training results) -1 week after leakage ..282

Figure 308. Actual Leakage Location(X) - Neural Network training results -5 weeks after leakage 283
Figure 309. Actual Leakage Location(Y) - Neural Network training results -5 week after leakage 283
Figure 310. Actual Leakage Rate - Neural Network training results -5 weeks after leakage ...284
Figure 311. Errors in Leakage Rate (Neural Network training results) -5 weeks after leakage 284
Figure 312. Actual Leakage Location(X) - Neural Network training results -8 weeks after leakage 285
Figure 313. Actual Leakage Location(Y) - Neural Network training results -8 weeks after the leakage 285
Figure 314. Actual Leakage Rate - Neural Network training results -8 weeks after leakage 286
Figure 315. Errors in Leakage Rate (Neural Network training results) -8 weeks after leakage 286
Figure 316. Leakage location(X) - Neural Network results for all steps (training, calibration and verification)-clean pressure data 287
Figure 317. Leakage location(Y) - Neural Network results for all steps (training, calibration and verification)-clean pressure data 287
Figure 318. Leakage rate - Neural Network results for all steps (training, calibration and verification)-clean pressure data 288
Figure 319. Leakage location(X)- Neural Network results for all steps (training, calibration and verification)-noisy pressure data 288
Figure 320. Leakage location(Y)- Neural Network results for all steps (training, calibration and verification)-noisy pressure data 289
Figure 321. Leakage rate- Neural Network results for all steps (training, calibration and verification)-noisy pressure data 289
Figure 322. R-ILDS leakage location prediction, run1: well D-9-6 leaks 23 Mcf/day 290
Figure 323. R-ILDS leakage location prediction, run2: well D-9-6 leaks 72 Mcf/day 290
Figure 324. R-ILDS leakage location prediction, run3: well D-9-6 leaks 93 Mcf/day 291
Figure 325. R-ILDS leakage location prediction, run4: well D-9-7 leaks 32 Mcf/day 291
Figure 326. R-ILDS leakage location prediction, run5: well D-9-7 leaks 61 Mcf/day 292
Figure 327. R-ILDS leakage location prediction, run6: well D-9-7 leaks 87 Mcf/day 292
Figure 328. R-ILDS leakage location prediction, run7: well D-9-8 leaks 27 Mcf/day 293
Figure 329. R-ILDS leakage location prediction, run9: well D-9-8 leaks 101 Mcf/day 293
Figure 330. R-ILDS leakage location prediction, run9: well D-9-8 leaks 101 Mcf/day 294
Figure 331. R-ILDS leakage rate prediction, run1: well D-9-6 leaks 23 Mcf/day 294
Figure 332. R-ILDS leakage rate prediction, run2: well D-9-6 leaks 72 Mcf/day 295
Figure 333. R-ILDS leakage rate prediction, run3: well D-9-6 leaks 93 Mcf/day 295
Figure 334. R-ILDS leakage rate prediction, run4: well D-9-7 leaks 32 Mcf/day 296
Figure 335. R-ILDS leakage rate prediction, run5: well D-9-7 leaks 61 Mcf/day 296
Figure 336. R-ILDS leakage rate prediction, run6: well D-9-7 leaks 87 Mcf/day 297
Figure 337. R-ILDS leakage rate prediction, run7: well D-9-8 leaks 27 Mcf/day 297
Figure 338. R-ILDS leakage rate prediction, run8:well D-9-8 leaks 48 Mcf/day 298
Figure 339. R-ILDS leakage rate prediction, run9: well D-9-8 leaks 101 Mcf/day 298
Figure 340. Sensitivity analysis of the reservoir parameters on R-ILDS leakage location prediction Well D-9-6.....299

Figure 341. Sensitivity analysis of the reservoir parameters on R-ILDS leakage location prediction Well D-9-7 299
Figure 342. Sensitivity analysis of the reservoir parameters on R-ILDS leakage location prediction Well D-9-8 300
Figure 343. Sensitivity analysis of the reservoir parameters on R-ILDS leakage rate prediction Well D-9-6 300
Figure 344. Sensitivity analysis of the reservoir parameters on R-ILDS leakage rate prediction Well D-9-7 301
Figure 345: Sensitivity analysis of the reservoir parameters on R-ILDS leakage rate prediction Well D-9-7 301
Figure 346. R-ILDS prediction for leakage rate in well D-9-6 (variable rate) 302
Figure 347. R-ILDS prediction for leakage rate in well D-9-7 (variable rate) 302
Figure 348. Neural network predictions for the leakage rate for the case that PDG is in Injection well, D-9-6 results 303
Figure 349. Neural network predictions for the leakage rate for the case that PDG is in Injection well, D-9-7 results 303
Figure 350. Neural network predictions for the leakage rate for the case that PDG is in Injection well, D-9-8 results 304
Figure 351. Neural network predictions for the leakage location for the case that PDG is in Injection well 304
Figure 352. R-ILDS Leakage location prediction for well D-9-6, PDG in Injection well 305
Figure 353. R-ILDS Leakage location prediction for well D-9-7, PDG in Injection well 305
Figure 354. R-ILDS Leakage location prediction for well D-9-8, PDG in Injection well 306
Figure 355. Neural network results for Cumulative leaked gas -cap-rock leakage 307
Figure 356. Neural network results for leakage location(X) -cap-rock leakage 307
Figure 357. Neural network results for leakage location(Y) -cap-rock leakage 308
Figure 358. R-ILDS prediction for cumulative leaked gas, Blind Run 1(Cap-rock Leakage) 308
Figure 359. R-ILDS prediction for cumulative leaked gas, Blind Run 2(Cap-rock Leakage) 309
Figure 360. R-ILDS prediction for cumulative leaked gas, Blind Run 3 (Cap-rock Leakage) 309
Figure 361: R-ILDS prediction for cumulative leaked gas, Blind Run 3 (Cap-rock Leakage) 310
Figure 362: R-ILDS prediction for cumulative leaked gas, Blind Run 3 (Cap-rock Leakage) 310
Figure 363. Neural network training results for Leakage Index (one, two and three-well leakage) 311
Figure 364. Neural network training results for Leakage Index (one and three-well leakage) 311
Figure 371. Identify the time step for pressure data. 313
Figure 372. Dialog box for identification of the location of real-time pressure data. 314
Figure 373. Flow Chart describing the Intelligent Leak Detection System. 315
Figure 374. Software is reading pressure data. No leakage is detected. 316
Figure 375. Pressure behavior is unusual and there is a possibility of leakage. 317
Figure 376. Leakage is detected. Leakage location and amount is shown in the form 318
Figure 377. Input excel file format 319

LIST OF TABLES

Table 1. List of Industrial Advisory Committee 26
Table 2 . Datasheet for all 5 candidate sites....27
Table 3. 5 Spot CO_2 EOR Wells Information....30
Table 4. Anthropogenic test Injection Well Information....31
Table 5. Formation Top and Thickness (Citronelle, Al)....32
Table 6. Reservoir Components Data 33
Table 7. Reservoir Characteristics Data....33
Table 8. Log Interpretation results for Citronelle....47
Table 9. Log Interpretation results for Citronelle....51
Table 10. Log Interpretation results for Citronelle....52
Table 11. Porosity and permeability values for the injection well D-9-7 based on different logs.61
Table 12. Porosity and permeability for different reservoir realizations....61
Table 13. Top and Bottom of well D-9-1 and D-4-14 based on Geological Model....64
Table 14. Porosity based on Resistivity and Induction log and Density Porosity for well D-9-8..67
Table 15. Reservoir Thickness at the location of the wells in ARI and WVU Models 80
Table 16. Number of grid blocks in case 3 87
Table 17. Different predefined parameters for 10 different simulation runs based on cumulative injection and duration of injection 90
Table 18. CO_2 Plume extension size over time (in the first layer) for different rock types 97
Table 19. CO_2 Plume extension size over time (in the first layer) for different permeability ratios 98
Table 20. Plume extension size over time in the first layer for different gas relative permeability curves....99
Table 21. CO_2 Plume extension size over time in the first layer for different maximum residual gas saturations 101
Table 22. CO_2 Plume extension size over time (in the first layer) for different brine densities..104
Table 23. Plume extension size over time (in the first layer) for different boundary conditions 106
Table 24. Core porosity and Permeability from Core Data 113
Table 25. Reservoir parameters that tuned for history matching 118
Table 26. Pressures mismatch values for changing different reservoir parameter....121
Table 27. Reservoir parameters and properties (base case model) 124
Table 28 - Leakage rates observed in real cases (Loizzo 2010)....149
Table 29. CO_2 Leakage rates assigned for the wells D-9-2, D-9-6 and D-9-10....161
Table 30. Descriptive statistics and summarization of 504 hourly Δp data points in the observation well (D-9-8) 163
Table 31 . Verification Dataset 172
Table 32. Results for neural network verification....174
Table 33. Blind run ILDS predictions....175
Table 34: Calibration data set 181
Table 35: leakage rates and locations for ILDS validation 183
Table 36. Changes in reservoir Property Parameter 197
Table 37. CO_2 leakage rates for multi-well leakage....222
Table 38. Leakage Index for different single and multi-well leakage scenarios....223

Table 39. CO_2 leakage rates for the blind runs-two well leakages 224
Table 42. Basic Wells Information 230
Table 40. Different combination of leaking wells.....249
Table 41 Data Sumerization of noisy and De-noised ΔP for 3 weeks after the leakage 253

EXECUTIVE SUMMARY

Primary objective for geologic CO_2 sequestration is to confine injected CO_2 for a long period of time. If a leakage from a geological CO_2 sequestration site occurs, it is crucial to find the approximate amount and the location of the leak, in a timely manner, in order to initiate proper remedial activities.

An overwhelming majority of research and development for storage site monitoring has been concentrated on atmospheric, surface or near surface monitoring of the sequestered CO_2. The main premise of this study is that in the event of a leakage in a geological CO_2 sequestration site, the CO_2 must move (at the reservoir level) before it can reach the surface. Movement of fluids in reservoirs are associated with pressure differences. Therefore, if pressure changes in the reservoir can be *(a)* detected, and *(b)* analyzed effectively, one might be able to identify and characterize such a leak, long before any surface or near surface leakage detection technology can effectively be utilized.

This study aims to monitor the integrity of CO_2 storage at the reservoir level, in real-time and analyze and report the location and amount of CO_2 leakage soon after such incident takes place. This work is concentrated on developing in-situ CO_2 Monitoring and Verification technology based on the implementation of Permanent Down-hole Gauges (PDG) or "Smart Wells" (for the detection purposes) along with Artificial Intelligence and Data Mining (for the analysis of the detected signals in order to identify the amount and the location of the leak). The technology attempts to identify the characteristics of the CO_2 leakage by de-convolving the pressure signals collected from the Permanent Down-hole Gauges (PDG).

The concept of "Smart Field" is rapidly gaining support and popularity in the oil and gas industry. Hundreds of millions of dollars have been invested to successfully develop highly sensitive Permanent Down-hole Gauges (PDG) that is capable of successful operation in harsh environment for very long periods of time. PDGs collect and transmit high frequency data streams to the remote offices to be analyzed and used for reservoir management. The industry is now working on the state-of-the-art software solutions that can take maximum advantage of the large amount of data that is collected, transmitted and stored in data historians using PDGs.

PDGs monitor the pressure changes in the formation and transmit high frequency data streams to the surface. The pressure changes in the reservoir are indications of fluid flow (movement) in the formation which during the post-injection time-frame are indicators of a potential leakage in the system. The complex and highly convoluted real-time data transmitted by multiple PDGs is cleansed, summarized, processed and modeled using state-of-the-art Artificial Intelligence and Data Mining (AI&DM) technology in order to identify the approximate location and amount of the CO_2 leakage that has caused the pressure change in the reservoir.

The process implemented in this study follows a four-step procedure to accomplish its objective. First step is the development of a base reservoir model for an existing CO_2 sequestration site> Citronelle Dome in Alabama has been selected for this project. In the second step, actual field data (CO_2 injection) is used to history match the base model. The third step of the process includes generation of multiple leakage scenarios using the history matched reservoir model and collection of the high frequency pressure signals that results from the imposed leakage in the system. Finally, during the fourth step of the process, the high frequency pressure signals are processed and analyzed using an innovative machine learning and pattern recognition technology in order to identify the location and the amount of the leakage in the system.

Citronelle field, a saline aquifer reservoir, located in the state of Alabama (Figure 1) was considered as the basis for this study. Step 1 of this project included the development of a reservoir model for the Citronelle saline aquifer. Reservoir simulation model for CO_2 injection at

Citronelle dome was developed and history matched with real field data. This model acknowledged “Lateral Heterogeneity”.

Structural maps for 17 sand layers (most extensive ones that were targeted for CO_2 injection) were generated by interpretation and correlation of 14 well logs. The location of the well logs and three cross sections for correlating the wells are shown in Figure 2. Based on correlation between wells, 17 top maps were generated representing lateral heterogeneity in the reservoir.

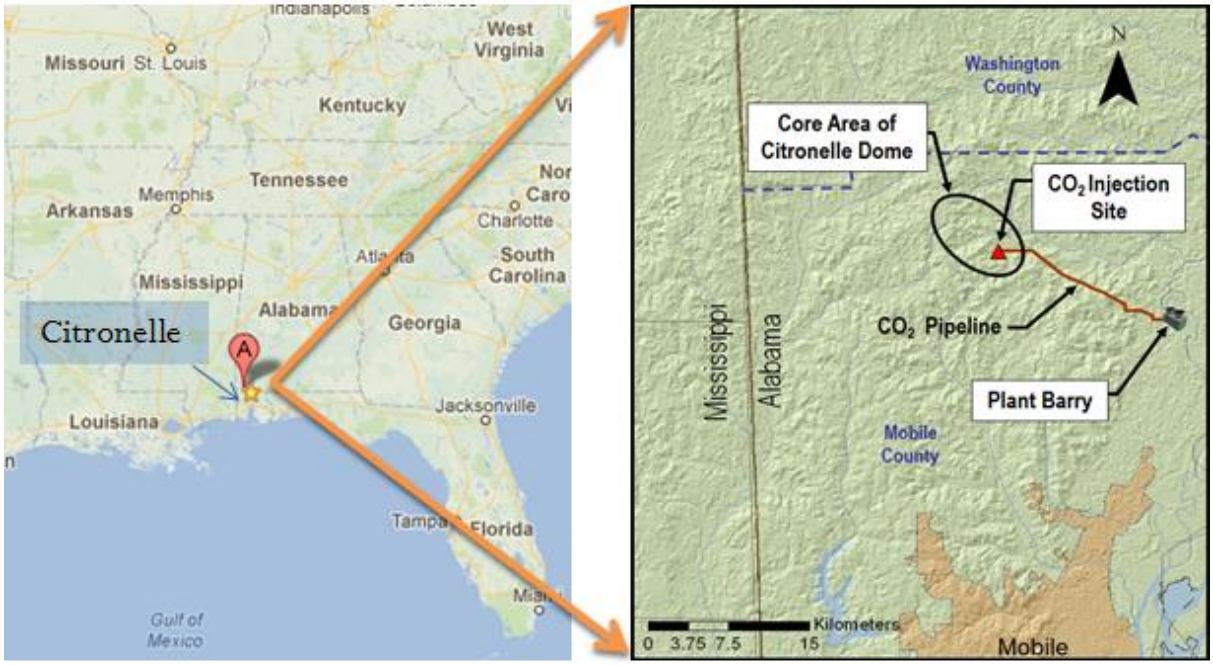

Figure 1. Location of the Citronelle Dome in the State of Alabama, the United States of America.

The same well logs were used to generate thickness (isopach) maps for all the layers. In order to make porosity maps, 40 well logs were analyzed and interpreted. Three different porosity maps were generated for each sand layer (51 total porosity maps for the entire reservoir). Permeability of the reservoir was obtained using porosity-permeability correlations from core analysis.

Installed PDGs at the injection well and an observation well were modeled as part of the numerical modeling of this asset. Real-time pressure signals from the PDGs were used to history match the numerical model (Step 2). Quality of the history matched model and its capability to predict (in forecast mode) reservoir performance is demonstrate in Figure 3.

Upon completion of the history matching process, different CO_2 leakage scenarios were designed and modeled. High frequency pressure data from the model (representing the PDGs response to pressure changes in the reservoir) were generated using the history matched numerical model. Figure 4 is an example of pressure signal in one of the PDGs that results from a potential leakage in the reservoir.

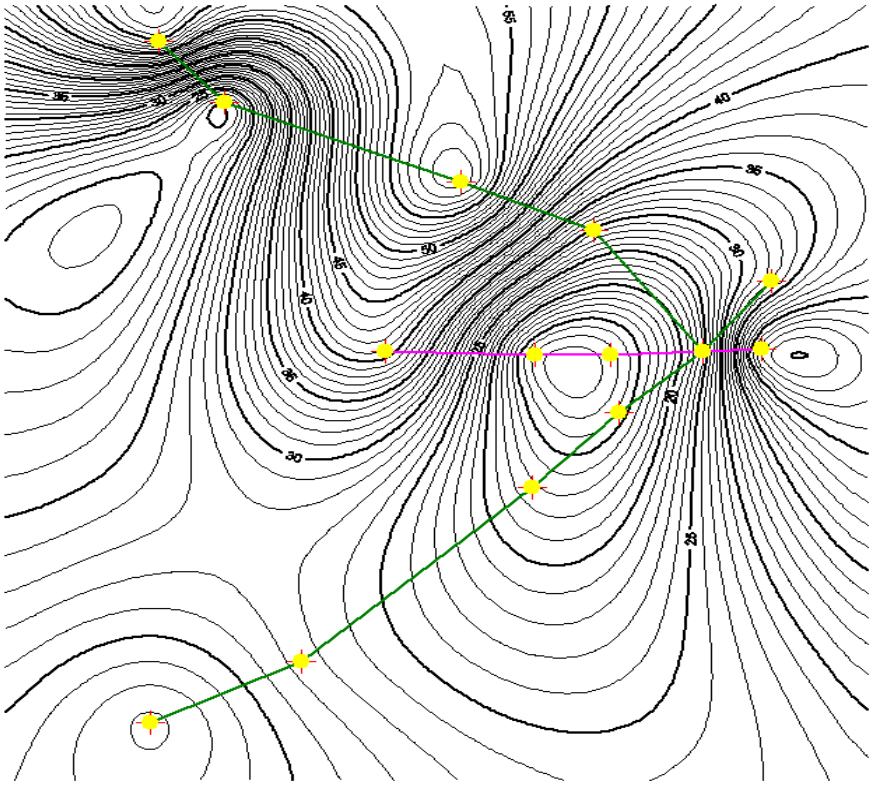

Figure 2. The location of the well logs and three cross sections for correlating the wells.

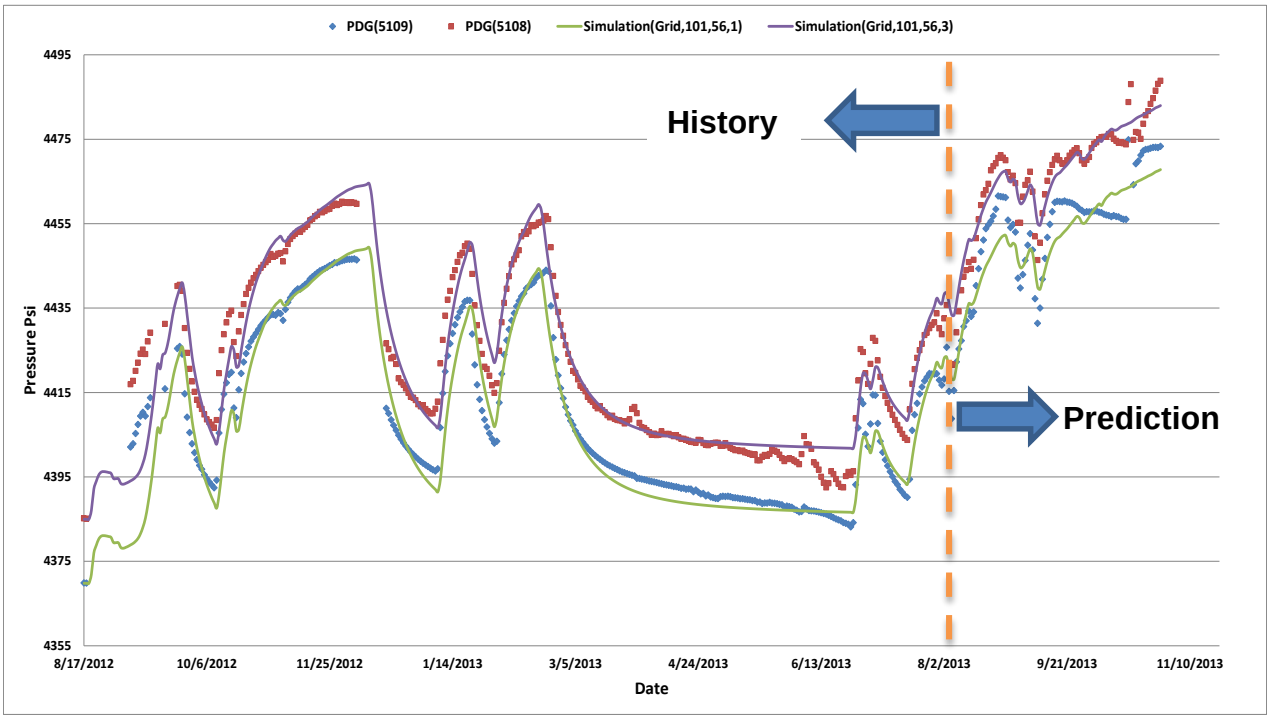

Figure 3. Quality of the history match of the reservoir simulation model.

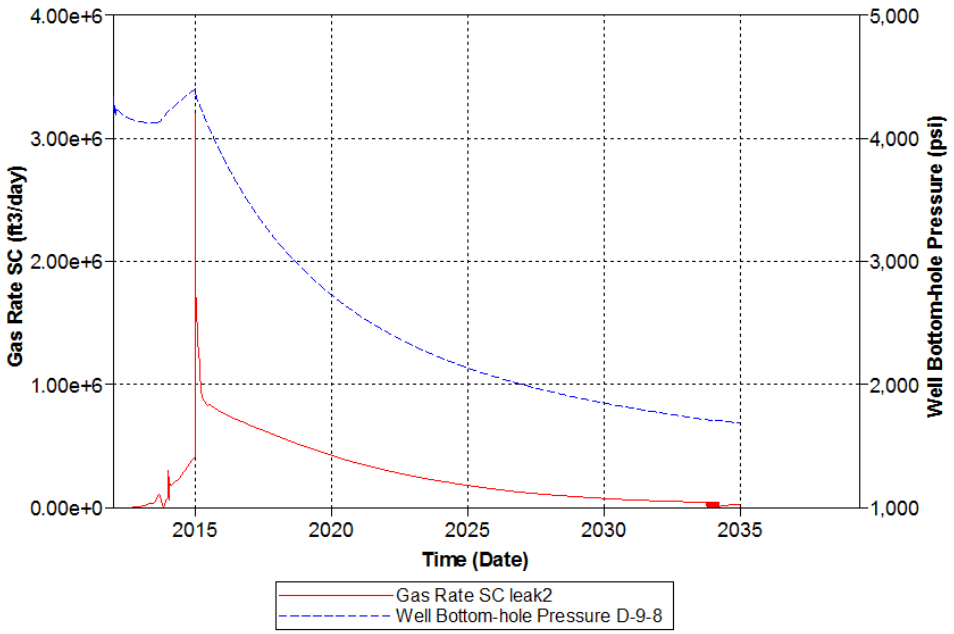

Figure 4. Modeling the CO_2 leakage from the abandoned wells in the Citronelle Dome.

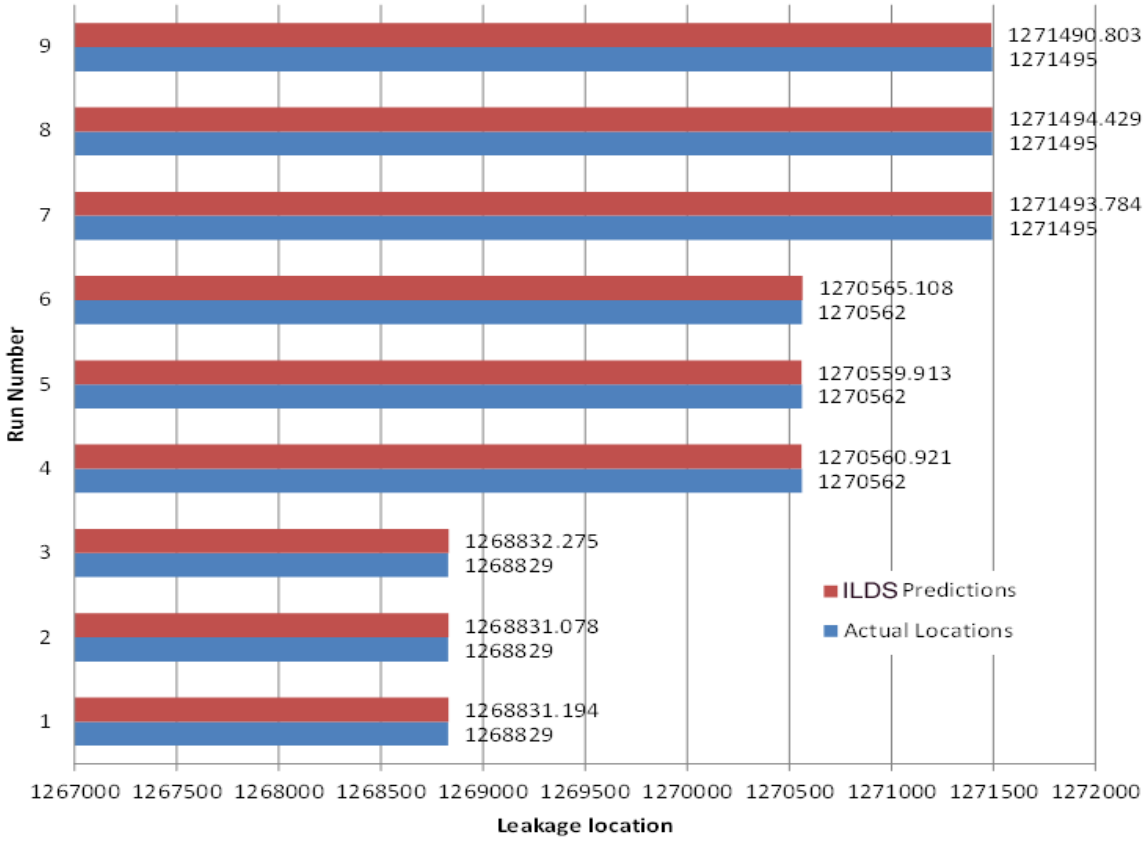

Figure 5. Accuracy of the Intelligent Leakage Detection System (ILDS) in identifying the location of the leakage.

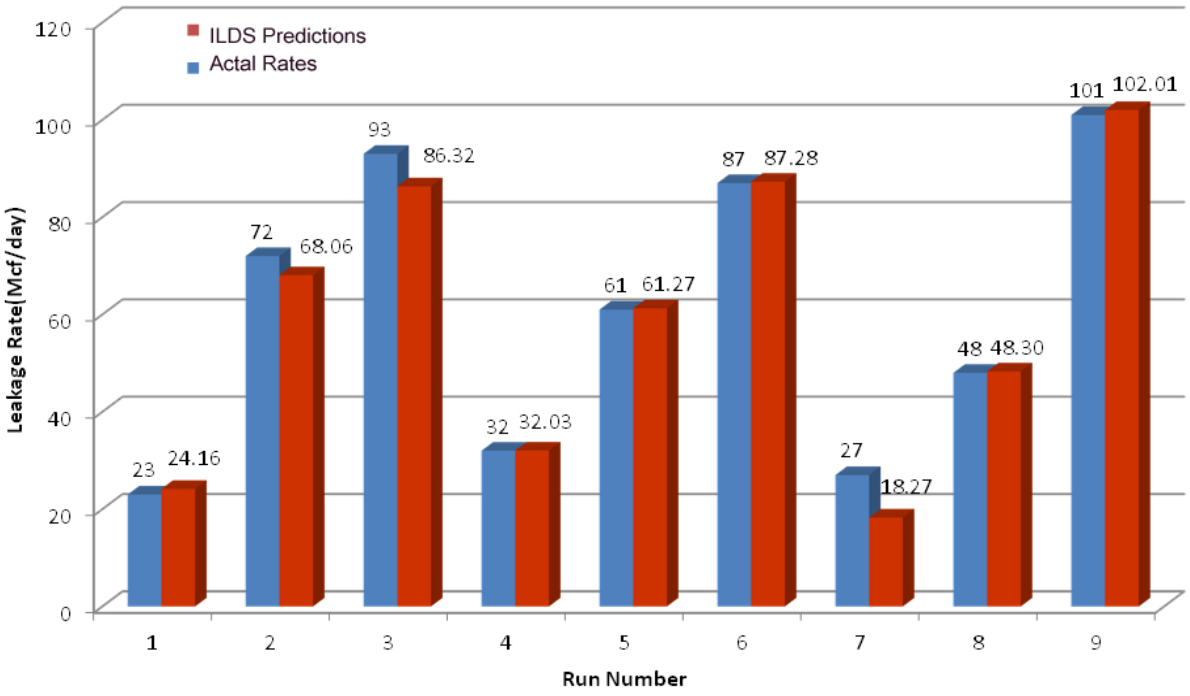

Figure 6. . Accuracy of the Intelligent Leakage Detection System (ILDS) in identifying the amount of the leakage.

Since the behavior of pressure signals (generated due to the modeled leakage) are too complex to be de-convoluted using any existing mathematical formulations, a Machine Learning-based technology was introduced for this purpose (Step 4). Figure 5 and Figure 6 show the accuracy that can be achieved using this technology to detect a leak at the reservoir level within hours of the occurrence. These figures demonstrate that both the location and the amount of the leakage can be identified using the Intelligent Leakage Detection System (ILDS).

The Intelligent Leakage Detection System (ILDS) was developed as the result of this project using an innovative machine learning and pattern recognition technology (Figure 7).This report summarizes the efforts toward the development of the Intelligent Leakage Detection System (ILDS). The ILDS is able to detect leakage characteristics in a short period of time (less than a day from its occurrence) demonstrating the capabilities of the system in locating and quantifying leakage characteristics subject to complex rate behaviors.

Furthermore, this project evaluated the performance of the ILDS under following conditions:

a. Multiple well leakages,
b. Leakage in multiple vertical locations in a given well,
c. Leakage occurring in the cap rock,
d. Availability of additional monitoring wells,
e. Presence of pressure drift,
f. Presence of noise in the pressure sensor, and finally
g. Uncertainty in the reservoir model.

Figure 7 shows the interface of the ILDS. The Intelligent Leakage Detection System (ILDS) is capable of being deployed online and perform real-time analysis. In other words, ILDS can receive, analyze, process and provide results in real-time.

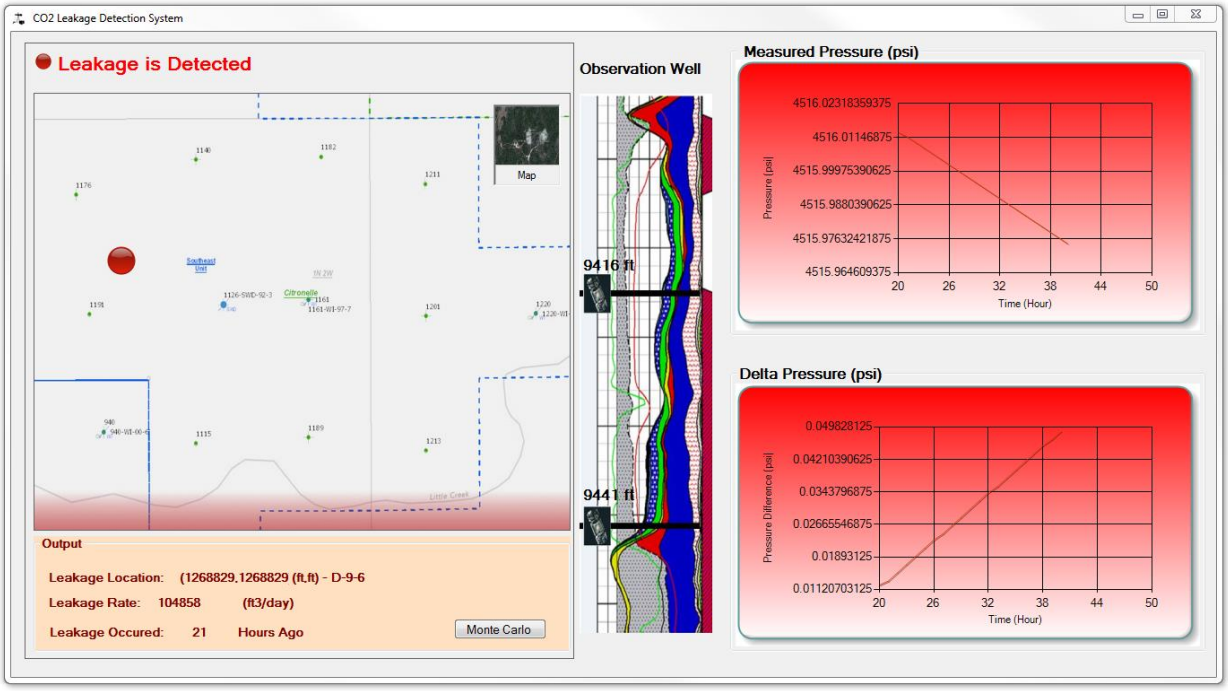

Figure 7. A snapshot of the interface developed for the Intelligent Leakage Detection System (ILDS).

During this project, the West Virginia University team was supported by CONSOL Energy, Advance Resources International (ARI), Battelle, and Schlumberger. Professionals from these organizations formed an industry advisory group providing peer review, valuable insight, guidance, and critical observations throughout the life of the project, ensuring a robust and practical technology that can be used in the field.

SITE SELECTION

CITRONELLE FIELD- SALINE AQUIFER

Selection of a suitable CO_2 sequestration site was the first step in this project. The selected site should provide required data to build a geological model. The geological model would serve as the foundation for the dynamic model that has been developed and used throughout this project.

In order to kick off the site selection procedure, an Industrial Advisory Committee (IAC) was established consisting of five experts from the industry with experience and clear track record in Carbon Capture and Storage. This committee provided technical advice to the project team throughout the life of the project. The first task of the Industrial Advisory Committee (IAC) was assisting the project team in selecting a site for the project. Table 1 shows the list of individuals that serve in the Industrial Advisory Committee (IAC).

Table 1. List of Industrial Advisory Committee

Name	Affiliation
Neeraj Gupta	Battelle
Dwight Peters	Schlumberger
George Koperna	ARI
Grant Bromhal	DOE-NETL
Richard Winschel	CONSOL

Initially, committee agreed that data availability for building simulation model is one of the key criteria for site selection. Five potential sites were discussed:

- Citronelle Site: Operated by Denbury. Phase III Regional Partnership. ARI can help provide the geological model.
- Mt. Simon Site: FutureGen Site in Illinois, Battelle has performed the geological modeling.
- MRCSP Site: Phase III Regional partnership, Battelle has performed the geological modeling.
- Illinois Basin (Decatur) Site: Rob Finely (USGS) has access to the geological model; some simulation modeling has already been performed.
- Otway Site: Site is in Australia.

The datasheet shown in Table 2 was sent to all the member of advisory committee. The members were asked to provide any and all information or contact points for any of the candidate sites. Following the conversation that the WVU team had with George Koperna from ARI, it was agreed to provide WVU with the Citronelle field geo-cellular model. ARI was performing the reservoir modeling for the phase III, southeast regional CO_2 sequestration partnership.

Table 2 . Datasheet for all 5 candidate sites

Site Reference	Contact Person	Affiliation	Email	CO2 Source	Our Information	Supplemental Information
Citronelle- Denbury	George Koperna	ARI	gkoperna@adv-res.com	25 Mwatt Mobil Alabama Power Plant	• Injection Starts at January 2011, • Injection in 1500 ft above Oil Field, • Some logs are available, • 2D Seismic will be available • 3D Seismic might be done within 2 years.	• Previous production history • Injection plan and history • Type of formation • Geocellular model and geological characteristics • State and characteristics of injected CO2
Mt. Simon - Mattoon FutureGen	Mark McKoy, Bill Gwilliam, Dick Winschel - Signe Wurstner	NETL/ CONSOL / Battelle			• 2D Seismic is available, • 1200 ft thickness • Geological model is done by Battelle, • First Well in 2010	• Previous production history • Injection plan and history • Type of formation • Geocellular model and geological characteristics • State and characteristics of injected CO2
MRCSP Site, Regional Partnership Phase III	Neeraj Gupta, Joel Sminchak, David Ball,	Battelle			Field to be announced	• Previous production history • Injection plan and history • Type of formation • Geocellular model and geological characteristics • State and characteristics of injected CO2
Illinois Basin Decatur	Rob Finely	Illinois GS			• 2D Seismic and 3D Seismic performed • Some simulation models have been run. • Injection starts next year • A Geocellular model exists	• Previous production history • Injection plan and history • Type of formation • Geocellular model and geological characteristics • State and characteristics of injected CO2
Otway-Australia	Justin Gleir / Grant Bromhal	DOE	Justin.Glier@netl.doe.gov Grant.Bromhal@netl.doe.gov		• Depleted gas reservoir • One injection well • One monitoring well • One production well • Geocellular and simulation model exist	• Previous production history • Injection plan and history • Type of formation • Geocellular model and geological characteristics • State and characteristics of injected CO2

SELECTION OF RESERVOIR MODELING SOFTWARE

After a comprehensive study that included examining major reservoir simulation models that are available in the market, the WVU team decided to use the numerical simulation and visualization package (BUILDER/GEM/RESULTS) from Computer Modeling Group (CMG). The criteria for selecting this simulation model to be used in our project included availability (of the software and personnel for support), ease of use, and willingness of the provider of the package to work with the university. This package has been used extensively by this team and the team members are able to use the software with a high proficiency.

BACKGROUND STUDY ON CANDIDATE SITES

Citronelle in Mobile Alabama was selected as a candidates for this project. Upon selection of this site as a prime candidate, the group started a background study on this field. A brief background on this site that was eventually selected as the site to be used for this project is provided in Appendix 1.

Comprehensive studies on this field can be found in literature from different groups of researchers mainly in Alabama University and the Southeast Regional Carbon Sequestration Partnership. Citronelle was discovered on 1955. It produces from the Rodessa formation (lower Cretaceous). 414 active and shut in well exist in this field. The Citronelle Dome is a giant, salt-core anticline in the eastern Mississippi Interior Salt Basin of southern Alabama that is located near several large-scale, stationary, carbon-emitting sources in the greater Mobile area. The dome forms an elliptical, four-way structural closure containing opportunities for CO_2-enhanced oil recovery (CO_2-EOR) and large-capacity saline reservoir CO_2 sequestration.

The Citronelle oil field, located on the crest of the dome, has produced more than 169 million bbls of 42–46° API gravity oil from sandstone bodies in the Lower Cretaceous Rodessa Formation. The top seal for the oil accumulation is a thick succession of shale and anhydrite, and the reservoir is under-filled such that oil-water contacts are typically elevated 30–60 m (100–200 ft.) above the structural spill point. Approximately 31–34% of the original oil in place has been recovered by primary and secondary methods, and CO_2-EOR has the potential to increase reserves by up to 20%.

Structural contour maps of the dome demonstrate that the area of structural closure increases upward in section. Sandstone units providing prospective carbon sinks include the Massive and Pilot sands of the lower Tuscaloosa Group, as well as several sandstone units in the upper Tuscaloosa Group and the Eutaw Formation (Figure 8). Many of these sandstone units are characterized by high porosity and permeability with low heterogeneity. The Tuscaloosa-Eutaw interval is capped by up to 610 m (2000 ft.) of chalk and marine shale that are proven reservoir seals in nearby oil fields. Therefore, the Citronelle Dome can be considered a major geologic sink where CO_2 can be safely stored while realizing the economic benefits associated with CO_2-EOR (Esposito 2008). Citronelle field is the location for the anthropogenic CO_2 Injection field test in southeast regional CO2 sequestration partnership.

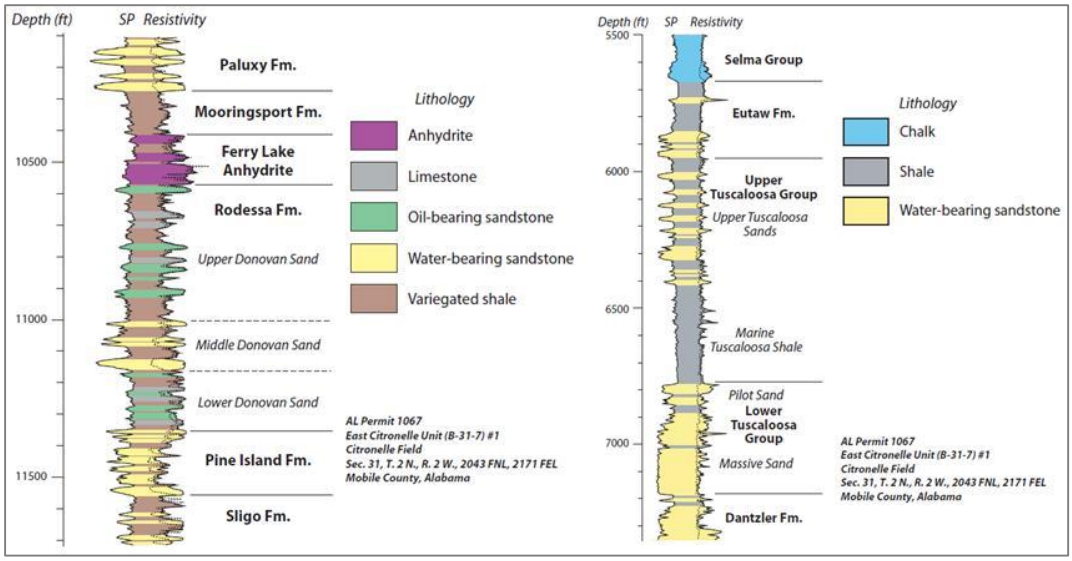

Figure 8. Rodessa Oil and Saline Reservoirs (Left) - Tuscaloosa-Eutaw Saline Reservoirs (Right)

Source for the CO_2 capture is at Alabama Power's Barry Electric Generating Plant, located in Mobile County. Plant Barry is located approximately 10 miles from the Citronelle Oil Field, the ultimate destination of a pipeline that will link the coal-fired CO_2 source and the saline formation that will be used for the demonstration project. Data confirms that the geology surrounding Plant Barry and within the area of the Citronelle Oil Field is regionally very similar to the geologic setting of the larger Gulf Coast area.

Beginning in 2011, between 100,000 and 150,000 tons of CO_2 per year – the equivalent of emissions from 25 megawatts of the plant's generating capacity – was the source for the SECARB project. The CO_2, after capture, is transported to the Citronelle Oil Field and injected into the Paluxy Formation, a saline sandstone reservoir that is located immediately above the oil field and is regionally significant as a safe sequestration target throughout the southeastern Gulf Coast.

Based on the R&D objectives of a CO_2 Injection test project, SECARB planned an extensive MVA program for its field activities. Each site was well instrumented with multiple sensor arrays. Standard off-the-shelf technologies were tested in carbon sequestration applications. In addition, novel new tools and techniques will be tested and evaluated (SECARB 2014). These MVA plans can very well be compared to the MVA technologies that is developed this project.

Process of selecting a test site for injection pilot and detailed study of its geology, determination of oil-CO_2 minimum miscibility pressure has been completed. The injection well is B-10-10#2 which previously was a producer and was converted to a water injector in 2008. The Injector is located in a 5 spot with 4 producers (B-19-7, B-19-8,B-19-9 and B-19-11) developed in the upper Donovan 14-1 and 16-2 sandstone units. Well B-19-10 was initially considered in the 5 spot but

was replaced by B-19-11 because of operational problems (Figure 9). All relevant information for these wells was gathered through the Alabama Geological Survey website[1].

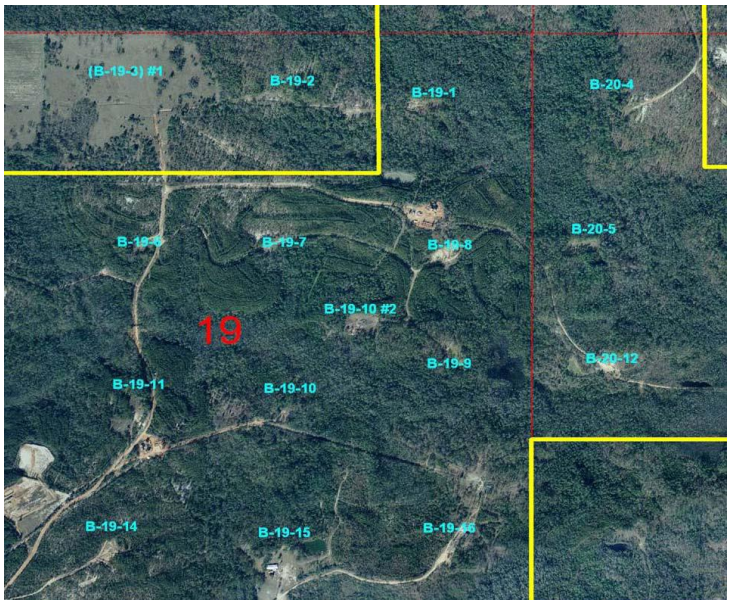

Figure 9. Map of the 5 spot CO_2 – EOR

Simulation results from University of Alabama at Birmingham were thoroughly studied. The 5 spot model is simulated for a water injection followed by a CO_2 -EOR period. Results of these models simulated by both SENSOR (Coats Engineering, Inc.) and MASTER 3.0 simulator show an increase in oil recovery by CO_2 injection. Another scenario of water alternating gas (WAG) recovery is also simulated by SENSOR and shows that this method might be preferred when the CO_2 has a limited supply (Walsh 2010).

Table 3. 5 Spot CO_2 EOR Wells Information

Well Name	Type	Latitude	Longitude	Spud Date	Perfs
B-19-7	Producer	31.12338	-88.2169	12/6/1962	10863-11458; 11014-20; 11042-48; 11416-24
B-19-8	Producer	31.12373	-88.2127	4/29/1963	10904-11561
B-19-9	Producer	31.12351	-88.2127	1/19/1963	10962-68, 10984-11000, 11024-40, 11394-401
B-19-10 #2	Injector	31.12156	-88.2149	1/26/1982	10988-92, 11031-38, 11395-99
B-19-11	Producer	31.11962	-88.2208	10/25/1962	10784-795, 10840-862, 10954-11001, 11012-046

[1] http://www.gsa.state.al.us

At the time this project was to be started, another pilot project in Citronelle, AL was about to start. This pilot was a CO_2 storage project in saline aquifer (Paluxy formation) as part of the phase III South Eastern Carbon Sequestration Partnership. This was an anthropogenic test with large volume of CO_2 injection into a saline aquifer with capture of CO_2 from power plant Barry. Denbury Resources Incorporation participated in the early planning stages of the project to inject CO_2 into the saline formation and to monitor CO_2 containment. Alabama Power Company's Plant Barry, near Bucks, Alabama, was the source of CO_2, approximately 12 miles from the Southeast Citronelle Unit.

The project capability included capturing approximately 125,000 metric tons of anthropogenic CO_2 per year. A pipeline was constructed from Plant Barry to Denbury's Southeast Citronelle Unit, and the CO_2 was injected into saline Paluxy sandstones at depths of approximately 10,000 feet. These sandstones are separated from the deeper Rodessa oil reservoir by the impermeable Ferry Lake Anhydrite. One new injection well and one new monitoring well were planned. Injection was planned to continue for four years at a rate of 125,000 tons per year. After finishing of injection, the sequestered CO_2 would be monitored for an additional four years in order to determine how well the CO_2 has been contained.

A numerical model from this site was received from Advanced Resources International. An area of about 9000 acre with a 50 by 50 Cartesian grid (Grid Size = 400 ft. by 400 ft) was modeled. The model contained 17 sand bodies in 51 simulation layers. Average permeability was 88 md for the entire formation and average porosity was 19.3 %.

The model has one injection well penetrating all 17 sand bodies with thickness of about 10 to 80 ft. each. Total thickness of the paluxy formation is about 1100 ft. in southeast unit. All 17 sand bodies except for the number 14^{th} are surrounded (at least partially) by Carter-Tracy (Limited extent) aquifers in the model. The injection target is the saline Paluxy sandstones at the depth of approximately 10,000 feet. The Paluxy formation represents a regressive sequence. Injection well is well D-9-7 which was previously plugged and abandoned on 09/12/08.

Table 4 and Table 5 provide some detail information regarding the perforations of well D-9-7 and the formation tops used in the model.

Table 4. Anthropogenic test Injection Well Information

Well Name	Type	Latitude	Longitude	Spud Date	Perfs
D-9-7	Injector	31.06519	-88.18172	11/19/1961	10900-02, 10966-70, 10975-79, 11027-40, 11069-80

Table 5. Formation Top and Thickness (Citronelle, Al)

Formation Tops	Depth (ft bgs)	Interval Thickness (ft)
Bottom of Fresh Water (<1,000 mg/l)	~1,000	
Base of USDW (<10,000 mg/l)	~1,200	
Selma Chalk Group (seal)	4,560	1,310
Eutaw	5,870	150
Tuscaloosa Group		
Upper Tuscaloosa	6,020	720
Middle Tuscaloosa (seal)	6,740	210
Lower Tuscaloosa	6,950	410
Washita-Fredericksburg (seal)	7,360	2,040
Paluxy Formation (target)	9,400	1,110
Mooringsport Formation	10,510	240
Ferry Lake Anhydrite	10,750	190
Rodessa Formation (oil reservoir)	10,940	-

RESERVOIR SIMULATION AND MODELING

ARI SIMULATION MODEL

The base model being used for simulation by the WVU team was received from Advanced Resources International. The model represents the injecting target-Paluxy, between the depths of 9,040 feet to 10,476 feet. The model that has an area of approximately 9000 acres, is built using a 50 x 50 x 51 Cartesian grid with a total number of grid blocks equal to 138,975. The size of each grid is 400 ft. x 400 ft. An average permeability 88 md and an average porosity 19.3% are used as constant parameters for the entire formation in the model.

Table 6 and Table 7 provide more details on the information used in the ARI model.

Table 6. Reservoir Components Data

Reservoir Pressure		**230 F**	
Water Properties		Compressibility=3.2E-6 1/psi	
Components	Critical Pressure, Psi	Critical temperature, F	Acentric factor
CO_2	72.8	304.2	0.225
C1	45.4	190.6	0.008

Table 7. Reservoir Characteristics Data

Total blocks	**50x50x51=138975 blocks**
Block size	400x400 feet
Permeability(I.J.k)	88 md
Porosity	20%
Global Composition (C1,CO_2)	0.01
Aquifers	There are 16 aquifers in which leakage is allowed

Relative Permeability Curves

Relative permeability curves which are used in the model are shown in the following figures.

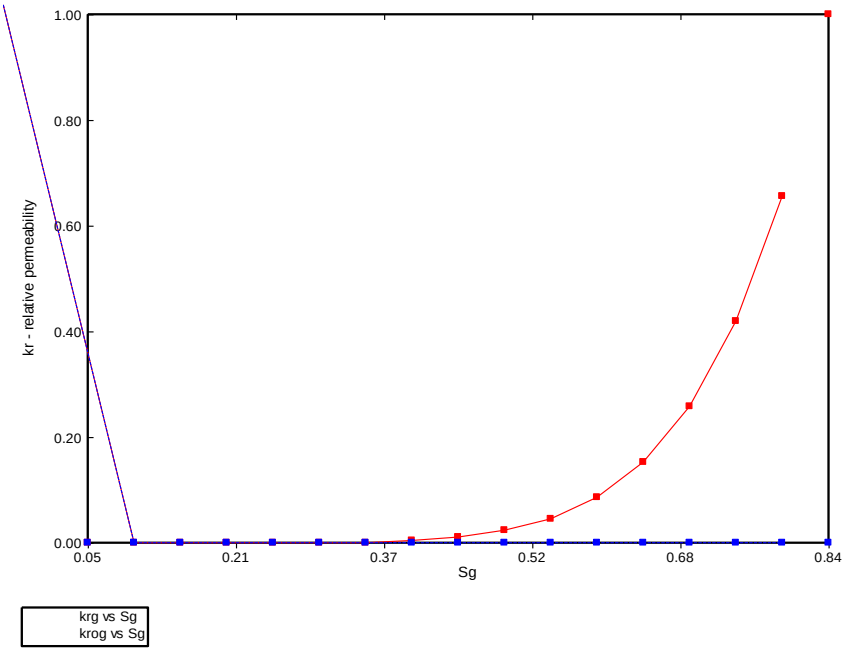

Figure 10. Gas Relative Permeability (Red) - Oil Relative Permeability (Blue)

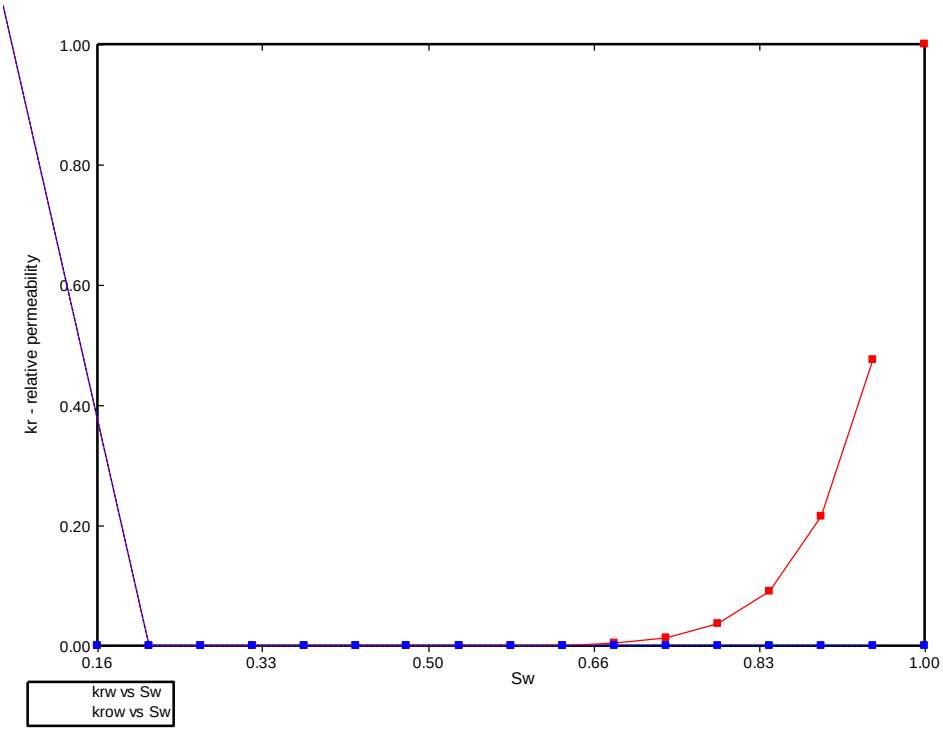

Figure 11. Water Relative Permeability (Red) - Oil Relative Permeability (Blue)

The model has 51 simulation layers, which form 17 sand layers with thickness of about 10 to 80 ft. each. A 3-D view of the simulation model is shown in the following graphs.

Figure 12. Citronelle Model Structure

Injection Scenarios and Simulation Results

The WVU team has performed several simulation Scenarios with different injecting CO_2 amount followed by a certain monitoring time to examine the extent of the CO_2 plum after injection. The different scenarios are chosen based on the target amount of injection which is reported for this test project.

The Gas saturation result shows how well the CO_2 is contained after injection for each scenario. The figures below show the gas saturation plume around the injection well.

Scenario 1

In this scenario, CO_2 is injected into the target formation with the amount of 100,000 tons per year for four years starting on January 2010.

After injection, a period of 100 years monitoring is followed. The figures below show how CO_2 travels around the injection well along the entire formation, each figure shows the Gas (CO_2) saturation before injection, end of injection, 50 years after injection, and at the end of 100 years of monitoring, respectively.

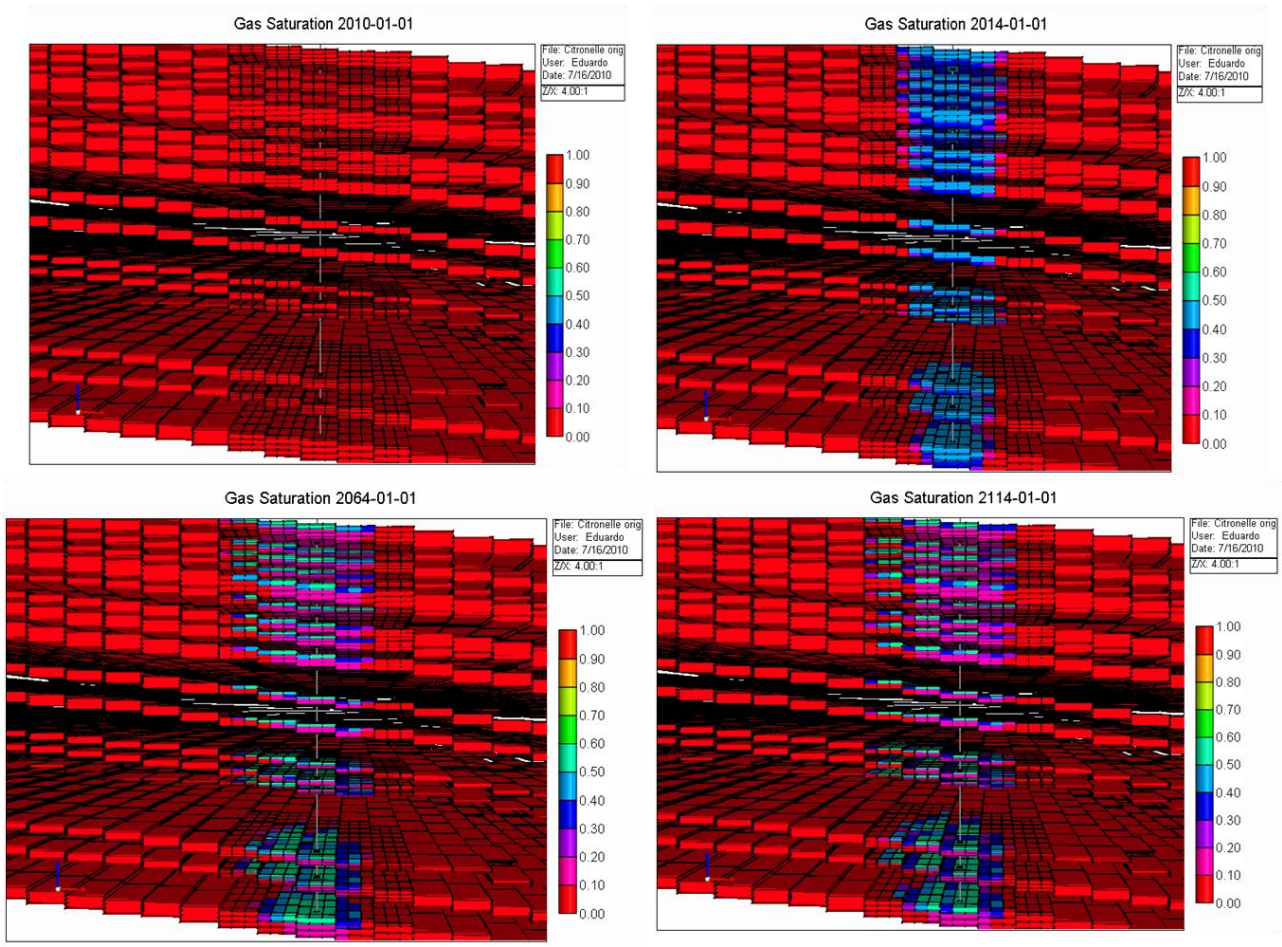

Figure 13. Gas Saturation around the injection well - Scenario 1

Following graphs show the gas (CO_2) rate and well pressure during the injection and the monitoring period.

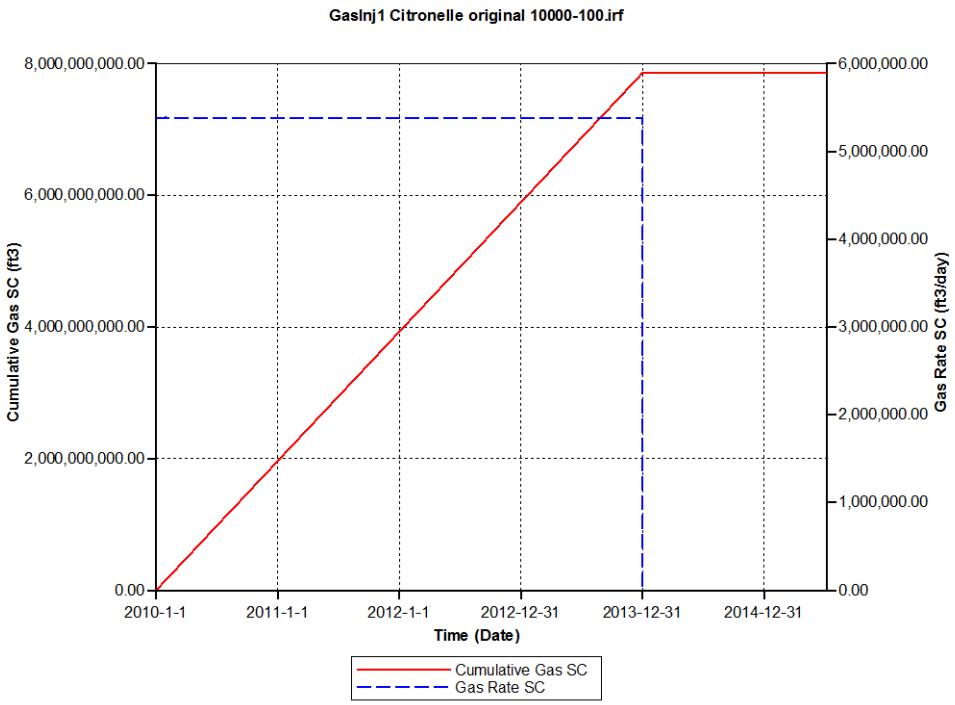

Figure 14. Cumulative Gas Rate & Gas rate Standard Condition at the injection period

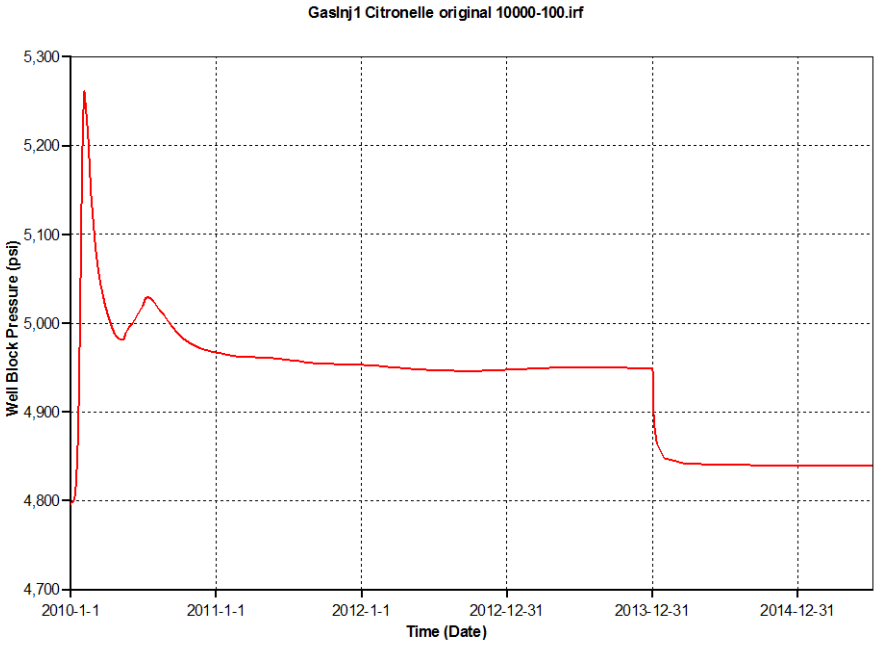

Figure 15. Well Block Pressure at the injection period

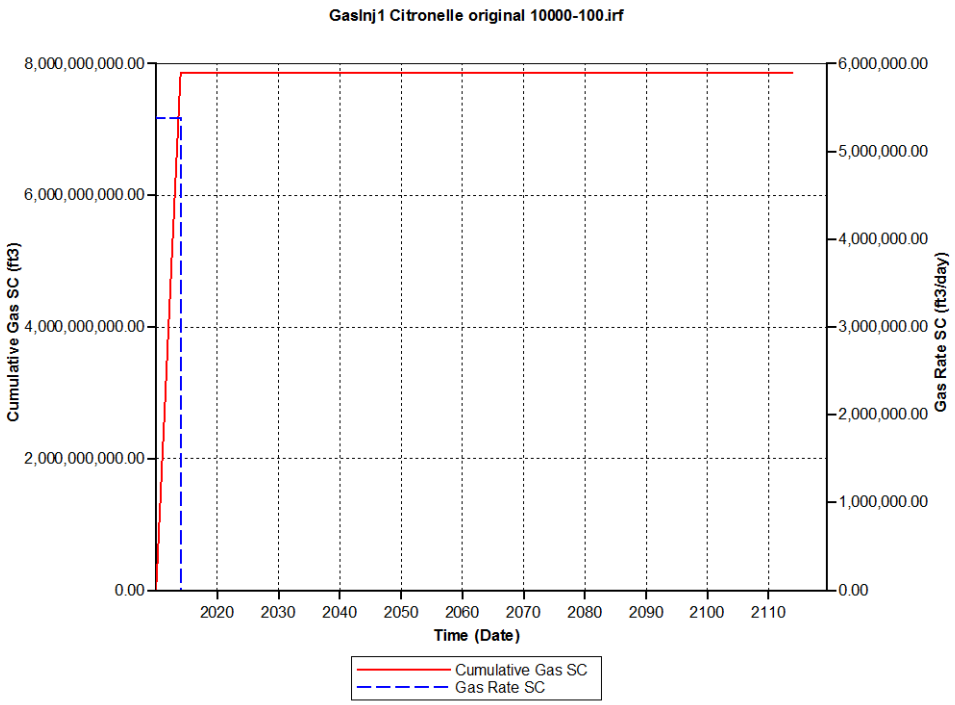

Figure 16. Cumulative Gas Rate & Gas rate Standard Condition at the monitoring period

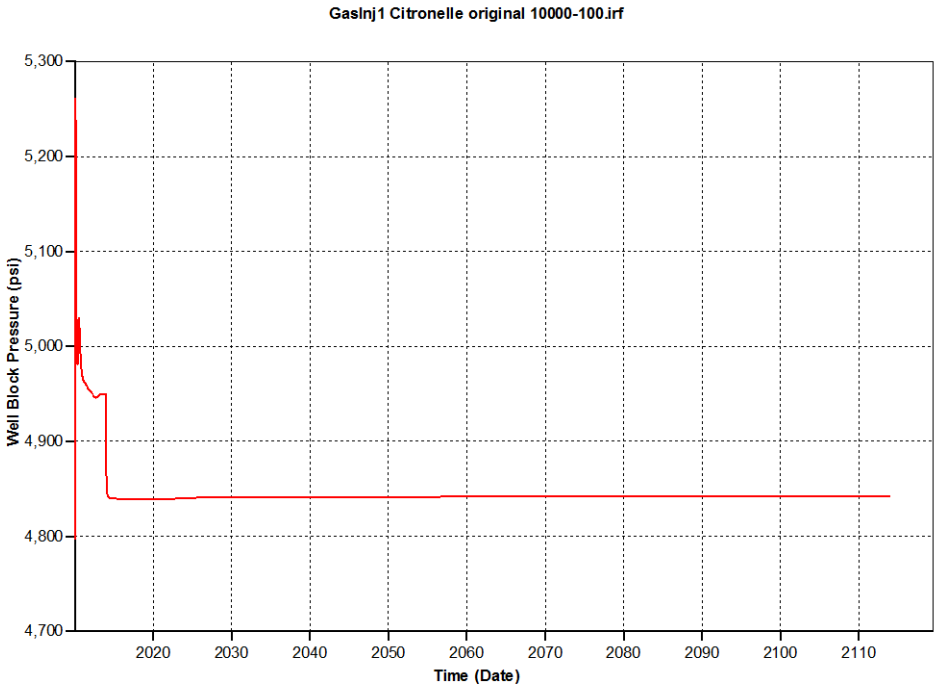

Figure 17. Well Block Pressure at the monitoring period

Scenario 2

In this scenario, CO_2 is injected into the target formation with the amount of 125,000 tons per year for four years starting on January 2010.

After injection, a period of 100 years monitoring is followed. The figures below show how CO_2 travels around the injection well along the entire formation, each figure shows the Gas (CO_2) saturation before injection, end of injection, 50 years after injection, and at the end of 100 years of monitoring, respectively.

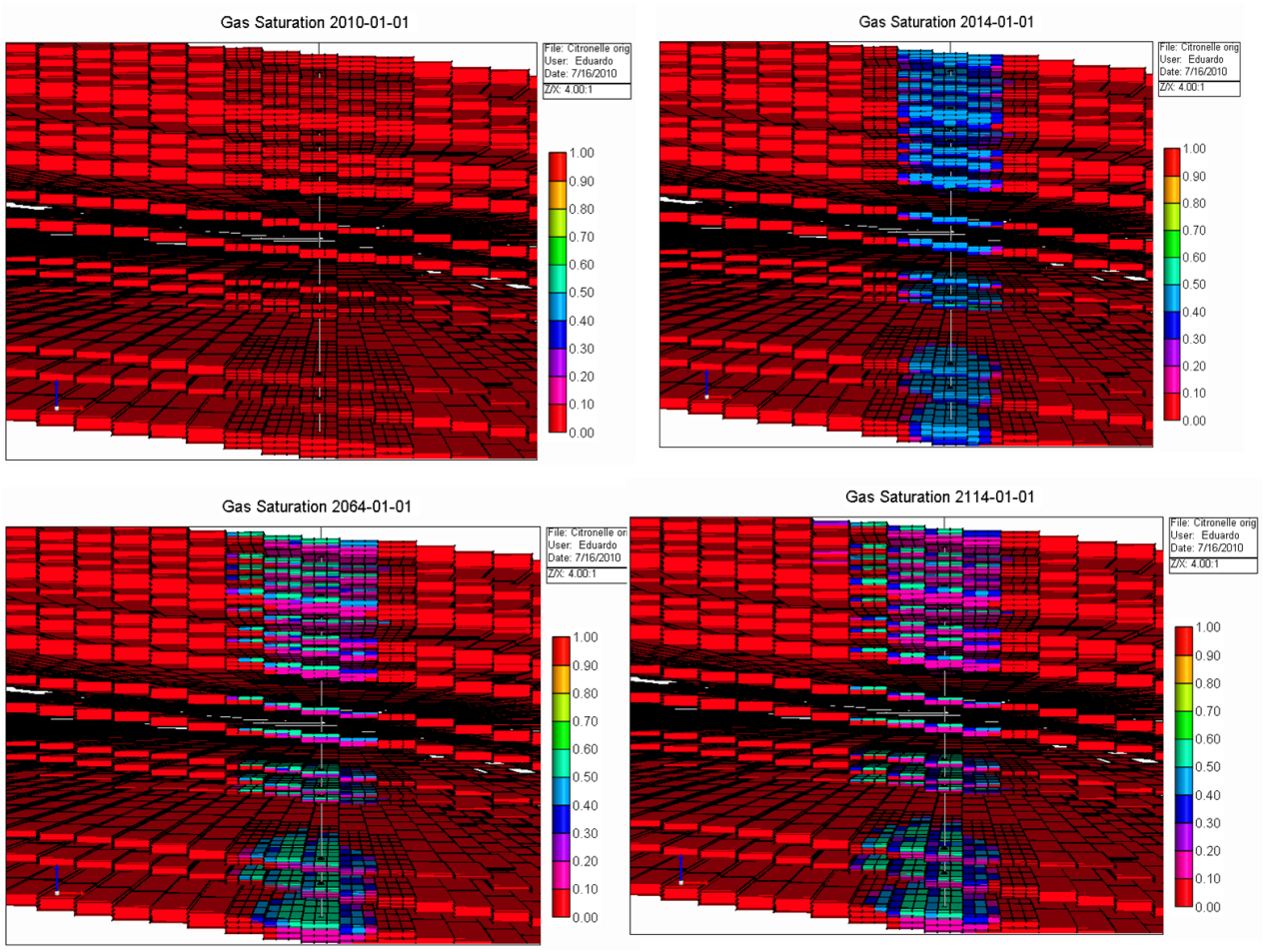

Figure 18. Gas Saturation around the injection well - Scenario 2

Following graphs show the gas (CO_2) rate and well pressure during the injection and the monitoring period.

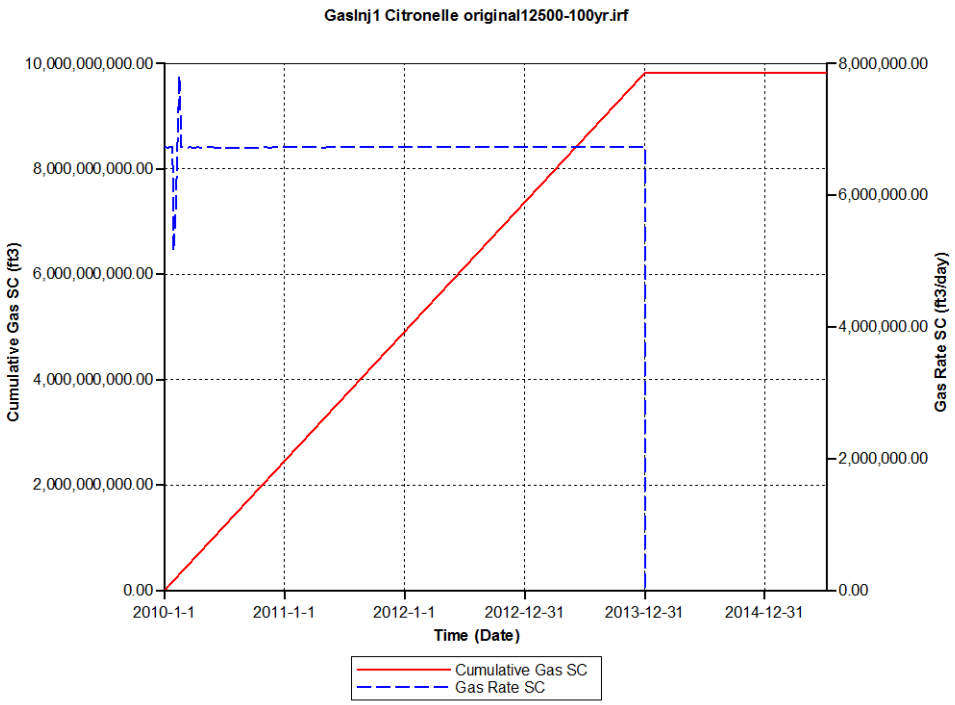

Figure 19. Cumulative Gas Rate & Gas rate Standard Condition at the injection period

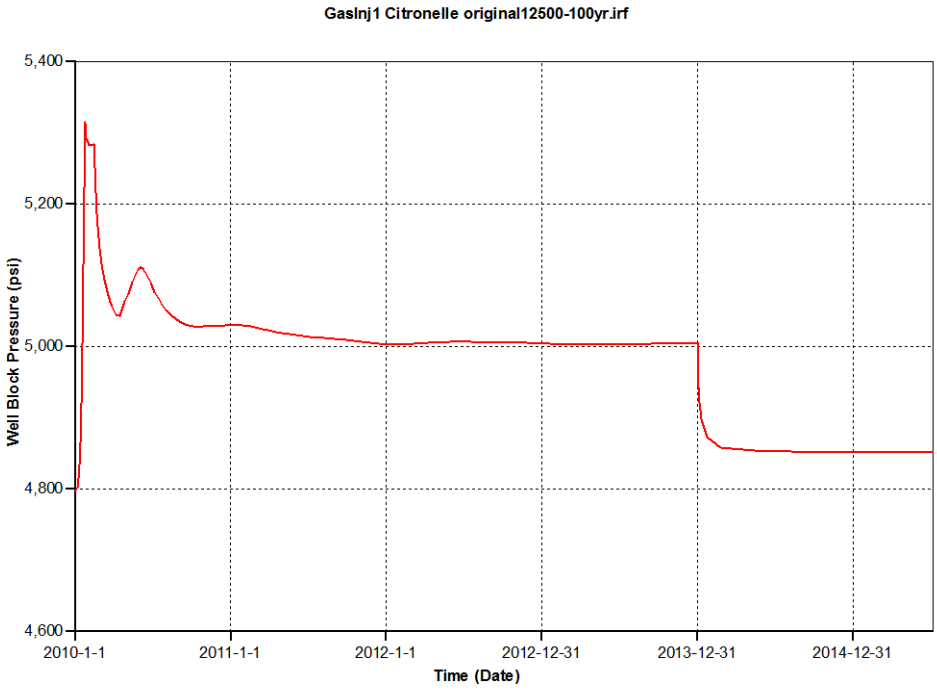

Figure 20. Well Block Pressure at the injection period

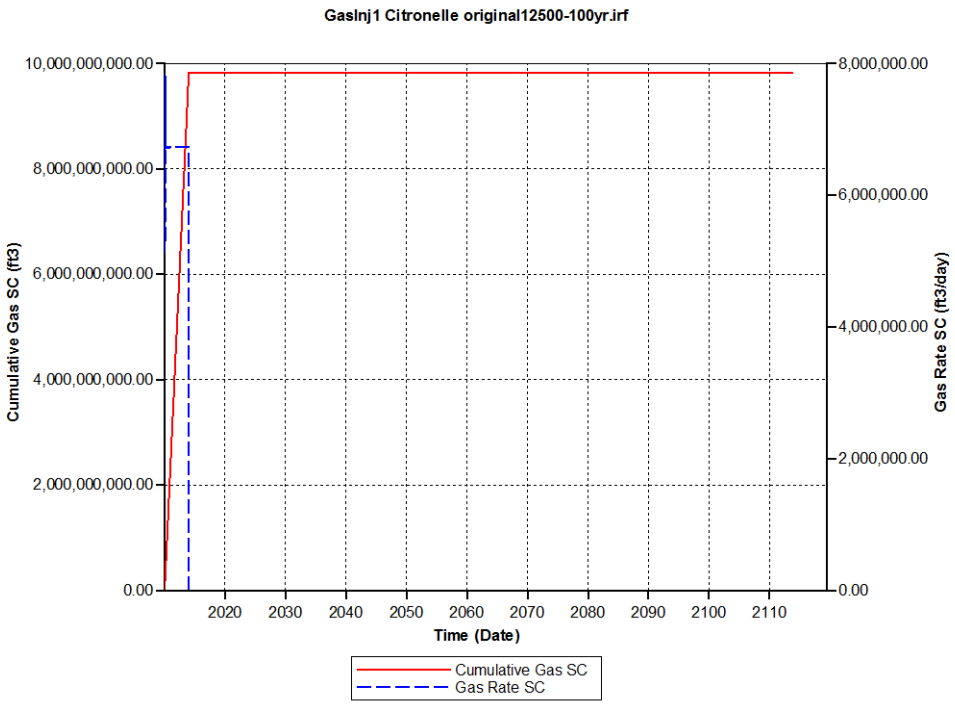

Figure 21. Cumulative Gas Rate & Gas rate Standard Condition at the monitoring period

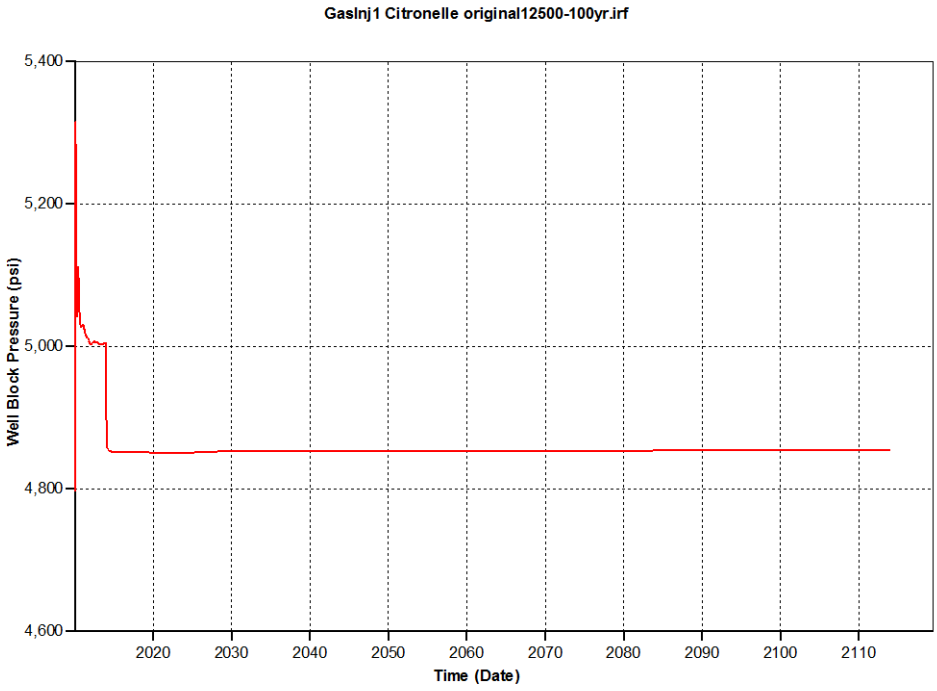

Figure 22. Well Block Pressure at the monitoring period

Scenario 3

In this scenario, CO_2 is injected into the target formation with the amount of 150,000 tons per year for four years starting January 2010.

After injection, a period of 100 years monitoring is followed. The figures below show how CO_2 travels around the injection well along the entire formation, each figure shows the Gas (CO_2) saturation before injection, end of injection, 50 years after injection, and at the end of 100 years of monitoring, respectively.

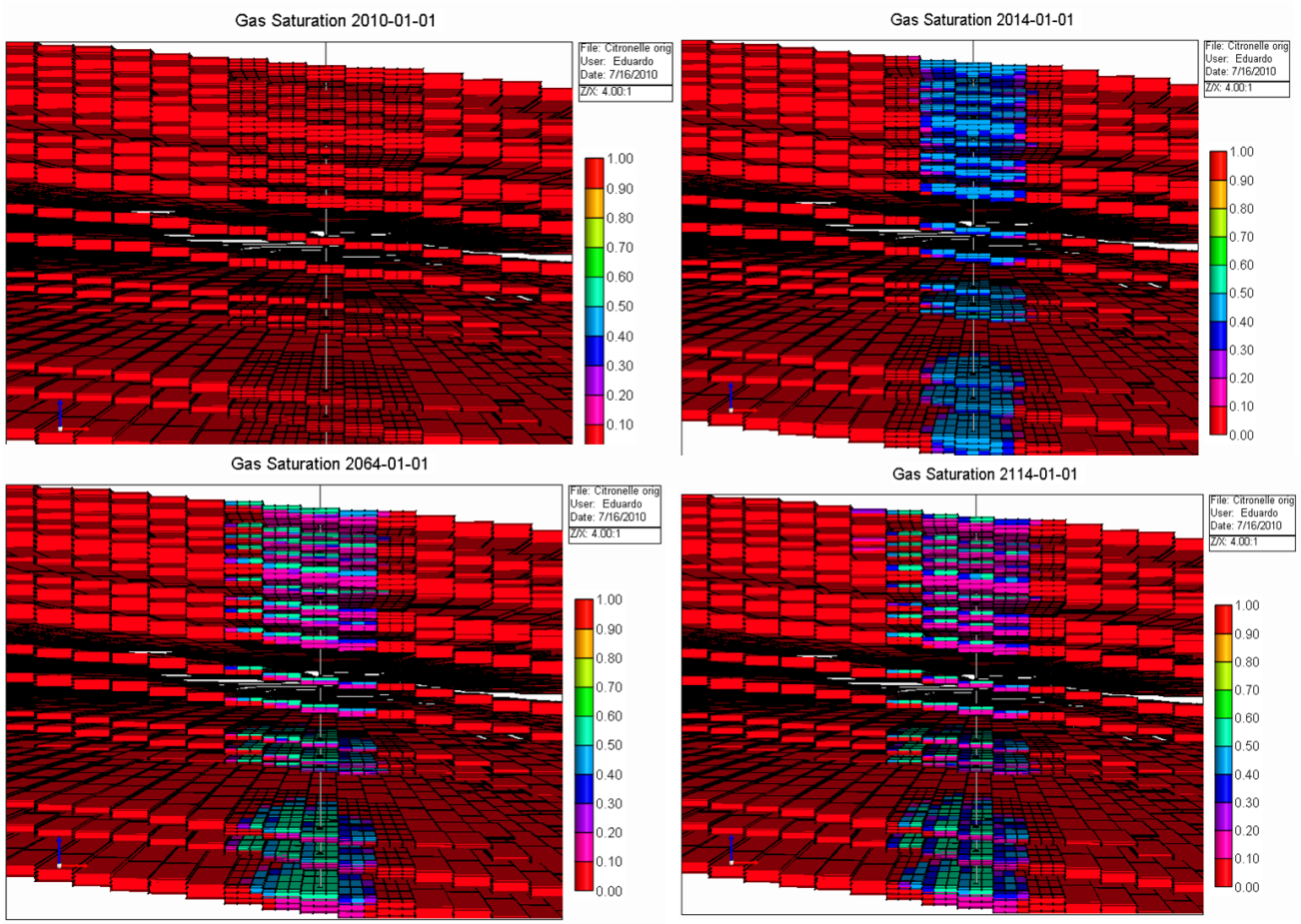

Figure 23. Gas Saturation around the injection well - Scenario 3

Following graphs show the gas (CO_2) rate and well pressure during the injection and the monitoring period.

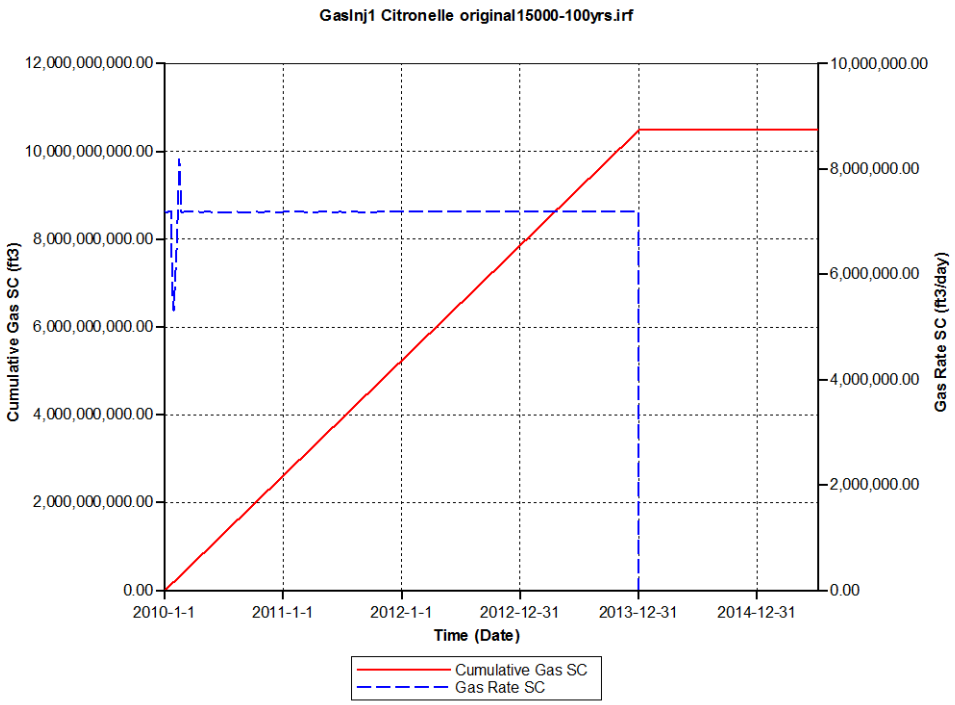

Figure 24. Cumulative Gas Rate & Gas rate Standard Condition at the injection period

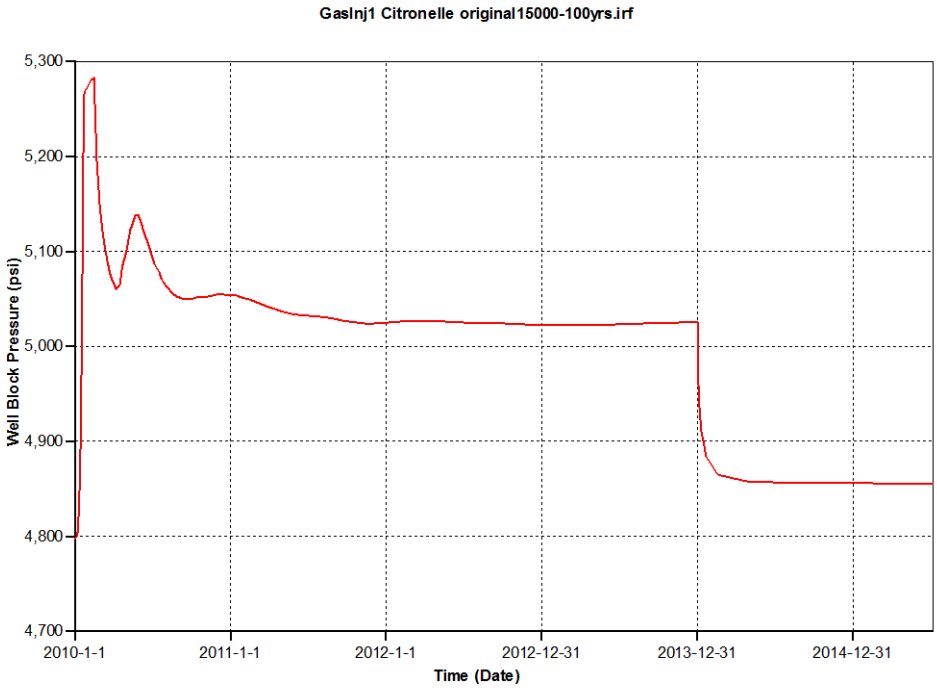

Figure 25. Well Block Pressure at the injection period

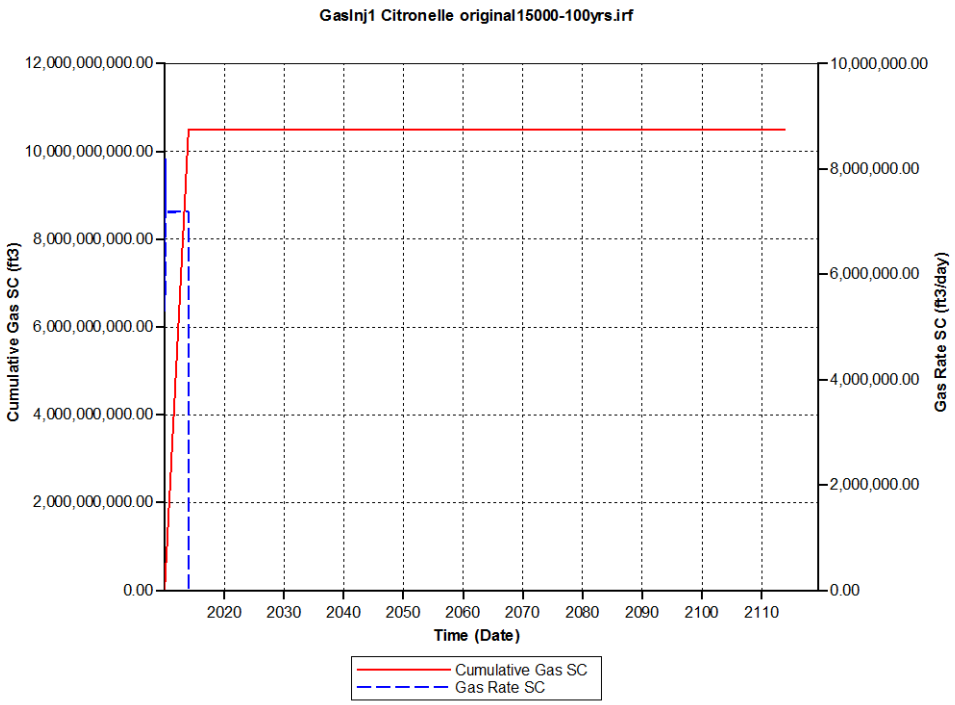

Figure 26. Cumulative Gas Rate & Gas rate Standard Condition at the monitoring period

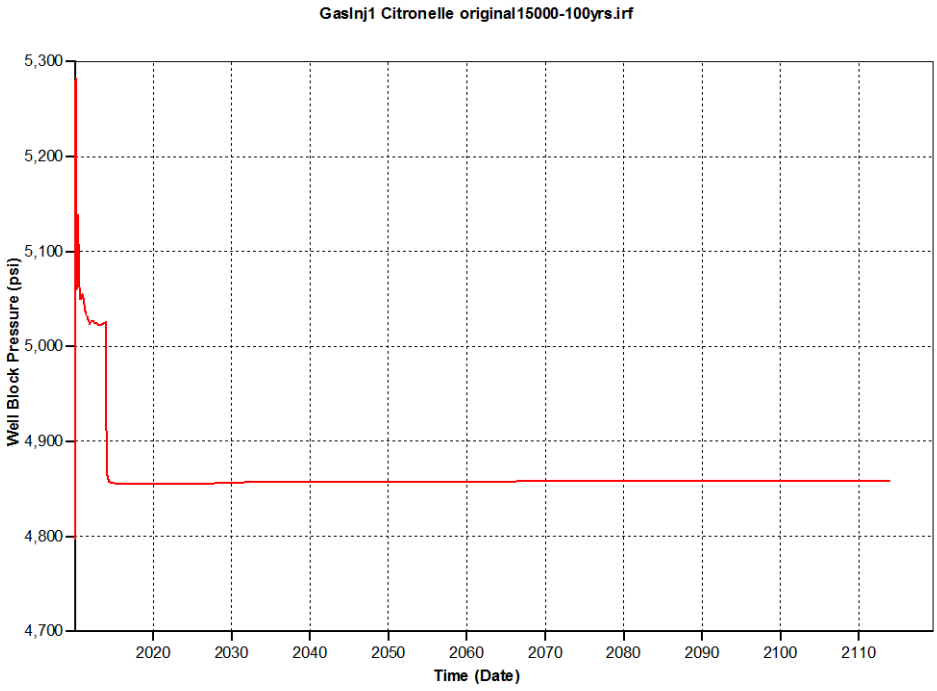

Figure 27. Well Block Pressure at the monitoring period

These simulation runs demonstrated that 100 years after the stop of injection, approximately 60 to 70% of the CO_2 plum penetrates mostly the upper part of the sand layers, while the remaining 30% are distributed among the middle and bottom sand layers.

DEVELOPING LATERAL HETEROGENEITY FOR THE FIELD (THE WVU MODEL)

The WVU team continued the search for more geological data on the Citronelle Field. At the end of August 2010, the WVU team received a complete report on SECARB Phase III anthropogenic test project (Advance Resources International [ARI] Report). This report covers all the background studies that have been performed on this field by ARI.

In line with the data gathering efforts, the WVU team started looking for any available well logs from the field, especially the closest wells to the injection well. These logs were ordered from the Alabama geological survey and were interpreted at WVU. Porosity values are interpreted from these well logs and the permeability is calculated based on an equation used in ARI report. The interpretation procedure will be covered later in this report.

The simulation model which was received from ARI has an average value for porosity and permeability. However based on the ARI report these values are calculated from a well log at the well D-9-7. The WVU team decided to incorporate the vertical heterogeneity extracted from the well log into the numerical model in order to have a better understanding of the fate of CO_2 in different depths of the reservoir.

The data for the Citronelle field presented in the ARI report provided the porosity and permeability data for the injection well D-9-7. Simulation of the injection with just this data would not present a very realistic picture of CO_2 plum in the reservoir. Our simulation runs suggested that the CO_2 plum can be expected to reach as far as 1 mile away from the injection well. Thus to generate a realistic model that captures the heterogeneity of the formation in the lateral direction, the WVU team obtained well logs from wells up to 1 mile away from the injection well.

The wells whose logs were obtained for generating the heterogeneity were D-4-14,D-4-15,D-4-16,D-9-2,D-9-3,D-9-6, D-9-8,D-9-10, D-9-10,D-10-5,D-10-12. The logs obtained were induction logs with formation resistivity values from 1400 ft to 11600 ft. The region of interest on the logs was the injection zone from about 9400 ft to about 10500 ft.

All logs were digitized to be used for the calculation of porosity. To calculate the porosity corresponding to each resistivity, the Archie equation provided in the ARI report was used.

$$\emptyset = \left(\frac{a}{\left(\frac{Rt}{Rw}\right) * Sw^{n}} \right)^{1/m}$$

Where

a = tortuosity factor = 1; default value

m = cementation factor = 2.25; best match to Citronelle oilfield porosity logs

n = saturation exponent = 2; common default value

R_w = resistivity of the formation water = 0.045; best match to Citronelle oilfield porosity logs

S_w = Water saturation =0.95; assume only residual gas saturation

φ = porosity

R_t = True formation resistivity = obtained from logs.

The true formation resistivity for each of the injection zones was read from the digitized logs and the porosity at each data point was obtained by using the equation above. The digitized logs included the resistivity value every six inches, thus our porosities were calculated at six inch intervals. To find the porosity of each zone, the porosity thickness was calculated for each one of the injection zones and divided by the thickness of the zone using the following equation:

$$\emptyset ave = \frac{\sum \emptyset h}{\sum h}$$

Therefore, average porosities for each of the injection zones were calculated. The next step was generating the permeability for the injection zone. The ARI report shows that for most of the logs obtained from the Citronelle field, the general relationship between porosity and permeability is given by the following equation:

$$k = 0.013e^{0.377\emptyset}$$

Once the permeability was calculated for each injection zone using the above equation, lateral heterogeneity in all injection zones were introduced into the geological model. Results of these calculations are shown in Table 8.

Numerical Modeling

The Simulation model was modified based on the parameters gathered from the document provided by ARI. This document, discusses the new changes that have occurred in the CO_2 sequestration plan. These changes were implemented in the model, the amount of permeability and porosity in sandstone layers were updated with the new values in the document (SECARB 2010). The injection well in the model was completed and perforated in 11 sandstone layers. Other layers were closed to injection in the model.

The ARI document also states that the injection well has a maximum bottom hole pressure constraint of 6,300 psi to avoid of surpassing the fracture pressure during the CO_2 injection. Another constraint that was imposed in the model was the maximum CO_2 injection rate of 9.45 million standard cubic feet per day.

Preliminary results of the model are shown in following graphs (Figure 28and Figure 29).

Table 8. Log Interpretation results for Citronelle

Well Name	D-9-6		D-4-15		D-10-5		D-10-12		D-4-16		D-9-3	
Sand Layer	Φ	K(md)	Φ	K(md)	Φ	K(md)	Φ	K(md)	Φ	K(md)	Φ	K(md)
9460	0.14	8.52	0.19	75.65	0.11	2.63	0.14	8.52	0.22	232.69	0.16	19.45
9520	0.16	19.45	0.11	1.95	0.12	3.14	0.11	2.25	0.24	617.53	0.13	4.81
9540	0.11	2.25	0.13	4.81	0.14	8.52	0.11	1.95	0.22	232.69	0.10	1.71
9570	0.11	2.25	0.15	12.33	0.13	4.81	0.11	1.95	0.10	1.49	0.11	2.63
9620	0.12	3.14	0.16	19.45	0.10	1.71	0.12	3.83	0.14	8.52	0.14	6.25
9670	0.12	3.14	0.19	75.65	0.14	8.52	0.14	8.52	0.12	3.14	0.13	4.81
9710	0.14	8.52	0.16	19.45	0.12	3.14	0.15	9.79	0.12	3.14	0.19	75.65
9740	0.14	8.52	0.19	75.65	0.10	1.71	0.11	1.95	0.15	9.79	0.12	3.83
9800	0.16	19.45	0.13	4.81	0.16	19.45	0.11	2.63	0.11	2.25	0.13	4.81
9900	0.13	4.81	0.12	3.83	0.12	3.83	0.14	6.25	0.11	2.63	0.14	6.25
9970	0.13	4.37	0.22	232.69	0.13	4.37	0.11	2.25	0.12	2.92	0.11	2.25
10060	0.13	4.37	0.12	3.83	0.12	4.00	0.14	6.25	0.12	3.83	0.13	4.37
10100	0.13	4.81	0.12	3.14	0.13	4.81	0.12	3.14	0.11	1.95	0.13	4.81
10130	0.13	4.81	0.12	3.14	0.13	4.81	0.12	3.14	0.11	1.95	0.13	4.37
10310	0.14	6.25	0.16	19.45	0.13	4.18	0.13	4.81	0.13	4.81	0.16	19.45
10370	0.12	3.14	0.14	8.52	0.14	8.52	0.13	4.81	0.15	13.40	0.15	11.38
10470	0.16	19.45	0.14	8.52	0.12	3.14	0.13	4.37	0.22	232.69	0.13	5.32
10500	0.13	4.81	0.11	2.25	0.26	1477.78	0.11	2.12	0.13	4.81	0.11	2.25
Well Name	D-4-14		D-9-8		D-9-2		D-9-10		D-5-7		D-9-11	
Sand Layer	Φ	K(md)	Φ	K(md)	Φ	K(md)	Φ	K(md)	Φ	K(md)	Φ	K(md)
9460	0.14	7.68	0.19	77.81	0.10	1.24	0.14	7.08	0.11	1.95	0.14	8.50
9520	0.15	11.54	0.22	199.03	0.16	16.56	0.11	2.08	0.10	1.34	0.12	2.76
9540	0.14	8.08	0.16	21.38	0.11	2.05	0.12	2.76	0.12	2.90	0.11	2.25
9570	0.11	2.25	0.13	4.79	0.10	1.45	0.12	2.70	0.12	3.28	0.12	3.20
9620	0.14	6.61	0.18	38.43	0.12	2.91	0.13	6.05	0.10	1.40	0.12	2.82
9670	0.14	7.74	0.16	21.19	0.10	1.38	0.12	3.54	0.12	2.85	0.12	4.02
9710	0.13	5.28	0.26	1084.88	0.11	2.32	0.11	1.84	0.14	7.58	0.11	1.94
9740	0.22	282.02	0.19	57.30	0.11	2.33	0.11	2.34	0.10	1.40	0.12	3.06
9800	0.18	37.14	0.20	107.93	0.13	5.26	0.11	2.40	0.12	3.34	0.12	2.69
9900	0.15	13.86	0.13	5.15	0.14	7.39	0.13	5.95	0.10	1.37	0.12	3.79
9970	0.13	5.04	0.17	33.11	0.11	2.55	0.11	2.35	0.12	3.74	0.12	4.02
10060	0.12	3.76	0.12	3.45	0.10	1.68	0.12	3.27	0.10	1.36	0.12	3.23
10100	0.21	122.09	0.12	3.10	0.11	2.44	0.11	2.06	0.11	2.57	0.12	3.71
10130	0.13	4.98	0.13	4.07	0.11	2.25	0.11	2.41	0.14	6.23	0.12	3.18
10310	0.14	6.84	0.13	4.67	0.13	6.02	0.13	4.07	0.15	11.64	0.13	4.98
10370	0.14	6.81	0.17	24.80	0.12	2.97	0.11	1.99	0.10	1.68	0.15	11.30
10470	0.22	245.11	0.22	236.92	0.12	3.79	0.10	1.37	0.12	2.99	0.10	1.55
10500	0.13	5.13	0.14	6.79	0.15	9.70	0.14	6.21	0.12	3.47	0.12	3.38

Figure 28. CO_2 Gas mole fraction at the end of the injection

Figure 29. CO_2 Gas mole fraction after 10 years of monitoring

Permeability Realizations

Following correlation between porosity and permeability was used by ARI, In order to generate the permeability map used in their model.

$$k = 0.020e^{0.425\emptyset}$$

The WVU team later added another correlation between porosity and permeability in order to make the trend lines more representative of the actual data. This new correlation is shown below. And the results of these correlations as trend lines and actual data is shown in Figure 30.

$$k = 0.013e^{0.377\emptyset}$$

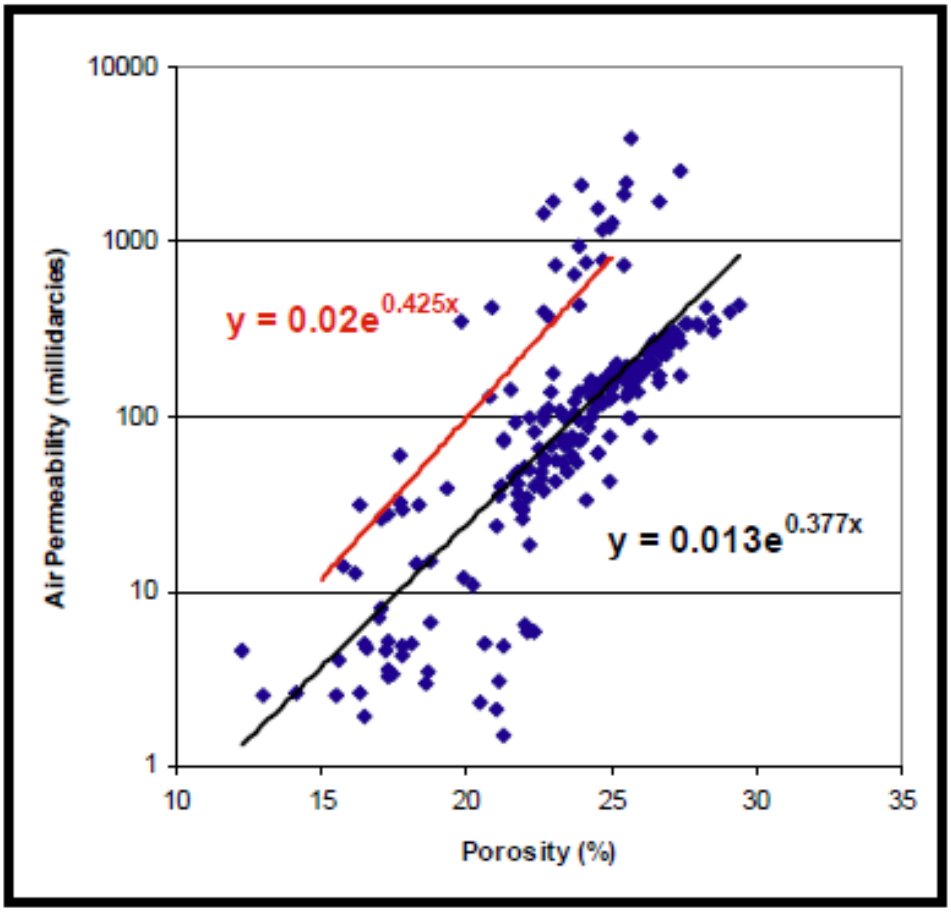

Figure 30.The porosity-permeability correlation proposed by ARI

Base on the data presented in this figure, a large number of data points fall outside of the trend lines; moreover several other data points do not follow the trends identified by the correlations presented above. In order to rectify this, four different clusters were identified and ranked as the

best to the worst rock types. The correlation between the porosity and permeability for the four different realizations were defined. (Figure 31). The interpretation of the well logs and calculation of porosity and permeability based on the cluster analyses shown in Figure 31 are listed in Table 9 and Table 10.

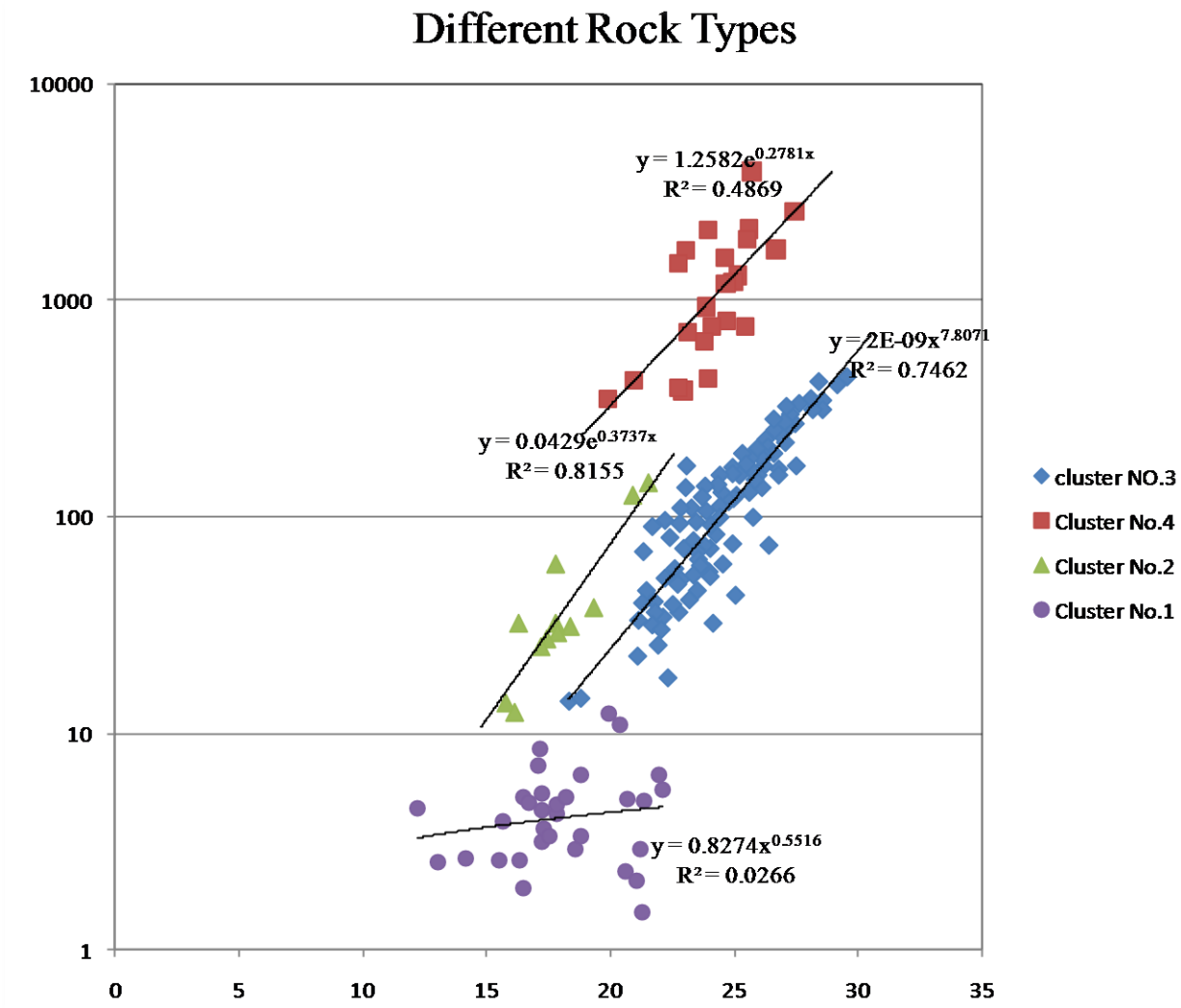

Figure 31.The porosity-permeability correlation in different rock types

Table 9. Log Interpretation results for Citronelle

Well Name		D-18-16		D-8-2		D-16-4		D-9-5		B-33-13		D-10-4		D-8-7	
Log Number		1047EL		1057EL		1059EL		1190EL		1204EL		1211EL		994EL	
Sand Layer	Depth Range(ft)	Φ	K(md)	Φ	K(md)	Φ	K(md)	Φ	K(md)	Φ	K(md)	Φ	K(md)	Φ	K(md)
9460	9444-9476	0.116	3.931	0.124	6.620	0.130	5.913	0.116	6.179	0.105	2.241	0.131	5.955	0.121	7.143
9520	9513-9528	0.125	4.498	0.106	2.289	0.146	16.210	0.127	6.183	0.117	3.248	0.171	37.120	0.119	4.409
9540	9534-9549	0.108	3.103	0.116	4.747	0.128	5.578	0.142	10.217	0.098	1.302	0.142	9.574	0.093	1.081
9570	9562-9584	0.134	6.618	0.142	29.493	0.101	1.758	0.089	0.879	0.091	0.983	0.121	6.299	0.092	1.003
9620	9596-9638	0.139	12.302	0.104	5.651	0.125	5.696	0.148	23.149	0.117	6.016	0.110	2.470	0.101	3.400
9670	9660-9679	0.107	3.596	0.129	5.625	0.111	2.893	0.108	2.825	0.123	4.472	0.159	19.662	0.119	6.094
9710	9695-9717	0.124	5.337	0.092	1.102	0.090	1.113	0.080	0.636	0.089	0.927	0.113	2.745	0.107	3.583
9740	9730-9748	0.123	5.402	0.114	3.593	0.141	14.163	0.121	5.512	0.109	2.140	0.116	3.721	0.104	1.976
9800	9775-9806	0.098	2.653	0.116	4.090	0.108	3.254	0.115	6.712	0.101	2.166	0.123	5.540	0.103	3.122
9900	9886-9903	0.123	4.509	0.101	1.468	0.133	5.723	0.116	3.742	0.101	1.553	0.128	4.661	0.095	1.320
9970	9954-9977	0.097	1.527	0.136	6.550	0.102	1.884	0.108	2.650	0.098	1.392	0.135	7.043	0.106	2.898
10060	10055-10069	0.117	3.129	0.123	4.232	0.098	1.339	0.090	1.028	0.110	2.339	0.133	5.652	0.129	5.113
10100	10099-10113	0.088	0.891	0.106	1.922	0.132	5.702	0.114	3.293	0.120	3.373	0.137	7.099	0.132	5.493
10130	10121-10134	0.113	2.816	0.111	2.672	0.110	2.635	0.120	3.250	0.112	2.544	0.125	4.102	0.143	8.732
10310	10302-10318	0.128	4.696	0.147	11.876	0.106	1.850	0.127	4.477	0.138	7.413	0.118	3.018	0.137	6.751
10370	10362-10381	0.135	6.495	0.101	1.489	0.149	11.878	0.150	11.747	0.100	2.304	0.133	6.113	0.145	9.921
10470	10454-10484	0.091	1.646	0.093	1.236	0.131	5.529	0.124	5.966	0.122	3.742	0.133	5.873	0.087	1.053
10500	10491-10508	0.137	7.292	0.136	7.276	0.111	2.530	0.130	4.935	0.116	2.874	0.095	1.199	0.129	5.162
Well Name		D-8-1		D-5-9		D-5-16		D-17-11		D-9-7		D-9-15		D-5-1	
Log Number		1075EL		1119EL		1120EL		1125El		1126EL		1127EL		1128El	
Sand Layer	Depth Range(ft)	Φ	K(md)	Φ	K(md)	Φ	K(md)	Φ	K(md)	Φ	K(md)	Φ	K(md)	Φ	K(md)
9460	9444-9476	0.123	7.140	0.108	3.944	0.114	5.003	0.165	27.138	0.096	1.442	0.118	4.439	0.123	4.765
9520	9513-9528	0.103	2.516	0.101	1.570	0.128	8.996	0.147	10.560	0.090	1.375	0.113	2.715	0.099	1.377
9540	9534-9549	0.116	4.239	0.092	1.253	0.095	1.280	0.154	13.788	0.081	0.635	0.089	0.874	0.098	1.325
9570	9562-9584	0.092	1.086	0.150	15.780	0.101	2.110	0.141	8.076	0.100	1.755	0.094	1.121	0.146	11.307
9620	9596-9638	0.102	2.097	0.107	2.569	0.151	22.722	0.119	4.484	0.106	6.768	0.112	3.076	0.133	10.216
9670	9660-9679	0.143	10.573	0.103	2.617	0.122	7.468	0.125	4.668	0.122	7.249	0.114	3.187	0.104	2.505
9710	9695-9717	0.141	10.042	0.090	1.261	0.093	1.804	0.100	1.391	0.095	1.579	0.108	2.822	0.116	4.414
9740	9730-9748	0.082	0.688	0.136	6.755	0.086	0.796	0.101	1.456	0.087	0.877	0.086	0.832	0.092	1.705
9800	9775-9806	0.114	5.196	0.094	1.232	0.124	4.500	0.105	1.967	0.105	3.135	0.109	3.792	0.134	6.891
9900	9886-9903	0.116	3.139	0.126	4.256	0.085	1.113	0.112	2.347	0.100	1.540	0.106	1.885	0.082	0.787
9970	9954-9977	0.104	2.576	0.130	5.054	0.128	4.586	0.121	3.935	0.086	1.265	0.100	1.615	0.094	1.494
10060	10055-10069	0.121	3.418	0.116	2.950	0.118	3.072	0.114	2.535	0.098	1.568	0.108	2.310	0.098	1.498
10100	10099-10113	0.102	1.671	0.094	1.576	0.098	1.425	0.098	1.267	0.094	1.302	0.108	2.370	0.091	1.108
10130	10121-10134	0.115	2.859	0.102	2.066	0.119	3.263	0.134	9.475	0.085	0.928	0.121	3.556	0.097	1.567
10310	10302-10318	0.146	11.499	0.145	9.902	0.115	2.692	0.101	1.565	0.102	92.269	0.088	0.922	0.115	3.575
10370	10362-10381	0.156	16.247	0.103	2.369	0.125	4.235	0.095	1.147	0.090	1.711	0.109	2.427	0.136	6.865
10470	10454-10484	0.093	1.818	0.119	3.268	0.105	2.102	0.102	1.662	0.090	1.227	0.103	2.122	0.117	3.085
10500	10491-10508	0.125	4.728	0.114	2.696	0.117	3.260	0.117	3.502	0.070	0.406	0.079	0.575	0.101	1.549
Well Name		D-9-4		D-9-9		D-6-5		D-9-1		B-32-10					
Log Number		1132El		1189EL		1174EL		1182EL		1149El					
Sand Layer	Depth Range(ft)	Φ	K(md)	Φ	K(md)	Φ	K(md)	Φ	K(md)	Φ	K(md)				
9460	9444-9476	0.119	5.304	0.119	6.876	0.115	3.989	0.132	15.867	0.083	0.705				
9520	9513-9528	0.116	3.903	0.155	14.628	0.120	4.667	0.101	2.115	0.085	0.763				
9540	9534-9549	0.131	6.561	0.092	1.036	0.118	4.241	0.155	15.834	0.121	4.527				
9570	9562-9584	0.096	1.855	0.131	13.590	0.097	2.084	0.117	3.203	0.103	2.250				
9620	9596-9638	0.130	7.717	0.102	2.977	0.105	2.078	0.125	5.830	0.092	1.448				
9670	9660-9679	0.113	3.481	0.097	1.661	0.122	3.958	0.123	4.008	0.093	1.140				
9710	9695-9717	0.073	0.455	0.115	3.453	0.127	6.185	0.095	1.256	0.107	2.329				
9740	9730-9748	0.090	1.096	0.086	0.796	0.136	6.523	0.131	6.429	0.099	1.573				
9800	9775-9806	0.103	2.799	0.101	2.204	0.115	3.908	0.117	3.537	0.107	2.576				
9900	9886-9903	0.105	2.428	0.136	6.653	0.126	4.468	0.118	3.325	0.087	0.832				
9970	9954-9977	0.105	1.886	0.132	5.619	0.108	2.806	0.116	3.337	0.113	3.334				
10060	10055-10069	0.086	0.894	0.126	4.333	0.081	0.698	0.131	5.314	0.121	3.412				
10100	10099-10113	0.117	2.939	0.116	3.211	0.127	4.570	0.124	3.962	0.107	2.038				
10130	10121-10134	0.124	3.972	0.126	5.558	0.109	2.133	0.113	2.481	0.117	3.000				
10310	10302-10318	0.143	8.856	0.110	2.307	0.122	3.717	0.137	7.314	0.141	8.235				
10370	10362-10381	0.138	7.235	0.117	3.425	0.128	4.603	0.108	2.323	0.102	2.260				
10470	10454-10484	0.104	2.556	0.119	3.775	0.108	3.228	0.096	1.930	0.110	2.256				
10500	10491-10508	0.125	4.281	0.083	0.698	0.093	1.065	0.138	7.265	0.128	5.115				

Table 10. Log Interpretation results for Citronelle

Log Number		850EL		778EL		833EL		873EL		886EL		888EL		1044EL	
Sand Layer	Depth Range(ft)	Φ	K(md)	Φ	K(md)	Φ	K(md)	Φ	K(md)	Φ	K(md)	Φ	K(md)	Φ	K(md)
9460	9444-9476	0.119	16.772	0.154	39.312	0.128	6.725	0.122	17.825	0.117	3.756	0.135	7.030	0.092	1.207
9520	9513-9528	0.084	1.469	0.112	7.820	0.135	6.775	0.122	8.601	0.088	1.232	0.169	26.918	0.112	4.423
9540	9534-9549	0.112	4.143	0.068	0.451	0.134	7.217	0.137	8.620	0.065	0.319	0.147	10.686	0.102	2.006
9570	9562-9584	0.117	5.100	0.129	7.788	0.142	9.347	0.089	2.659	0.085	2.970	0.148	11.509	0.106	2.708
9620	9596-9638	0.084	3.406	0.108	5.761	0.098	2.000	0.073	1.457	0.116	11.014	0.117	3.454	0.140	16.643
9670	9660-9679	0.075	0.929	0.094	3.892	0.112	2.448	0.081	2.492	0.096	2.173	0.093	2.096	0.083	0.700
9710	9695-9717	0.115	4.246	0.142	8.482	0.128	4.990	0.064	0.316	0.113	2.908	0.067	0.342	0.097	2.091
9740	9730-9748	0.140	7.887	0.065	0.321	0.103	2.600	0.079	1.135	0.070	0.467	0.070	0.393	0.077	0.531
9800	9775-9806	0.107	2.641	0.084	1.523	0.125	6.195	0.075	0.714	0.098	3.274	0.097	1.898	0.124	5.173
9900	9886-9903	0.093	1.898	0.118	3.651	0.115	3.013	0.062	0.277	0.110	2.224	0.070	0.511	0.099	2.331
9970	9954-9977	0.113	2.857	0.116	3.950	0.102	1.634	0.086	1.608	0.100	1.441	0.118	4.207	0.119	3.524
10060	10055-10069	0.128	4.709	0.130	5.015	0.129	4.920	0.130	5.619	0.119	3.494	0.078	0.825	0.118	2.977
10100	10099-10113	0.135	6.248	0.117	4.344	0.098	1.377	0.100	1.420	0.147	10.468	0.125	4.119	0.109	2.244
10130	10121-10134	0.085	1.478	0.128	4.771	0.110	2.137	0.113	2.844	0.141	8.321	0.133	5.663	0.101	1.558
10310	10302-10318	0.057	0.227	0.145	9.544	0.127	4.474	0.101	2.627	0.114	6.923	0.100	2.080	0.082	0.712
10370	10362-10381	0.092	1.985	0.143	8.737	0.111	2.432	0.143	9.141	0.067	0.402	0.126	4.910	0.138	7.148
10470	10454-10484	0.088	1.237	0.076	0.994	0.106	2.544	0.087	1.643	0.090	2.306	0.138	9.602	0.124	4.893
10500	10491-10508	0.121	3.468	0.083	1.543	0.101	3.325	0.135	6.324	0.091	2.430	0.110	2.403	0.115	2.754

Log Number		888EL		913EL		944EL		948EL		967EL		968EL		1032EL	
Sand Layer	Depth Range(ft)	Φ	K(md)	Φ	K(md)	Φ	K(md)	Φ	K(md)	Φ	K(md)	Φ	K(md)	Φ	K(md)
9460	9444-9476	0.135	7.030	0.175	39.115	0.091	1.067	0.128	9.712	0.121	4.788	0.136	12.735	0.158	21.412
9520	9513-9528	0.169	26.918	0.138	9.736	0.102	2.498	0.140	13.511	0.110	2.655	0.132	6.232	0.112	2.694
9540	9534-9549	0.147	10.686	0.175	35.558	0.084	0.730	0.154	14.663	0.114	3.207	0.083	0.959	0.129	5.334
9570	9562-9584	0.148	11.509	0.139	7.671	0.110	7.794	0.146	10.130	0.093	1.088	0.079	0.679	0.115	3.549
9620	9596-9638	0.117	3.454	0.116	5.276	0.101	2.789	0.107	3.993	0.111	4.084	0.095	2.591	0.142	9.361
9670	9660-9679	0.093	2.096	0.095	1.115	0.112	4.536	0.086	0.802	0.087	0.855	0.122	5.201	0.151	14.620
9710	9695-9717	0.067	0.342	0.156	26.523	0.106	2.737	0.136	23.358	0.084	0.749	0.104	2.173	0.123	3.769
9740	9730-9748	0.070	0.393	0.115	4.456	0.093	1.518	0.094	1.943	0.106	2.061	0.116	3.931	0.150	12.092
9800	9775-9806	0.097	1.898	0.147	14.127	0.112	3.221	0.087	1.035	0.103	2.091	0.097	2.115	0.132	6.289
9900	9886-9903	0.070	0.511	0.102	1.819	0.085	0.890	0.109	2.152	0.087	0.858	0.080	0.656	0.080	0.768
9970	9954-9977	0.118	4.207	0.142	9.052	0.100	1.897	0.120	3.441	0.127	5.278	0.135	6.273	0.123	4.121
10060	10055-10069	0.078	0.825	0.092	0.984	0.081	0.770	0.143	9.159	0.109	2.325	0.093	1.537	0.113	2.533
10100	10099-10113	0.125	4.119	0.082	0.729	0.127	4.511	0.096	1.228	0.120	3.323	0.122	3.627	0.117	3.038
10130	10121-10134	0.133	5.663	0.109	2.585	0.081	0.658	0.126	4.733	0.116	2.767	0.123	3.903	0.110	2.286
10310	10302-10318	0.100	2.080	0.107	2.198	0.136	6.720	0.127	4.513	0.147	11.009	0.118	3.241	0.146	11.328
10370	10362-10381	0.126	4.910	0.106	2.175	0.137	7.032	0.140	7.833	0.141	8.517	0.127	4.547	0.145	10.076
10470	10454-10484	0.138	9.602	0.110	2.390	0.127	7.016	0.128	5.146	0.104	2.399	0.099	2.317	0.108	3.275
10500	10491-10508	0.110	2.403	0.104	2.286	0.097	1.251	0.123	3.924	0.143	8.699	0.122	3.788	0.108	2.203

Log Number		969EL		990EL		991EL		1014EL		1020EL	
Sand Layer	Depth Range(ft)	Φ	K(md)	Φ	K(md)	Φ	K(md)	Φ	K(md)	Φ	K(md)
9460	9444-9476	0.116	4.943	0.142	10.218	0.113	3.427	0.066	2.412	0.160	19.354
9520	9513-9528	0.118	3.392	0.138	7.359	0.121	4.234	0.068	0.669	0.091	1.184
9540	9534-9549	0.078	0.547	0.132	5.642	0.124	4.206	0.044	0.217	0.086	0.807
9570	9562-9584	0.085	0.761	0.137	8.641	0.110	2.462	0.086	0.800	0.136	8.258
9620	9596-9638	0.096	2.108	0.150	15.549	0.107	2.730	0.076	0.740	0.103	3.046
9670	9660-9679	0.114	4.963	0.125	4.353	0.136	6.668	0.062	0.389	0.164	21.921
9710	9695-9717	0.109	2.839	0.125	4.326	0.079	0.585	0.051	0.176	0.076	0.509
9740	9730-9748	0.072	0.440	0.119	3.494	0.113	3.353	0.056	0.303	0.108	3.344
9800	9775-9806	0.124	5.685	0.125	4.160	0.101	2.081	0.077	0.784	0.107	3.261
9900	9886-9903	0.081	0.676	0.107	1.890	0.093	1.139	0.045	0.136	0.114	2.968
9970	9954-9977	0.116	4.051	0.107	2.055	0.115	2.698	0.055	0.303	0.123	4.120
10060	10055-10069	0.114	2.575	0.110	2.380	0.091	1.092	0.068	0.488	0.131	5.308
10100	10099-10113	0.096	1.668	0.108	2.004	0.113	2.620	0.043	0.126	0.117	3.175
10130	10121-10134	0.112	2.386	0.120	3.556	0.110	2.134	0.039	0.107	0.129	4.886
10310	10302-10318	0.086	1.278	0.131	5.475	0.127	4.690	0.053	0.190	0.130	5.133
10370	10362-10381	0.126	4.293	0.128	4.693	0.146	10.123	0.047	0.148	0.126	5.131
10470	10454-10484	0.129	5.641	0.117	3.004	0.102	1.995	0.044	0.137	0.078	0.595
10500	10491-10508	0.110	2.329	0.108	2.033	0.130	5.207	0.092	1.007	0.133	6.034

NUMERICAL MODELING (PERMEABILITY REALIZATIONS)

The original simulation model was modified based on the derived porosity and permeability from the well logs. Preliminary results of the simulation runs are shown in the following figures. The new (revised) porosity and permeability distributions are shown in Figure 32 and Figure 33, respectively.

The distribution of injected CO_2 into saline formation is initially dominated by gravity segregation which is related to the permeability anisotropy of the saline formation.

The CO_2 mole fraction at the end of injection period in both heterogeneous and homogeneous models is shown in Figure 34 and Figure 35, respectively. Please note the major differences in CO_2 plum distributions in the reservoir as the heterogeneities mentioned above are introduced in the model. Figure 36 and Figure 37 illustrate CO_2 mole fraction after 30 years of monitoring in both models. The permeability in homogenous model is higher compared to the heterogeneous model, causing more rapid dispersion of injected CO_2 over a wider area. This, in turn will cause wider plume and higher CO_2 concentration in the homogenous model.

Since CO_2 is more mobile than brine, in the homogenous formation model, viscous fingering is dominant while in the heterogeneous formation gravity segregation has more substantial impact. Figure 37 demonstrates the change in the CO_2 mole fraction over 30 years of monitoring in the heterogeneous model.

Due to the density differences between CO_2 and brine, buoyancy force has a significant influence on the CO_2 gas distribution in the reservoir and causes the CO_2 plume to migrate upward. This can be clearly seen in the simulation model results.

Gas saturation in the area of review (AoR) after the injection period and at the end of the monitoring period is demonstrated in Figure 39 through Figure 42 . The layers with the higher permeable in the homogenous model have more gas saturation. The layers with the lower permeability in the heterogeneous model have smaller plume extent and higher saturation due to lower mobility of the CO_2 Plume. The homogenous model with its higher permeability has a larger plume extent and lower saturation due to rapid dispersal of the gas from the injection zone. The change in gas saturation over the 30 years of monitoring period is shown in Figure 43.

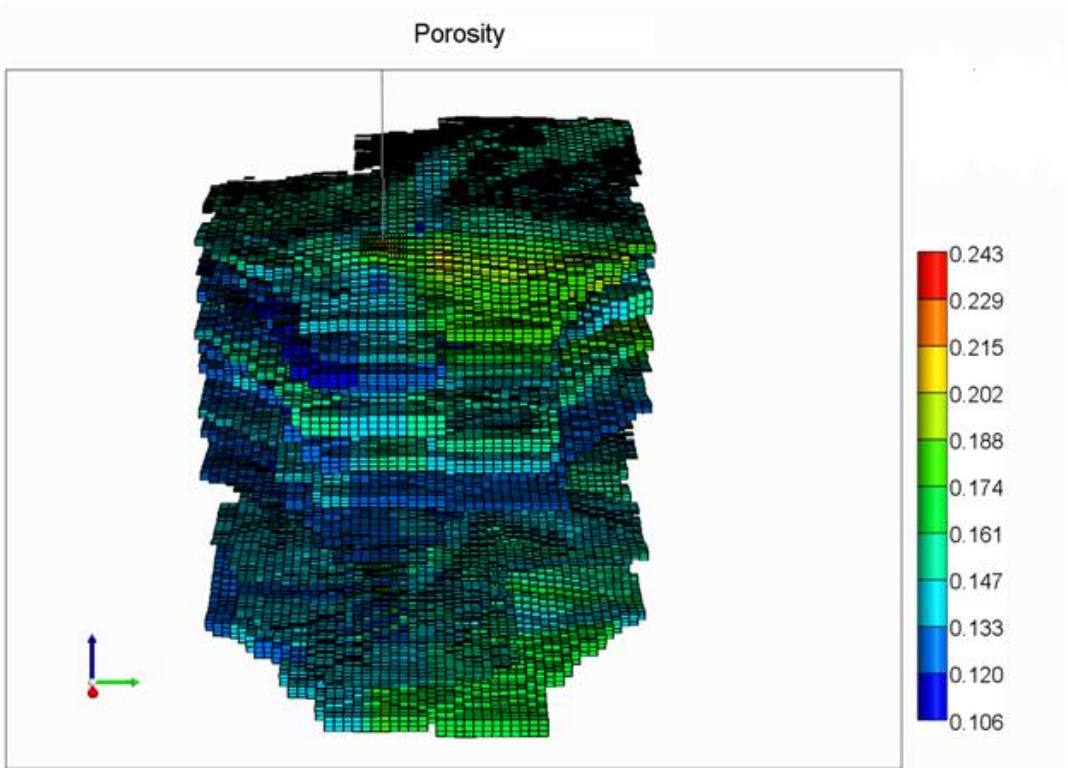

Figure 32. New and revised porosity distribution

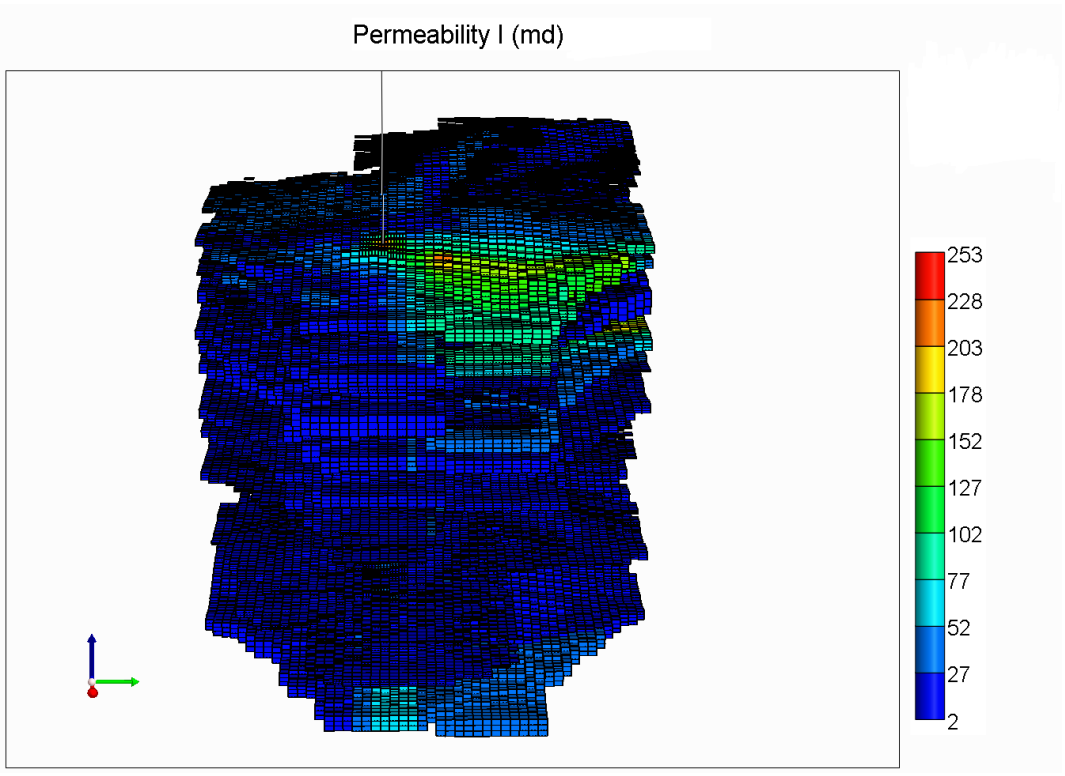

Figure 33. New and revised permeability distribution

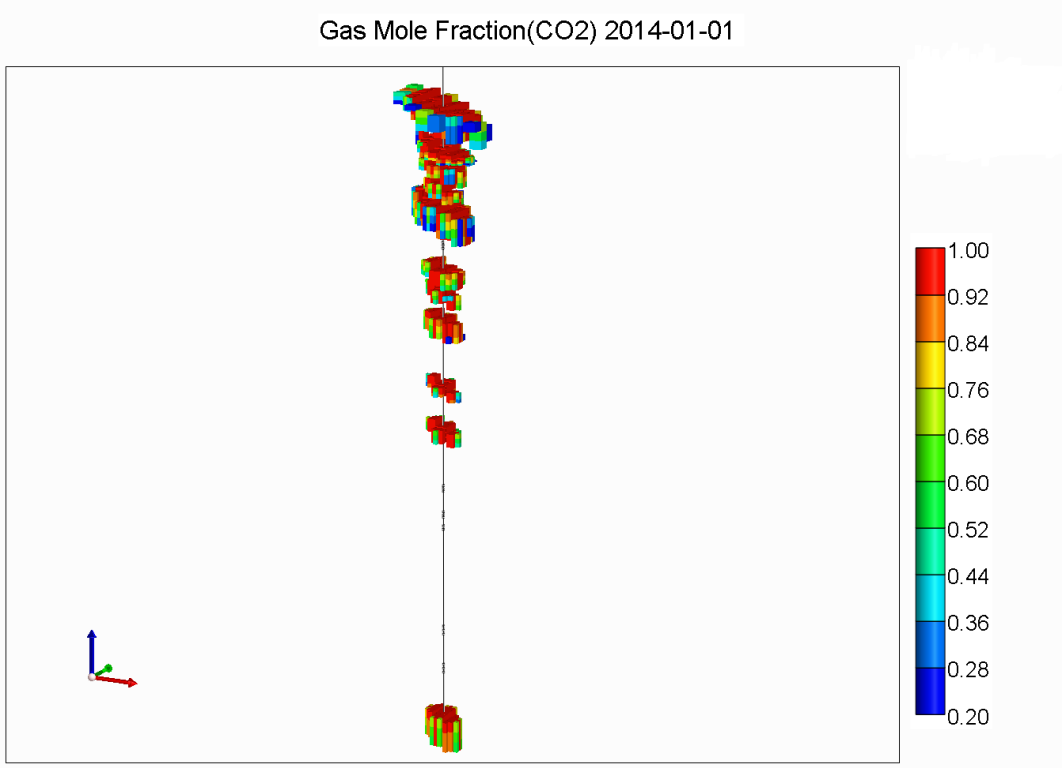

Figure 34. CO_2 mole fraction at the end of the injection period in heterogeneous model

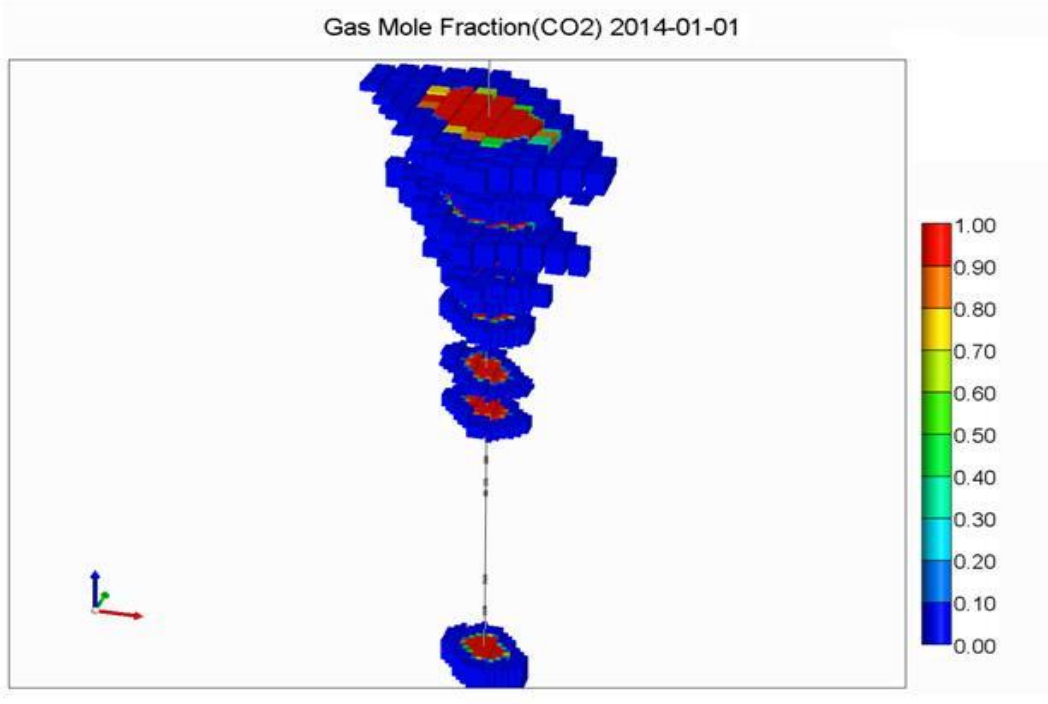

Figure 35. CO_2 mole fraction at the end of the injection period in homogenous model

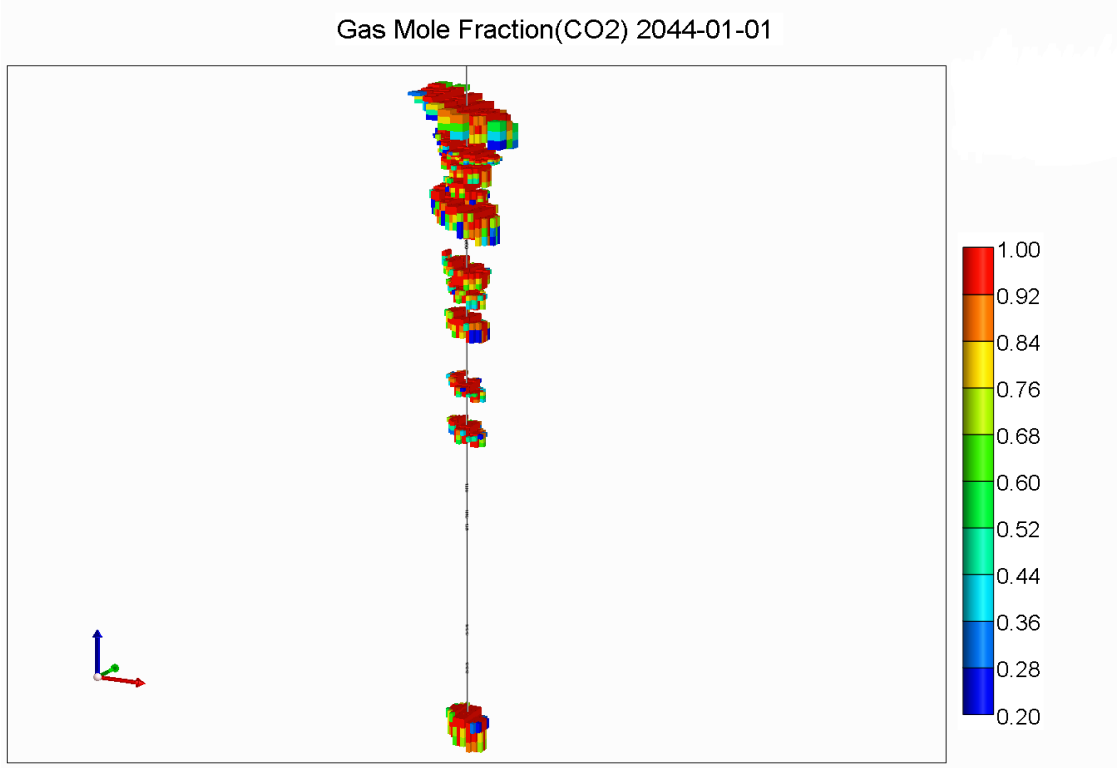

Figure 36. CO_2 Gas mole fraction after 30 years of monitoring in heterogeneous model

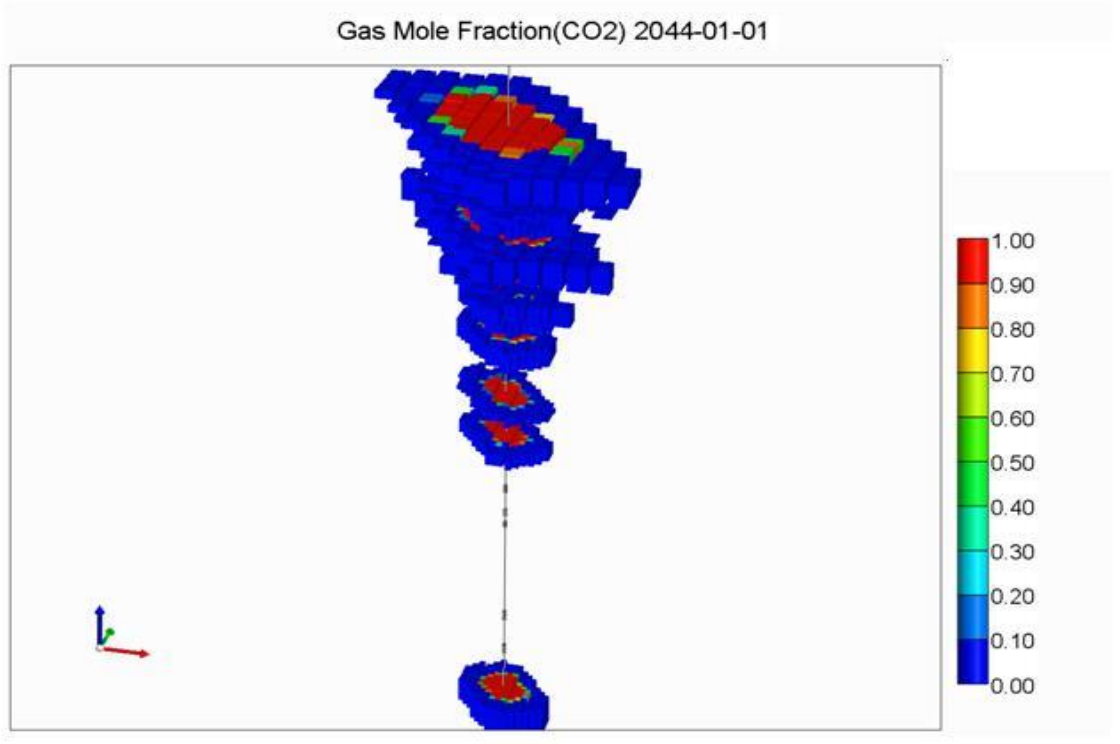

Figure 37. CO_2 Gas mole fraction after 30 years of monitoring in homogenous model

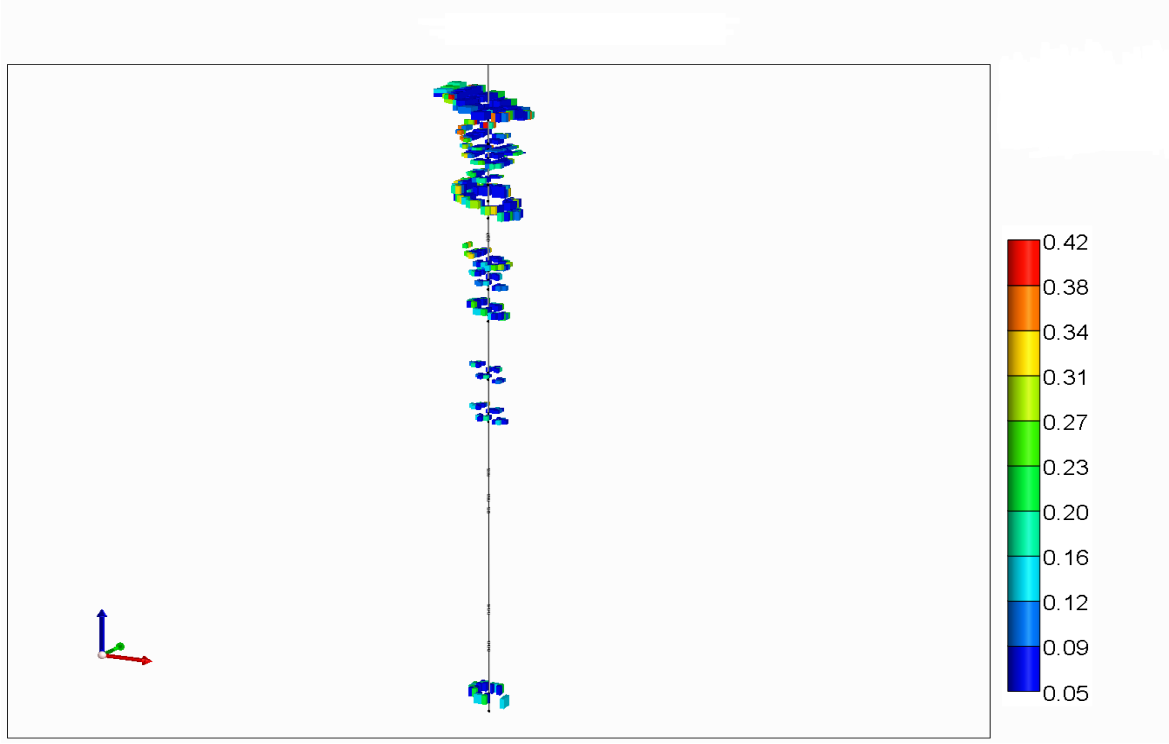

Figure 38. Change in CO_2 Gas mole fraction over 30 years of monitoring in heterogeneous model

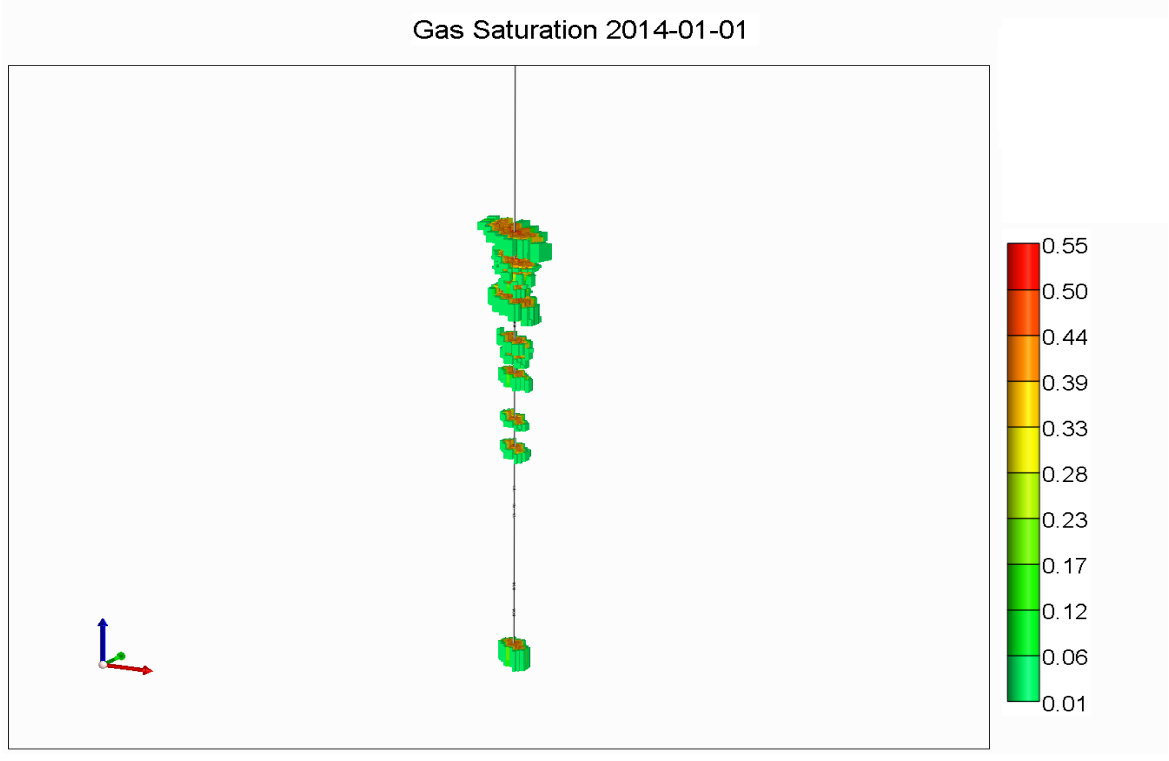

Figure 39. Gas Saturation at the end of the injection in heterogeneous model

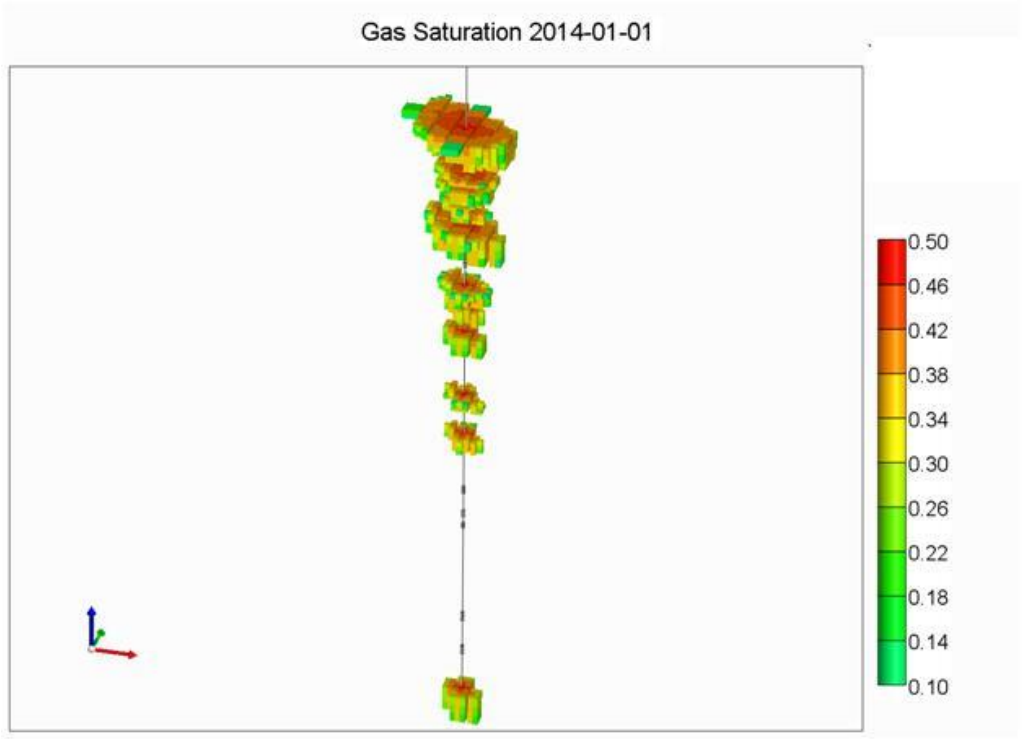

Figure 40. Gas Saturation at the end of the injection in homogenous model

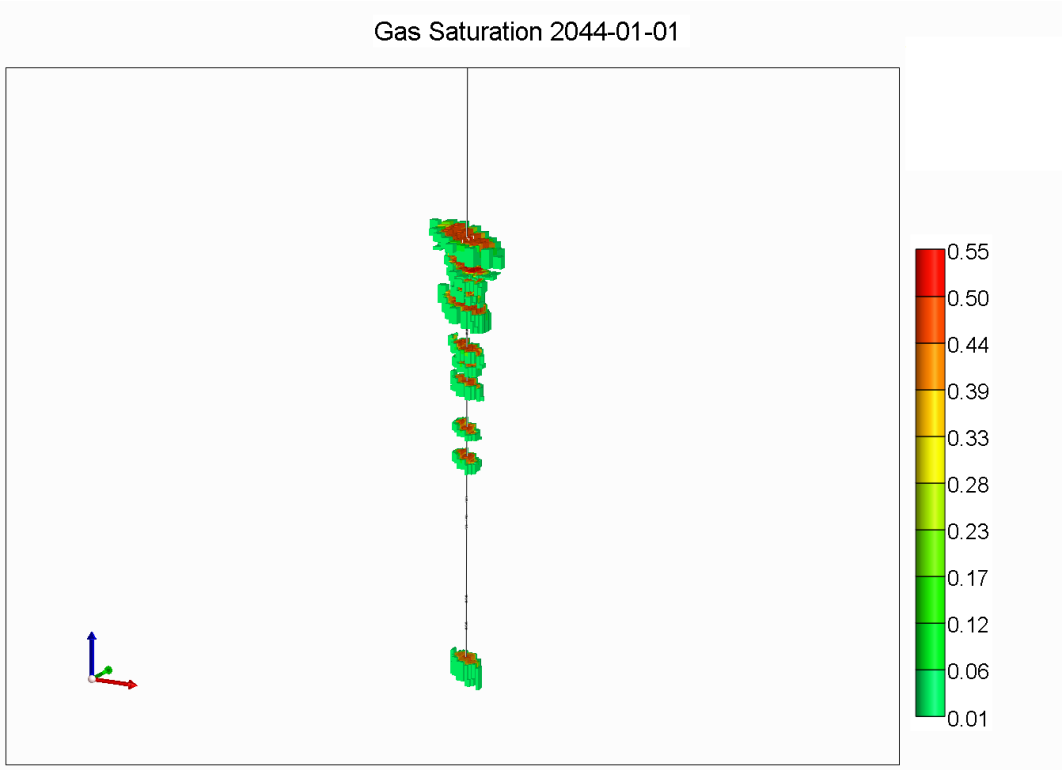

Figure 41. Gas saturation after 30 years of monitoring in heterogeneous model

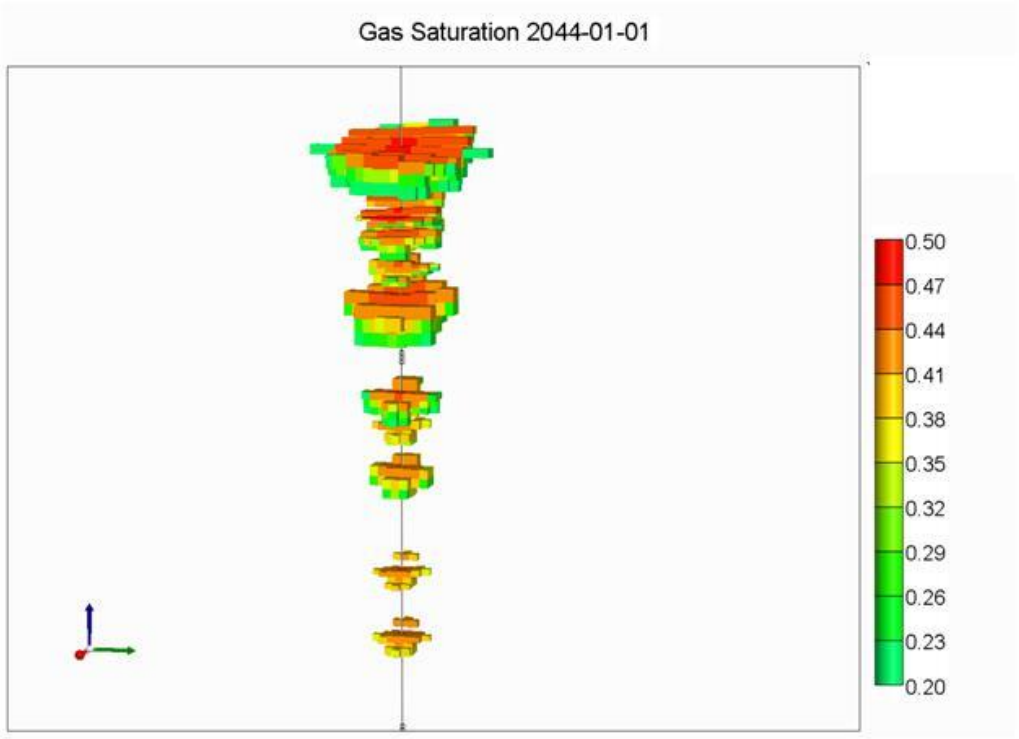

Figure 42. Gas Saturation after 30 years of monitoring in homogenous model

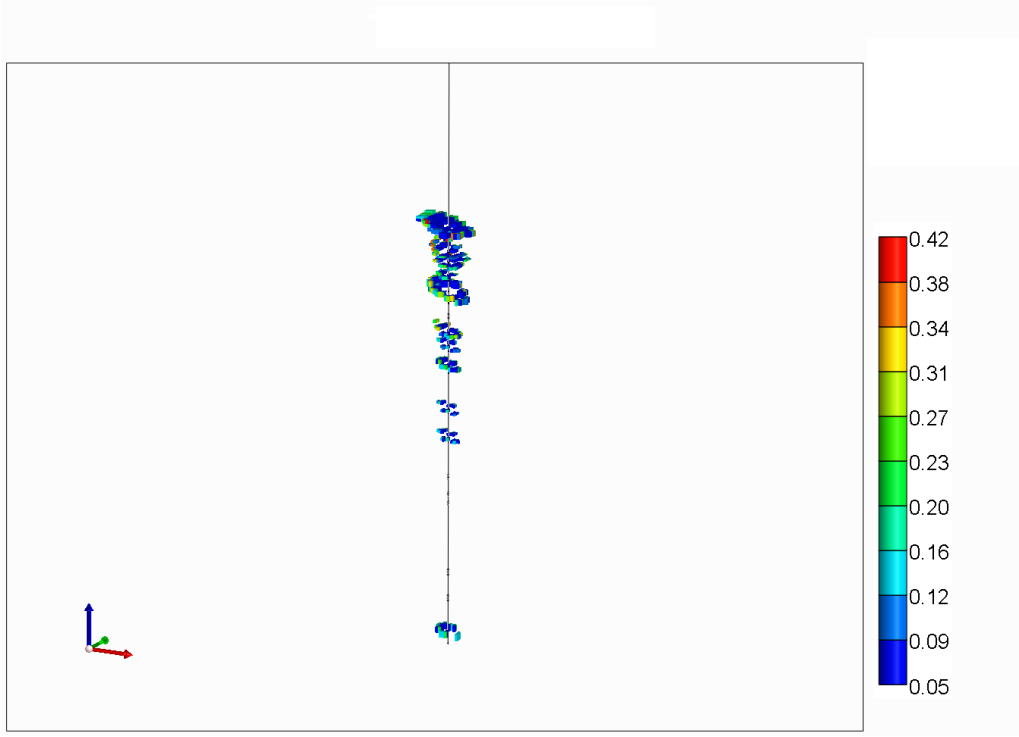

Figure 43. Change in gas saturation over 30 years of monitoring in heterogeneous model

The Area of Review (AoR) is defined as the farthest reach of the tangible CO_2 plume. This value has been reported to be 1,200 ft. from the injection well. Based on the result of our models (homogeneous and heterogeneous models), CO_2 will be extent approximately 1,800 ft. from the proposed injection well. This has been demonstrated in Figure 44.

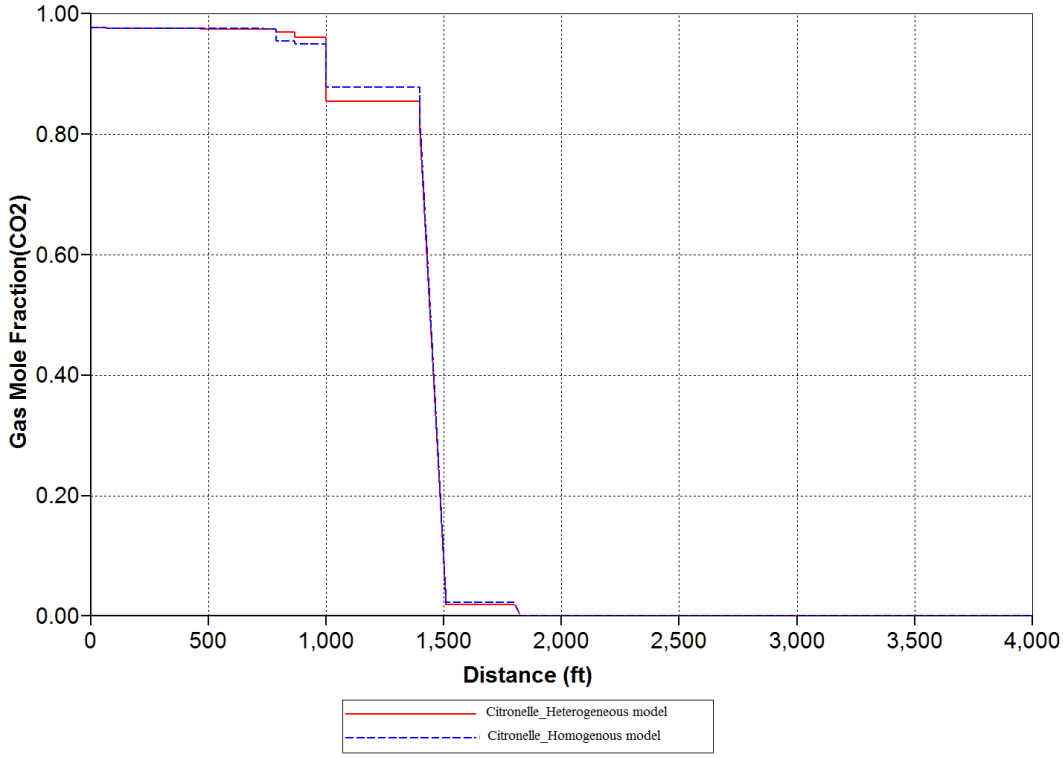

Figure 44. The distribution of CO_2 around the injection well D-9-7 in both heterogeneous and homogenous models.

The objective of this section of the report was to demonstrate the issues that the WVU team had identified with the original model. The conclusion of the study up to this point was that in order to have a realistic view of distribution of CO_2 in this formation, a more serious effort need to be put forward in order to develop a robust numerical model for this project.

Given the WVU team's experience with the oil and gas industry, and the state-of-the-art static and dynamic model development, it became obvious that the existing numerical model will not pass the potential scrutiny by the oil and gas professionals. Therefore, to base this project on a solid foundation, the WVU team decided to develop a new and robust static model and use it as the basis for the dynamic flow model. What is covered in the next several sections is a summary of the efforts that resulted in the numerical model developed by the WVU team for this project for the Citronelle field.

GEOLOGICAL MODEL DEVELOPMENT

In the original model the resistivity logs were used to calculate porosity. Then the porosity-permeability correlations were utilized to generate the permeability maps. Using induction log to calculated porosity results in large differences in porosity and consequently permeability vales. Results of such calculations for the injection well D-9-7 are shown in Table 11.

This problem were investigated even further by incorporating the difference in the porosity and permeability calculations into multiple reservoir realizations. The differences between these realizations are shown in Table 12. The porosity and permeability maps based on the log data for different realizations were created and used to modify the simulation model.

Table 11**.** Porosity and permeability values for the injection well D-9-7 based on different logs

log		Resistivity log		Induction Log	
Well Name		D-9-7		D-9-7	
Sand Layer	Depth Range(ft)	Φ	K(md)	Φ	K(md)
9460	9444-9476	0.10	1.442	0.22	229.976
9520	**9513-9528**	**0.09**	**1.375**	**0.20**	**98.295**
9540	9534-9549	0.08	0.635	0.19	64.263
9570	**9562-9584**	**0.10**	**1.755**	**0.18**	**42.013**
9620	9596-9638	0.11	6.768	0.21	150.352
9670	**9660-9679**	**0.12**	**7.249**	**0.16**	**17.957**
9710	9695-9717	0.09	1.579	0.19	64.263
9740	**9730-9748**	**0.09**	**0.877**	**0.18**	**42.013**
9800	9775-9806	0.10	3.135	0.18	42.013
9900	**9886-9903**	**0.10**	**1.540**	**0.18**	**42.013**
9970	9954-9977	0.09	1.265	0.18	42.013
10060	**10055-10069**	**0.10**	**1.568**	**0.19**	**64.263**
10100	10099-10113	0.09	1.302	0.19	64.263
10130	**10121-10134**	**0.09**	**0.928**	**0.18**	**42.013**
10310	10302-10318	0.10	1.600	0.19	64.263
10370	**10362-10381**	**0.09**	**1.711**	**0.18**	**42.013**
10470	10454-10484	0.09	1.227	0.19	64.263
10500	**10491-10508**	**0.07**	**0.406**	**0.19**	**64.263**

Table 12. Porosity and permeability for different reservoir realizations

Realization	Porosity Log	Permeability Correlation
R1	Homogenous	Homogenous
R2	Resistivity	28.8185 * { Porosity } ** 1.1063
R3	Resistivity	0.0429 * EXP (37.3657 * { Porosity })
R4	Resistivity	5 * EXP10 (6) * { Porosity } ** 7.682
R5	Resistivity	1.2582 * EXP (27.814 * { Porosity })
R6	Induction	28.8185 * { Porosity } ** 1.1063
R7	Induction	0.0429 * EXP (37.3657 * { Porosity })
R8	Induction	5 * EXP10 (6) * { Porosity } ** 7.682
R9	Induction	1.2582 * EXP (27.814 * { Porosity })

Based on the geological information which is provided in the report (SECARB 2010), two cross sections A-A' and B-B' had been considered for log analysis in order to build the original geological model. The wells which are located on these two cross sections are shown in Figure 45 and the target well in both cross sections is injection well D-9-7.

By going through the well logs, it was noticed that the top and thickness of the sand layers in the original simulation model do not match those from the well logs. As it is shown in Figure 46, the sand layers in the injection well D-9-7 are picked based on the highest resistivity and highest SP values. Using the same logic in other wells located on the cross sections, logs and geological model are not compatible with each other.

To demonstrate this problem clearly, the top and the bottom of first (from above) five sand layers in the geological model, Table 13, is displayed on the corresponding log in Figure 47 and Figure 48 for well D-9-1 and D-4-14 respectively. Well D-4-14 is located near the injection well on cross section A-A' and well D-9-1 has the same position on cross section B-B'.

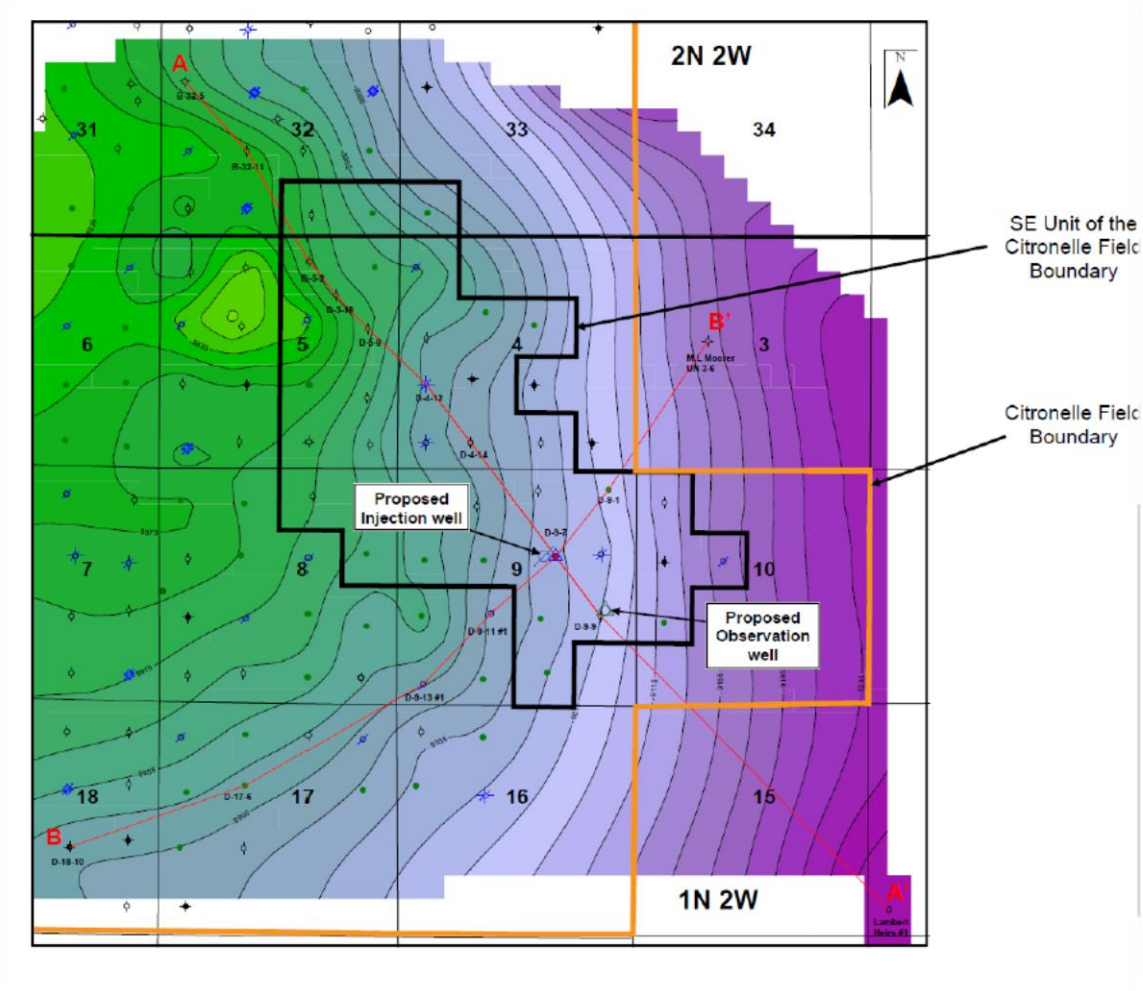

Figure 45. The location of cross section A-A' and B-B' and the wells on them, ARI report[7]

Sand Layer	Sand Layer Top and Bottom (feet below sea-level)	Thicknes s (ft)
9420	9,414 – 9,421	6
9430	9,427 – 9,438	12
9460	9,444 – 9,476	32
9520	9,513 - 9,528	15
9540	9,534 - 9,549	15
9570	9,562 - 9,584	22
9620	9,596 - 9,638	42
9670	9,660 - 9,679	19
9710	9,695 - 9,717	22
9740	9,730 - 9,748	18
9800	9,775 - 9,806	30
9840	9,833 - 9,843	10
9870	9,868 - 9,874	6
9900	9,886 - 9,903	18
9940	9,929 - 9,939	10
9970	9,954 - 9,977	24
10030	10,016 - 10,025	9
10040	10,037 - 10,049	11
10060	10,055 - 10,069	15
10100	10,099 - 10,113	15
10130	10,121 - 10,134	13
10230	10,223 - 10,231	7
10310	10,302 - 10,318	16
10370	10,362 - 10,381	20
10400	10,396 - 10,412	16
10470	10,454 -10,484	31
10500	10,491 - 10,508	18

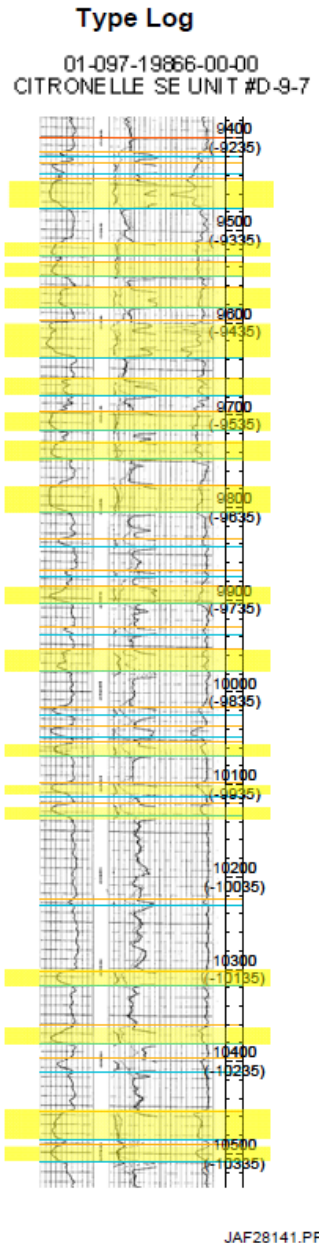

Figure 46. The sand layers of injection well D-9-7 and its corresponding well log, the report (SECARB 2010).

Table 13. Top and Bottom of well D-9-1 and D-4-14 based on Geological Model

D-9-1		D-4-14	
top	bottom	top	bottom
9312.9	9323.6	9226.5	9231.6
9323.6	9334.3	9231.6	9236.7
9334.3	9345	9236.7	9241.8
9377.6	9380.767	9281.6	9287.567
9380.767	9383.933	9287.567	9293.533
9383.933	9387.1	9293.533	9299.5
9399.8	9403.9	9304	9308.433
9403.9	9408	9308.433	9312.867
9408	9412.1	9312.867	9317.3
9437.7	9440.633	9326.7	9328.733
9440.633	9443.567	9328.733	9330.767
9443.567	9446.5	9330.767	9332.8
9468.8	9478.167	9349.8	9370.167
9478.167	9487.533	9370.167	9390.533
9487.533	9496.9	9390.533	9410.9

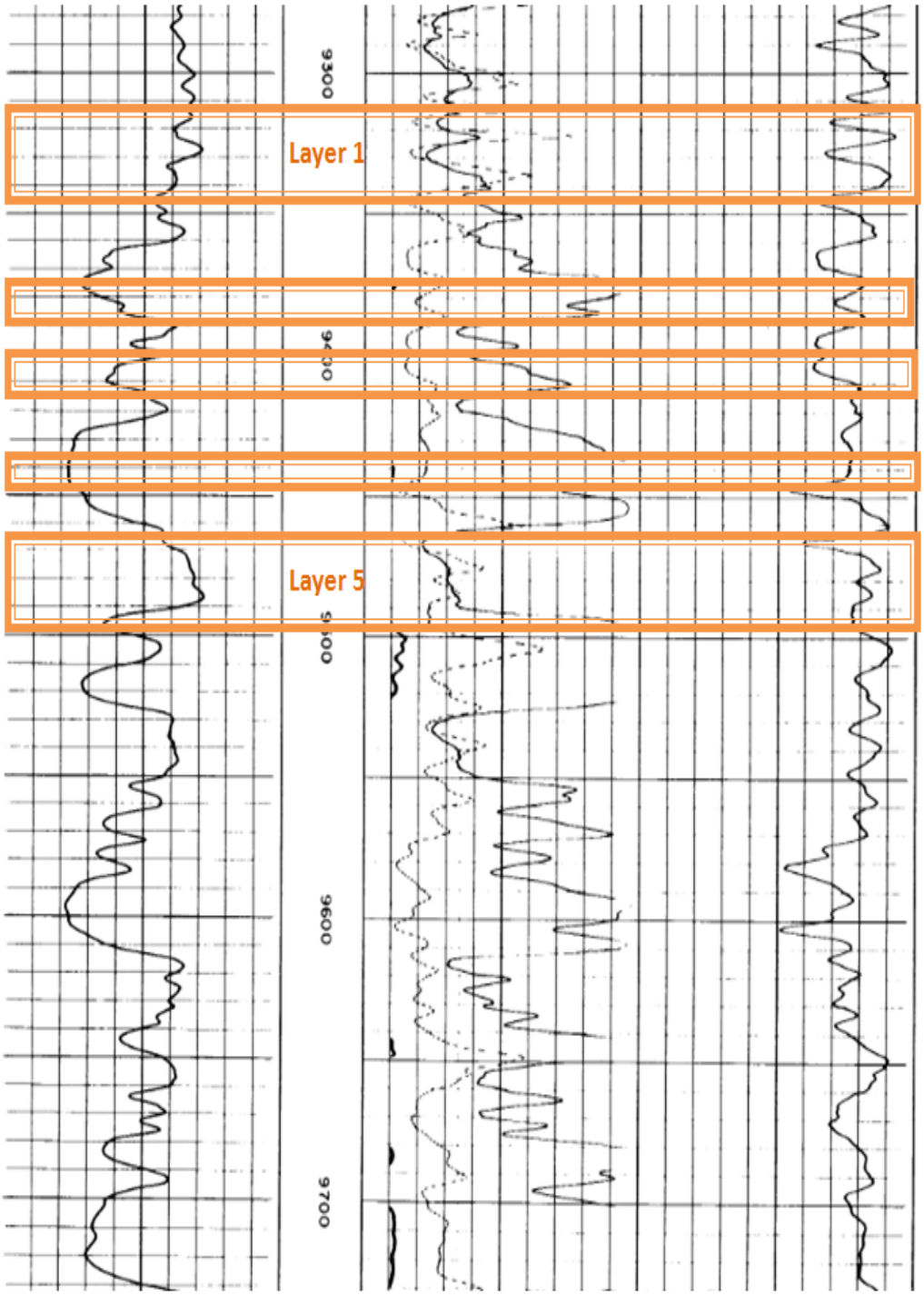

Figure 47. The location of top five sand layers on the resistivity and SP log based on the geological model, Well D-9-1

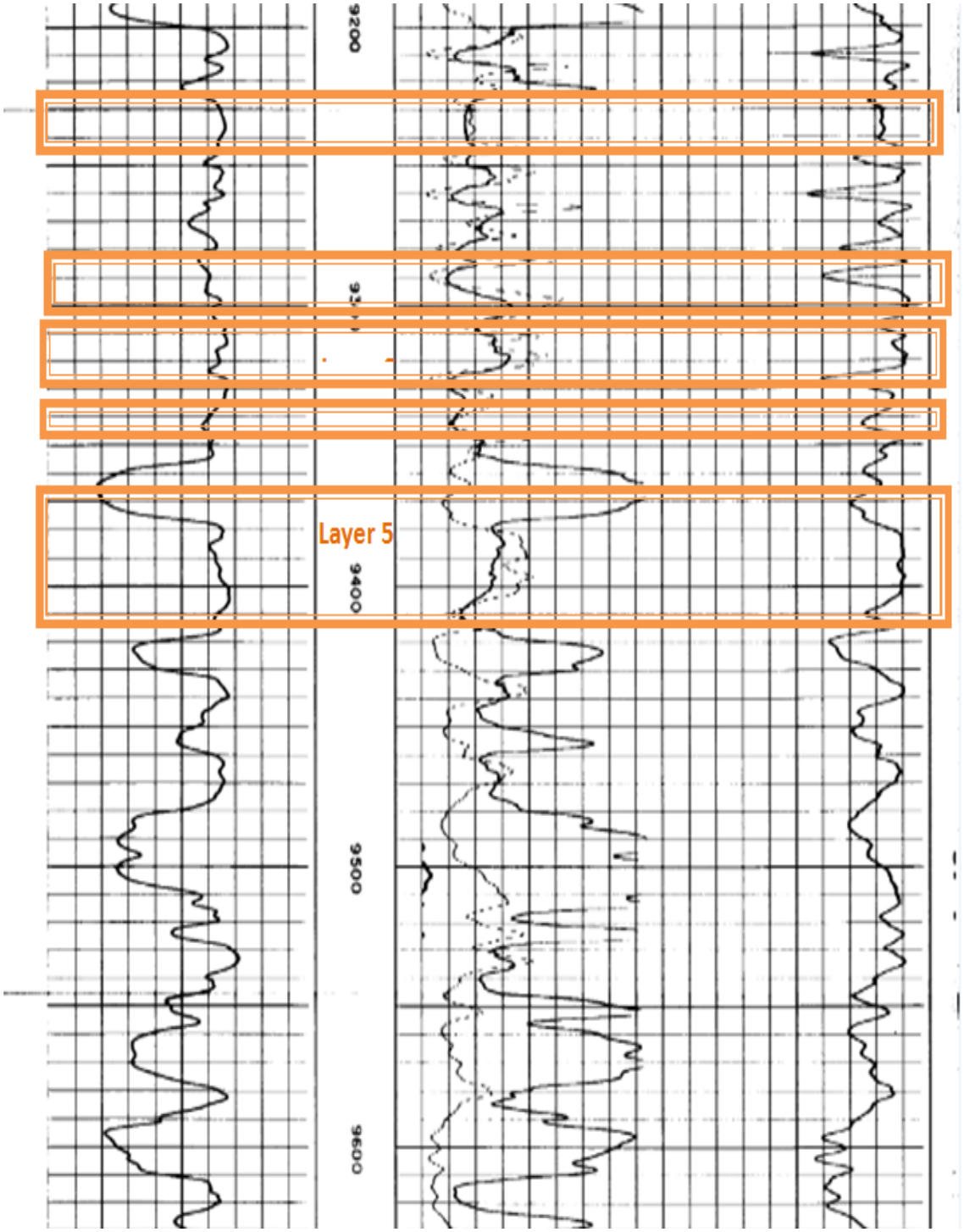

Figure 48. The location of top five sand layers on the resistivity and SP log based on the geological model, Well D-4-14

The core and well log data for well D-9-8 were obtained. This well is considered as the observation well and is close to the injection well. The new density log was interpreted for this well and was compared to the one that was already available. The latter interpreted values are different from the former ones (Table 14). The top and bottoms are not matching with the geological model either. The information from this well can be included in the previous maps in order to modify the top and thickness distribution.

Considering the aforementioned observations, a new geological model was built. This new WVU geological model honors all the information obtained from the well log and the cores.

Table 14. Porosity based on Resistivity and Induction log and Density Porosity for well D-9-8

D-9-8				new log	D-9-8				new log
top	bottom	ϕ(resistivity)	ϕ(Induction)	Dendity Porosity	top	bottom	ϕ(resistivity)	ϕ(Induction)	Dendity Porosity
9300.5	9314.1	0.1357	0.1534	0.2227	9648.2	9658.1	0.1160	0.1596	0.1847
9314.1	9327.8	0.1487	0.1597	0.1217	9658.1	9667.9	0.1769	0.2139	0.1658
9327.8	9341.4	0.1524	0.1787	0.1986	9752.7	9759.1	0.0892	0.1711	0.1868
9359.2	9363.0	0.1038	0.1847	0.1860	9759.1	9765.6	0.0809	0.1774	0.1659
9363.0	9366.8	0.0864	0.1877	0.1867	9765.6	9772.0	0.0755	0.1669	0.2010
9366.8	9370.6	0.0866	0.1701	0.2303	9822.8	9829.9	0.1214	0.1313	0.2719
9391.2	9399.5	0.1170	0.1986	0.2593	9829.9	9836.9	0.1280	0.1272	0.2313
9399.5	9407.9	0.0964	0.2047	0.2095	9836.9	9844.0	0.1263	0.1237	0.2218
9407.9	9416.2	0.1011	0.2272	0.2242	9925.8	9929.3	0.1300	0.1259	0.2391
9432.1	9436.0	0.1030	0.3135	0.2292	9929.3	9932.9	0.1282	0.1313	0.1552
9436.0	9439.9	0.1492	0.3620	0.2121	9932.9	9936.4	0.1332	0.1578	0.1444
9439.9	9443.8	0.0997	0.1967	0.3000	9967.7	9969.7	0.1136	0.1745	0.1215
9462.4	9476.5	0.1535	0.1470	0.1798	9969.7	9971.6	0.1015	0.1785	0.1212
9476.5	9490.6	0.1347	0.1941	0.1266	9971.6	9973.6	0.0982	0.1765	0.1170
9490.6	9504.7	0.0952	0.1910	0.1858	9971.4	9972.9	0.0977	0.1781	0.2020
9503.6	9506.8	0.0914	0.2218	0.2053	9972.9	9974.4	0.0987	0.1746	0.1926
9506.8	9510.0	0.0931	0.2138	0.2059	9974.4	9975.9	0.0985	0.1734	0.1480
9510.0	9513.2	0.0854	0.2082	0.2111	10159.2	10162.3	0.0966	0.1464	0.1144
9561.8	9571.6	0.1415	0.1489	0.2003	10162.3	10165.3	0.0869	0.1242	0.4468
9571.6	9581.4	0.1141	0.2218	0.2591	10165.3	10168.4	0.0805	0.1178	0.2384
9581.4	9591.2	0.1009	0.2569	0.2294	10231.6	10241.3	0.1319	0.1425	0.0685
9599.0	9605.2	0.0829	0.1968	0.2419	10241.3	10251.1	0.1057	0.1590	0.2492
9605.2	9611.5	0.1074	0.2922	0.2542	10251.1	10260.8	0.1177	0.1291	0.2613
9611.5	9617.7	0.1150	0.2251	0.2101	10324.3	10341.2	0.1279	0.1374	0.1252
9638.4	9648.2	0.1499	0.1871	0.1449	10341.2	10358.2	0.1153	0.1755	0.1336
					10358.2	10375.1	0.1044	0.1438	0.1230

WVU NUMERICAL MODELING BASED ON POROSITY LOGS

With incorporating the data obtained from well log interpretation, a vertically and laterally heterogeneous model was generated that honored all the detail information extracted from a large number of wells. The original simulation model was modified based on the derived porosity and permeability from the resistivity logs for nine different reservoir realizations.

Preliminary results of the simulation runs are shown in the following figures. The porosity and permeability distributions are shown in Figure 49 to Figure 57.

Figure 49. Porosity Distribution, Realization case number 1

Figure 50. Porosity Distribution, Realization case number 2

Figure 51. Porosity Distribution, Realization case number 3

Figure 52. Porosity Distribution, Realization case number 4

Figure 53. Porosity Distribution, Realization case number 5

Figure 54. Porosity Distribution, Realization case number 6

Figure 55. Porosity Distribution, Realization case number 7

Figure 56. Porosity Distribution, Realization case number 8

Figure 57. Porosity Distribution, Realization case number 9

As mentioned before, the Area of Review is defined as the farthest reach of the tangible CO_2 plume. This value has been reported to be 1,200 ft. from the injection well. Based on the results

of the WVU models (9 realizations), CO_2 will reach up to a distance of approximately 1,800 ft. from the proposed injection well in the model with highest amount of injected CO_2. This has been demonstrated in Figure 58. The possibility of CO_2 injection into reservoir has been studied in these cases as well. The result is illustrated in Figure 59.

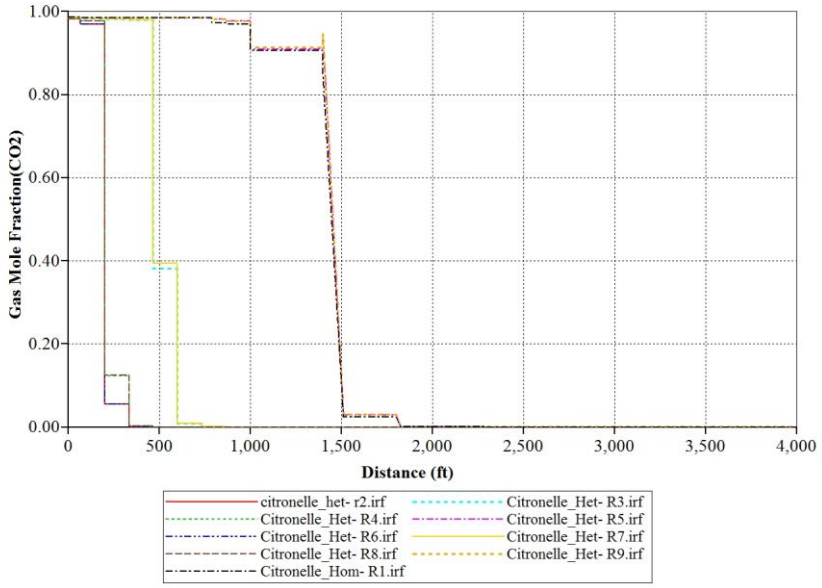

Figure 58. The distance of CO_2 extension from the injection well D-9-7 in whole nine models

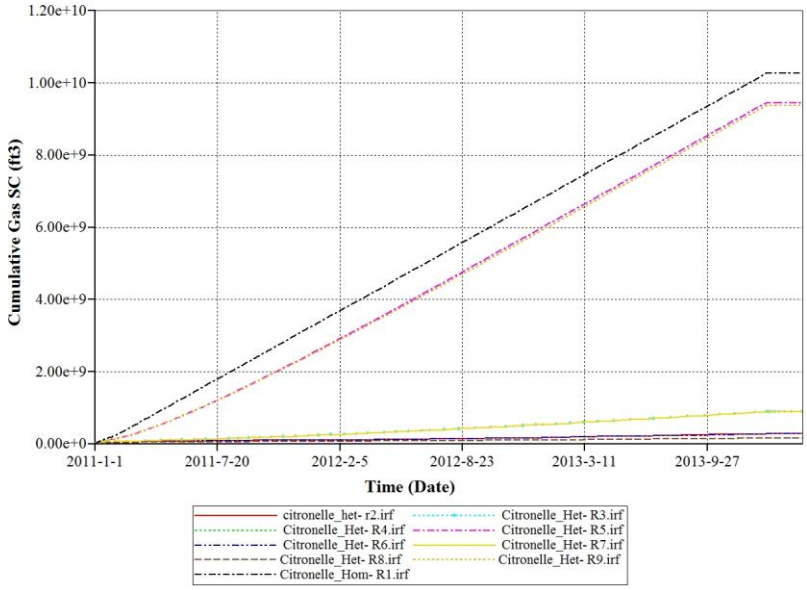

Figure 59. Cumulative Gas against Time for all different realization cases

GEOLOGICAL MODEL-SAND LAYER DEVELOPMENT

As it was mentioned before, two cross sections A-A' and B-B' have been considered for log analysis in order to build the geological model. The wells which are located on these two cross sections are shown in Figure 60 and the target well in both cross sections is injection well D-9-7. As it was mentioned in the previous section, going through the well logs of some of the existing wells it was noticed that the top and thickness of the sand layers in the original simulation model do not match those from the well logs. Since logs and geological model were not compatible with each other, a new geological model was created by the WVU team.

Geographix software was used to accomplish the building of the new WVU geological model. For the WVU geological model three different cross sections A-A', B-B' and C-C' were considered (Figure 61). The injection well D-9-7 is the well which was considered as a reference well in all three cross sections. Figure 61 shows the location of the wells on the cross sections.

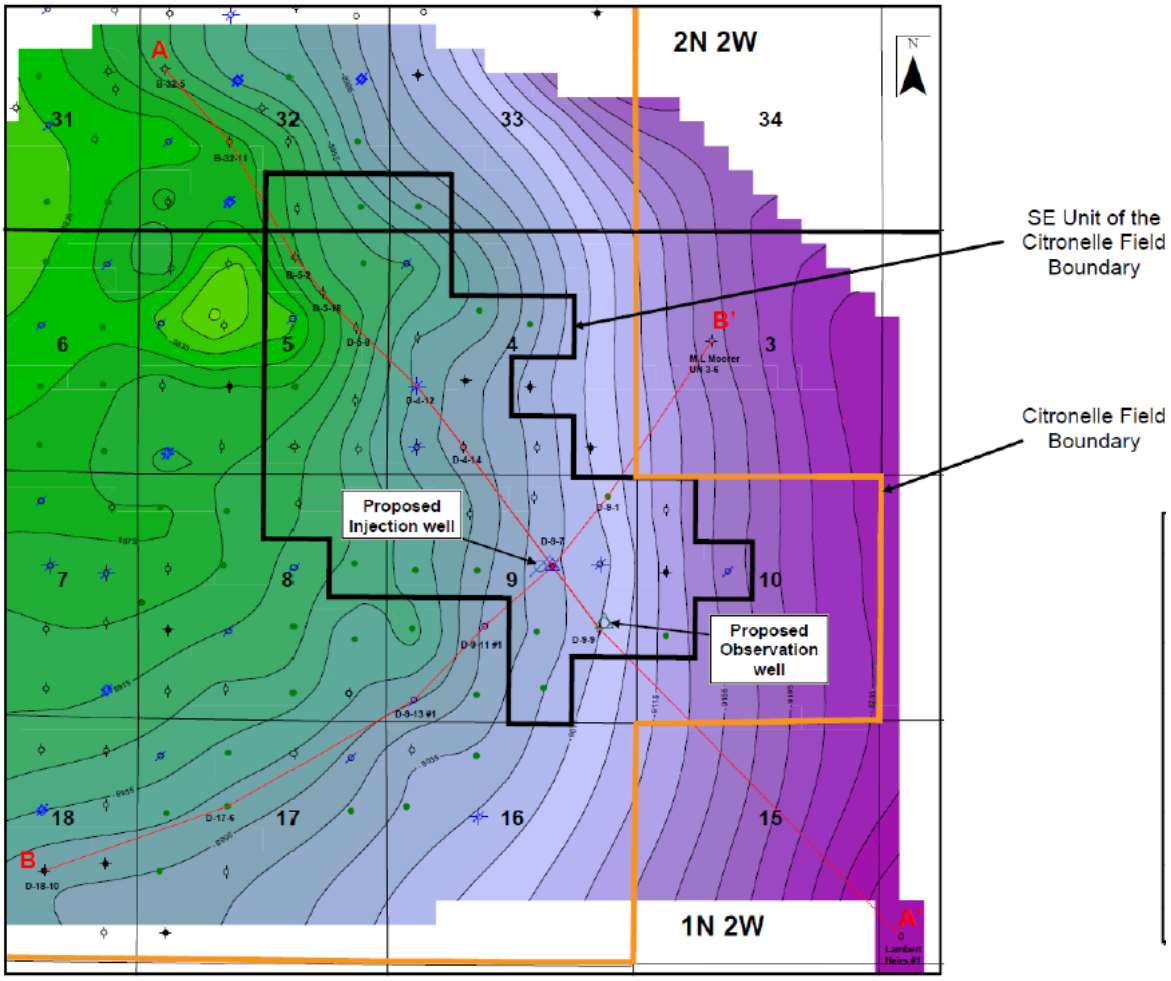

Figure 60. The location of cross sections A-A' and B-B' and the wells on them, ARI report

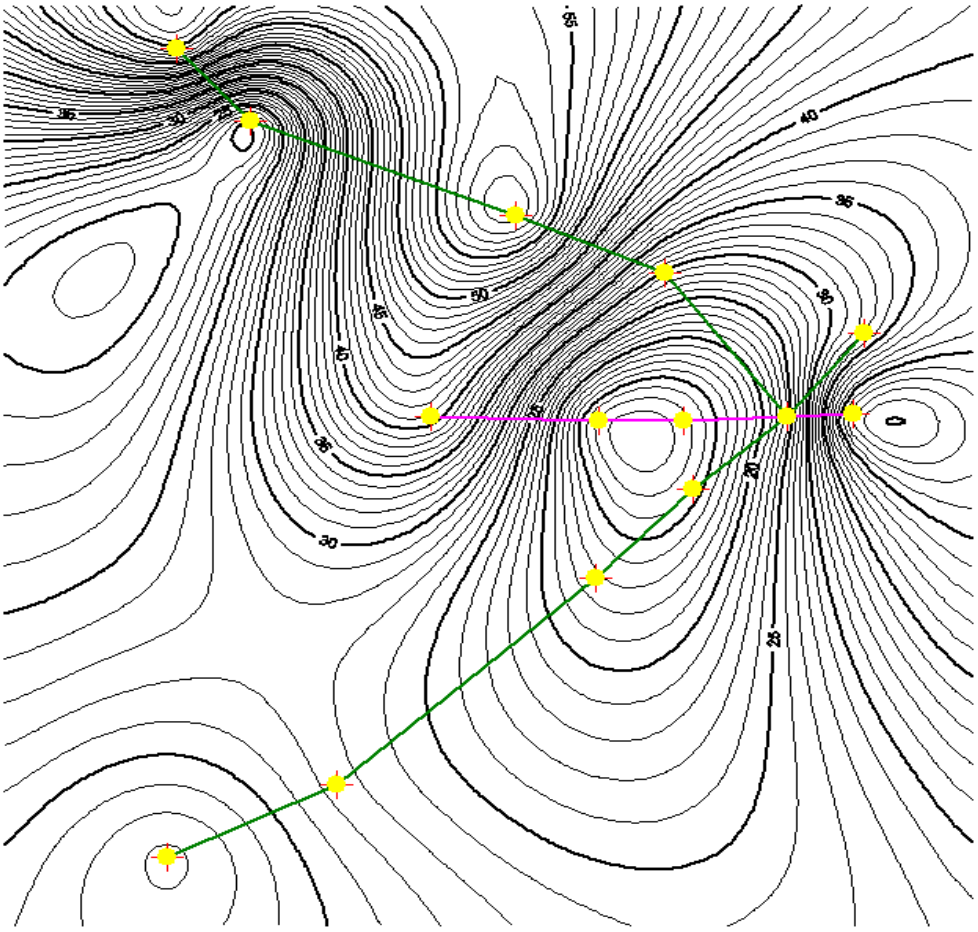

Figure 61. The location of cross section A-A', B-B' and C-C' and the wells on them, WVU Model

As it is shown in Figure 46, in ARI Model the sand layers in the injection well D-9-7 are picked based on the highest resistivity and highest SP values. The same trend and also cutoff value have been used to pick exactly the same layers as shown in injection well D-9-7 (Figure 63). The template for resistivity and SP logs for the injection well has been applied for the rest well logs.

By going through the same procedure in other wells on cross sections, the sand layers have been selected and structural as well as isopach maps were created. The guide for selecting the sand layers in each well was finding the same pattern of resistivity and SP logs seen in the injection well in other wells.

To clearly demonstrate the work that has been done, the picked sand layers on the cross sections A-A', B-B' and C-C' are shown in Figure 64, Figure 65 and Figure 66 respectively.

Since there is not enough information available and GR log does not exist for all the wells, in creating the structural map, there is no option to calculate the shaliness of each layer. Hence the Net to Gross thickness value in the model has been set to one.

Sand Layer	Sand Layer Top and Bottom (feet below sea-level)	Thicknes s (ft)
9420	9,414 – 9,421	6
9430	9,427 – 9,438	12
9460	9,444 – 9,476	32
9520	9,513 - 9,528	15
9540	9,534 - 9,549	15
9570	9,562 - 9,584	22
9620	9,596 - 9,638	42
9670	9,660 - 9,679	19
9710	9,695 - 9,717	22
9740	9,730 - 9,748	18
9800	9,775 - 9,806	30
9840	9,833 - 9,843	10
9870	9,868 - 9,874	6
9900	9,886 - 9,903	18
9940	9,929 - 9,939	10
9970	9,954 - 9,977	24
10030	10,016 - 10,025	9
10040	10,037 - 10,049	11
10060	10,055 - 10,069	15
10100	10,099 - 10,113	15
10130	10,121 - 10,134	13
10230	10,223 - 10,231	7
10310	10,302 - 10,318	16
10370	10,362 - 10,381	20
10400	10,396 - 10,412	16
10470	10,454 -10,484	31
10500	10,491 - 10,508	18

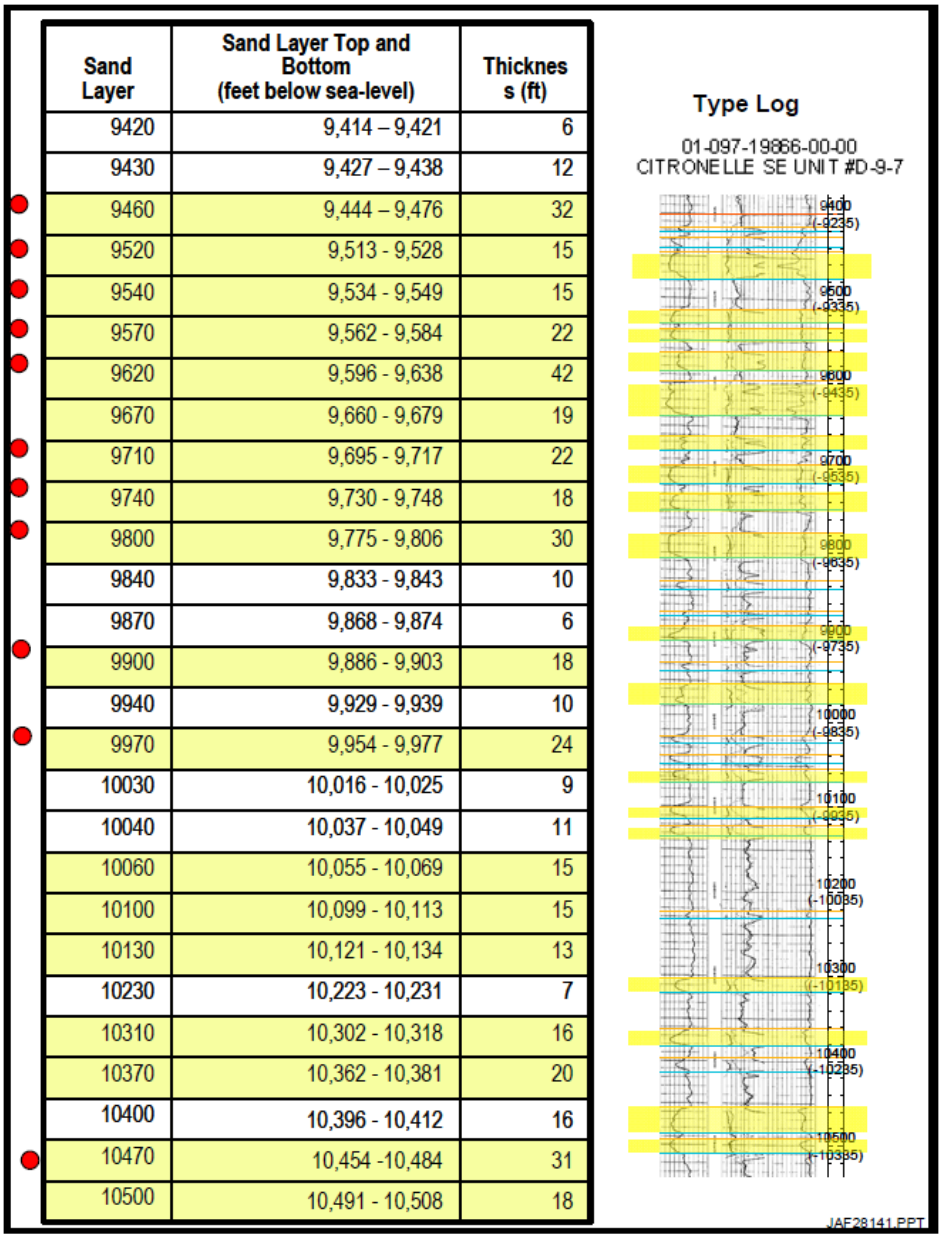

Figure 62. The sand layers of injection well D-9-7 and its corresponding well log, in the SECARB report (SECARB 2010).

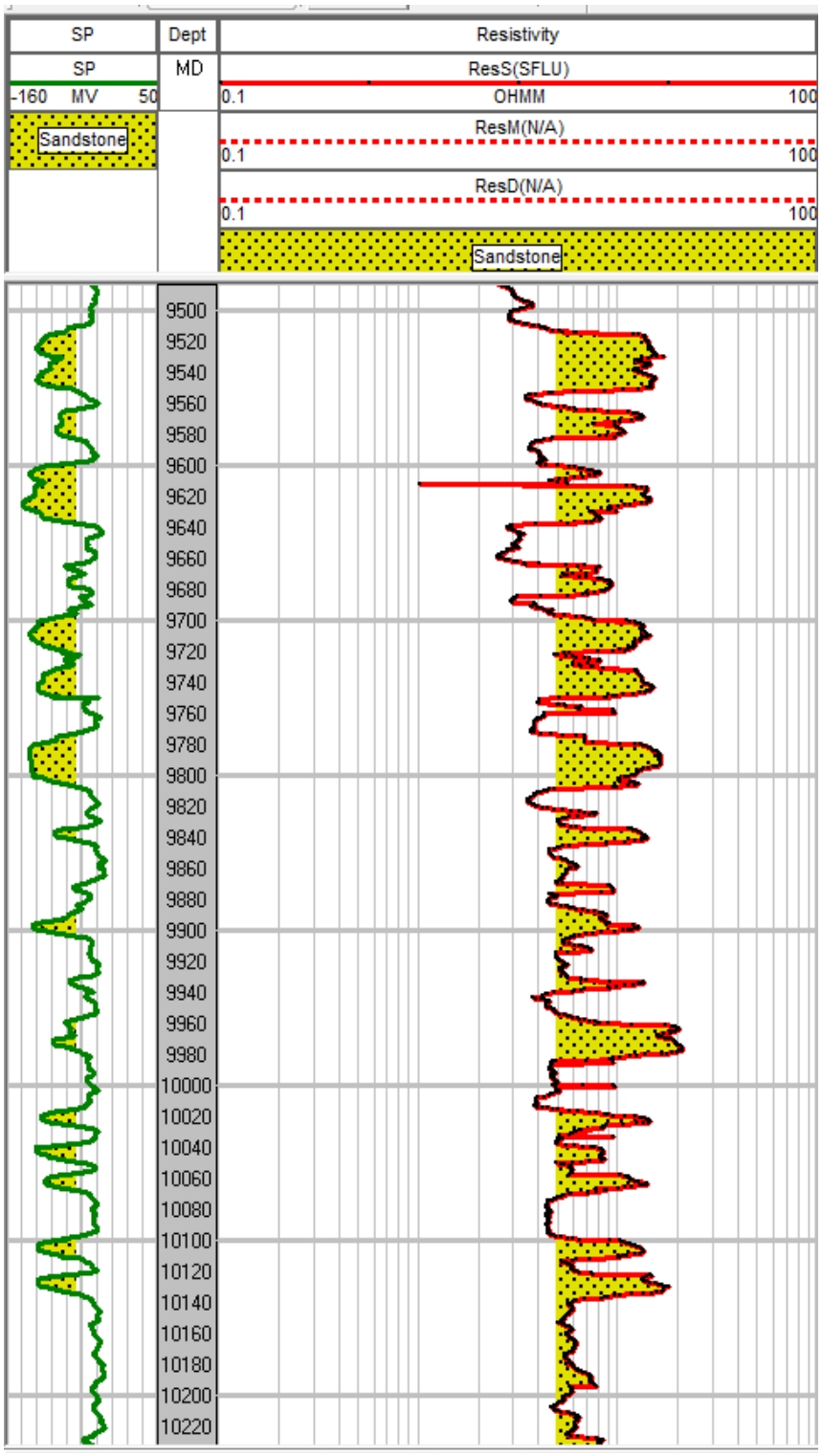

Figure 63. The sand layers of injection well D-9-7 and its corresponding well log, the WVU Model

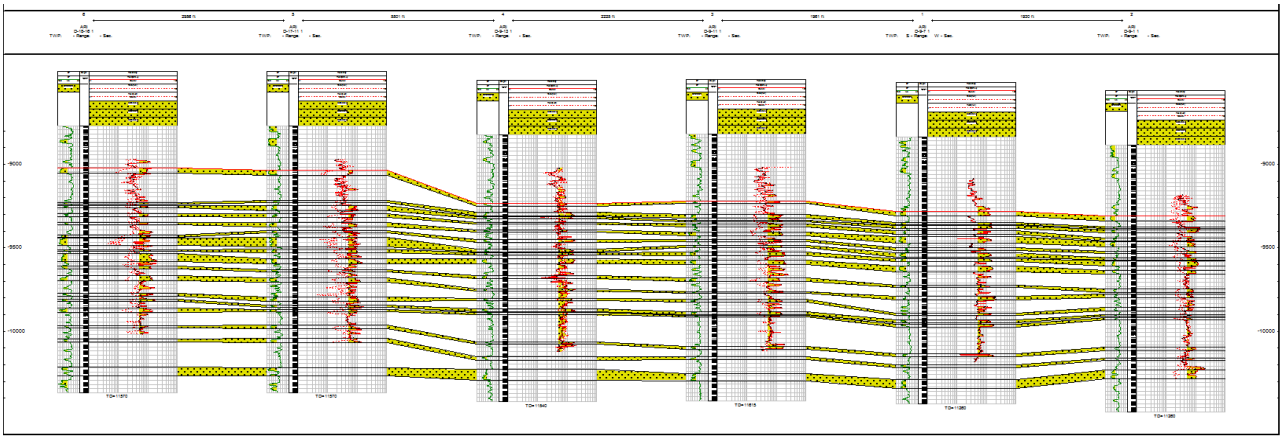

Figure 64. Sand layers on Cross section A-A', the WVU Model

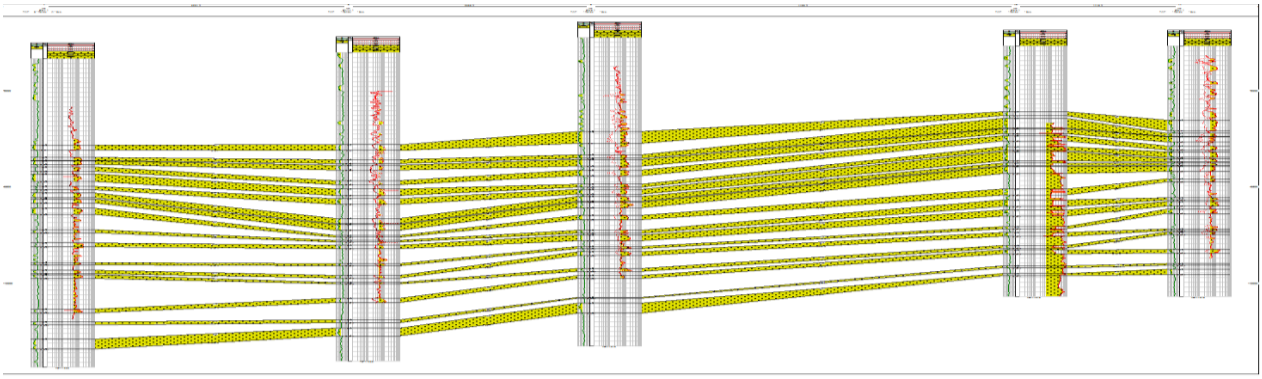

Figure 65. Sand layers on Cross section B-B', the WVU Model

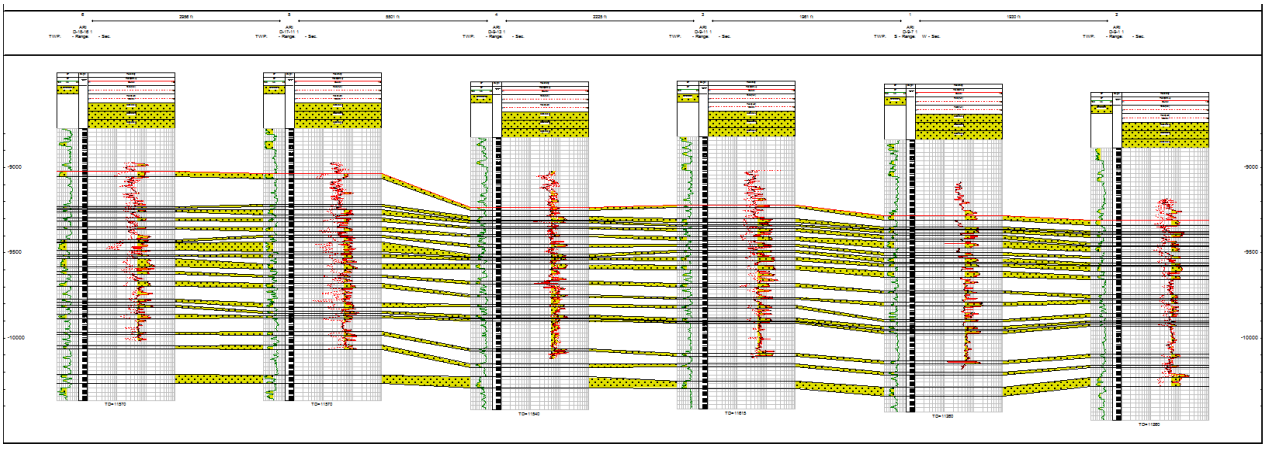

Figure 66. Sand layers on Cross section C-C', the WVU Model

The final structural maps from Geographix have been imported into CMG. The Grid top and thickness are shown in Figure 67 and Figure 68 .

Figure 67. Grid tops in WVU Model

Figure 68. Grid Thickness in WVU Model

Upon further comparison between the models from ARI and WVU, two main differences can be detected; namely: reservoir thickness and geological dip angle of the reservoir. Table 15 shows the sand layer thickness of the wells which are located on the cross sections for both models. The WVU model has thicker layers and the geological dip for the WVU model is less than what came in the report for the ARI model. Figure 69 shows the cross plots of both reservoirs.

Table 15. Reservoir Thickness at the location of the wells in ARI and WVU Models

Wells	D-9-7	D-18-16	D-4-14	D-5-5	D-5-9	D-6-1	D-8-7
WVU Model	435.2	267.6	360.2	349.5	406.5	238.8	397.8
ARI Model	435.2	194.7	319.1	234.6	299.9	154.6	320.9
Wells	D-9-1	D-9-11	D-9-13	D-9-14	D-9-5	D-9-6	D-9-8
WVU Model	348.6	315.2	310.6	299.8	376.1	414.9	351.6
ARI Model	279.4	345.2	323.1	312.8	354.9	398.2	369.2

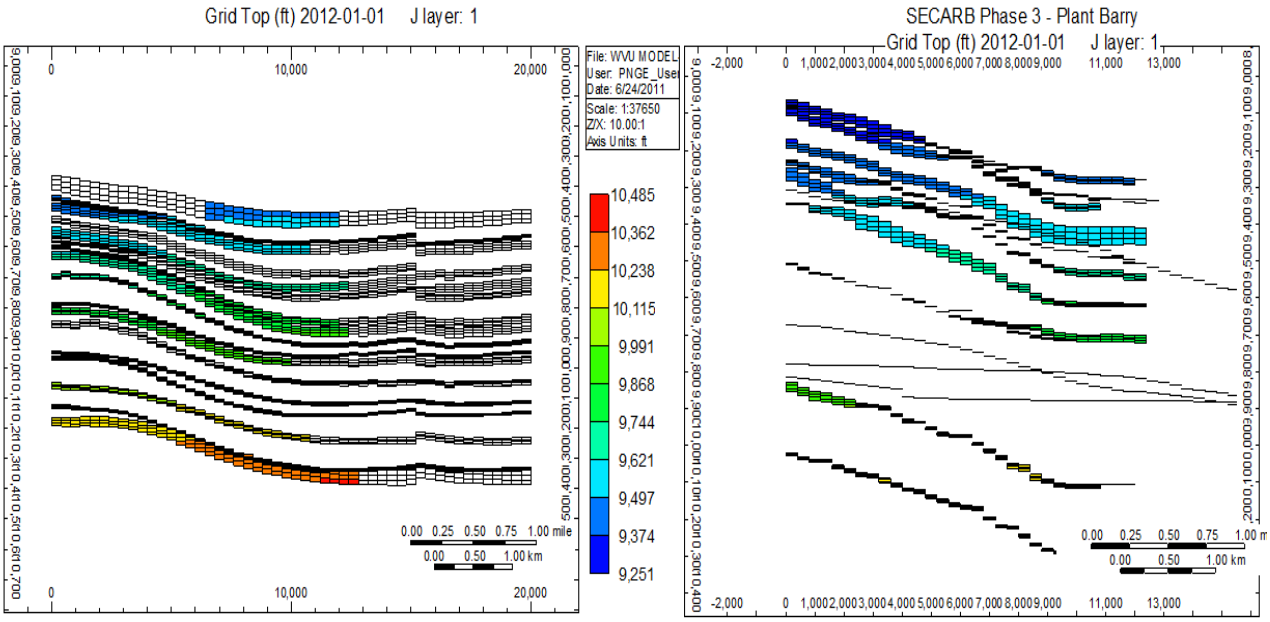

Figure 69. Geological dip of the reservoir, the WVU Model (left) and the ARI Model (right)

Developing Lateral Heterogeneity for the Field: New Approach

Figure 70, shows the proposed porosity-permeability correlation provided in the report (SECARB 2010). Based on the data shown in this figure, a large number of outliers can be detected; moreover many of the data points are not following the trends identified (by straight lines) in the figure. There are new core data of Paluxy formation from the observation well D-9-8 which can be added to these points as well. In order to rectify the problem of the outliers and consider new points, five different clusters were determined and ranked as the best to the worst rock types.

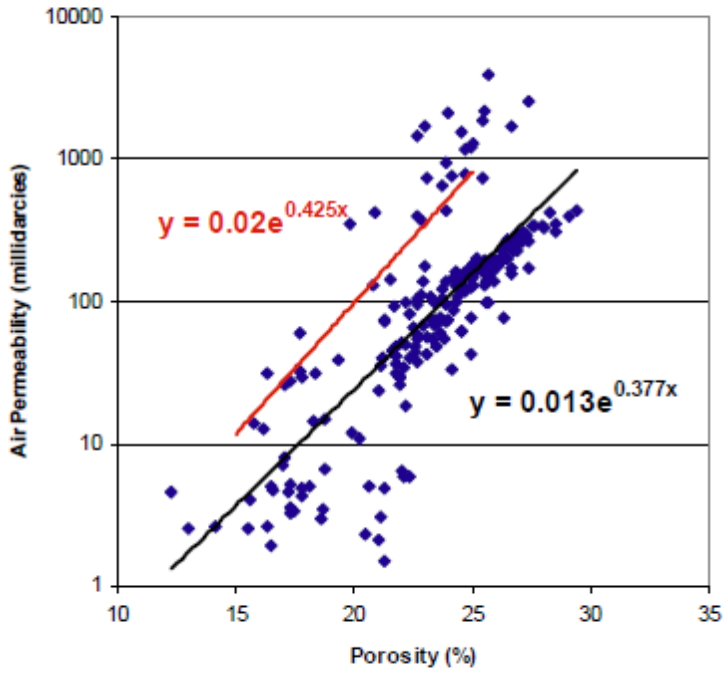

Figure 70. The porosity-permeability correlation proposed by ARI

The porosity values coming from the log and the core analysis show a good match in well D-9-8. However, using the porosity-permeability correlation suggested in the report (SECARB 2010) and shown in the above figure, large differences between permeability calculated from the correlation and permeability from the core data can be observed (Figure 71). This issue arise the necessity of having a more reliable porosity-permeability correlation.

The new correlations between the porosity and permeability for the five different rock types were defined and are shown in Figure 72.

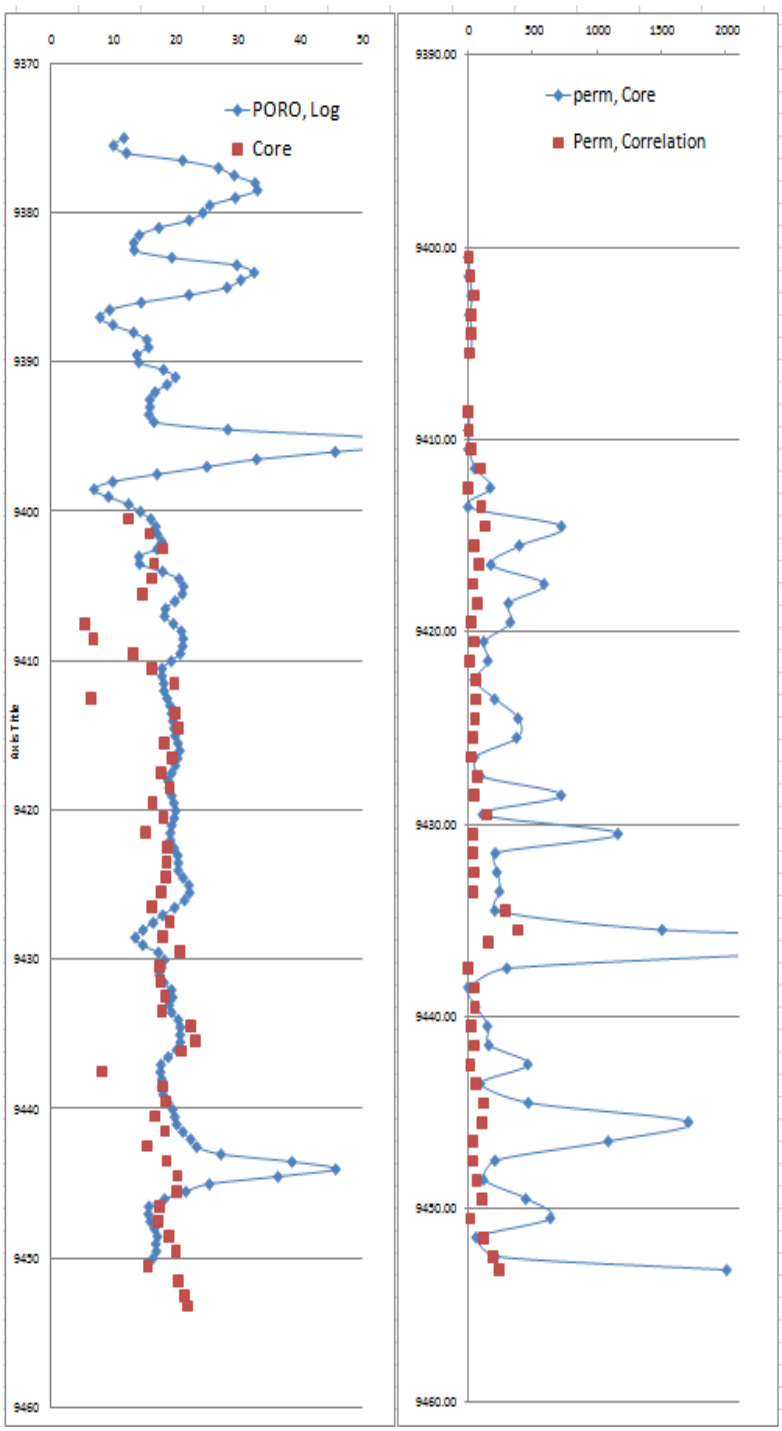

Figure 71. Porosity - permeability relation between core and log in D-9-8

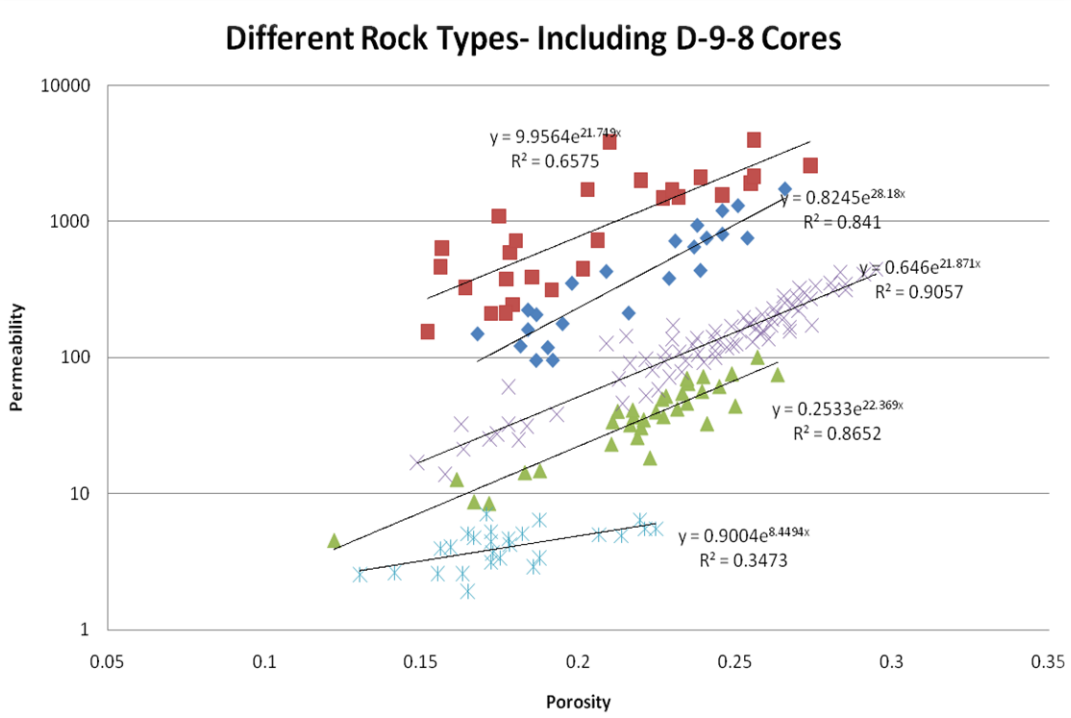

Figure 72. The porosity-permeability correlation in different rock types

WVU Numerical Model - Initial Results

The induction logs have been used to interpret the porosity values. The porosity-permeability correlations have been utilized to generate the permeability maps using the interpreted porosity values. Figure 73 illustrates the porosity distribution in WVU model.

Cartesian grid has been used for the WVU model which has the same dimension as the ARI model. It has the dimension of 50∗50∗51 with Δx and Δy equal to 400 ft. The same rock and fluid properties have been applied to the model.

The first concern in the reservoir model is the extension of CO_2 plume originating from the injection well. Three simulation models, the old and the new model from ARI[2] and the WVU model, were examined for this purpose. The results of the simulation runs are shown in the following figures. The CO_2 extension is shown in each graph in the first sand layer which has the most CO_2 saturation. Also the CO_2 distribution in whole sand layers is depicted in both models, the WVU and the ARI Model.

[2] A modified model was later received from ARI. The modified model is referred to the “New” ARI Model.

Figure 73. Porosity distribution in the WVU Model

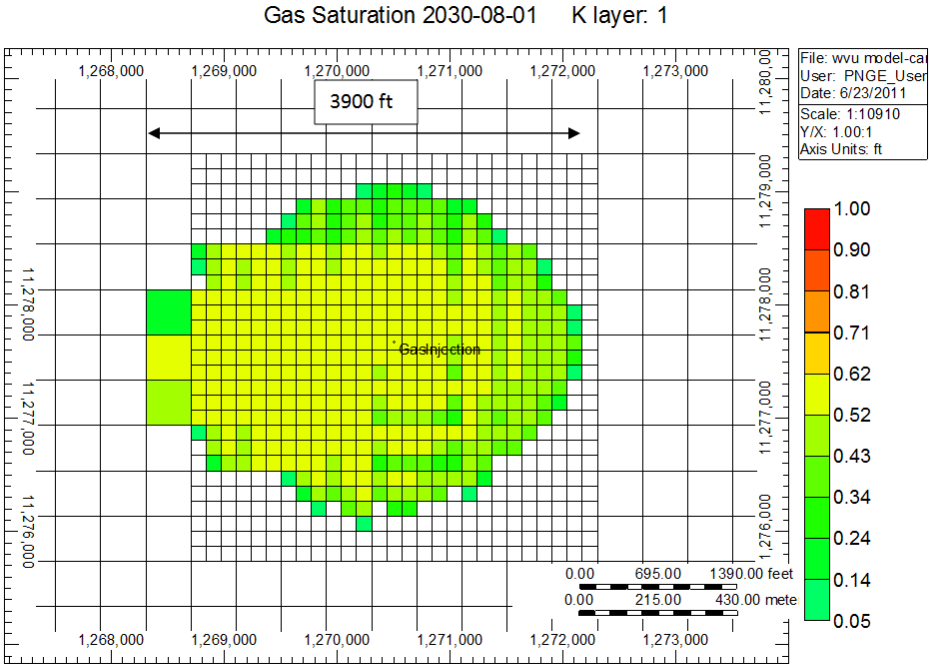

Figure 74. The extension of CO_2 plume in WVU Model

Figure 75. Gas Saturation in the WVU Model

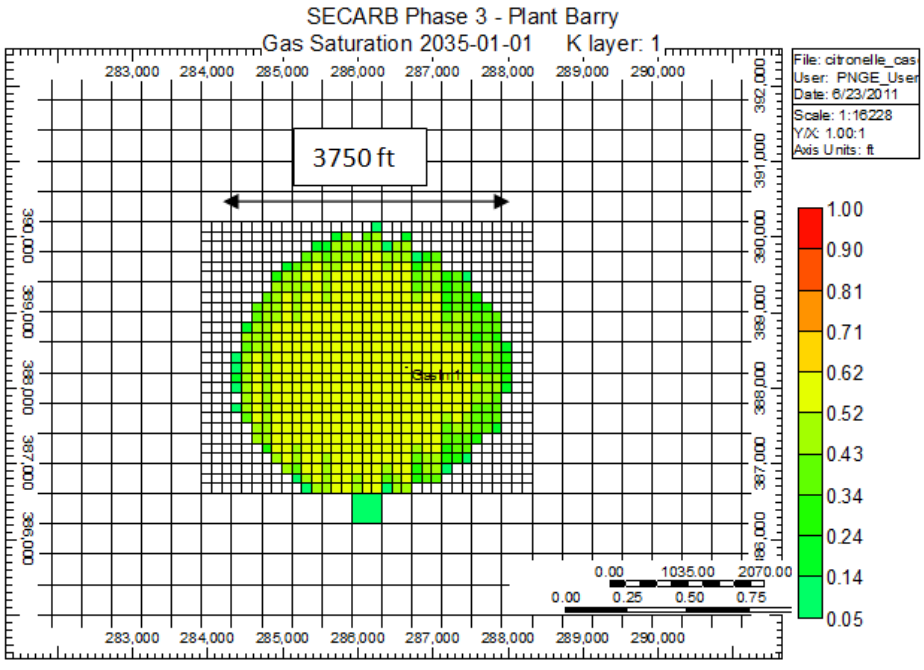

Figure 76. The Extension of CO_2 Plume in the ARI New Model

Figure 77. Gas Saturation in the ARI New Model

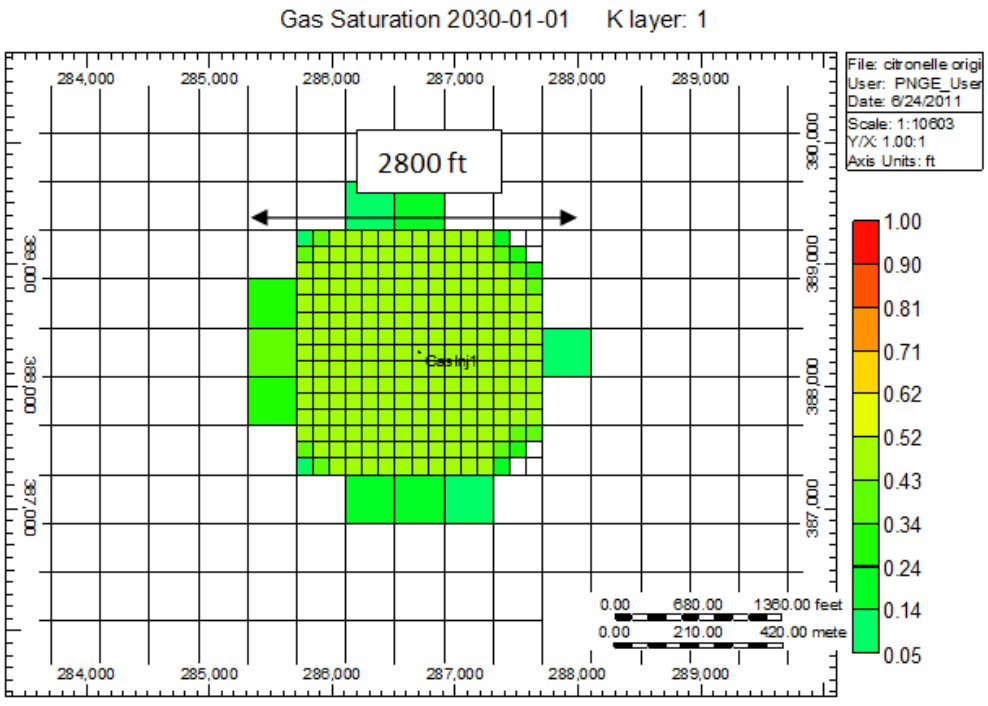

Figure 78. The extension of CO_2 Plume in the ARI Old Model

GRIDDING SENSITIVITY ANALYSIS

Three different grid geometries were considered in order to examine the effect of the number and size of the grid blocks on the accuracy of the Citronelle numerical model results. The first case (Figure 79) consisted of 50 grid blocks in i and j directions and 51 layers in k direction. The size of each coarse grid block is 400ft by 400ft. The second case consisted of 2419 coarse grids and 729 fine girds in the AoI (Area of Investigation). The size of the each fine grid in the second case is 133 ft. by 133 ft. (Figure 80). In the 3rd case (Figure 81) the model included 4 different grid types where the size of grids changes from totally coarse (400 * 400 ft.) to tally fine (66.7*66.7ft). Table 16 lists the total number of each grid type.

Table 16. Number of grid blocks in case 3

Grid Type	Coarse	1	2	Fine	Total
Number of Grids	2305	384	666	900	4255

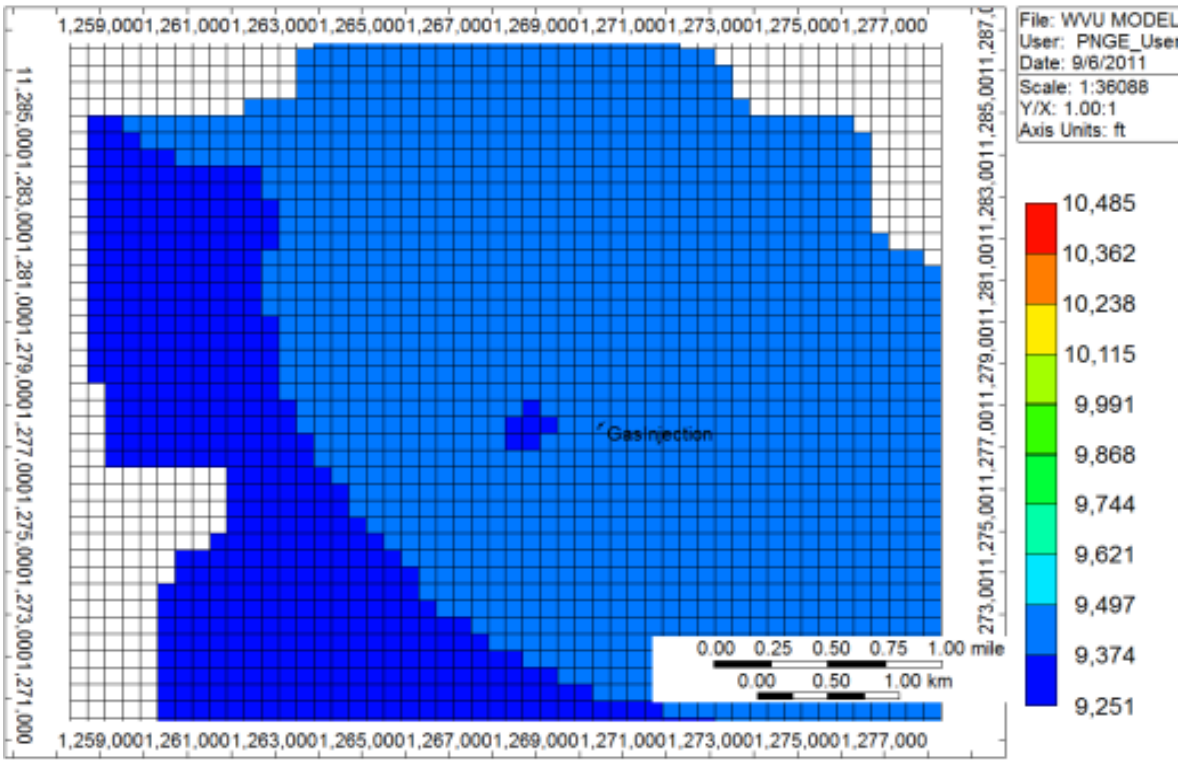

Figure 79. Citronelle model with all coarse grid-blocks (case 1)

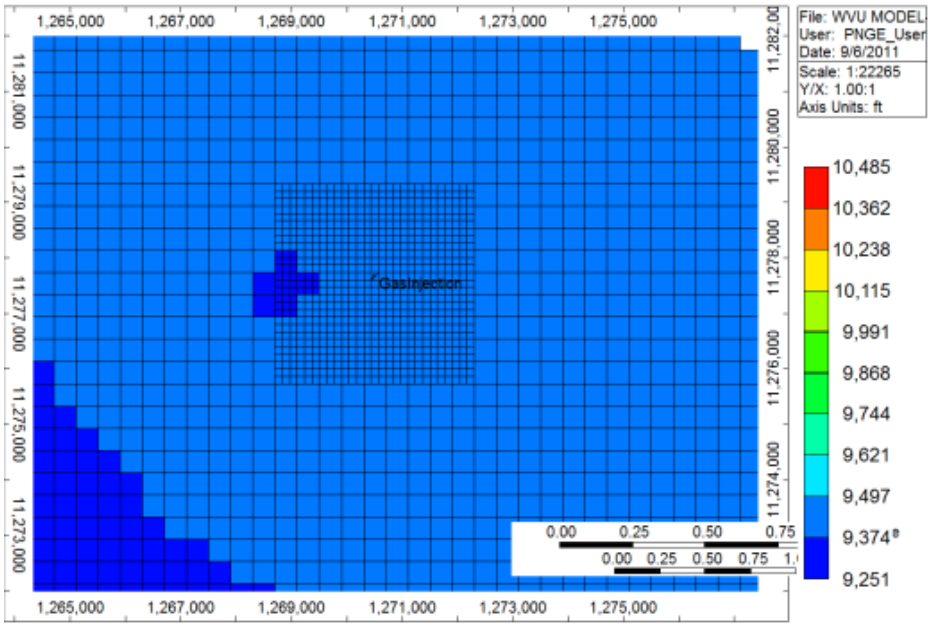

Figure 80. Citronelle model with coarse and fine grid-blocks (case 2)

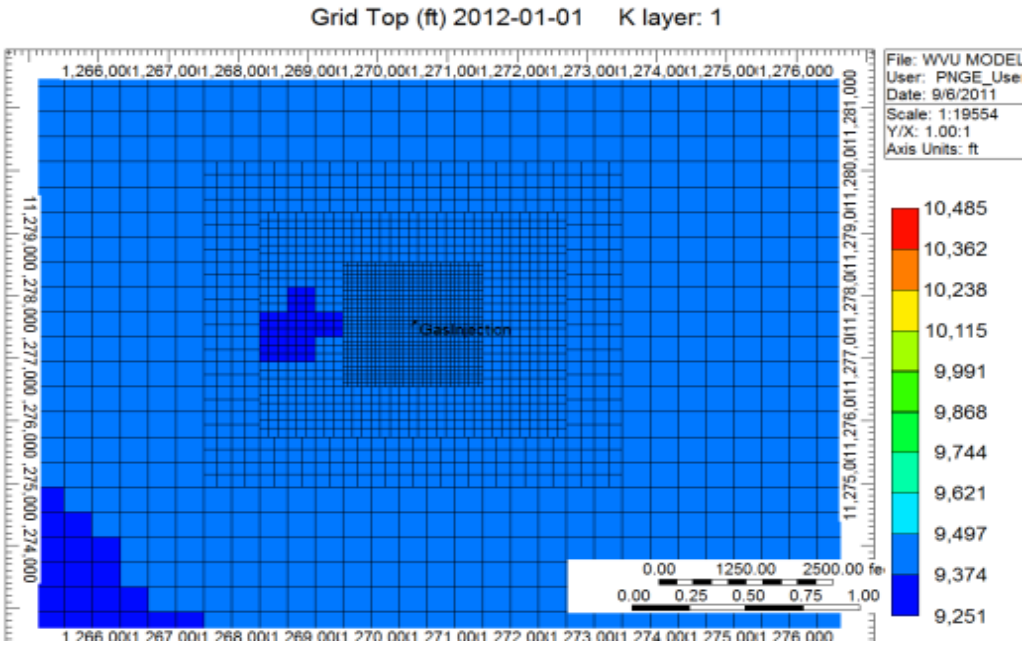

Figure 81. Citronelle model having 4 types of grid-blocks (case 3)

As the number of grid blocks increases, higher spatial resolution is achieved which leads to more accurate results. It should be mentioned that the run time for case 1(coarse grids) is much less than the case with 4 types of grid blocks. Figure 82 and Figure 83 illustrate the effect of number of grids in CO_2 saturation profile in a grid close to the injection well and at the location of observation well.

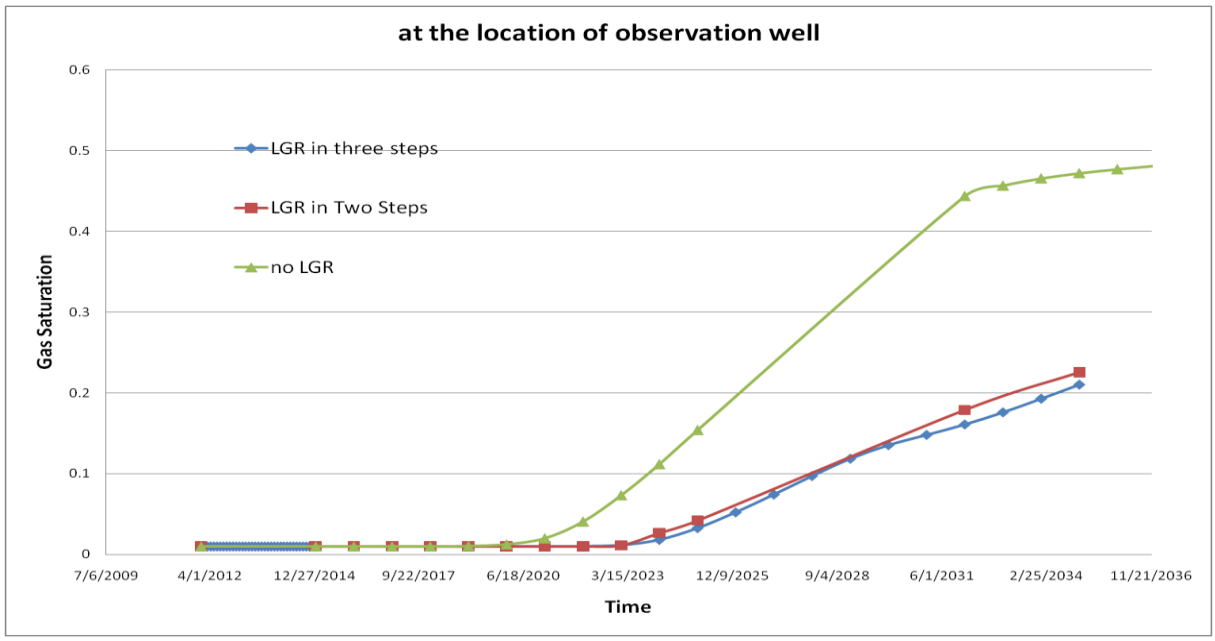

Figure 82. CO_2 Saturation at the location of the observation well

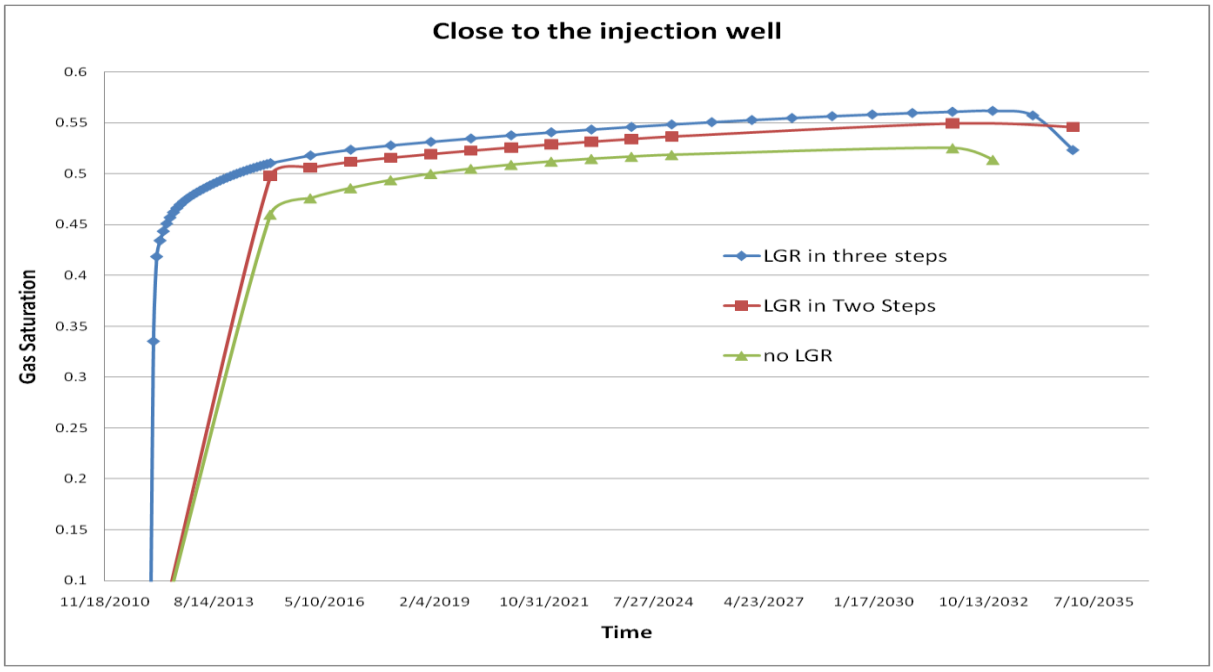

Figure 83. CO_2 Saturation at the a grid close to the injection well

DESIGNING DIFFERENT INJECTION SCENARIOS

One hundred different scenarios were designed based on the duration of injection and cumulative amount of injection. Latin Hypercube algorithm was used in order to select only 10 out of these scenarios as representative simulation runs. Table 17 lists the criteria for the ten selected simulation runs.

Table 17. Different predefined parameters for 10 different simulation runs based on cumulative injection and duration of injection

Base	base value for injection		3	10,348	36
Run	Latin Hypercube coefficients		L (years)	G (MM ft^3)	months of injection
1	0.2249	0.3159	3.2	19,884	38.2
2	0.1745	0.8746	2.8	45,900	33.7
3	0.8494	0.7186	7.9	38,635	94.4
4	0.9301	0.1756	8.5	13,351	101.7
5	0.0109	0.0071	1.6	5,504	19.0
6	0.4041	0.565	4.5	31,483	54.4
7	0.3453	0.9803	4.1	50,821	49.1
8	0.5861	0.4749	5.9	27,288	70.7
9	0.6851	0.6384	6.6	34,901	79.7
10	0.7742	0.2527	7.3	16,941	87.7

The injection rate increases monthly for all the scenarios. The idea behind making these runs is to investigate the impact of change in cumulative injected CO_2 and duration of injection on the reservoir pressure and CO_2 saturation. These characteristics are also important for the investigation of Area of Review (AoR) and Post Injection Site Care (PISC).

For example a comparison between pressure and saturation distribution for the base case run and Run#7 is shown in Figure 84, Figure 85, Figure 86 and Figure 87.

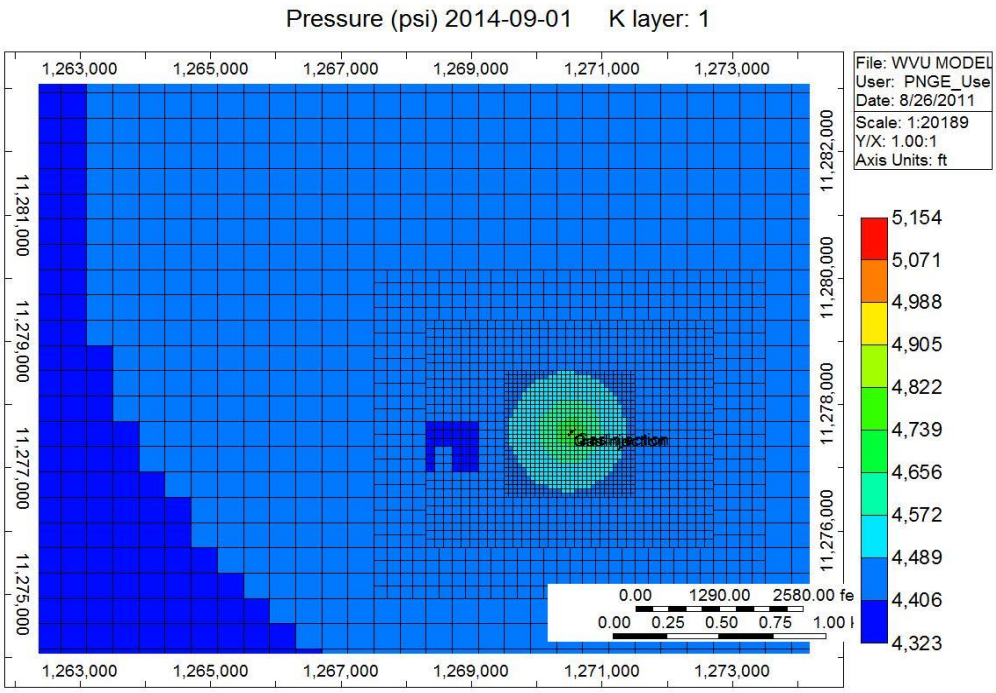

Figure 84. Pressure distribution for the base case

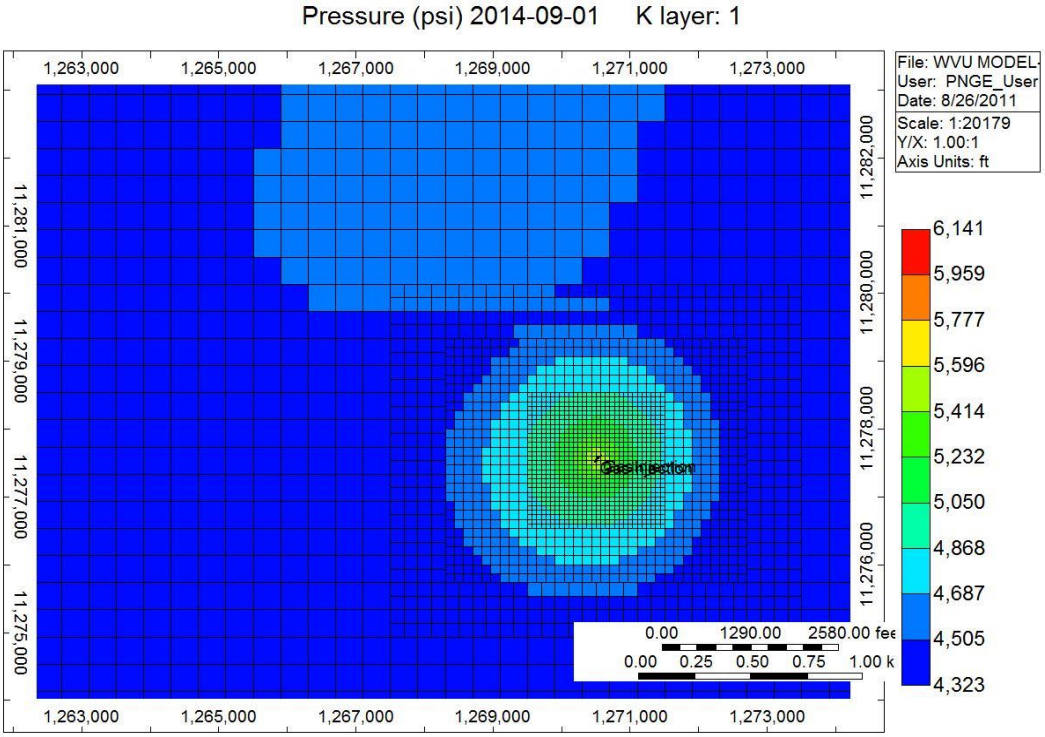

Figure 85. Pressure distribution for Run7 (L=4years, G=5E10 ft3)

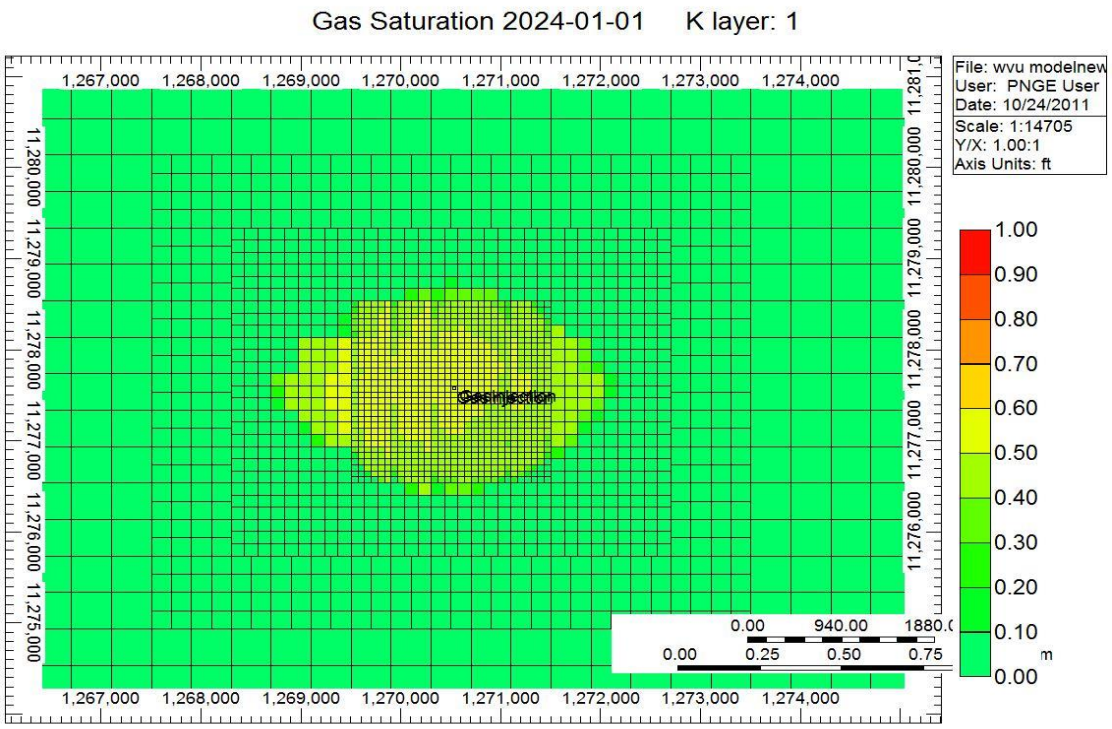

Figure 86. Saturation distribution for the base case

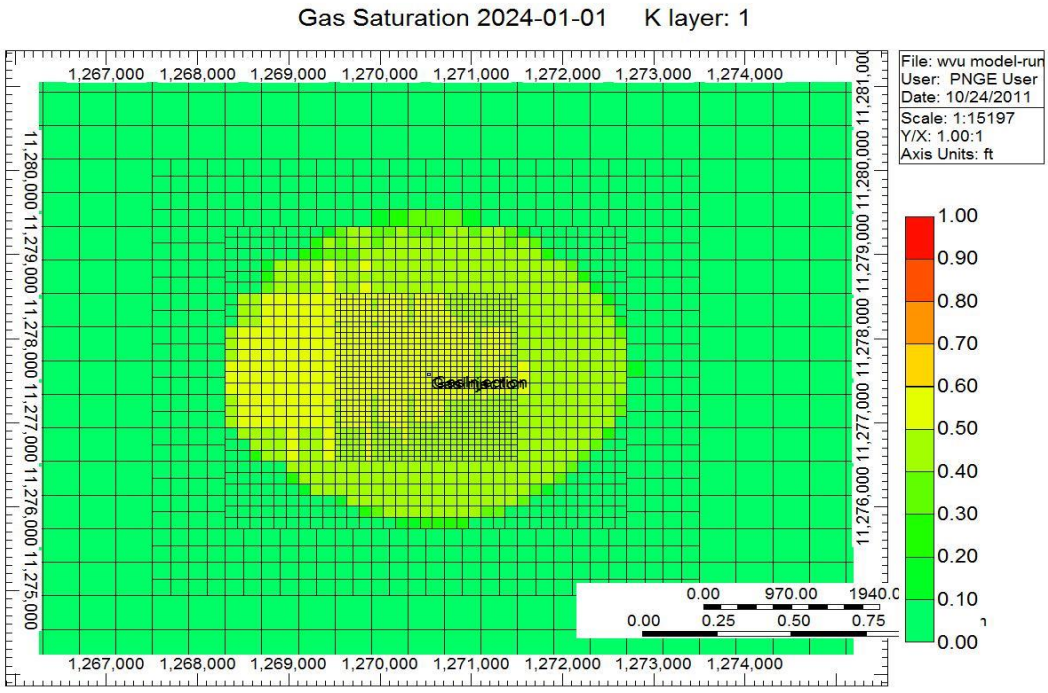

Figure 87. Saturation distribution for Run7 (L=4years, G=5E10 ft3)

SENSITIVITY ANALYSIS ON RESERVOIR SIMULATION RESULTS

Initial reservoir simulation runs showed that maximum extension of the CO_2 plume takes place in the first (top) layer and sixth layer of the reservoir. This is mainly due to the fact that these layers represent sands with higher permeability values, which cause CO_2 to migrate further from the injection well. As it is shown in Figure 88, the plume area has a major diameter of about 4,933 ft, 500 years after the end of injection. CO_2 plume extension in all the target layers (vertically) is shown in Figure 89.

Two Pressure Down-hole Gauges (PDG) are installed in the project's observation well (D-9-8#2). This observation well is located 820 ft. to the east of the injection well. These PDGs can provide real time pressure and temperature measurements. The actual pressure data can be used for reservoir monitoring (especially CO_2 leakage detection) in addition to history matching. Therefore, the main focus of this section of the project is to analyze the reservoir simulation pressure behavior at the location of the PDGs in the observation well.

Pressure in the observation well increases from 4,400 psi to 4,727 psi (maximum pressure) during the 3 years of injection (from 2012 to 2015). After the injection stops, the pressure decreases gradually to 4,660 psi after 1 year (stabilized pressure). Finally the reservoir pressure in the observation well follows a gentle decline with a stable trend from 4,660 to 4,653 psi over 500 years (Figure 90).

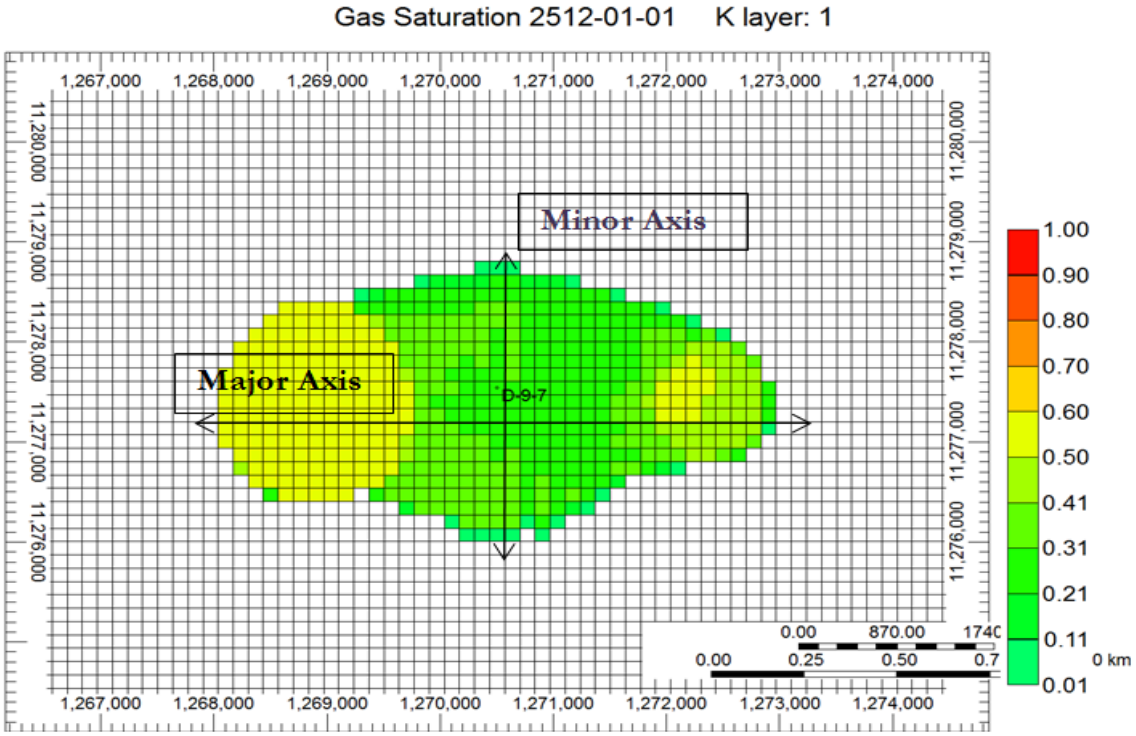

Figure 88. CO_2 Plume extension in the first layer 500 years after injection

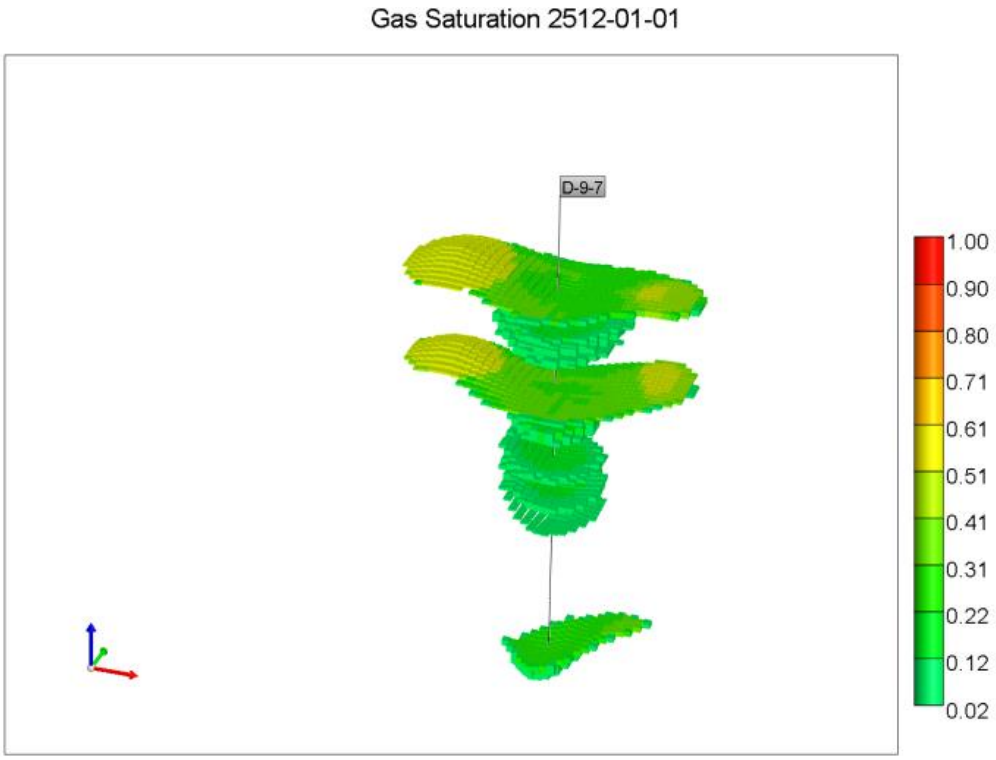

Figure 89. CO_2 Plume extension in all layers 500 years after injection

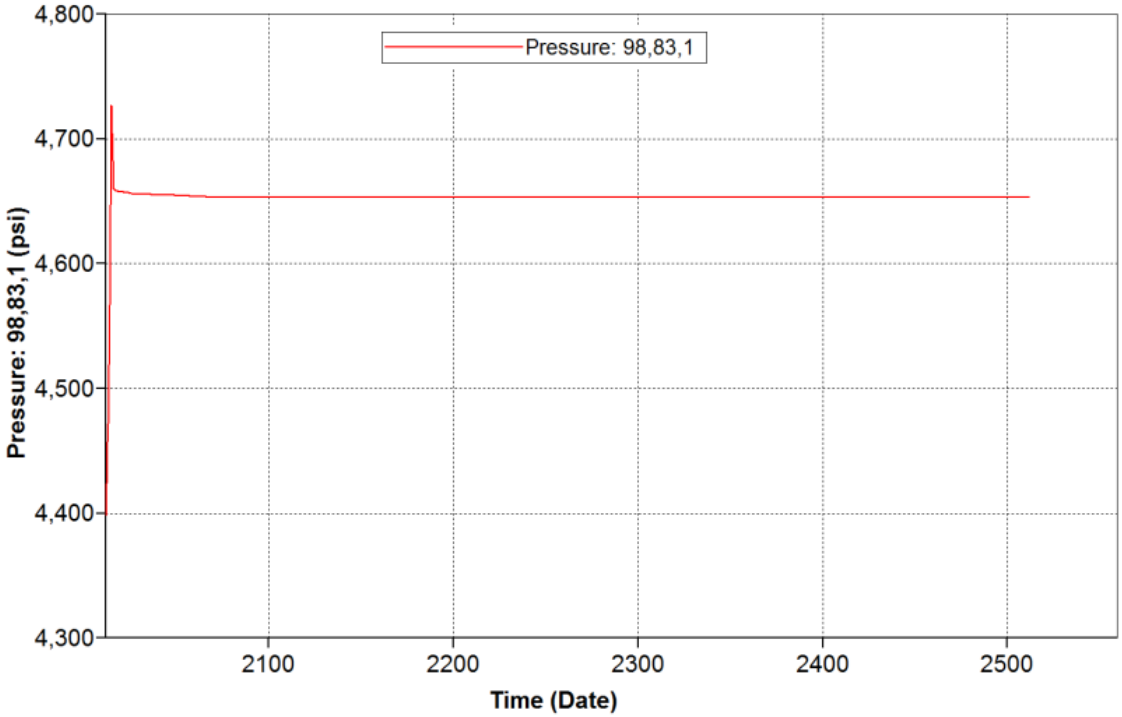

Figure 90. Pressure behavior in the observation well (base case model)

SENSITIVITY ANALYSIS

In this section, sensitivity of the numerical simulation model to several reservoir properties is presented. The procedure for the sensitivity analysis is as follows: one parameter is modified at a time (within a given uncertainty range) and the corresponding impacts on the reservoir pressure (at the observation well) and the CO_2 plume extension are investigated. Reservoir parameters that were analyzed in this study included permeability (rock type), gas relative permeability, maximum residual gas saturation (hysteresis), vertical to horizontal permeability ratio, boundary condition, brine compressibility, and density.

Since the CO_2 plume extension shape is elliptical, the magnitude of the major and minor axis (Figure 88) can characterize the CO_2 plum distribution after 5, 50 or 500 years of injection. Additionally, to analyze the reservoir pressure behavior, we focused on maximum and stabilized pressures (at the end of injection).

PERMEABILITY

From here forward, the contribution of each of the parameters to reservoir pressure and plume extension are discussed. In this reservoir model, porosity originates from maps that are generated by the interpretation of 40 well logs. Figure 91 shows porosity-permeability cross-plots. As was mentioned before in this report, in order to have a reliable porosity-permeability correlation, the data points are clustered into 5 different rock types, ranging from “Very Tight” to “Very Conductive” rock types. The initial porosity-permeability data gathered from well D-9-8 (observation well) core analysis, represents a “Conductive Rock Type”. This correlation was used in the base model. During the sensitivity analysis, “Average Rock Type” ($K = 0.64e^{21.87\varphi}$) and Very Conductive ($K = 9.964e^{21.74\varphi}$) rock types are introduced to the reservoir simulation model.

For the “Average Rock Type”, due to the lower permeability values, CO_2 injectivity decreases. Thus, it is not possible to inject/store the all the CO_2 according to planned target (Figure 92). Injectivity of CO_2 is the same for both “Conductive” and “Very Conductive” rock types. We can see the results for pressure in Figure 93. Since the stabilized reservoir pressure changes very gently during the 500 years after the stop of the injection; we show the results for only the 20 years after the injection. This is done so that more details can be observed in the figure.

By decreasing the permeability (use of “Average Rock Type”), CO_2 injectivity decreases to 60% of the target value, resulting in reduced reservoir pressure compared to the base case. For higher permeability (“Very Conductive Rock Type”), stabilized reservoir pressure is 42 psi less than the base case, due to the higher conductivity that prevents more pressure build up. Additionally, an increase in the permeability, enhances the CO_2 and brine displacement, which leads to larger CO_2 plume extensions. This can be seen in Table 18.

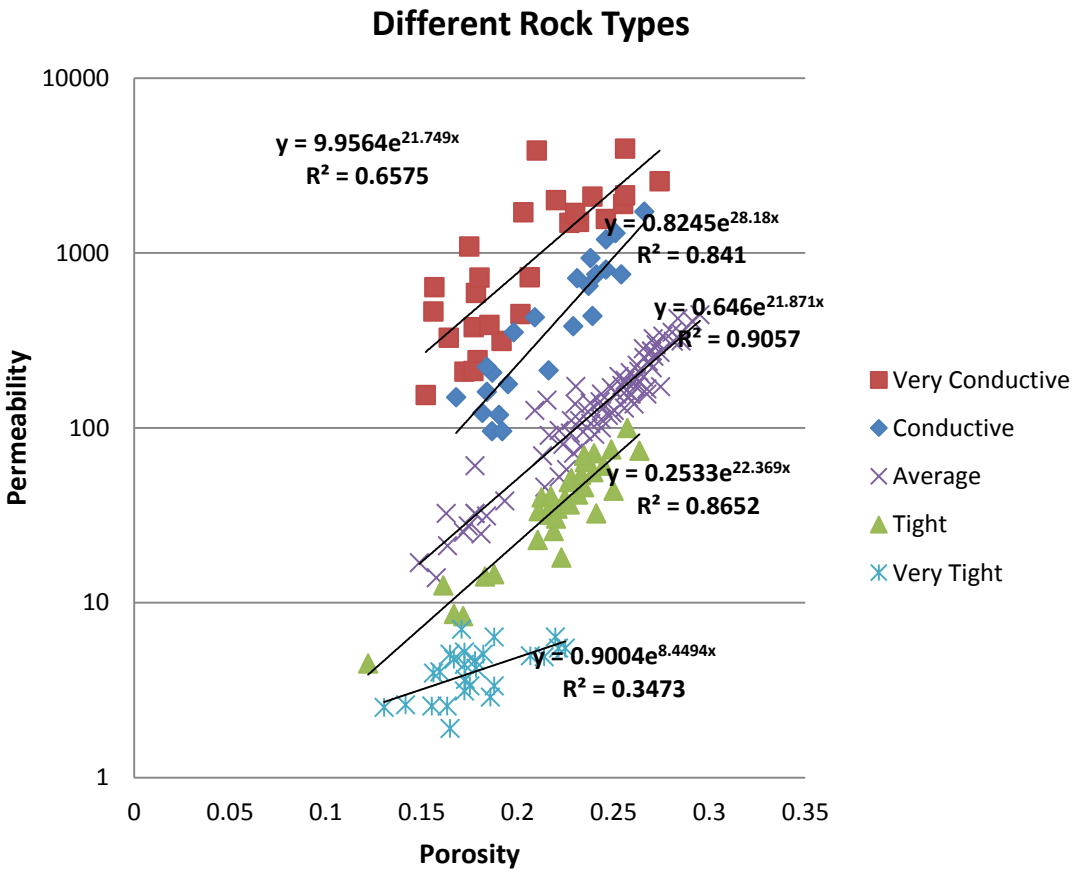

Figure 91. Porosity-permeability cross-plot

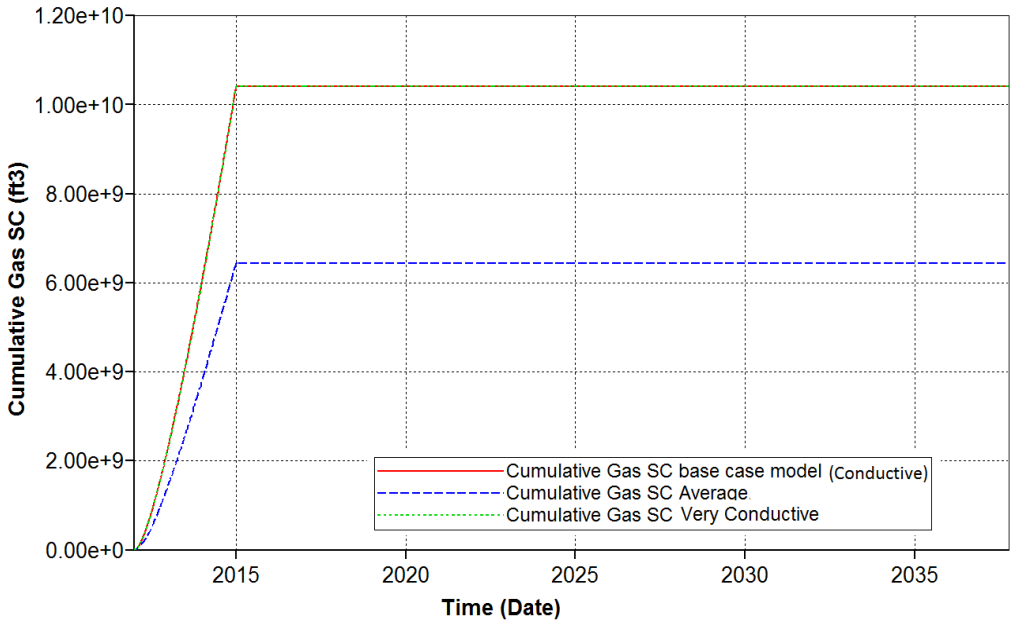

Figure 92. CO_2 injectivity for different rock types

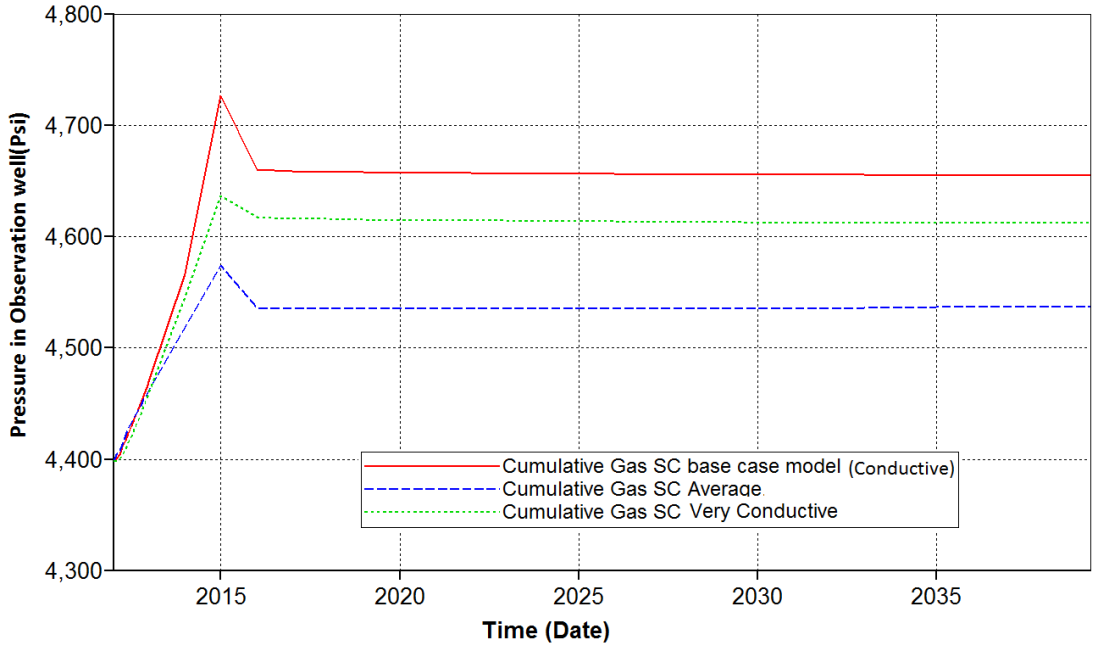

Figure 93. Reservoir pressure in observation well for different rock types

Table 18. CO_2 Plume extension size over time (in the first layer) for different rock types

			Permeability		
			Base Case (K=0.824e^28.18 φ)	Average (K=0.64e^21.87 φ)	Very Conductive (K=9.964e^21.74φ)
CO_2 Plume Extension	5 Years after Injection	Minor Axis(ft)	2133	1600	2533
		Major Axis(ft)	2400	1733	3200
	50 Years after Injection	Minor Axis(ft)	2533	1867	2800
		Major Axis(ft)	4000	2133	4667
	500 Years after Injection	Minor Axis(ft)	2667	2133	2667
		Major Axis(ft)	4933	3733	5067

PERMEABILITY RATIO

Typically, vertical permeability is determined as a ratio to horizontal permeability. In this study, for the base case model, K_v/K_h is considered to be 0.1. For the sensitivity analysis; we assigned values of 0.3, 0.5, and 0.7 to the K_v/K_h. As shown in Figure 94, an increase in the K_v/K_h generates less pressure build up during the injection. However, after the transition time, increase in the stabilized pressure value, corresponds to increase in vertical to horizontal permeability ratio. Also, the size of the CO_2 plume slightly increases for higher K_v/K_h, especially for 5 and 50 years after injection (Table 19).

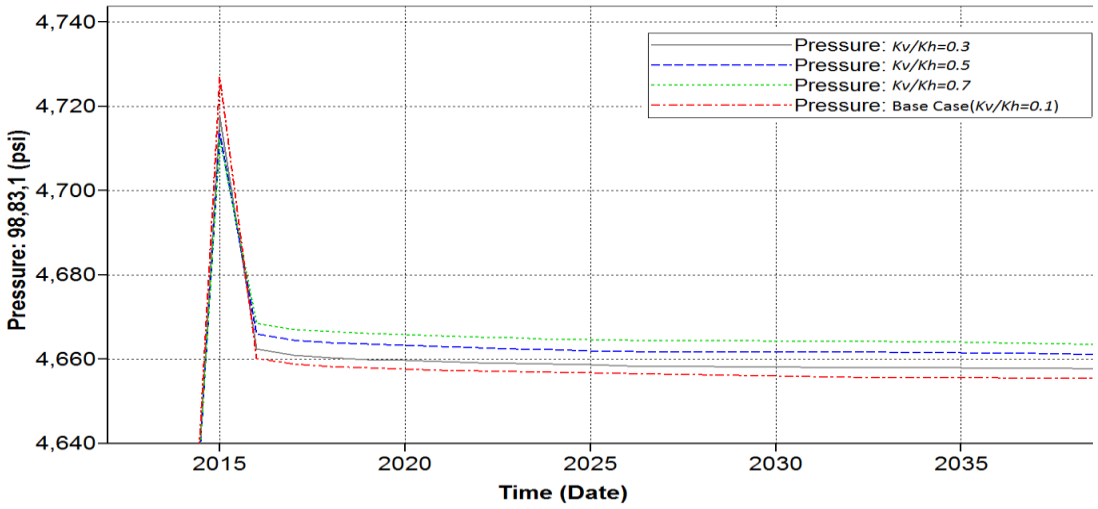

Figure 94. Reservoir pressure in observation well for different permeability ratio

Table 19. CO_2 Plume extension size over time (in the first layer) for different permeability ratios

			Vertical to Horizontal Permeability Ratio			
			Base Case	K_v/K_h=0.3	K_v/K_h=0.5	K_v/K_h=0.7
CO_2 Plume Extension	5 Years after Injection	Minor Axis(ft.)	2133	2133	2133	2267
		Major Axis(ft.)	2400	2533	2667	2800
	50 Years after Injection	Minor Axis(ft.)	2533	2667	2667	2667
		Major Axis(ft.)	4000	4133	4267	4400
	500 Years after Injection	Minor Axis(ft.)	2667	2667	2800	2800
		Major Axis(ft.)	4933	4933	5067	5067

GAS RELATIVE PERMEABILITY CURVES

Four different gas (CO_2) relative permeability curves were generated so that two of them represent higher and two represent lower values of relative permeability at any given gas saturation, compared with the base case (Figure 95).

It is worth mentioning that the curves with the higher gas (CO_2) relative permeability values have lower residual gas saturations and vice versa. The results are shown in Table 20 and Figure 96. Higher gas (CO_2) relative permeability curves represent lower residual gas saturation that can mobilize CO_2 phase earlier (at lower gas saturations). Therefore, CO_2 moves further resulting in larger CO_2 plume extension. Additionally, higher gas relative permeability increases the stabilized reservoir pressure. Reversely, lower gas relative permeability leads to less extensive plume and lower stabilized reservoir pressure.

Table 20. Plume extension size over time in the first layer for different gas relative permeability curves

			Gas Relative Permeability				
			Base Case	K_{rg} Low2	K_{rg} Low1	K_{rg} High1	K_{rg} High2
CO_2 Plume Extension	5 Years after Injection	Minor Axis(ft.)	2133	1867	2000	2133	2400
		Major Axis(ft.)	2400	2133	2266	2533	2800
	50 Years after Injection	Minor Axis(ft.)	2533	2133	2267	2667	2933
		Major Axis(ft.)	4000	2800	3467	4267	4533
	500 Years after Injection	Minor Axis(ft.)	2667	2400	2533	2800	2933
		Major Axis(ft.)	4933	4133	4533	5067	5467

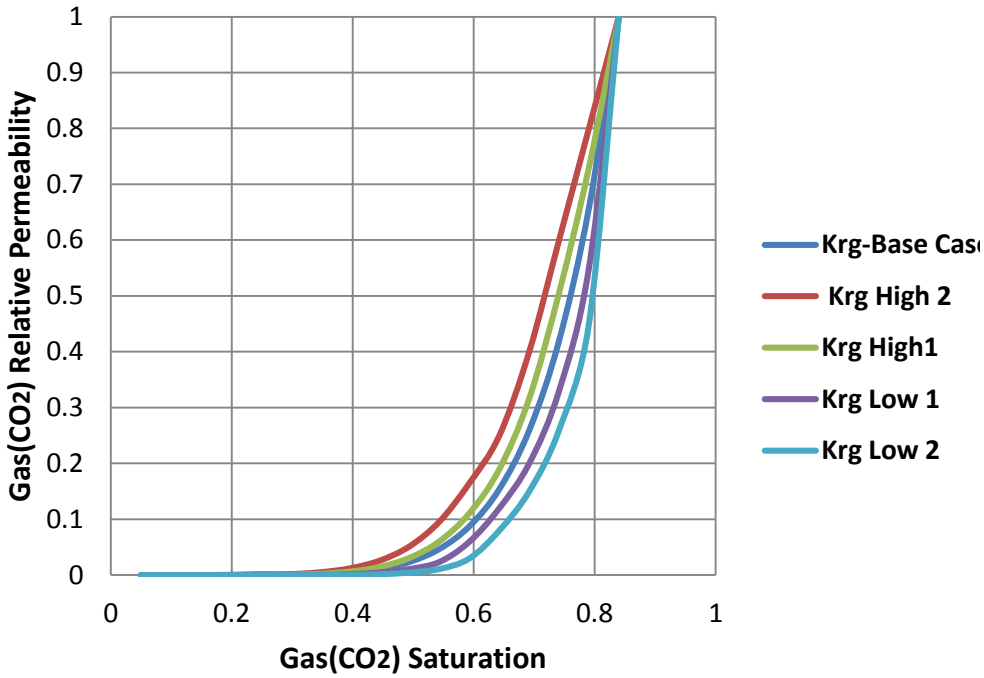

Figure 95. Different gas relative permeability curves

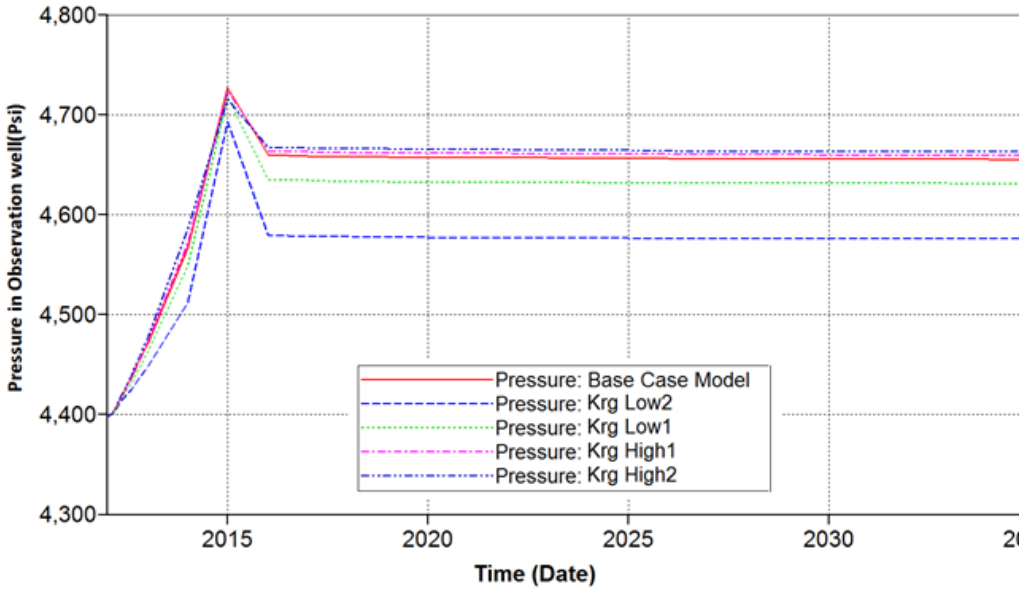

Figure 96. Reservoir pressure in observation well for different gas relative permeability curves

MAXIMUM RESIDUAL GAS SATURATION

Generally, drainage relative permeability curves are provided for the reservoir simulation model. When the maximum residual gas saturation is introduced, the imbibition gas relative permeability curve can be determined based on the drainage curve. During CO_2 movement in the reservoir, water imbibition causes a portion of gas phase to be trapped in the pores (residual trapping). Therefore, when the maximum residual gas saturation increases, more gas is trapped, resulting in less mobile CO_2 and consequently a smaller CO_2 plume extension (Table 21). Changing maximum residual gas saturation has no significant impact on the reservoir pressure.

Table 21. CO_2 Plume extension size over time in the first layer for different maximum residual gas saturations

			Maximum Residual Gas Saturation(Hysteresis)			
			Base Case	0.05	0.1	0.2
CO_2 Plume Extension	5 Years after Injection	Minor Axis(ft)	2133	2133	2133	2133
		Major Axis(ft)	2400	2400	2400	2400
	50 Years after Injection	Minor Axis(ft)	2533	2533	2533	2400
		Major Axis(ft)	4000	4000	3867	3733
	500 Years after Injection	Minor Axis(ft)	2667	2800	2533	2533
		Major Axis(ft)	4933	4933	4800	4533

BRINE COMPRESSIBILITY

In a closed geologic system, the amount of CO_2 that can be injected into the saline reservoir is mostly dependent on the availability of the additional pore space that can be provided due to brine compressibility. Additionally, compressibility determines how much injected fluid contributes to reservoir pressure build up or brine volume change (also can be referred to as a change in brine density).

As observed in Figure 97, an increase in brine compressibility results in lowering the maximum and stabilized reservoir pressures. For higher brine compressibility, injected CO_2 results in more changes in brine density rather than generating pressure build up in the reservoir. Changing brine compressibility shows no considerable influence on the CO_2 plume extension.

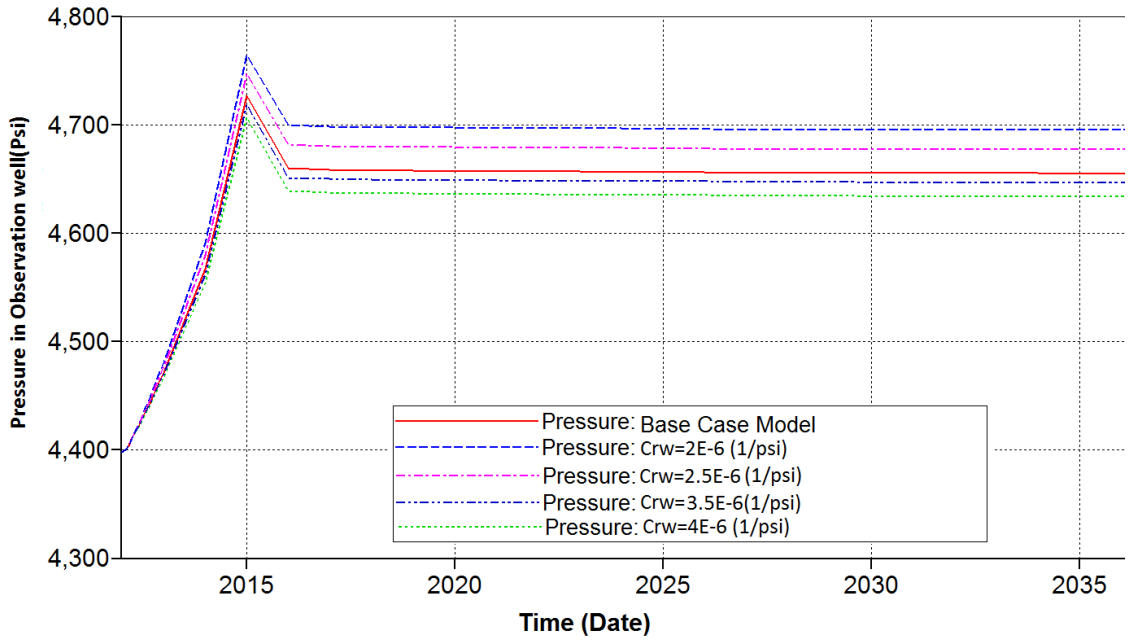

Figure 97. Reservoir pressure in observation well for different brine compressibility

BRINE DENSITY

The impact of a change in brine density on the reservoir pressure can be analyzed by considering the fact that denser the brine is, the less compressible it is, allowing more pressure build up during and after CO_2 injection. As it is illustrated in Figure 98, higher brine density contributes to more pressure gain for the reservoir (both maximum and stabilized pressures).

The influence of the brine density on CO_2 plume extension is addressed by the driving mechanism that governs fluid movement in the reservoir. During CO_2 injection, viscous forces makes the CO_2 move forward, and after injection is completed, buoyancy would be the dominant driving force. The density difference between the brine and the CO_2 determines the magnitude of the buoyant force. Higher brine density results in greater density differential and consequently, more buoyance force. Therefore an increase in brine density accounts for more buoyant force to be exerted to the CO_2 plume resulting in larger extensions (Table 22).

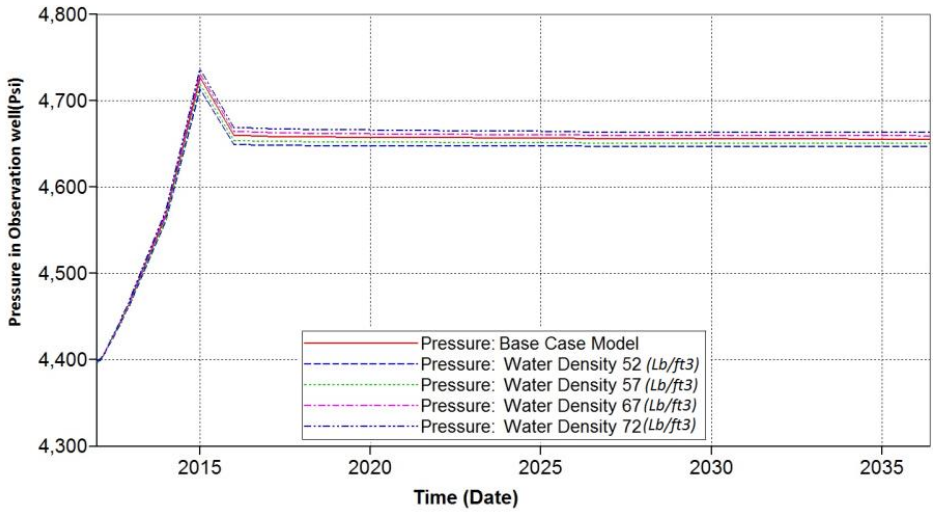

Figure 98. Reservoir pressure in observation well for different brine densities

Table 22. CO_2 Plume extension size over time (in the first layer) for different brine densities

			Brine Density(lb/ft3)				
			Base Case	52	57	67	72
CO_2 Plume Extension	5 Years after Injection	Minor Axis(ft)	2133	2133	2133	2133	2133
		Major Axis(ft)	2400	2267	2400	2533	2667
	50 Years after Injection	Minor Axis(ft)	2533	2533	2533	2533	2667
		Major Axis(ft)	4000	3467	3733	4133	4133
	500 Years after Injection	Minor Axis(ft)	2667	2533	2667	2800	2800
		Major Axis(ft)	4933	4667	4933	4933	5066

BOUNDARY CONDITION

In this section, we assume that the saline reservoir in the Paluxy formation is not a closed system. A Fetkovich aquifer which keeps the reservoir pressure constant at the reservoir boundaries is assigned to the East, East- South and East-South-West edges of the reservoir (Figure 99). As shown in Figure 100, reservoir pressure behavior in the closed system (no flow boundaries at all edges) is significantly different compared to other cases. First, maximum reservoir pressure at the end of injection is high. Second, the stabilized pressure reaches a constant value at higher pressures.

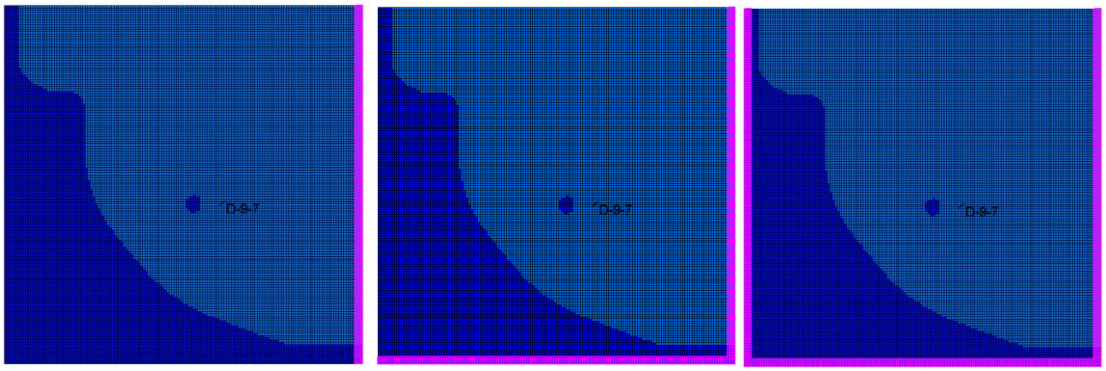

Figure 99. Different locations for constant pressure boundary (Fetkovich aquifer) – Presence of the aquifer is indicated by the pink line next to the boundary.

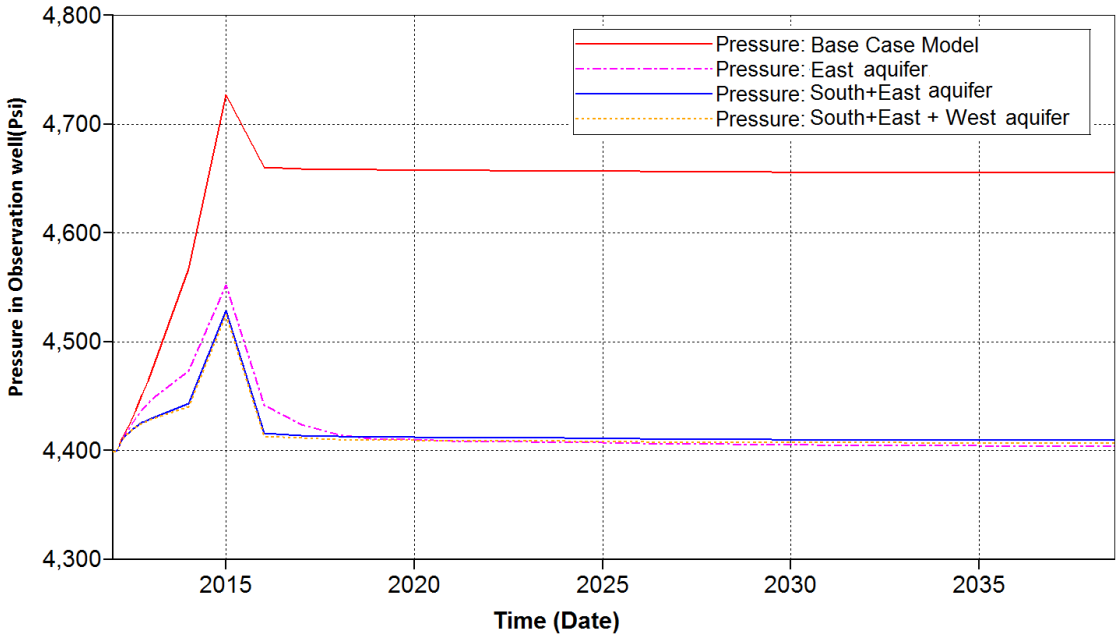

Figure 100. Reservoir pressure in observation well for different boundary conditions.

Changing the boundary condition of the reservoir from closed to constant pressure, affects reservoir pressure behavior significantly. When Fetkovich aquifers are placed at the edges of the reservoir, maximum pressure build up decreases notably. In addition, stabilized reservoir pressure comes back to native reservoir pressure after a while when injection is ceased. Table 23 summarize the impact of the reservoir boundary on the plum extension.

Table 23. Plume extension size over time (in the first layer) for different boundary conditions

			Reservoir Boundary (Fetkovich Aquifer)			
			Base Case	East	East+ South	East+ South+ West
CO_2 Plume Extension	5 Years after Injection	Minor Axis(ft)	2133	2133	2267	2267
		Major Axis(ft)	2400	2400	2667	2800
	50 Years after Injection	Minor Axis(ft)	2533	2533	2667	2667
		Major Axis(ft)	4000	4000	4133	4133
	500 Years after Injection	Minor Axis(ft)	2667	2800	2800	2800
		Major Axis(ft)	4933	5066	5066	5066

In this section, all the steps for reservoir simulation model development for CO_2 injection in the Paluxy saline reservoir of the Citronelle Dome were explained. The model was used to predict storage performance behavior. Sensitivity analyses was performed to study the impacts of reservoir uncertainty on the reservoir pressure in the observation well and CO_2 plume extension. The results of sensitivity analysis can be considered for risk assessment in addition to history matching the reservoir simulation model while actual field measurements (pressure data) are available. The main findings can be summarized as follows:

- Rock type (permeability) contribution to CO_2 injectivity, reservoir pressure and CO_2 plume extension is significant. Higher permeability represents more extensive CO_2 plume and less reservoir pressure gain. Also an increase in vertical to horizontal ratio leads to higher stabilized pressure and CO_2 plume extension.

- It is observed that an increase in gas (CO_2) relative permeability results in a higher stabilized pressure and a larger CO_2 plume extension. Additionally, higher maximum residual gas (CO_2) saturation results in more residual trapping, and therefore, lower CO_2 plume extension.

- Brine compressibility plays a role in reservoir pressure build up, especially in a closed geologic system. When brine compressibility rises, we observe a decrease in stabilized reservoir pressure.

- Density of brine is the parameter that affects both reservoir pressure and CO_2 plume extension. Denser brine causes more buoyancy force, which drives CO_2 to move further and distributes in more area. Also higher brine density values contribute to more reservoir pressure build up.

- Changing the boundary condition of the reservoir from closed to constant pressure, affects reservoir pressure behavior significantly. When Fetkovich aquifers are placed at the edges of the reservoir, maximum pressure build up decreases notably. In addition, stabilized reservoir pressure comes back to native reservoir pressure after a while when injection is ceased.

HISTORY MATCHING OF THE RESERVOIR SIMULATION MODEL

COLLECTING INJECTION DATA

The objective of carbon capture and sequestration in Citronelle filed is to inject 9.48MMcf/day of CO_2 during three years (starting at the beginning of 2012). Due to some operational constrains, the injection started on August 20, 2012 with the rate of 918 Mcf/day. After that the CO_2 injection rate increased with an oscillating trend (due to operational difficulties) until the 28th of September when it reached to 9 MMcf/day. From that time injection stopped for 14 days and then it started with almost stable trend(around 9 MMcf/day) up to the 29th of November(2012). During this 3months period, the average CO_2 injection rate was about 6.26 MMcf/day (66% of the injection target was achieved). The daily injection rate from the beginning up to end of the November is shown in Figure 101. These injection rates were used in the Reservoir Simulation Model as the input constrains.

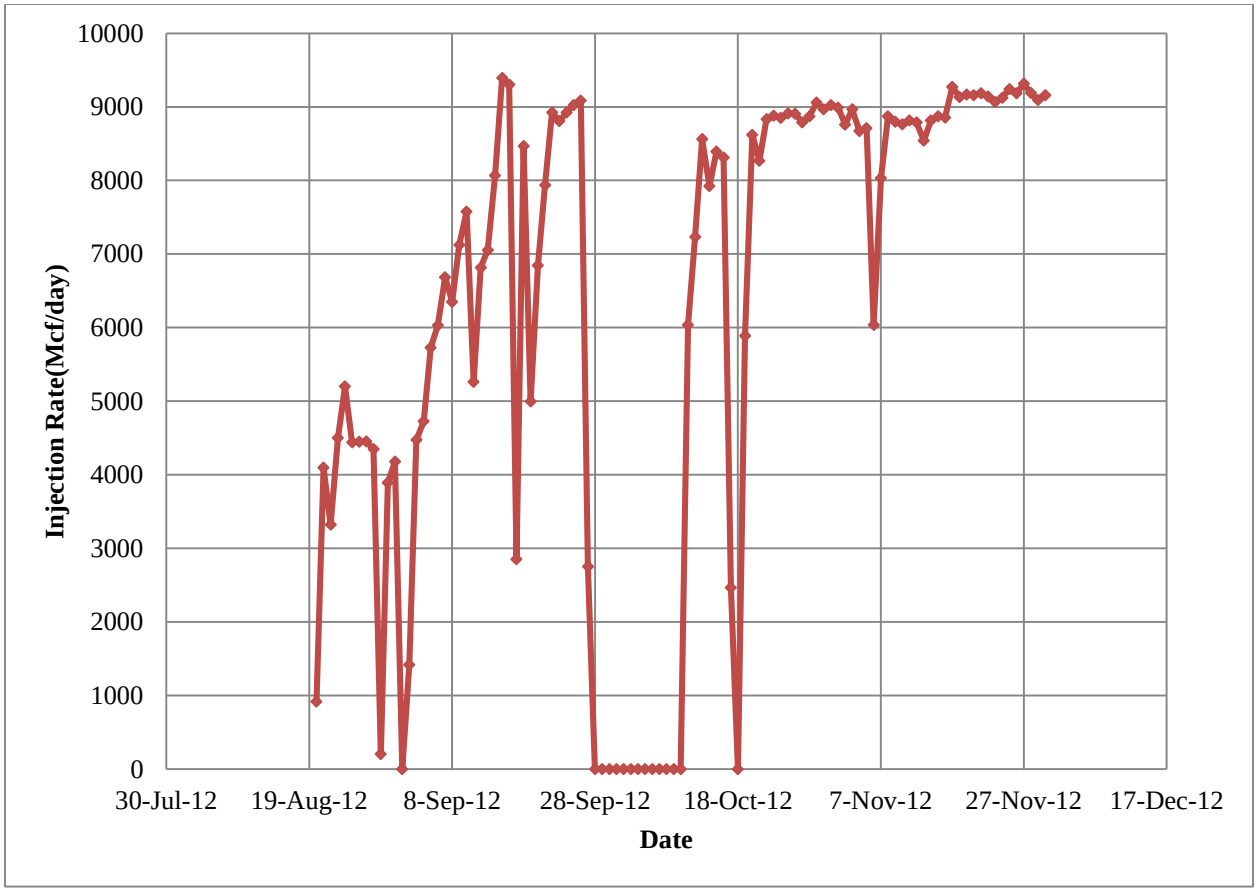

Figure 101. CO_2 Injection rate history

COLLECTION OF PRESSURE DATA (DE-NOISING AND AVERAGING)

As explained in previous sections, high frequency real time pressure data from two PDGs are available on a minute by minute basis from August 17th, 2012. These high frequency and noisy data should be processed in order to be used for history matching.

In order to perform the history matching, first we de-noise the pressure data by Daubechies wavelets 10 in five levels. The de-noising results for 1 day pressure data (9/10/2012, 1440 records) and the entire data (103,750 records) are illustrated in Figure 102 and Figure 103.

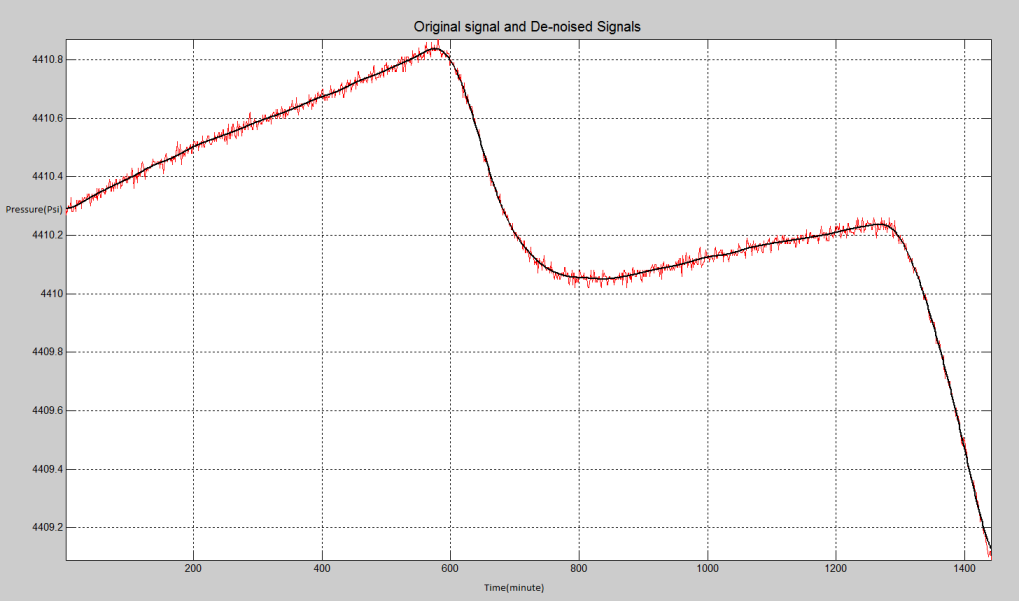

Figure 102. Original (noisy) and De-noised Pressure data in one day (9/10/2012)

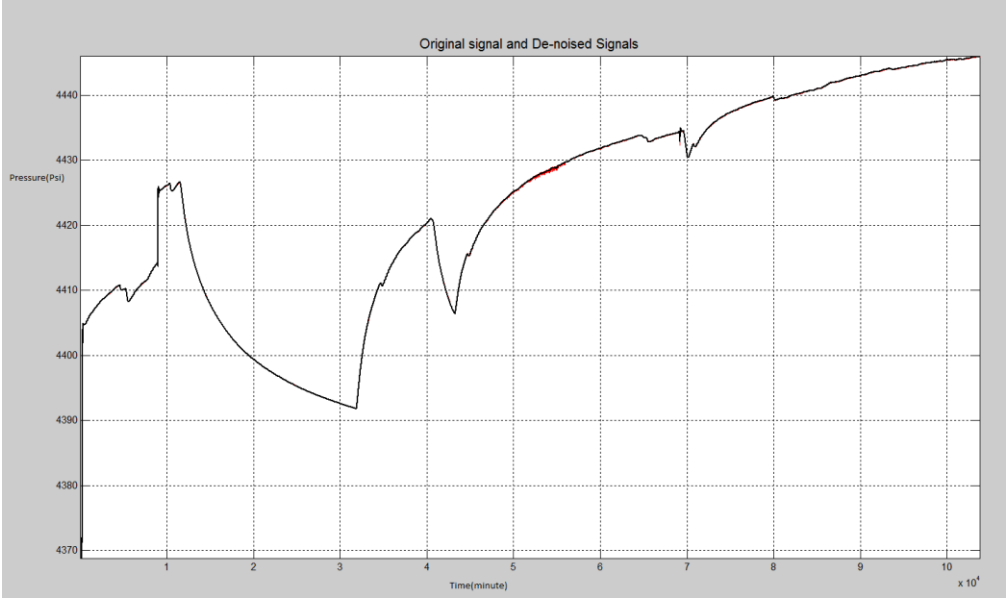

Figure 103. Original (noisy) and De-noised Pressure data for the entire interval

After preprocessing (de-noising is referred to as a pre-processing procedure) the high frequency pressure data it is necessary to do data summarization over time. As it was mentioned earlier the pressure data from the PDGs is collected every minute. Therefore, for each day 1440 data points are available. For the history matching of the reservoir simulation model, it is possible to run the model by setting each time step equal to one minute, and then try to match the actual with the simulated pressure data. But this approach is computationally expensive and impractical. Therefore the pressure data is summarized by averaging over every day. The results of real time pressure data on a daily basis is illustrated in Figure 104.

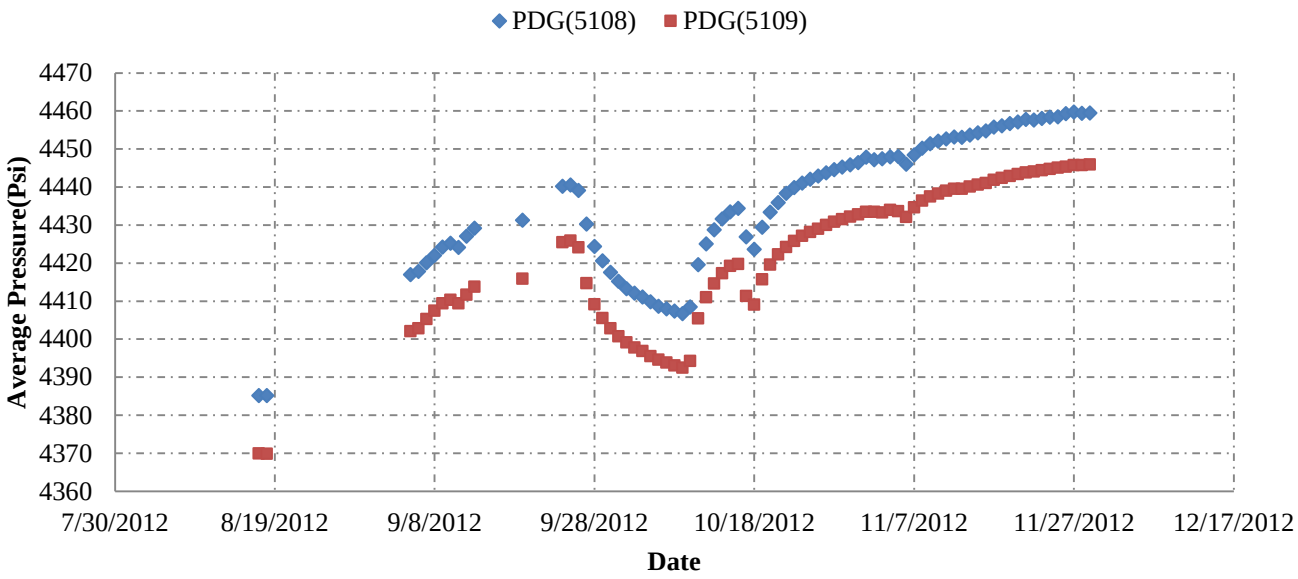

Figure 104. Daily averaged Pressure data from 2 PDGs

A comprehensive explanation and analysis of the de-noising process has been included in this report as an appendix. Details of the de-noising analysis can be found in Appendix 2.

IN-SITU CO_2 BEHAVIOR VALIDATION - EARLY INJECTION DATA

The reservoir simulation model was built using Computer Modeling Group's (CMG) software application called "GEM". Geological structure of the model includes 17 sand layers representing 51 simulation layers (Figure 105). The model is a 125x125x51 models having 125 grid blocks in X, and Y directions and 51 layers in Z direction. Δx and Δy equal to 133.3 ft.

Well logs from 40 offset wells that are within the area of study have been acquired and interpreted in order to generate the porosity maps. The initial model was assumed to be homogeneous with the absolute permeability of 460 md (for the entire reservoir). Relative permeability curves from the history-match of the injection pilot test at the Mississippi Test Site were used (trapped gas saturation was considered to be 7.5 percent). For the reservoir simulation, the injection well was operated with maximum bottom-hole pressure limit of 6,300 psi and an injection rate constraint. The density of saline water was set to 62 lb/ft^3 and its compressibility was set to $3x10^{-6}$ (psi^{-1}) at 14.7 psi. The reference pressure was set to be 4,393 psi at 4,015 ft.

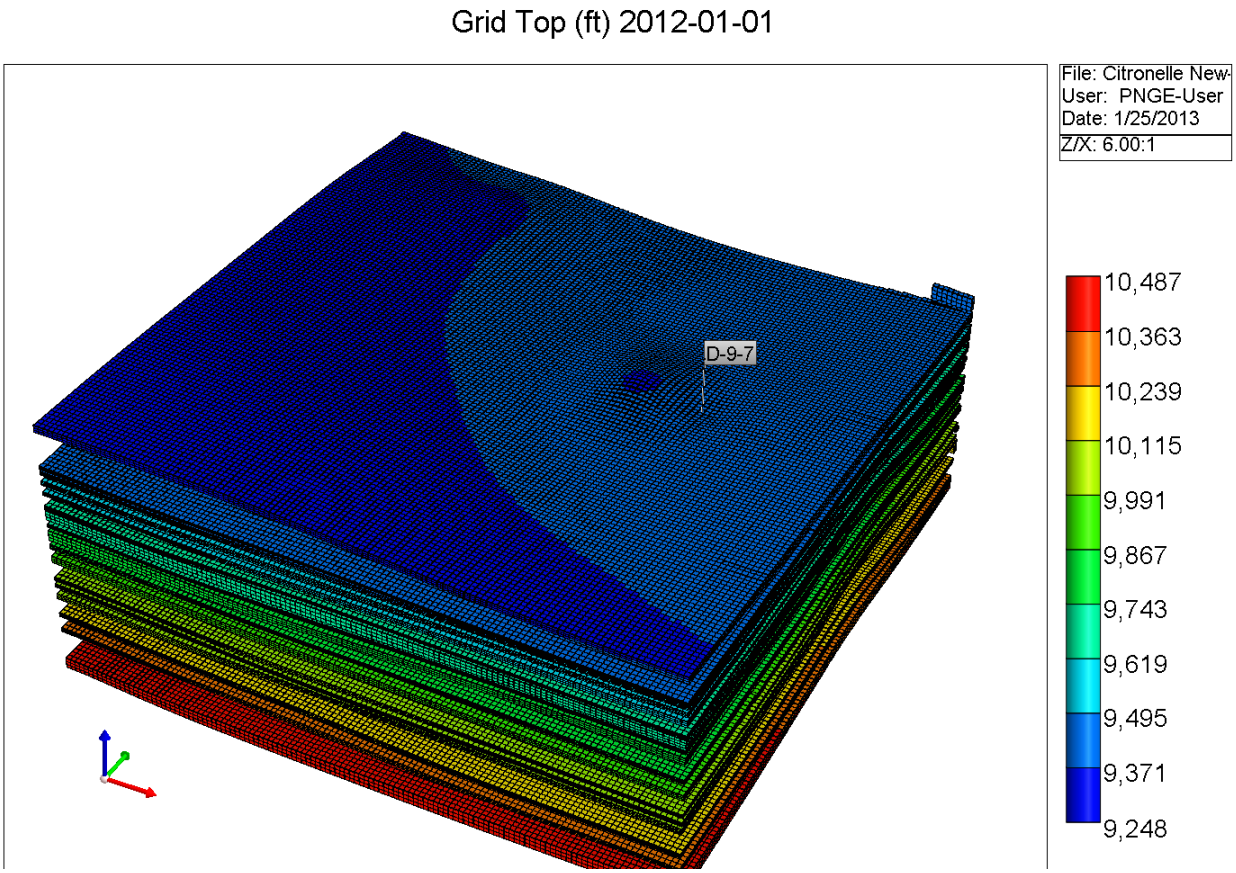

Figure 105. The Grid tops of the reservoir Simulation Model

In Figure 106 pressure result at the two PDGs location from the reservoir simulation model (the base model) is compared to the actual data. It should be mentioned that the average Block pressure for the corresponding grid blocks (101,56,1 and 101,56,3) with the exact coordinates of the PDGs (5109, 5108) are compared with the actual data.

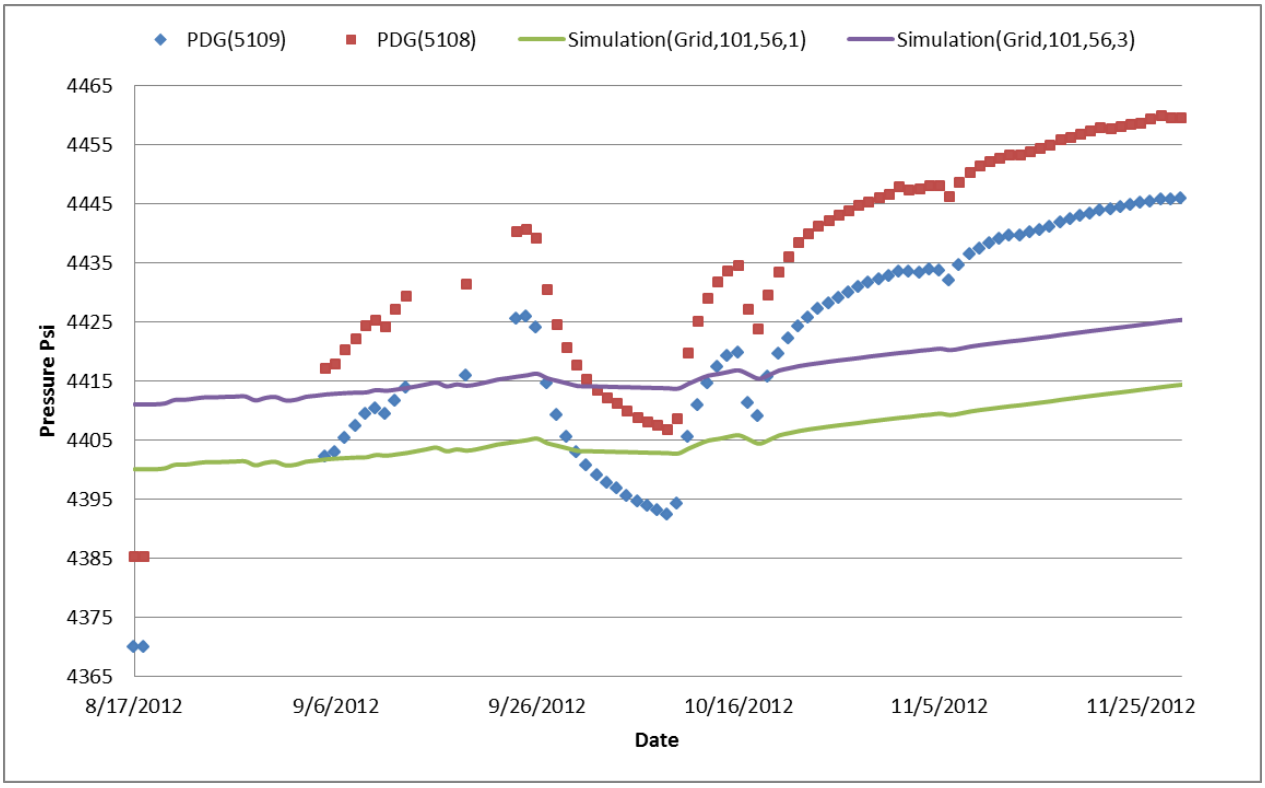

Figure 106. Comparison between actual PDG data and simulation results –base case

The objective of the history matching is to modify some of the reservoir parameters and characteristics in the reservoir simulation model such that the gap (dis-similarity in magnitude and behavior) of the model results and the actual pressure measurements reduces to a minimum. The first parameter modified is absolute permeability. As mentioned in the previous sections of this report, five different clusters were determined in the porosity-permeability cross plots that corresponded to five rock types. The rock types were identified as the best to the worst rock types (Figure 107) based on the data shown in Figure 107. We had selected the “Average Rock Type” for the base model.

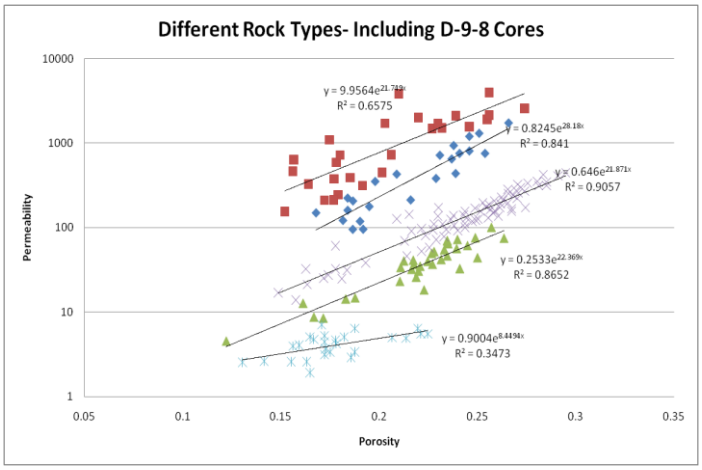

Figure 107. Different rock types based relationship between porosity and permeability

Table 24. Core porosity and Permeability from Core Data

Sand Name	Thickness (ft)	Porosity (%)	Hz Perm (md)	V Perm (md)
9460-1	15	18	290	180
9460-2	5	22	1,830	1,100
9460-3	5	17	220	130
9460-4	1	20	1,340	810
9460-5	4	18	280	170
9460-6	1	21	1,040	630
9520	15	18	170	80
9540	13	18	170	80
9570	22	19.3	90	90
9620	41	21.8	1,230	1,140
9710	15	18.2	190	90
9740	15	17	100	40
9800	28	18.4	210	110
9900	12	16	60	20

The results of the pressure data when the "Conductive Rock Type" was considered in the model are shown in Figure 108. From here forward, most of the simulation runs are considered to have the permeability values corresponding to the "Conductive Rock Type" ($K=.825e^{28.1\phi}$)

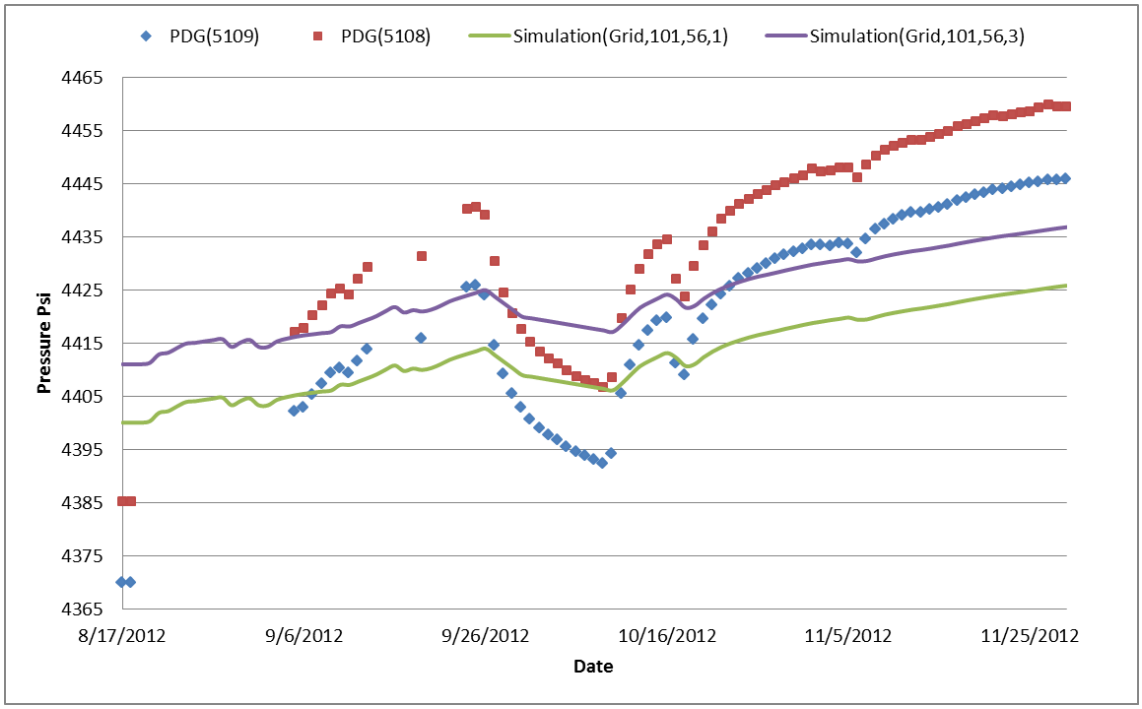

Figure 108. Comparison between actual PDG data and simulation results –Modified Permeability

An important point that was observed by analyzing the pressure behavior is the difference between actual initial pressure and the simulated initial pressure. To adjust the observed difference, the reference pressure at 9,416 ft was changed to 4,370 psi. Another observation is that the difference between pressure readings from PDGs (P @ 9,441 ft – P @ 9,416 ft = 4,385 - 4,370 = 15 psi) is not the same as the difference between the 2 corresponding grid blocks (P @ 101, 56, 3 - P @ 101, 56, 1 = 4,411 – 4,400 = 11psi) knowing the fact that both PDGs and Grid blocks are exactly 25 ft apart. This means that the pressure gradient between the PDGs is 0.613 psi/ft while it has the value of 0.428 psi/ft between the grids. This means that the brine density should be higher than what was set in the simulation model. Brine density at the reservoir conditions can be calculated by the following equation:

$$\tilde{\rho}_{br} = \tilde{\rho}^{0}_{br}\left[1 + c_{br}\left(p - p^{0}\right)\right]$$

In order to keep the brine compressibility the same as the initial value, new density of brine should be set as 87 lb/ft^3. It should be mentioned that the brine compressibility can also be changed in order to have the same brine density at the reservoir level. The results for the case that reference pressure and brine density were changed are shown in Figure 109 and Figure 110 (it should be mentioned that since the PDGs depths are not exactly at middle of grid blocks a modification based on the elevation difference was performed so that the grids represent the same initial

pressure as PDGs). The results for modified Brine compressibility, reservoir boundary and horizontal permeability are shown in detail in Appendix 3.

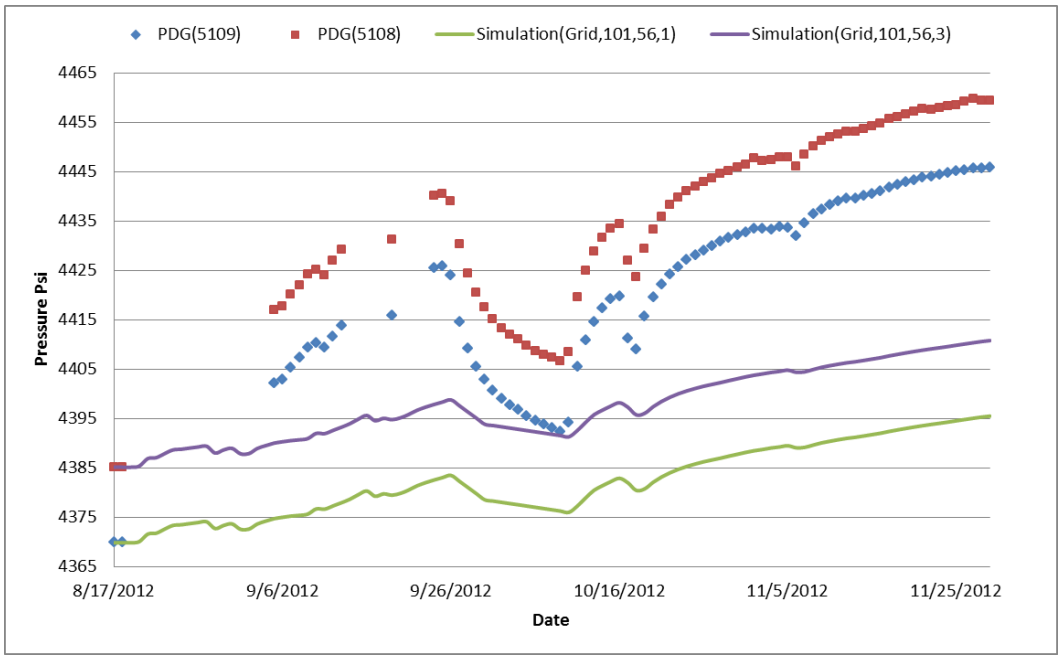

Figure 109. Comparison between actual PDG data and simulation results –Modified reference pressure and brine density

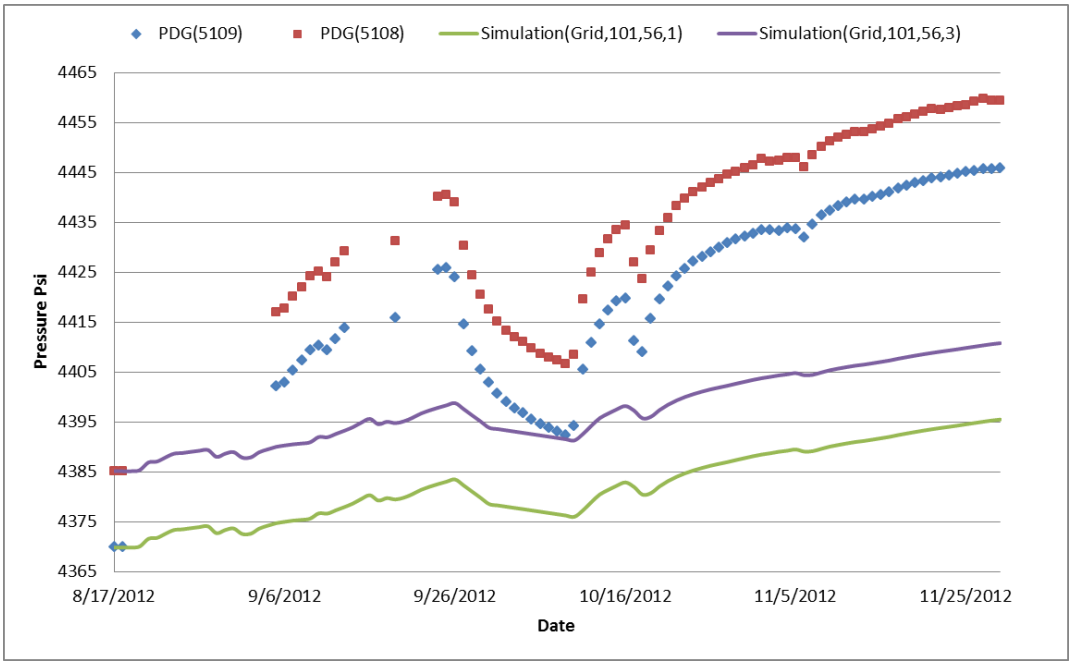

Figure 110. Comparison between actual PDG data and simulation results –Modified reference pressure and brine density

The effect of vertical to horizontal perm ratio, rock -fluid compressibility, water viscosity, porosity and boundary of the reservoir was studied on simulation pressure results. By tuning the mentioned parameters, although simulation pressure results convert towards the actual measurements, but the mismatch between simulation and actual pressure remains high.

The next step that improved the simulation results considerably was modification of vertical transmissibility in order to control vertical communications between the layers. The transmissibility multiplier was set to zero for the layers that are subject to no CO_2 injection (due to either high shaliness or very high permeability that causes rapid gas movement). By making transmissibility modification, the trend in simulated pressure responses started to approach that of actual pressure (Figure 111).

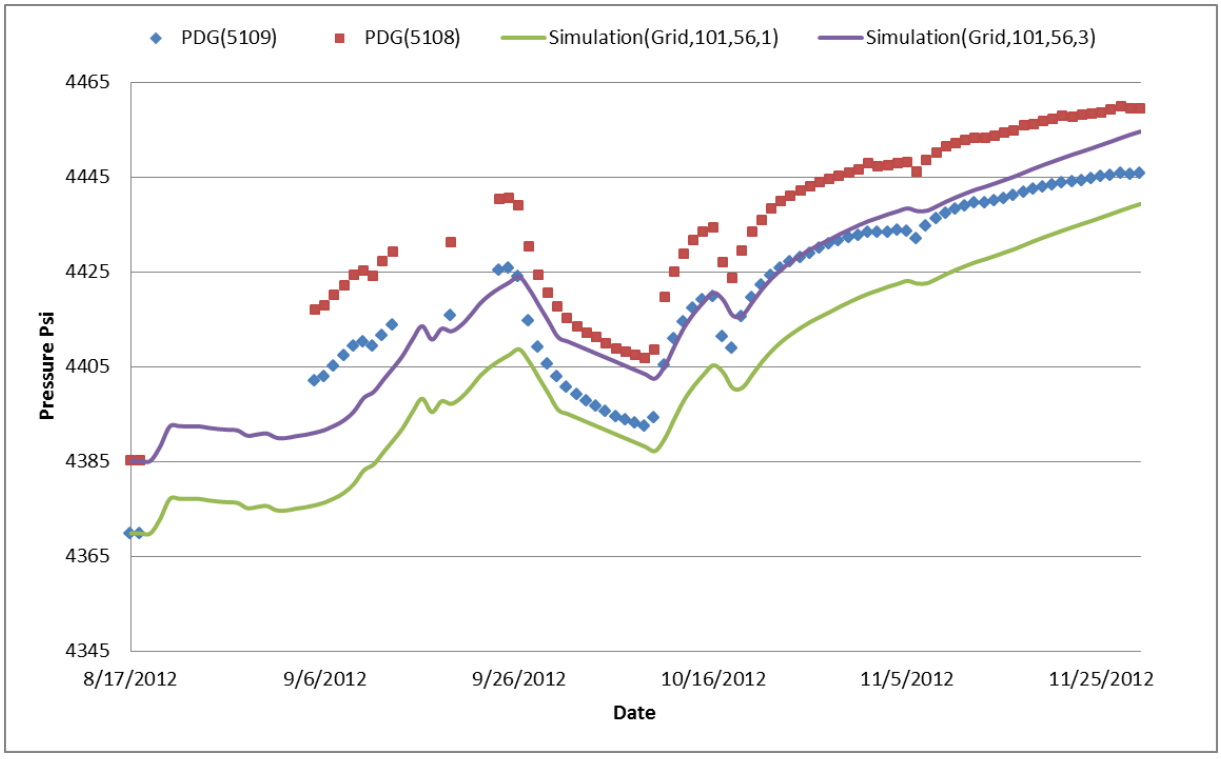

Figure 111. Comparison between actual PDG data and simulation results –modified transmissibility multiplier

From here forward, we try to apply the changes on the simulation model with modified absolute permeability, initial pressure, brine density and more importantly vertical transmissibility multiplier. The next step was to investigate the effect of relative permeability curves on the simulation pressure results. The original relative permeability curves (gas and water) that initially were used in the simulation model came from a Mississippi Storage pilot plan, located 70 miles from the Citronelle site.

There are two important features that characterize relative permeability curves. The first feature is immobile or irreducible phase saturation below which, the corresponding phase (water or gas) cannot move. The other important characteristic of relative permeability curve is the curvature.

This feature has considerable influence on fluid movement in the reservoir model. To investigate the effect of these relative permeability features on the simulated pressure behavior, we defined ranges of relative permeability values in the vicinity of the original curves. Both irreducible phase saturation and curvature of relative permeability changed in a reasonable range. The generated curves are shown in Figure 112.

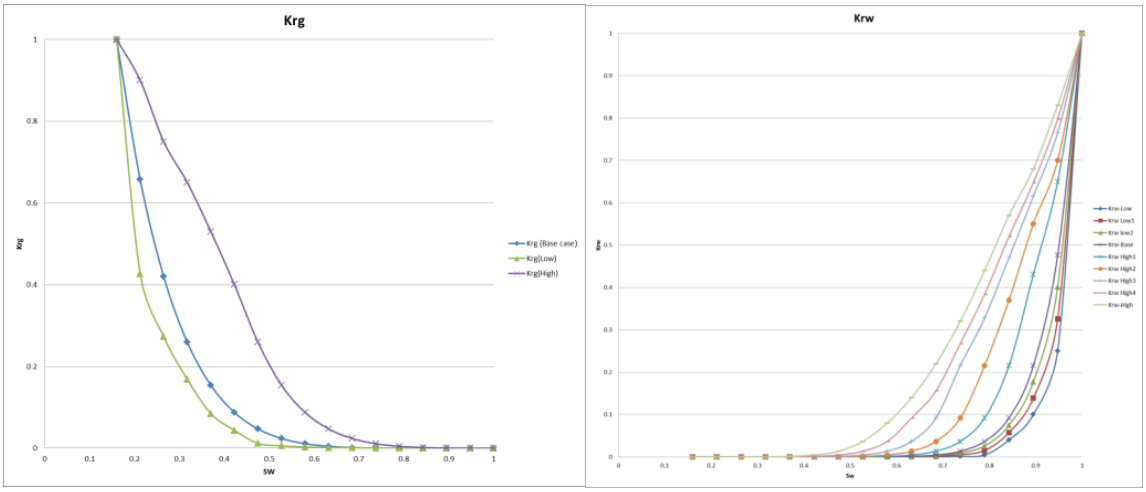

Figure 112. Relative permeability curves (Right: water relative permeability, Left: gas relative permeability)

We tested the effect of both gas and water relative permeability curves on the pressure behavior. Higher curvature and lower irreducible phase saturation increased the simulated pressure results. By adjusting the relative permeability curves, we obtained reasonably good match between simulated pressure results and actual field measurements.

In Figure 113 the best history match results based on changing the gas relative permeability is illustrated. Also in the Appendix 3, we show how simulation pressure history behaves with respect to different reservoir boundary conditions, absolute and relative permeability.

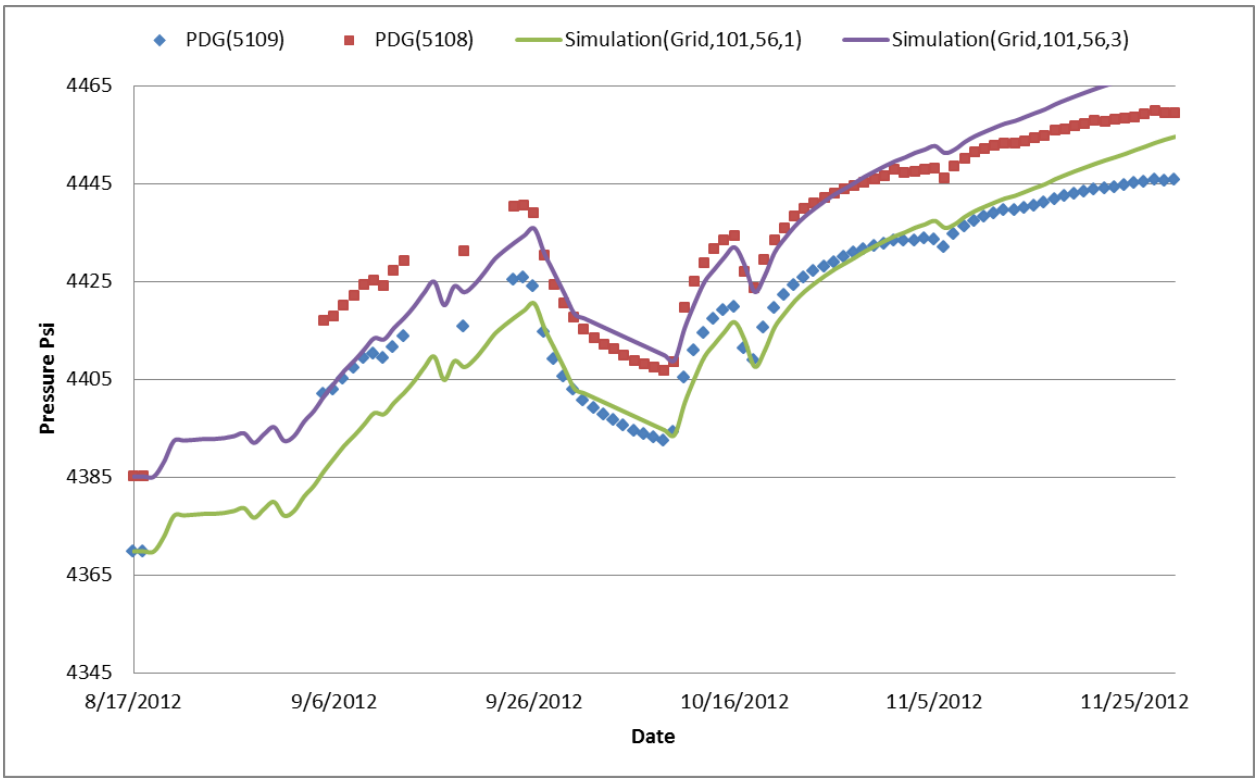

Figure 113. Comparison between actual PDG data and simulation results –modified gas relative permeability

As these studies were ongoing, more field data became available including actual injection and pressure (coming from PDGs in observation well) from 8/19/2012 to 11/30/2012. The injection rate and pressure data were in daily and in per minute basis, respectively. In order to keep the consistency between to different available data and also decrease computational time and effort for reservoir simulation, minute-based pressure data was averaged to daily basis. Several reservoir parameters were tuned (as shown in Table 25) in order to minimize the mismatch between actual field data and simulation results. The best history matched results during the mentioned time interval are shown in Figure 114.

Table 25. Reservoir parameters that tuned for history matching

Matching Parameter
Absolute Permeability
Brine Density
Reference Pressure
Transmissibility Multiplier
Reservoir Boundary
Relative Permeability

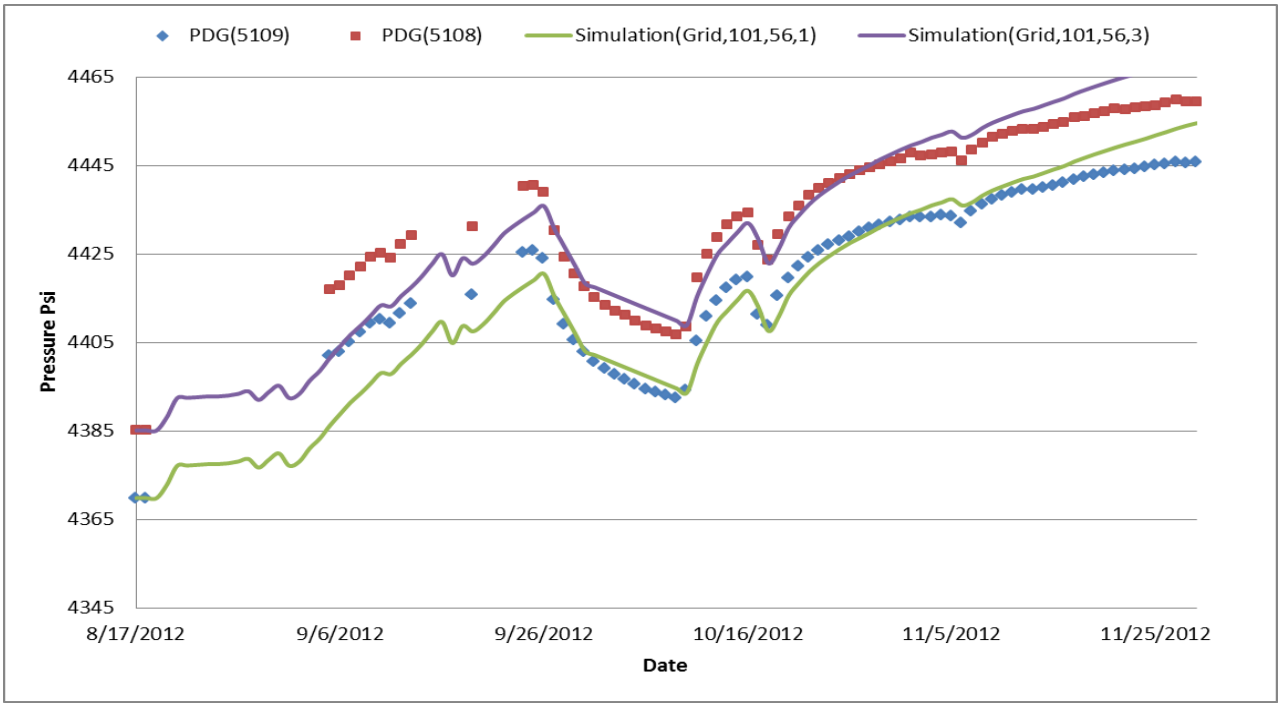

Figure 114. Comparison between actual PDG data and simulation results –modified gas relative permeability-best history matched results with no additional data

Available field data for two more months (December2012 and January 2013) were considered for history matching. The reservoir simulation predicted the pressure data for the two new months using the best history matched model. The results for the reservoir pressure are overestimated by reservoir simulator model.

Comparison between reservoir simulator and actual pressure data is shown Figure 115

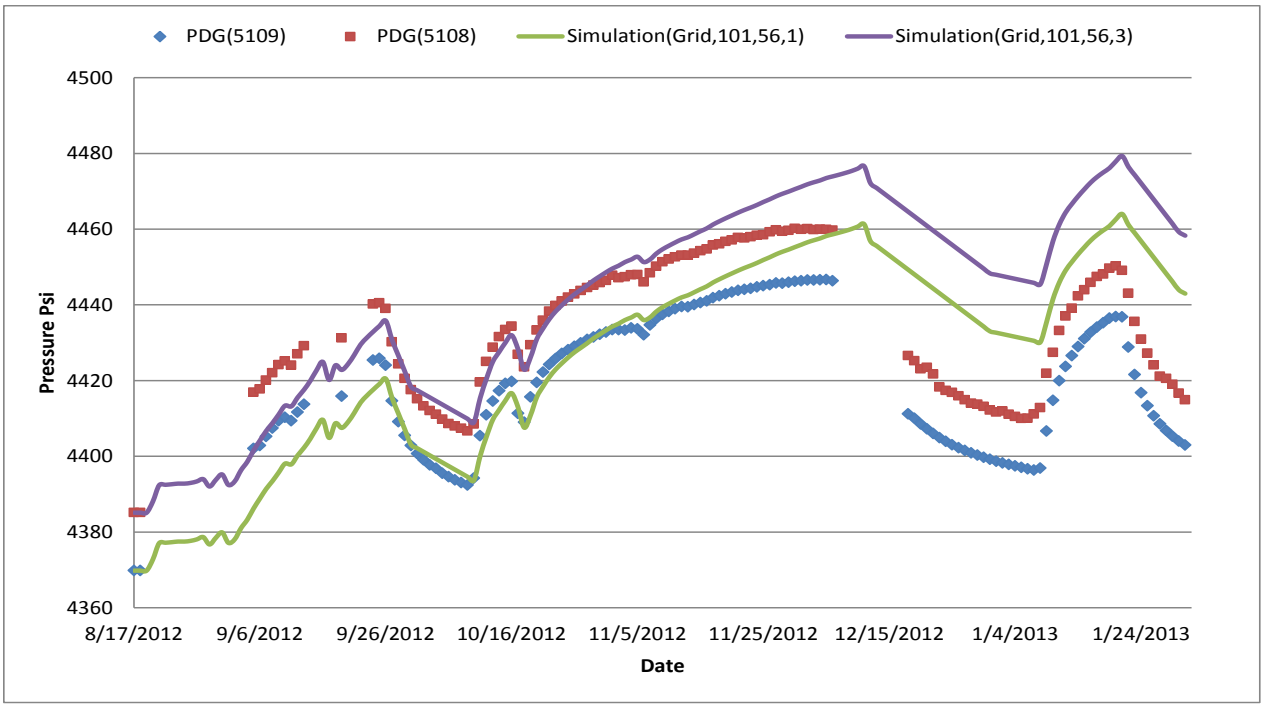

Figure 115. Comparison between actual PDG data and simulation results –modified gas relative permeability-best history matched results with additional data

Several reservoir parameters were tuned again, aiming to reduce the overall mismatch between the actual field data and simulation results (those recently acquired – the new two months of data). These parameters modified: absolute permeability, brine compressibility, brine viscosity, relative permeability, reservoir boundary condition and vertical to horizontal permeability ratio. In order to compare the mismatch between reservoir simulation predictions and actual field data, an objective function that measures the difference between simulated and actual data was used according to the following equation:

$$OF = \sqrt{\frac{\sum_{t=1}^{Nt}(P_t^s - P_t^m)^2}{Nt}}$$

Where $P_t^s and P_t^m$ are simulated and measured pressure values at each time step (day) and *Nt* is the total number of measurements. The values of the mismatch or the objective functions are shown in Table 26.

Based on the results of the models we learned that higher brine compressibility (4e-6 1/psi) represents the lowest mismatch with actual data. The pressure results for this model are shown in Figure 116. All the history match results are illustrated in Appendix 3.

Table 26. Pressures mismatch values for changing different reservoir parameter

Tuned Reservoir Parameter	Pressure Mismatch Value(OF,Psi)
Reduced μ_w	16.89
New Boundary	20.01
Reduced K(half of the base)	20.94
Brine Compressibility=4e-6/psi	16.34
K_v/K_h=0. 9	16.99
K_{rw} low	17.08
K_{rw} High2	18.75
K_{rw} High3	20.815
K_{rg} low	20.21
K_{rg} high	20.7

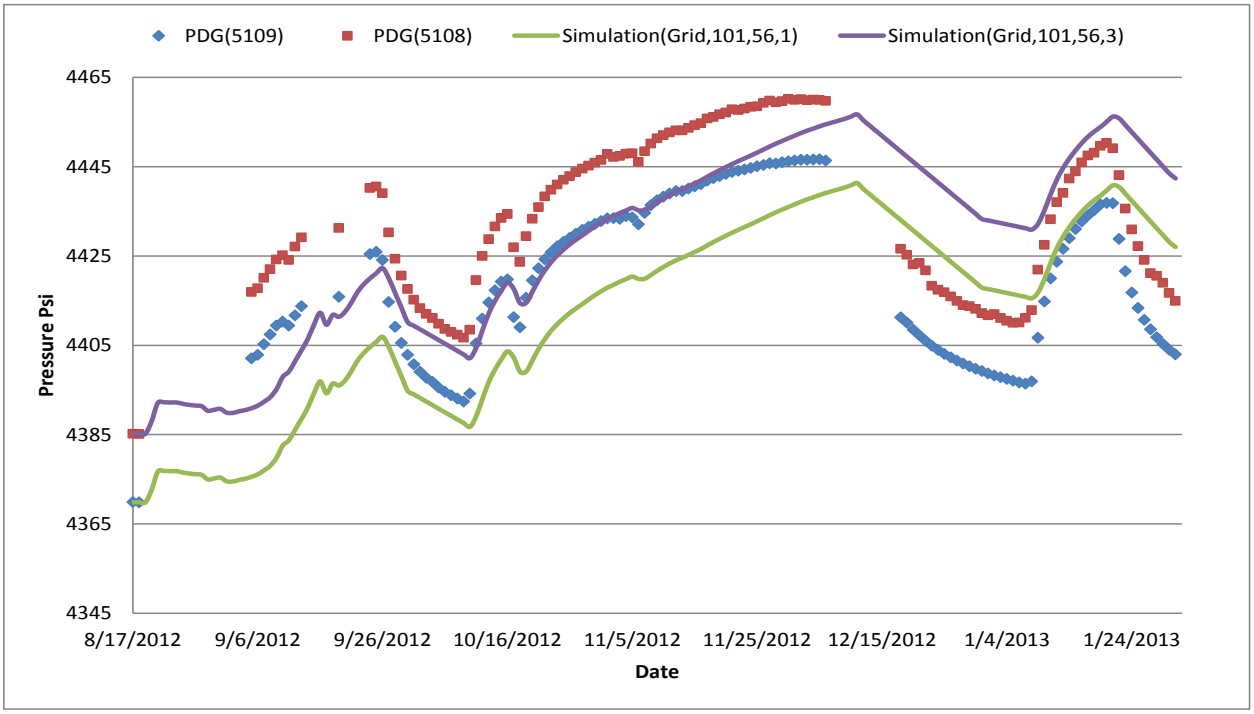

Figure 116. Comparison between actual PDG data and simulation results –results with lowest mismatch (modified brine compressibility)

IN-SITU CO_2 BEHAVIOR VALIDATION - ENTIRE INJECTION DATA

In previous section, in-situ CO_2 behavior validation was initiated for the reservoir simulation model based on the availability of the field data. The first set of available data (injection rate and pressure data from observation well) belonged to a time period from 8/19/2012 to 11/30/2012. A second set of data which covered two more months (December 2012 and January 2013) became available upon completion of the first set of history matching efforts. Once this new set of data was received it was considered for continuation of history matching. The history matching process of almost eleven months of injection rate and pressure data is presented in this section. Locations of injection and observation wells are shown in Figure 117.

Figure 117. Location of the injection and observation well in the area of interest

During the entire year the injection process was almost stable, although it experienced some periodic shutdown. The daily injection rate from the beginning up to August, 2013 is shown in

Figure 118. These injection rates were used in the reservoir simulation model as the input constrains for the history matching process.

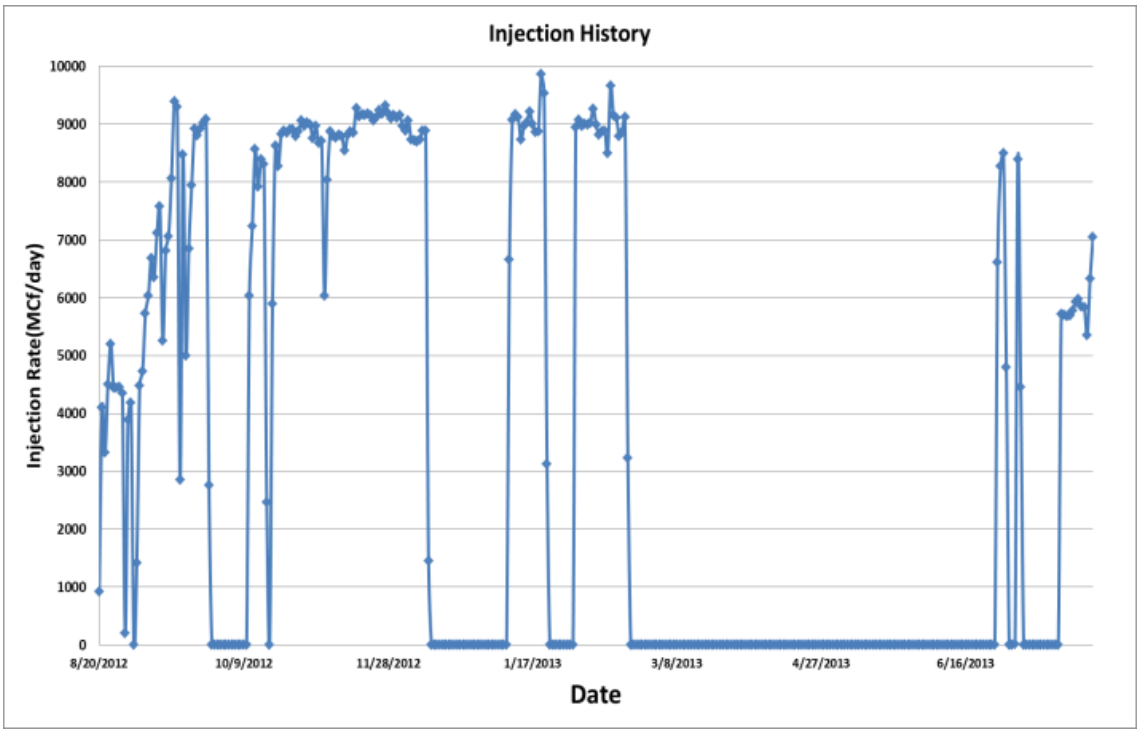

Figure 118. CO_2 injection history at Citronelle field

In the observation well (D-9-8#2) at Citronelle field (Figure 117), two Pressure Down-hole Gauges (PDG-5108/5109) are installed at different depths (9,416 and 9,441 ft TVD) in order to provide real time pressure and temperature readings during and after the injection period. The pressure data is available from mid-August 2012 till the end of September 2013, recorded on one-minute basis (1,440 records per day). The pressure data was summarized by averaging over each day. The actual pressure data on a daily basis is illustrated in Figure 119.

Initially a base case reservoir model was developed considering reservoir properties that are summarized in Table 27. Porosity maps for each simulation layer were acquired by interpretation of 40 well logs. In this model, operational constrains were the actual CO_2 injection rates (Figure 118). Furthermore, maximum bottom-hole pressure limit of 6,300 psi was also imposed as additional operational constraint. The solubility of CO_2 in the brine was not considered in the base model. Block pressure for the grids corresponding to the PDGs were compared with the actual data. Simulated pressure data using the base model are plotted against actual pressure history in Figure 120.

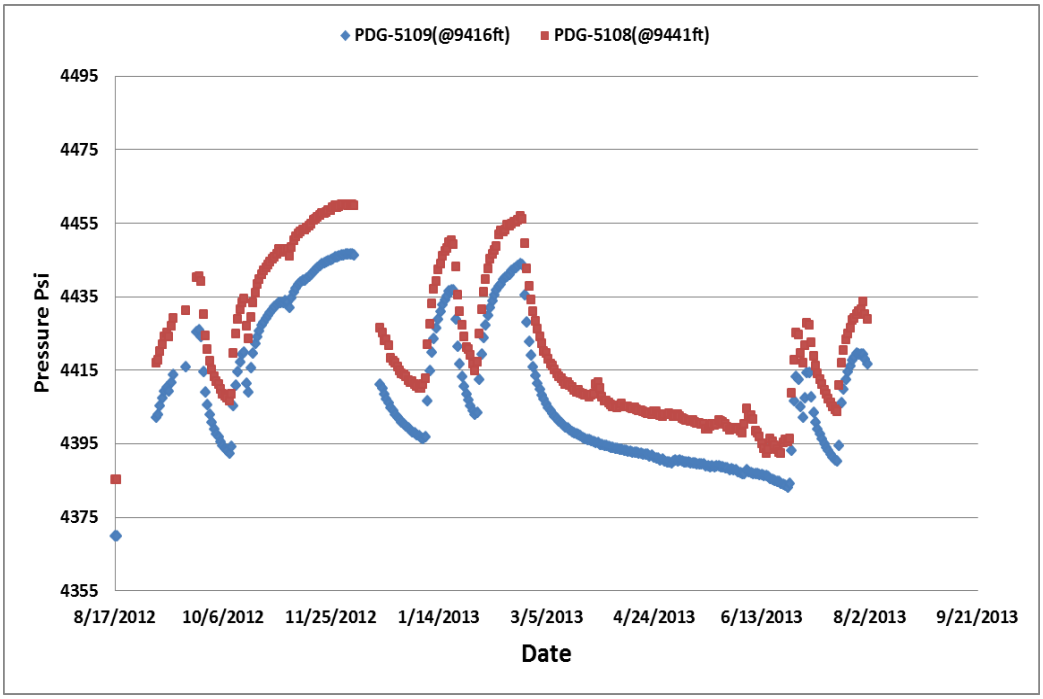

Figure 119. Daily pressure data from PDGs @ observation well

Table 27. Reservoir parameters and properties (base case model)

Parameter	Value	Parameter	Value
Permeability(md)	460(all grids)	Water density(lb/ft3)	62
Temperature(◦F)	230	Water viscosity(cp)	0.26
Salinity(ppm)	100000	Water compressibility(1/psi)	3.2E-6
Residual gas saturation	0.35	Kv/Kh(permeability ratio)	0.1
Residual water saturation	0.6	Pressure reference@9415ft(psi)	4393

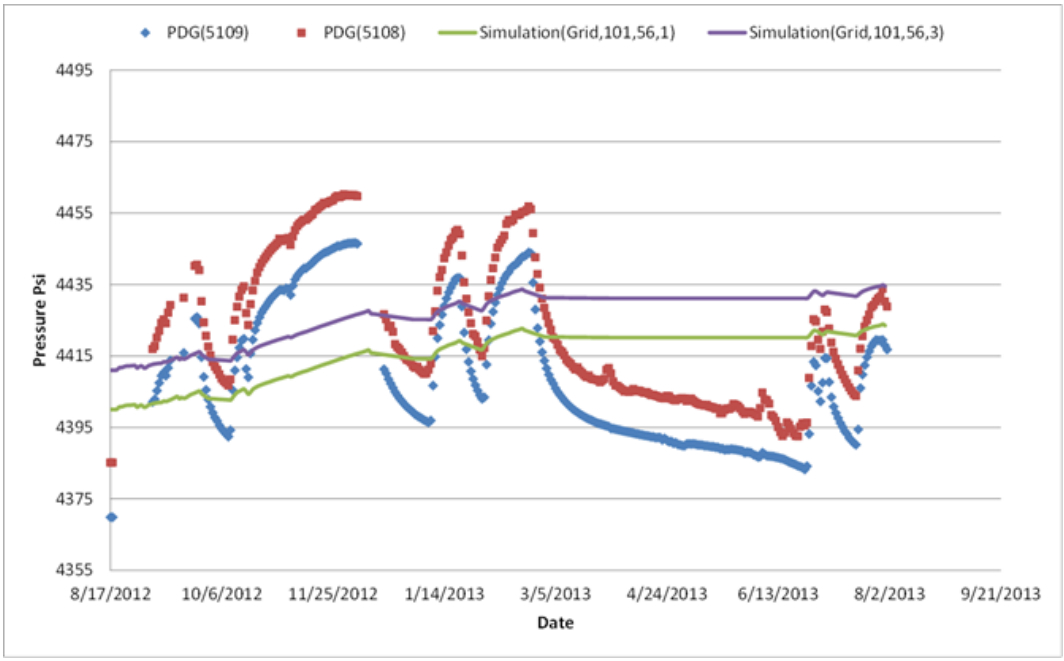

Figure 120. Model's pressure results and actual history for the base model

A thorough sensitivity analysis was performed to study the effects of several reservoir parameters on pressure behavior in the observation well. As expected, the results of sensitivity analysis showed that permeability (rock type) contributed significantly to injectivity, CO_2 plume extension and reservoir pressure. By use of Alabama's southwestern Dataset, porosity-permeability cross-plots (Figure 121) were generated for the Paluxy formation core data. Available data from the cores taken from injection well demonstrated the dominance of conductive rock type ($k=0.824e^{28.18\varphi}$) in the vicinity of the injection area. Also, vertical to horizontal permeability ratio was calculated to be 0.58 using core data analysis.

Modification of pressure references, brine density and permeability in addition to zero transmissibility between the sand and shale layers resulted in pressure predictions illustrated in Figure 122.

Please note that a more thorough explanation of how this process was conducted (but for the first set of pressure and injection rate data) was provided in the previous section. Therefore, in this section we just mentioned the highlights and the corresponding results of the history matching process for the larger data set.

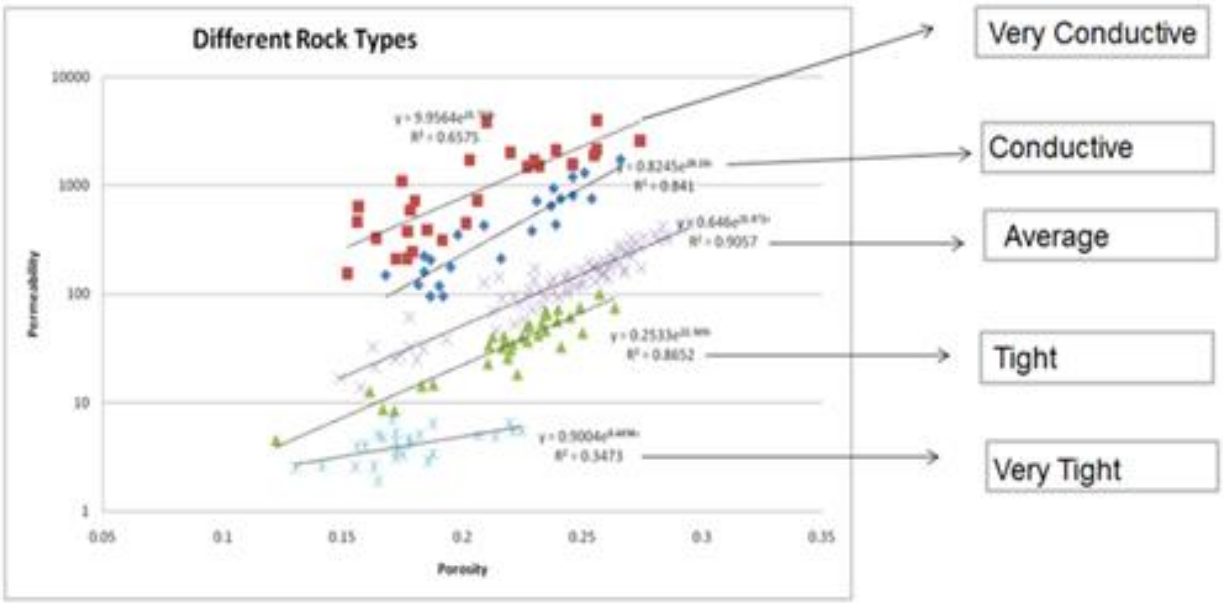

Figure 121. Porosity-permeability cross plot

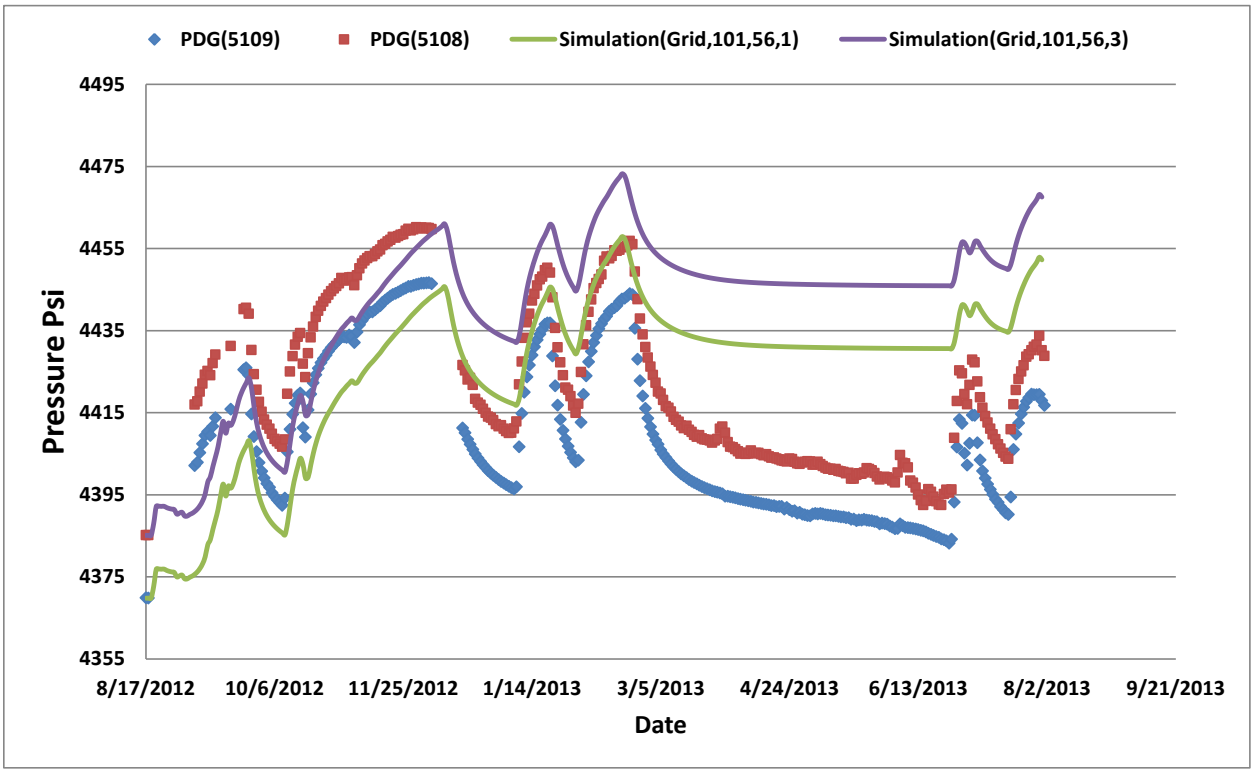

Figure 122. Model's pressure results and actual history; modified, pressure reference, brine density and permeability

By Implementation of the modified parameters in the model, a closer match between the simulated and the actual pressure data as well as the pressure gradient was achieved. However, modeled pressure predictions did not follow PDGs pressure trend correctly. As it is shown in Figure 122, reservoir simulation results underestimated actual data during first four months after the injection, and overestimated the rest of pressure history.

Additionally, simulated pressure drawdowns reached a stable trend much faster, compared to the actual data. This behavior can be explained by the fact that higher permeability (in the model) resulted in lowering the time that pressure drawdown got to a steady trend. Therefore, it was necessary to decrease the permeability in the model to adjust pressure drawdown behavior. On the other hand, lowering the permeability led to CO_2 injectivity reduction. As a result, reservoir model was divided into two regions:

A. grids in the vicinity of the injection (zone 20*20 grids around the injection well), and
B. grids outside the injection (zone-Figure 123).

To correct model's pressure drawdown trend, dual modification in reservoir permeability was done by decreasing permeability in region "a" and increasing permeability in region "b".

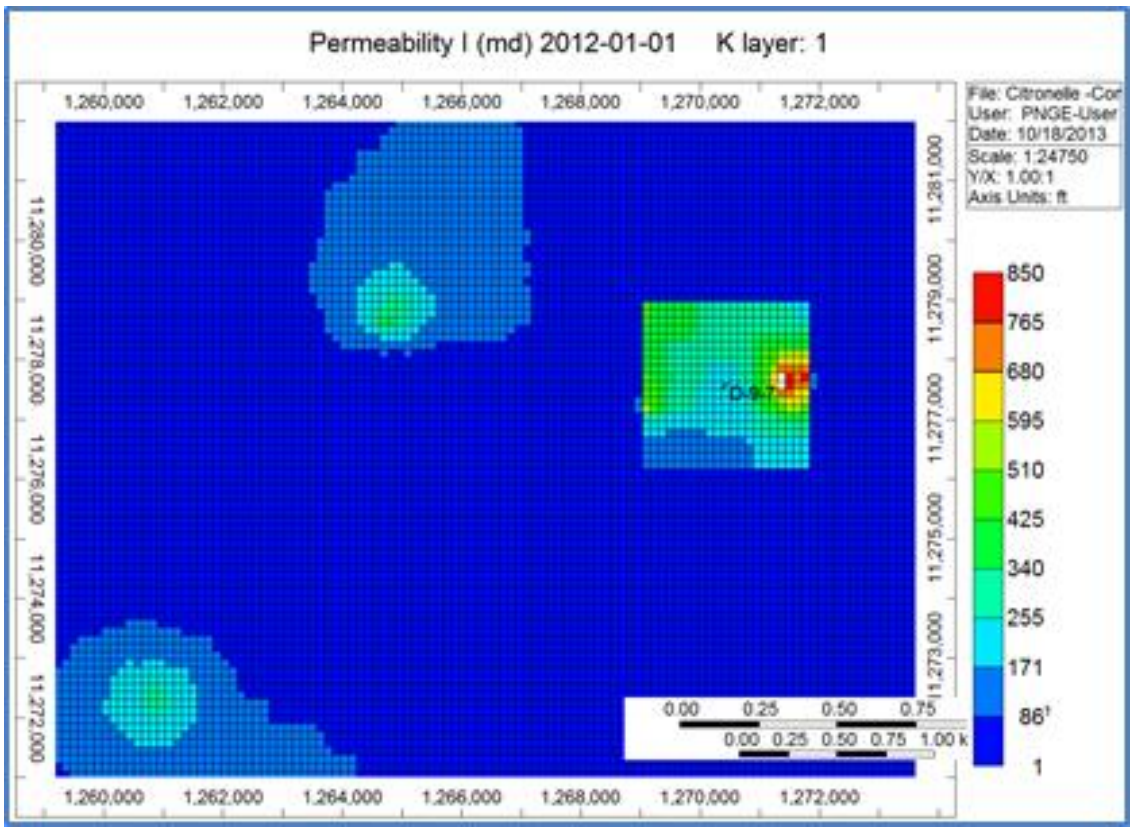

Figure 123. Two permeability regions in the reservoir

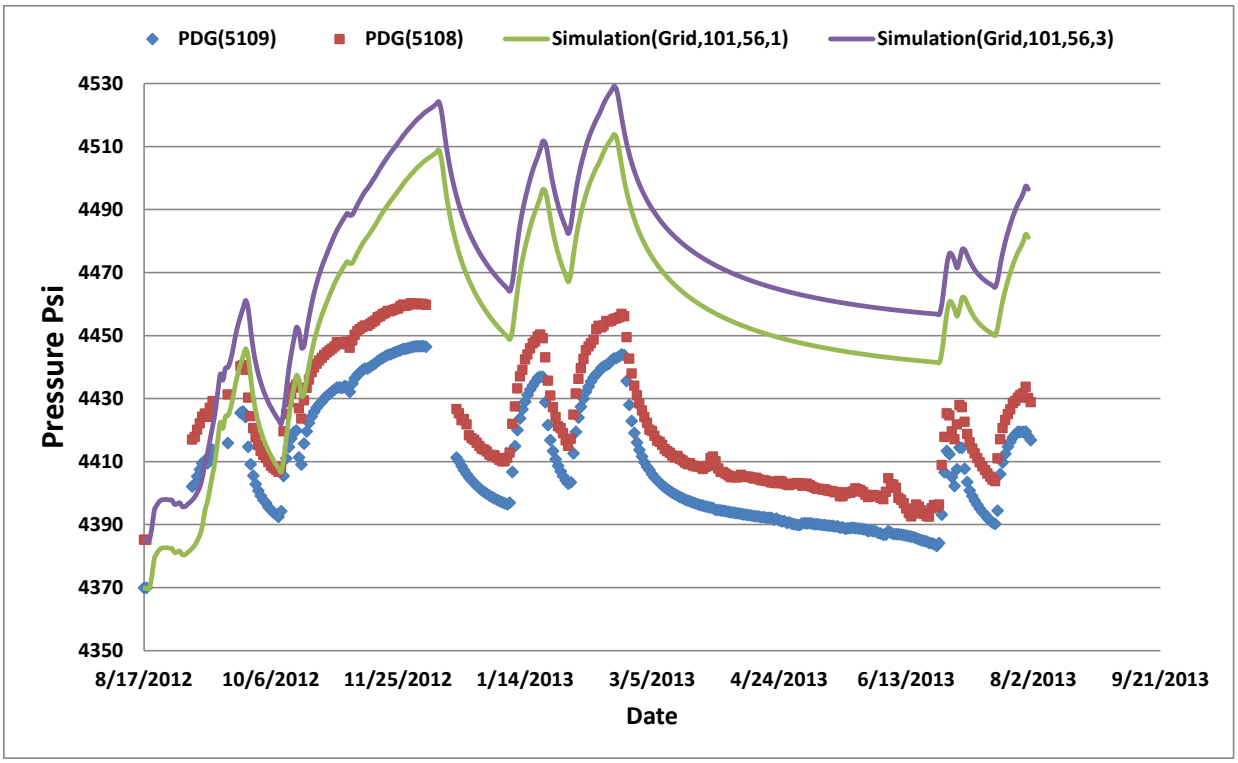

Figure 124. Model's pressure results and actual history; modified permeability in different reservoir regions

As it is shown in Figure 124, although modifications in the model's permeability improved pressure drawdown behavior, pressure predictions were overestimated considerably (compared to the actual PDG data). To lower pressure results, solubility of CO_2 in the brine (aqueous phase) was incorporated in the model. More importantly, volume modifier was assigned to the grids at the eastern boundary of the reservoir (Figure 125-left). This accounted for the fact that reservoir boundary and volume might be larger than what was assigned in the model.

To develop geological model, top and thickness of sand layers were picked for log data of 14 wells (crossing at injection well) and then correlated with one another as shown in Figure 125 - right. Due to the limited amount of information (just two well logs) at the east side of the injection well, it was not possible to estimate the extension of the sand layer on that area. Therefore, it was probable to have more reservoir volume beyond the boundary of the geological model.

Adding more volume to the reservoir (sand layers) resulted in lowering the modeled pressure behavior. After activating CO_2 solubility in the brine phase and tuning the "volume modifier", a good match between the model behavior and the actual pressure data, with less than 0.001% average error was achieved (Figure 126).

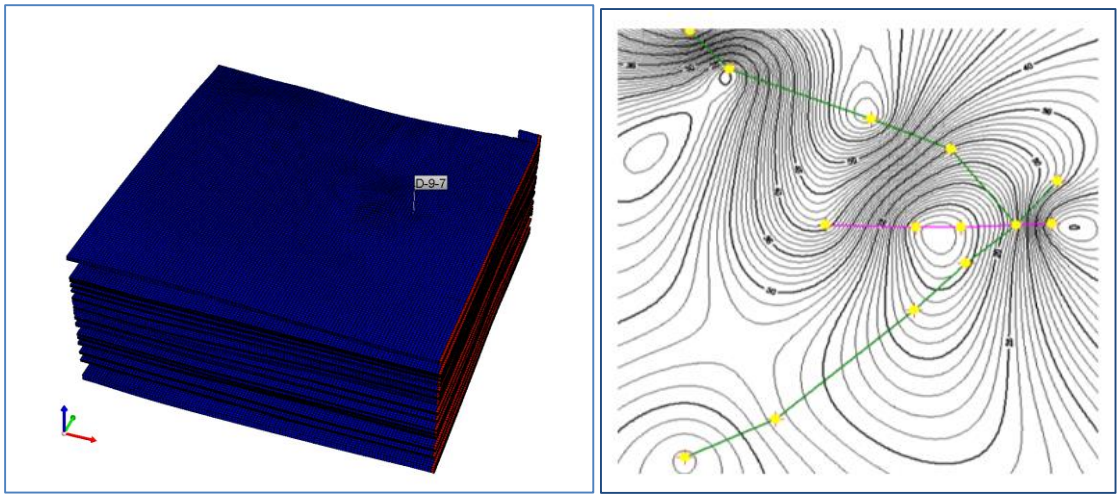

Figure 125. Increased volume modifier at the east boundary (left) and well cross sections (right)

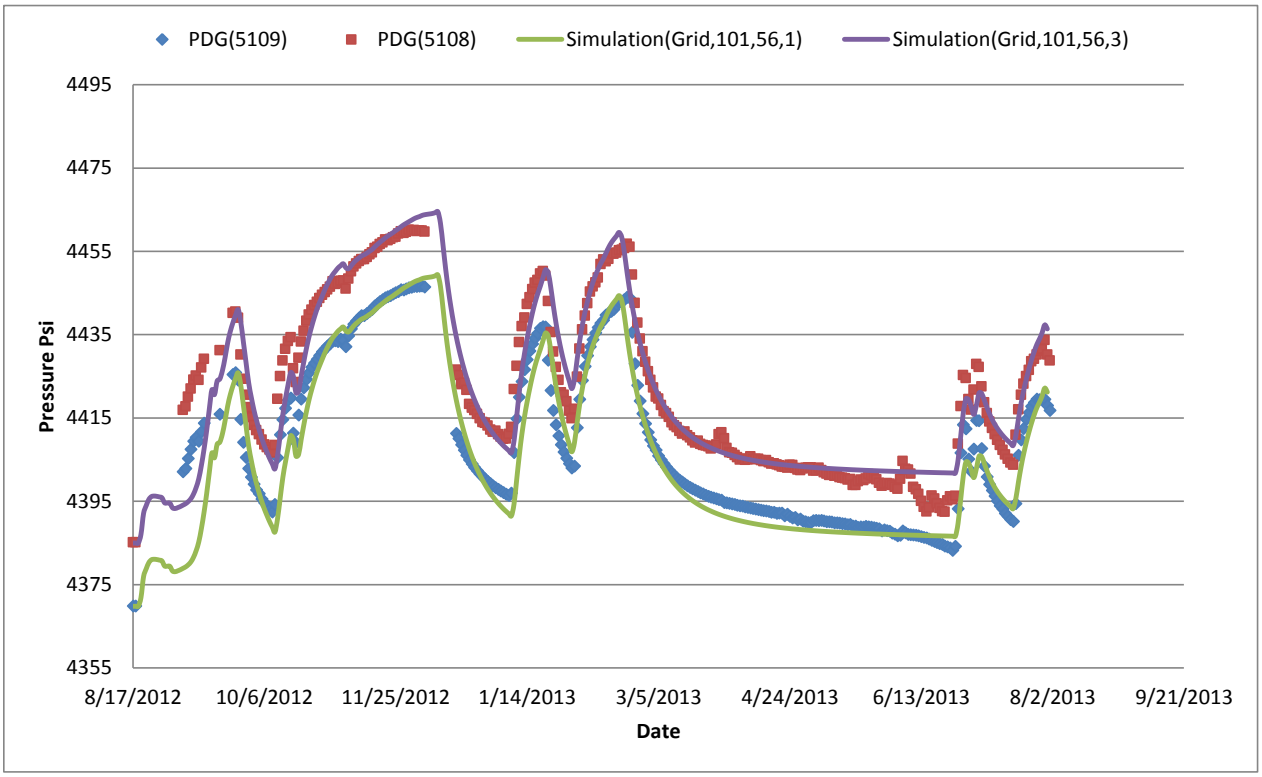

Figure 126. Model's pressure results and actual history; final history match

HISTORY MATCHED MODEL VALIDATION

As showed in the previous section, especially in Figure 126, the history matched model showed good precision in generating ten months of pressure results which resembled the actual field measurements. In order to study predictability of reservoir model, last three months (from August 1rd to October 30th, 2013) of actual injection/pressure was set aside in advance during the history matching process and was utilized in order to validate the history matched model's predictive capability.

During these three months, CO_2 was injected steadily according to targeted rate of 9.48 MMcf/day (Figure 127 and Figure 128). The Injection process experienced few shutdowns that resulted in average rate to be 7.98 MMcf/day. Consequently, reservoir pressure increased during August 2013, followed by some drawdowns (due to no injections) in September 2013 and gentle buildup during the last month.

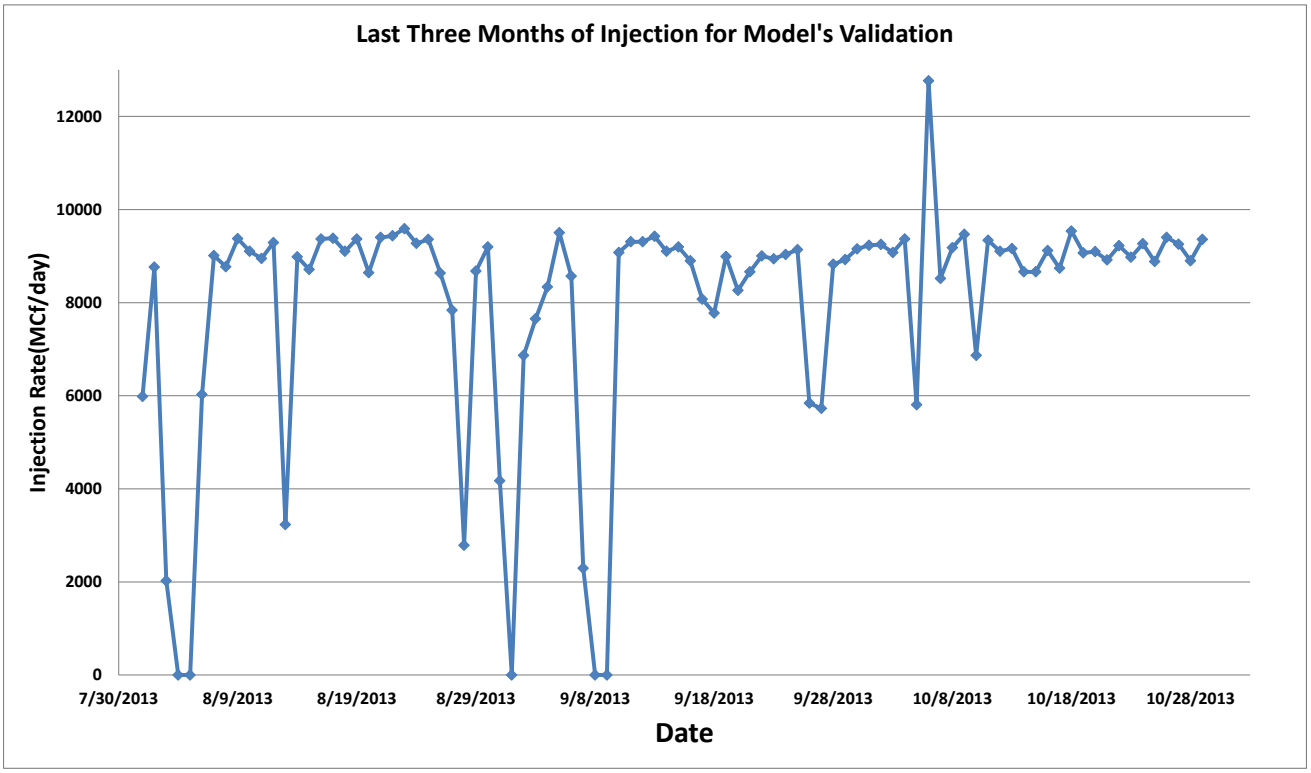

Figure 127. Last three months of injection rate

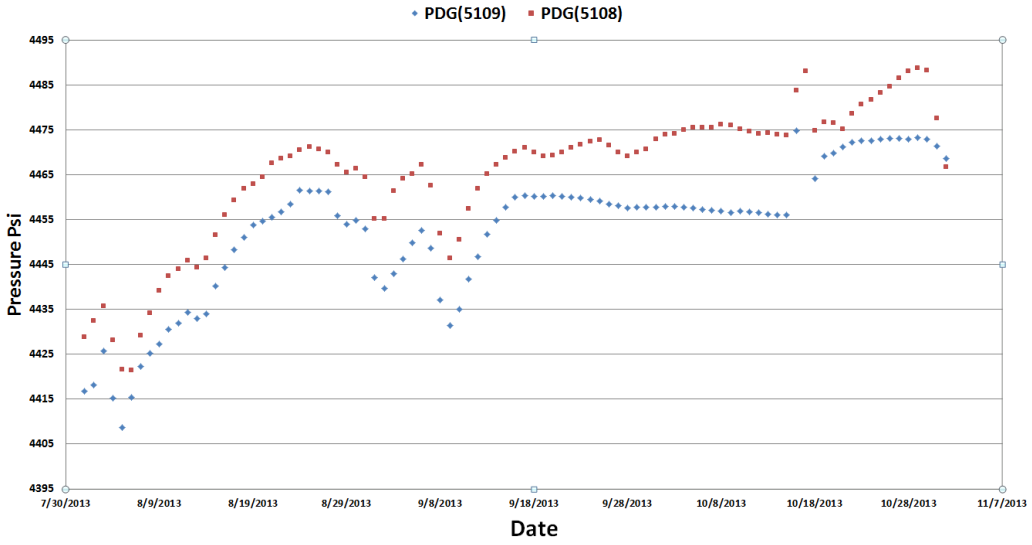

Figure 128. Daily pressure data for last three months of injection

The history matched model was deployed in forecast mode and the operational constraints (injection rates) were imposed. The model generated the corresponding pressure signals at the observation well. Model's pressure prediction results were plotted versus actual measurements from the field (Figure 129). Model's predictions have accurately captured the trend of the actual data as shown in this figure. The average error for the two permanent downhole gauges are 0.12% and 0.073%, respectively.

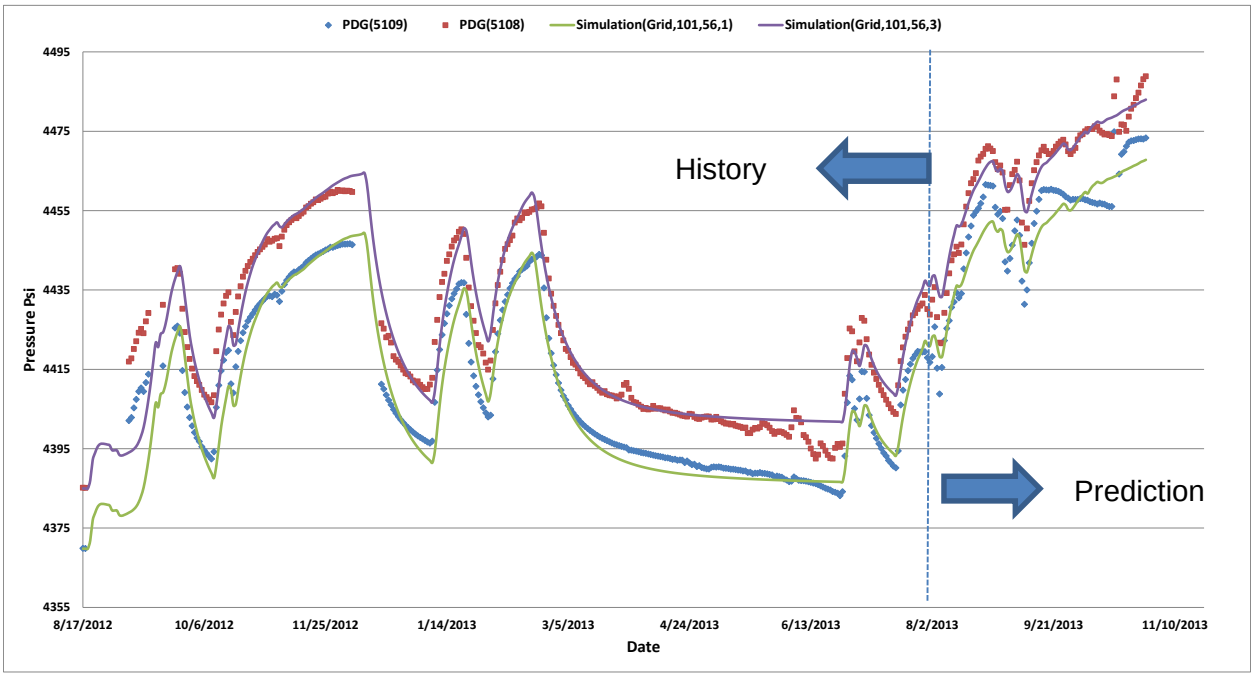

Figure 129. Model's pressure result and actual data for prediction and history

Model Integrity Verification

A time window of 500 years was considered to be investigated for the long term behavior of the reservoir based on the results of the latest validated history matched model (Figure 129). The results also used to verify if any CO_2 leakage happens in the reservoir because of some numerical or non-physical effects.

There are two main parameters to be considered for the long term monitoring of CO_2 sequestration, as reservoir pressure and CO_2 plume extension. The well bottom-hole pressure at well D-9-8#2 which is the observation well is shown in Figure 130. Reservoir pressure starts from the initial value of 4,380 psi and reaches to the maximum value of 4,628 psi at the end of the injection period. Then, it takes almost a year for the reservoir pressure to decline from the maximum value to 4,525 psi to the final, settled and almost constant value of 4,517 psi, 500 years after the injection is completed (Figure 130).

CO_2 plume extension in the first layer and 500 years after the injection (for all layers), are shown in Figure 131 and Figure 132. The maximum plume extension spreads almost 4,800 ft. in the East-West direction and almost 2,800 ft. in the south-north direction.

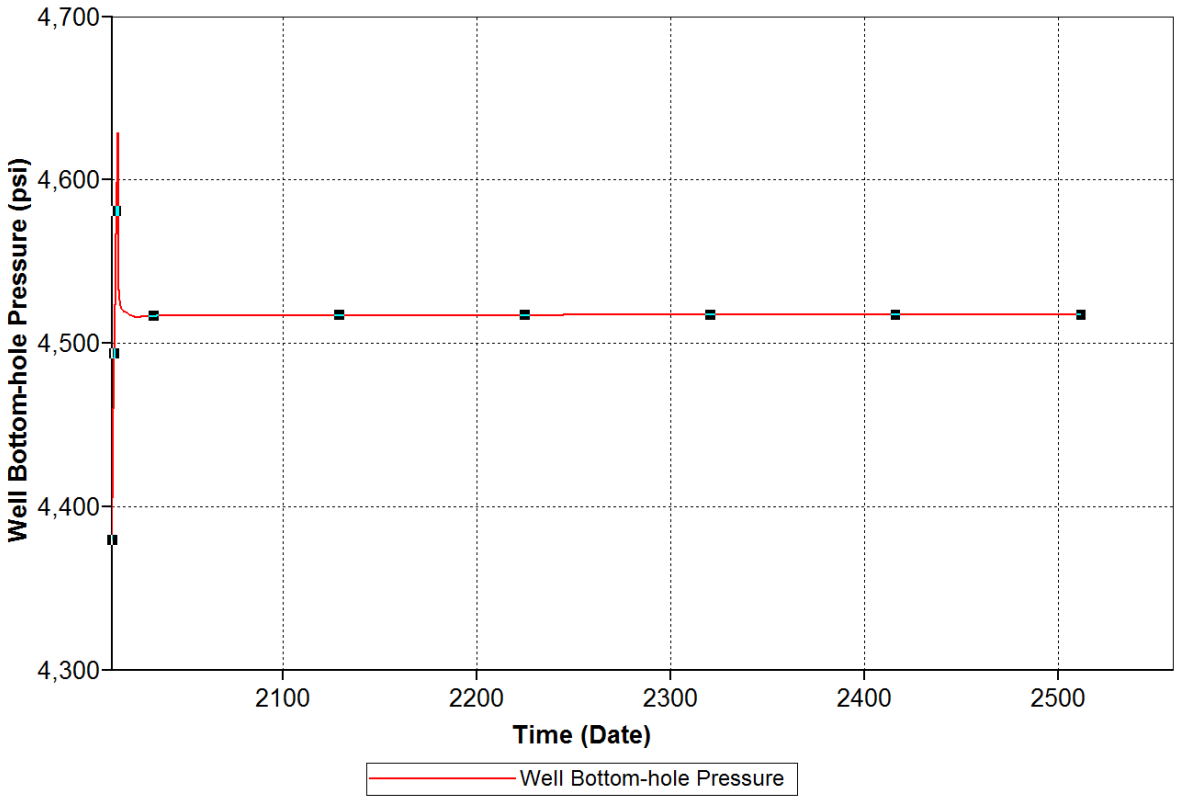

Figure 130. Pressure behavior in observation well during 500 years post injection (latest history matched model)

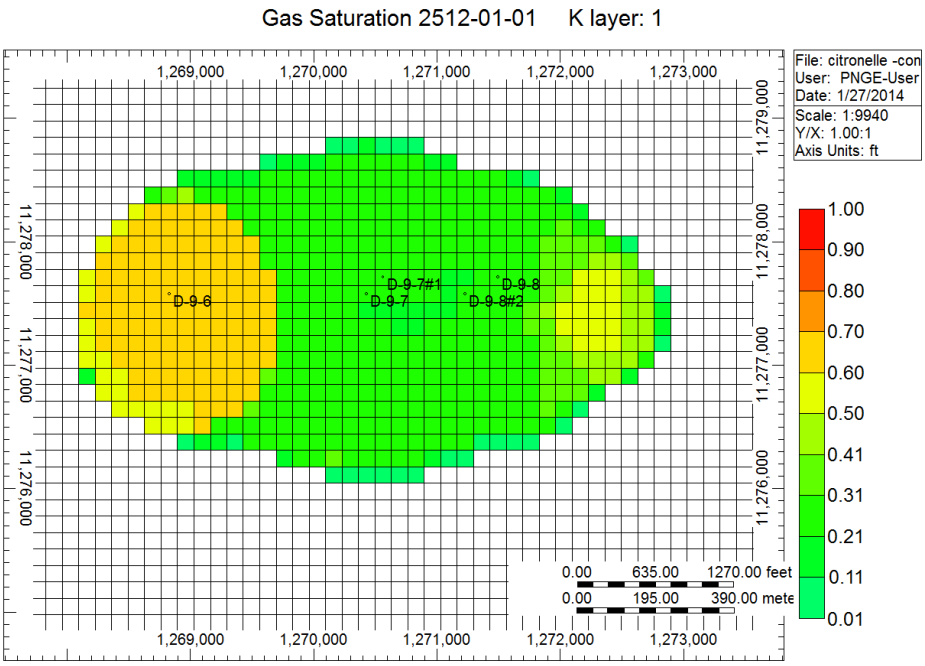

Figure 131. CO_2 plume extension in the first layer (500 years after injection-latest history matched model)

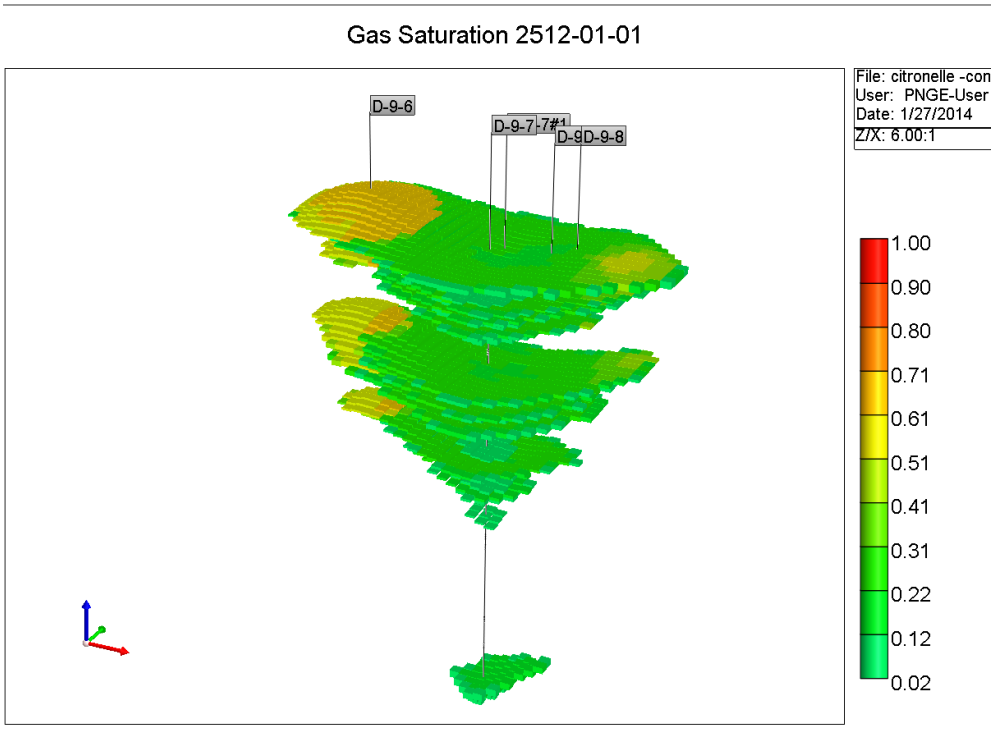

Figure 132. CO_2 plume extension in all the layers (500 years after injection-latest history matched model)

LEAKAGE MODELING

Typically there are 3 main sources for the leakage in CO_2 storages reservoirs; faults, wells and high permeability zones. Based on the geological report (SECARB 2010), no fault exists in the vicinity on CO_2 injection well. But there are different types of wells in the AOR (Area of Review).The most recent Citronelle numerical model (The model developed by the WVU team) shows that the distance of CO_2 plume from the injection well will reach as far as 2,200 ft. away from the injection well. Therefore, abandoned wells in this extended area (around 34 water disposal, dry whole, injector, producer, and observation wells) would be candidates for potential leakage. The leakage can be determined by four parameters; leak radius, permeability, length and location. These parameters can be assigned to each candidate well and the effect of leakage on the reservoir behavior (especially pressure) can be investigated.

High permeability zones can be formed by the reaction of the CO_2 with specific type of clays which forms dehydrate clays in the cap rock. Also there is the possibility that increasing reservoir pressure cracks the cap rock and provides a conduit for CO_2 to leak. Since the chemical reaction between CO_2 and clay mineral was not considered in this model, only potential CO_2-induced fractures are studied.

First, the leakage was introduced to the reservoir model by adding a CO_2 production well in the plume area of the homogeneous model for Citronelle field. Due to the high number of grids and complexity, the iterations did not converge and no results achieved in this trial. So it was decided to work on the simpler model to avoid convergence problems. A 2-D model with same properties of the Citronelle model was built (Figure 133).

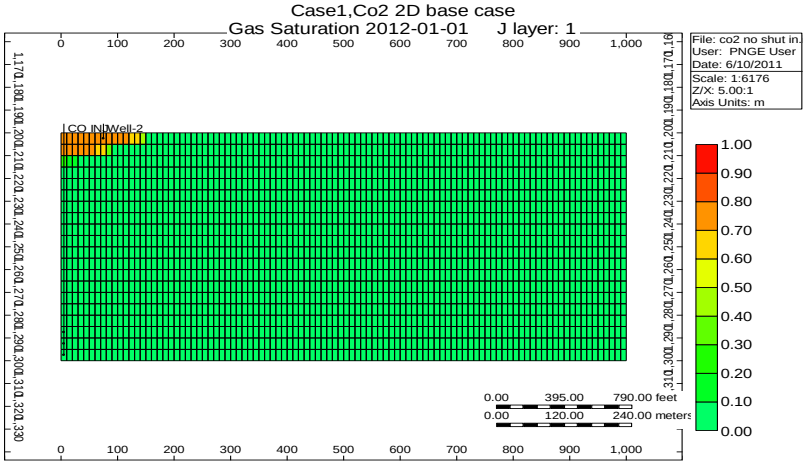

Figure 133. Saturation profile in 2-D model

Two different constrains were set for the leakage well; minimum bottom-hole pressure and leakage rate. Different values for mentioned parameters were considered in order to evaluate pressure behaviors of the reservoir. There is a threshold value for minimum reservoir pressure,

below which there would be no flow of CO_2. In this model if the reservoir pressure reaches 30,000 kpa (4,351 psi) there would be no flow from the leakage well (Figure 134).

Different leakage rates also were considered. As the amount of the leakage rate decreases, the duration of the CO_2 production incrases until the reservoir pressure reaches to the minimum flowing pressure (Figure 135).

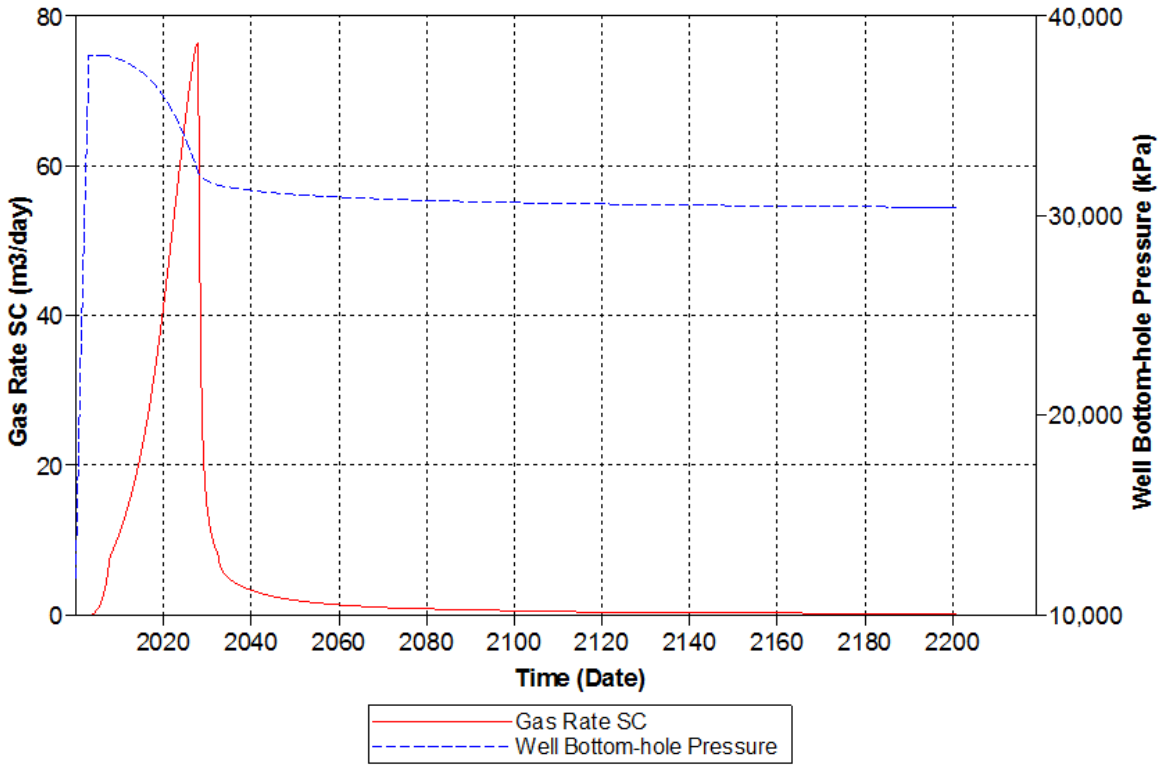

Figure 134. Reservoir pressure and leakage rate at min BHP 25000kpa

As pressures changes in the reservoir, the pressure on one side of the seal may differ more and more from pressures on the other side; that is, a pressure drop begins to appear across the cap rock. When this pressure drop becomes sufficiently large, the seal provided by the cap rock may be breached, and flow across the breach may occur.

This type of leakage was simulated in the 2-D model. In this type of leakage CO_2 starts flowing from production well when a specific pressure difference between the reservoir pressure and assigned minimum bottom-hole pressure is achieved. At this time there would be a jump in the CO_2 rate. While CO_2 is leaking through the cap rock, the reservoir pressure drops and the cap rock leak starts closing (Figure 136).

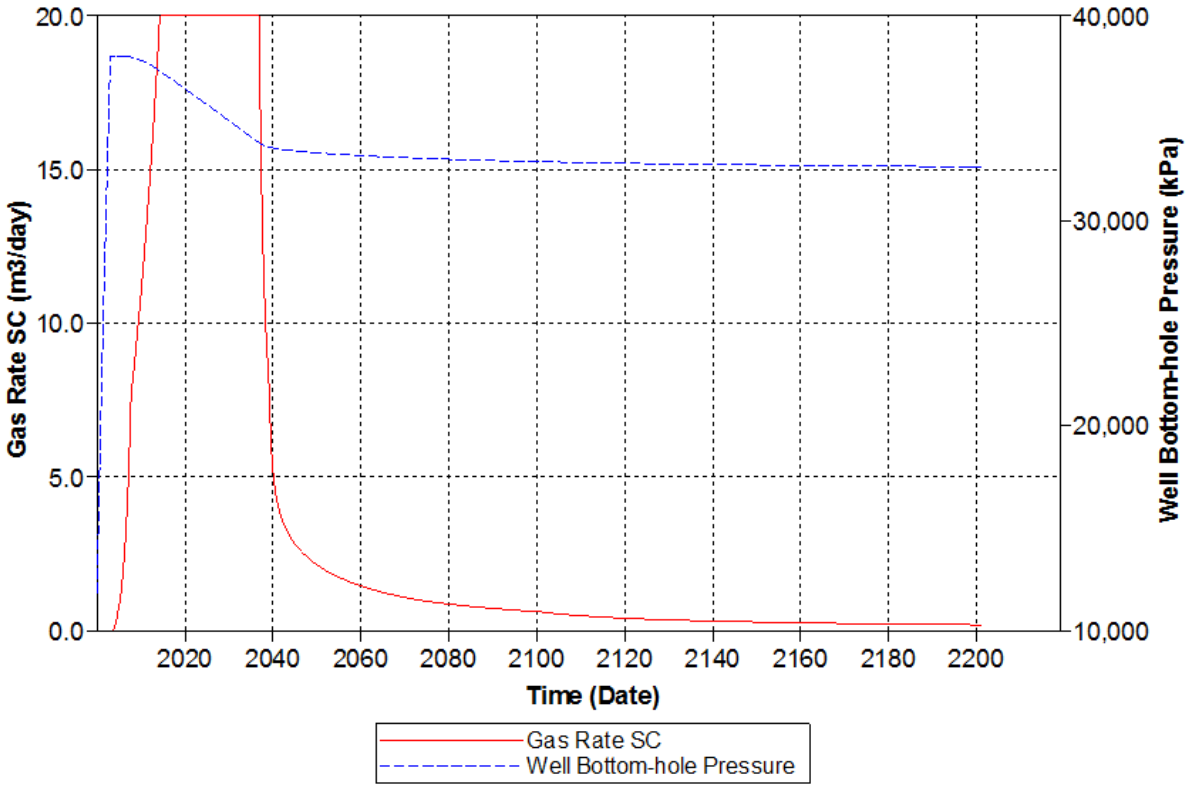

Figure 135. Reservoir pressure and leakage rate at Surface Gas rate 20SM3/day

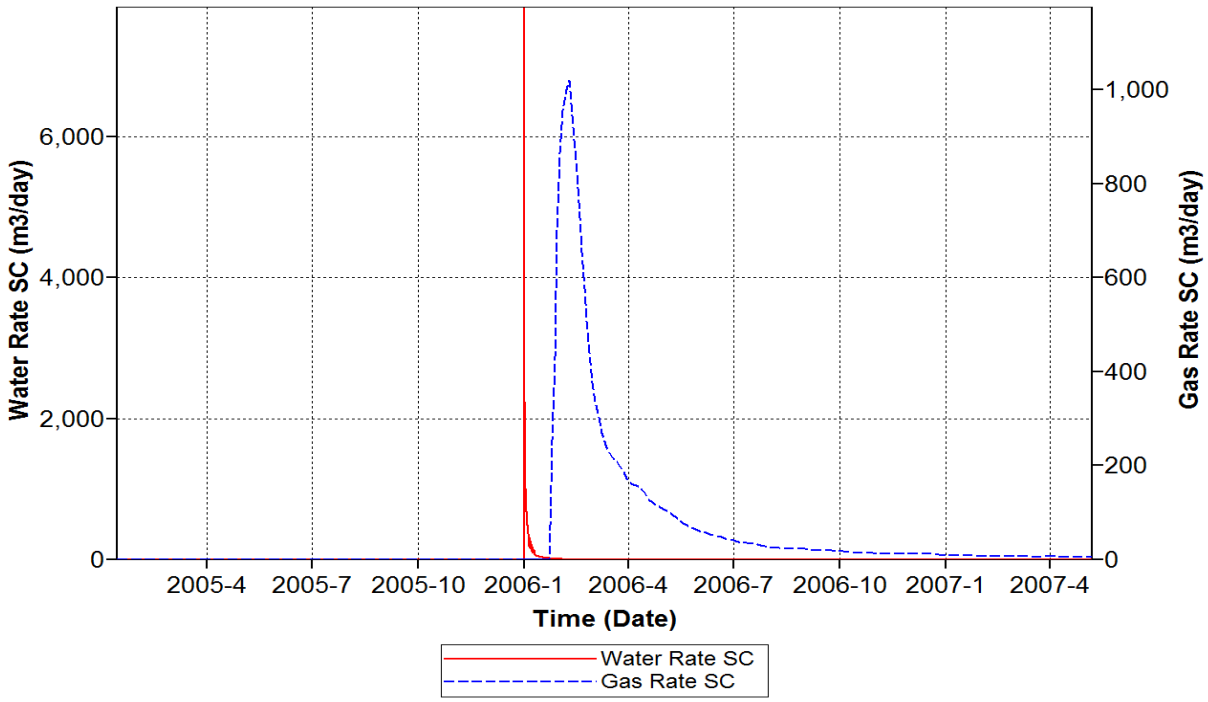

Figure 136. Leakage rate for Cap Rock leakage

In the next step the top layer of the final Citronelle model (that was history matched) was selected to model the leakage[3]. A total of 4 actual wells were identified to be in the plum extension area within the time domain of the interest in this project. These are: injection well (D-9-7), observation well (D-9-8) and 2 other existing wells (Figure 137).

For this case, at first a cap rock leakage was assigned to Well-Leak 2. A jump of the gas rate in Figure 138 represents the leakage. Furthermore, the pressure decline in the observation well also is an indication of the presence of the leak.

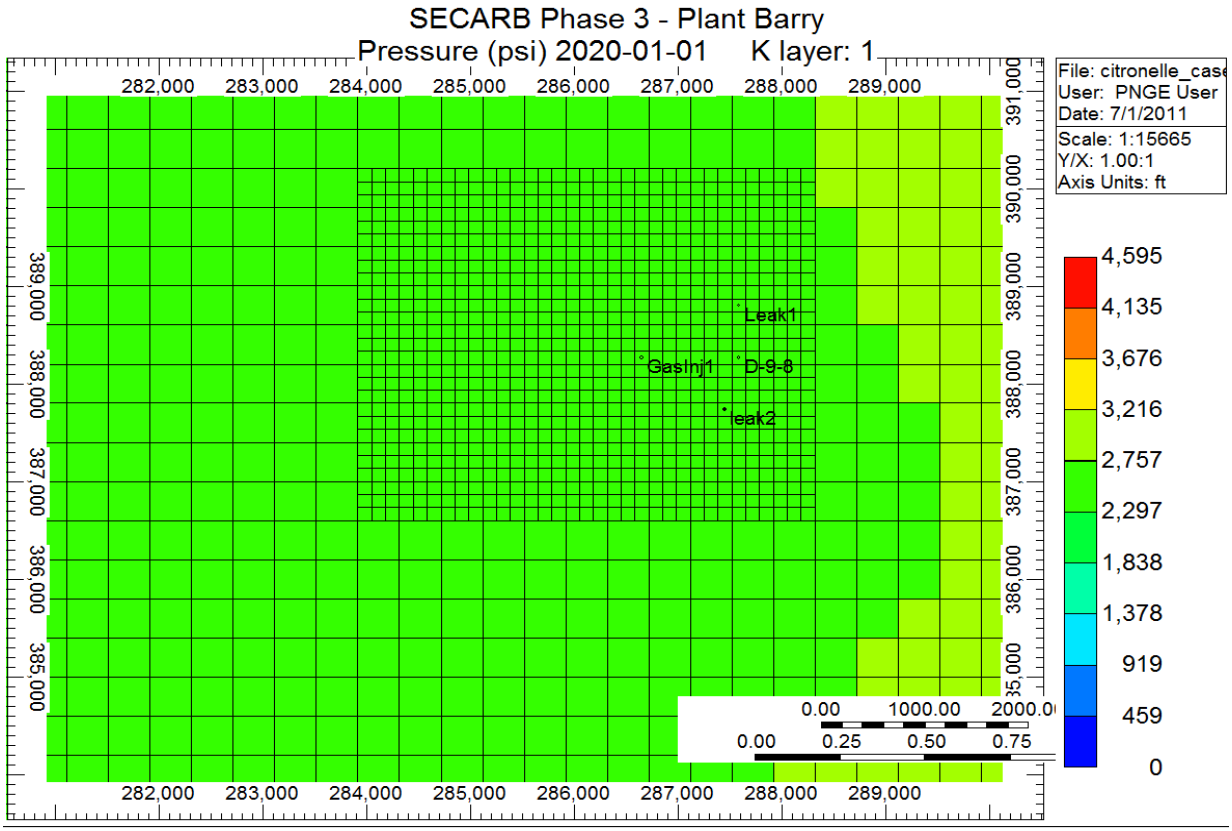

Figure 137. Location of the injection, observation and 2 leakage wells in the first layer of the Citronelle field

The main objective of this section of the study was to determine the number of wells that are prone to leakage and investigate the characterization of the reservoir behavior when CO_2 leakage occurs. To investigate the number of possible well locations that are disposed to leakage, it is necessary to know the extension of the CO_2 plume. Based on the WVU and the ARI studies regarding the AoR (Area of Review), the maximum diameter of the CO_2 plume ranges from 2,800 ft. (ARI model) to 3,900ft (WVU model) as depicted in Figure 139.

[3] Working on the whole field requires a lot of run time and leads to numerical convergence issues.

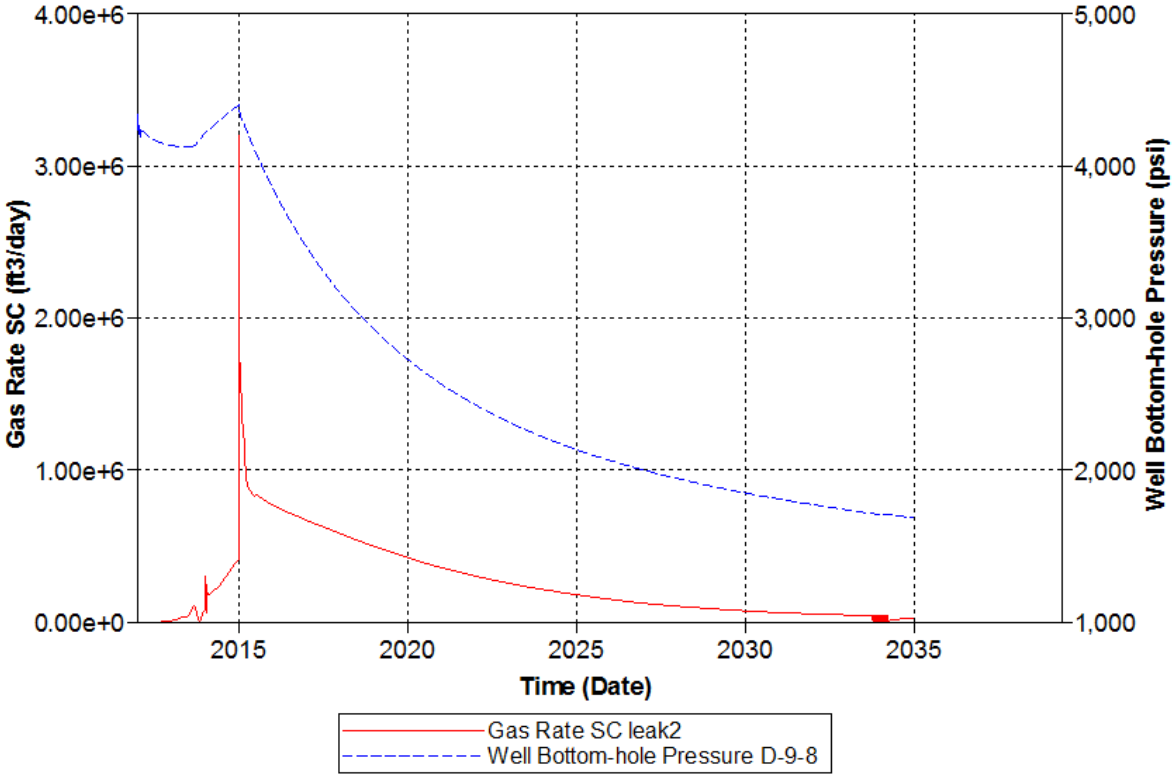

Figure 138. Leakage rate at leak2 and pressure profile in observation well (D-9-8)

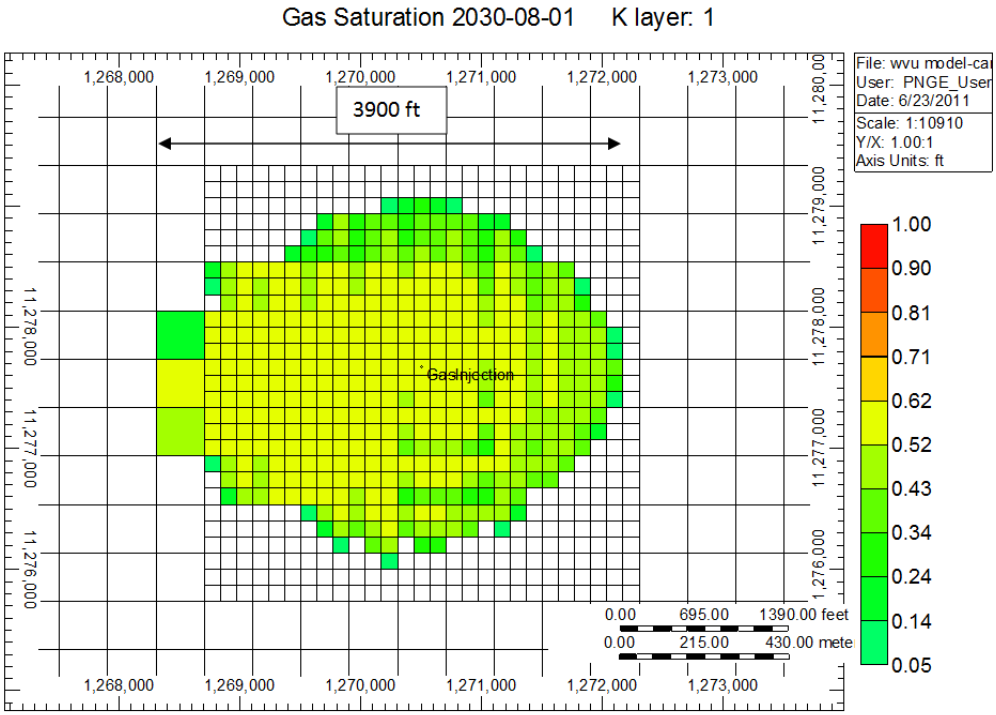

Figure 139.The extension of CO_2 plume in WVU Model

It should be mentioned that the maximum CO_2 plume extension occurs in the first layer (Figure 140). Therefore it is unlikely that CO_2 reaches to the existing wells in the other layers.

According to the Denbury Resources report (SECARB 2010) there are 34 wells in the radius of one mile from the injection well (12 oil producer, 5 water injection and 17 abandoned wells). Based on the realization which resulted in maximum CO_2 extension, a total of 7 wells (D-9-1, D-9-2, D-9-3, D-9-6, D-9-9, D-9-10, D-9-11) can be potential candidates for CO_2 leakage as it is shown by red circle in Figure 141.

Figure 140. Gas Saturation in different layers of the Citronelle aquifer (WVU Model)

As mentioned before, the maximum extension of the plume exists in the first layer of the reservoir. Therefore, this layer (Figure 142) – including CO_2 injection well (D-9-7), observation well (D-9-8) and 4 existing wells (D-9-1, D-9-3, D-9-9, D-9-11) - was considered for the simulation of the CO_2 leakage through the wells (cap rock fracture, fault and high permeability zone leakages are not addressed in this study).

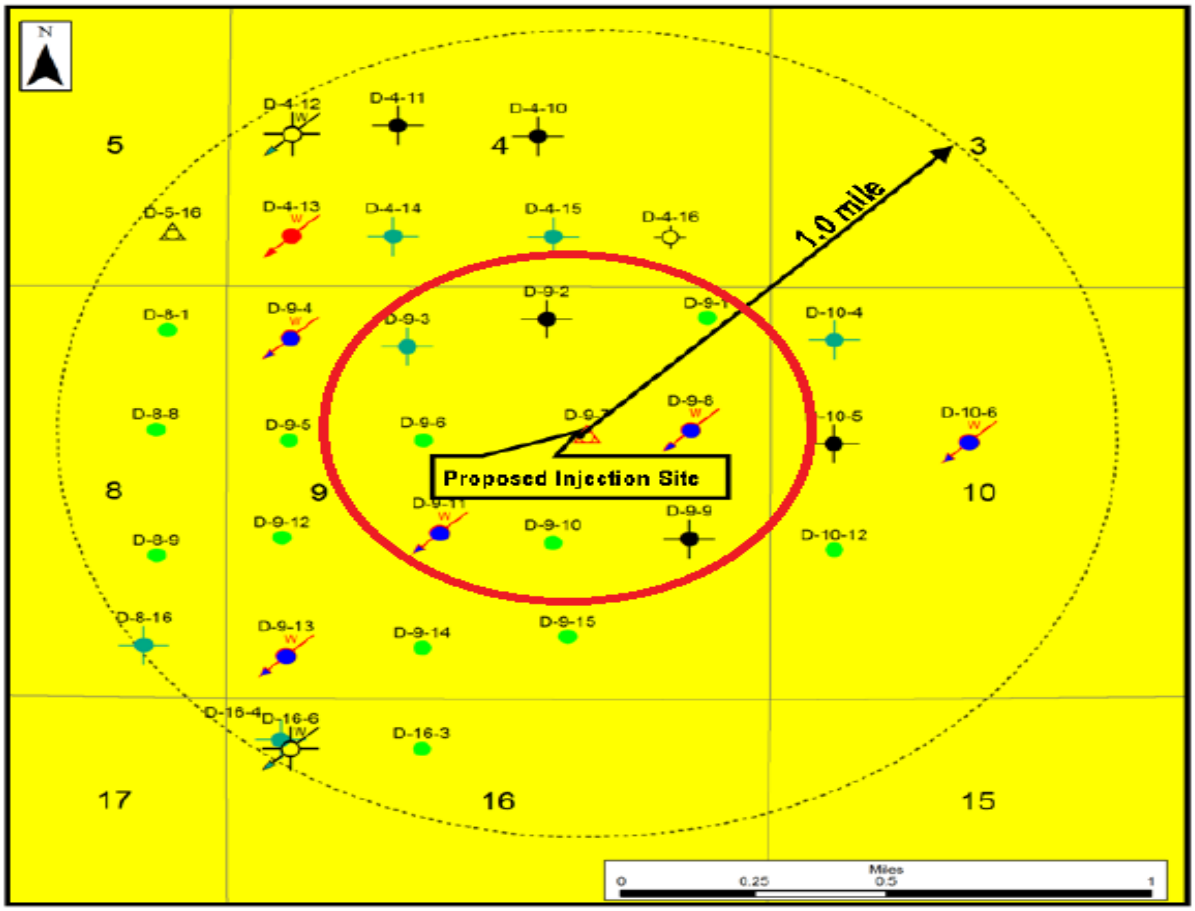

Figure 141. Location of Wells within 1.0 Mile of the Proposed Injection Site

The leakage rate is highly dependent on water production. The WVU team was able to model leakages due to the presence of an existing well and leakage due to cap rock fracturing (there is no fault in this reservoir) within the CMG software that is used for the numerical modeling in this project is able to. In the cap rock leakage, it is possible to assume that the water can also leak through the induced fractures. But this assumption cannot be valid for the well leakage because of the characteristics of the flow paths. The water rate in the well leakage should be restricted to very small values in order to represent the reality more accurately.

First, it is necessary to investigate the effect of the water which is produced along with the CO_2 through a leakage from the well in the Citronelle Model. The leakage has been simulated by considering one of the wells as the leakage location. CO_2 leakage rate has been set as the model constraint with the value of 175,000 ft^3/d. Figure 143 shows the results of this simulation run.

As it is shown in Figure 143 , water production begins after almost one and a half year in this case. Hence, the pressure behavior recorded in observation well is due to both gas and water production.

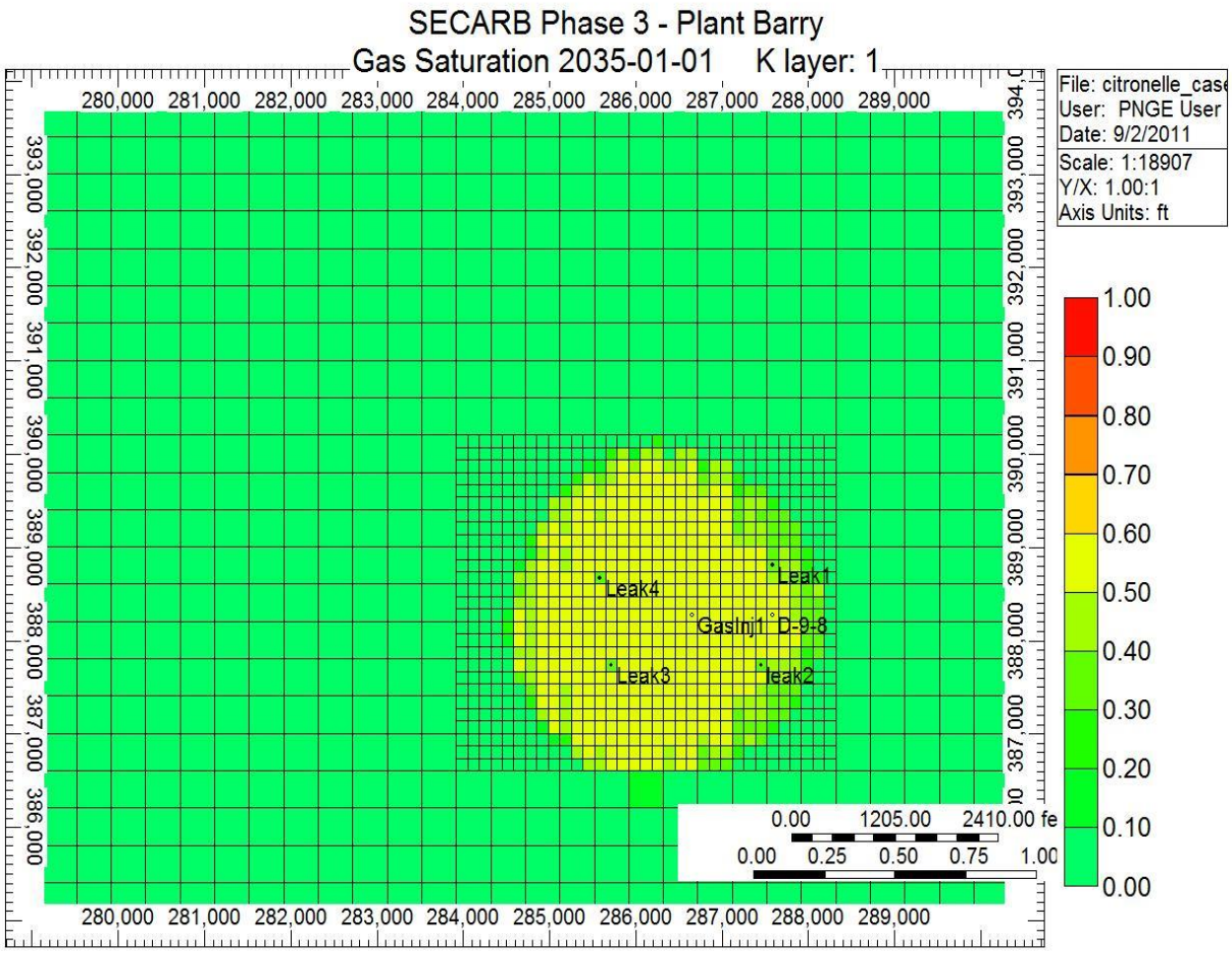

Figure 142. Location of the injection, observation and 4 leakage wells in the first layer of the Citronelle field

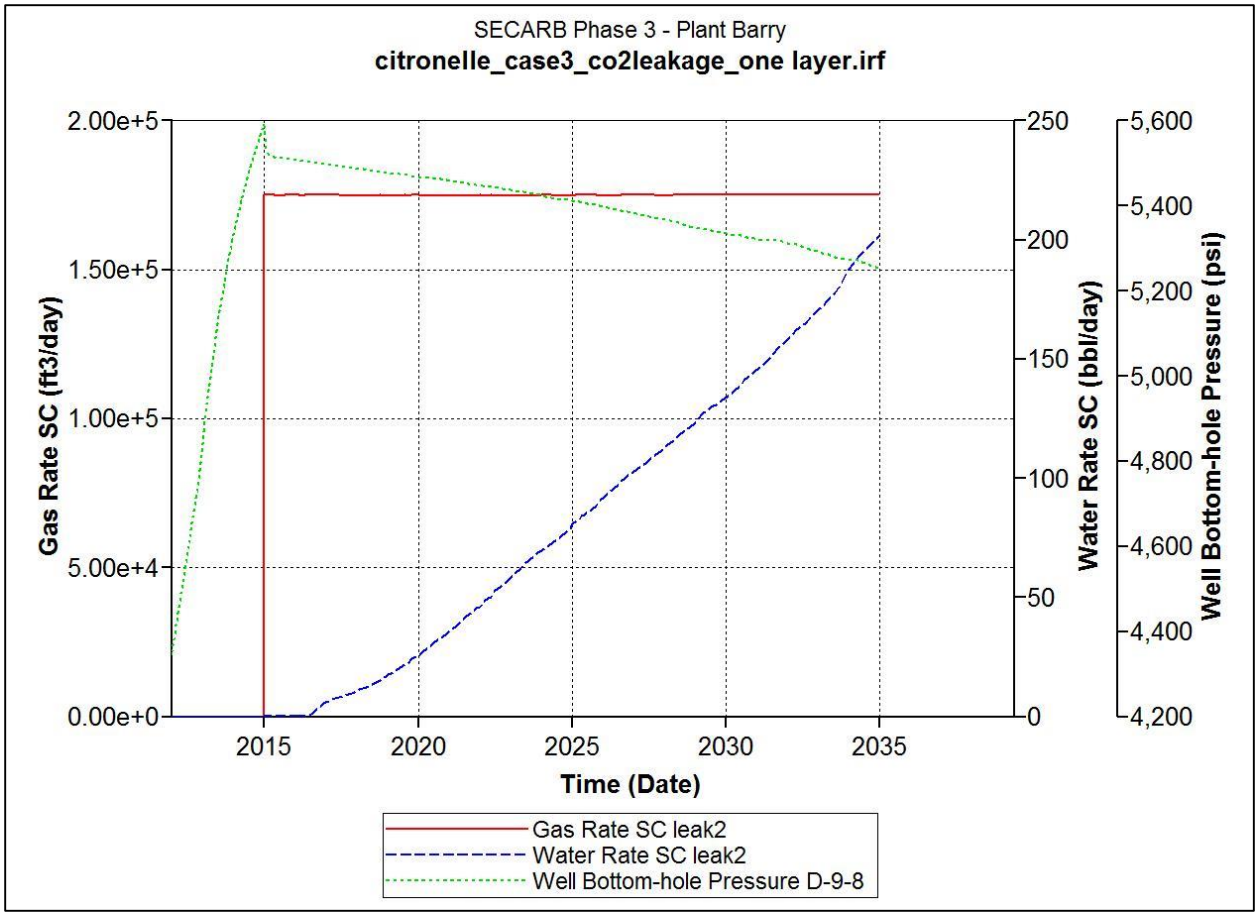

Figure 143. Pressure behavior of the reservoir during leakage of CO_2 and water

In order to minimize the effect of water production on the pressure behavior, its value has been set to be 1 bbl/day. The results of this situation are illustrated in Figure 144. In this case the well produces CO_2 at a fixed rate for almost one and half year. After that, the CO_2 leakage rate starts decreasing significantly since the water reaches to the leaking well. CO_2 is trapped in the Citronelle geologic formation due to hydrodynamic mechanism in which formation water is compressed and displaced due to high injection pressure in order to provide pore space for CO_2.

When gaseous or supercritical CO_2 phase is being produced, water finds its way back to the pores that have already been occupied by the gas. Once all the CO_2 surrounding a leaky well escapes through the leakage well, water reaches to that well and starts production from the well in the model. This is not possible in reality.

To determine the maximum and minimum leakage rate, the CO_2 production for one leakage well was varied incrementally. Based on the results, maximum leakage rate for one well was determined to be about 1,750 MCFD (Figure 145). It should be mentioned that there is no lower limit for the leakage rate.

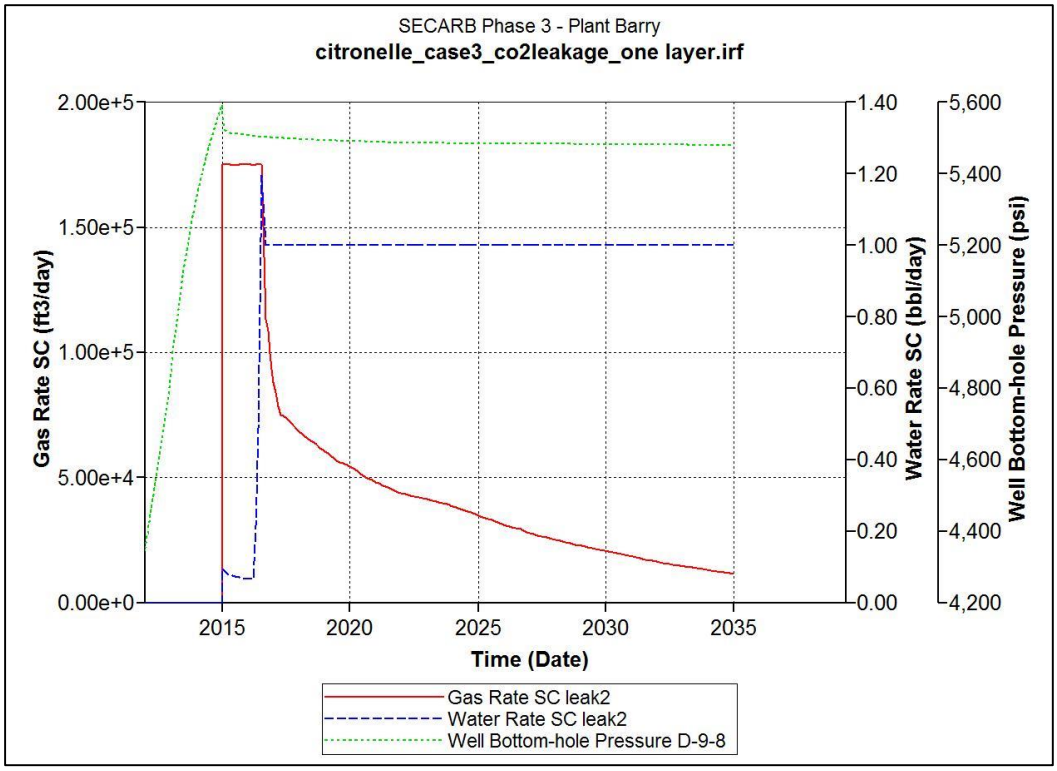

Figure 144. Pressure behavior of the reservoir during leakage of CO_2 with 1 bbl/day water constraint

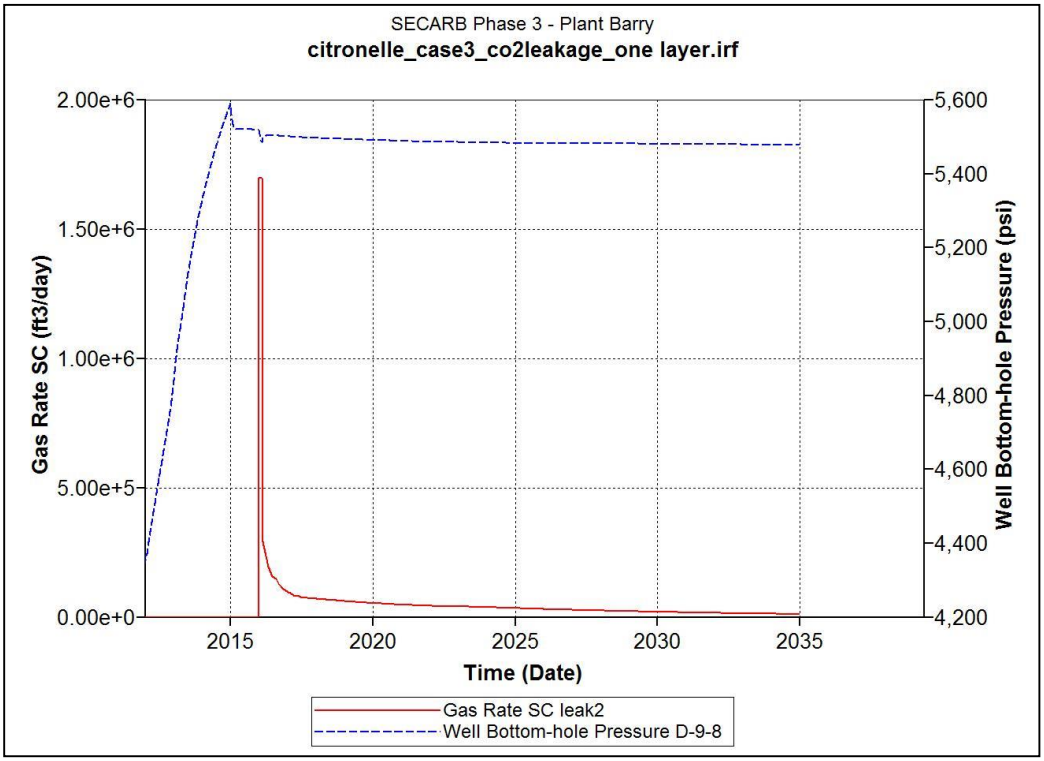

Figure 145. Maximum leakage rate through one well

The most important subsurface indicator that can be used in order to determine the amount of CO_2 leaking through a well is reservoir pressure. The effect of different leakage rates on the behavior of the observation well pressure (D-9-8) was investigated. To do so, the leakage rate was decreased incrementally from 175 MCFD to 50 MCFD. It is should be noted that "1 bbl/day" water production constraint was considered for the leakage well in order to prevent water leaking through the well and to maximize CO_2 leakage. Figure 146 and Figure 147 demonstrate the results of the leakage rate investigation.

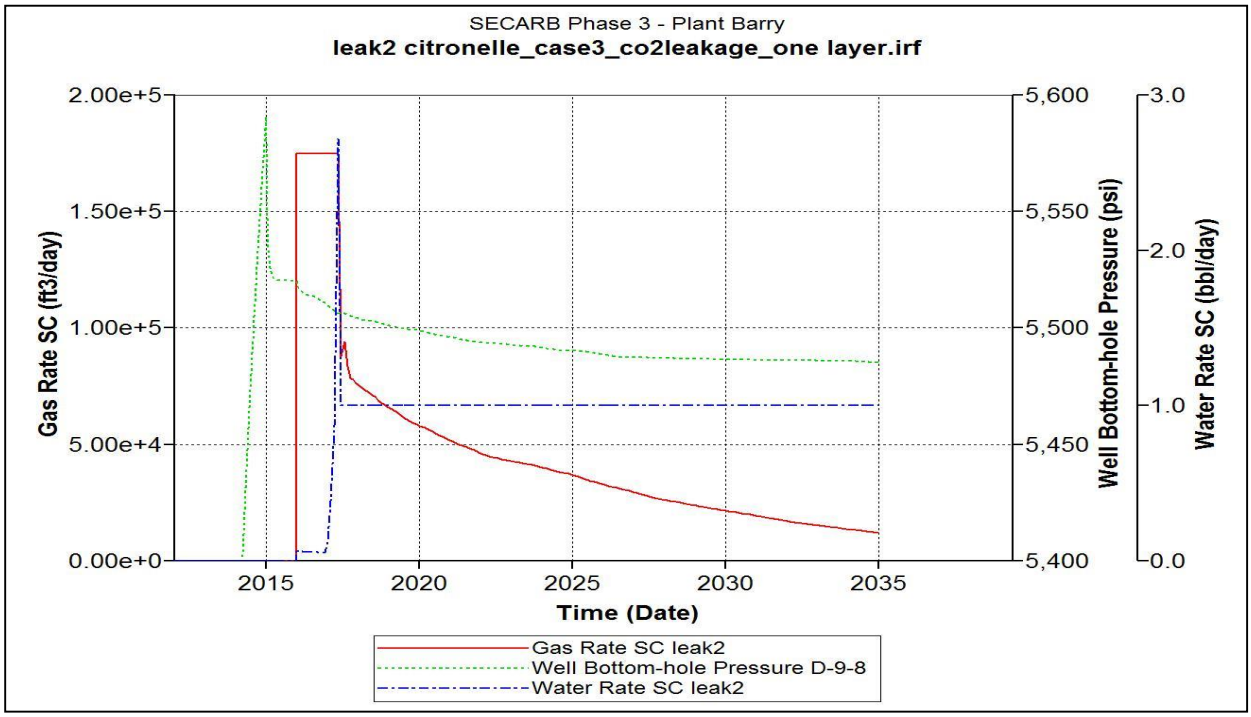

Figure 146. Pressure behavior in the observation well (D-9-8) for the leakage rate =175000 scf/day

For all the cases the value of cumulative produced leaked gas is the same. This means that for the high leakage rate scenarios, the duration that we can see a plateau in CO_2 leakage (production) is less than lower rate scenarios. The maximum amount of pressure drop in the observation well due to the leakage is about 30 psi.

For example for the leakage rate of 1,750 MCFD the pressure of the observation well decreases 10 psi annually (the leakage takes 3 years). However, when the leakage rate is 50 MCFD, the pressure in the observation well declines only 3 psi per year.

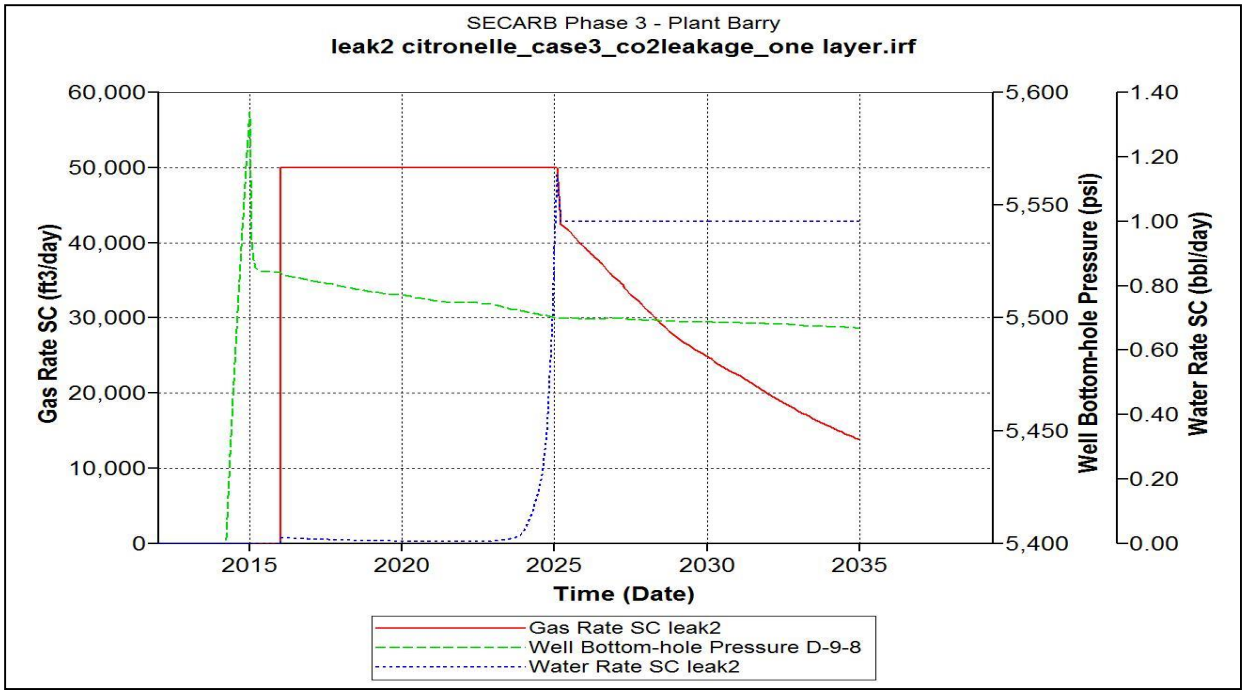

Figure 147. Pressure behavior in the observation well (D-9-8) for the leakage rate =50000 scf/day

The effect of the leakage through 2 wells also was studied. Two existing wells were assigned as the probable sources of leakage. Different sets of leakage rates were considered for the wells. The results for the scenario that both wells leak at 175,000 scf/day, and the case that one well leaks at 175,000 scf/day and the other at 50,000 are shown in Figure 148 and Figure 149.

It should be mentioned that in some cases the effect of the leakage from two wells is the same as leakage from a single well. Hence, it might not be possible to distinguish 1 or 2 leakages by just one sensor in the observation well. If additional sensors are placed in different locations, it would be possible to determine the location and the amount of the leakage more accurately by knowing the location of the sensors and the pressure profile recorded by each sensor.

In the last case, effect of CO_2 leakage from all 4 wells in the Citronelle field was studied. All of these wells (D-9-1, D-9-3, D-9-9, and D-9-11) were subject to CO_2 leakage rate of 175,000 scf/day and water rate of 1 bbl/day. Each well produces at the constant CO_2 rate until all the CO_2 which is surrounding the well is produced and water reaches the bore hole.

When all the wells start leaking, the pressure in the observation well (D-9-8) drops at the maximum rate. As the leakage stops at any well (based on the location of the well in the plume area), the slope of the pressure decline in the observation well decreases. When all the wells stop leaking, there would be no further decline in the pressure of the observation wells.

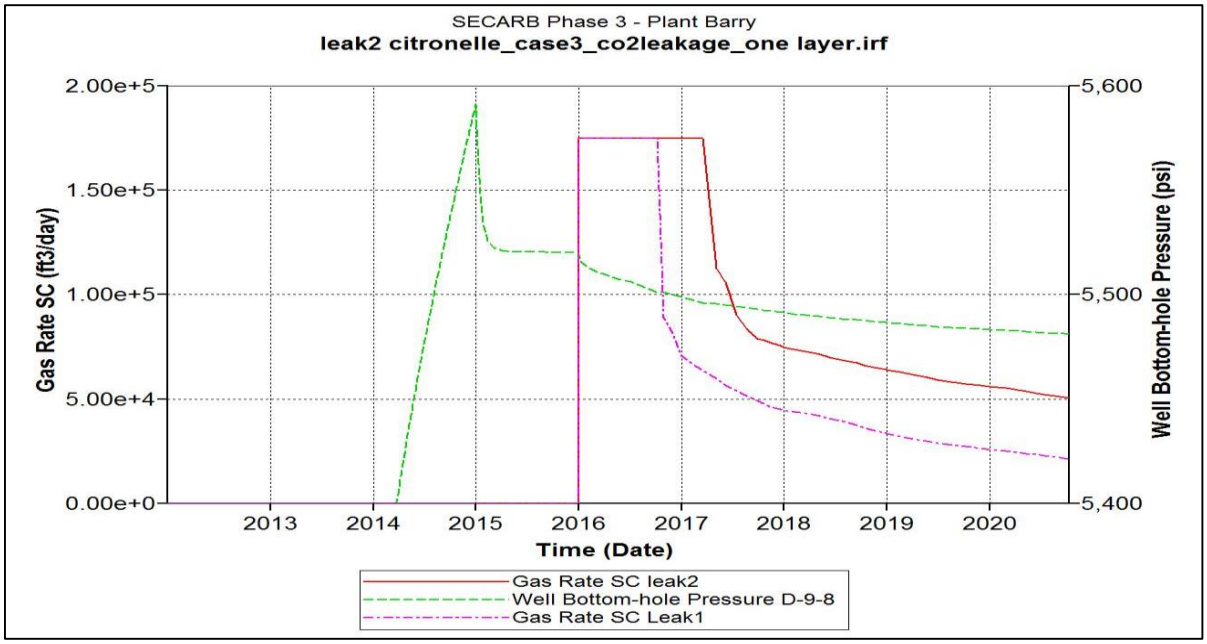

Figure 148. Pressure behavior in the observation well (D-9-8) for the leakage rate = 175,000 scf/day of two wells

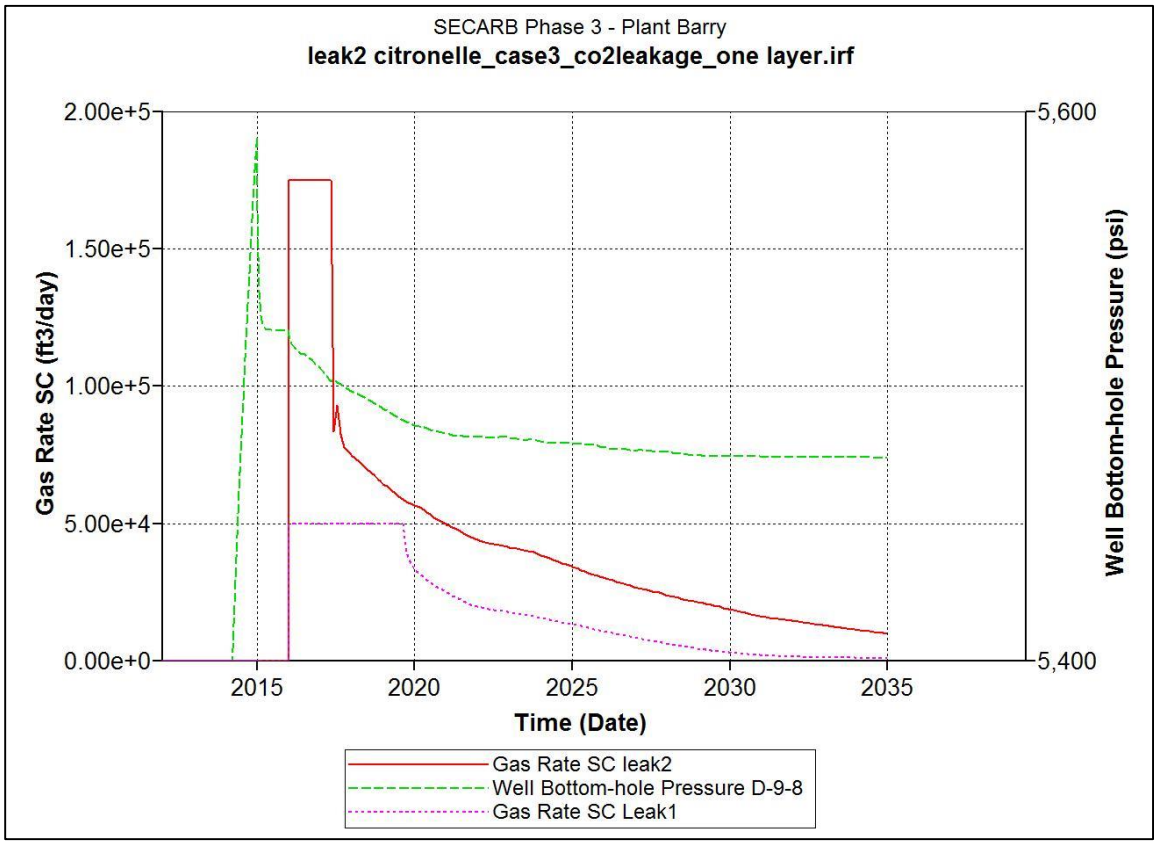

Figure 149. Pressure behavior in the observation well (D-9-8) for the leakage rate = 175,000 & 50,000 scf/day in two wells.

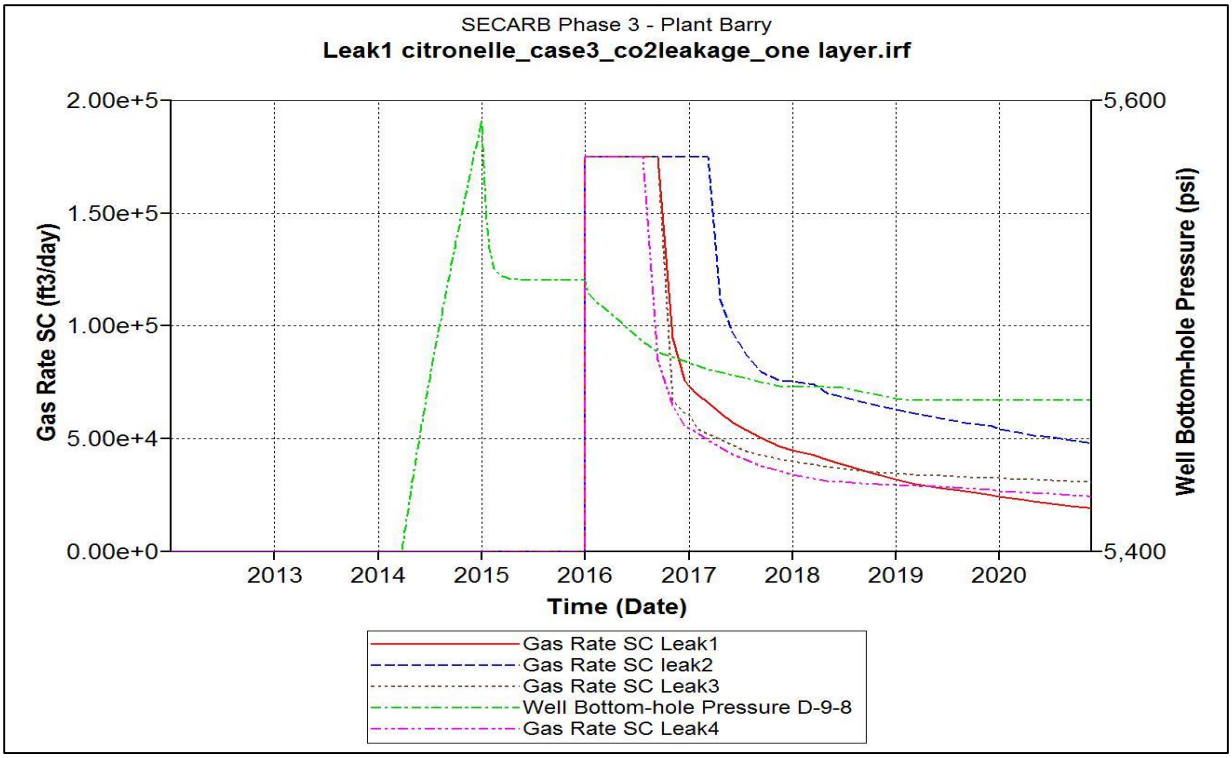

Figure 150. Pressure behavior in the observation well (D-9-8) for the leakage rate = 175,000 & 50,000 scf/day of 4 wells

DATA PREPARATION FOR THE INTELLIGENT LEAK DETECTION SYSTEM (ILDS)

To implement the technology developed in this project in an actual CO_2 storage site, the technology must be implemented in the form of a software application and put online and on-site. Development and demonstration of such a software application is presented in this report. The main engine of the ILDS software application includes a series trained data-driven models that are capable of de-convolving complex pressure signals from the PDGs into location and rate of the CO_2 leakage in a sequestration site.

Development of the Intelligent Leakage Detection System (ILDS) requires that following steps to be completed:

1. A history matched model of the CO_2 storage site be developed and validated.
2. The validated, history matched model is used to generate a series of leakage scenarios.
3. Real-time pressure data (from the modeled PDGs) due to a variety of leakage scenarios are collected.
4. The collected pressure data are used to train a set of data-driven models, as the heart and main engine of the ILDS, using machine learning and pattern recognition technology.
5. The data-driven models are tested and validated for accuracy, and are embedded in the ILDS.
6. Pressure signals from the PDGs in the storage site are uploaded into the ILDS and passed through the trained data-driven models.
7. ILDS response by identifying the location and the amount (rate) of the CO_2 leakage in the system.

In this report we demonstrate how a software implementation of the ILDS can be applied to the Citronelle storage site. Since use of pressure data that are received in high frequency streams from Permanent Down-hole Gauges (PDG) are required, a set of simulation runs are designed and executed and pressure behavior (signals) in the observation wells (D-9-7 and D-9-8) as a function different leakage scenarios (rates and locations) are generated.

Total of nine wells (D9-7 or injection well, D-9-1, D-9-2, D-9-3, D-9-6, D-9-8, D-9-9, D-9-10 and D-9-11) are located in the Area of Investigation. There are pressure gauges in the wells D-9-8 and D-9-7 (Figure 151).

In this model CO_2 is injected in 10 reservoir layers for 3 years with the rate of 500 ton/year (9,480,600 ft^3/day). The maximum CO_2 plume extension is about 3,800 to 4,000 ft. away from the injection well. The focus is on the different leakage scenarios. The leakage rates that have been used in the simulation scenarios are based on published observation (Loizzo 2010). The leakage rates considered in the simulation runs to generate pressure signal data are shown in Table 28.

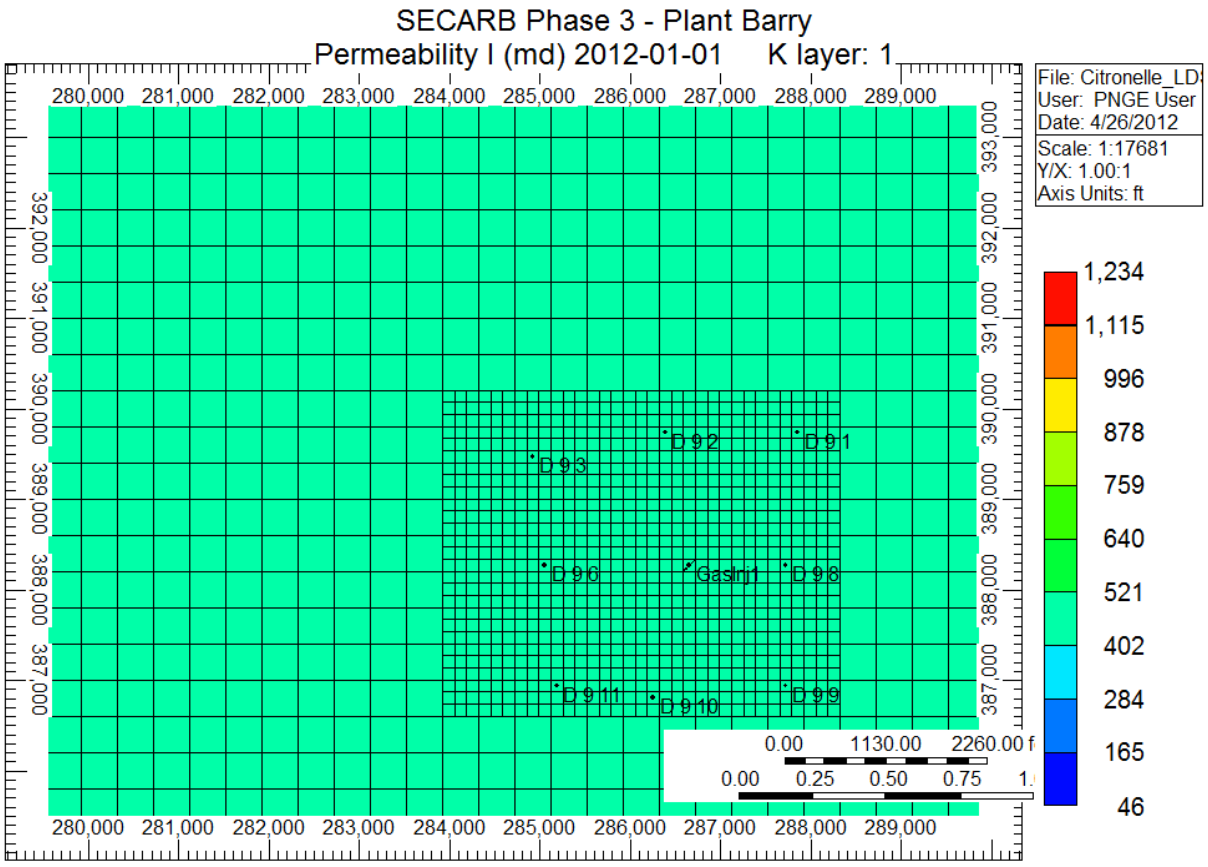

Figure 151. Reservoir model with the existing wells in Area of Investigation

Table 28 - Leakage rates observed in real cases (Loizzo 2010)

Ton/year	ft3/day
35	1837.5
100	5250
210	11025
800	42000
1400	73500
1900	99750
2300	120750
2500	131250
10000	525000
100000	5250000

Based on published data (Loizzo 2010) the leakage rates of the order of 35 - 100 tons/year are considered as small leakages. The rates that range from 100 to 800 tons/year are the ones that typically happen in the underground CO_2 storage projects. 93% of the wells have a leak rate smaller than 1,400 ton/year. A major event which may result in fatalities and extreme damages requires the leak rate of the order of 10,000 to 100,000 ton/year.

We assigned the rates shown in Table 28 to all the wells. Figure 152 shows that the CO_2 plum extension in this site (within 500 years) will only reach three of the wells (wells D 9-6, D 9-2 and D9-10). Therefore, the simulation runs and data generation in this project is concentrated around the potential leakage from these three wells.

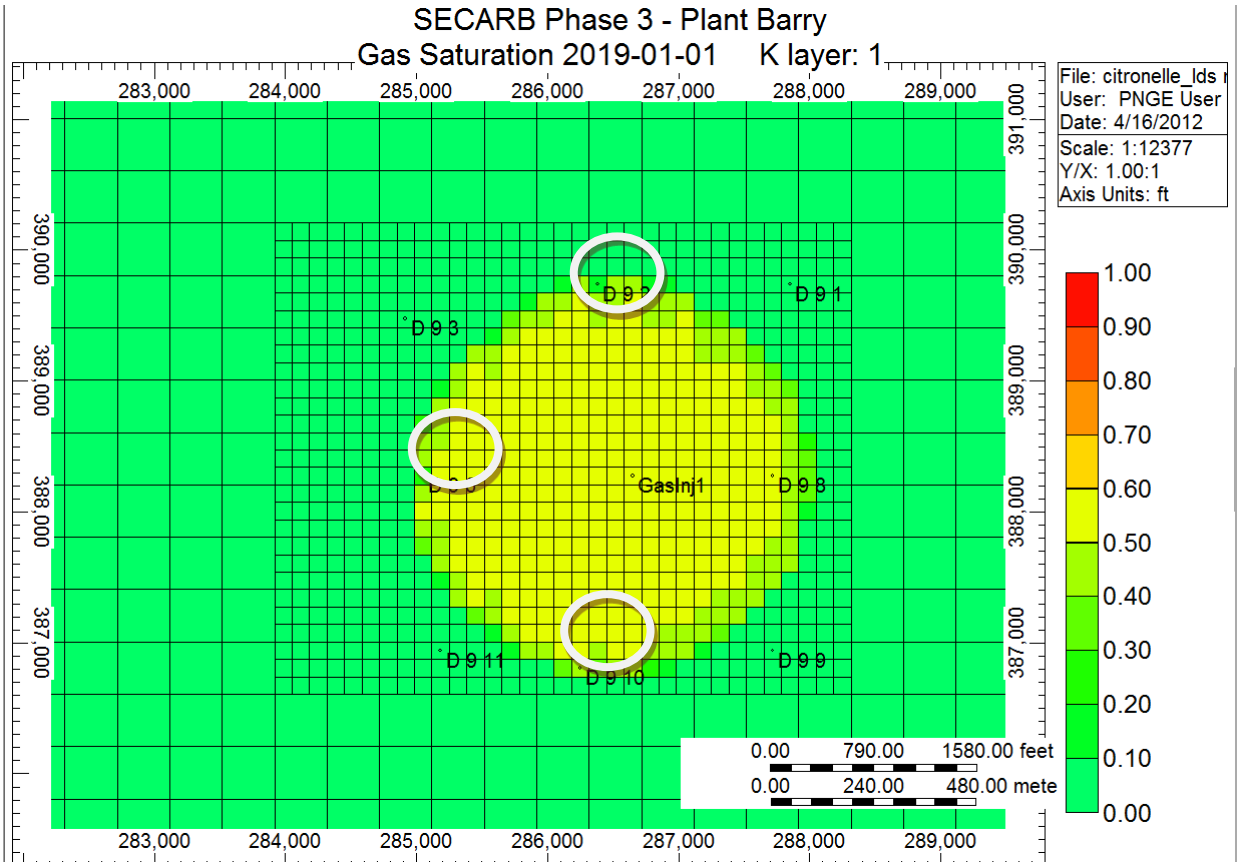

Figure 152. Location of the wells that represent leakage rates in Table 1.

There are different types of Permanent Down-hole Gauges in the oil industry which represents various working specifications. One of the most reliable ones is named “reserve CQG crystal quarts gauge” which is designed for a wide range of pressure conditions (up to 15,000 psi) and the resolution of better than 0.004 psi. Based on the resolution of this down-hole pressure gauge we used the reservoir simulation pressure results for the observation and injection wells with the accuracy of 0.005 psi.

To start, pressure values in the observation and the injection wells are generated in the case with no leakage, to be used as reference. For the observation well (D-9-8) the pressure rises from 4,344 to 4,443 psi during 3 years of injection period (2012 to 2015). After the injection stops, the pressure decreases sharply from 4,443 to 4,395 psi. This change in pressure takes place in a period of three months. Finally, the reservoir pressure in the observation well follows a gradual and stable decline from 4,395 to 4,393 psi during 20 years (Figure 153).

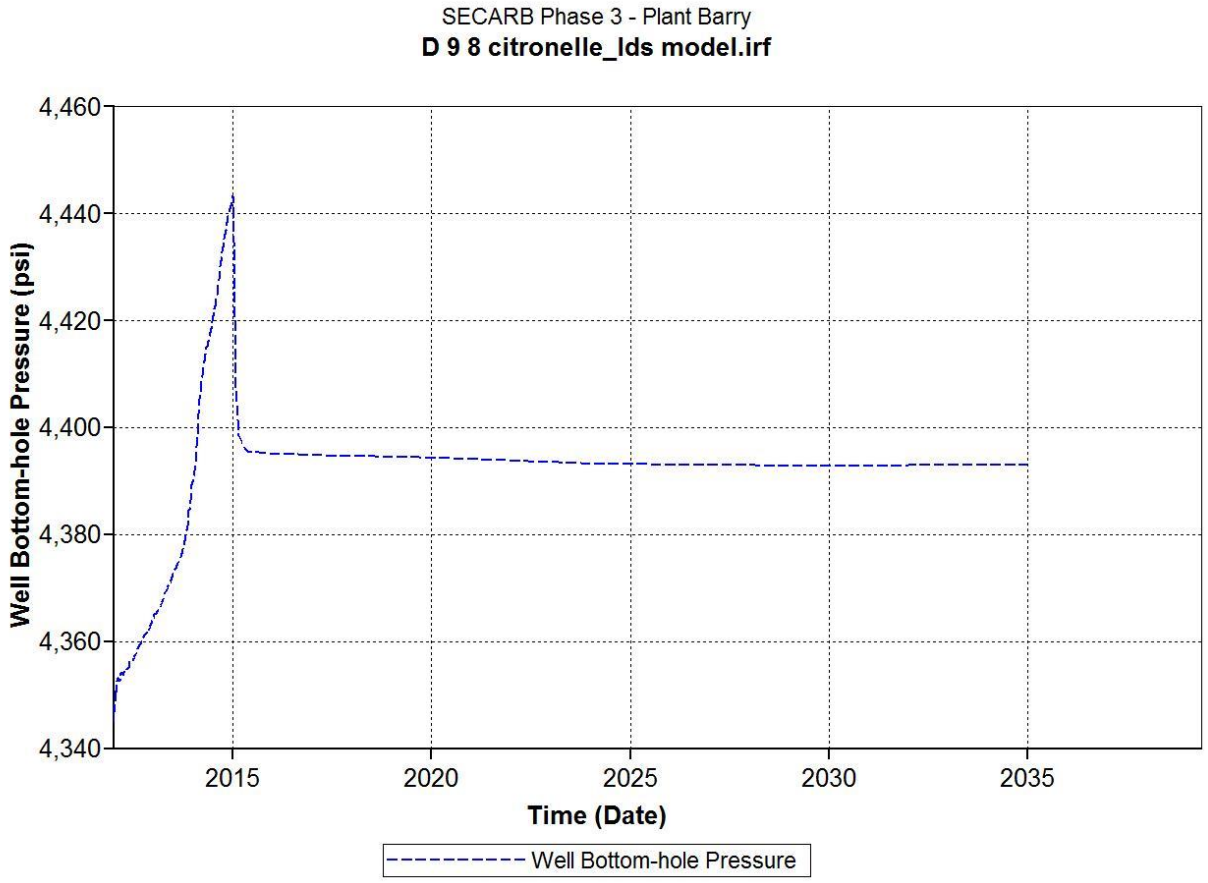

Figure 153. Pressure behavior in well D-9-8 in the case that no leakage happens

From here forward, the difference between the reference pressure signals (when no leakage is occurring in the system) and pressure signals due to any given leakage scenario that is collected at the observation wells, are referred to as ΔP. In this section we present the case of leakage from a single well.

As mentioned earlier, three wells showed potential to leak with the rates shown in Table 28. In all these cases the pressure behavior in the observation well and injection well show almost the same trend when the leakage duration increases. For brevity, we just show the results of the cases that well D-9-6 was subject to different leakage rates in Table 28.

For the first case, the leakage rate of 1,830 ft^3/day was considered for well D-9-6. The leakage starts in 01/01/2017, two years after the end of injection. At this time we can assume that CO_2 is in equilibrium with the reservoir and there is no sudden change in the pressure. The frequency of the pressure recordings is one day (this can be increased to hourly for high frequency data generation). As it is shown in Figure 154 and Figure 155, after the leak starts, there is a change in the pressure difference (ΔP). The magnitude of this change in ΔP is between -0.05 and 0.05 psi.

Based on the fact that the reservoir pressure decreases due to the leakage of CO_2, it is expected that ΔP ($P_{leak} – P_{no\ leak}$) have a positive value, therefore, negative values are not acceptable. They are mainly because of numerical dispersion. These negative values should be disregarded and replaced with zero during the training of the data-driven models. This pressure behavior is almost the same for the leakage rate equal to 5,250 ft^3/day.

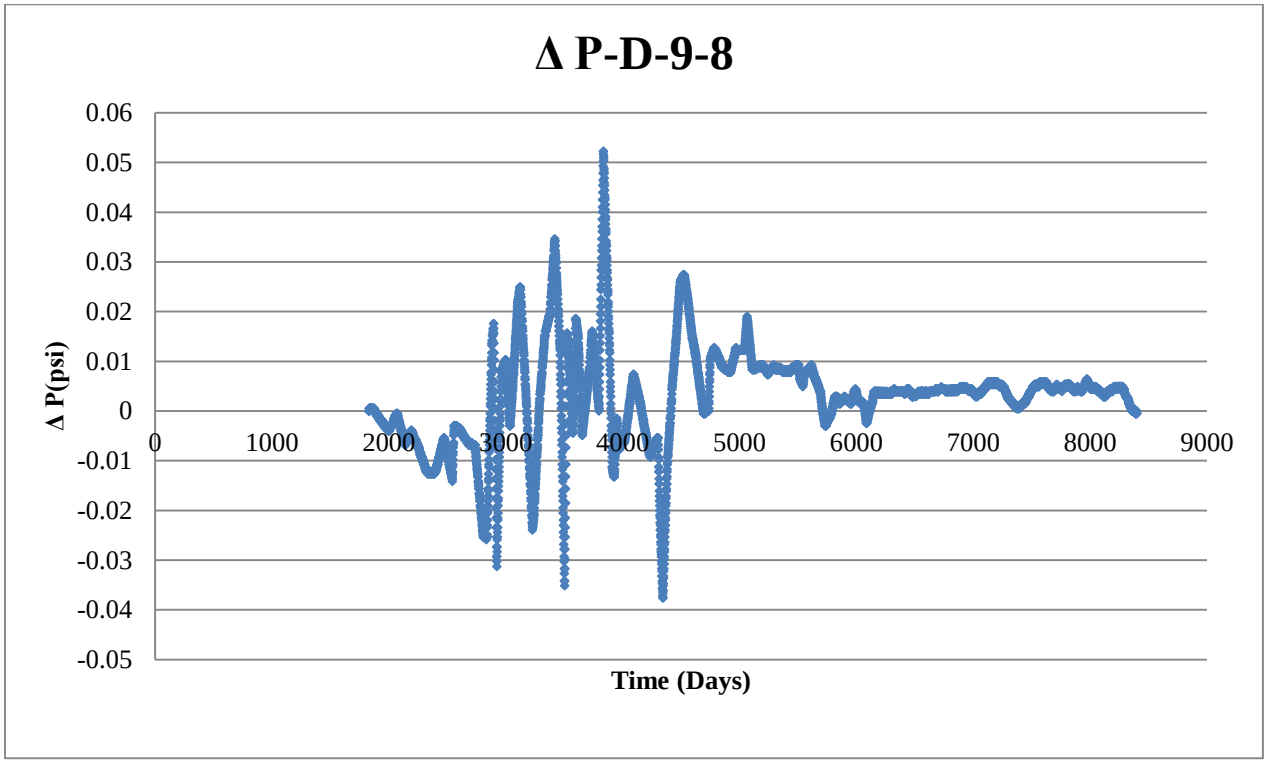

Figure 154. ΔP in well D-9-8 in the case that well D-9-6 leakage rate is 1,830 ft^3/day.

In the situation that leakage rate from the well D9-6 was set at 11,025 ft^3/day no negative values for ΔP in the well D-9-8 were observed (Figure 156). The only fact is that during the post leakage time, some fluctuation in ΔP behavior (ranging between 0 and 0.1 psi) is observed. This behavior may result in incorrect pattern recognition analysis. The pressure behavior which can be measured in the injection well (D-9-7) is more reasonable after the leakage (Figure 157). The

pressure difference reaches 0.04 psi in a year and remains constant for almost 4,000 days. Then it gradually increases to 0.06 psi.

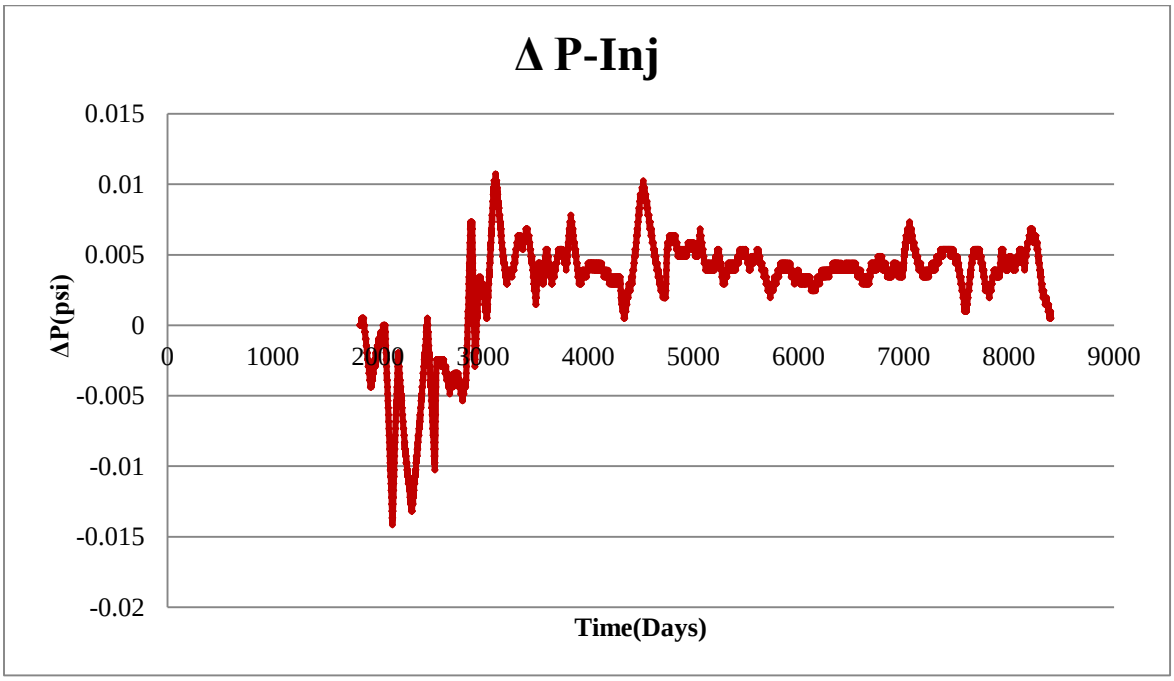

Figure 155. ΔP in Injection well in the case that well D-9-6 leakage rate is 1,830 ft^3/day.

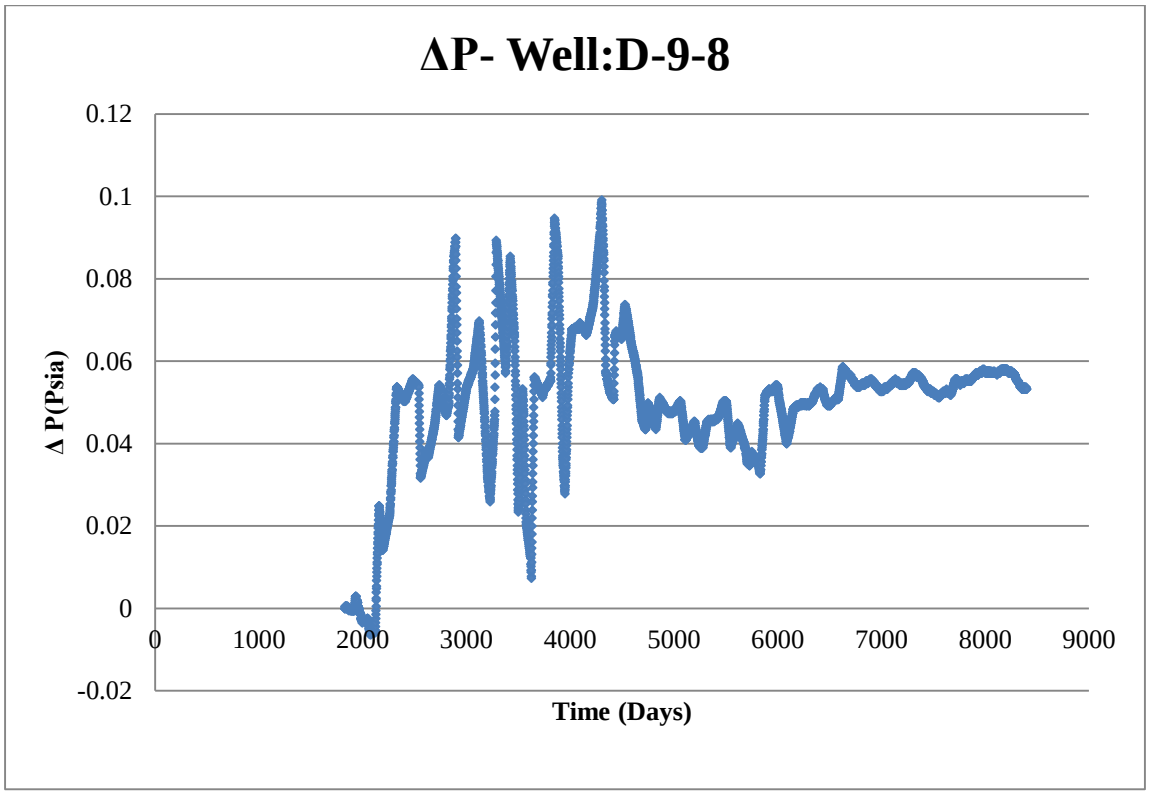

Figure 156. ΔP in well D-9-8 in the case that well D-9-6 leakage rate is 11,025 ft^3/day.

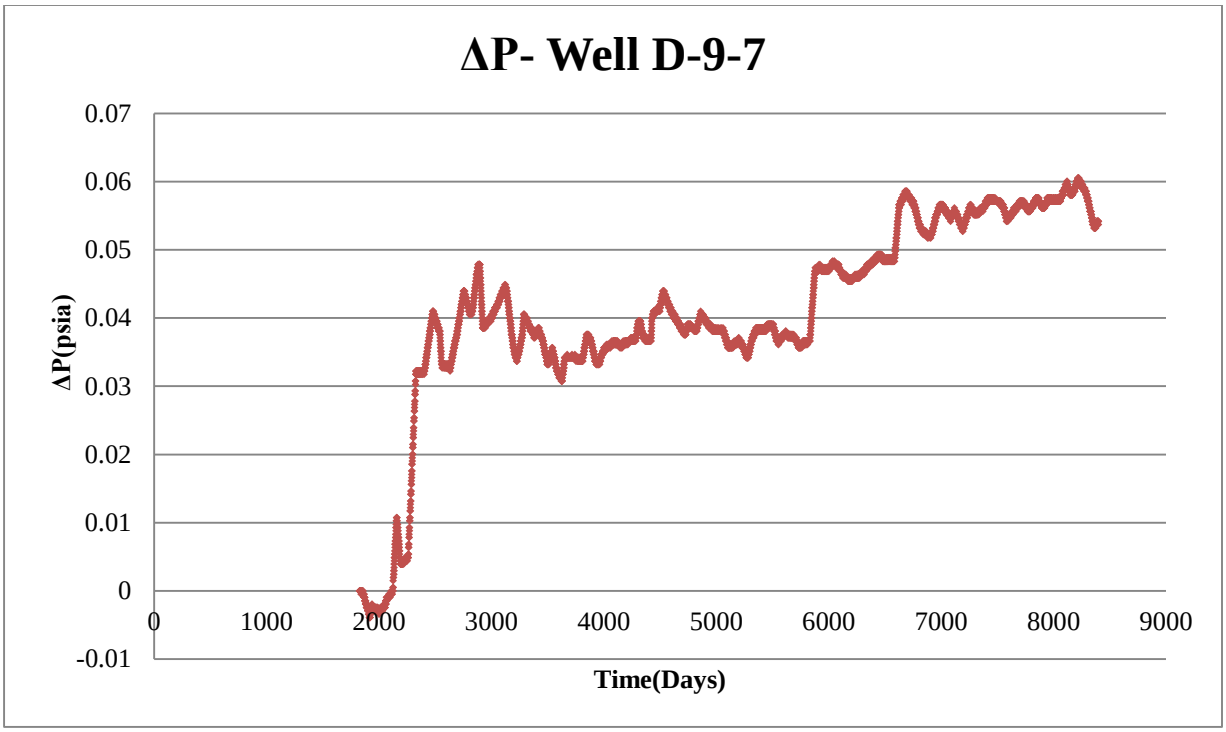

Figure 157. ΔP in well D-9-8 in the case that well D-9-7 leakage rate is 11,025 ft^3/day.

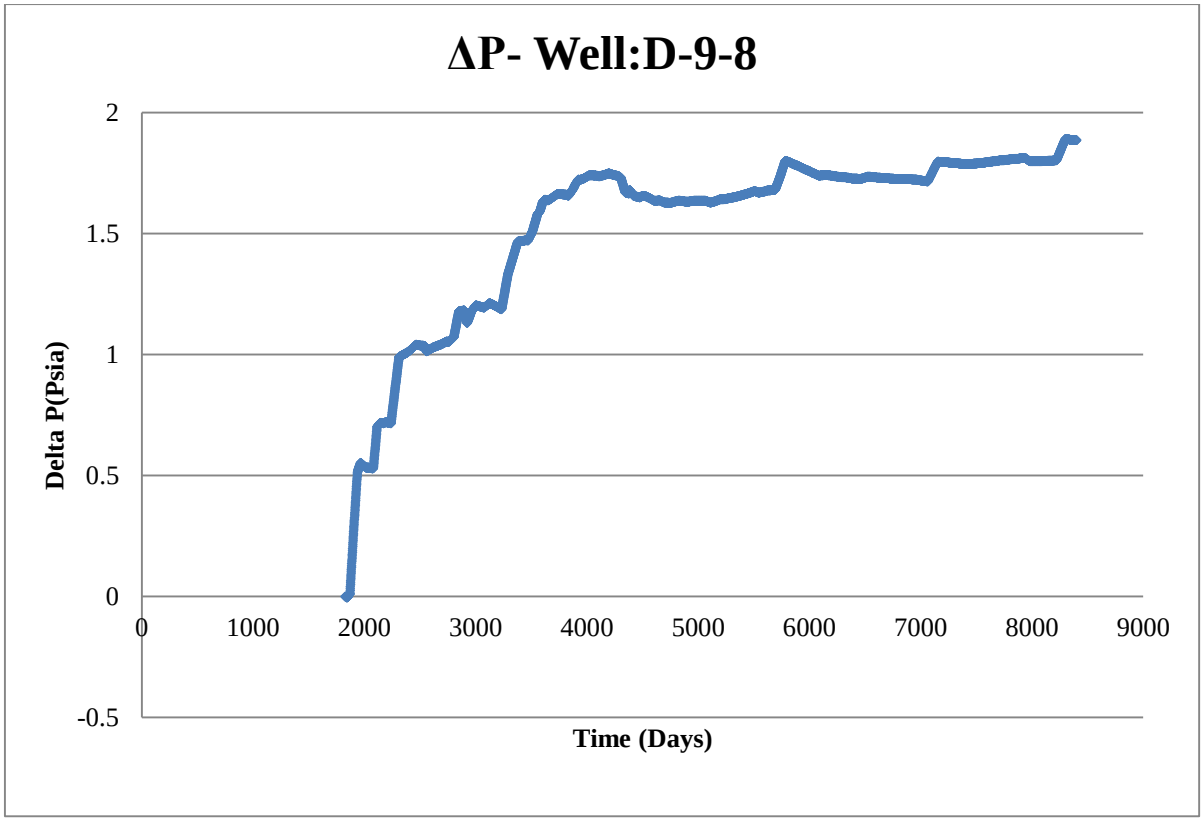

Figure 158. ΔP in well D-9-8 in the case that well D-9-6 leakage rate is 42,000 ft^3/day.

For the case that the assigned leakage rate for well D-9-6 is equal to 42,000 ft^3/day, the pressure difference behavior in both injection (D-9-7) and observation wells (D-9-8) follows almost the same trend. ΔP in well D-9-8 increases sharply to 1.5 psi at the beginning of post leakage time for 2,000 days followed by a plateau (Figure 158). ΔP in the injection well (D-9-7) shows a similar behavior (Figure 159).

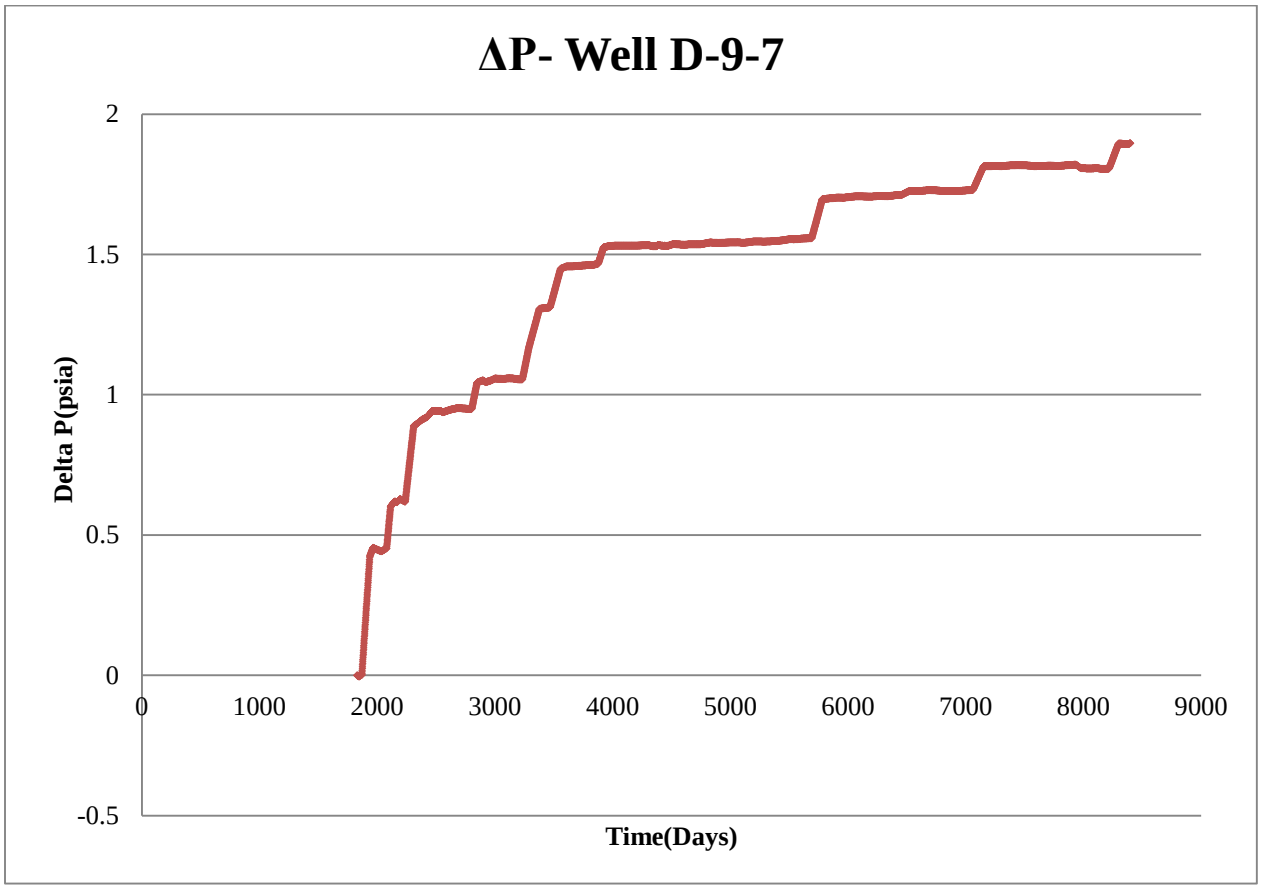

Figure 159. ΔP in Injection well in the case that well D-9-6 leakage rate is 42,000 ft^3/day.

When the Leakage rate in well D-9-6 reaches to 73,500 ft^3/day, pressure difference in both observation and injection wells follows the same logarithmic trend (Figure 160, Figure 161). It means that the rate of increase of the ΔP in the early times during the post leakage period is more than the later times. ΔP in the first 3 months after the leakage reaches to 0.54 psi in the injection well (D-9-7) and 0.67psia in the observation well (D-9-8) are shown in the following figures.

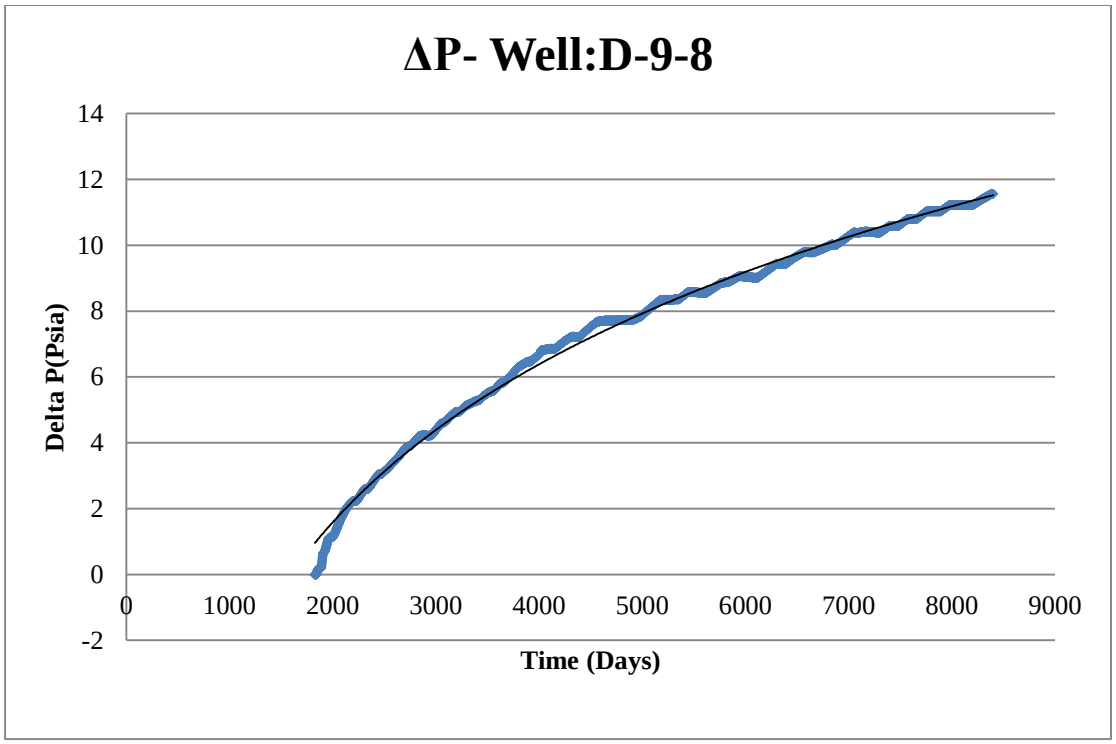

Figure 160. ΔP in well D-9-8 in the case that well D-9-6 leakage rate is 73,500 ft^3/day.

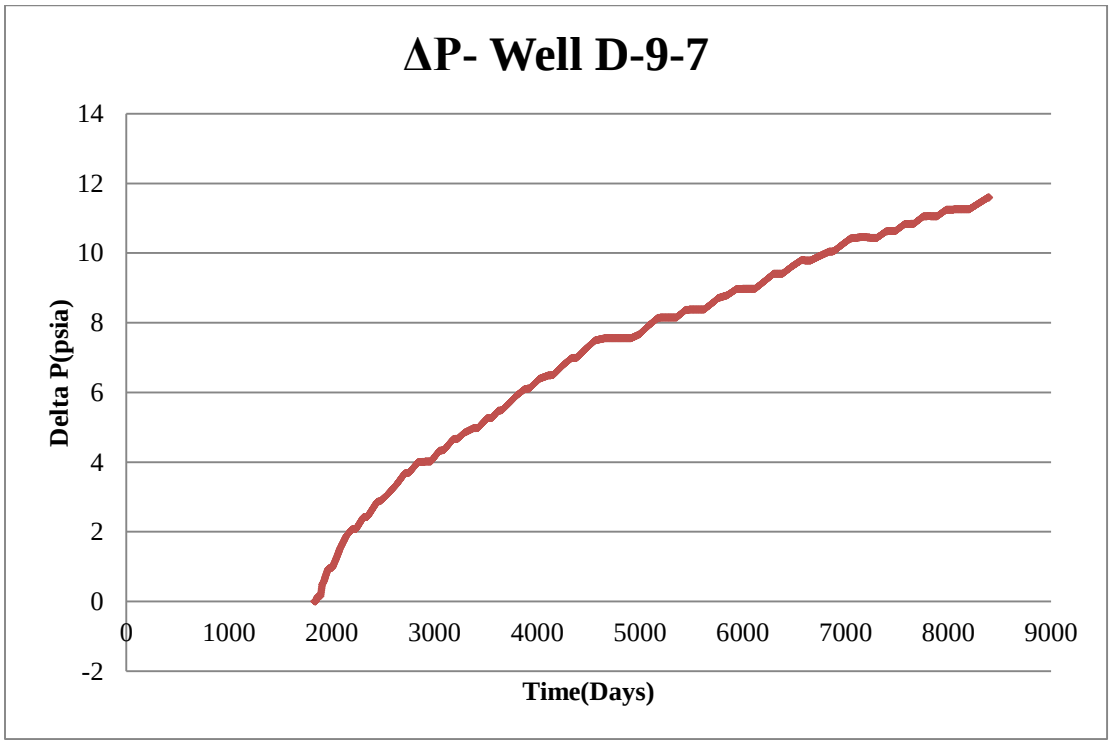

Figure 161. ΔP in injection well in the case that well D-9-6 leakage rate is 73,500 ft^3/day

The leakage rates of 99,750, 120,750 and 131,259ft^3/day were assigned for the well D-9-6. The trend of ΔP for the mentioned rate is also logarithmic. It should be noted that as the leakage rate increases, we can observe that ΔP in the observation and injection well raises proportional to the rate. For instance ΔP in the observation well (D-9-8), after 3 months of the leakage from well D-9-6 at the rates of 99,750, 120,750 and 131,259 ft^3/day are 0.94, 1.66 and 2.22 psi, respectively. It is worthy to mention that we cannot increase the leakage rates above 131,259 ft^3/day since the amount of the CO_2 around the well D-9-6 is not enough to support flow rates of the CO_2.

LEAKAGE IN WELLS D-9-2 AND D-9-10

The procedure for assigning different leakage rates to well D-9-2 and analyzing the ΔP in the injection and observation wells is the same as those of well D-9-6, but the pressure behavior is not the same.

For the leakage rate of 42,000 ft^3/day, we can see the logarithmic behavior for the ΔP trend (Figure 162). Also the amount of ΔP during the same time interval when a leak happens in well D-9-2 is higher compared to D-9-6 leakages. Another point is that the ΔP trend in the observation and injection down-hole gauges becomes linear instead of logarithmic when the well D-9-2 leaks with the rate of 99,750 ft^3/day (Figure 163).

For well D-9-10 we cannot see any logarithmic trend in ΔP behavior respect to time when the CO_2 leakages occurs. Most of the trends are considered linear. The results of the ΔP trends for all three wells are presented in Appendix 4.

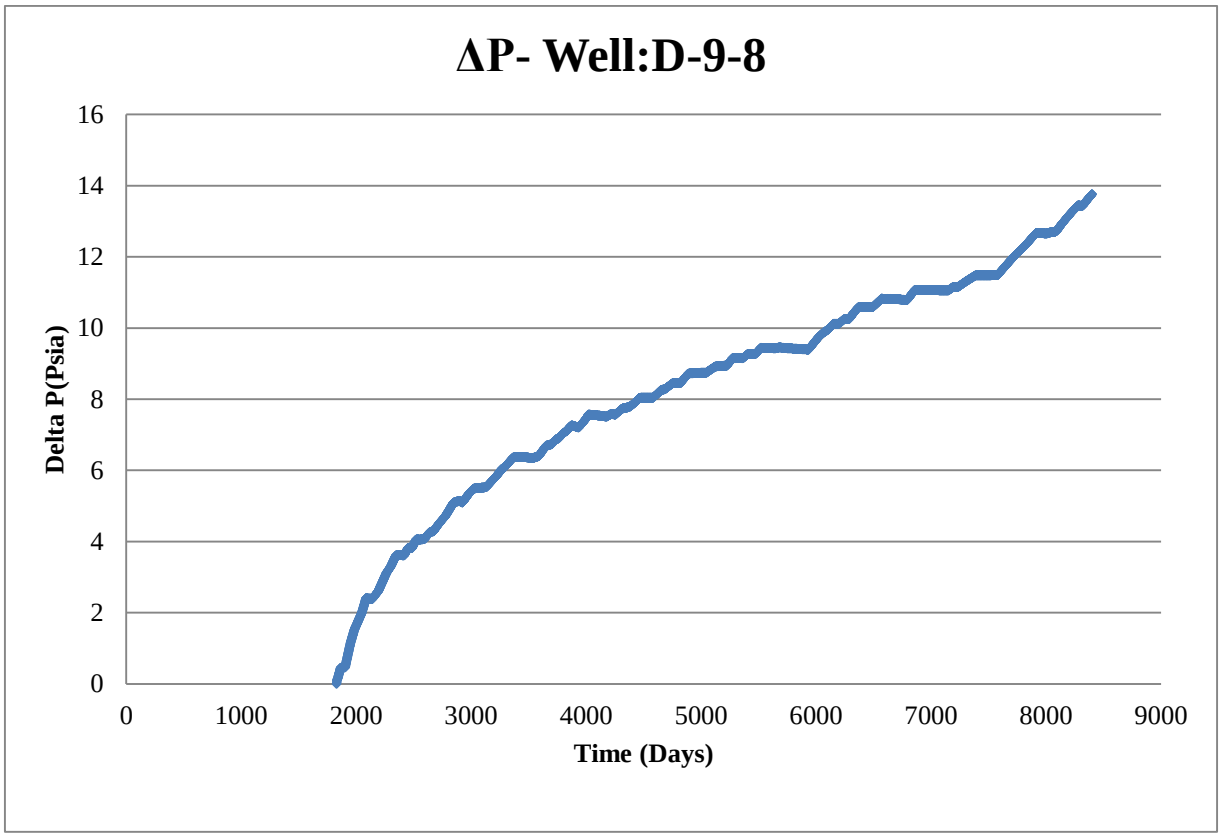

Figure 162. ΔP in well D9-8 in the case that well D-9-2 leakage rate is 42,000 ft^3/day.

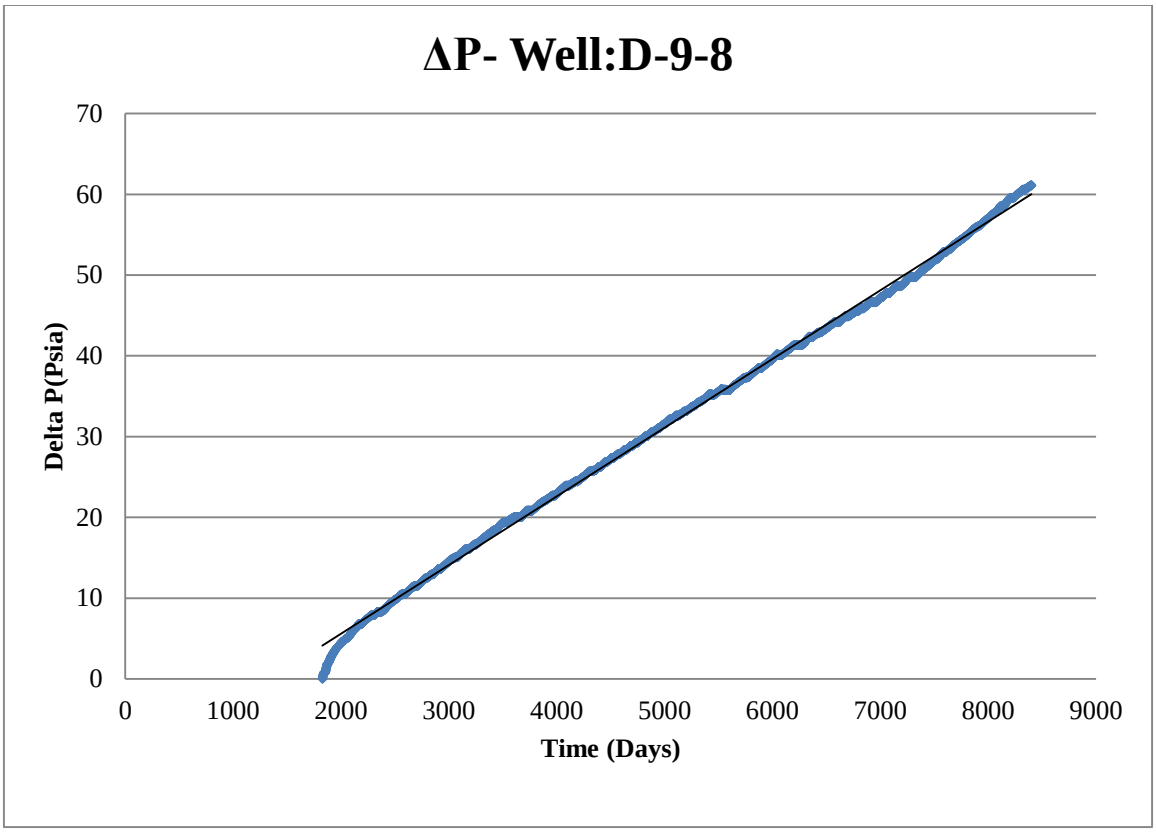

Figure 163. ΔP in well D9-8 in the case that well D-9-2 leakage rate is 99,750 ft^3/day.

INTELLIGENT LEAKAGE DETECTION SYSTEM

PROCESSING OF HIGH FREQUENCY DATA STREAMS – DATA SUMMARIZATION

Citronelle reservoir simulation model was used to generate high frequency pressure data (pressure reading from observation and injection well). The injection scenario used to generate the pressure signals included 500 ton/year (9,480,600 ft3/day) into 10 reservoir layers of the Pluxy formation. Figure 164 demonstrates the extent of the maximum CO_2 plume extension 4 years after the end of injection. Based on the extension of the CO_2 plum, wells D-9-2, D-9-6 and D-9-10 can be included within the reach of the CO_2 plum, and therefore, are considered for the leakage study.

In order to generate high frequency pressure data in observation and injection well, due to the leakage from the wells mentioned above, twenty different CO_2 leakage rates- in the range of real leakage rates observed in actual cases- were assigned to the wells D-9-2, D-9-6 and D-9-10. These CO_2 leakage rates are shown in Table 29.

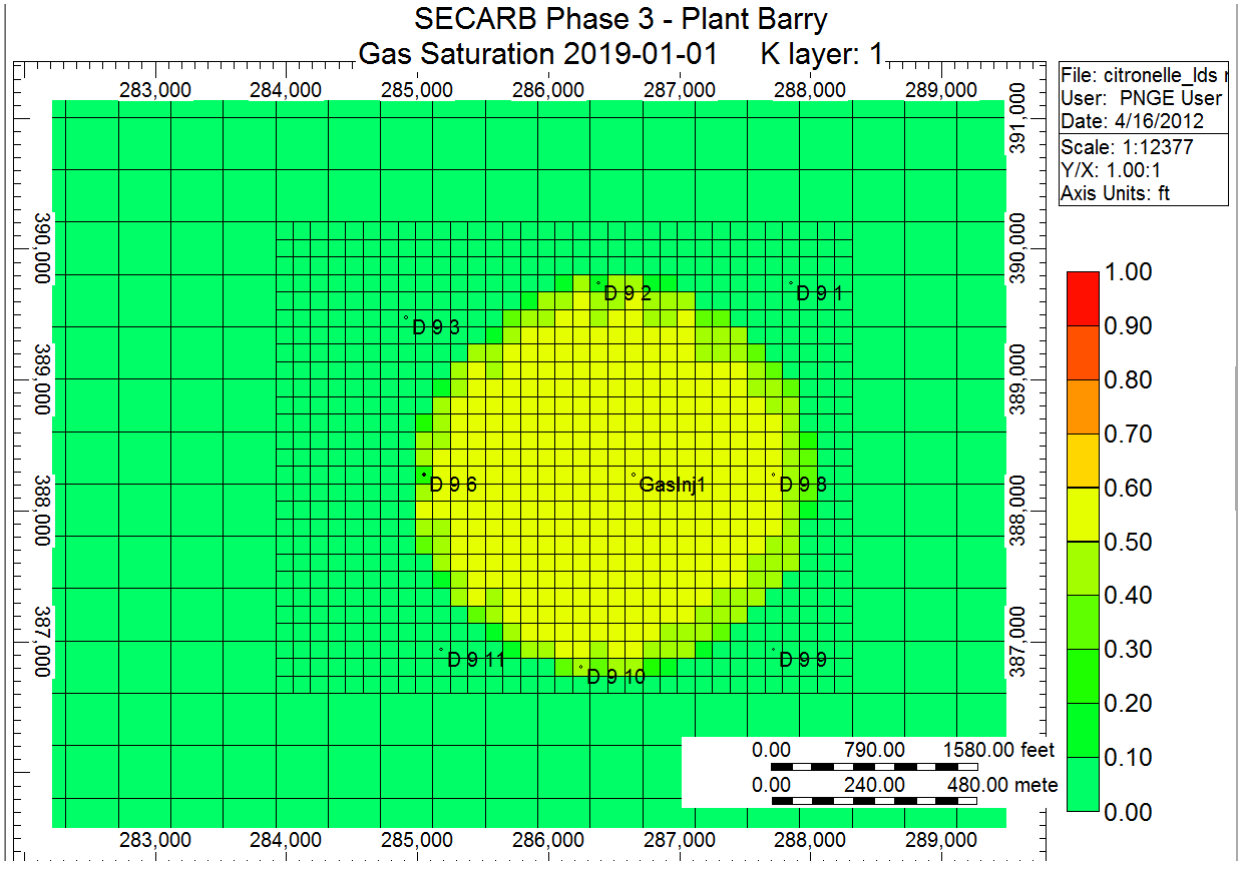

Figure 164.CO_2 Plume Extension in the first layer of the Citronelle Field 4 years after the end of injection

Table 29. CO_2 Leakage rates assigned for the wells D-9-2, D-9-6 and D-9-10

Leakage rate			
Ton/year	ft3/day	Ton/year	ft3/day
286	15000	1333	70000
381	20000	1429	75000
476	25000	1524	80000
571	30000	1619	85000
667	35000	1714	90000
762	40000	1810	95000
857	45000	1905	100000
952	50000	2000	105000
1048	55000	2095	110000
1143	60000		
1238	65000		

At each CO_2 leakage scenario it is considered that leakage starts 2 years after the end of injection (1/1/2017). For each CO_2 leakage rate, reservoir simulation run was performed at one hour time steps. The duration of leakage is 6 months. We also performed a simulation with no leakage. In this case the bottom-hole pressure in the observation well starts increasing during the injection until it reaches to its maximum at the end. After end of injection, the pressure drops until reservoir reaches the equilibrium. The typical time for this period is about 4 to 5 months. After that, the bottom-hole pressure becomes almost constant.

When a CO_2 leakage takes place in one of the wells, it creates a pressure change in the reservoir. This pressure change can be observed in the observation well. Therefore the difference between pressure in the observation well, in the case that no leakage exists and when a leakage happens, is considered as the leakage indicator. This pressure difference (or Δp) behavior can characterize the specifications of the leakage, specifically the location and the amount of CO_2 being leaked.

For example the magnitude of Δp is directly proportional to the amount of the CO_2 leakage rate. Also the shape of the Δp as a function of time is related to the location of the leakage. As an example Δp history (high frequency-hourly basis) in the observation well, for the case that well D-9-6 leaks with the rate of 30,000 ft3/day is shown in Figure 165. For all the leakage rate scenarios in Table 29 (3 wells leak individually) high frequency Δp values were generated for both injection and observation well.

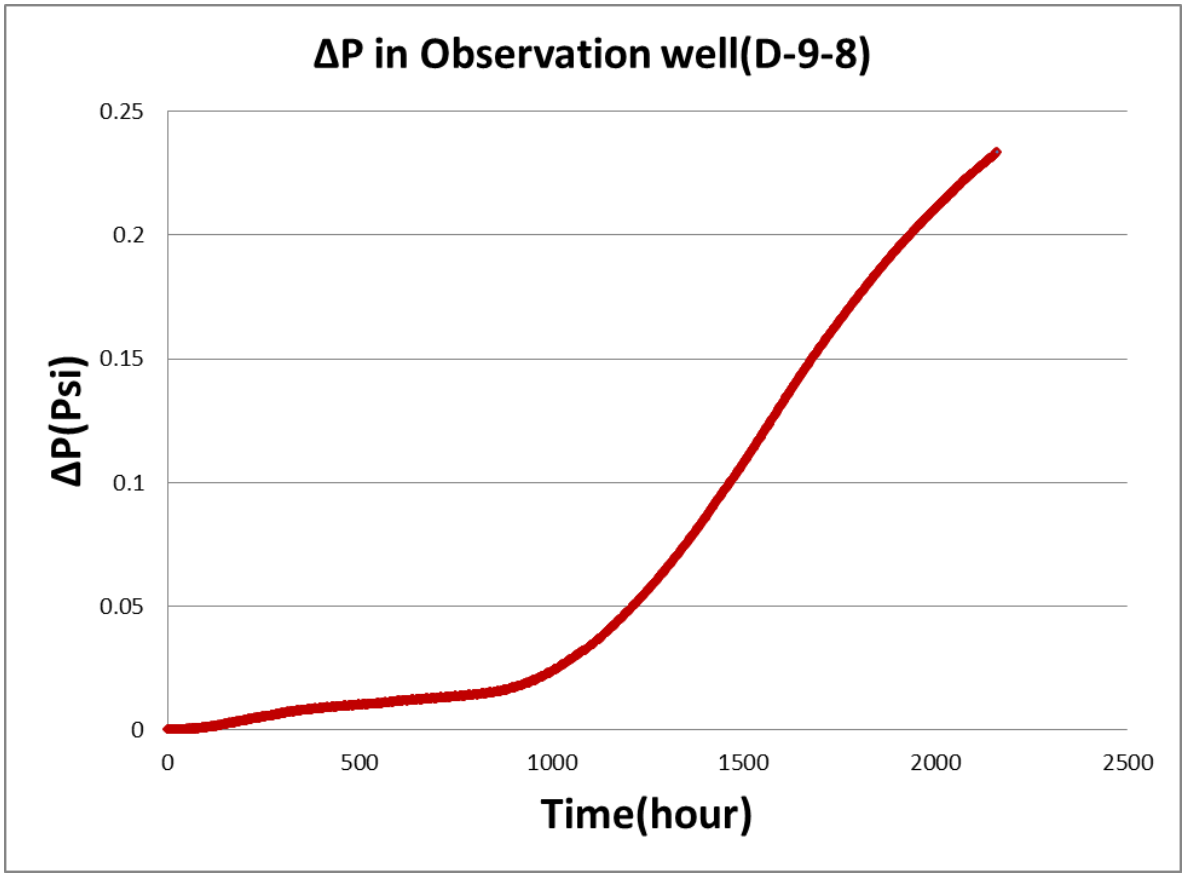

Figure 165. ΔP in injection well in the case that well D-9-6 leakage rate is 30000ft3/day

Data Summarization

Normally the data that is transmitted from the PDG sensors include Noise. The First step in processing such data streams is removing the noise associated with the data. The next step is summarizing the high frequency PDG data and transforming the data into a format that can be used by the pattern recognition technology.

Based on the characteristics of the ∆p extracted from the high frequency data streams, “Descriptive Statistics” was used for data summarization. Descriptive Statistics quantitatively describes the main features of a collection of data and provides simple summaries about the sample and about the observations that have been made. These summaries form the basis of the initial description of the data that will be used by the pattern recognition technology.

The parameters that can represent and summarize a large amount of data can be listed as: Mean, Standard Error, Median, Mode, Standard Deviation, Sample Variance, Kurtosis, Skewness, Range, Maximum, Minimum and Sum. For example the descriptive statistics and summarization of 504 hourly ∆p data points in the observation well (D-9-8) for the case that well D-9-6 leaks with the rate of 110,000 ft3/day is listed in Table 30.

Table 30. Descriptive statistics and summarization of 504 hourly ∆p data points in the observation well (D-9-8)

Descriptive statistics	
Mean	0.05297658
Standard Error	0.00344277
Median	0.01220703
Mode	0
Standard Deviation	0.07729008
Sample Variance	0.00597376
Kurtosis	1.0883939
Skewness	1.52563822
Range	0.28369141
Minimum	-0.0004883
Maximum	0.28320313
Sum	26.7001953
Count	504

Another way to represent large numbers of data points that can also be implemented in the neural network training and pattern recognition is Curve Fitting. In this process a curve is constructed, providing a mathematical function that has the best fit to a series of data points. The shape of ∆p history curve is different respect to the location of the leakage. Therefore, it is not possible to determine a typical curve (linear, exponential…) to fit all the data points.

The only curve that can provide a good fit for ∆p points is a "Polynomial" curve. In this project 4th degree polynomial curve was used to fit ∆p points for different leakage rates and leakage locations. For instance for the case that well D-9-6 leaks with the rate of 30,000 ft3/day (Figure 165), following polynomial function represents the best fit with the $R^2 = 0.9992$:

$$\Delta p = - 7x10^{-14}\, t^4 + 3x10^{-10}\, t^3 – 3x10^{-07}\, t^2 + 0.0001t - 0.0085$$

The coefficients and intercept of the above mathematical relationship can be used for pattern recognition and Neural Network Training.

PREPARATION OF HIGH FREQUENCY DATA FOR PATTERN RECOGNITION

Data Partitioning for Neural Network Modeling

In order to make neural network model, first of all it is necessary to prepare the data set including input and output features. In this project, our aim is to determine the location and amount of leakage based on the data that is provided by PDGs reading. Therefore, latitude and longitude (X, Y) of the leaking well (D-9-2, D-9-6 and D-9-10) and the CO_2 leakage rate are the output features of the Neural Network. The CO_2 leakage rates are shown in Table 29.

The actual input data that we receive directly from PDGs are pressure readings from observation well or in another word, the difference between pressure readings during the leakage and no leaking condition (Δp). As explained in the previous section, the Δp readings at different times (hourly basis) are summarized using descriptive statistics. For initial study the pressure information (PDG readings) in observation after 1 week of leakage in hourly basis was selected.

Prior to the input data selection, KPI[4] or key performance indicator analysis should be completed in order to determine which parameters are more influential to be considered as inputs. The first KPI test was performed on the location of leakage (coordinates of the possible leaking wells); to see which parameters are more effective. The results of the key performance indicator analysis for the location of the leakage are shown in Figure 166 and Figure 167.

Rank	Feature	% Degree of Influence
1	Skewness	100
2	Kurtosis	89
3	Range	12
4	Standard Deviation	11
5	Standard Error	11
6	Sum	11
7	Sample Variance	9
8	Maximum	8
9	Mean	6
10	Median	1

Figure 166. Key performance indicator analysis results for the latitude of the leakage.

Based on the key performance indicator results, skewness, kurtosis and range (or maximum) have the most influence on identifying the location of the leakage and mean and median are in the least degree of importance. Therefore the median was not selected as the input data for Neural Network Training.

[4] These analysis were performed using IDEA™, a software application provided by Intelligent Solutions, Inc.

The same analysis was performed to see the effect of each parameter on the CO_2 leakage rate. According to the results of the KPI (Figure 168), skewness, kurtosis and Maximum have the most effects on the CO_2 leakage rate. Also it is concluded that the median has the least effect on the leakage rate.

Rank	Feature	% Degree of Influence
1	Skewness	100
2	Kurtosis	44
3	Standard Error	15
4	Range	15
5	Maximum	15
6	Standard Deviation	14
7	Sum	14
8	Sample Variance	9
9	Mean	2
10	Median	1

Figure 167. Key performance indicator analysis results for the longitude of the leakage.

Rank	Feature	% Degree of Influence
1	Skewness	100
2	Kurtosis	57
3	Maximum	19
4	Standard Deviation	19
5	Mean	18
6	Sum	18
7	Range	18
8	Sample Variance	15
9	Standard Error	15
10	Median	1

Figure 168. Key performance indicator analysis results for the CO_2 leakage rate.

According to the key performance indicator analysis results, we decided to select 10 inputs (Mean, Standard Error, Mode, Standard Deviation, Sample Variance, Kurtosis, Skewness, Range, Maximum, and Sum) for Neural Network training. In this case we assigned 20 different CO_2

leakage rates to 3 leakage locations(wells D-9-2,D-9-6 and D-9-10).As a result totally 60 different records including 10 input parameters for each were considered for neural network training. For this data set, intelligent data partition was used for the segmentation of the records in which 80% of data were allocated for neural network training, 10% for network calibration and 10% for verification. Therefore 48 records will be used for training, 6 for calibration and 6 for verification.

NEURAL NETWORK ARCHITECTURE DESIGN

Error Back-propagation is one of the popular learning algorithms that was used in this study. For this algorithm just one hidden layer was provided. Based on the 10 inputs - 3 outputs, 12 neurons in the hidden layer and one random seed number were allocated for the neural network (Figure 169). The random numbers initialize the weights on the neural network prior to the training.

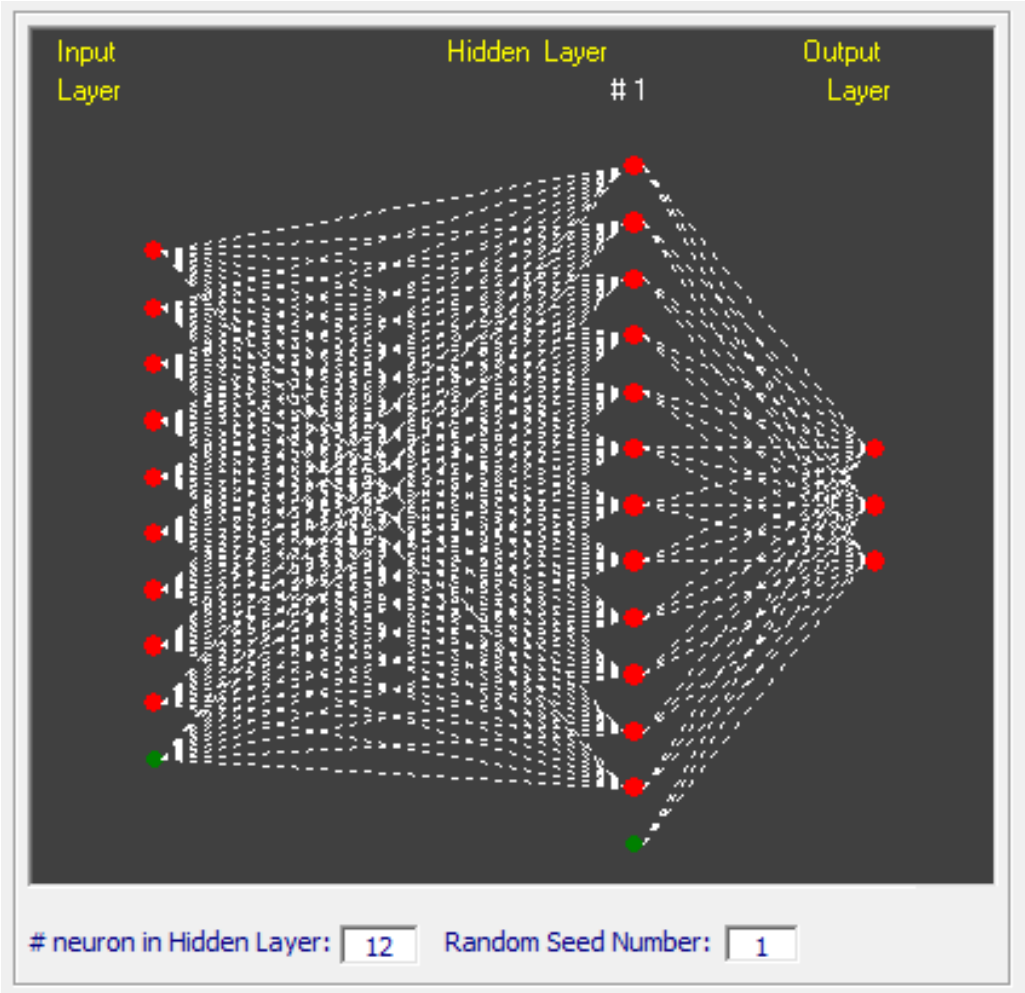

Figure 169. Neural network architecture

As shown in Figure 169 , there are two sets of synaptic connections in the network. First is the synaptic connections between the input layer and the hidden layer, and the second set of connections are those between the hidden layer and the output layer. Since we used “Vanila “ and “Enhance “ networks[5], for each connection set, 2 parameters as Momentum and Learning rate are assigned. “Learning Rate” which is an indication of how fast the network learns the information presented. This is usually a moderate to low number (between 0 and 1). Small

[5] IDEA™, from Intelligent Solutions, Inc.

learning rate value may prolong the learning process and slow it down to a crawl. Momentum is an extra push to the learning process that serves two purposes. First, it may accelerate the learning process, and second, it has the potential to kick the solution out of the local minima, that usually exists in the search space and causes the solutions to converge pre-maturely. In this project Learning rate and Momentum are considered 0.3 and 0.8 respectively. Also Logistic activation function was used to connect input layers to the hidden layers.

The next step is to identify how and when to save the trained network. It is recommended to save the network that has achieved the best training set, or the calibration set. Also the network can be saved after 1 epoch (or more) of training. Each epoch of training is completed when all the records in the training set have been visited by the network once.

NEURAL NETWORK TRAINING AND CALIBRATION

In the first step it was decided to train a network that relates the location of the leakage (X and Y coordinates) to the summarized pressure readings (Table 30) from observation well (D-9-8). The results of the neural network training and calibration of the X coordinate of the leakage after 15,000 epochs[6] are shown in Figure 170 and Figure 171.

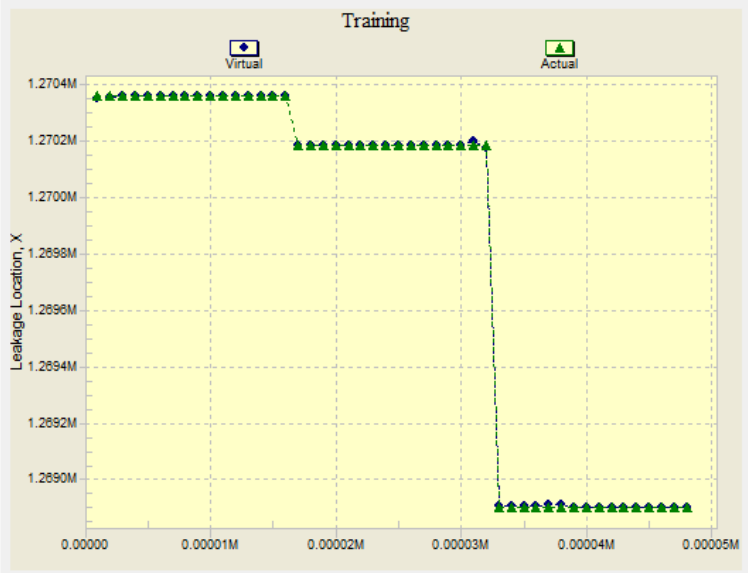

Figure 170. Neural Network training results for the leakage location(X)

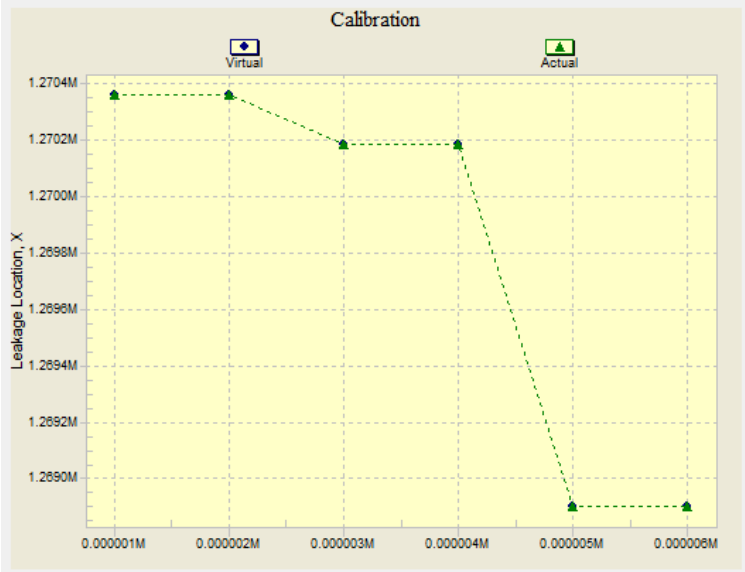

Figure 171. Neural Network Calibration results for the leakage location(X)

[6] Each epoch is defined as an iteration of the training of the neural network with all available data.

The best results for the training set were achieved after 14,993 epochs with minimum average error of .00071. For calibration set data the best results were saved at Epoch 13,455 with the minimum average error of .0012. The results for the CO_2 leakage rate training and calibration are illustrated in Figure 172 and Figure 173.

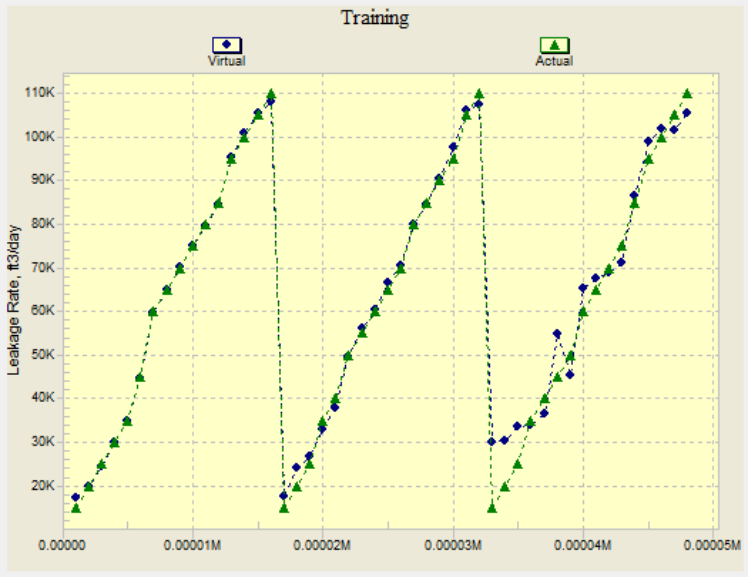

Figure 172. Neural Network training results for the leakage rate

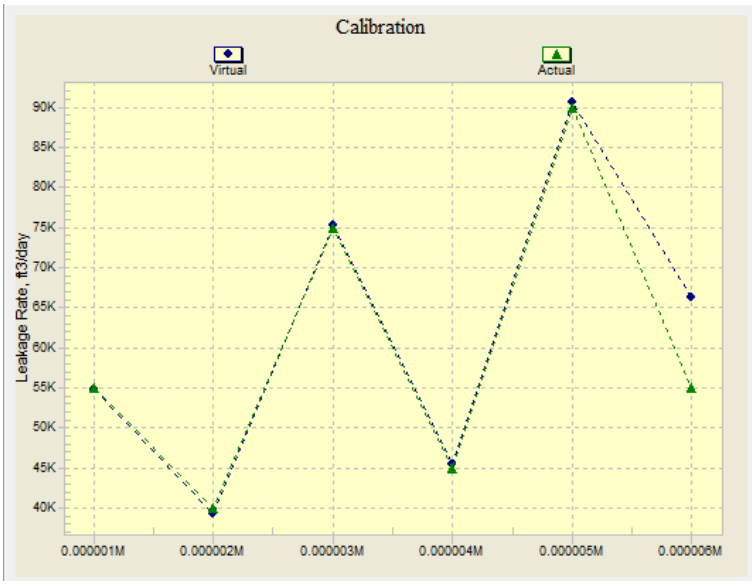

Figure 173. Neural Network calibration results for the leakage rate

In order to investigate the effect of more data assimilation in neural network training, we prepare the summarized pressure data set (weekly basis) for 8 weeks after CO_2 leakage happens. The neural network training and calibration results for the week 1, 5 and 8 are shown in the next section. A comprehensive results are included in Appendix 5.

PATTERN RECOGNITION ANALYSIS

Neural Network Validation

In order to develop the Intelligent Leakage Detection System (ILDS), a set of high frequency pressure data was generated corresponding to different CO_2 leakage characteristics. In the reservoir simulation model of the CO_2 injection in the Citronelle field (Paluxy Formation), it was observed that CO_2 plume extension would reach to the three existing wells (D-9-2, D-9-6 and D-9-10) at the end of 2017.Twenty Different CO_2 leakage rates ranging from 15 to 110 Mcf/day were assigned to each well in order to generate high frequency pressure data. The behavior of ΔP (the difference between pressure data in the case that no leakage is happening and when we have a leakage in the well) is the indicator of leakage characteristics as shown in Figure 174.

For each leakage scenario, the pressure difference data (ΔP) were collected from the observation well and summarized by descriptive statistics. By doing so, the data would be in proper format for pattern recognition. The hypothetical leakage started at the beginning of year 2017 and the pressure data were collected on hourly basis. The time window of one week was considered in order to summarize the pressure data (Figure 175).

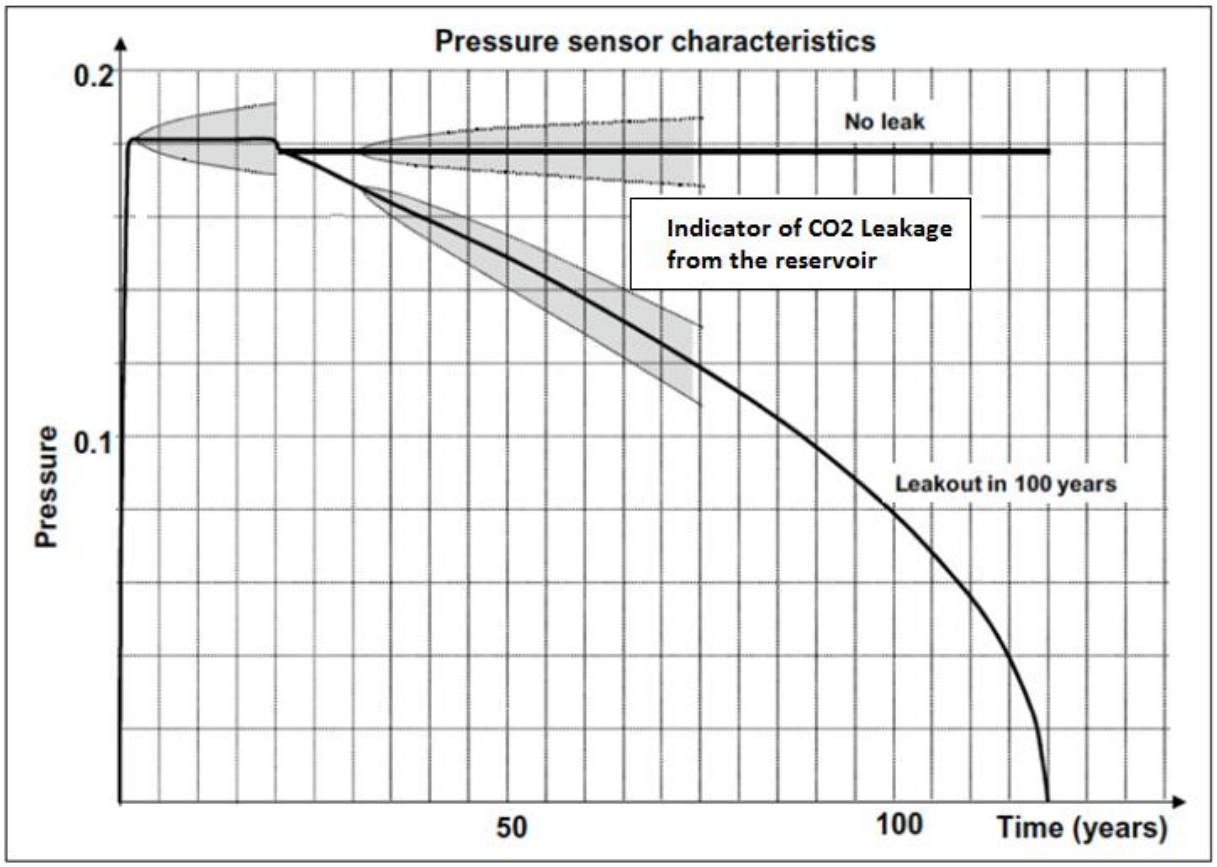

Figure 174. Pressure difference when no leakage happens compared to the case that leakage occurs

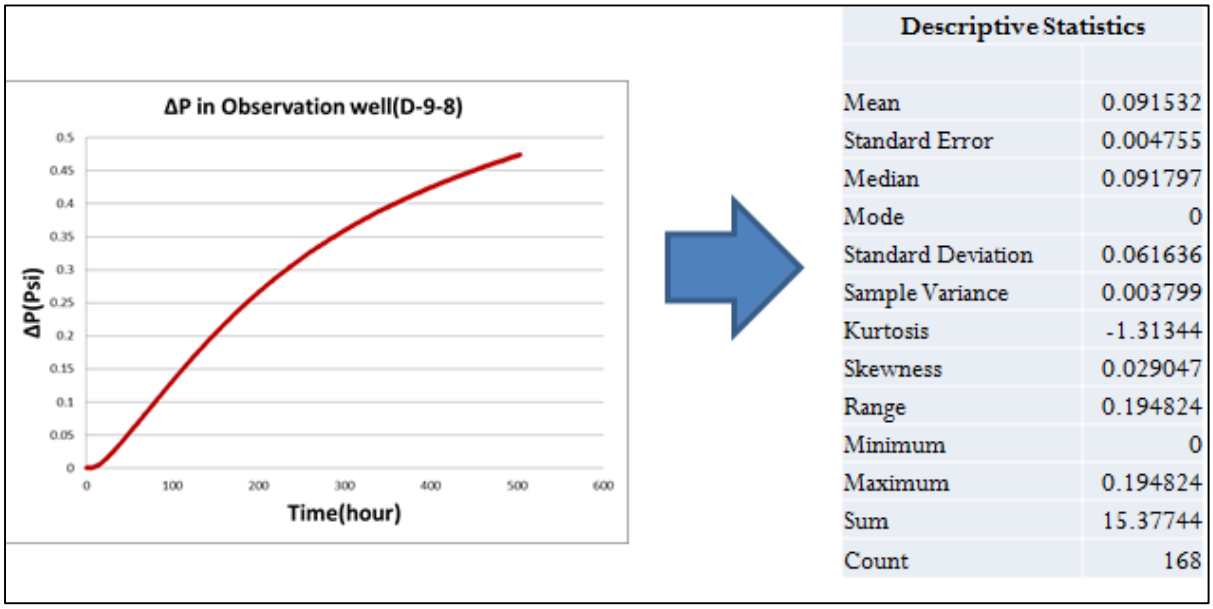

Descriptive Statistics	
Mean	0.091532
Standard Error	0.004755
Median	0.091797
Mode	0
Standard Deviation	0.061636
Sample Variance	0.003799
Kurtosis	-1.31344
Skewness	0.029047
Range	0.194824
Minimum	0
Maximum	0.194824
Sum	15.37744
Count	168

Figure 175. Pressure difference in Observation well and the corresponding descriptive statistics

The data set for neural network Training and Calibration was generated based on 60 different leakage scenarios. For each scenario, specific CO_2 leakage rate was assigned to one well (out of the three wells that are prone to the leakage). The aggregation of the descriptive statistics parameters of the high frequency pressure data for all the 60 scenarios formed the data set for pattern recognition.

Table 31 . Verification Dataset

Leakage Location, X	Leakage Location, Y	Leakage Rate, ft3/day
1270184.28	11276221.98	30,000
1270184.28	11276221.98	65,000
1270359.36	11279158.24	70,000
1270359.36	11279158.24	75,000
1268902.52	11277566.74	55,000
1268902.52	11277566.74	105,000

It is worthy to note that summarized pressure data are the inputs for neural network and Leakage location and rates are the output. This input-output selection is due to the fact that real time pressure data (summarized) is going to be fed into neural network to determine the location and amount of CO_2 leakage. The date set was partitioned to three sections for training, calibration and verification of neural networks.

For the verification of the predictive capabilities of the neural networks, 10 percent of the data were set aside for the final analysis. These data would be used to test the validity of the neural networks that were trained and calibrated. In other words, the verification data set, determines the power of the neural network for prediction. In this case 6 records out of the 60 records were set aside for verification. The data records used for verification are shown if Table 31.

The verification results for the leakage location are shown in Figure 176 and Figure 177. Based on the results shown in these two figures, it can be concluded that neural networks for clean pressure data (including no associated noise) are well trained. The R^2 for verification data records corresponding to latitude and longitude of leakage location is equal to 1.

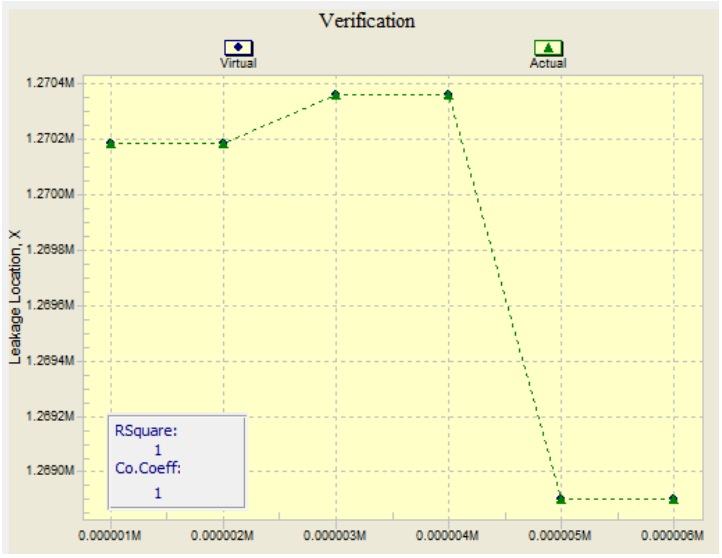

Figure 176. Verification results for leakage location(X) - clean data

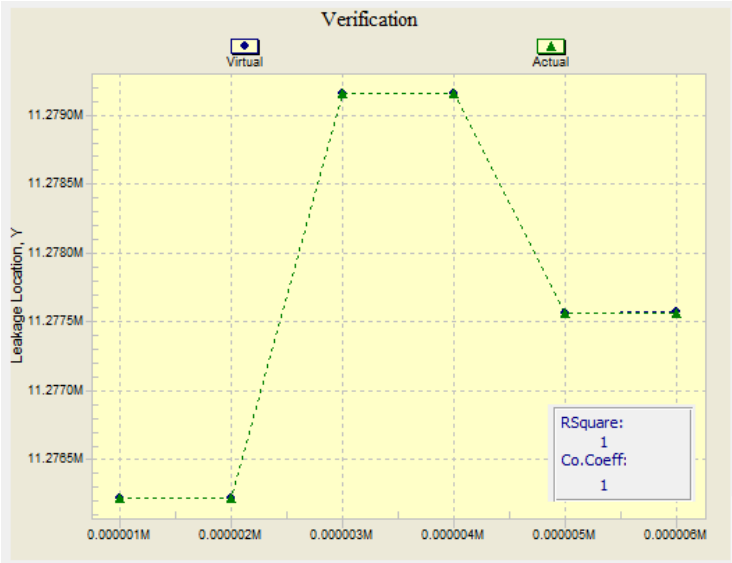

Figure 177 . Verification results for leakage location(Y) - clean data

The verification results for CO_2 leakage rate are shown in Figure 178. There is only one point for leakage rate that lies out of the general trend for predictions. This leads to a R^2 of about 0.4. It is worthy to mention that R^2 for training and calibration are 0.94 and 0.99, respectively. As a result, although we see a low value for R^2 in verification section, higher values of R^2 for training and calibration makes the overall predictability of the network to be reasonably high. The results for neural network verification are shown in Table 32. Detail results for overall neural network training, Calibration and verification are summarized in Appendix 5.

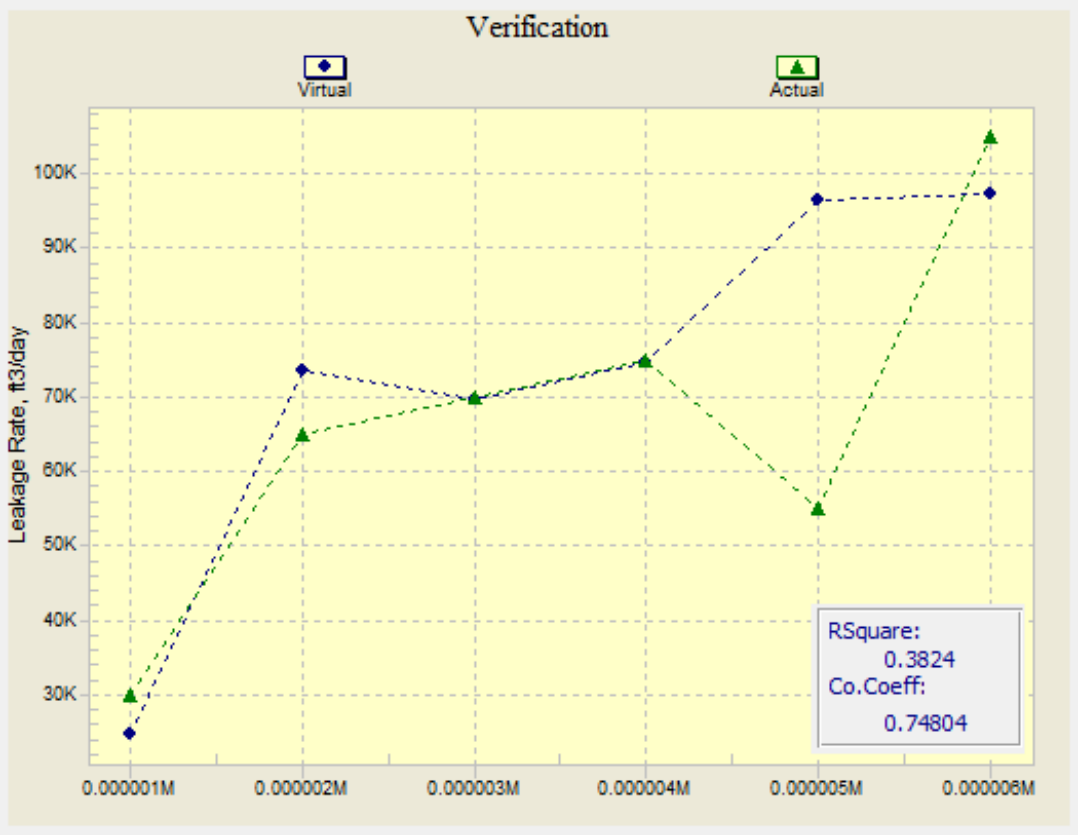

Figure 178. Verification results for leakage rate

Table 32. Results for neural network verification

N.Net Leakage Location, X	N.Net Leakage Location, Y	N.Net Leakage Rate, ft3/day
1270184.64	11276223.67	24770.36
1270184.89	11276223.64	73583.62
1270359.14	11279157.49	69651.10
1270359.15	11279157.48	74652.59
1268902.65	11277565.91	96394.92
1268902.55	11277568.66	97346.52

Blind run Validation

In order to validate the performance of the ILDS, 3 different CO_2 leakage rates (not seen by the Neural Network before) were assigned to possible leakage location (wells D-9-2, D-9-6, D-9-10) as blind runs. Pressure data from these runs were applied to the ILDS. The ILDS predications for CO_2 leakage location and rates are shown in Table 33 and Figure 179, respectively.

The predictions of the ILDS for the Leakage location show high accuracy in a way that the results are almost the same as actual values. For the low Leakage rate (26MCf/day), Neural Network predictions demonstrate minor difference with the actual values, nevertheless, the range of predicted rates is reasonably correct. For the higher leakage rates the ILDS prediction is noticeably precise.

Table 33. Blind run ILDS predictions

Run	Leakage Location(X) Actual	Leakage Location(X) ILDS	Leakage Location(Y) Actual	Leakage Location(Y) ILDS
1	1268902.53	1268903.05	11277566.74	11277569.97
2	1268902.53	1268902.78	11277566.74	11277565.13
3	1268902.53	1268902.55	11277566.74	11277567.57
4	1270359.37	1270359.03	11279158.24	11279157.46
5	1270359.37	1270359.11	11279158.24	11279157.51
6	1270359.37	1270359.17	11279158.24	11279157.44
7	1270184.29	1270184.53	11276221.98	11276223.47
8	1270184.29	1270185.16	11276221.98	11276224.14
9	1270184.29	1270183.81	11276221.98	11276222.66

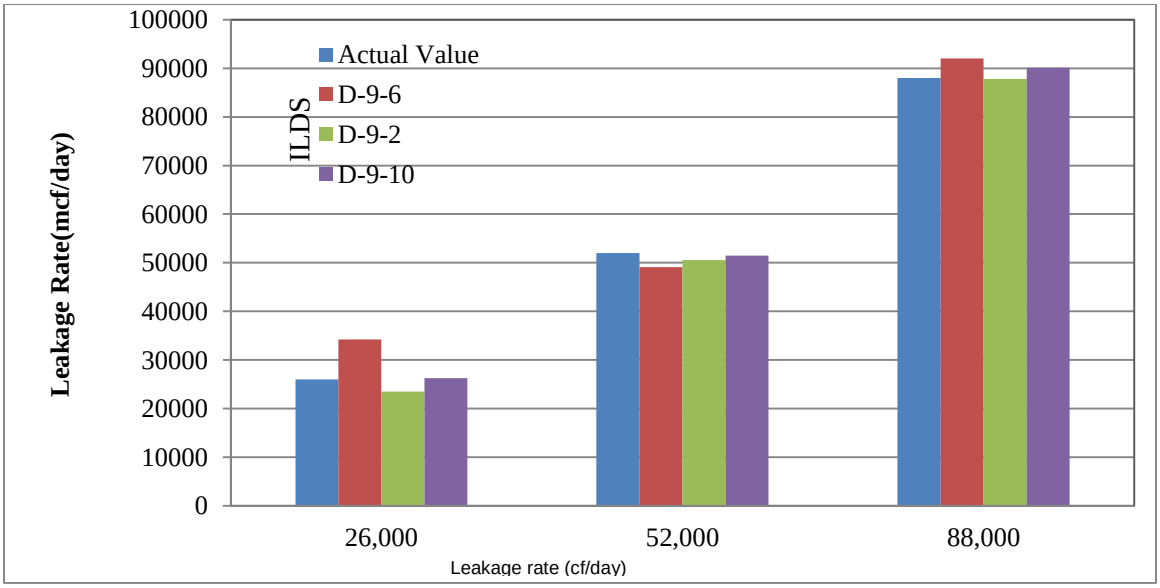

Figure 179. Results for blind runs, leakage rates

Neural Network Model Analysis

The initial results of the neural network training are illustrated in Figure 179 and Table 33 which compare actual data (Leakage rate and locations) with neural network predictions.

The neural network determines the location of the leaking well with high accuracy (R^2 = 1). However, for Leakage rates, neural network results cannot represent a few of the actual data correctly (R^2=0.92) specifically when the rates belongs to well D-9-6. In order to improve the results for CO_2 leakage rates predictions, an individual Neural Network was trained for each hypothetical leaking well. This approach was successful to enhance the prediction performance of the Neural Network model for the Leakage rate which is shown in Figure 180 (R^2=0.96).

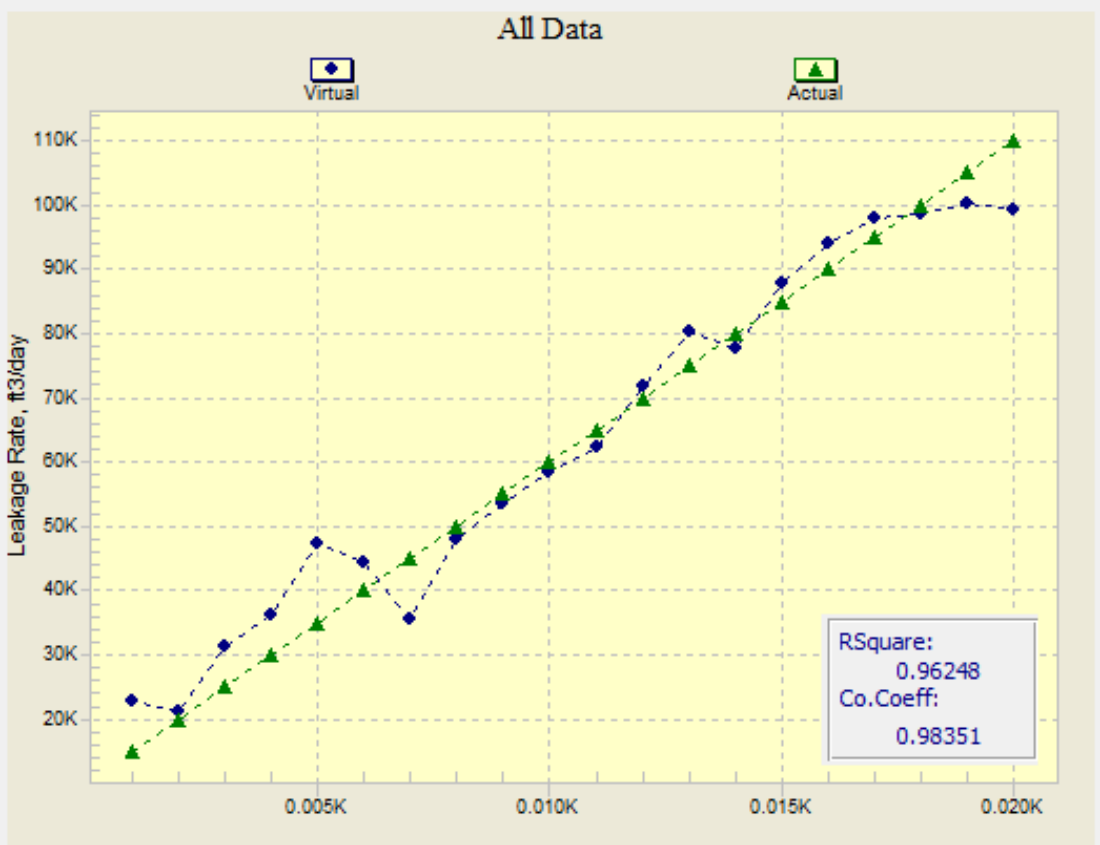

Figure 180. Neural Network pridiction for Leakage rate(network trained for each well individually)

Based on the Neural Network Modeling results we would design the ILDS in following way. At first the summarized pressure data are fed to the main Neural Network that predicts the location of the CO_2 leakage. Afterwards when the location is determined, the pressure data would be fed into the corresponding Neural Network that was designed for that specific location. Based on the initial results. Location and the amount of CO_2 leakage are quantified, using continuous monitoring of the reservoir pressure. Pattern recognition capabilities of Artificial Intelligence and Data Mining may be used as a powerful de-convolution tool for pressure behavior analysis.

INTELLIGENT LEAKAGE DETECTION SYSTEM DEVELOPMENT- HETEROGENEOUS MODEL

PATTERN RECOGNITION ANALYSIS

What was covered in the previous section was the application of the pattern recognition technology to the simpler version of the Citronelle numerical model[7]. In this section we summarize the result of applying the pattern recognition technology to the actual history matched model of the Citronelle field. The history matched model was used for modeling high frequency pressure signal behavior subject to various CO_2 leakage scenarios.

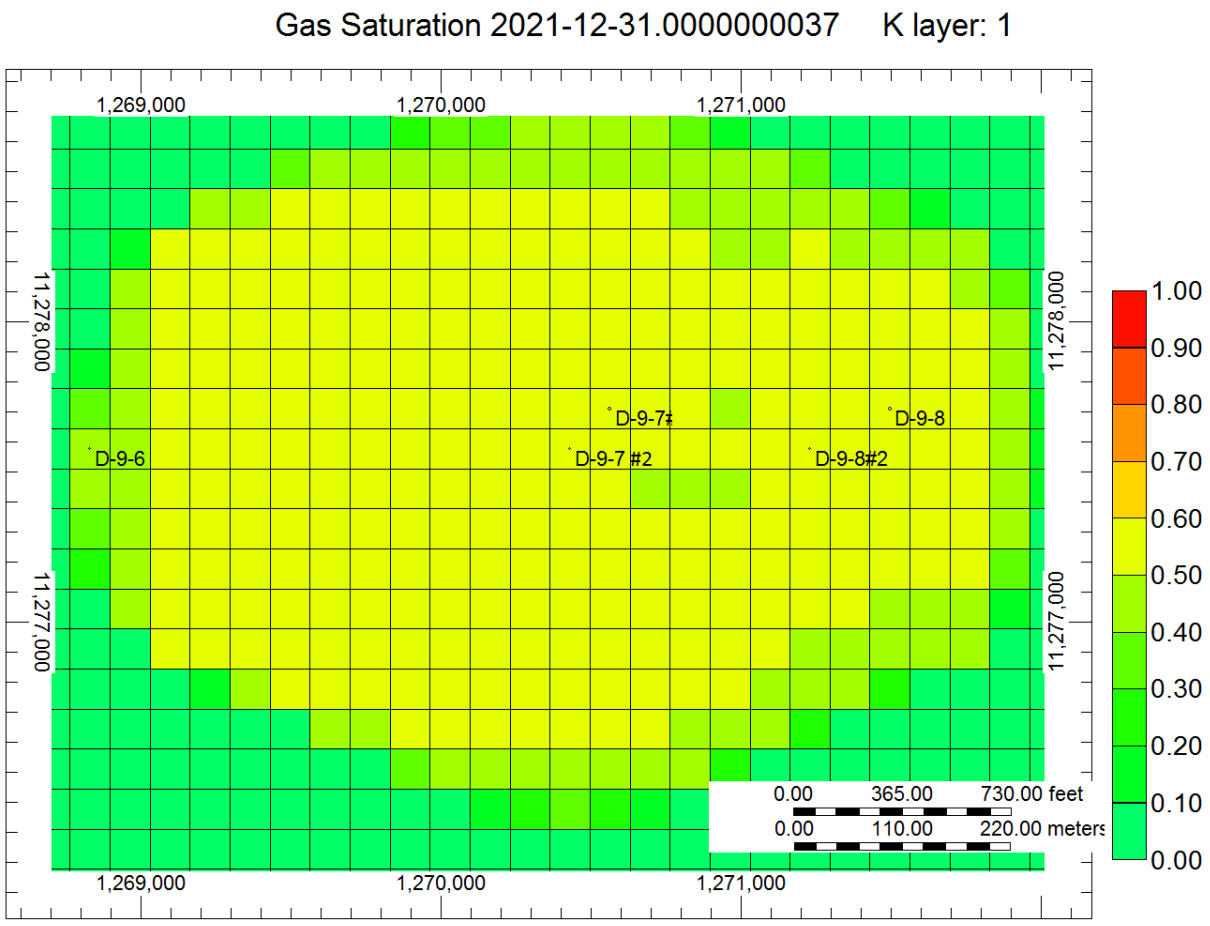

Figure 181. Location of five wells in the CO_2 plume area

Five different wells are located in the area of interest (the extension of the CO_2 plume - Figure 181). Each well would be prone to the leakage if the integrity of the well is compromised. Since wells D-9-7 (injection well) and D-9-8 (observation well) were drilled recently specifically for CO_2

[7] The model used in the previous section was essentially the non- history matched, base model. This was done to see the viability of the technology in a simpler case and learn from it when applying it to the real history matched model.

storage purposes, probability of CO_2 leakage through these wells was neglected. Wells D-9-6, D-9-7 and D-9-8 could experience some kind of leakage. When a leakage happens, a pressure change (ΔP) signal can be observed in the observation well. The pressure change signal in the observation well for the leakage rate of 65,000 cuf/day, at well D-9-7 is illustrated in Figure 182.

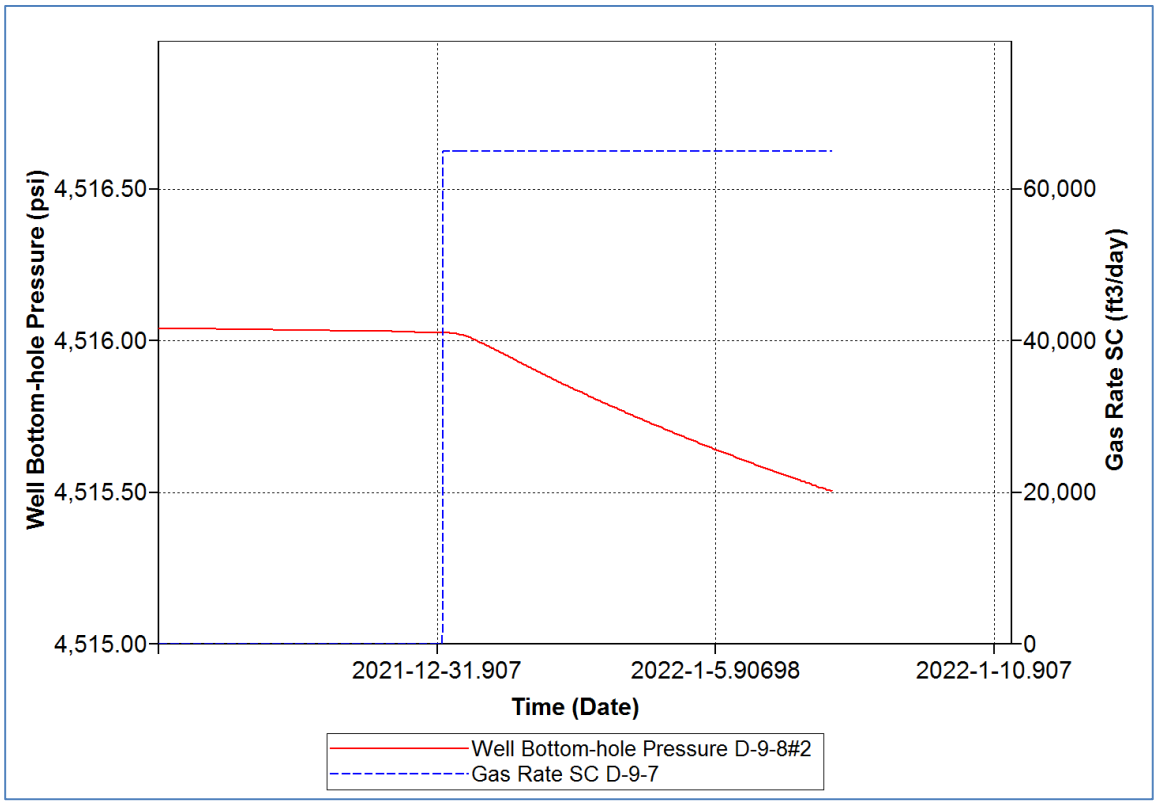

Figure 182. Reservoir Pressure in the observation Well (D-9-8)

NEURAL NET DATA PREPARATION

Intelligent Leakage Detection System (ILDS) consisted of a neural network that learned patterns that related the leakage characteristics (location and rate) to the corresponding pressure signals. In order to train the neural network, it was necessary to have pressure signals corresponding to each leakage scenario. Reservoir simulation was used to generate mentioned pressure signals.

Each well that was prone to the leakage (wells D-9-6, D-9-7 and D-9-8) experienced different leakage rates (in the range of 15,000 - 105,000 ft^3/day with 10,000 ft^3/day increments). The synthetic leakage initiated at 1/1/2022 and 168 pressure signals (collected on hourly basis) were recorded from the observation well (D-9-8). Descriptive statistics were used to summarize the pressure signals and to develop the data set for the neural network training.

Intelligent Data partitioning was used to divide the data set into Training (80%), Calibration (10%) and Verification (10%) portions. Then, data sets were analyzed by Key Performance Indicator (KPI) analysis in order to identify the relative impact of each input parameter (summarized

pressure data) on the output features. The results of KPI analysis (all the data points with maximum possible combinations) are shown in Figure 183.

Rank	Feature	% Degree of Influence
1	Skewness	100
2	Kurtosis	76
3	Standard Error	21
4	Range	20
5	Maximum	18
6	Sum	16
7	Standard Deviation	16
8	Mean	15
9	Sample Variance	12
10	Median	1

Rank	Feature	% Degree of Influence
1	Kurtosis	100
2	Skewness	45
3	Sample Variance	7
4	Standard Error	6
5	Sum	6
6	Mean	6
7	Maximum	5
8	Median	2
9	Range	2
10	Standard Deviation	1

Figure 183. Key performance indicator for Leakage location (left) and rate(right)

Neural Network Architecture Design

Back-propagation method was used for training the networks using all the parameters that were analyzed in key performance indicator as the input variables. Leakage location (X coordinate) and rate were set as the output parameters. Based on input-output selection, 10 neurons with one hidden layer formed the structure of the neural network (Figure 184). Input layers were connected to the hidden layers by logistic activation function. Also one random seed number was used to start initialization of neural network weights.

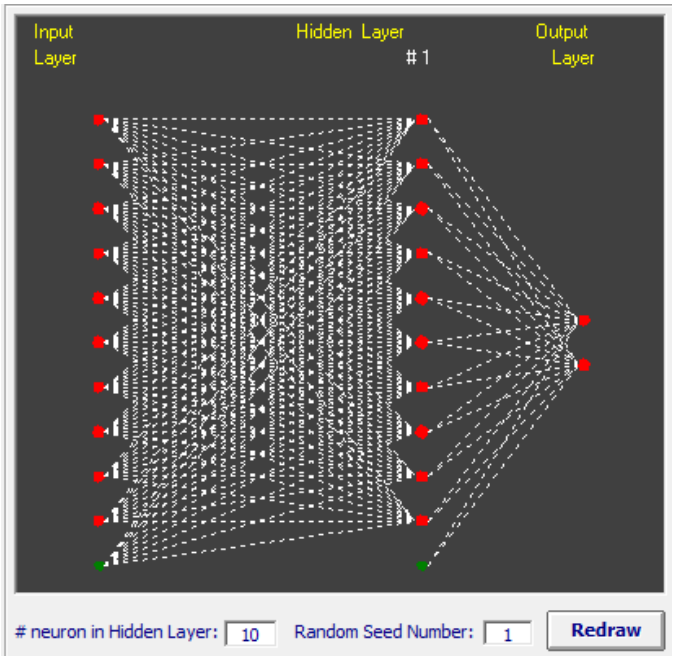

Figure 184. Neural Network architecture

NEURAL NETWORK TRAINING, CALIBRATION AND VERIFICATION

Training is a process during which data is introduced to the neural network for the purposes of identifying the best set of weights for the synaptic connections between all processing elements. The training algorithm is the set of mathematical equations that are used to find the most appropriate weight. This is usually done through an optimization process. The training algorithm used in this project is known as error back propagation. During the training a correlation is established between a set of multiple inputs (summarized pressure signals) and the output (leakage characteristics). Training is an iterative process which tries to minimize the average error through multiple epochs. When the error does not decline anymore (while the number of epochs continues to increase), the training process is considered to be complete.

Neural network training was stopped at epoch 112,693 when the minimum average error for the leakage locations and the leakage rate were 0.00043 and 0.000056, respectively (Figure 185 and Figure 186).

Figure 185. Neural Network training results for the leakage location(X)

Figure 186. Neural Network training results for the leakage rate

The calibration data was set aside in order to look over the training process and save the best training results. Additionally, calibration data set helped to avoid over training of the neural network models. In this neural network, three data points were considered for calibration (Table 34). The results for neural network predictions for the calibration data are shown in Figure 187 and Figure 188.

Table 34: Calibration data set

Leakage Location, X	Leakage Rate, ft3/day
1268829	25,000
1271495	35,000
1270562	75,000

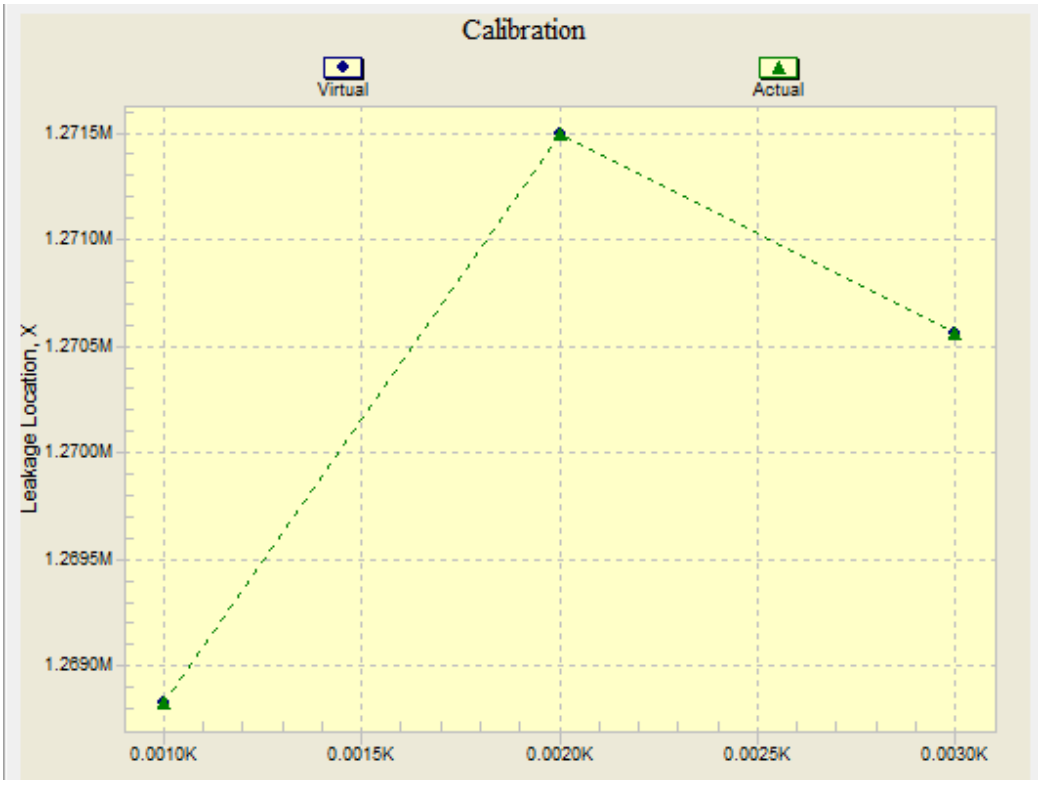

Figure 187. Neural Network Calibration results for the leakage location(X)

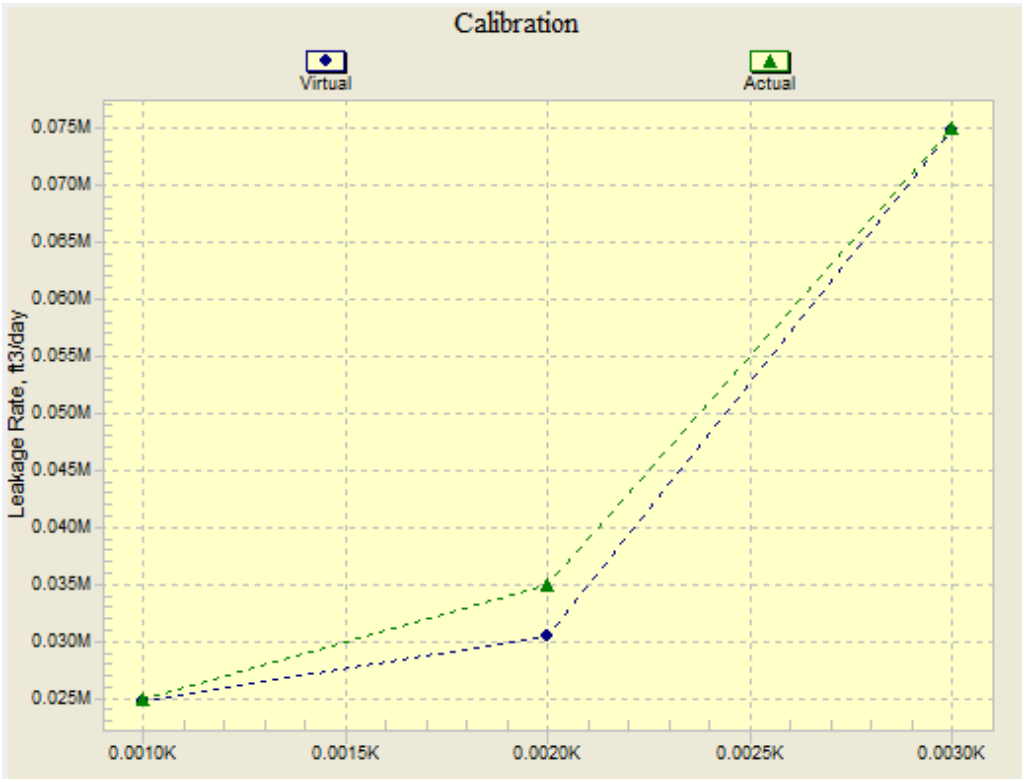

Figure 188. Neural Network calibration results for the leakage rate

NEURAL NETWORK VALIDATION

Validity of neural network predictions was tested by different methods. In the first method, 10% of data was not used during training and calibration processes. When the neural network was trained and calibrated, verification data was applied to the neural network to see how predictive the neural network model is. The verification results for the leakage rate obtained by the first method are shown in Figure 189.

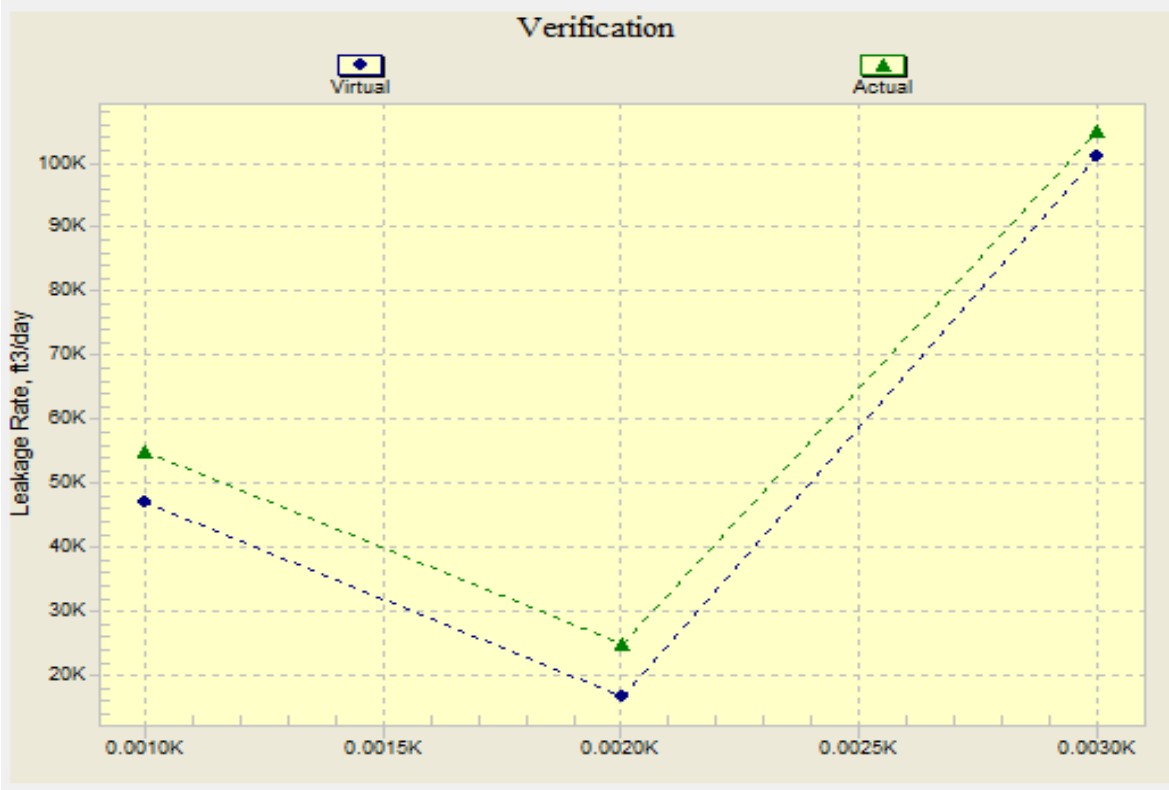

Figure 189: Neural Network Verification results for the leakage rate

Table 35: leakage rates and locations for ILDS validation

Run Number	Leakage Rate	Leakage Location	Well
1	23,000	1268829	**D-9-6**
2	72,000	1268829	
3	93,000	1268829	
4	32,000	1270562	**D-9-7**
5	61,000	1270562	
6	87,000	1270562	
7	27,000	1271495	**D-9-8**
8	48,000	1271495	
9	101,000	1271495	

In the second method, 9 different simulation runs were performed to generate pressure signals corresponding to the leakage rates that were not seen by the neural network during the training process. Three different leakage rates were assigned to each well (Table 35) and the pressure signals were collected and summarized by descriptive statistics. The results of the neural network predictions were compared with the data originally used in the simulation runs, to investigate the predictability of ILDS. Figure 190 and Figure 191 show the results of this exercise.

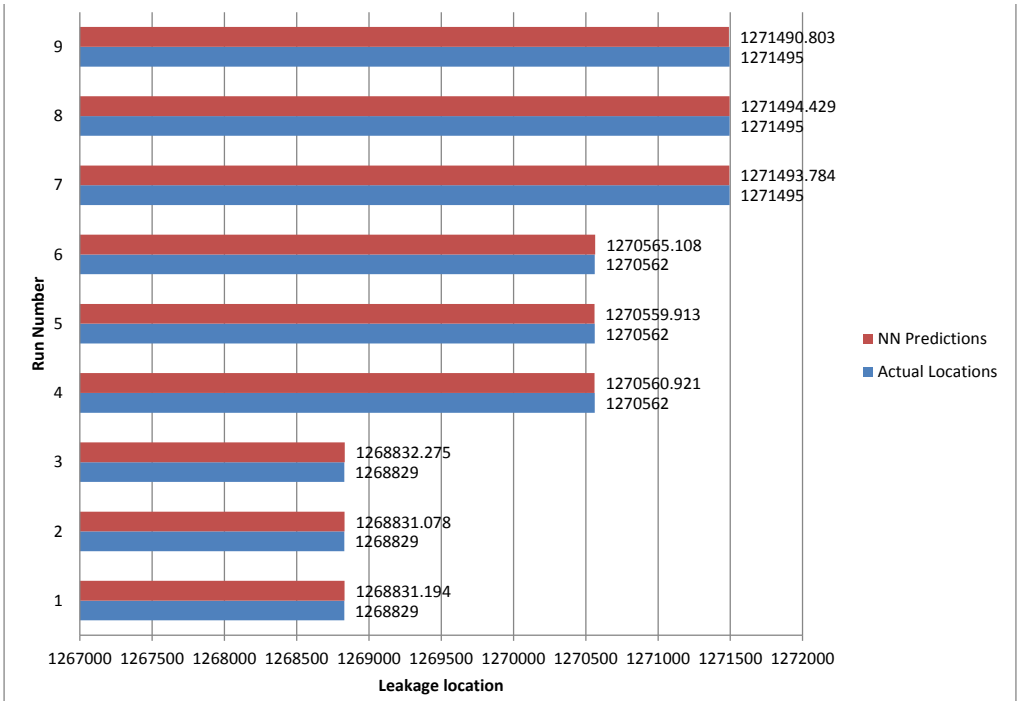

Figure 190. Results for neural network validation-leakage locations

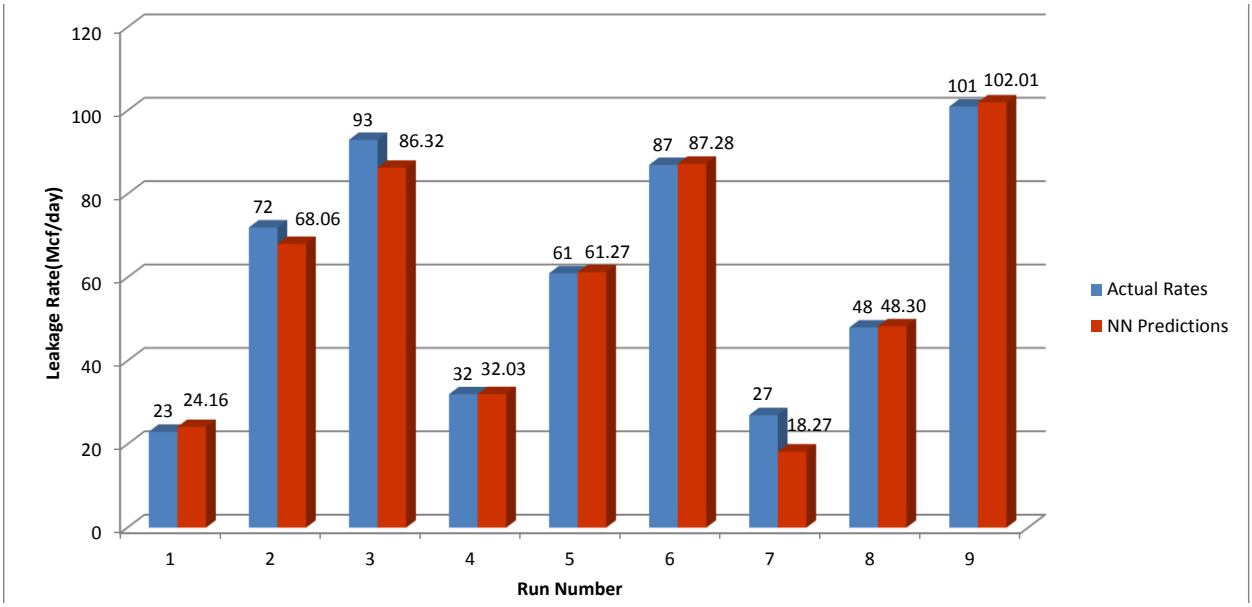

Figure 191: Results for neural network validation-leakage rate

NEURAL NETWORK MODEL ANALYSIS

The Neural Network prediction's precision can be analyzed by looking at the error plots and R^2 values. As it is shown in Figure 192, the R^2 for leakage location predictions is 0.99 which indicates high precision in neural network predictions. Additionally the error for leakage location prediction ranges between -5 to 7 ft. (actual leakage locations are: 1,268,829, 1,270,562, 1,271,495 ft). For leakage rate results (Figure 193); the R^2 is equal to 0.98 which shows very good prediction capabilities for the neural network models. The maximum errors for leakage rate predictions range from -5 to 9 Mcf/day which is less than 10 %.

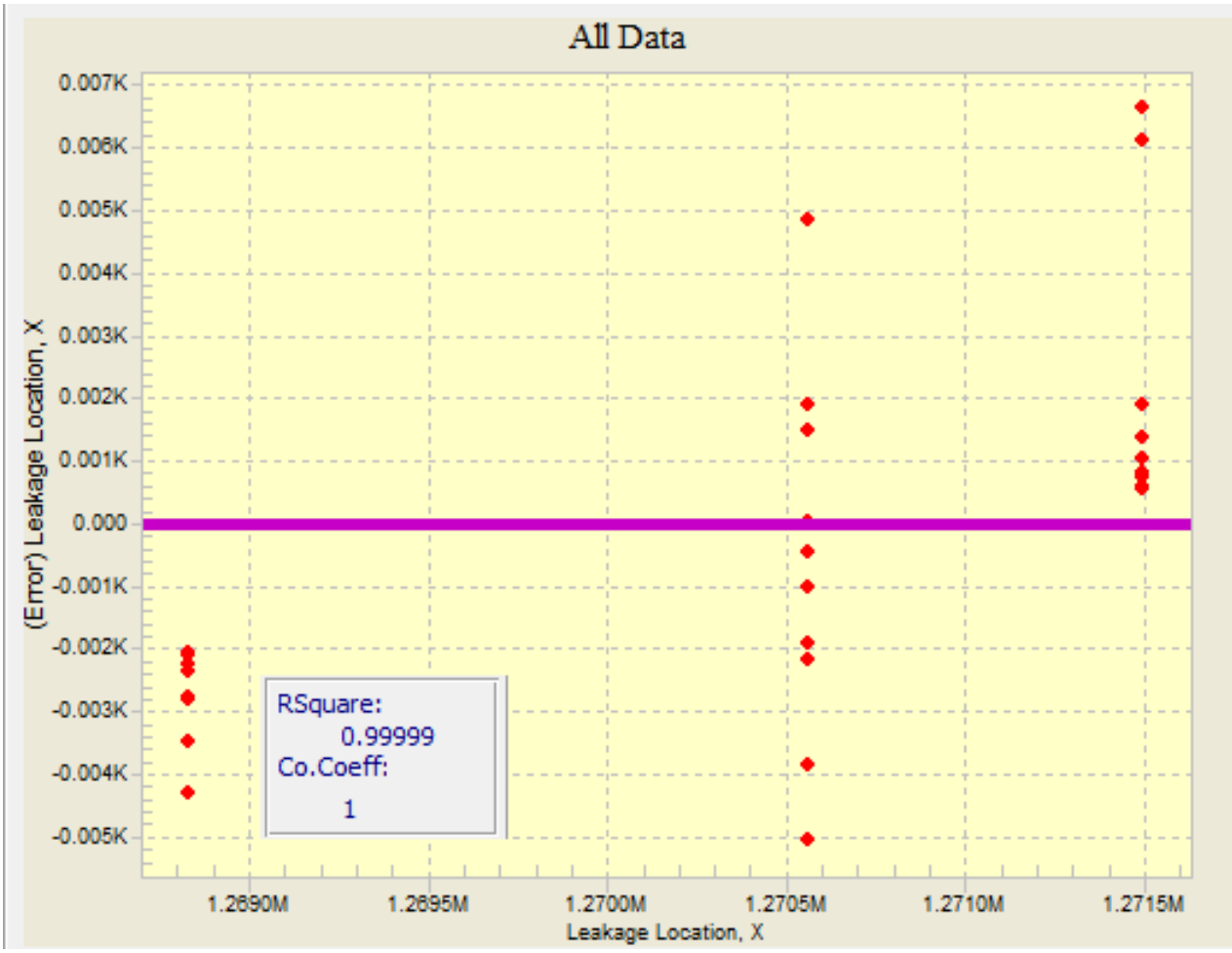

Figure 192. Neural Network prediction errors for Leakage location

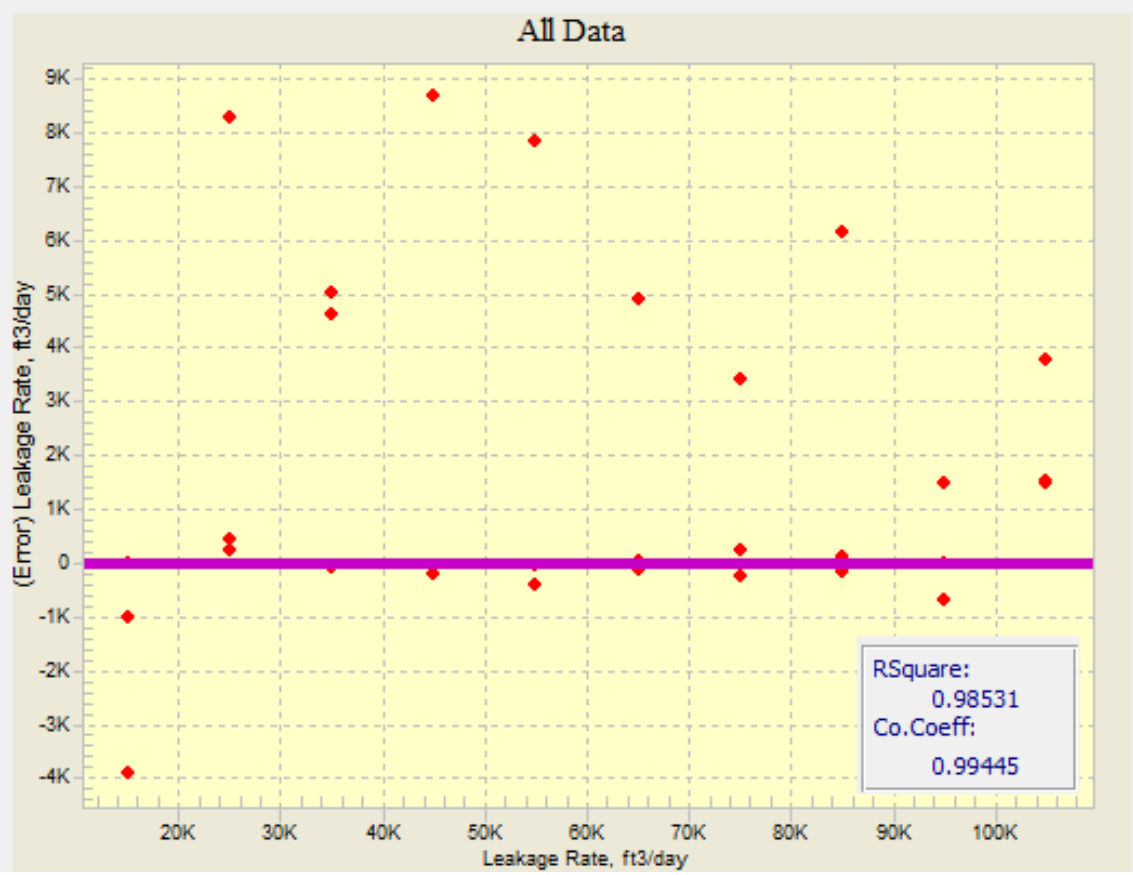

Figure 193. Neural Network prediction errors for Leakage rates

ILDS Enhancement and Evaluation

As part of a monitoring technique, an Intelligent CO_2 Leakage Detection System (ILDS) was developed for CO_2 storage project at Citronelle Dome. This system, which was designed based on Pattern Recognition Technology and Smart Wells, is able to identify the location and the amount of the CO_2 leakage at the reservoir level using real-time pressure data from PDGs.

The history matched reservoir simulation model (based on 11 months of actual injection/pressure data) was used for CO_2 leakage modeling studies. High frequency real time pressure streams were processed with a novel technique to form a new data driven Real-Time ILDS (RT-ILDS) which was able to detect leakage characteristics in a short period of time (less than one day after the initiation of a leakage). RT-ILDS also demonstrated high precision in quantifying leakage characteristics subject to complex rate behaviors. The performance of RT-ILDS was examined under different conditions as multiple well leakage, availability of additional monitoring well, uncertainty in the reservoir model, leakage at different vertical locations along the well and cap-rock leakage.

REAL-TIME INTELLIGENT LEAKAGE DETECTION SYSTEM (RT-ILDS)

Real-Time Intelligent Leakage Detection System (RT-ILDS) is a data driven monitoring package which receives real time pressure data and determines occurrence of a CO_2 leakage, and consequently predicts location and amount of the leak. This system originally was designed (and discussed in detail in previous sections of this report) in a way that it would receive pressure signals for a time interval, one week of hourly signals - 168 records after the leakage.

Summarized pressure data obtained by descriptive statistics was fed into trained neural networks to find leakage characteristics. In that system, it was necessary to wait till the end of the time interval to find leakage characteristics. A new method of data processing is discussed in this section for the development of Real-Time Intelligent Leakage Detection System (RT-ILDS). In this method the pressure data is analyzed in real-time considering the previous trend of the signals. By this method it is possible to determine leakage characteristics much faster in less than a day.

In order to process the data and convert it to a format which is appropriate for the pattern recognition technology, pressure signal based on thirty different CO_2 leakage scenarios were used. Each scenario was corresponded to a simulation run that modeled specific CO_2 leakage rate (ranging from 15 to 105 Mcf/day with 10 Mcf/day increments) at one of the three leakage locations (wells D-9-6, D-9-7, and D-9-8).

The specifications of the simulation runs and behavior of the pressure signal for each scenario was similar to those covered in detail in the previous sections. First, a threshold was assigned as .01 psi for the ΔP that is defined as: $(P_{No\ Leakage} - P_{Leakage})$, as the leakage indicator.

This threshold is actually equal to the precision of the PDGs that are currently used in the industry and that are currently installed in the observation well D-9-8. When this threshold is achieved, data processing starts by considering values of ΔP, pressure derivative, ΔP average, ΔP summation, ΔP standard deviation, ΔP skewness, and kurtosis for the past history of the data (in a given window of time – usually an hour).

The hourly pressure data for one week for each CO_2 leakage scenario were used to generate the data set for the neural network training, calibration and verification. The first 12 hours of the data after beginning of the leakage ($\Delta P > 0.01$ psi) were neglected from the data processing, since they proved not to be useful for our analysis.

Neural Network Data Preparation

Development of the RT-ILDS is mainly based on the training, calibration and verification of the neural networks that received the pre-processed real-time pressure data for each CO_2 leakage scenario as the input and the corresponding leak rate and location as the output. Initially, a neural network was trained to find a pattern between leakage location (output) and the corresponding pre-processed pressure signals. The entire data set for leakage location neural network consisted

of 3,527 data records which were partitioned into 2821, 353, and 353 records for training, calibration, and verification, respectively.

The influence of each input parameter on the output (leakage location) was determined by Key Performance Indicator (KPI) analysis. As it is illustrated in Figure 194, skewness, standard deviation and average of the ΔP are indicated to have the most impact on the output (leakage location).

It is worth mentioning that descriptive statistics for ΔP (in Figure 194 and Figure 195) data at each time step is calculated on a cumulative basis after pressure threshold of 0.01 psi (leakage indicator) is observed. For example, at time step 24 (after pressure threshold was detected), average, summation, standard deviation, skewness and kurtosis were calculated for 24 ΔP records (Cumulative). Derivative and ΔP are point values at time step 24. The last 12 data records and corresponding calculated parameters will be used in neural network training.

Rank	Feature	% Degree of Influence
1	Cum Skewness(DeltP)	100
2	Cum ST Dev(DeltP)	61
3	Cum Avereage(DeltP)	59
4	Delp	58
5	Cum Kurtosis(DeltP)	50
6	Cum Sum(DeltP)	26
7	Derivitive	2
8	Time(New)	1

Figure 194. Key performance Indicator for the Leakage Location

For leakage rate determination, one neural network was trained for each well separately. The number of input data records for each well is different due to implementing 0.01 psi threshold as the leakage indicator. For instance, 1,553 records were used to train leakage rate neural network for Well D-9-8. That data records were partitioned into 1243, 155, and 155 records for training, calibration, and verification, respectively. The results for Key Performance Indicator analysis for well D-9-8 which shows the impact of the input parameters on the CO_2 leakage rate are shown in Figure 195.

Rank	Feature	% Degree of Influence
1	Cum ST Dev(DeltP)	100
2	Delp	86
3	Cum Avereage(DeltP)	75
4	Derivitive	40
5	Cum Sum(DeltP)	36
6	Cum Skewness(DeltP)	5
7	Cum Kurtosis(DeltP)	3
8	Time(New)	1

Figure 195. Key performance Indicator for the leakage rate at well D-9-8

Results and Validation

Neural network training process attempts to calculate most proper weights that describes a pattern between leakage locations and the specified input data (pressure signals). The entire process consisted of number of epochs that attempts to minimize the error between actual and predicted results.

It was necessary to calibrate the training process by looking over the training results and finding the best training outcomes. When the error in the calibration reached a minimum value, the training process is stopped and the training process is identified as completed. The results for all the training processes (training, calibration, and validation) are shown in Figure 196 (CO_2 leakage location) and Figure 197 (CO_2 leakage rate in well D-9-8). For both leakage location and results, R-square is more than 0.99 which represents high precision.

In order to validate the performance of the RT-ILDS, a set of blind runs (not used for the neural network training) were designed, the simulation runs were performed and the appropriate data was collected and pre-processed to appropriate for mat for the application to the neural network models.

As it is shown in Table 35 nine total simulation runs were performed considering assignment of three CO_2 leakage rates at the possible locations of the leakage (wells: D-9-6, D-9-7, and D-9-8). Pressure signals which corresponded to each CO_2 leakage scenario were processed by applying the leakage threshold (0.01 psi) and generating ΔP, pressure derivative, ΔP average, ΔP summation, ΔP standard deviation, ΔP skewness, ΔP kurtosis at each time step.

For each leakage scenario, all the calculated parameters were fed to the RT-ILDS to get the prediction for leakage location and leakage rate. All the results for RT-ILDS prediction for each blind run are shown in Figure 198, Figure 199. All the details of the analysis are presented in Appendix 6.

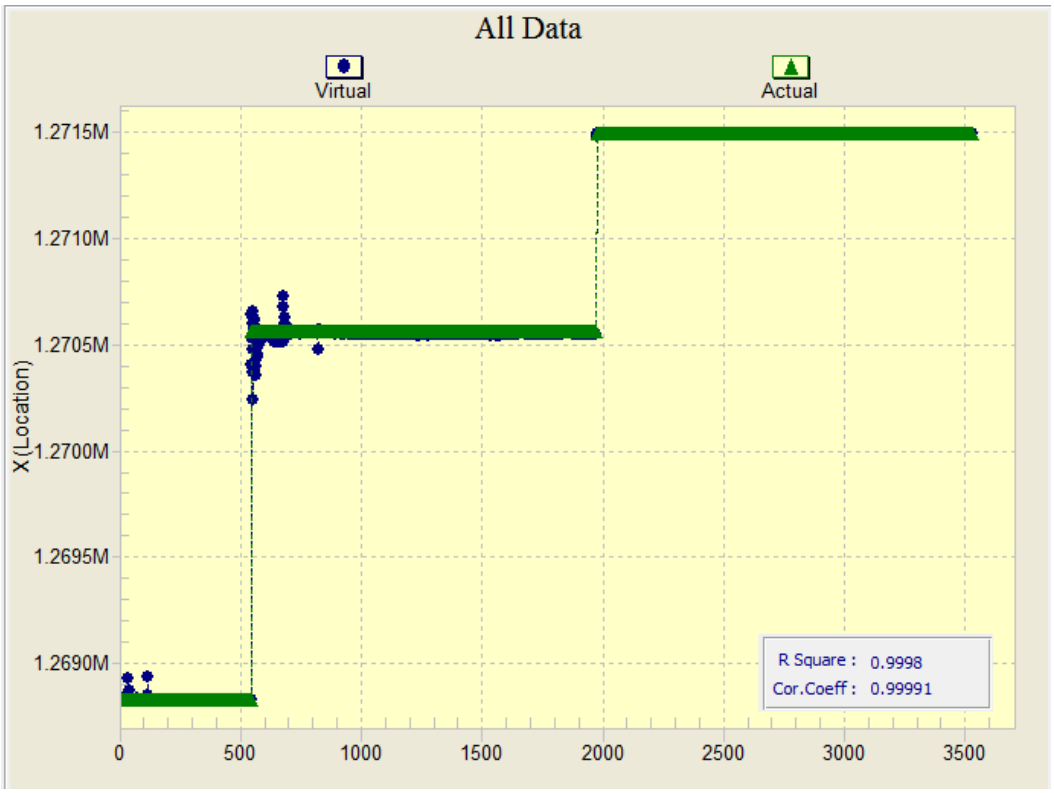

Figure 196. Neural network results for leakage location

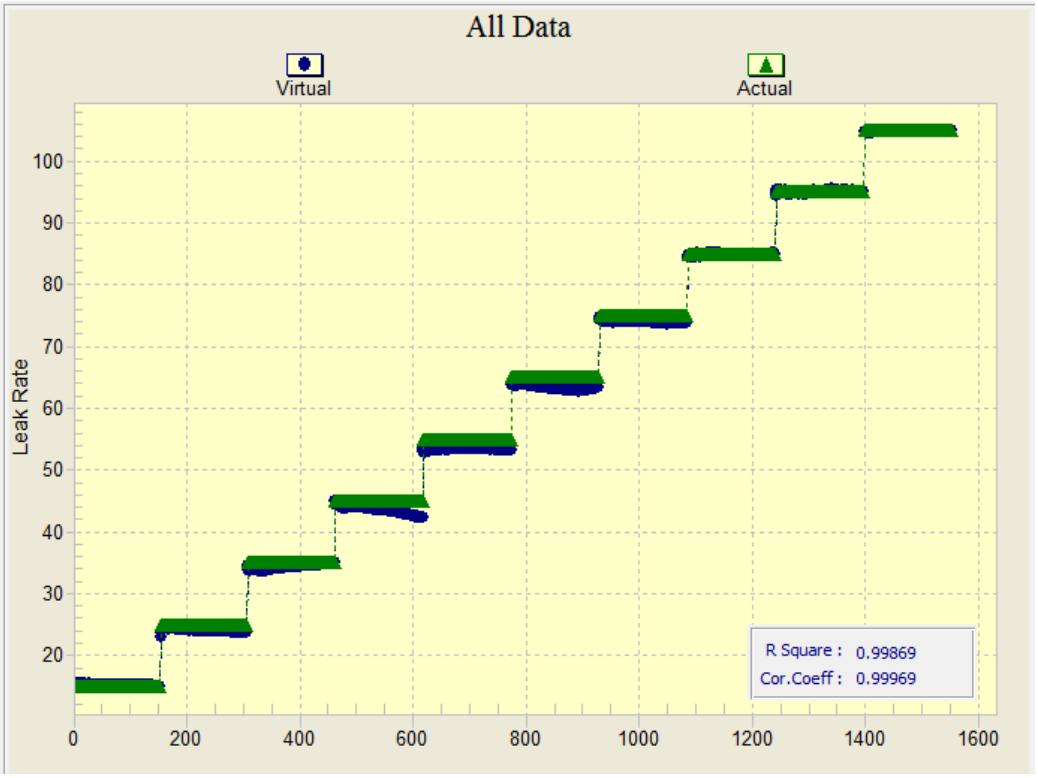

Figure 197. Neural network results for leakage rate in well D-9-8

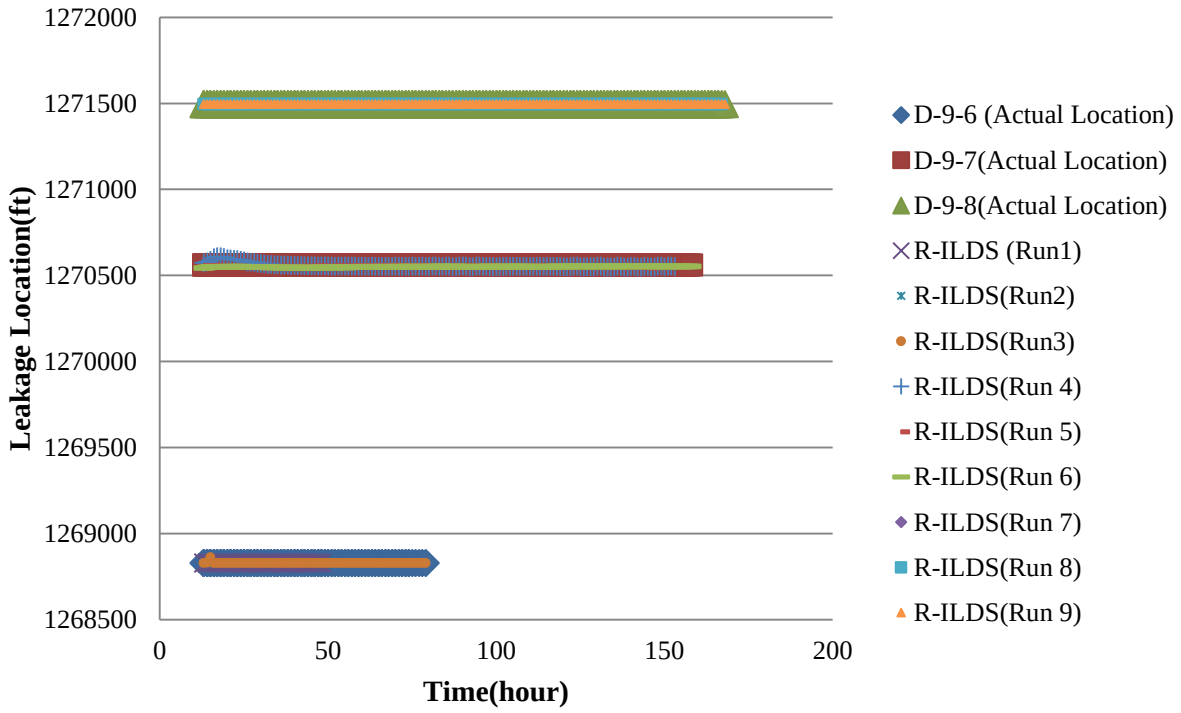

Figure 198. R-ILDS Leakage Location prediction, all blind runs

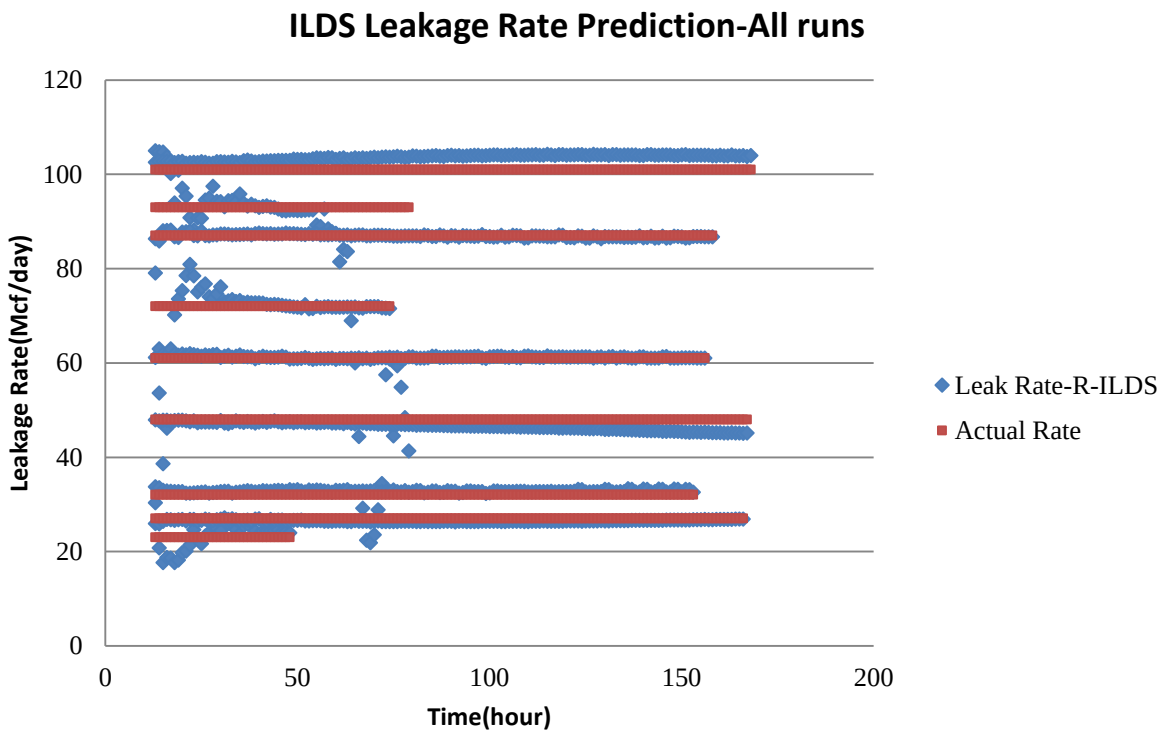

Figure 199. R-ILDS Leakage rate prediction, all blind runs

The precision of the neural network predictions can be quantified by R^2 parameter and the distribution of the errors. The neural network that was trained for leakage location, has an R^2 value that is practically equal to 1. The prediction's error histogram for locations of wells is shown in Figure 200.

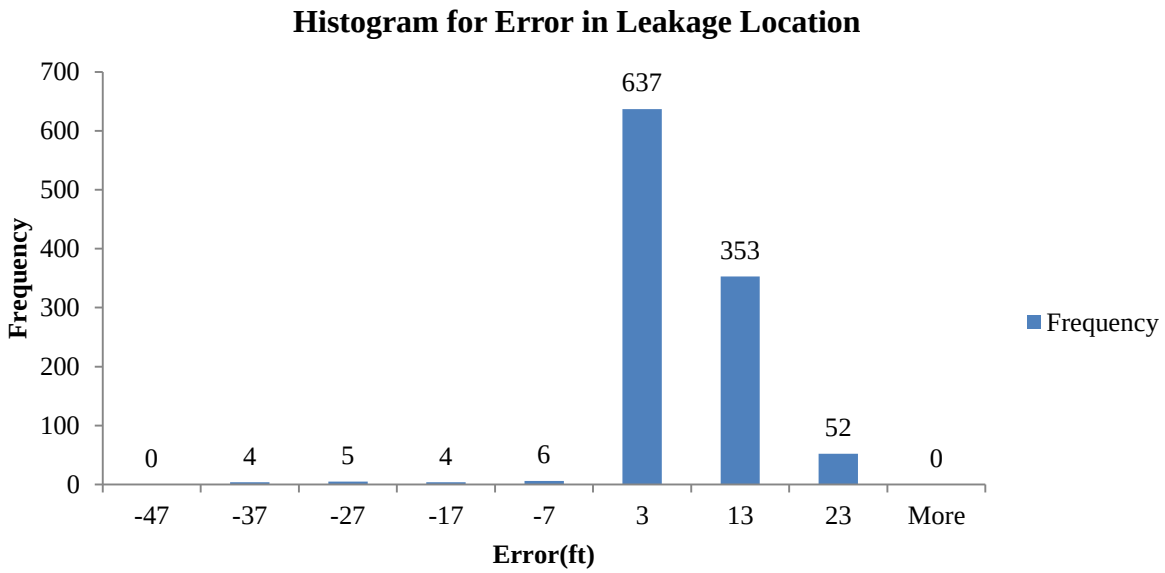

Figure 200. Histogram for the error in neural network's location prediction

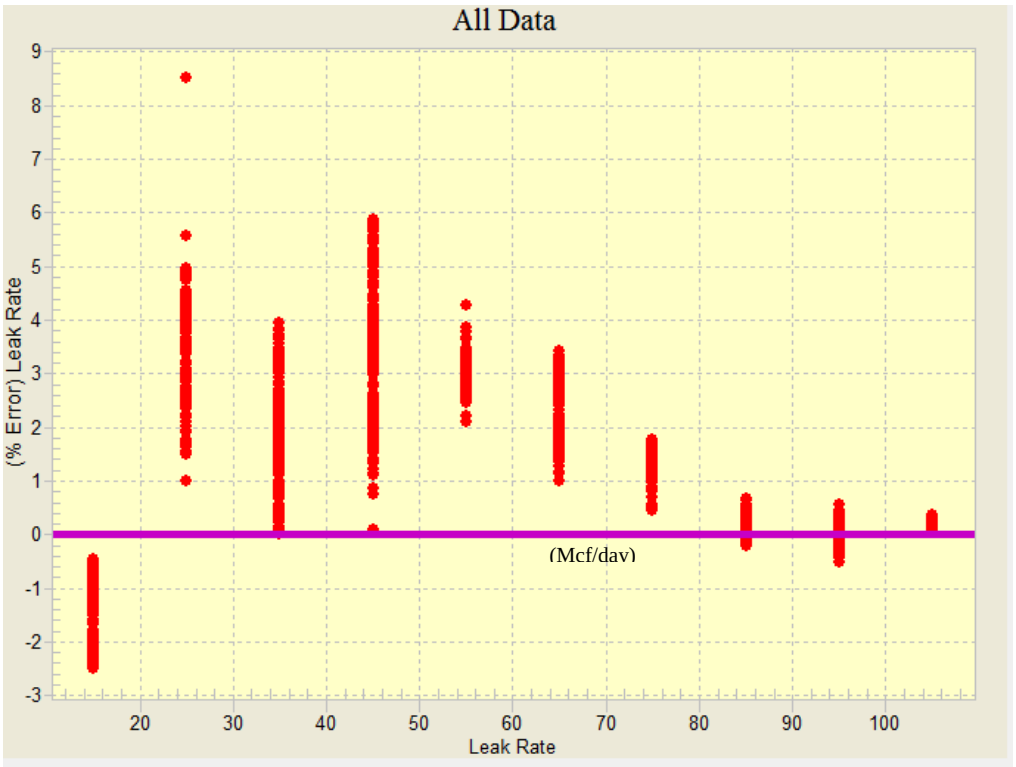

Figure 201. Neural network prediction errors for Leakage rates in well D-9-8

The average error for the leakage location is 3 ft. with the maximum error of 46 ft. The R^2 for the CO_2 leakage rate predictions is 0.998 which represents a good precision. The percentage error plot for leak rate at well D-9-8 is shown in Figure 201. The maximum error for the leakage rate is less than 9 %. The average error for CO_2 leakage rate predictions is less than 4% at well D-9-8.

DETECTION TIME

When CO_2 leakage occurs in the reservoir (from the existing wells, D-9-6, D-9-7, and D-9-8), there is a delay until Pressure Down-hole Gauges receive the generated pressure signal. The time that takes to detect CO_2 leakage depends on the Pressure Down-hole Gauge resolution and amplitude of the pressure signals. Resolution of the PDGs that were installed in observation well is 0.01 psi. Therefore, if the amplitude of an induced pressure signal due to CO_2 leakage is less than PDG resolution, it wouldn't be possible to detect the leak.

Another important parameter related to leakage detection timing is the amplitude of the pressure signal. The signal amplitude is proportional to the inverse distance from the location of the leakage to the location of the observation well. The distances of each possible leakage location (wells D-9-6, D-9-7, and D-9-8) to the observation well are shown in the Figure 202[8].

Figure 202. Distance of possible leakage locations to the observation well

[8] Please note that distance, as far as the transmission of the pressure transients are concerned, includes the impact of the permeability as well as the physical distance between two points. Furthermore, the accuracy of the permeability distribution is a function of the accuracy of the history matching process.

The induced pressure signal (as a result of the leakage in the reservoir) for the cases that each of three wells leak 55 Mcf/day is shown in Figure 203. As the leakage location gets closer to observation well, the amplitude of the pressure signal increases. RT-ILDS was developed based on the fact that pressure change threshold of 0.01 psi can be detected by PDGs.

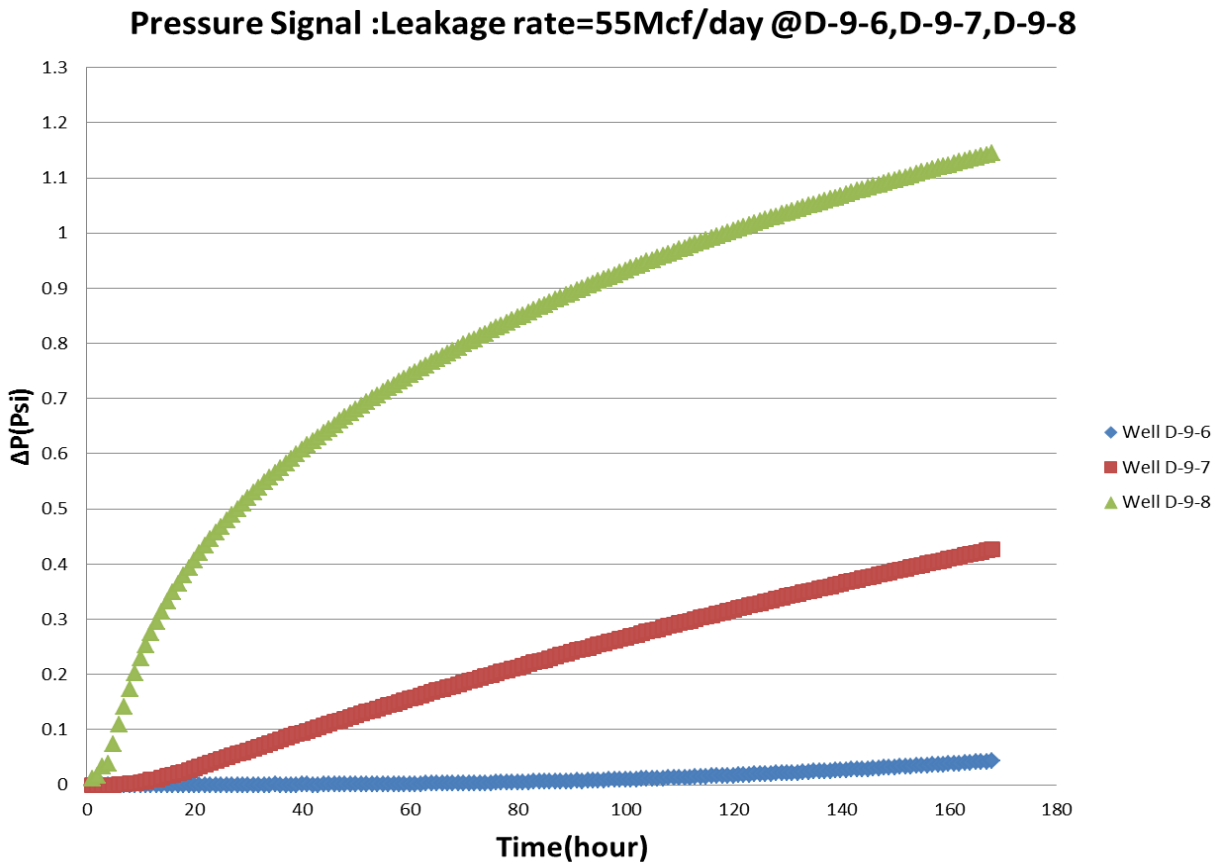

Figure 203. Comparison of pressure signal amplitude when wells leaked with the same rate

Also, the first 12 pressure data records (after reaching to ΔP=0.01 psi) were not included in RT-ILDS development. Based on mentioned criteria, detection times for different CO_2 leakage rates at each leakage location are plotted versus CO_2 leakage rate in

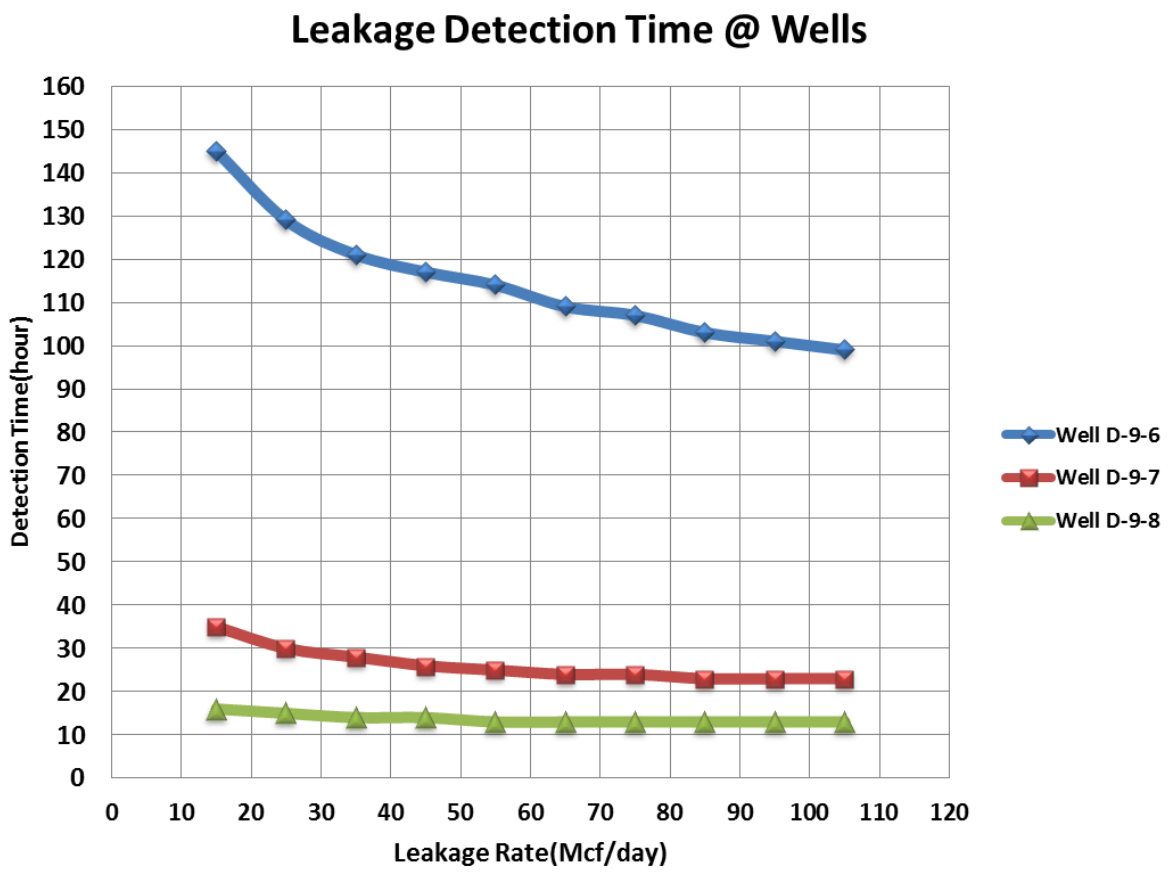

Figure 204. As the distance between the leakage source and the observation well decreases, pressure signal amplitudes increase and it takes less time to detect the leakage and provide valid results.

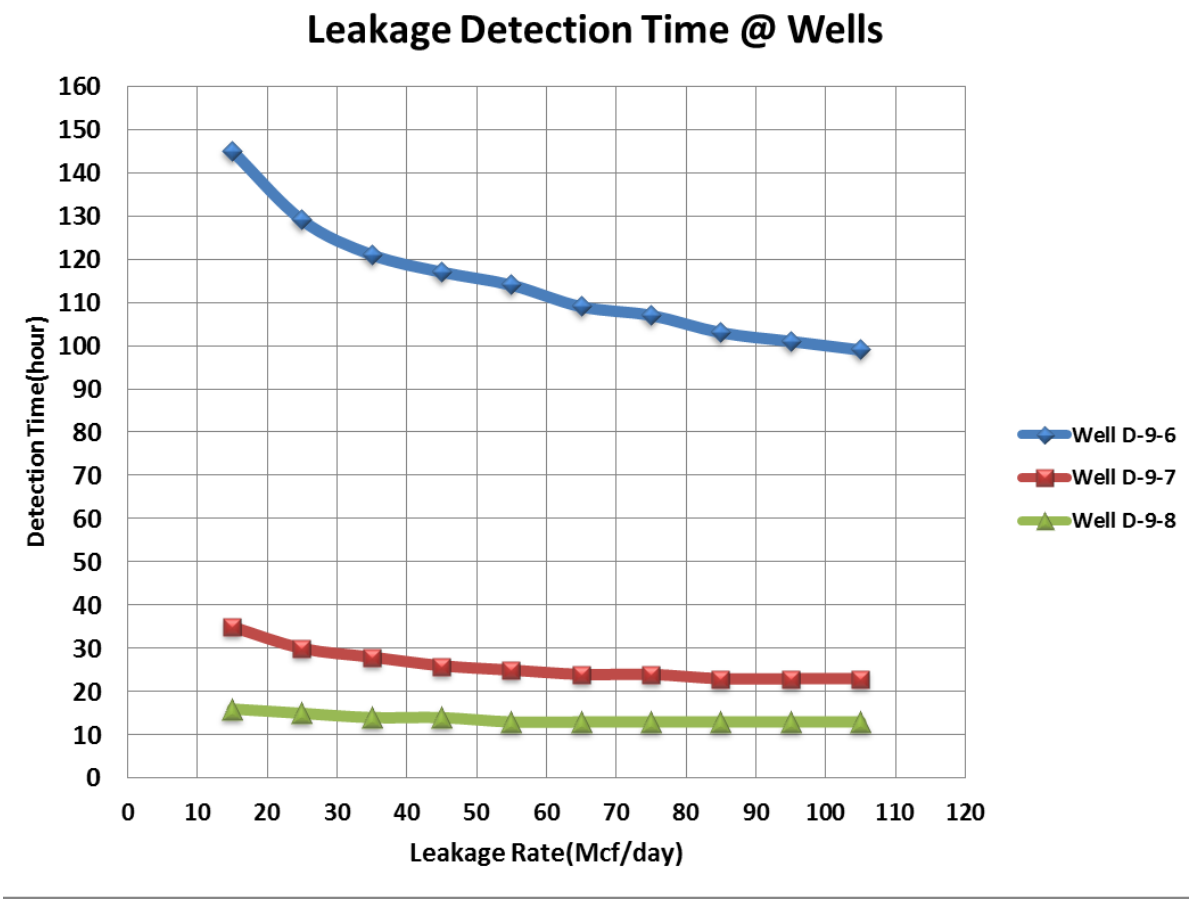

Figure 204. Detection time for each rate at different locations

TESTING RT-ILDS FOR MULTIPLE GEOLOGICAL REALIZATION

Reservoir simulation model for CO_2 injection at Citronelle saline aquifer was developed and history matched with real field data. This model acknowledged “Lateral Heterogeneity” in different ways. The first reservoir characteristics that played important role in making the reservoir model heterogeneous was the top of sand layers.

Structural maps for 17 sand layers (most extensive ones that were targeted for CO_2 injection) were generated by interpretation and correlation of 14 well logs. The location of the well logs and three cross sections for correlating the wells are shown in Figure 61. Based on correlation between wells, 17 top maps were generated representing lateral heterogeneity in the reservoir. The top map for the first sand layer is shown in Figure 67.

The same well logs were used to generate thickness (isopach) maps for all the layers. The example for grid thickness map (first sand layer) is shown in Figure 68. In order to make porosity maps, 40 well logs were analyzed and interpreted. Three different porosity maps were generated

for each sand layer (51 total porosity maps for the entire reservoir). The lateral heterogeneity for porosity is shown in Figure 73. In this model, permeability of the reservoir was obtained using porosity-permeability correlations from core analysis. This means that there are lateral heterogeneities for the permeability as well.

Multiple reservoir characteristics realizations were generated aimed at changing the parameters that control lateral heterogeneity in the reservoir. Reservoir porosity, sand layer top/thickness and vertical to horizontal permeability ratio were the main parameters to be modified for generating lateral heterogeneity realizations. All these parameters varied compared with the original value according to Table 36. For each realization, leakage rates equal to 70, 60 and 50 Mcf /day were assigned to wells D-9-6, D-9-7, and D-9-8, respectively.

Table 36. Changes in reservoir Property Parameter

Variation / Reservoir Parameter	2% UP	2% low	5% low	10% up	10% low
Porosity				X	X
Sand Layer Top	X	X			
Sand Layer Thickness			X		
Vertical to Horizontal Permeability Ratio				X	

The corresponding pressure signals (due to leakage from the wells) at the observation well, were collected, processed and fed to the RT-ILDS. It should be mentioned that after changing reservoir characteristics (like porosity or thickness), initial reservoir pressure and stabilization pressure after end of injection varied (compare with the initial history matched model). This means that $P_{No\ leakage}$ and consequently ΔP had to be recalibrated and recalculated.

To recalibrated and recalculated the ΔP, for each realization, a “No-Leakage” scenario was modeled and relevant data was extracted. Reservoir pressure signals at the observation well were collected for each realization. At this point, new ΔP values were calculated for each realization, having No-Leakage pressure data for all the cases.

As an example, ΔP –Original and ΔP –New for the realization that porosity of the reservoir lowered 10% and CO_2 leakage rate equal to 60 Mcf/day was assigned to well D-9-7, are shown in Figure 205.

Pressure signals from different CO_2 leakage rate scenarios and reservoir characteristic realizations were collected, processed and fed into the RT-ILDS. Detail results of all these exercises that demonstrated the robustness of the RT-ILDS are shown in Appendix 7.

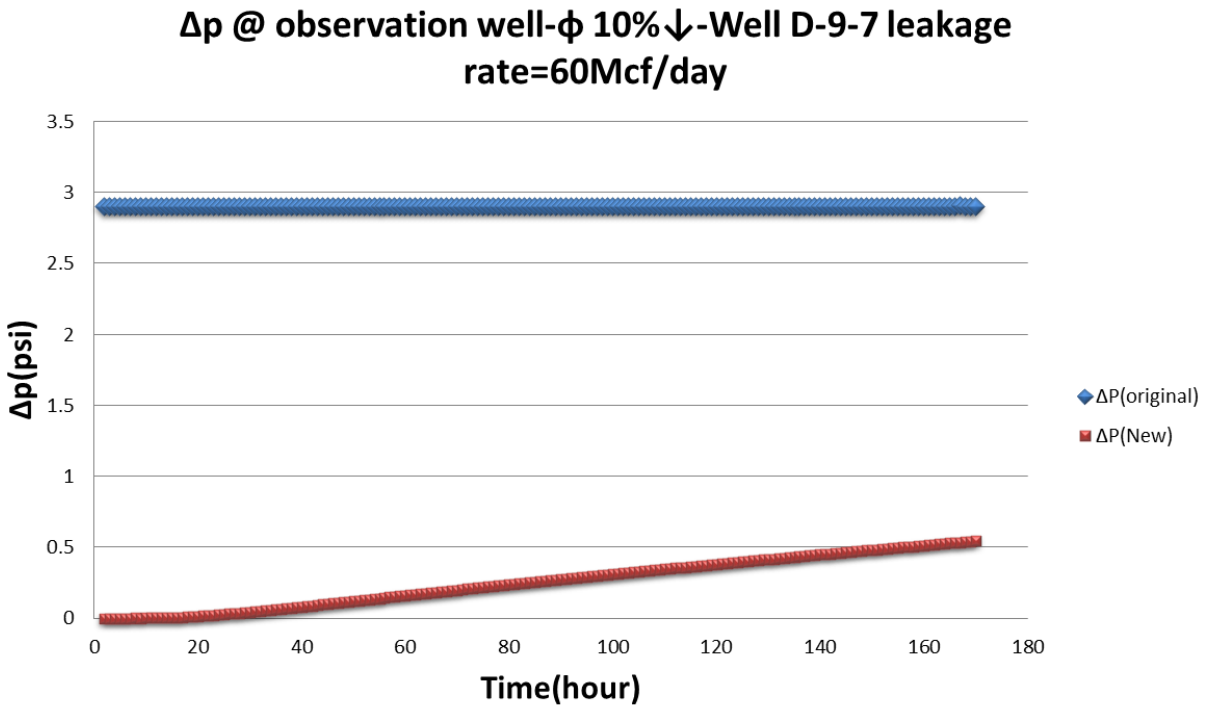

Figure 205. Original and new ΔP, at observation well subject to lowering reservoir porosity

First, the effect of each specific parameter on the RT-ILDS predictions for leakage location is explained. When the leakage (rate = 70 Mcf/day) took place at well D-9-6, RT- ILDS predicted the location for all the realization correctly except for the case that reservoir porosity decreased 10%. In this case, RT-ILDS prediction started deviating from the actual value (1,268,829 ft.) almost 35 hours after detecting the leakage. The location prediction from that time showed 1000 ft deviation from the actual value and then it gradually moved back to the actual value.

For the case that well D-9-7 leaked (rate = 60 Mcf/day), RT-ILDS location prediction represented almost 20 ft. error. In the situation that reservoir porosity decreased 10%, prediction values showed 20 ft. error early after leakage detection. Then, the error for R-ILDS location prediction slightly increased to 80 ft. This error is acceptable since the predicted location is still in the vicinity of the target leaking well (D-9-7).

When well D-9-8 was leaking with the rate of 50 Mcf /day, changing the reservoir characteristics showed no effect in R-ILDS location prediction apart from the case that reservoir porosity increased 10%. In this case, R-ILDS predicted the leakage location to be at well D-9-6.

The impact of model's specific parameters on RT-ILDS's prediction for leakage rate is as follow. RT-ILDS's predictions for CO_2 leakage rate at well D-9-6 were almost precise excluding the cases that reservoir porosity varied. The R-ILDS's results for CO_2 leakage rate were 105 Mcf/day (actual value = 70 Mcf/day) while reservoir porosity was changed ±10%.

Once well D-9-7 was leaking, change of main reservoir parameters showed very little impact of RT-ILDS's results for CO_2 leakage rate. The maximum error of 10 Mcf/day in the results was caused by decreasing reservoir porosity for 10%. It should be mentioned that CO_2 leakage rate for this well was 60 Mcf/day.

Finally, for the case that well D-9-8 was leaking 50 Mcf/day, RT-ILDS's results for CO_2 leakage rate were consistent with the actual value with the exception of the realizations with reservoir porosity change. Lowering reservoir porosity for 10% led to R-ILDS prediction to be 15 Mcf/day while increasing reservoir porosity resulted in 70 Mcf/day predictions.

All in all, the impact of models specific parameters was studied on the performance of RT-ILDS. For most of the cases, changes in the model's parameter did not show significant impact on RT-ILDS's results. The only parameter that impacted R-ILDS's predictions considerably for both CO_2 leakage rate and location was reservoir porosity. In reservoir simulation model that was developed for CO_2 injection at Citronelle filed, reservoir permeability was calculated by porosity-permeability correlation. Therefore, variation of reservoir porosity indirectly changes reservoir permeability. In other words, any change in reservoir porosity leaded to change in permeability as well.

Reservoir permeability plays very important role in fluid flow in the reservoir and consequently pressure signals coming from the observation well. Porosity change caused different fluid flow behavior and consequently different pressure signal behavior. As a result, RT-ILDS's results were impacted by variation of reservoir porosity.

DETECTION OF LEAKS AT DIFFERENT VERTICAL LOCATIONS ALONG THE WELLS

Based on the reservoir simulation results for CO_2 distribution and extension, it was observed that CO_2 plume reached to existing wells in reservoir mainly in layer 1 (Figure 206). Therefore all the synthetic leakages were assigned to the wells at layer 1 (the well was perforated just in that layer).

More investigation showed that CO_2 Plume was in contact with Well D-9-7 through 9 layers and Well D-9-8 in two layers. This means that CO_2 leakage could take place at different vertical locations along the well D-9-7. For that reason, the changes in the vertical leakage location were applied to investigate if the system was capable of detecting the leak and the rate regardless of where (vertically) the leak was initiated within a well.

It should be mentioned that two Pressure Down-hole Gauges were installed at well D-9-8 in the first layer of the reservoir. During the history matching process, based the reservoir pressure behavior in the observation well, it was concluded that the transmissibility of the shale layers that were inter-bedded in the sand layers was zero (Figure 207). This resulted in no communication between sand layers vertically. Therefore, if a leakage took place at well D-9-7 in layer 5, it would not be possible to observe the pressure change by the sensors located in layer 1. The pressure change in PDG located in well D-9-8#2 when well D-9-7 was leaking from layer 5 (50Mcf/day) is shown in Figure 208.

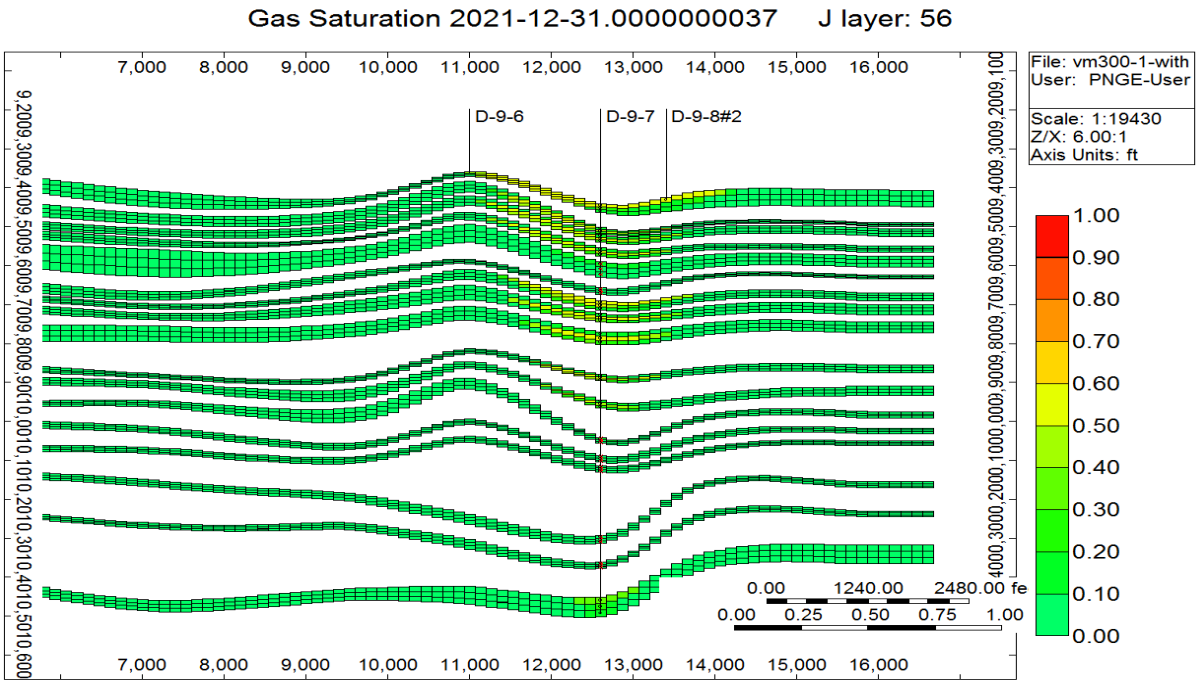

Figure 206. CO_2 plume extension in different layers

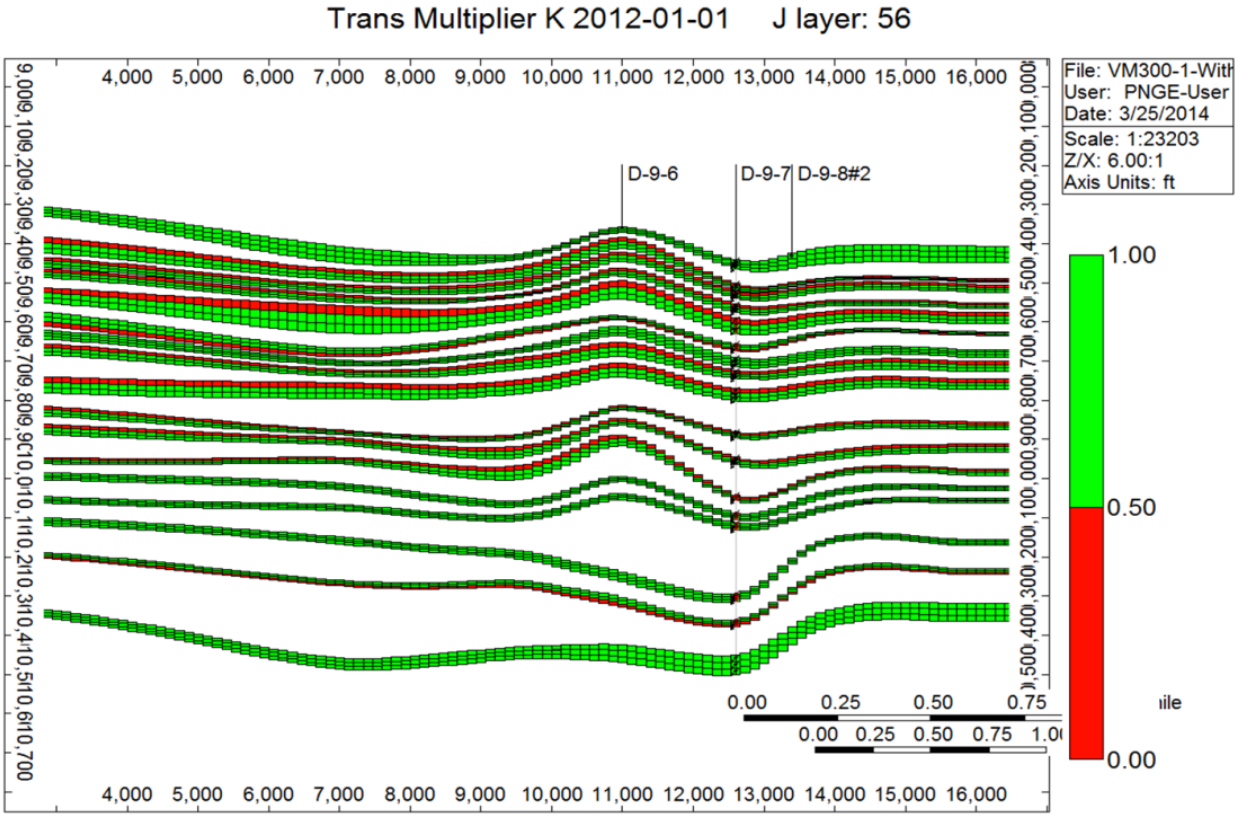

Figure 207. Transmissibility multiplier for shale layers

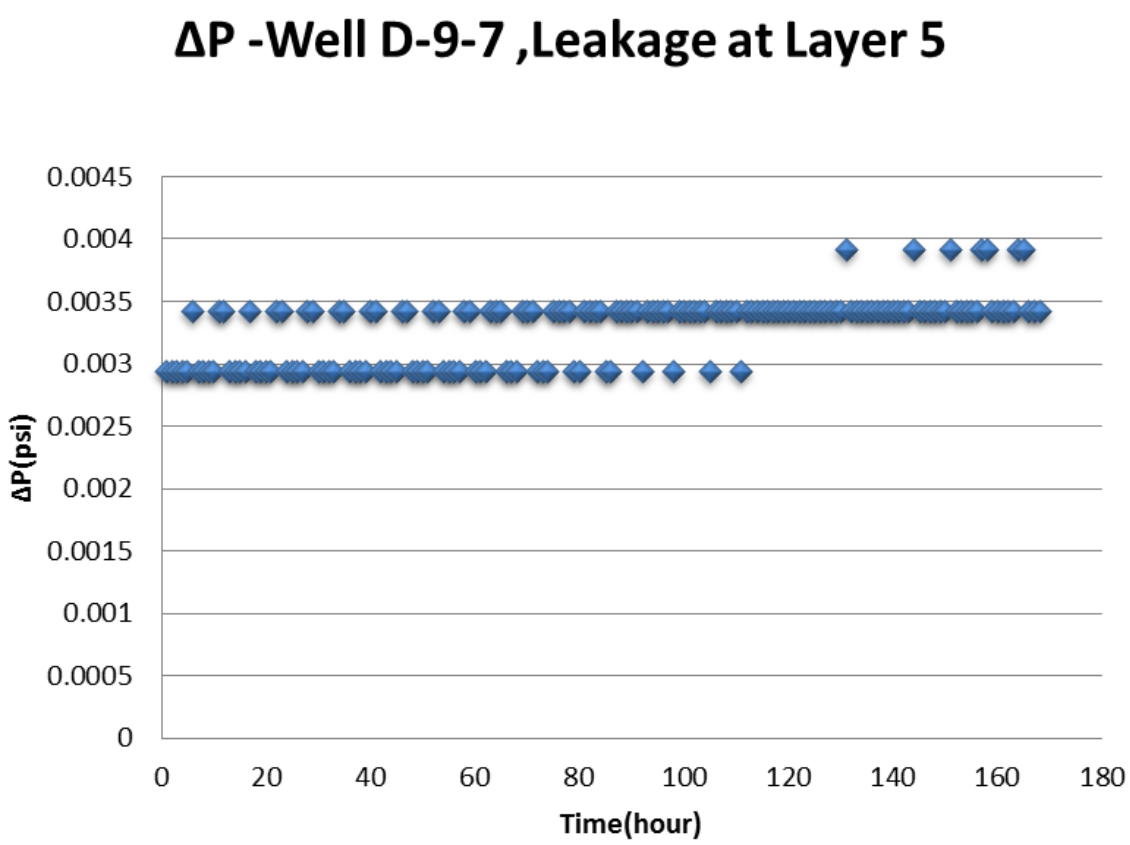

Figure 208. Pressure change in observation well when leakage initiated at layer 5

It was assumed that several Pressure Down-hole Gauges were installed at the observation well, at multiple sand layers in the reservoir. By making this assumption, it would be possible to measure pressure changes due to CO_2 leakage at every layer. Therefore, the corresponding pressure changes (ΔP), during a potential leakage at wells D-9-7 and D-9-8 were recorded, processed and provided to RT-ILDS. The RT-ILDS's results for CO_2 leakage location and rate are

shown In Figure 209, Figure 210 and

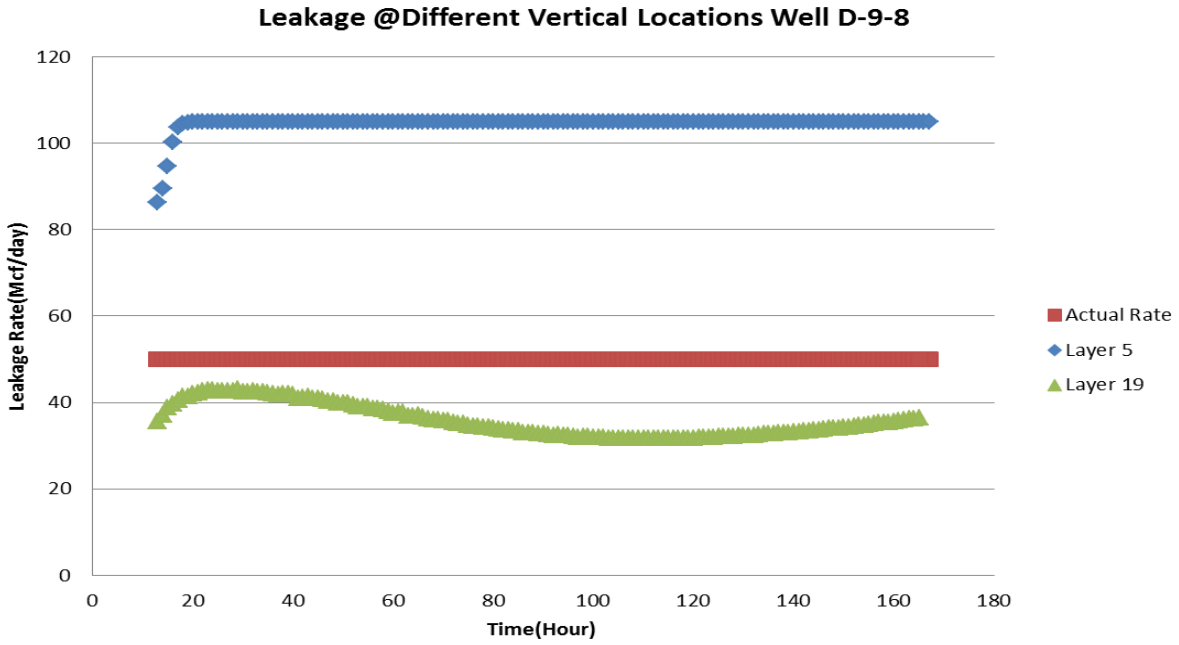

Figure **211**.

Based on the results for leakage location (Figure 209), it can be concluded that RT-ILDS is able to detect CO_2 location correctly when CO_2 leakage took place in well D-9-8 at different vertical locations (assuming existence of PDG in every layer).

When CO_2 leakage took place at well D-9-7, RT-ILDS predicted the leakage location correctly specially within 80 hours after the leakage (except the cases that well leaked form layer 5 and layer 29). After 80 hours from the detection time, the results started deviating from actual location of well D-9-7.

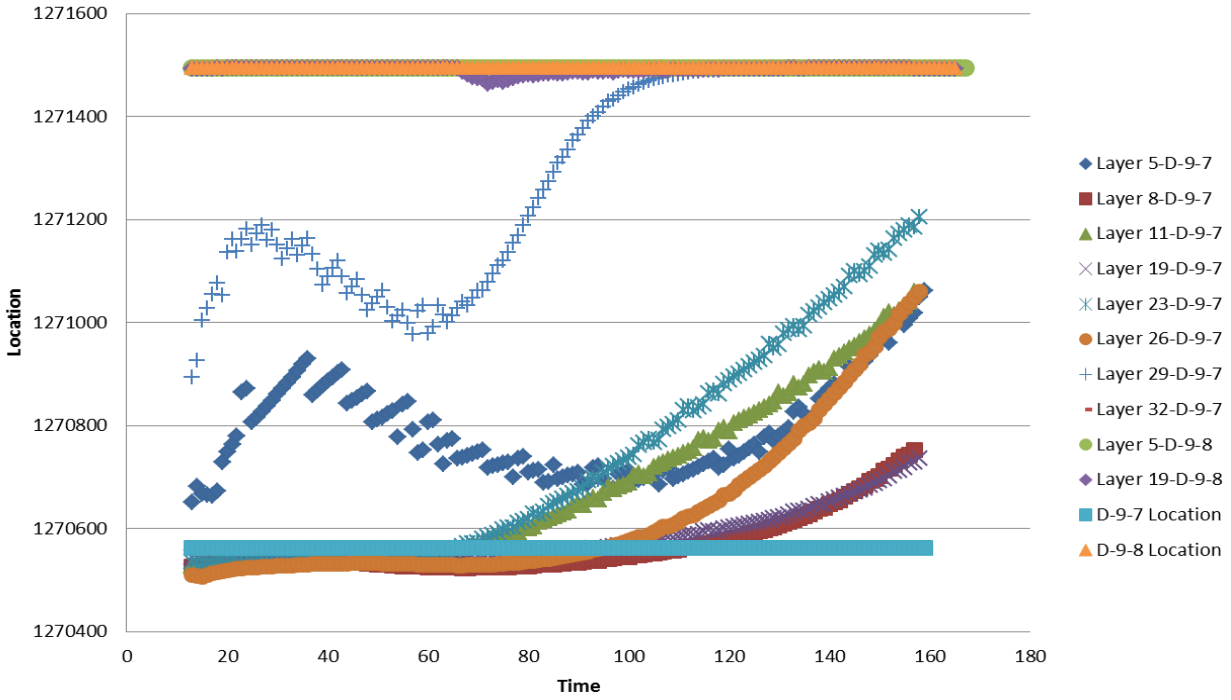

Figure 209. Leakage location prediction; leakage took place at different vertical locations

CO_2 leakage rate of 50 Mcf/day was assigned to each leakage scenario (different vertical locations along the well). For the case that well D-9-7 was leaking (Figure 210); RT-ILDS's leakage rate predictions were around 100 Mcf/day. When the leakage was from well D-9-8(at different layers), RT-ILDS predicted the rate for case that CO_2 leakage was from layer 19 correctly

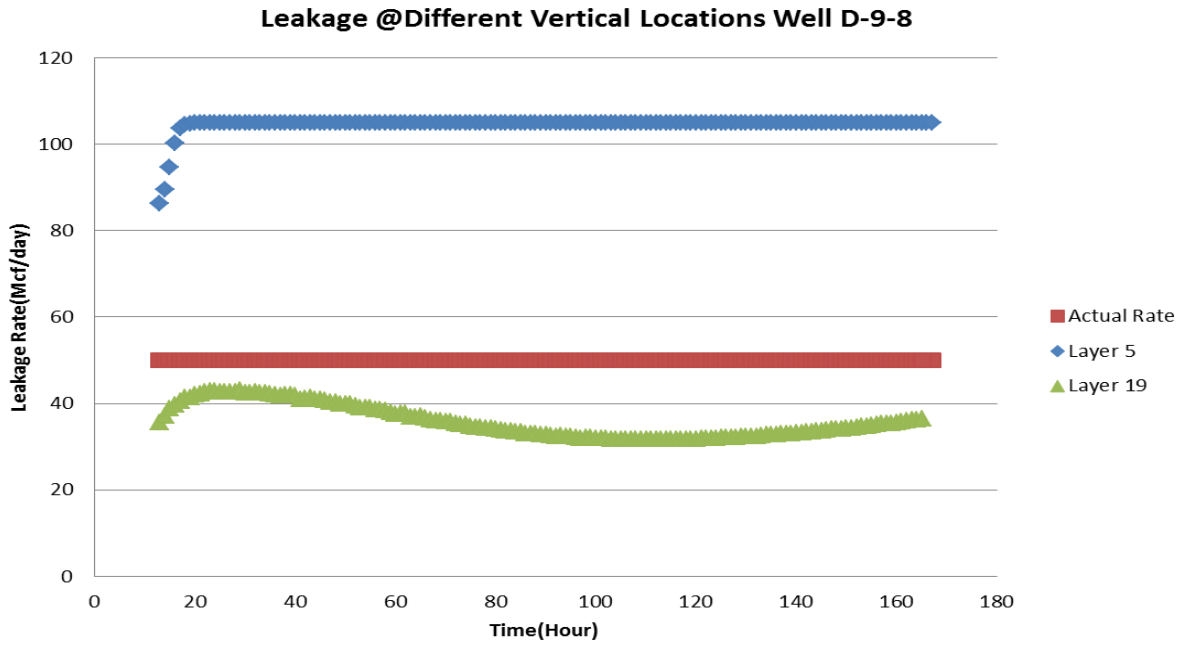

(

Figure **211**).

However the results for CO_2 leakage rate when leak was initiated from layer 5, was not satisfactory. The main reason for not having correct prediction for the cases that CO_2 leakage initiated at different vertical locations is that pressure signals are coming from different layers with completely different reservoir characteristics.

Therefore, these pressure signals cannot be exactly the same as the case the CO_2 leakage initiated from layer 1 (the RT-ILDS was developed based on pressure signals for different CO_2 leakage scenarios at layer 1).

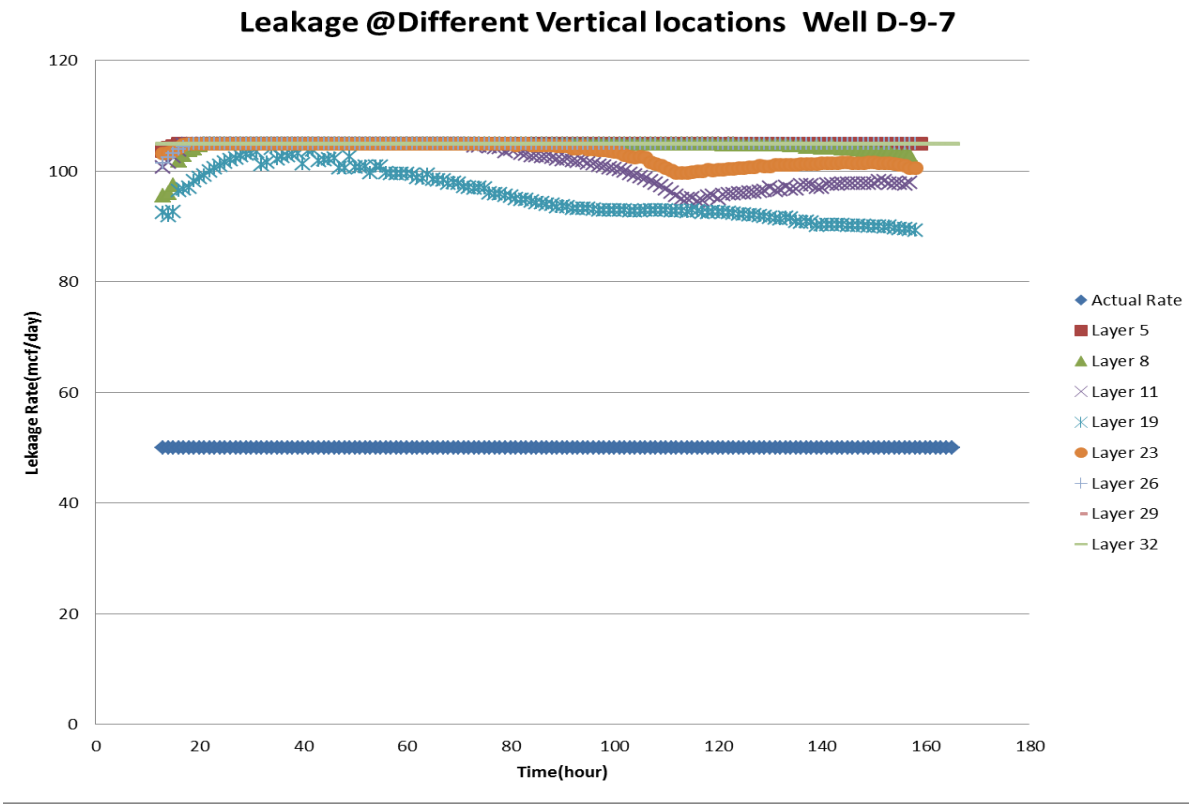

Figure 210. Leakage rate prediction at well D-9-7 when leakage took place at different vertical locations

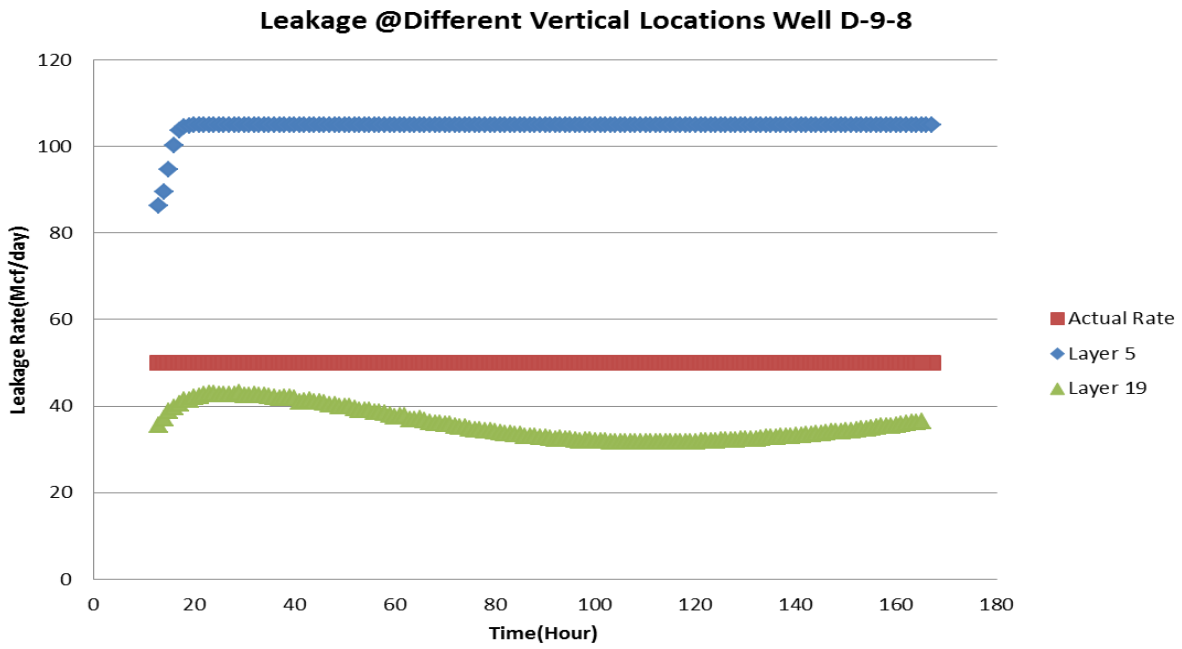

Figure 211. Leakage rate prediction at well D-9-8 when leakage took place at different vertical locations

EFFECT OF GAUGE ACCURACY OR PRESSURE DRIFT ON RT-ILDS RESULTS

One of the important parameters that affect the accuracy of the pressure measurements is Pressure Sensor Drift (PSD). Most of the Pressure Down-hole Gauges (PDGs) experience drift over their life time. PSD can be defined as a gradual malfunction of the sensor that may create offsets in pressure readings from the original calibrated form. Changes in reservoir temperature or pressure make the PDGs to respond differently depending on manufacturing characteristics. The scale of PSD changes according to working conditions and manufacturing specifications.

PSD can be measured as how much pressure readings deviated from the original value in a year (psi/year). Distributions of different PSD values are shown in Figure 212. For RT-ILDS, Pressure Sensor Drift (PSD) can act as a CO_2 leakage indicator. When ΔP of greater than 0.01 is recorded by the pressure sensor, RT-ILDS reports a leakage and starts processing the data to quantify leakage characteristics. For example PSD equal to 1 psi/year generates $\Delta P=0.01$, almost 88 hours after the initiation of the drift.

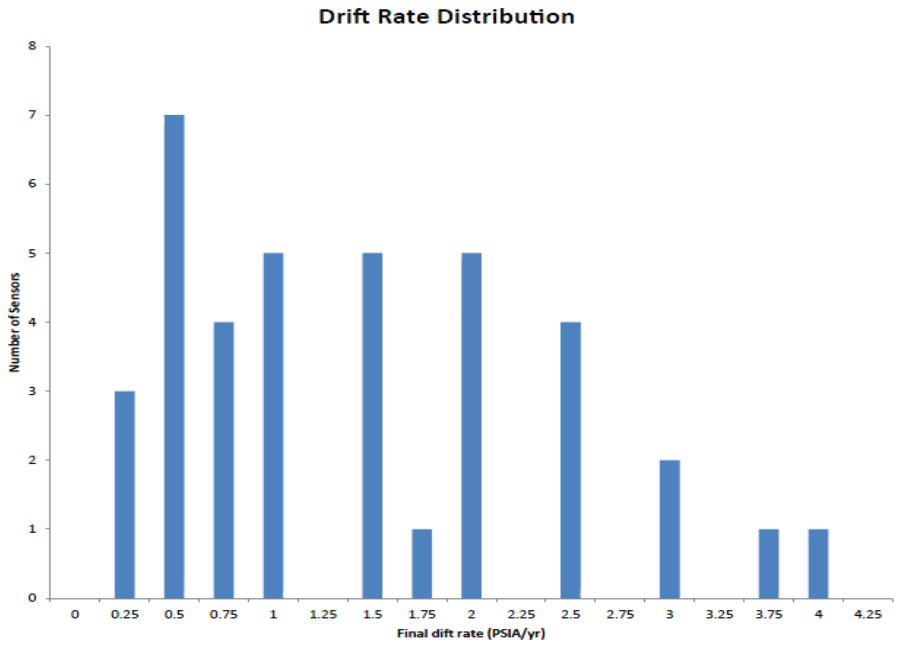

Figure 212. PSD distribution for the sensors

Based on the different values of reported PSDs (Figure 212), the times that RT-ILDS reports a leakage mistakenly are shown in Figure 213. This leakage is due to pressure gauge drift and not actual induced pressure change. PSD trends (are substitute for ΔP for actual leakage) over 168 hours were generated and applied to RT-ILDS. The RT-ILDS prediction results for CO_2 leakage location and rate are shown in Figure 214. RT-ILDS results for the leakage location at early times oscillate between wells D-9-6 and D-9-7. After 80 hours, all the results converge to Well D-9-6. This means that PSD makes ILDS to reports inaccurately that well D-9-6 is leaking.

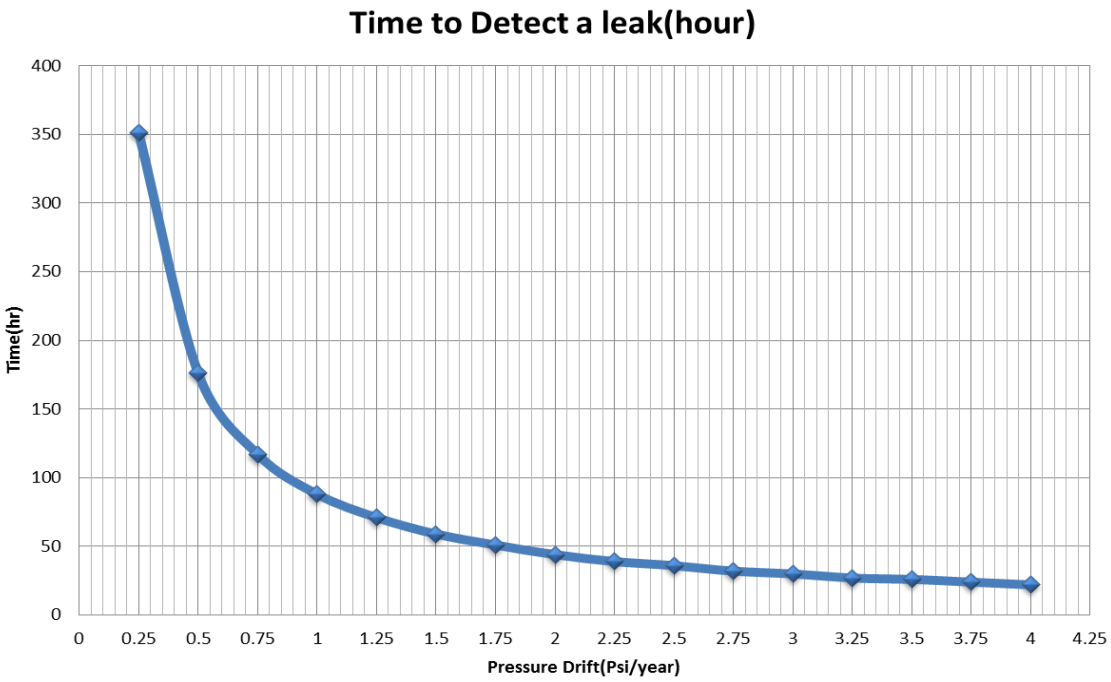

Figure 213. Time to report a leak based on different PSD values

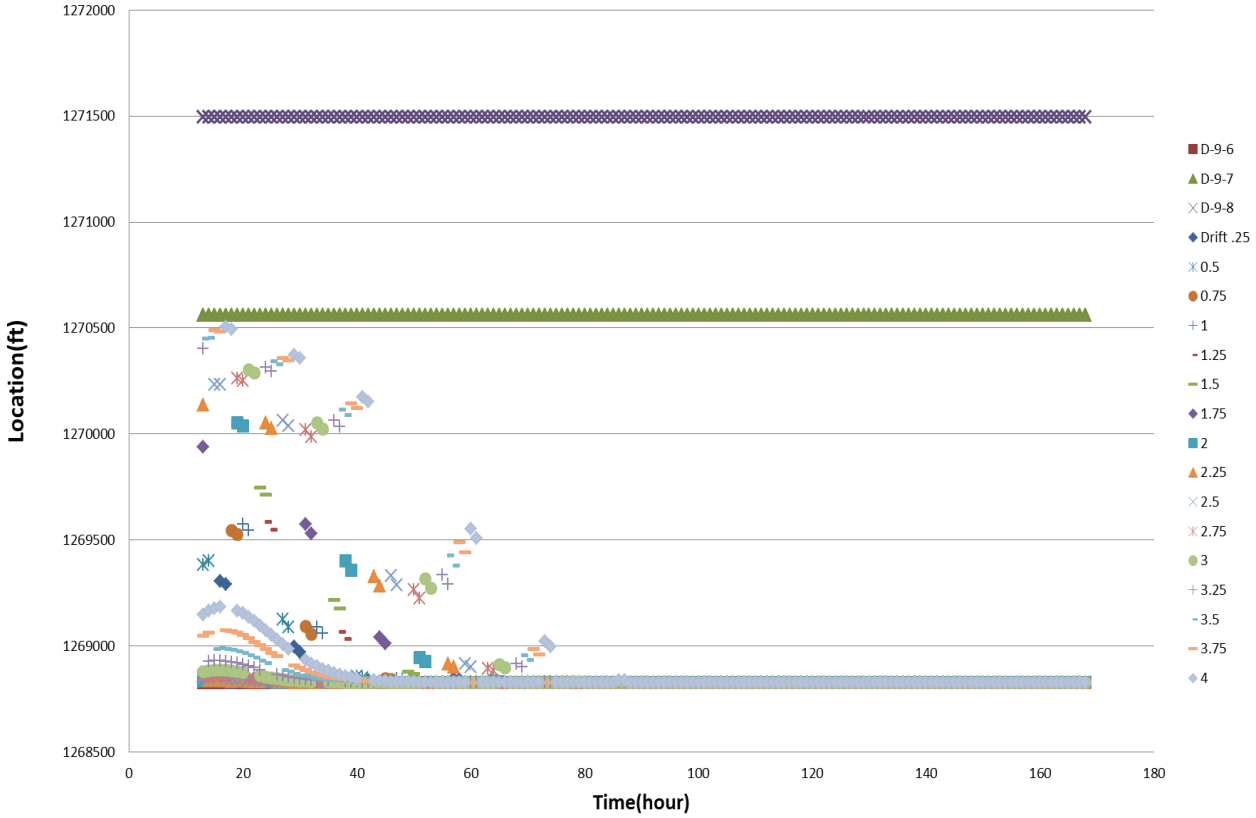

Figure 214. R-ILDS prediction for leakage location based on different drift values

USE OF WELL HEAD PRESSURE AT INJECTION WELL

Typically, there are three different reservoir pressure regimes during the injection and post injection. The first period refers to the start of the CO_2 injection until it ends (We refer to this time period as T1). At this Injection time (T1), reservoir pressure increases proportional to the amount of CO_2 injected and reaches to a maximum value at the end of injection period.

When the CO_2 injection ends, there would be a transition time (We refer to this time period as T2) when the reservoir pressure decreases until the brine and injected CO_2 reach a semi-equilibrium point. At the end of the transition time (T2), reservoir pressure remains almost constant (or decrease with a very slow trend) which can be referred to a steady state period (We refer to this time period as T3).

These three time cycles are shown in Figure 215. The objective of this study was to develop RT-ILDS for time cycle T3 when there had been no injection in the field and reservoir pressure reached to steady state trend. During this time period, since CO_2 injection is stopped, there is no fluid flow in the well and well head pressure would not change (it is possible to have well head pressure during the injection-T1). Therefore it is not possible to use well head pressure at the injection well for leakage detection in this study.

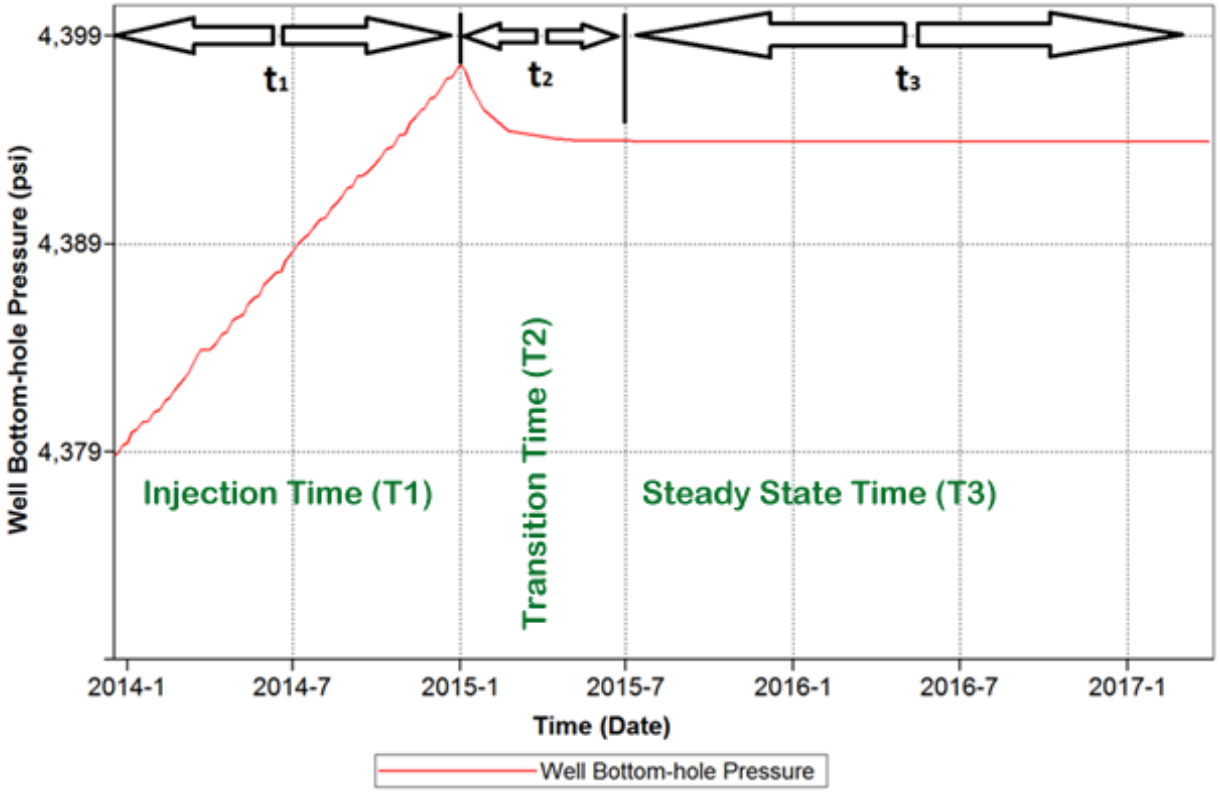

Figure 215. Different time cycles during and after CO_2 injection

The wells can be equipped with a pressure gauge that measures casing pressure (Figure 216). When there is only steady state production from tubing and no leakage occurs, the gauge measuring the casing pressure will show zero. Sometimes due to heating of the casing and completion fluids, the gauge measuring the casing pressure may not read zero.

By closing a needle valve, casing pressure should get back to zero. Otherwise, the casing represents Sustained Casing Pressure (SCP) which is an indicator for leakage; analysis of SCP can lead to determination of leakage pathway characterization on the same well (no other wells in that area). This is outside of the scope for this Study.

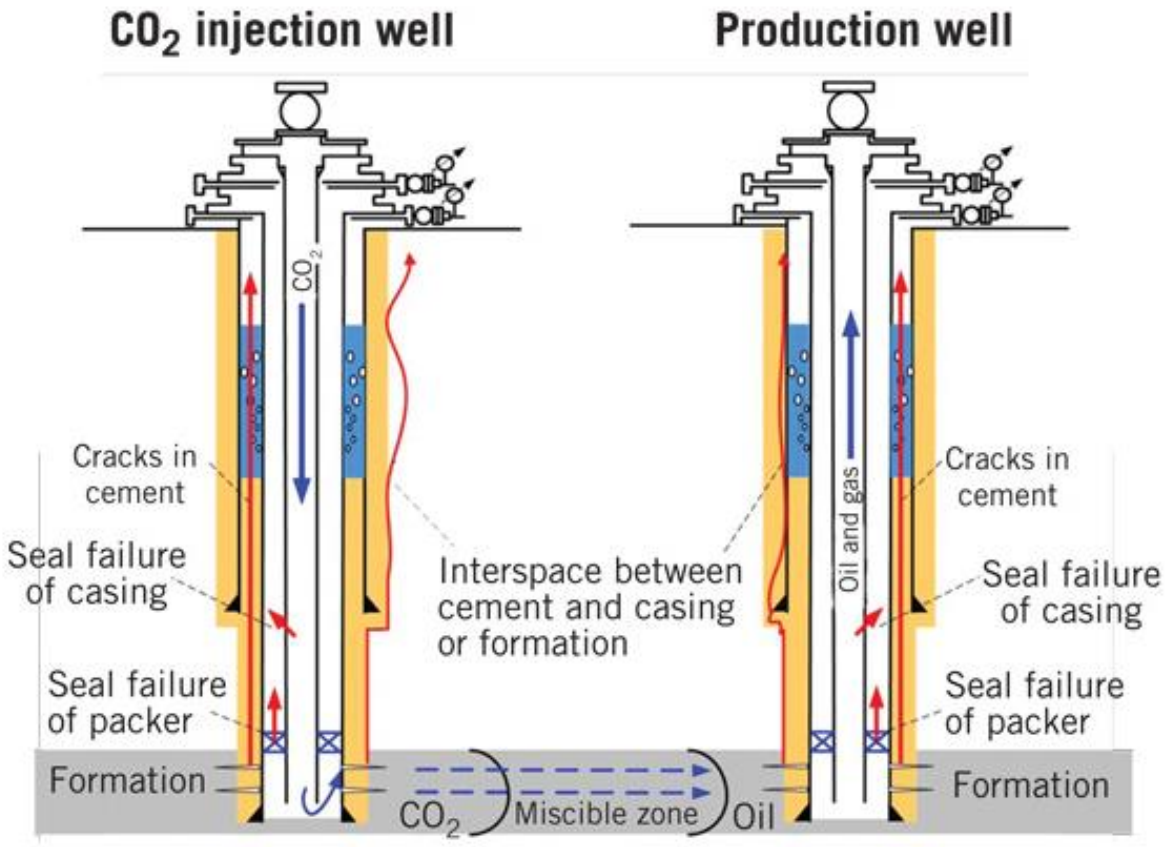

Figure 216. Sustained Casing Pressure

RT-ILDS FOR VARIABLE CO_2 LEAKAGE RATES

In previous sections, it was demonstrated that RT-ILDS is capable of incorporating pressure signals that were generated by CO_2 leakage rates with step function behavior (Figure 217). CO_2 leakages were initiated with a specific rate that remained constant as the time passed. In order to investigate the effect of variable CO_2 leakage on the performance of RT-ILDS, a set of simulation runs was designed to assimilate different CO_2 leakage rate behaviors such as linear, exponential and logarithmic.

The corresponding pressure signals for each variable rate function were included in leakage detection system development. Exponential and logarithmic CO_2 leakage rate functions are shown in Figure 218. Additionally, 20 different linearly changing CO_2 leakage rates were assigned to each possible leakage locations (well D-9-6, D-9-7, and D-9-8) in the reservoir simulation model (60 total simulation runs). Linear CO_2 leakage rates are shown in the Figure 219. The corresponding pressure signals for each CO_2 leakage scenario were collected, processed and sorted to form a data set which is appropriate for pattern recognition technology.

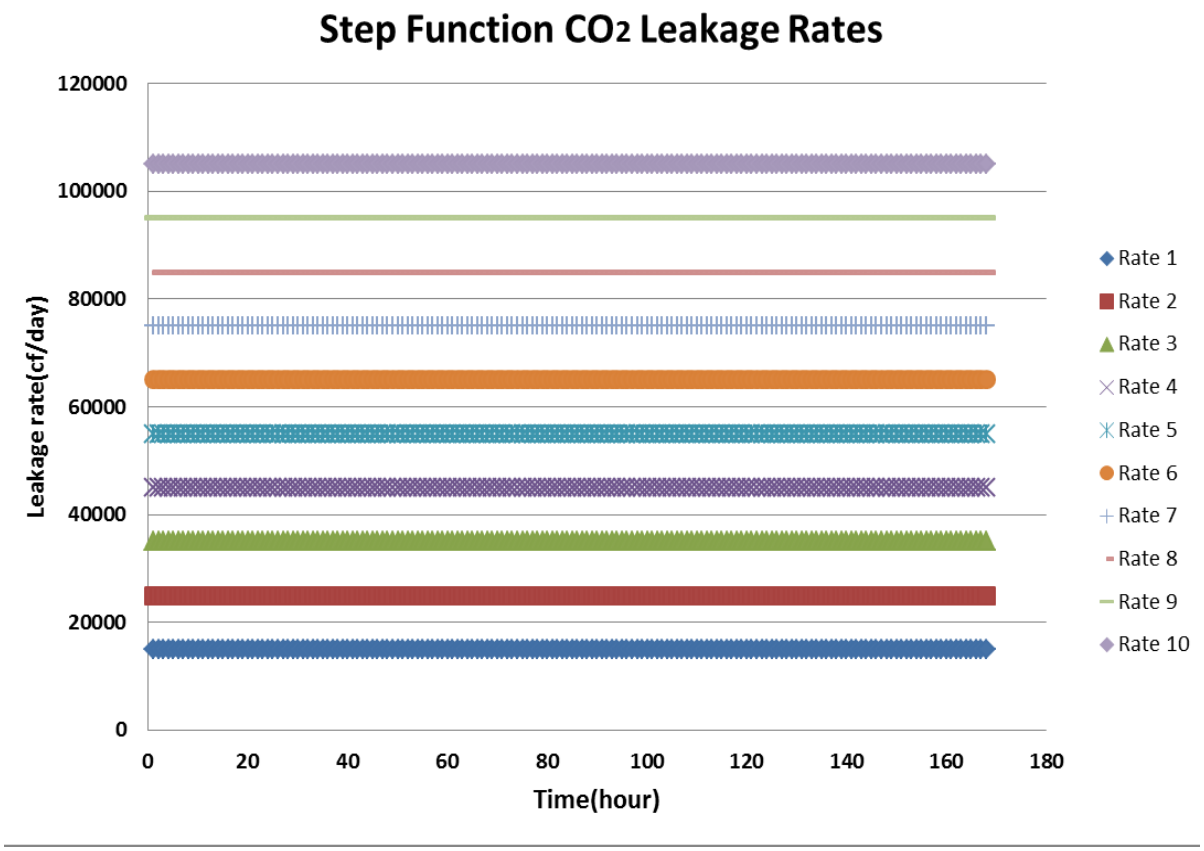

Figure 217. Step function CO_2 leakage rate

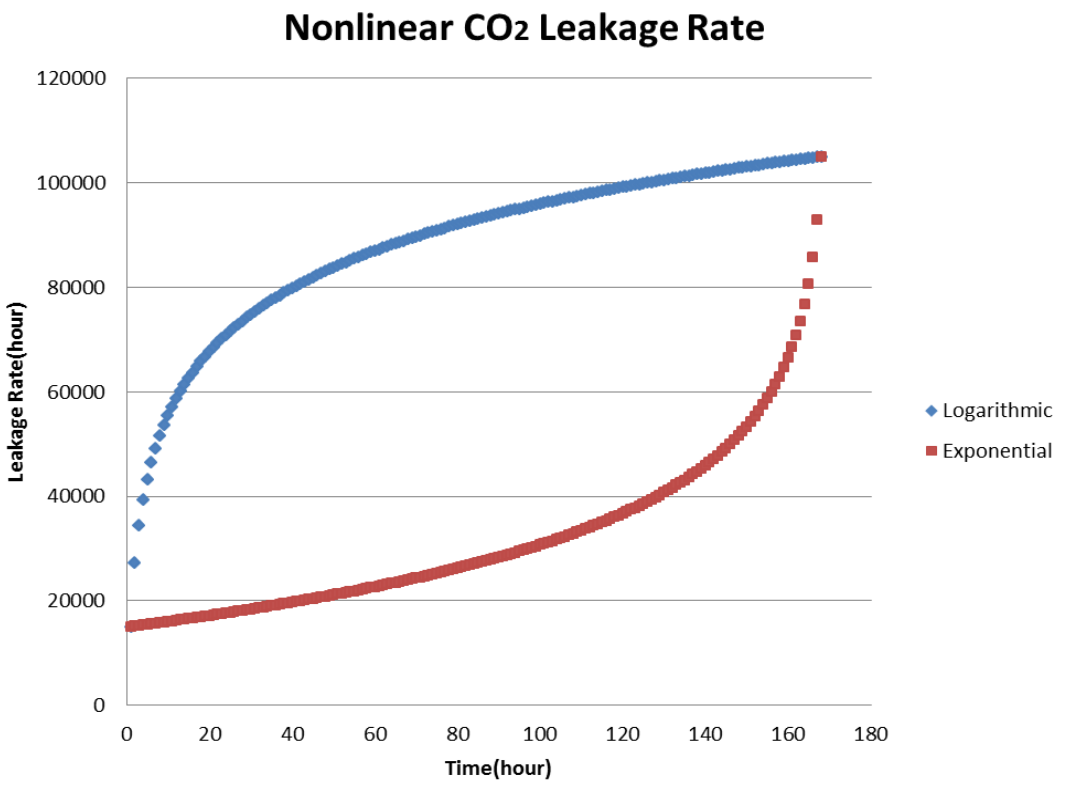

Figure 218. Logarithmic and exponential CO_2 leakage rates

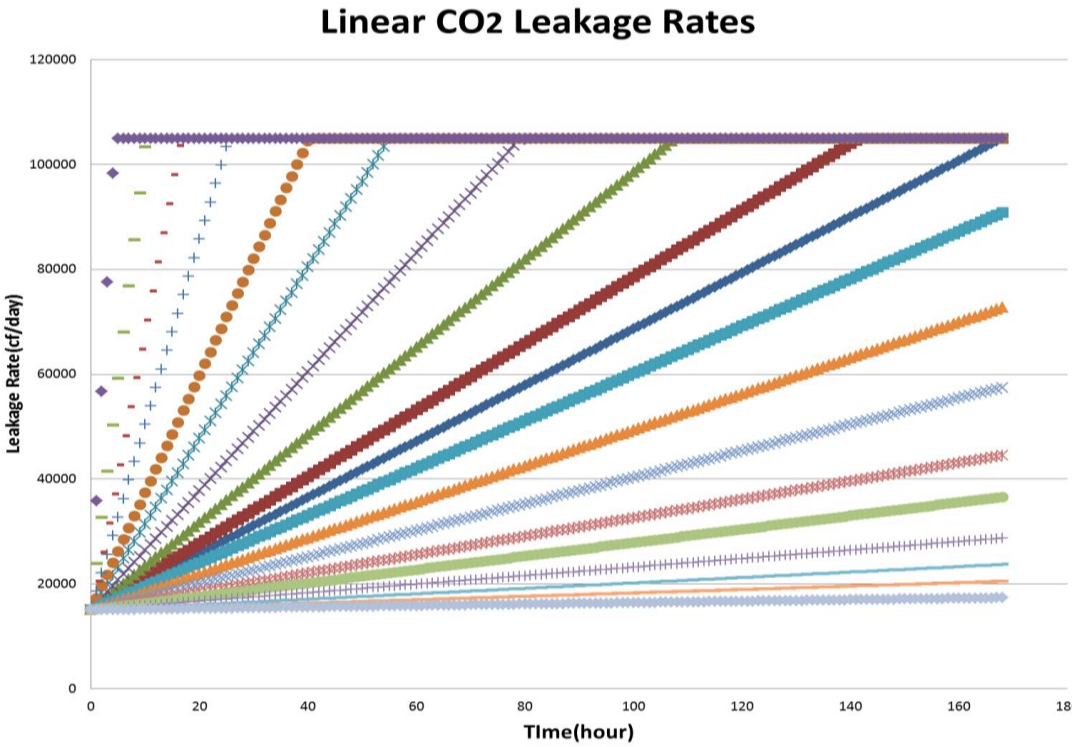

Figure 219. Linear CO_2 leakage rates

For CO_2 leakage location detection (with different leakage rate functions) all the pressure signals (coming from 60 simulation runs) as function of time and their calculated time-based descriptive statistics were lumped together to form input data set. Therefore, input data set included 10,950 data records that were partitioned into training, calibration and verification sets (80%, 10% and 10%, respectively). The outputs for this network were three leakage locations (wells D-9-6, D-9-7, and D-9-8).

Back-propagation neural network with 50 neurons in hidden layers was selected for training process. Neural network results (virtual versus actual) for CO_2 leakage location are shown in Figure 220. Neural network was able to find the pattern between leakage location and pressure signals with high precision (R^2 = 0.998)

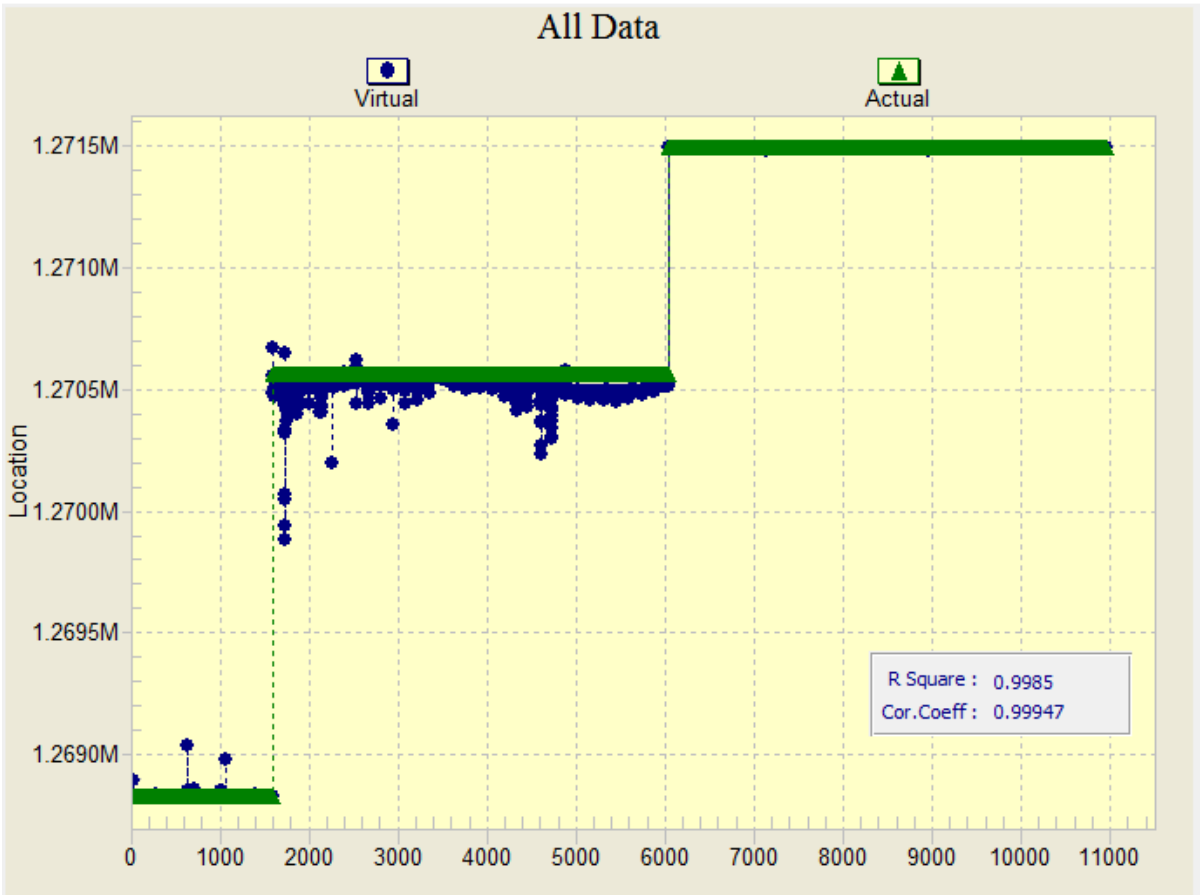

Figure 220. Neural network results for leakage location

Three neural networks were trained for each well individually to detect the leakage rate. The input data was the same as what was used for the leakage location training. However the output is CO_2 leakage rate at each specific time. It is different from that case the leakage rate remained constant as function on time.

The neural network architecture was almost the same as previous ones except the number of neurons in hidden layers. The results for CO_2 leakage rate (well D-9-8) are shown in Figure 221 (results for other wells are included in Appendix 4). Neural networks were able to determine a pattern between 32 different CO_2 leakage rate functions (as function of time) and corresponding pressure signals quite accurately (R^2 = 0.999).

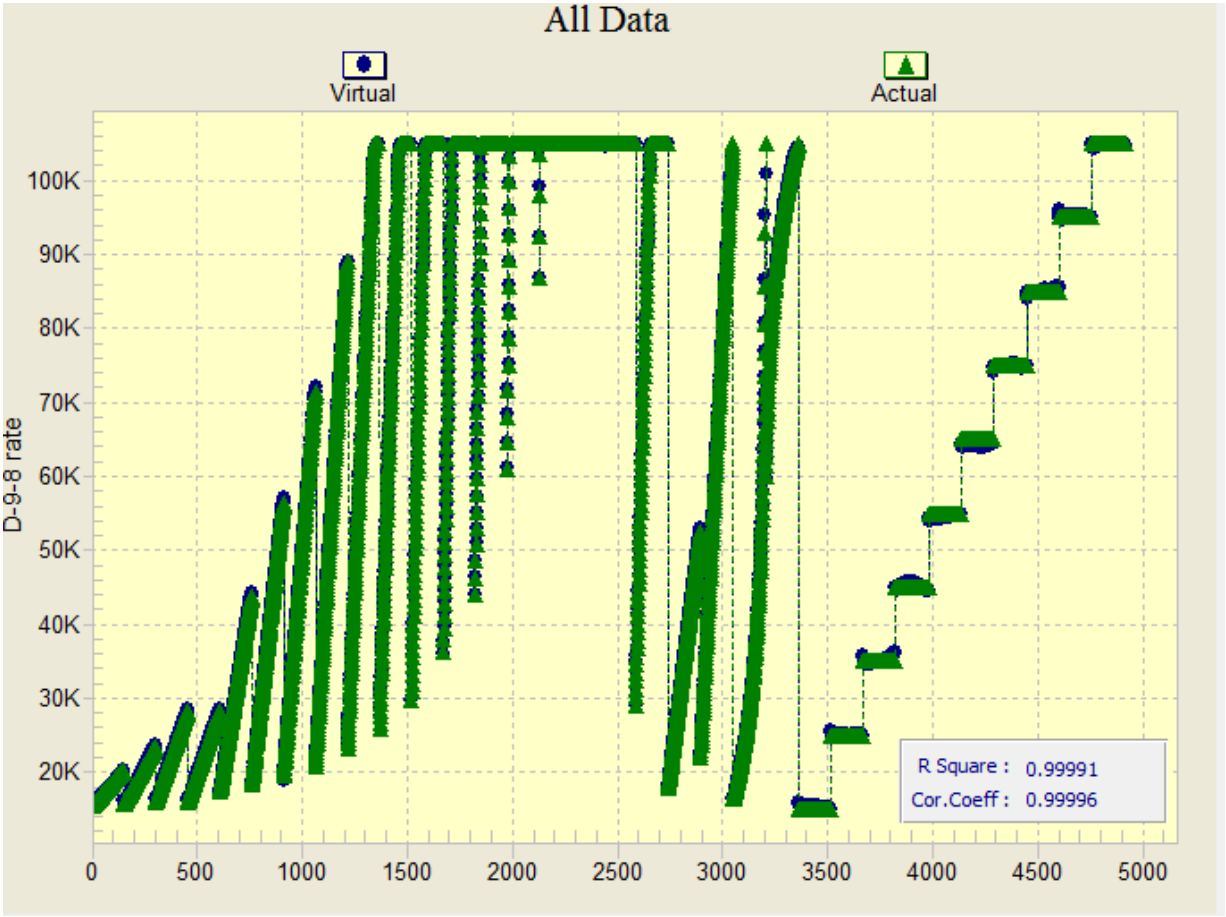

Figure 221. Neural network results for leakage rates at well D-9-8

In order to further validate the performance of the RT-ILDS, a complex CO_2 leakage rate as function of time was considered for the blind test of the system. This rate function represented logarithmic behavior at the beginning followed by a linear trend. The end part of the rate function showed exponential characteristic.

The rate function for the blind run is shown in Figure 222. This rate function was assigned to each of the leakage locations (D-9-6, D-9-7, and D-9-8) as the rate constraints and corresponding pressure signal from observation well (D-9-8) was collected. The pressure signals were processed to determine real time ΔP and calculated descriptive statistics values to be applied to the RT-ILDS and find the CO_2 leakage location and the rate. RT-ILDS predictions for leakage

location and rate (at well D-9-8) are shown in Figure 223 and Figure 224. (Details of all the results of this portion of the study are included in Appendix 8).

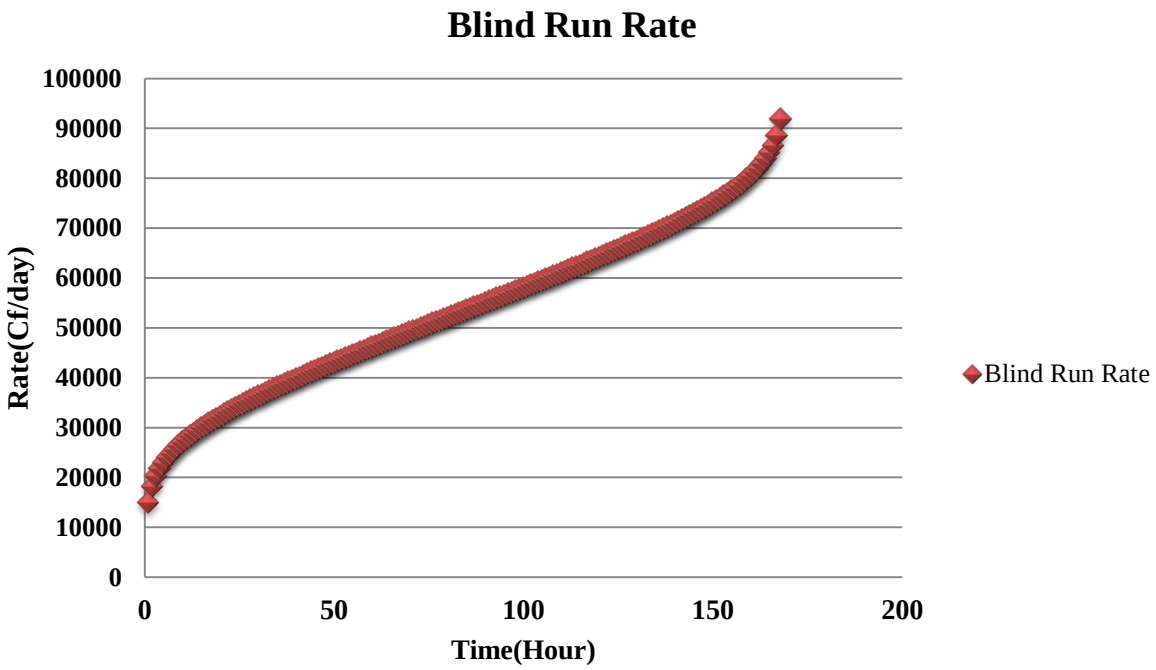

Figure 222. Rate function for the blind test of the ILDS.

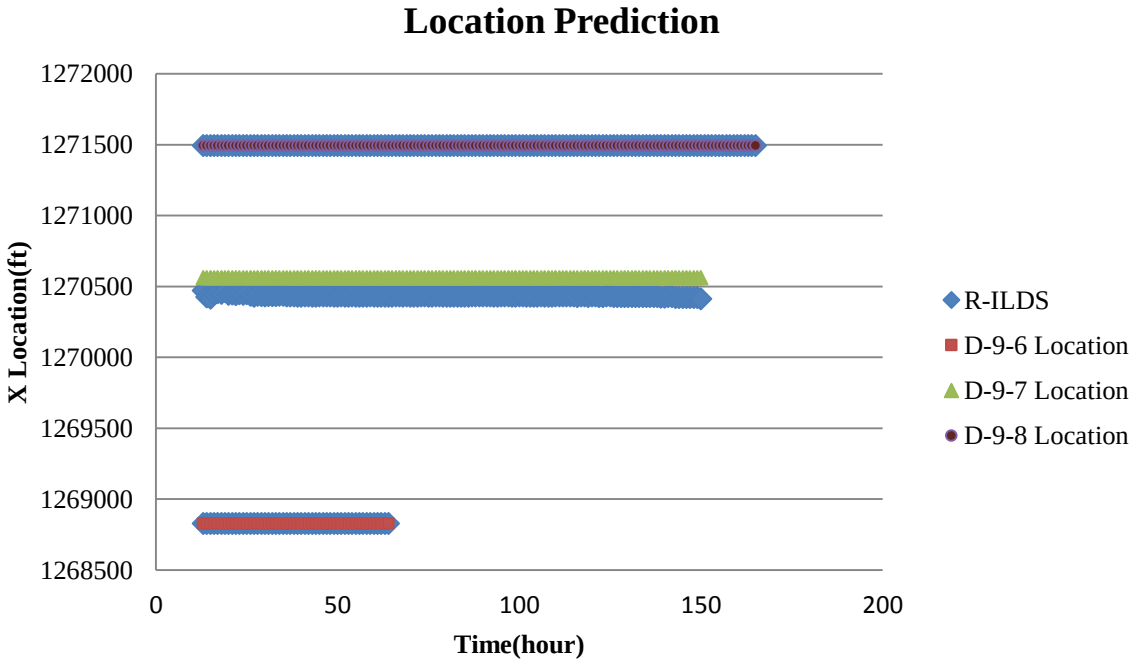

Figure 223. R-ILDS prediction for leakage location (variable rate)

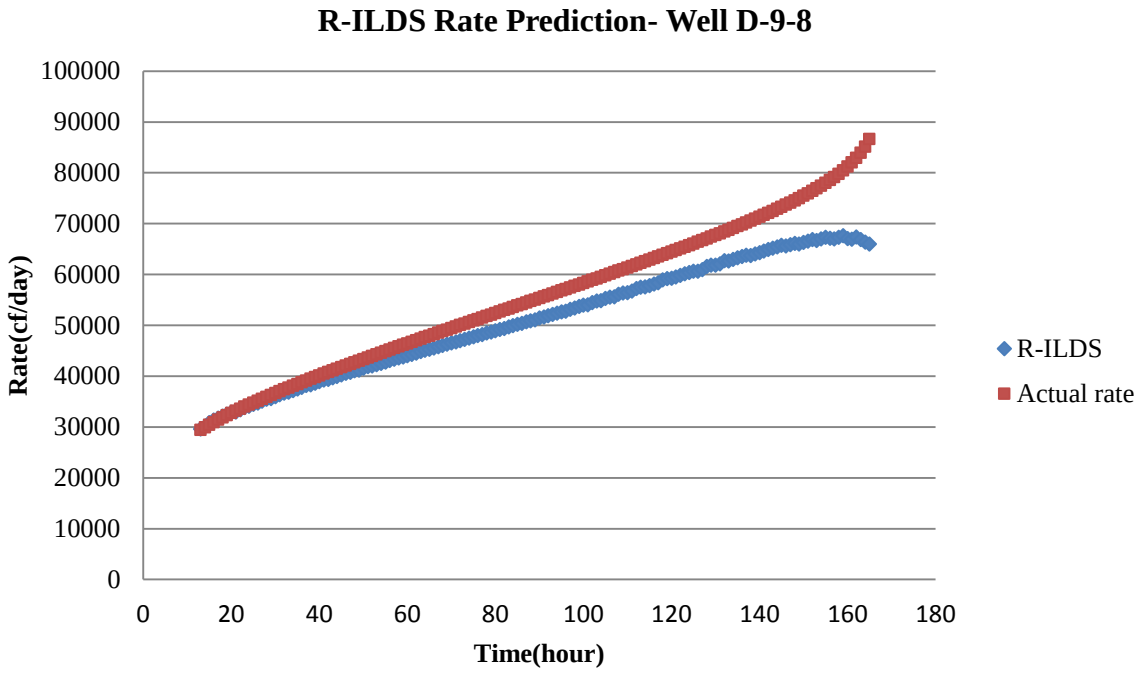

Figure 224. R-ILDS prediction for leakage rate in well D-9-8 (variable rate)

RT-ILDS predictions for the CO_2 leakage locations were reasonably accurate. RT-ILDS was able to predict the location of each well correctly. For the CO_2 leakage rate in well D-9-8, RT-ILDS prediction represented the actual rate especially at the early times.

RT-ILDS predicted just one value for rate at each time. In order to have range of rates rather than a single value, “Monte Carlo” simulation was used. Monte Carlo method is a computerized mathematical technique designed for explanation of risk in quantitative analysis and decision making.

Following steps are included in Monte Carlo simulation process:

1. Identification a range for possible inputs.
2. Generate random inputs from a probability distribution over the range.
3. Perform a large number of simulations with determined inputs
4. Collect, combine and analyses the results

The domain of the input parameters was defined by having Key Performance Indicator (KPI) analysis for leakage rate in Well D-9-8 (Figure 225).

Rank	Feature	% Degree of Influence
1	Cum Sum(DeltP)	100
2	Cum Avereage(DeltP)	80
3	Cum ST Dev(DeltP)	64
4	Cum Skewness(DeltP)	56
5	Derivative	51
6	Delta P	48
7	Time(New)	3
8	Cum Kurtosis(DeltP)	1

Figure 225. KPI for CO_2 leakage rate in well D-9-8

As it is shown in Figure 225, cumulative summation (ΔP), average (ΔP), standard deviation (ΔP) and skewness indicated the most impact on CO_2 leakage rate in well D-9-8. Based on the "±20%" rectangular probability distribution, 1000 random variables for each mentioned parameter were generated. Then, the trained neural network computed CO_2 leakage rate 1000 times based on combinations of the generated input variables.

Calculated leakage rates were sorted according to their relative frequency and cumulative probability. As an example at time 162 hr after leakage, the actual rate was 83 Mcf/day while RT-ILDS prediction showed 67.4 Mcf/day. Monte Carlo results provided a leakage rate range (Figure 226) that includes the actual rate.

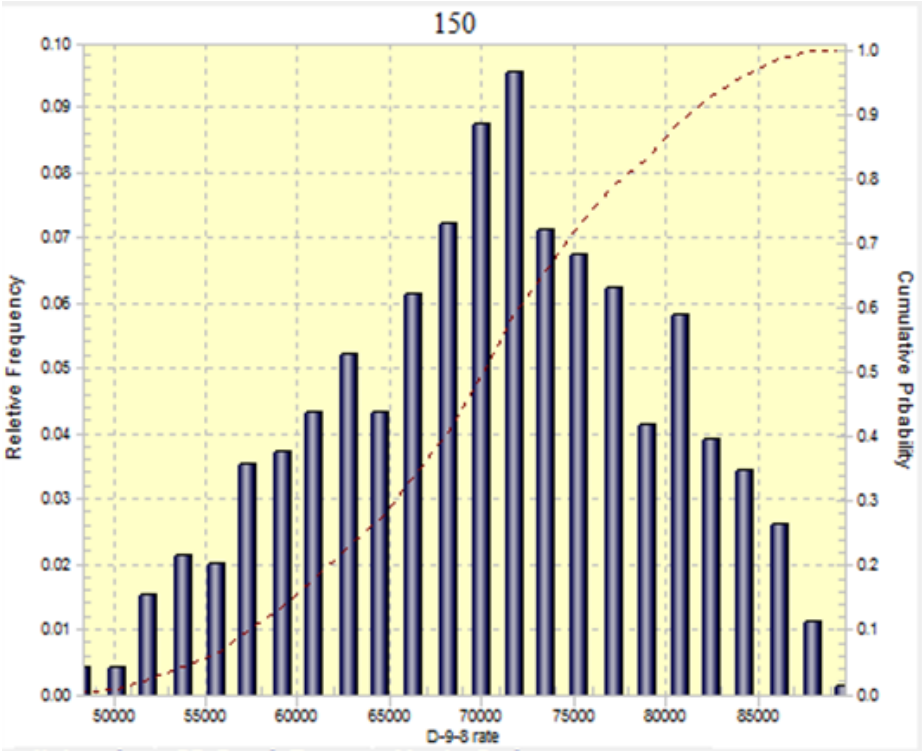

Figure 226. Relative frequency & cum. probability for the leakage rate at time 162 hr

USE OF PRESSURE DOWN-HOLE GAUGE (PDG) IN INJECTION WELL

Two Pressure Down-hole Gauges were installed in the well D-9-8 to measure and transfer real-time pressure data (Figure 227) to the surface. So fare, all the studies were performed based on the presence of PDG at observation well. At this section, it is assumed that a pressure down-hole gauge is installed in the Injection well (D-9-7) rather than observation well. This may reduce the need for drilling an observation well in the system.

All the reservoir simulations runs that addressed 30 different CO_2 leakage scenarios were repeated in order to generate high frequency pressure data at the injection well. The same procedure was used to apply this new sets of data (high frequency pressure data collected at the injection well) as the new engine of the RT-ILDS. The results for the RT-ILDS with new processing engine based on the presence of the PDG at the injection well are included in details in Appendix 9.

Figure 227. Location of the injection and observation well in the area of interest

According to the training results, RT-ILDS was able to predict the CO_2 leakage rates with good precision (CO_2 leakage rate R^2 were more than 0.99 for all three wells, D-9-6, D-9-7, and D-9-8). For the CO_2 leakage location, the RT-ILDS results were not representing the actual locations (CO_2 leakage location R^2 was 0.49). The reason for not having good results is that injection well is located approximately in the middle of wells D-9-6 and D-9-8 as shown in Figure 227 (Almost equal distance from both wells).

This symmetric characteristics of well locations, led to having the same pressure signals, when well D-9-6 or D-9-8 leaked (Figure 228). Since the injection well is located in the middle of CO_2 plume (based on reservoir characterization), it receives the same pressure signals from different leakages that are at the same distance to the well. Therefore it is not possible to detect the exact location correctly. PDG should be installed in location that represents distinct pressure signals from different leakage location. Otherwise the presence of second monitoring well is necessary to be able to detect CO_2 leakage location correctly.

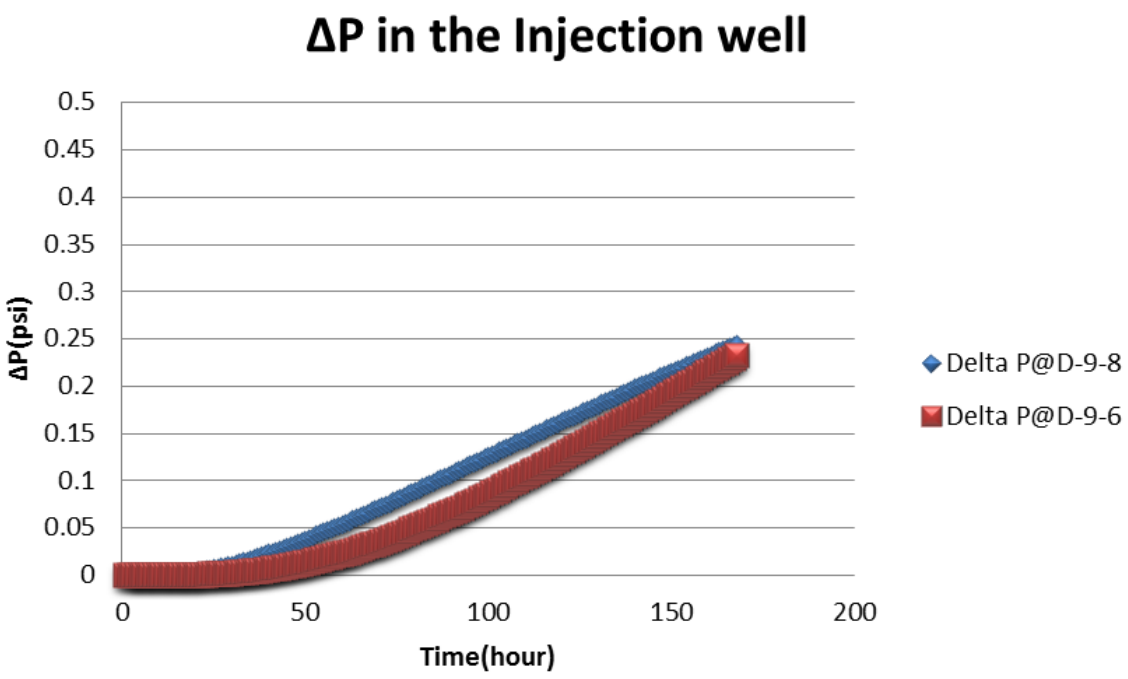

Figure 228. Pressure signals subject to leakages at well D-9-6 and D-9-8

LEAKAGE FROM THE CAP-ROCK

Initially, the reservoir was assumed to have a continuously sealed cap-rock that prevented any communication between the reservoir and formations above it. After the injection period, pressure on one side of the seal (in the target zone) would increase leading to a pressure difference across the cap-rock. When the pressure difference across the cap rock exceeds the fracture pressure, the seal layer breaches and provides a path for CO_2 to migrate to the other layers.

In order to model cap-rock leakage in the reservoir simulator, the pressure in the Dantzler sand located on top of the seal (

Table 5) was estimated by having the pressure gradient in the formation and its average depth. This pressure was assigned as the constraint for the cap rock leakage in the model. The pressure difference between two layers is the main driving force for CO_2 flow through the leakage path.

As an example, the reservoir pressure (in the observation well) and CO_2 leakage rate behavior for the case that cap rock leakage occurs (at 01/01/2022) in the North of the injection well (Figure 229) is shown in Figure 230. When the cap-rock fracture is initiated, large amount of CO_2 is released and leaked to the upper layer in very short period of time (less than a day). This high flow rate of CO_2 leakage causes sharp decline in the reservoir pressure.

As the reservoir pressure decreases, the driving force (pressure difference between reservoir and top sand layer) declines and less CO_2 leakage rate is observed. Typically ,the pressure signal that is created due to cap rock leakage represents higher amplitudes compare with the well leakages signals (that were studied in previous sections). Therefore a different RT-ILDS implementation was used to detect and quantify the characteristics of cap rock leakage.

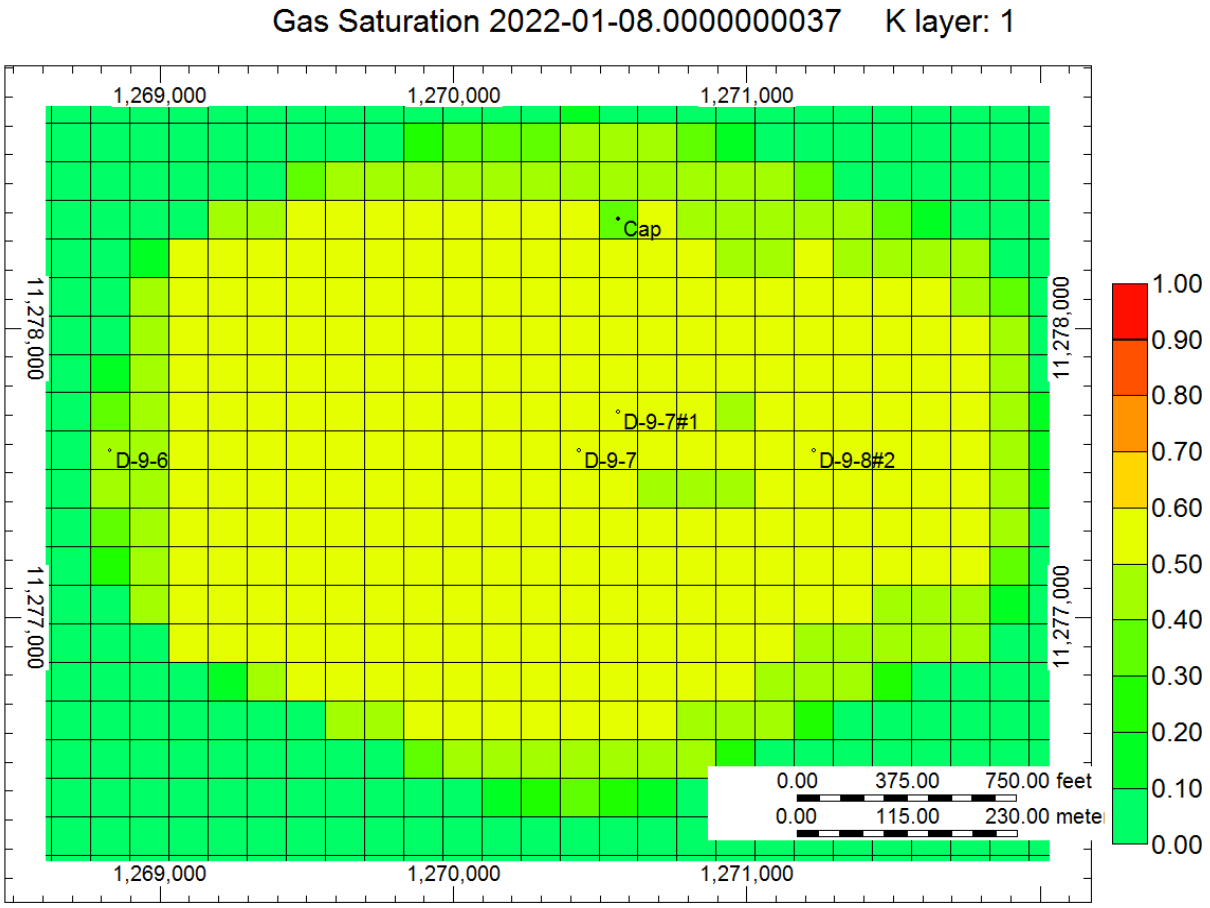

Figure 229. Cap-rock leakage location

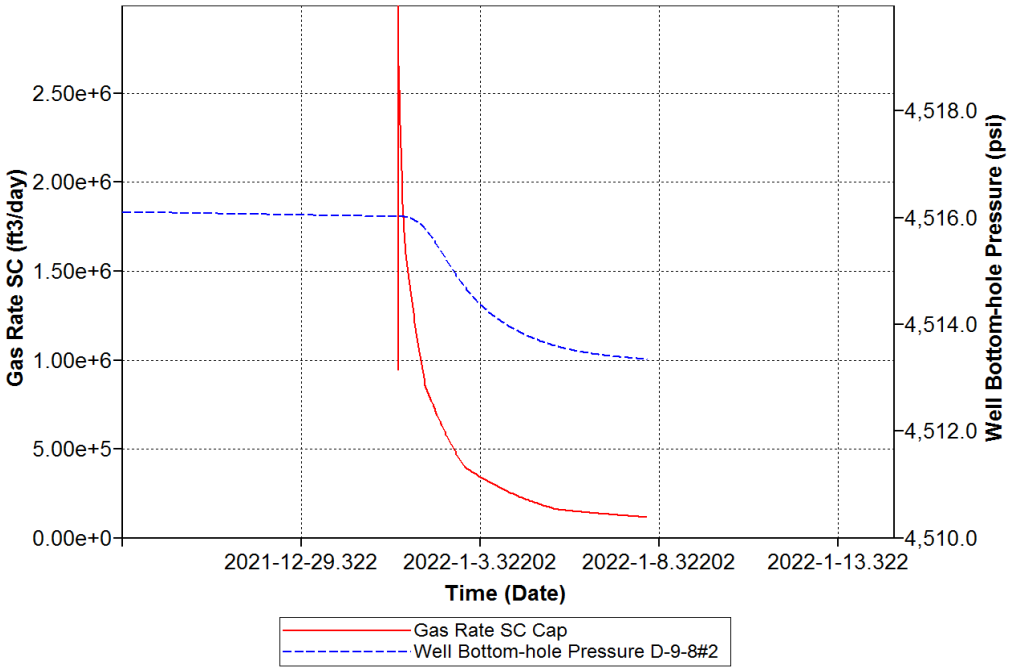

Figure 230. Pressure behavior in the observation well and CO_2 rate due to cap rock leakage

In order to develop the new implementation of the RT-ILDS for detecting the cap-rock leakage, 9 different simulation runs were designed based on the location of the leakage (Figure **231**). The only constrain for cap-rock leakage was pressure in the upper layer (Dantzler sand) which was assigned as the bottom–hole pressure for a synthetic well that was drilled in the leakage location.

As mentioned earlier, there is a sharp increase in the CO_2 leakage rate. To eliminate this peak in the CO_2 leakage rate behavior, cumulative amount of leaked CO_2 was used instead of rate. The training process is exactly the same as what was explained before. For each leakage scenario, the corresponding pressure signals were processed in real time by descriptive statistics to be used as the input for neural network.

The outputs for the neural network were the leakage location (x and y) and the cumulative leaked CO_2. Details results for the neural network training are shown in Appendix 10. The neural network results for cumulative leaked gas and x coordinate of leakage location were precise with R^2 equal to 0.97, and 0.99, respectively. For leakage location “y” coordinate the neural network predictions were not as accurate as the other ones (cumulative leaked gas and x coordinate). This might be due to the symmetric locations of cap-rock leakages respect of observation well in “y” direction.

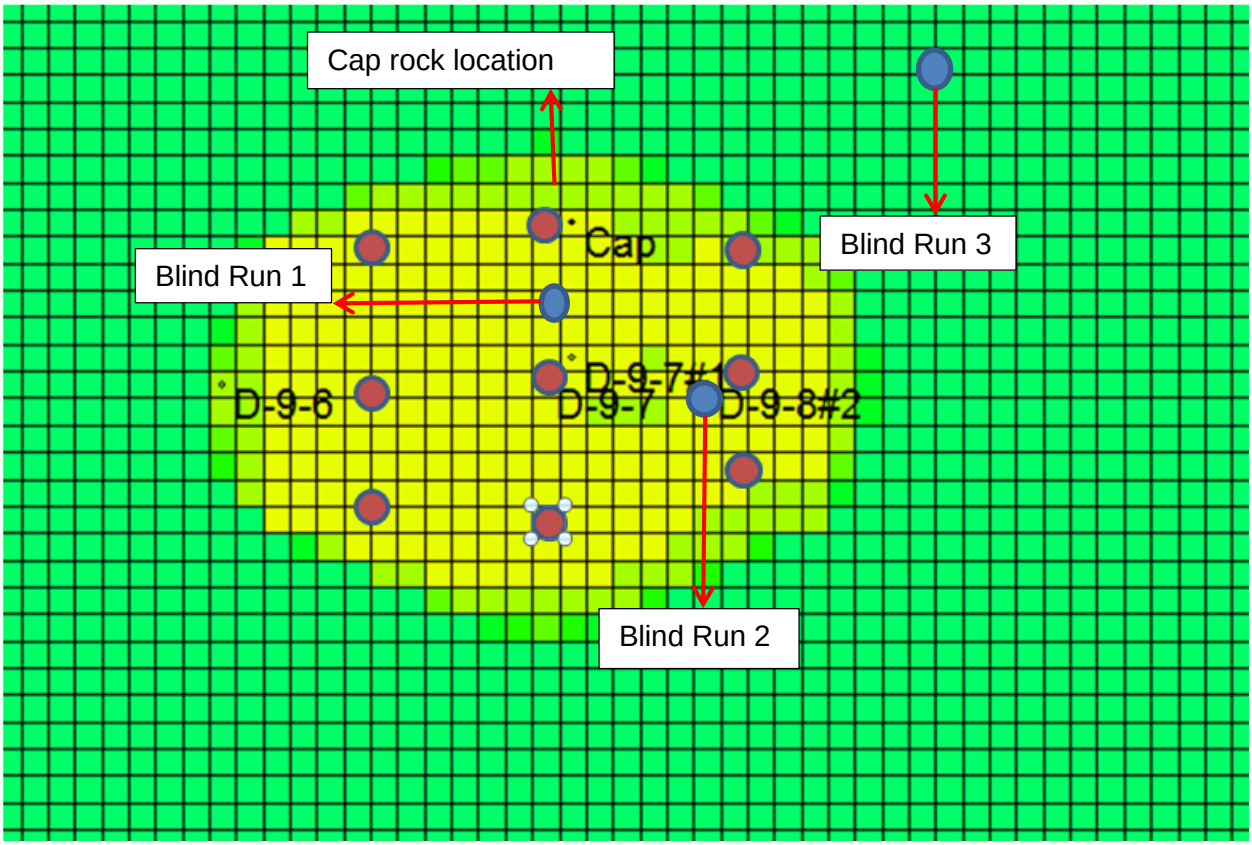

Figure 231. 9 different locations for cap-rock leakages and 3 blind runs

The final part for the verification of cap-rock R-ILDS was to design a set of blind runs that were not used during the neural network training process. Three cap-rock leakage locations were considered in the reservoir simulation model (Figure **231**). Two cap-rock leakage locations (out of three) were inside the range of the locations used for neural network training. The results for blind run verification are shown in Appendix 10.

It can be observed that for cumulative leaked rate, RT-ILDS results are almost the same as actual values for the first two blind run cases (were located in the range of locations). For the third blind run which was located outside the range, RT-ILDS results overestimated the actual value considerably. X-coordinate results were almost the same as actual locations except blind runs 2. For the Y coordinate results there were noticeable difference between actual values and RT-ILDS prediction. Overall, location of cap-rock leakage can be predicted as accurate as well-leakage due to symmetry of the location and impulsive and uncertain behavior of the leakage.

MULTI-WELL LEAKAGE

In the previous sections, a single well leakage was studied and analyzed. Since it possible that leakages take place from multiple locations, simultaneously, this section covers the capabilities of the RT-ILDS in detecting multiple leakages. To investigate multi-well leakage, combination of rates for two and three well leakages were assigned to the wells in the reservoir model according to Table 37.

Table 37. CO_2 leakage rates for multi-well leakage

Two Well			Three Well		
Leakage Rate(Mcf/day)			Leakage rate(Mcf/day)		
D-9-6	D-9-7	D-9-8	D-9-6	D-9-7	D-9-8
15	15	0	15	15	15
15	60	0	15	15	60
15	105	0	15	15	105
60	15	0	15	60	15
60	60	0	15	60	60
60	105	0	15	60	105
105	15	0	15	105	15
105	60	0	15	105	60
105	105	0	15	105	105
15	0	15	60	15	15
15	0	60	60	15	60
15	0	105	60	15	105
60	0	15	60	60	15
60	0	60	60	60	60
60	0	105	60	60	105
105	0	15	60	105	15
105	0	60	60	105	60
105	0	105	60	105	105
0	15	15	105	15	15
0	15	60	105	15	60
0	15	105	105	15	105
0	60	15	105	60	15
0	60	60	105	60	60
0	60	105	105	60	105
0	105	15	105	105	15
0	105	60	105	105	60
0	105	105	105	105	105

After performing simulation runs (start of leakage was at 1/1/2022) based multi-well leakage scenarios and processing all the corresponding pressure signals, it was required to train a neural network to differentiate between various combinations of well leakages. In this regard, a “Leakage Index” was defined based on the distance of each well from the observation well. Longer distances from the observation well resulted in selecting lower values for leakage index. The index values

ranged from 1 to 7 (higher values represent higher pressure signal amplitudes) according to distance to observation well and number of the leaking wells. All the scenarios can be divided into three classes as: single well leakages (indices: 1, 2, and 3), two well leakages (indices: 4, 5, and 6) and three well leakage (index: 7). The leakage index values are shown in Table 38

Table 38. Leakage Index for different single and multi-well leakage scenarios

Leaking Well	Leakage Index
D-9-6	1
D-9-7	2
D-9-8	3
D-9-6 & D-9-7	4
D-9-6 & D-9-8	5
D-9-7 & D-9-8	6
D-9-6 & D-9-7 & D-9-8	7

Several neural networks were trained considering different leakage indices as the output and processed pressure signals (ΔP) as the input. Detail results for this section are shown in Appendix 11. As it can be seen, it was not possible to get reasonable results for the neural networks. The main reason for not getting acceptable neural network training is that convolution of several pressure signals (generated by different combinations of well leakages) makes it very difficult for the networks to catch specific patterns out of final pressure signals.

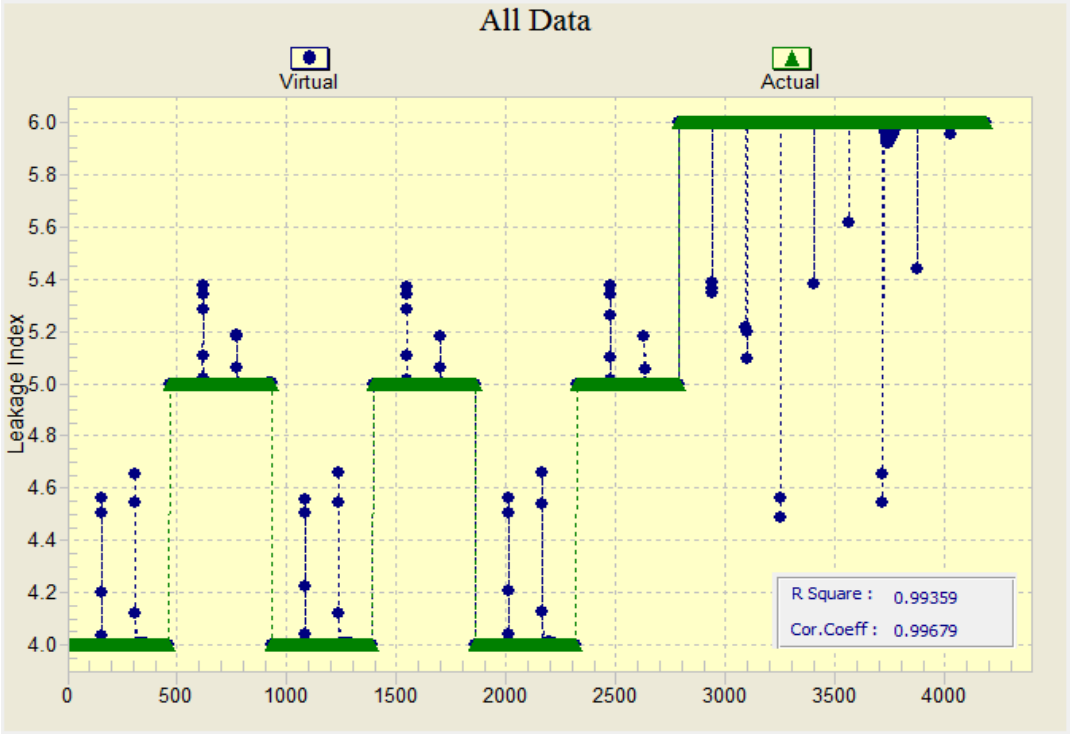

Figure 232. Neural network results for two-well leakage

In order to de-convolve mixed pressure signals (generated by multi-well leakages), existence of an additional pressure down-hole gauge was considered in the injection well (in addition to the observation well). The problem also was simplified in a way where only two well leakages were subject to investigation (leakage index values of 4, 5, and 6). Addition of one more pressure down-hole gauge brought in more information about pressure signals and the time that signals were observed by the gauges. For this case, a neural network was trained by Generalized Regression Neural Network GRNN, algorithm. The results for neural network training are shown in Figure 232.

By use of this new approach (adding more pressure gauge in the injection well), the results for neural network training improved significantly (R^2 equal to 0.9935). As a result, it became possible to differentiate which two wells were leaking by having pressure signals coming from two pressure down-hole gauges. The final step was to verity the practicality of the RT-ILDS which was devolved for multi well leakage. To do so, six simulation runs considering combinations of two-well leakages (Table 39) were performed.

Table 39. CO_2 leakage rates for the blind runs-two well leakages

Run	Two Well		
	Leakage Rate(Mcf/day)		
	D-9-6	D-9-7	D-9-8
1	40	80	0
2	80	40	0
3	40	0	80
4	80	0	40
5	0	40	80
6	0	80	40

The results for blind run verifications are shown in Figure 233. RT-ILDS was able to predict the leakage index correctly except for few hours at the early times after the leakages. Although the probability of two wells leak simultaneously is low, but with use of two pressure gauges installed in two distinct wells, it was possible to say which wells leak at the same time.

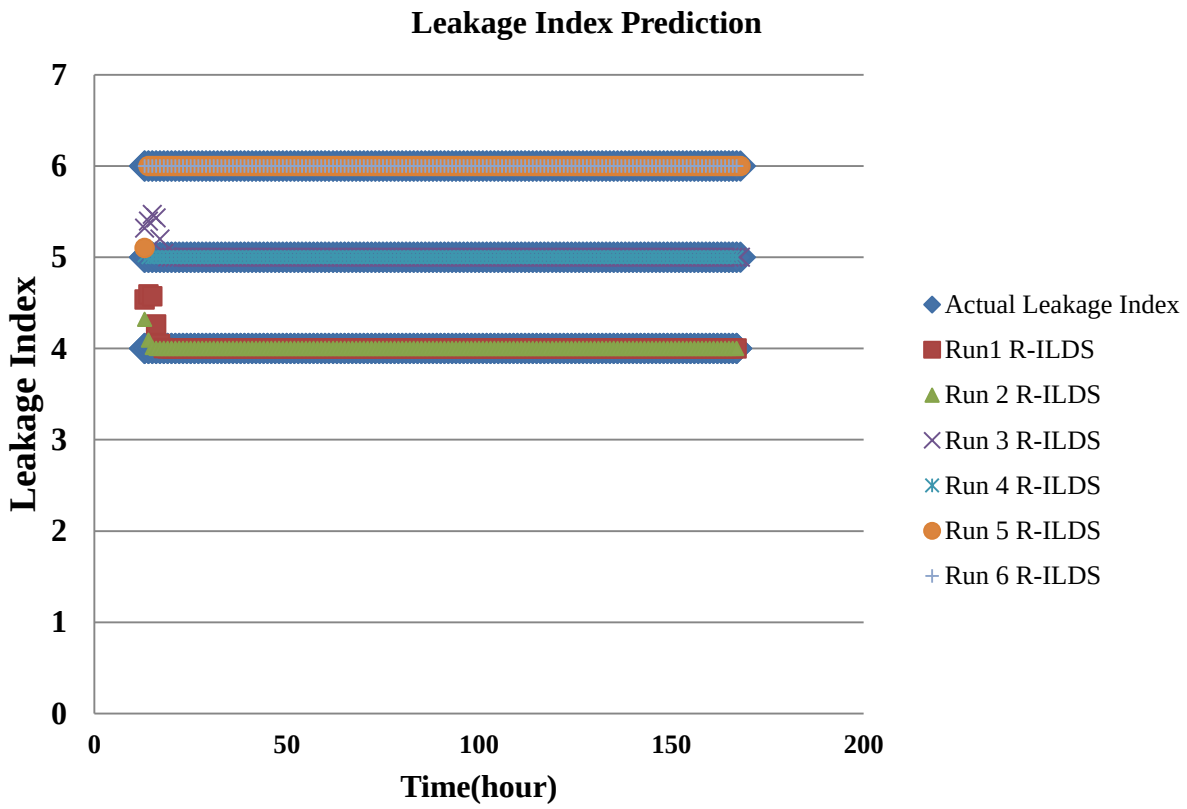

Figure 233. R-ILDS predictions for two-well leakages

ANALYSIS TO DEMONSTRATE THE PROJECT TECHNOLOGY'S ABILITY TO SUPPORT DOE'S GOAL OF LESS THAN 1% CO2 LEAKAGE OVER 100 YEARS

The objective of CO_2 sequestration in the Citronelle dome was to inject 9.4 MMcf/day (500 tons/day) of CO_2 into the saline aquifer at Paluxy formation for duration of three years. Therefore, the total injected value will be 10,293 MMcf or 547.5 Mton.

One percent of total injected value is 102.93 MMcf (5.47 ton). If 102.93 MMcf of CO_2 leak from the reservoir over 100 years, the corresponding daily leakage rate from one will be 2.85 Mcf/day or 0.15 ton/day. Three different reservoir simulation runs were performed by assigning 2.85 Mcf/day of CO_2 leakage rate to the three wells that were located in the CO_2 plume area. For each leakage location, the pressure change in the observation well was recorded. As it is shown in Figure 234 it takes 281 hours to detect the leakage from wells D-9-6, it takes 79 hours to detect the leakage from wells D-9-7, and it takes 12 hours to detect the leakage from wells D-9-8. Therefore RT-ILDS technology is able to detect leakages correspond to 1% on total injected value over 100 years within a reasonable time.

After the leakage is detected, remediation activities must be implemented to rectify the situation. Remediation activities are outside of the scope of this project.

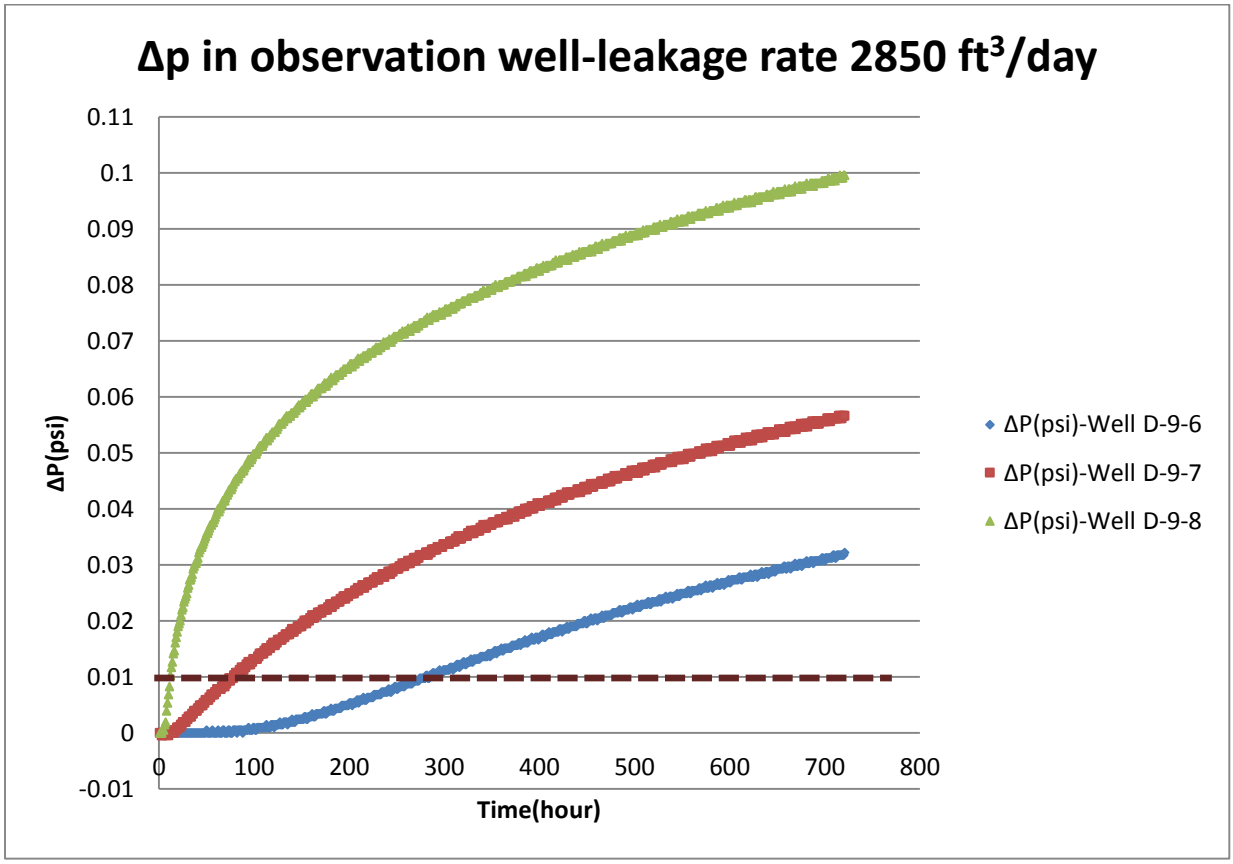

Figure 234. Pressure change in the observation well when leakage rate is 2850 ft^3/day or 1% of the total injected volume.

CONCLUSIONS

An Intelligent Leakage Detection System (ILDS) was developed. This modeling technology was implemented using Citronelle field, a saline aquifer reservoir, located in the U.S. The process included development and history matching a reservoir simulation model for CO_2 sequestration in the Citronelle field. The modeling and history matching included installed PDGs at the injection well and an observation well. High frequency pressure data from PDGs were generated using the history matched numerical model using different CO_2 leakage scenarios. ILDS incorporates machine learning technology for deconvolution of pressure signals.

It was demonstrated that the ILDS is able to detect leakage characteristics in less than a day from its occurrence. The performance of ILDS was examined under different conditions such as multiple well leakages, cap rock leakage, availability of an additional monitoring well, presence of pressure drift and noise in the pressure sensor and uncertainty in the reservoir model.

It is concluded that if there are impermeable (shale) layers between the sand (or carbonate) layers that are host of the CO2 injection, then, in order to have a system that can pick up leakage at any layer in the reservoir, all layers must have PDGs.

APPENDICES

APPENDIX1

CITRONELLE FIELD

The approximate surface area of the Citronelle oilfield is 16,380 acres which is located in Mobile County. The oilfield surrounds the city of Citronelle and covers portions of Township 2 North, Ranges 2 West and 3 West; and Township 1 North, Ranges 2 West and 3 West. This giant oil reservoir has 524 wells which 414 of the m are active now. The production rate of 50000 bbl/month has been reported.

The CO_2 captured from Alabama Power's Plant Barry, is transferred with a short pipeline to Citronelle field to be injected and stored into the brine saturated Paluxy formation at the depth of 9400-10500 ft. The location of the proposed injection well and observation well is shown in in Figure 235. Information about these two well can be found in Table 40.

The proposed storage area, southeast unit, is located more than 8000 ft. below the underground source of drinking water. It occupies about 1520 acres.

There are multiple thick layers with low permeability (shale intervals) in the formation of the proposed injection area that act as a barrier and help to stop the upward movement of buoyant fluid and brine.

The start of CO_2 injection will be 2011 and injection will be continued for up to three years. The total injection is up to 547,500 tons of CO_2 during these three years. The maximum bottom hole pressure constraint of 6300 psi is based on considering the pressure gradient of 0.6 psi/ft at 10500 ft.

Different porous and permeable sandstones layers in the Paluxy formation improve the CO_2 injectivity. Net sandstone layers thickness (11 sandstone flow units) is about 287 ft which is about %60 of the net sandstone thickness. The average porosity for the Paluxy sands is %19 and a thickness-weighted average permeability of 88 md was reported. So the high transmissibility of the Paluxy formation causes a little pressure gain during the injection. The maximum pressure difference for the injection well grid block is 520 psi at the top sand layer.

As the structure dip is so low (about 1.25 degree) at the proposed storage area, there is just a little post-injection up-dip migration.

The maximum plume extend based on the primary simulation results is 1200 ft. This value is defined as an "Area of Review". Two wells, the abandoned well D-9-7 and also an active injection well D-9-8 exist in this area. The migration of CO_2 toward the drinking water source is very unlikely as these two wells are constructed properly. Outside the area of review, in 0.8 mile there is shallow water well at the depth of 529 ft. No faulted or fractured zone within the Citronelle dome structure was found. So all in all, this proposed area is safe to consider as a suitable site for storage.

Table 40. Basic Wells Information

Proposed Injection Well no. 1		
survey, Abstract	Section 9, Township 1 North, Range 2 West	
well location	latitude	31.06486° N (NAD27)
	longitude	88.18201° W (NAD27)
spud date		Dec., 2010
completion date		Jan., 2011
total well depth		11800 ft below GL
elevation	Ground Level	161.36 ft
	Rig Floor	172 ft
injection zone	Paluxy Formation	9415-10520 ft
Injection Interval	Upper Paluxy Sandstone	9415-9810 ft
	Basal Paluxy Sandstone	10455-10520 ft
Proposed Observation Well no. 1		
survey, Abstract	Section 9 Township 1 North, Range 2 West	
well location	latitude	31.06163° N (NAD27)
	longitude	88.17822° W (NAD27)
spud date		Jan., 2011
completion date		Jan., 2012
total well depth		11800 ft below GL
elevation	Ground Level	147.83 ft
	Rig Floor	158 ft
injection zone	Paluxy Formation	9400-10530 ft

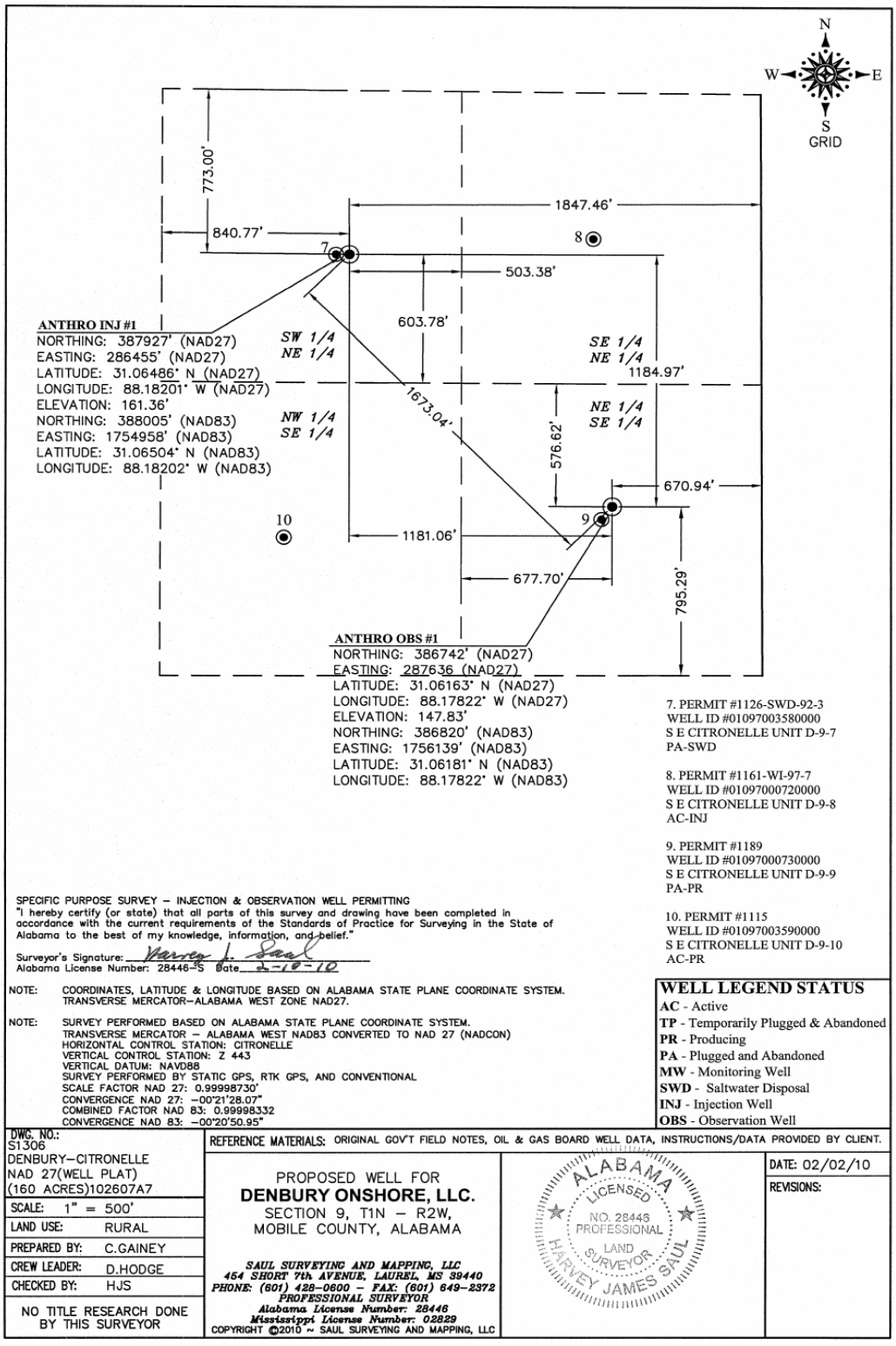

Figure 235 - survey plot showing the location of the proposed injection well, and the proposed observation

APPENDIX 2

THE DE-NOISING PROCESS

DE-NOISING OF PERMANENT DOWN HOLE GAUGE DATA USING WAVELETS

Permanent downhole gauges have been installed in more than 1000 wells worldwide. The continuous pressure measurement allows the operator to make adjustments to the well to optimize recovery. Past experience indicates that permanent down hole gauges are cost-effective even for the single use of well monitoring to assist operational management (Athichanagorn[3]). Additional value could be derived by analyzing the pressure data for reservoir information or using it during history matching.

An operator will attempt to maximize the value from the investment in a permanent downhole gauge acquisition system. However, in practice lots of permanent downhole gauge data have been archived or even discarded because of the lack of tools to process the data. This is because permanent downhole long term measurements are prone to different kinds of errors than data from a short well test. In the traditional well test, the pressure response of the reservoir is measured carefully under a strictly controlled environment. In the case of long term reservoir monitoring using permanent pressure gauges, the well and the reservoir and its fluid composition may undergo dynamic changes. The well may be stimulated or worked over causing the gauge to record invalid measurements.

The pressure data may also be stored at low precision or the system may malfunction creating superfluous outliers and noise. Flow rate data are often not available in the permanent downhole gauge acquisition system. Athichanagorn[3] developed an interpretation methodology for long-term pressure data records from permanent downhole gauges. This methodology is useful when flow rates data are not available or not complete. If flow rates prior to a transient are available, a transient can be analyzed using conventional well testing methods but the data may still be preprocessed using the data processing tools developed by Athichanagorn (Athichanagorn 2002) implemented algorithms to remove outliers and noise from a data set using wavelet transform signal processing. Since the amount of data collected by the permanent downhole gauges is very large, an algorithm to reduce the number of data to a manageable size by eliminating redundant information was also implemented. In order to interpret the permanent long-term data, a complete history of flow rates and the time of flow rate changes are needed, and these records are often unavailable. So Athichanagorn (Athichanagorn 2004) developed algorithms to detect the times at which flow rate changes occur (the break points) and to reconstruct unknown or uncertain flow rates from the pressure data.

Guan et al (Guan 2004) described wavelets as mathematical functions which are used to separate a given function into different components. These components however retain the basic information about the original signal thus allowing the original signal to be reconstructed. There are in existence different types of wavelets, which lend themselves to different applications, there is the Haar wavelet, which is the first wavelet proposed and there is the Daubechies wavelet, which has been the most widely used wavelets in signal processing(de-noising and compression), image compression to name a few processes. Guan et a l. also report the use of thresholding

methods to filter the data from PDG's, a soft thresholding method for the discontinuous regions of the data, and a hard thresholding method for the continuous regions of the chart.

Unlike Fourier transforms which are limited to signals that do not change over time, Wavelet transforms are well suited for transient data such as those we receive from PDG's.

With respect to data compression, Bernasconi et al. (Bernasconi 1999) reported that by using a Wavelet transform algorithm, data compression ratios of 15:1 were achieved without any data degradation upon decompression. Higher compression ratios of up to 50:1 have been reported without significant deterioration of the original data upon decompression

Althichanagorn et al. proposed a 7 step process for data processing data from PDG's. The first steps involves using the wavelet transform to remove outliers from the collected data and then to de-noise the data. We can obviously determine outliers by merely observing the data trend and observing those points that do not follow the general trend of the data.

Kikani et al. (Kikani 1998)report that data is reduced at each level by a factor of 2. Thus by using a DB wavelet to decompose to a level of 10, a stream of data with 12000 points can be reduced to 6 points. Obviously this is an extreme case and we will probably stop at level 7 with 47 points so that the general trend of the data. But this highlights the power of the Wavelet transform in the compression of data.

Dr. Stark (Stark 2005) describes wavelets transforms and how to compute them using the Matlab software. He presented several exercises showing the merits of the wavelet transforms over the Fourier transform. In one such exercise, the two methods are used to represent an "attack" signal and the Fourier transform misses several peaks of the original signal while the wavelet captures all the significant portions of the original signal. Thus a lot of people in literature have described compression using Fourier transform as "lossy" data compression as part of the original signal is typically lost during the transformation.

Two methods of wavelet analysis are presented in Dr. Stark's book; Dicrete Wavelet analysis and Continuous Wavelet analysis. The names imply that the continuous wavelet analysis deals with transforms of continuous time signals, and vice versa with the discrete wavelet analysis.

Dr. Stark discusses transforming signals into wavelets and the subsequent reconstruction of the original signal. This is of interest to our research as after de-noising our signal we would like to reconstruct the original signal we started with before we proceed to compression of the data.

The Wavelet Toolbox in MATLAB allows one to perform a number of analyses on either 1 dimensional or 2 dimensional data. For our Research we only deal with 1 dimensional data. Figure 236 shows a flow chart of how one would expect to de-noise the data using the transform.

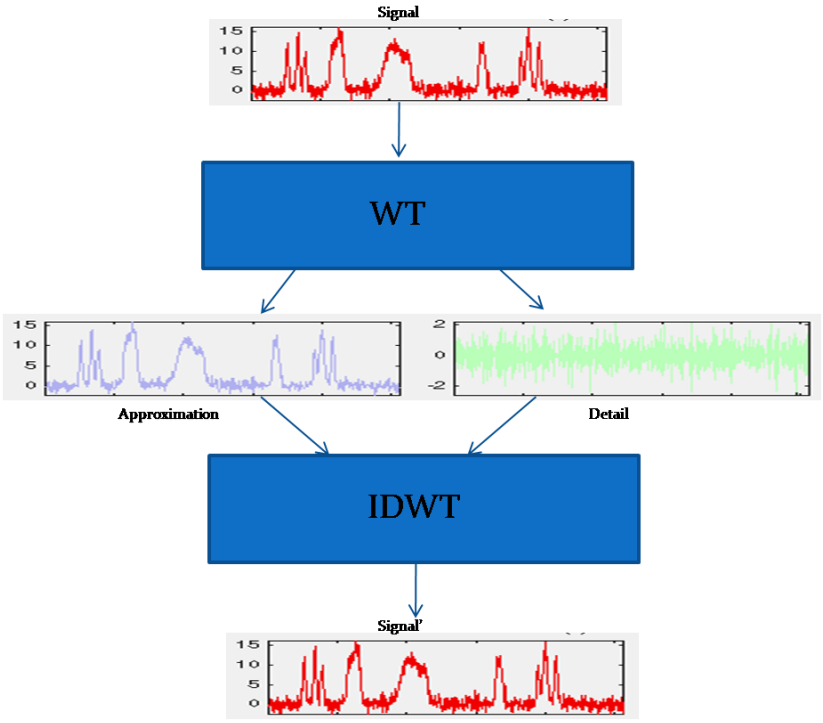

Figure 236. Wavelet Transform and Inverse Wavelet Transform Flow Chart

There are sample signals saved in the toolbox to serve as demos and we have focused on the signal for electrical consumption with time. Figure 237 below shows the original demo signal.

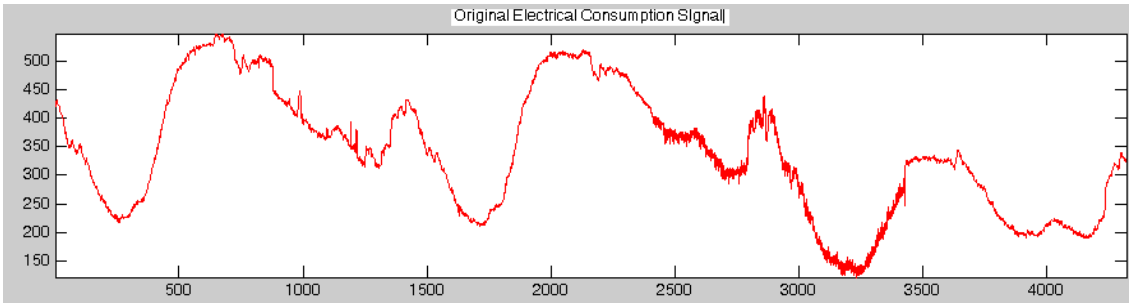

Figure 237. Original Noisy Signal for Electrical Consumption

There are a number of operations which can be performed on the original signal such as de-noising, compression and decomposition. The software also presents the user with a number of wavelets to use for the analysis, such the Haar wavelet, the DB wavelet, the orthogonal wavelet.

For this analysis the DB wavelet has been used. The reason for choosing this wavelet was simply to follow the examples in the book. The first analysis was in de-noising the signal provided. After

selecting the de-noise button, there is a default thresholding of the signal performed by the software. The user can go in and manually reduce the threshold and clean up the signal more or simply use the default settings of the software. Following de-noising, the signal is saved. Figure 238 is a comparison of the original signal to the de-noised signal.

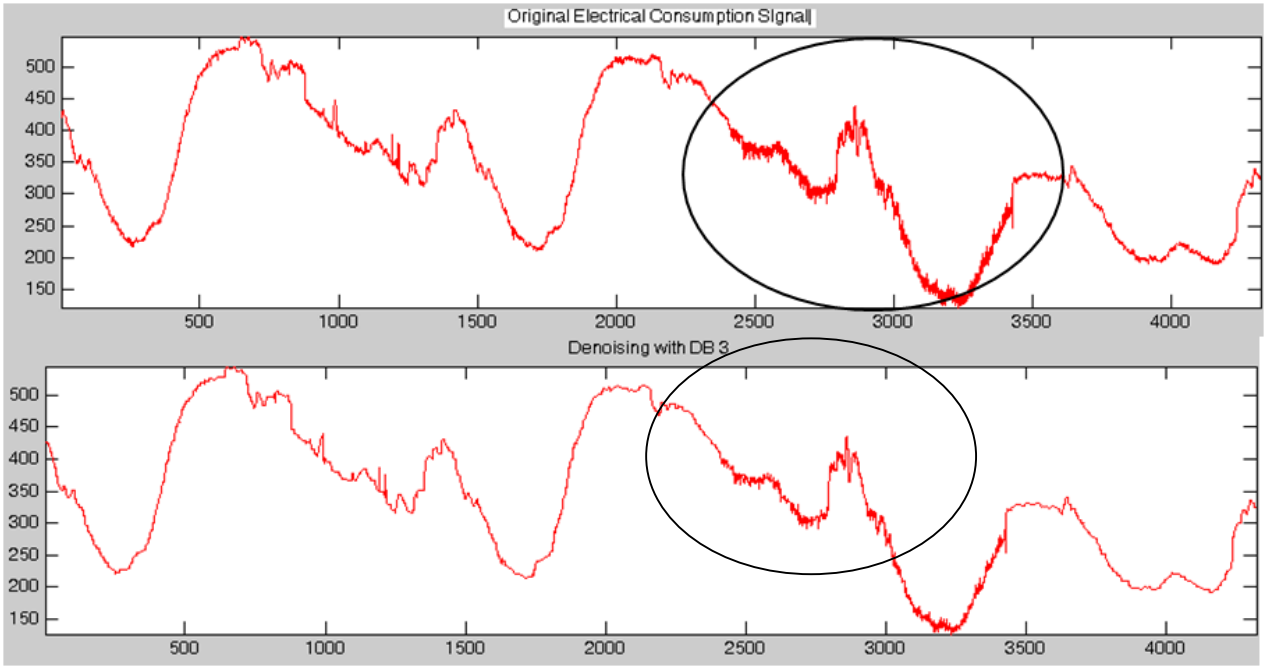

Figure 238. De-noised Signal Using Wavelets

Looking at the comparison of the two signals above, a reduction in the noise can be noted when comparing the original signal to the de-noised signal

The objective of this part of work is to illustrate the feasibility of using wavelets in de-noising data obtained from permanent downhole gauges. Once de-noised, the data will then be summarized and ready for further analysis.

METHODOLOGY OF DE-NOISING USING WAVELET

To accomplish the stated objectives, the following steps are taken.

1. Read the data pressure data into Matlab
2. Perform Wavelet De-noising using Matlab
3. Write and summarize the data into Microsoft excel

Reading Pressure Data into Matlab

To generate the data used for de-noising, a reservoir model was generated using a reservoir simulator (CMG IMEX). The data was imported into excel and noise was simulated and added to

it. A function was generated to add noise to the data from the simulator to simulate a real injection case.

Noise = 2.5*Randbetween (-20,20)

Figure 239 shows the comparison between the original data and noisy data.

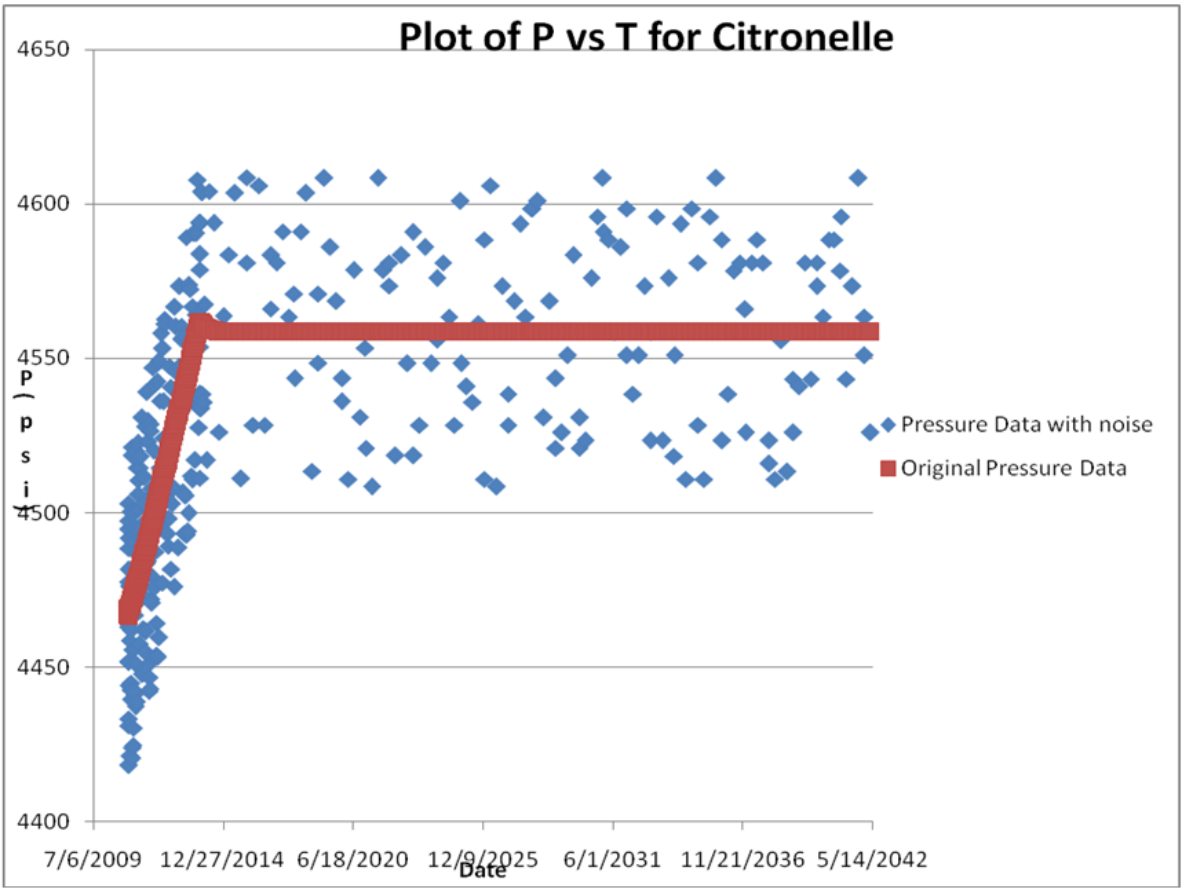

Figure 239. Comparison of Noisy and Simulated Data

A code was generated to read the data into Matlab. The code is shown below.

C = xlsread('filename.xls')

Figure 240 shows a screen shot of data being read into Matlab.

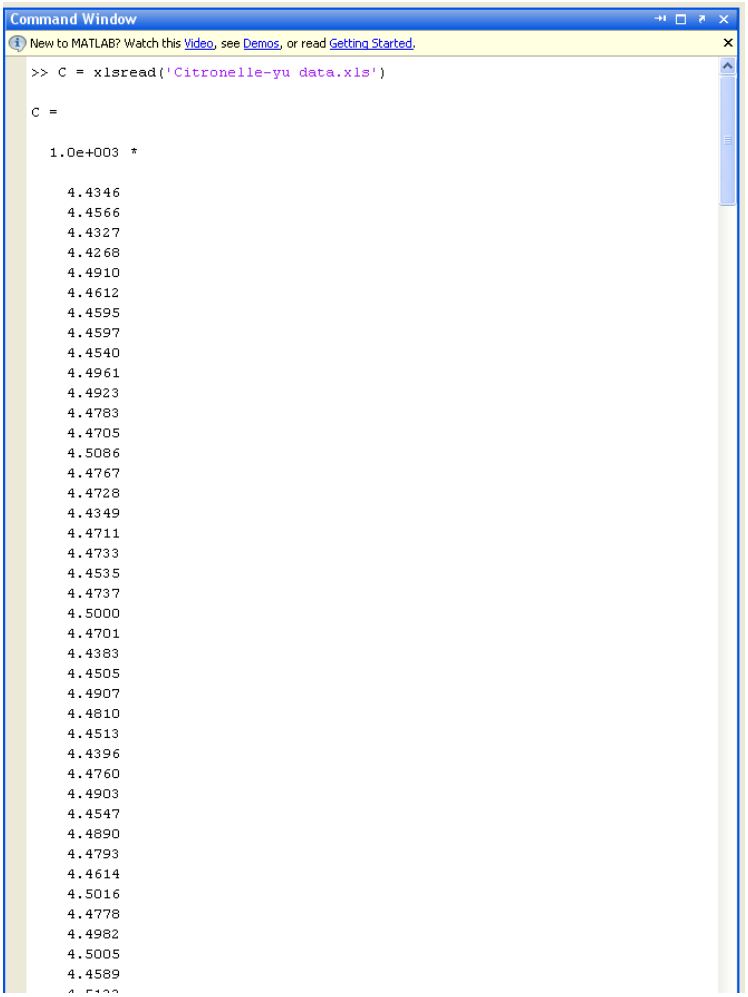

Figure 240. Screenshot of data reading

PERFORM WAVELET DE-NOISING USING MATLAB

The code to de-noise the data is shown below and makes use of wavelet transforms of the sym family. We use this wavelet due to the fact that it is able to provide useful surface texture features. The code used to de-noise is shown below

```
sig = C;

[sden,cfs] = cmddenoise(sig,'sym4',5,'s');

subplot(2,1,1); plot(sig,'r'); axis tight

hold on; plot(sden,'k');

title('Original and denoised superimposed signals')

subplot(2,1,2); plot(sden,'k'); axis tight
```

```
title('Denoised signal')
```

A screen shot of the program upon executing is shown below in Figure 241.

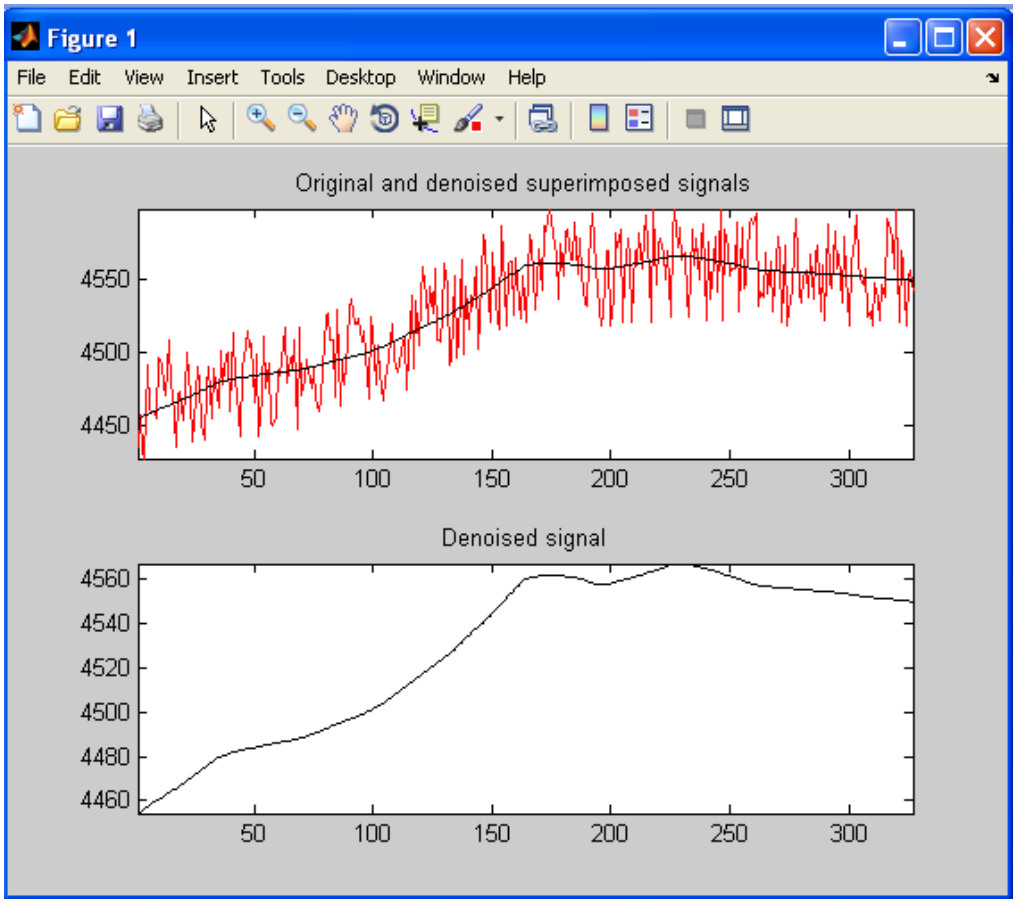

Figure 241. Application of code to noisy data

To Write data into Excel

To write data into excel, the following code was used

```
xlswrite('Denoiseddata.xls', sden')
```

A snapshot of this is shown in Figure 242.

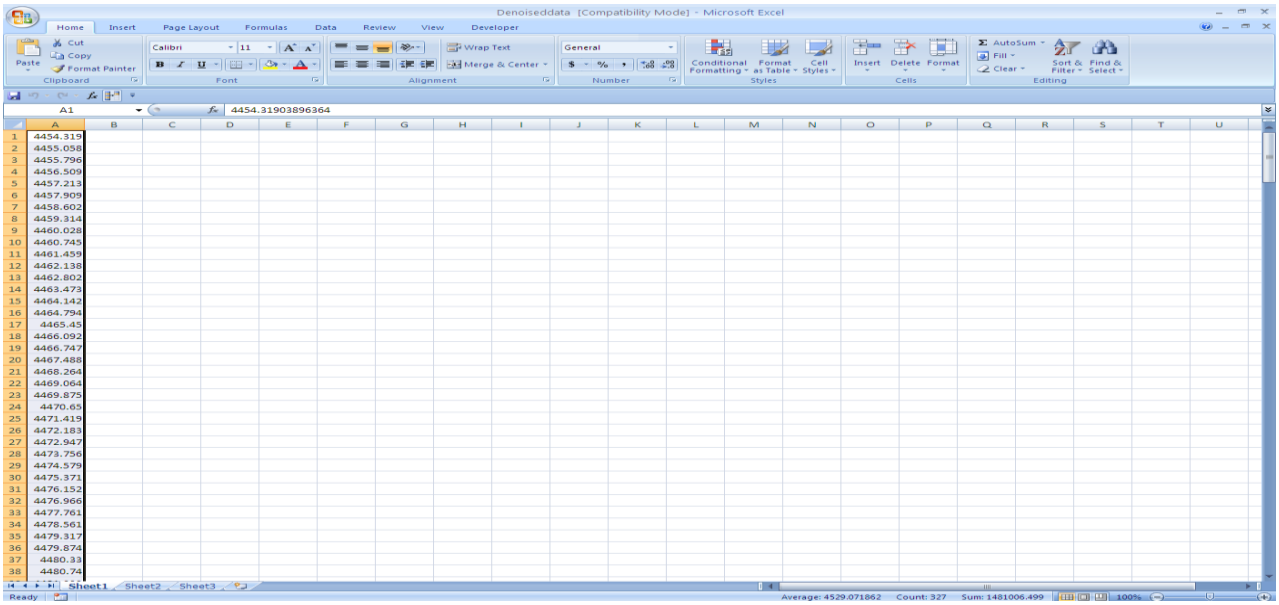

Figure 242. Screen shot of de-noised data in excel

The results of application of the wavelets can be seen in Figure 243 where the data obtained after De-noising is compared to the noisy data and the original data from the reservoir simulator.

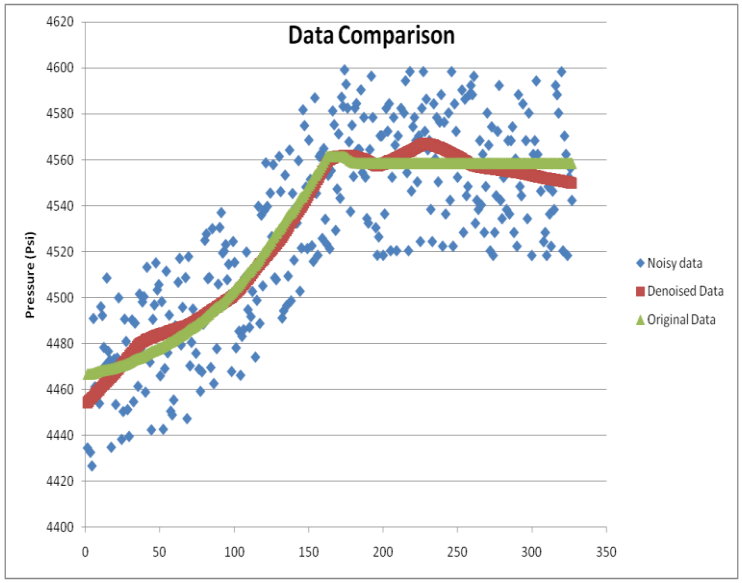

Figure 243. De-noising data comparison

It was observed that different decomposition levels of the wavelets could be used, but the higher the level of decomposition, the better the noise removal. The smaller the level of decomposition the more artifacts of the noisy signal remain.

The maximum error between the de-noised data obtained and the original data was 0.27%. This shows a good applicability of wavelets to noise reduction.

HIGH FREQUENCY DATA GENERATION

Reservoir Modeling

The main objectives of this work were generating high frequency data from flow model, simulating noise by distorting the data and finally pre- processing and summarizing high frequency distorted data for the next step (Pattern Recognition).

For this study the grid geometry of WVU reservoir simulation model was changed to provide high resolutions data for pattern recognition analysis. This model consists of 150 by 150 grids in I and J direction (Figure 244) with the size of 133*133 ft. Totally 51 layers in the vertical direction was considered for modeling this reservoir.

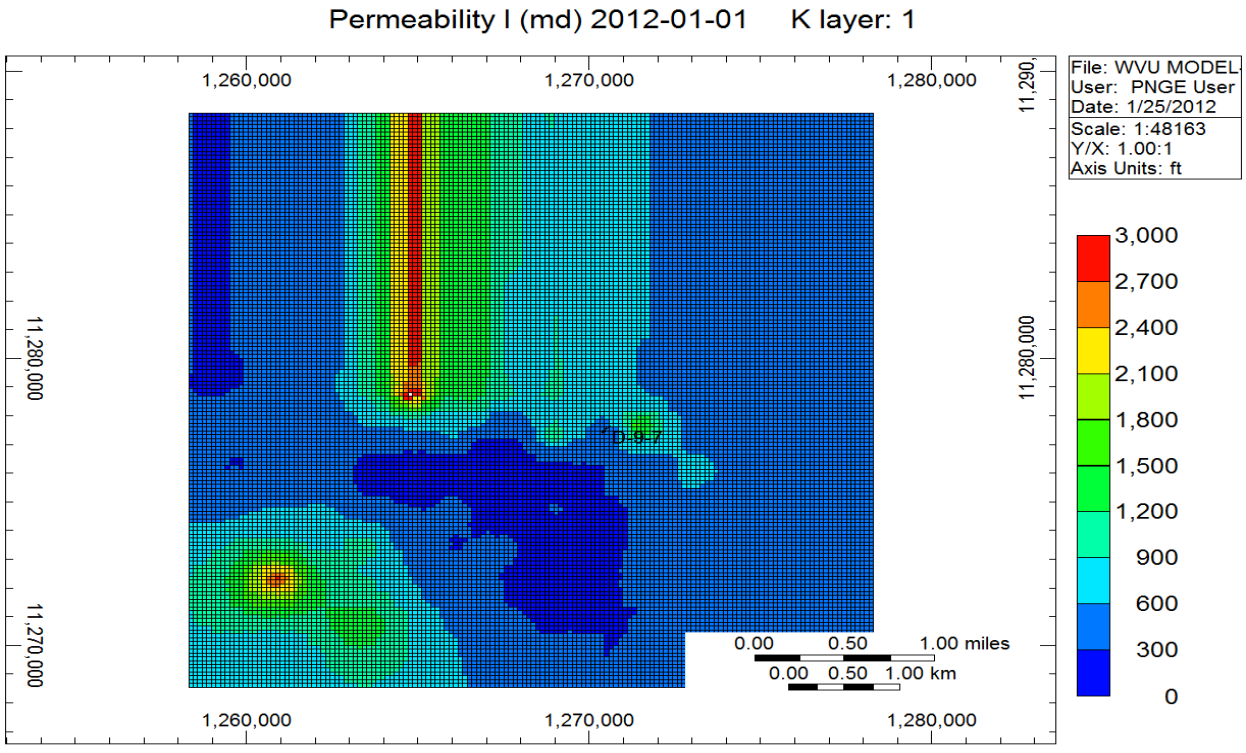

Figure 244. Totally fine grid model with heterogeneous permeability

Also in this model a correlation between porosity and permeability was considered to introduce heterogeneity to the reservoir. Based on available core and log data from the same layer (Paluxy) of the Citronelle surrounding Fields, a core plot of permeability versus porosity was generated.

Because the data was so scattered, it was not possible to find an appropriate and unique pattern that relates permeability to the porosity. Therefore the data was divided to 5 different categories based on the magnitude of permeability and R^2 (Figure 245). These 5 categories represent very poor, poor, average, good and excellent rock conductivity respect to CO_2 plume extension in the reservoir.

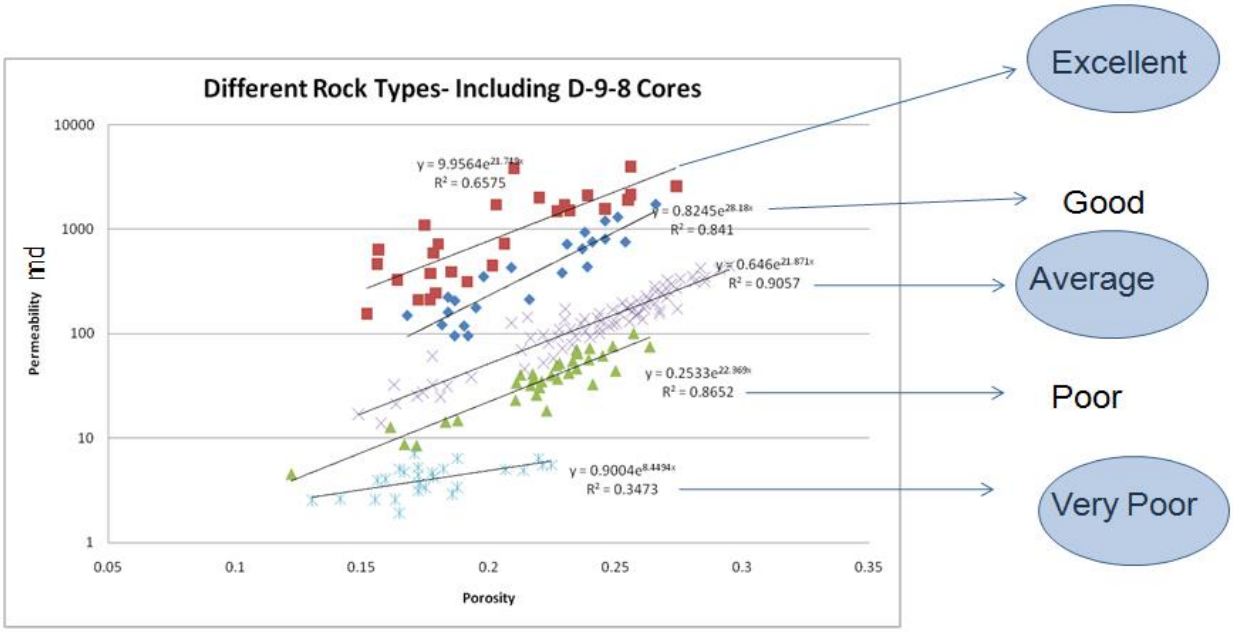

Figure 245. 5 different permeability realizations based on the rock conductivity

In the case that “Excellent” permeability was assigned to the reservoir (Figure 244) maximum CO_2 plume extension (about 4000 ft.) was observed in the top layer (Figure 246). The second largest CO_2 plume was observed in the 19th vertical layer.

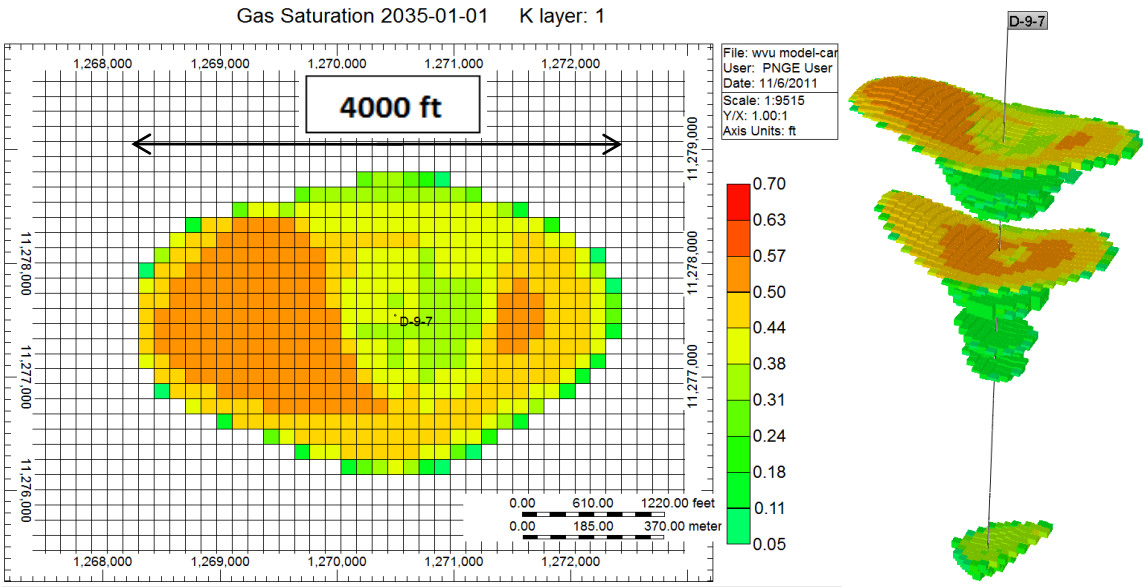

Figure 246. CO_2 Plume extension in different layers of the reservoir

The maximum extension of the plume can be seen in the first layer of the reservoir. This layer (Figure 247 and Figure 247) ,which includes CO_2 injection well (D-9-7), observation well (D-9-8) and 3 existing wells (D-9-2, D-9-6, D-9-10,) - was considered for the simulation of the CO_2 leakage through the well (permeability and injection were increased to enlarge plume extension in South –North direction and consequently CO_2 reaches to well D-9-2 and D-9-10 for high frequency data generation based on different leakage scenarios).The extension of the plume is different from the previous study because here the heterogeneity affects the shape and extension of the CO_2 plume(in previous model the permeability for all the grids in the reservoir were set to 400 md).

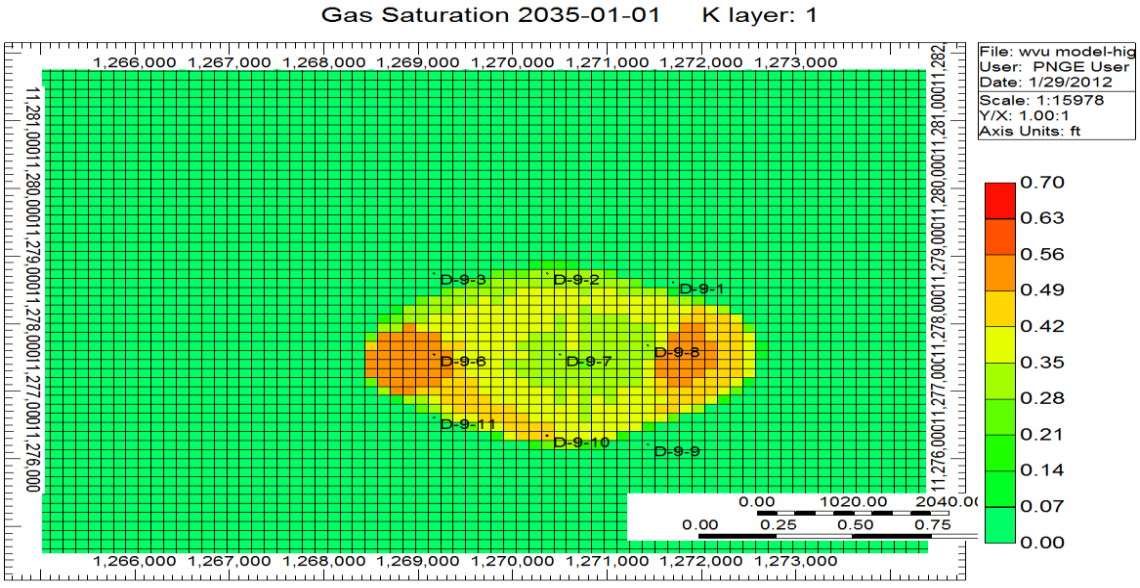

Figure 247.CO_2 Plume extension in first layer of the reservoir and location of the wells

HFD Generation

Totally 12 different leakage scenarios were studied based on the leakage rate and combinations of the wells that experience the leakage. For each scenario, the pressure behavior in the observation well (D-9-8) was recorded from the simulation results to generate high frequency data with noise and outlier

The next step was to generate high frequency data for pressure in the observation well (D-9-8) during the injection and equilibrium period (post injection). In order to do so, reservoir simulation run was performed based on “1-day” time step. The daily pressure results were converted to hourly results by using linear interpolation. Therefore high frequency (hourly based) pressure records were generated for well D-9-8 during 3 years of injection and 20 years after the end of injection (Totally 201623 data points were recorded for pressure).

Adding Noise and Outliers

There are in general, two types of measurement errors when managing long-term data, **Noise** is a group of data points that scatter around the trend of the overall data but lie in the same neighborhood as the true data and **Outliers,** that are data points that lie away from the trend of data. Because the data outlier is isolated, it causes a discontinuity in the data stream. Both of them can be identified from their misalignment with the rest of the data.

The raw data in the hourly base are coming from the numerical simulator which here is CMG. The data include 23 years of pressure data at the observation well (D-9-8). In the real case these data are coming from the Permanent Down-hole Pressure Gauges installed at the D-9-8. Since in the real case these data are including the noise and outliers, these items have been added artificially. The noise generation process includes adding maximum two percent of the pressure range to the data. For the outlier points maximum pressure of 30 psi has been considered. The noise and outliers were distributed in a randomly manner to the different points (Figure 248, Figure 249 and Figure 250). White noise has been used to generate distorted pressure data.

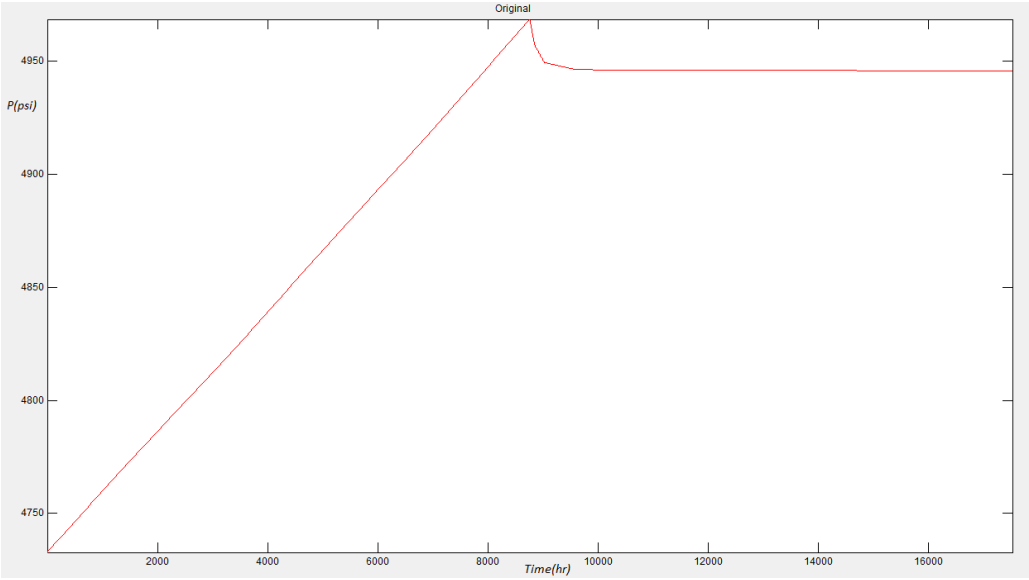

Figure 248. Pressure data for 2 years (year 2014 to 2016) without any noise

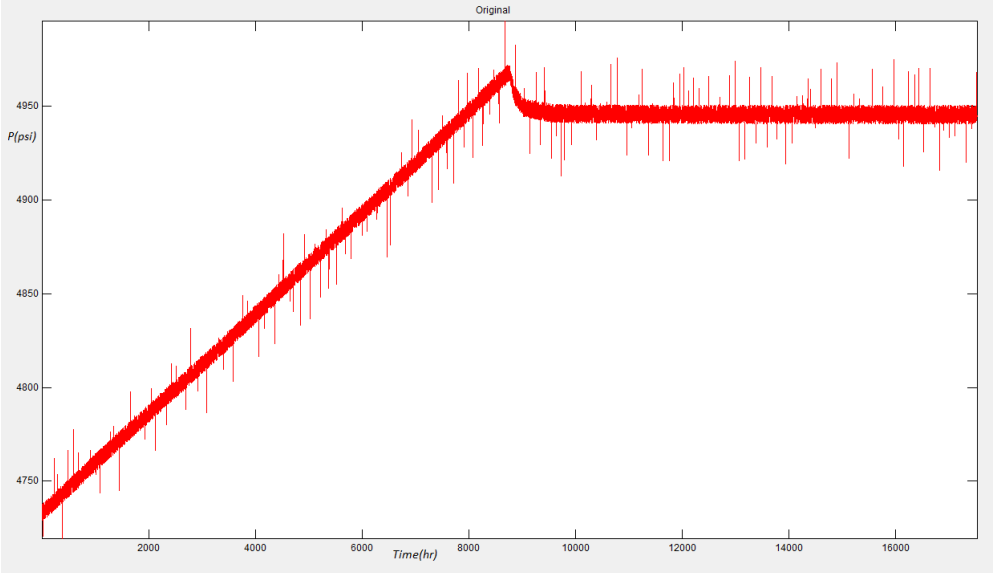

Figure 249. Pressure data for 2 years (year 2014 to 2016) after adding the noise and outlier

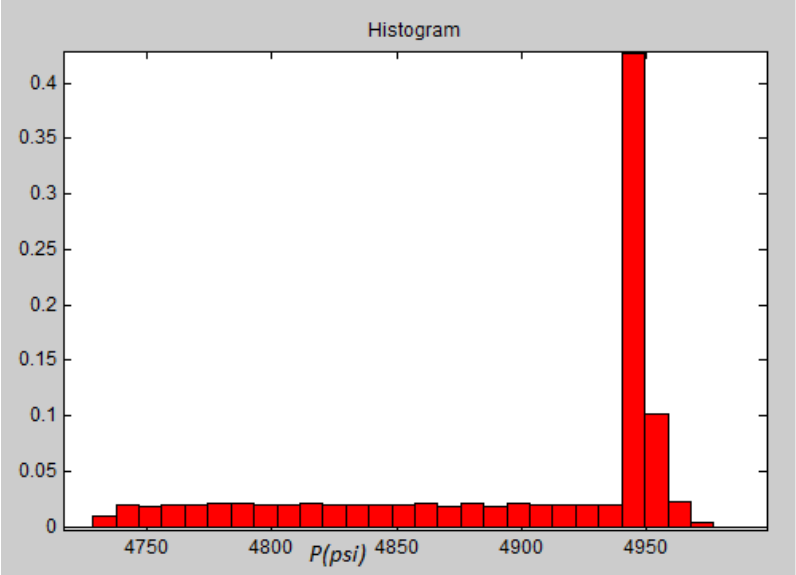

Figure 250. Histogram Pressure data for 2 years (year 2014 to 2016) after adding the noise and outlier

DE-NOISING AND DATA SMOOTHING

In order to extract the most representative features from the data and reduce fluctuations, a procedure called **de-noising** is commonly applied. Most of the de-noising methods tend to smear out sharp features in the data. The method being used in this project is denominated the **Wavelet Thresholding Method** which generally preserves most of these features.

Wavelets are mathematical functions that divide or separate data into different frequency components, and then study each component with a resolution matched to its scale, basically provides a multi-resolution framework for data representation. They have advantages over traditional Fourier methods in analyzing physical situations where the data contains discontinuities and sharp features.

The general de-noising procedure consists of 3 different steps. First of all the noisy data should be divided to N levels, following by decomposition of the data at level N. After that for each level from 1 to N, a threshold should be considered and then soft thresholding should be applied to the detail coefficients. Finally the data is reconstructed using the original approximation coefficients of level N and the modified detail coefficients of levels from 1 to N.

The important step in de-noising data is threshold selection method for each level. Three threshold selection rules are implemented in this study as: Rigorous SURE, Heuristics SURE and Fixed form threshold. The results of de-noising the data implementing 3 mentioned thresholding methods for the case that no leakage occurs in the reservoirs are depicted in Figure 251, Figure 252 and Figure 253.

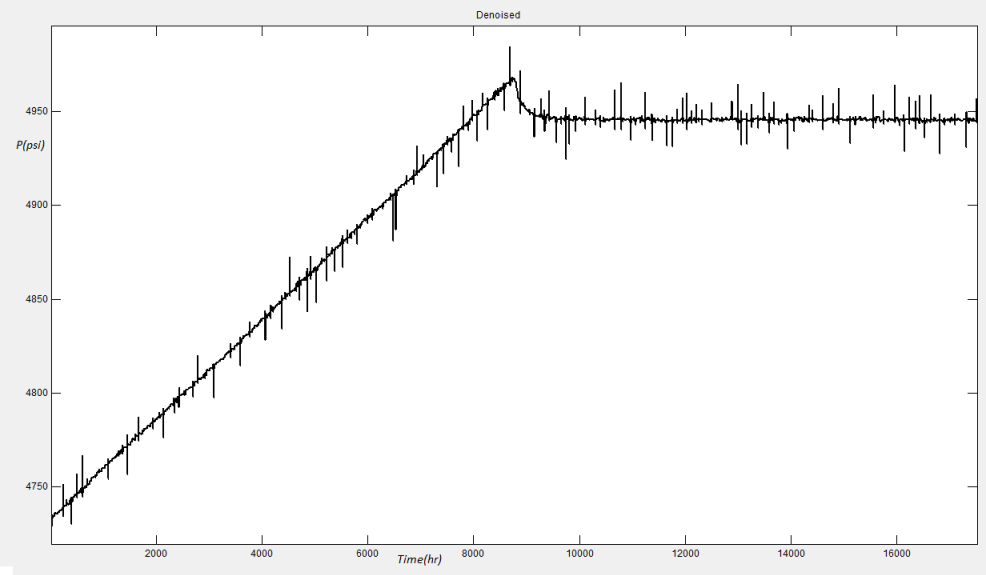

Figure 251. Rigorous SURE thresholding method

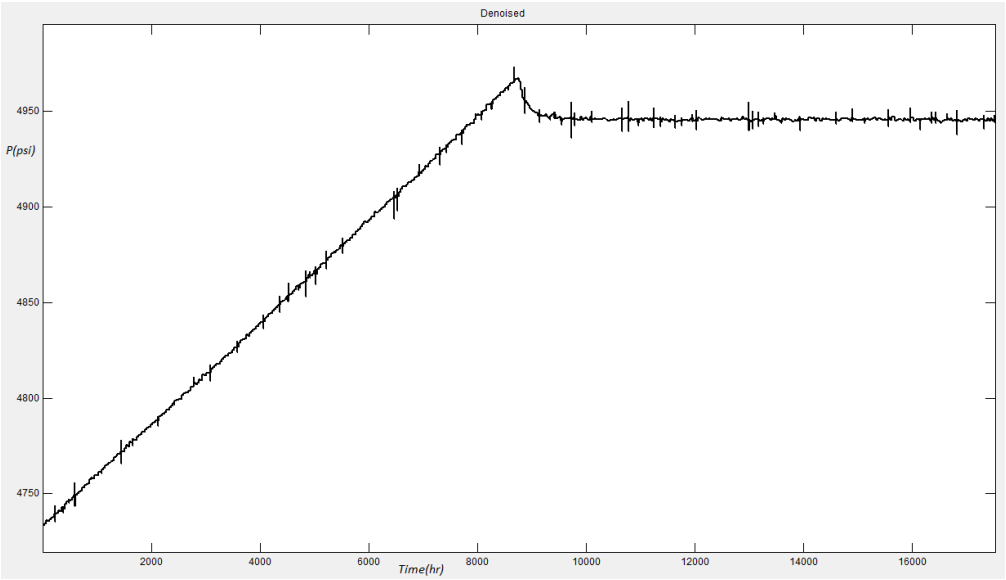

Figure 252.Heuristics SURE thresholding method

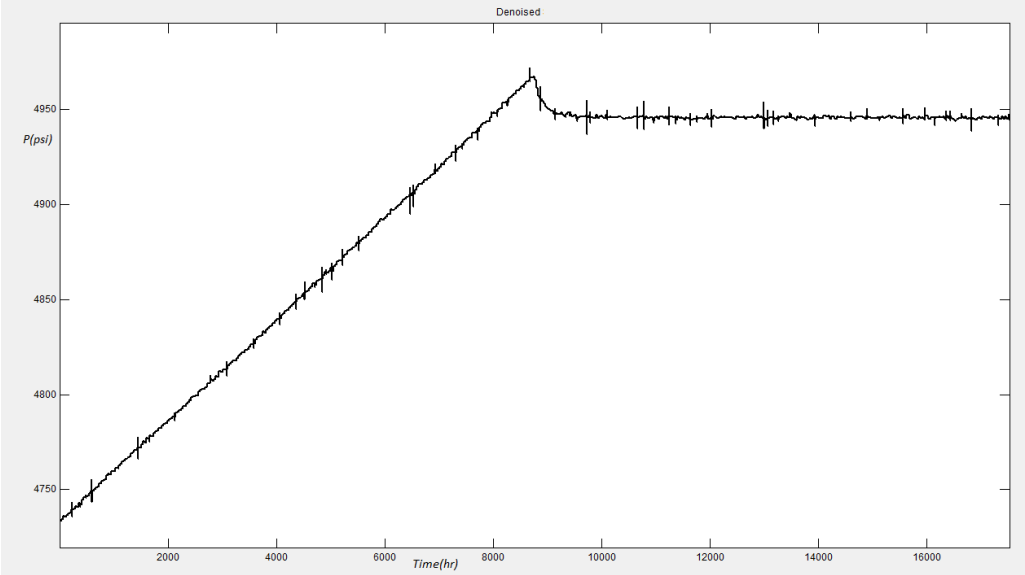

Figure 253.Fixed form threshold method

Comparison between the results shows that by using Fixed form Threshold method, noise and outliers can be removed more effectively. Hence Fixed form Threshold was used for de-noising pressure results for all different leakage scenarios.

Also several methods have been developed regarding wavelet shrinkage and thresholding. The main two thresholding methods are the soft-thresholding and hard-thresholding method. The main difference between them is that the soft-thresholding method consists on analyzing the difference between the wavelet coefficients and the chosen threshold smoothing the data once the wavelet transform is applied. In the hard-thresholding method, wavelets coefficients whose absolute values are less than the threshold are set to zero. Depending on the scale and particular characteristics of the data either method can be used and the result is a cleaned-up data that will still show important details. Based on the results, the soft thresholding shows better effectiveness in removing outliers. This method (soft) is applied for de-noising in this study.

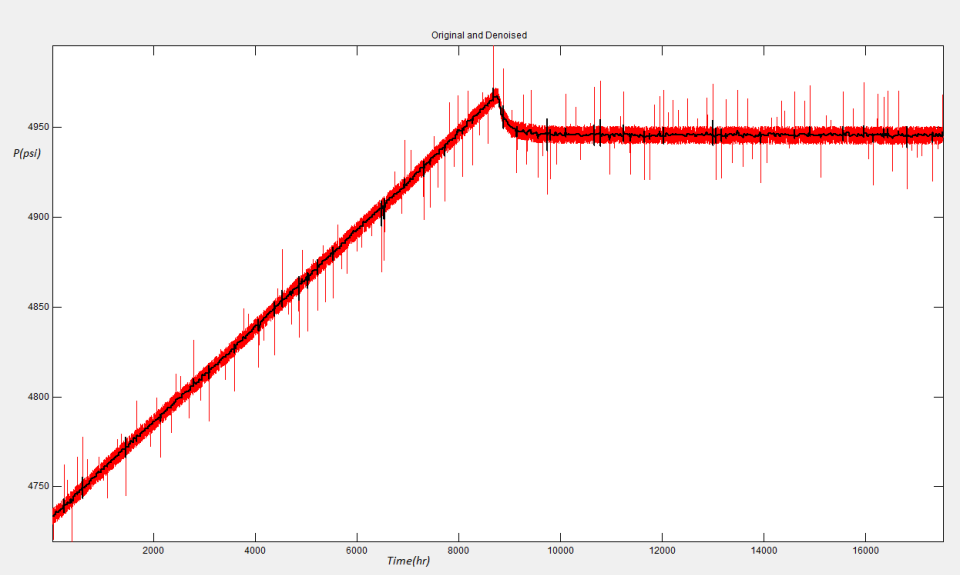

Figure 254. Soft thresholding (red: noisy data, black: de-noised data)

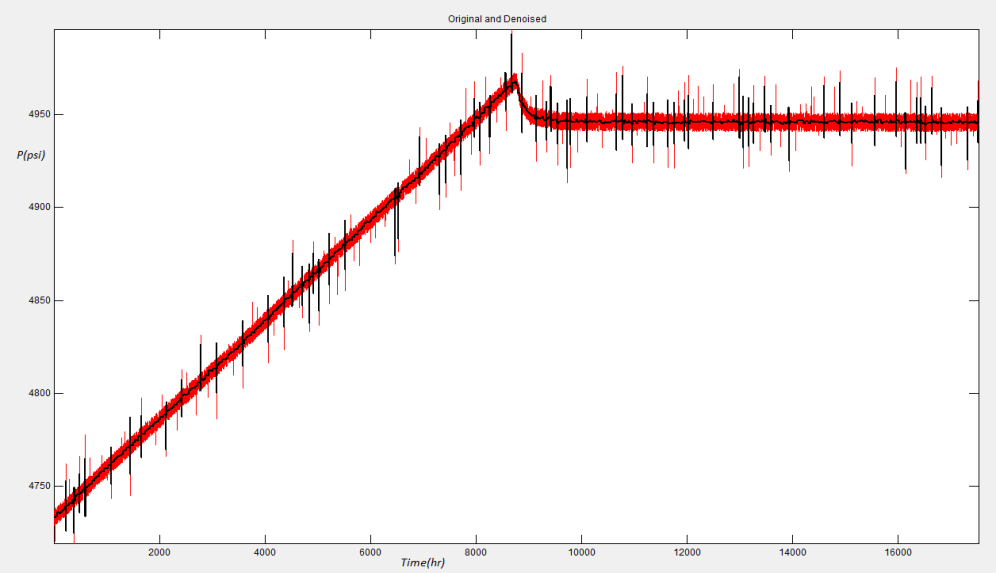

Figure 255. Hard thresholding (red: noisy data, black: de-noised)

After first time of de-nosing the data it can be seen that still some outliers were converted to the small noises. If the de-noising process is repeated for the de-noised data, it is possible to decrease the magnitude of the remaining noises a little bit. This can be seen in Figure 256 where the de-noised data reprocessed again.

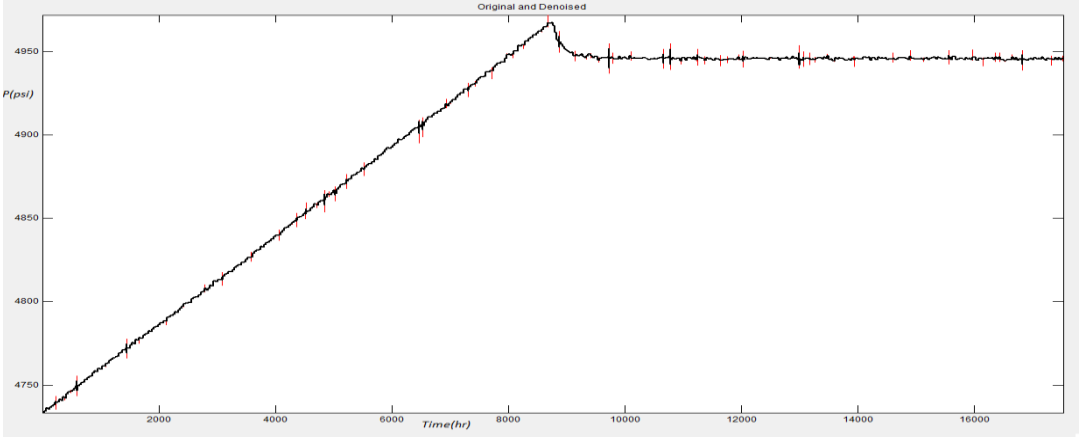

Figure 256. Reprocessing the de-noised data (red: noisy data, black: de-noised data)

Finally we performed the de-noising process for 12 different leakage scenarios that occurs in the first layer of the Citronelle field. Different combination of leaking wells and leakage rates for the wells D-9-2, D-9-6 and D-9-10 were considered according to

Table 41. The pressure in the observation well converted to high frequency data with added noise and outliers. At the end the noises and outliers removed by Soft-Fixed Form Threshold method. The results of de-noising the pressure data in all the scenarios is shown in figure 14 to 26. The results represent the pressure in the observation well during the post injection period.

Table 41. Different combination of leaking wells

Scenario	Well Status			Constraints Injection Gas Rate, ft3/d		
	D-9-2	D-9-6	D-9-10	D-9-2	D-9-6	D-9-10
1	"OPEN"	"OPEN"	"OPEN"	2.00E+06	2.00E+06	2.00E+06
2	"OPEN"	"OPEN"	"OPEN"	1.00E+06	1.00E+06	1.00E+06
3	"OPEN"	"OPEN"	"OPEN"	1.50E+06	1.50E+06	1.50E+06
4	"CLOSE"	"OPEN"	"OPEN"	-	1.00E+06	1.00E+06
5	"CLOSE"	"CLOSE"	"OPEN"	-	-	1.00E+06
6	"CLOSE"	"OPEN"	"CLOSE"	-	1.00E+06	-
7	"OPEN"	"CLOSE"	"CLOSE"	1.00E+06	-	-
8	"CLOSE"	"OPEN"	"CLOSE"	-	2.00E+06	-
9	"OPEN"	"CLOSE"	"OPEN"	2.00E+06	-	2.00E+06
10	"OPEN"	"CLOSE"	"CLOSE"	2.00E+06	-	-
11	"CLOSE"	"CLOSE"	"OPEN"	-	-	2.00E+06
12	"CLOSE"	"OPEN"	"CLOSE"	-	1.00E+06	-

DETERMINATION OF NOISE DISTRIBUTION AND LEVEL

There are two pressure down-hole Gauges (PDG) installed in the observation well (D-9-8#2) in Citronelle field. These gauges are located at the depth of 9416ft and 944 ft) with the intention of providing real time pressure and temperature data during and after injection period. The pressure data is available from 8/17/2012 to 11/29/2012 at every minute. It should be mentioned that there are some gaps in the pressure records due to onsite computer failure. The pressure trends from the PDGs are illustrated in Figure 257.

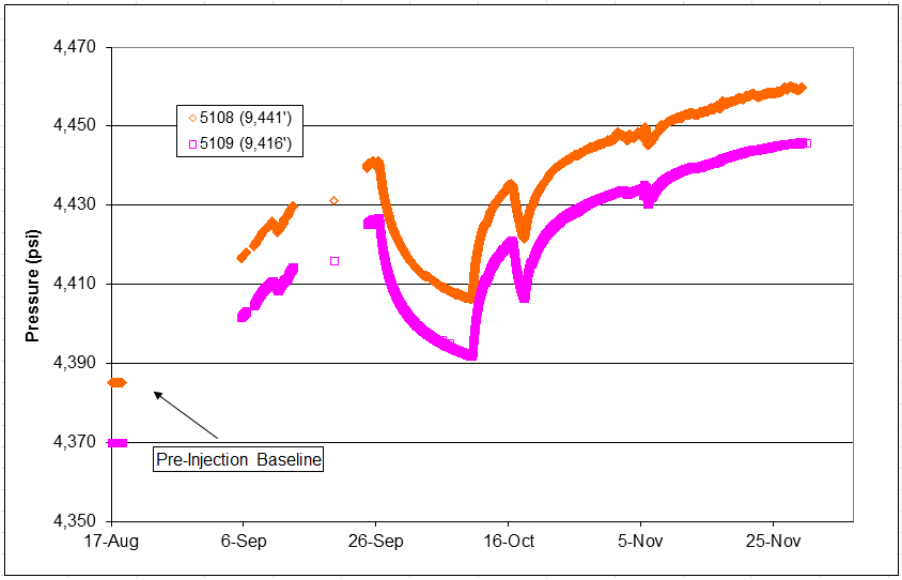

Figure 257. Monitoring Well (D-9-8#2) PDG data

Up to this point it has been assumed that associated random noise have continuous uniform distribution (or rectangular distribution), since we did not have access to actual data; which means that in the interval of the assigned noise (2% of pressure value) the chance of picking any random value is equally probable. Having access to actual pressure data enables us to analyze the characteristics of the noise in a practical way.

In order to prepare high frequency data for pattern recognition (and also de-noising process) it is necessary to evaluate the noise behavior. There are two main features in the noisy pressure data that requires a more detailed analysis, namely: Noise distribution and Noise level.

The noise level can be determined by knowing the difference between actual data and the fitted curve of the same data over a predefined time interval (with no fluctuation in the data).

$$Ni = P_{actual} - P_{fitted} \rightarrow Noise\ Level = \left(\frac{1}{n-1}\sum_{i=1}^{n} N_i^2\right)^{1/2}$$

6,500 pressure records in the interval of 26th to 29th of September, when the pressure trend has no sharp transients, were selected. Generalized Regression Neural Network (GRNN) was used to determine the fitted curve of the selected data. The results of curve fitting are shown in Figure 258.

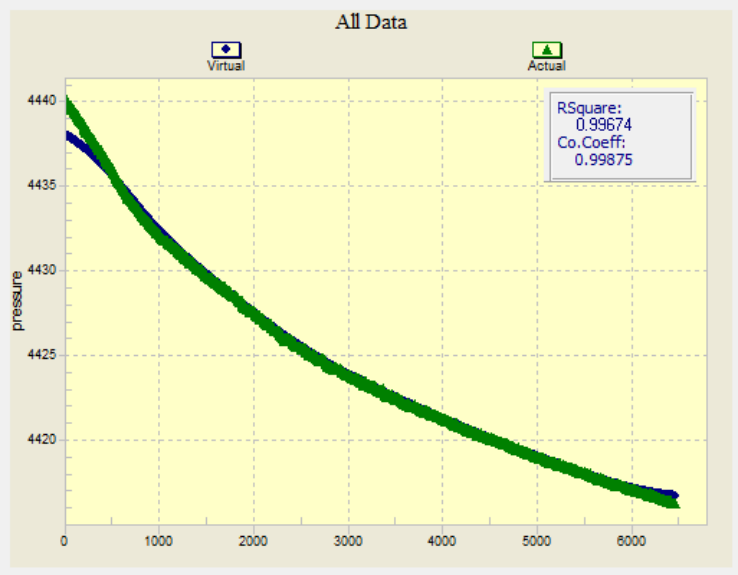

Figure 258. GRNN results for fitted pressure curve

According to the abovementioned formula the noise level is 0.08 Psi. The maximum and minimum value of the *Ni* is equal to 0.185 and -0.282 respectively. The frequency distribution of the noises was generated as well. Based on the results it can be concluded that the noises represent Normal or Gaussian distribution (Figure 259). Therefore the noise with the mentioned characteristics will be added to the pressure data acquired from different realization built and run using reservoir simulation. The noisy and de-noised data would be preprocessed to be transformed into a format that is suitable for pattern recognition analysis.

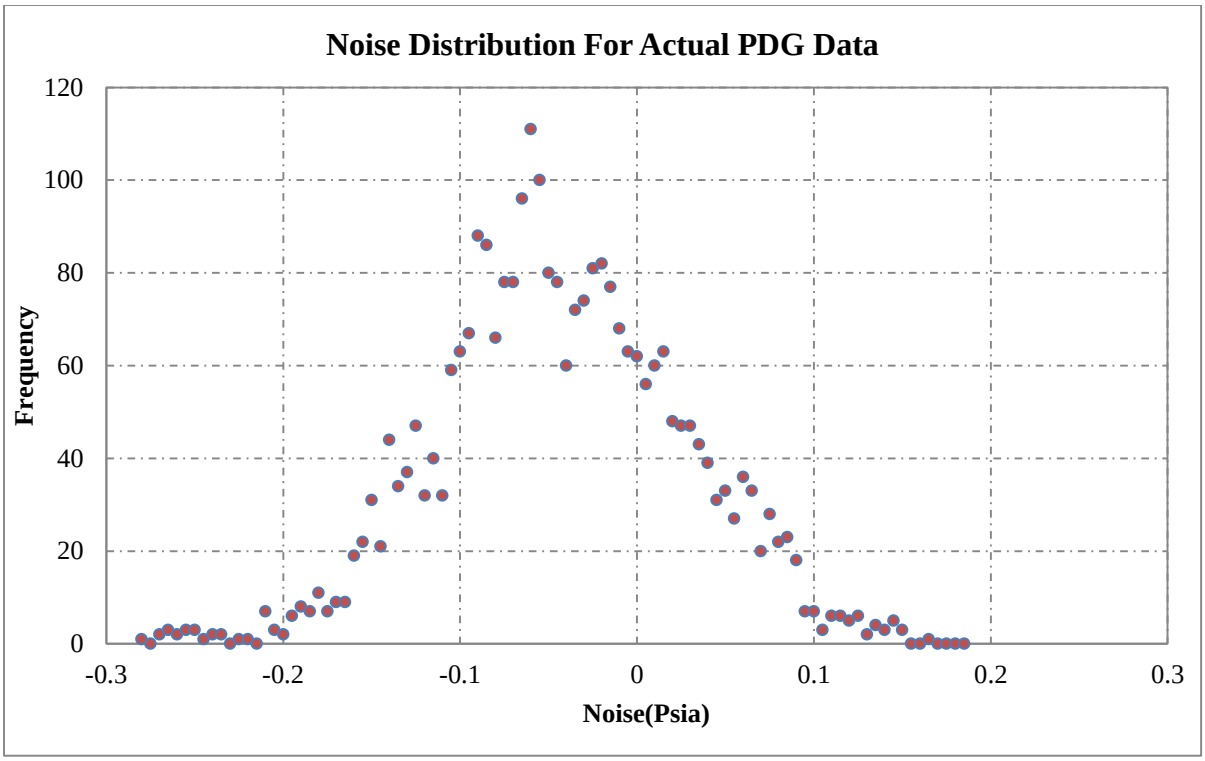

Figure 259. Noise distribution for actual PDG data (6500 records, Normal Distribution)

ADDING NOISE TO THE SIMULATION DATA, DE-NOISING AND DATA SUMMARIZING

Three wells (D-9-2, D-9-6 and D-9-10) were considered as the possible locations of the CO_2 leakage in the reservoir simulation model. For each of these candidates, twenty CO_2 leakage rates- in the range of real leakage rates observed in actual cases- were set as the constraint and corresponding pressure changes in the observation well were recorded (representing PDG data). Those pressure data was considered to be clean with no noise or outlier. The noise with the same characteristic (mentioned earlier) was added to the pressure data. The data was processed afterward in order to perform data cleansing. Based on the characteristic of the noise in this case, "Daubechies wavelets 10" in five levels were used to decompose the noisy data. After decomposition to 5 levels, a threshold was assigned to each level to remove the outliers. Then the processed data from each level were combined to reconstruct the De-noised data. It is worthy to mention that for each leakage scenario (leakage location and rate) the corresponding pressure difference readings ($\Delta p = P_{(No\ leakage)} - P_{(Leakage)}$) were summarized over a predefined period of time by descriptive statistics in order to extract the main and most important features of real time data. In this case we also summarize noisy and De-noised pressure data over three time periods (1,2 and 3 weeks after leakage - pressure readings are hourly basis) to prepare data for pattern recognition technology and Neural Network development. An example of pressure data from simulator, the same data with normal distributed noise and cleansed (De-noised) data when CO_2 leakage occurs in well D-9-6 leaks with the rate of 30 Mcf/day are shown in Figure 260. The results of pressure data summarization for both noisy and de-noised records are listed in

Table 42.

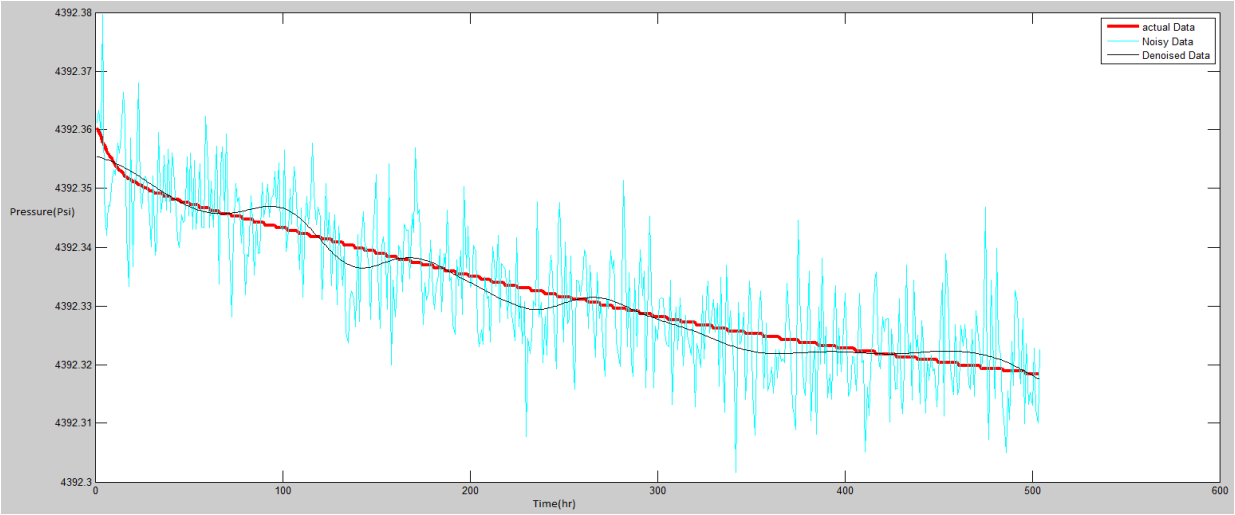

Figure 260. Presure data from simulator(red),added noise(green) and denoised (black) when well D-9-6 leaks with the rate of 30Mcf

Table 42 Data Sumerization of noisy and De-noised ΔP for 3 weeks after the leakage

	Noisy ΔP			De-noised ΔP		
	Week1	Week2	Week3	Week1	Week2	Week3
Mean	0.001	0.003	0.005	0.001	0.003	0.005
Standard Error	6.00E-04	4.44E-04	3.79E-04	1.81E-04	1.88E-04	1.75E-04
Median	0.001	0.003	0.005	0.000	0.004	0.006
Mode	-0.022	-0.022	-0.022	-0.003	-0.003	-0.003
Standard Deviation	0.008	0.008	0.009	0.002	0.003	0.004
Sample Variance	6.05E-05	6.61E-05	7.24E-05	5.52E-06	1.18E-05	1.55E-05
Kurtosis	2.936	2.934	2.881	2.083	1.820	1.992
Skewness	0.070	-0.044	-0.114	0.487	-0.111	-0.480
Range	0.043	0.051	0.053	0.008	0.013	0.014
Minimum	-0.022	-0.022	-0.022	-0.003	-0.003	-0.003
Maximum	0.021	0.030	0.031	0.005	0.010	0.011
Sum	0.138	1.149	2.670	0.123	1.142	2.663
Count	168	336	504	168	336	504

PERFORMING PATTERN RECOGNITION ANALYSIS

NEURAL NETWORK ARCHITECTURE DESIGN

The Neural Networks architecture for Noisy and De-noised ΔP data are designed as explained previously. In one case all the parameters from Descriptive statistics were selected as the input. In other Case the Number of inputs was decreased to 6, namely: Kurtosis, Skewnes, Maximum, Sum, Standard deviation and Mean. Since the number of outputs is three (Leakage location X, Leakage location Y and Leakage Rate), the number of hidden layers are designed to be ten (Figure 261).

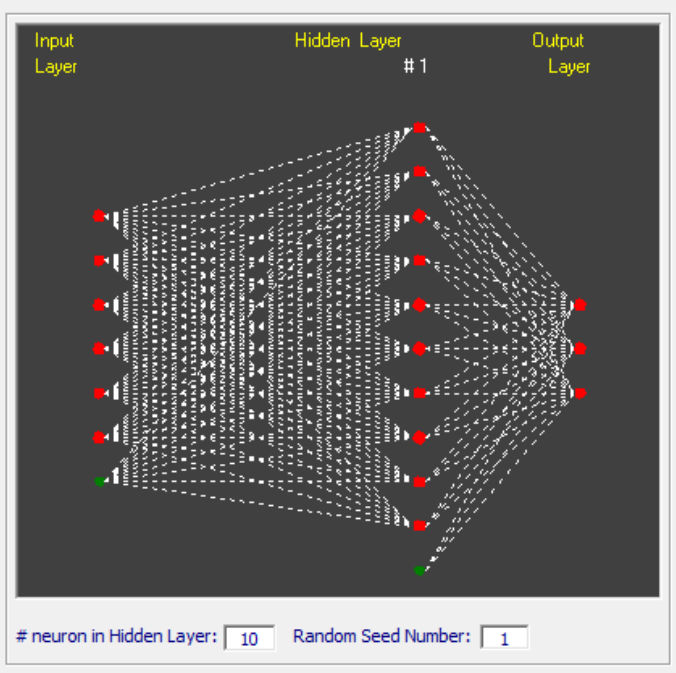

Figure 261. Neural Network architecture

NEURAL NETWORK TRAINING AND CALIBRATION

The actual input data consists of 60 set of CO_2 leakage scenarios (20 different leakage rates for each leaking well). By using intelligent data partitioning 48 cases are assigned for training and 6 cases for calibrating the Neural Networks. The outputs in all the neural networks are CO_2 leakage coordinates (X, Y) and rate. The results of the neural network training for the leakage location (Y) and leakage rate with de-noised pressure data after 3 weeks of leakage are shown in Figure 262 and Figure 263.

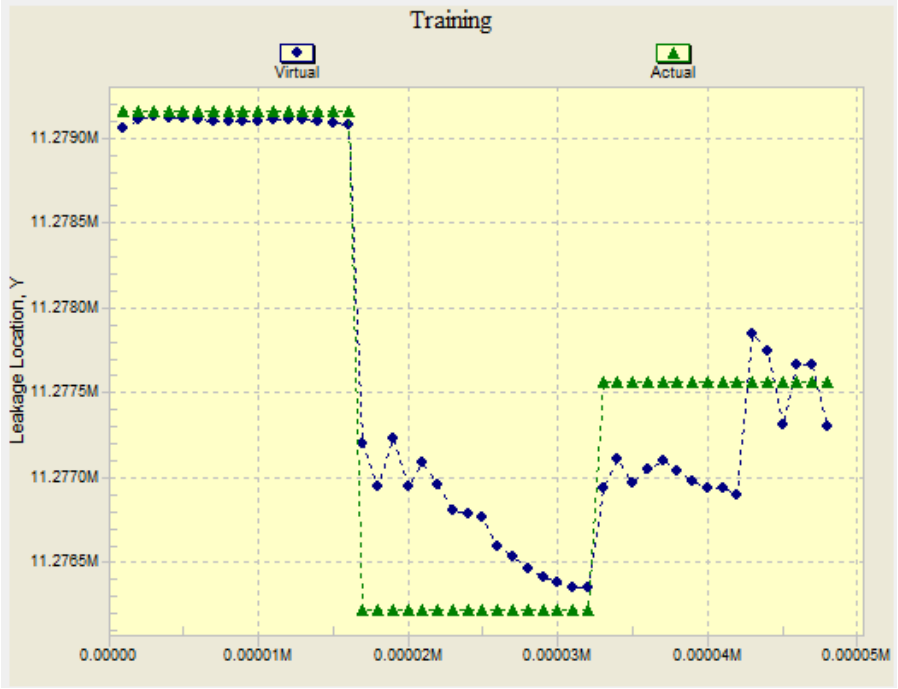

Figure 262. Neural network training results for the leakage location; de-noised pressure data after 3 weeks of leakage

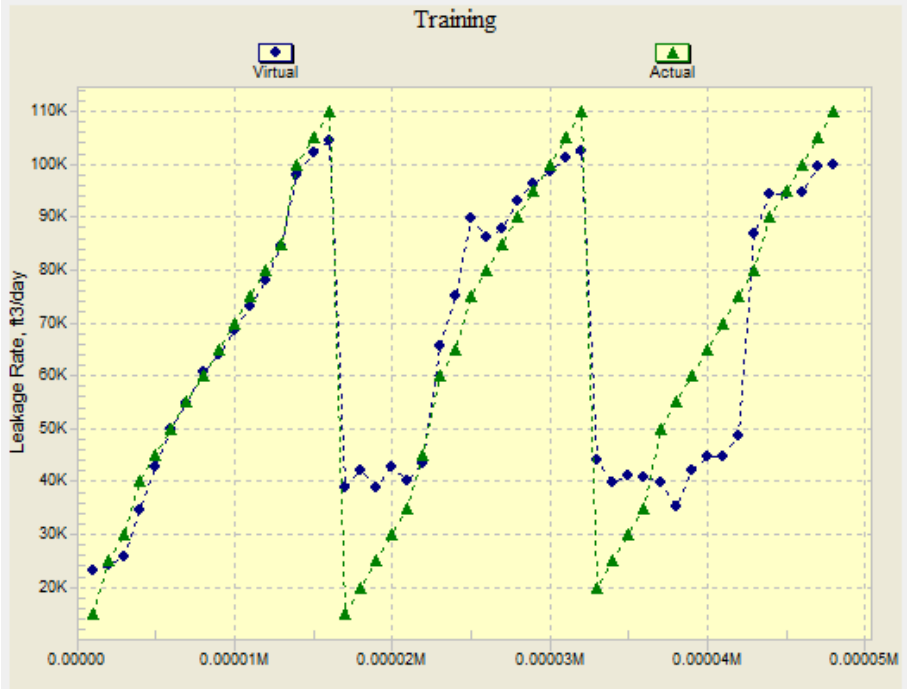

Figure 263. Neural network training results for the leakage Rate; de-noised pressure data after 3 weeks of leakage

The maximum errors in the training the leakage rate mostly happens in low leakage rates. The results of the neural network calibration for the Leakage location (Y) and leakage rate when de-noised pressure data after 3 weeks of leakage are shown in Figure 264 and Figure 265.

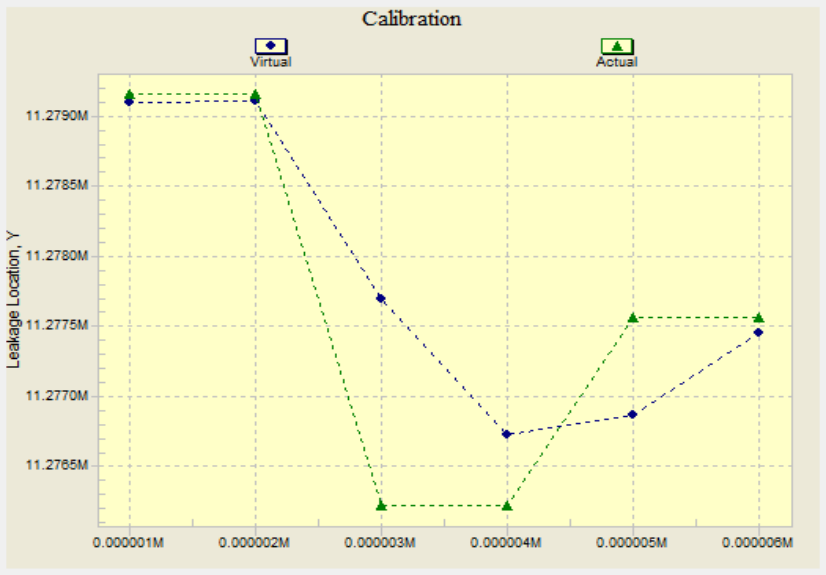

Figure 264. Neural network calibration results for the leakage location Y; de-noised pressure data after 3 weeks of leakage

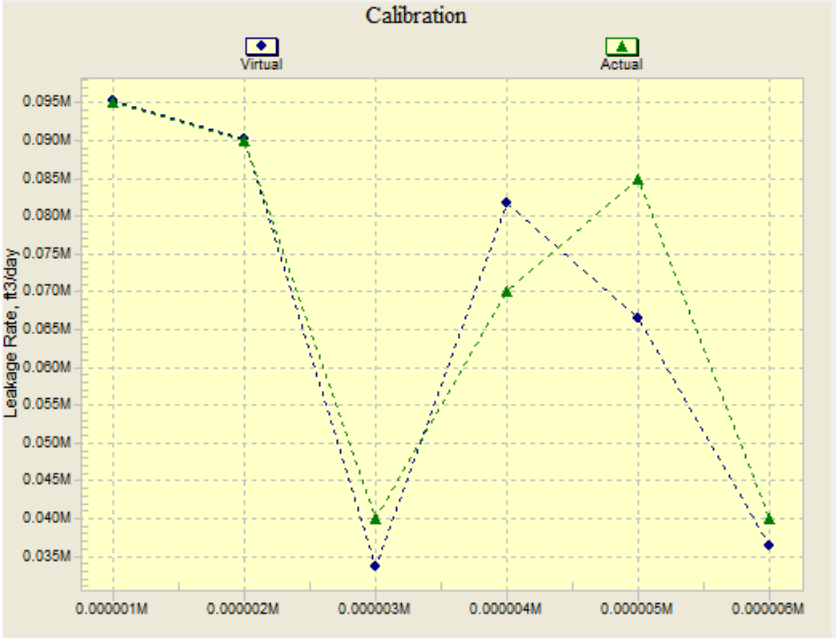

Figure 265. Neural network calibration results for the leakage rate; de-noised pressure data after 3 weeks of leakage

NEURAL NETWORK VALIDATION FOR NOISY DATA

In previous section, it was proved that Intelligent Leakage Detection System (ILDS) performs precisely when the real time pressure data is clean. There is some noise associated with real time pressure data. In order to investigate the robustness of the ILDS performance while noisy pressure data are transmitted from the observation well, the actual noise are added to the clean pressure data (generated by reservoir simulator for each Leakage scenario). The clean and noisy pressure records from observation well, when well D-9-6 leaks with rate of 35Mcf/day, are shown in Figure 266.

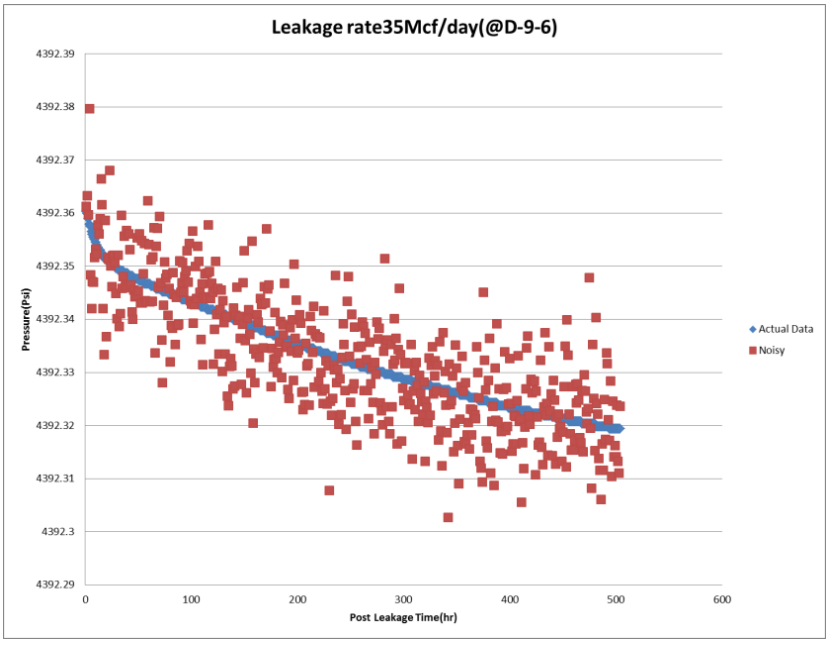

Figure 266. Clean (blue) and Noisy (red) high frequency pressure data from observation well

The first step for processing high frequency noisy pressure records is data cleansing. There are some accepted de-noising methods that have been widely used in the industry and academia. Initially we used Wavelet threshold method. In de-noising process generally the noisy data should be divided to different levels (decomposition). After that for each level, a threshold should be considered in order to remove the data that lies out of the threshold. Finally the data is reconstructed using the modified data from each level. An example of distorted pressure data which goes under de-noising process is depicted in Figure 267.

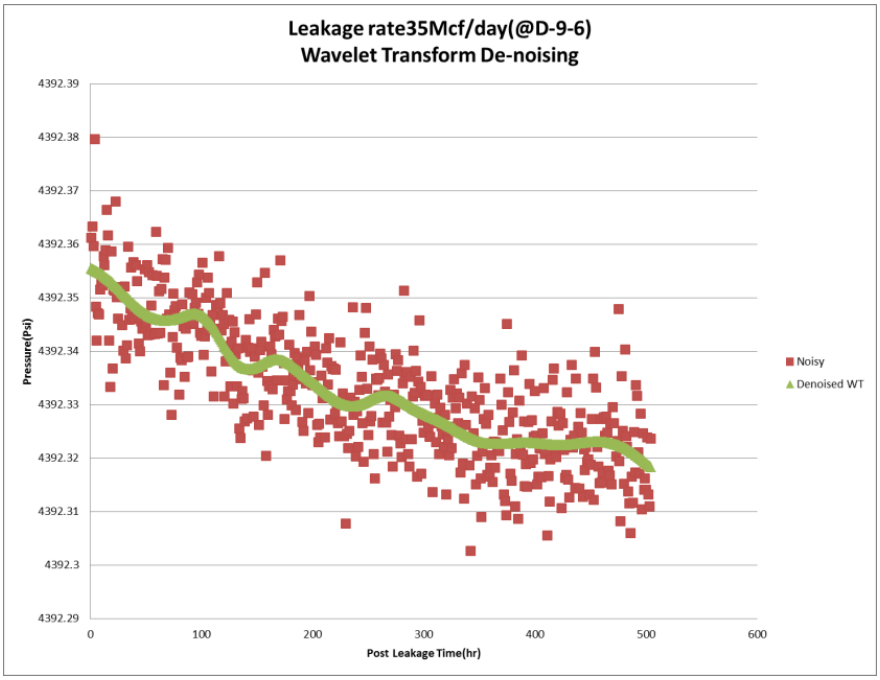

Figure 267. Noisy and De-noised pressure data using Wavelet threshold method

The main concern for using Wavelet threshold method for data cleansing is that, the de-noised data generally follows the trend of noisy data. This is mostly the case when leakage rates are low and corresponding real time pressure signal changes in the observation well are in a narrow range. This oscillating pattern of de-noised data changes the parameters that we got by data summarization of clean data. Especially the parameters like skewness and kurtosis that play important role in leakage location detection. In order to alleviate the effect of noise and clean the data in a way that represent behavior of pressure trend, we used GRNN (General Regression Neural Networks). GRNN is a type of probabilistic neural networks that requires just some small portion of data records for training. That specification of GRNN is advantageous since it would be able to capture the underlining trend and functionality of the large amount of data with few samples. When we are dealing with high frequency noisy pressure data, it would be better to use GRNN rather than Wavelet threshold method. Because the GRNN uses smaller portion of data, the presence of the noise cannot generally affect the calculated trend. This would be the case especially when the frequency of data increases. Therefore GRNN can be considered to be a very useful tool to de-noise high frequency pressure data. The results for de-noising pressure records by GRNN are shown in Figure 268. By comparing the resulted trends from Wavelet threshold de-noising method and GRNN with the original clear data, it can be concluded that GRNN method performs better.

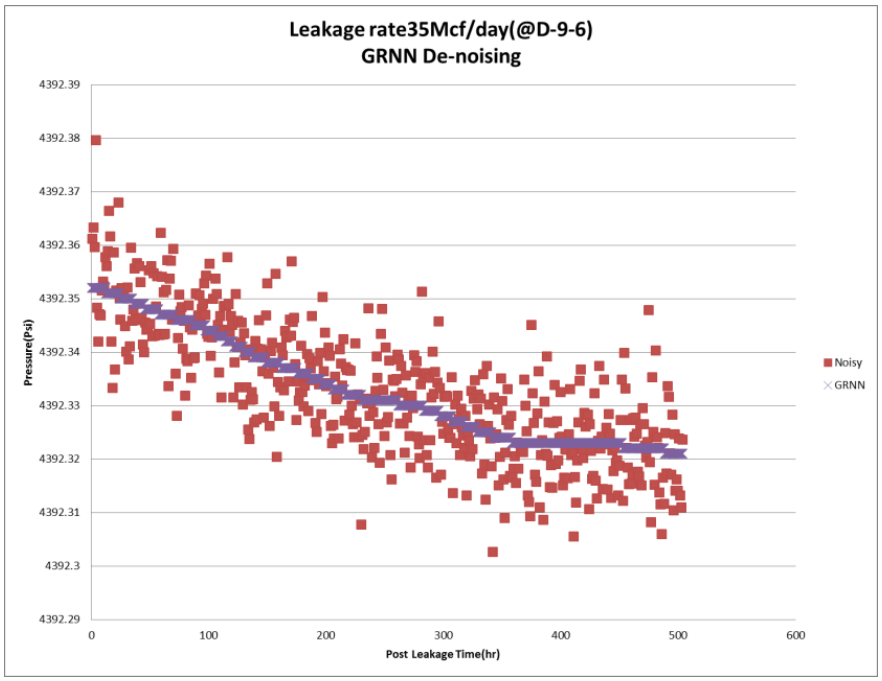

Figure 268. Noisy and De-noised pressure data using GRNN

In order to facilitate ILDS with the capability of receiving noisy pressure data, we added noise to the clean pressure data (generated by reservoir simulator for each leakage scenario). Then the noisy pressure data was cleansed by GRNN and summarized using descriptive statistics. Finally neural network was trained based on GRNN de-noised pressure data. The verification results for leakage location are shown in Figure 269 and Figure 270.

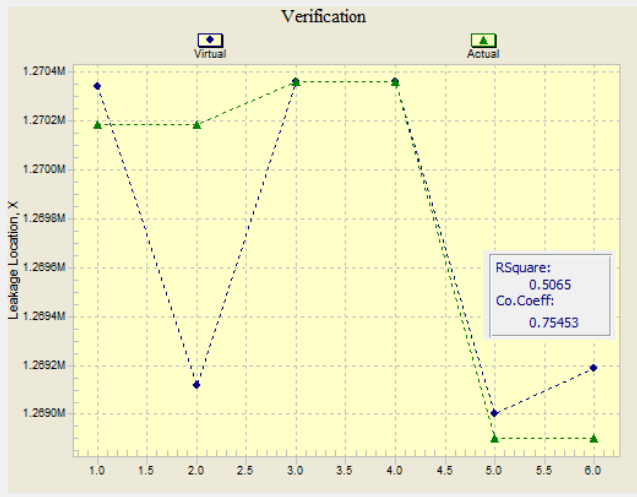

Figure 269. Verification results for leakage location(X)-noisy data

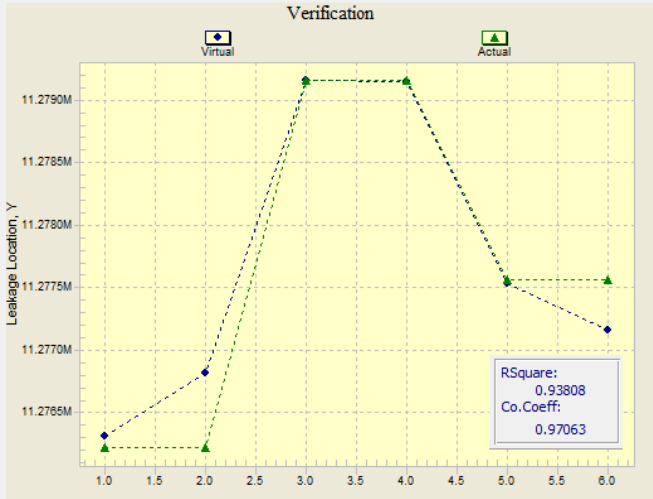

Figure 270. Verification results for leakage location(Y)-noisy data

As we can see from the abovementioned figures the R^2 value for X and Y coordinates for verification results are 0.5 and 0.94, respectively. Although the prediction ability of the neural networks verification decreases due to existence of the noise, but still it is able to predict the location with reasonable accuracy. The results for Leakage rate verification are shown in Figure 271. For verification of leakage rate when the pressure data is noisy, the R^2 is 0.77 which represents decent accuracy.

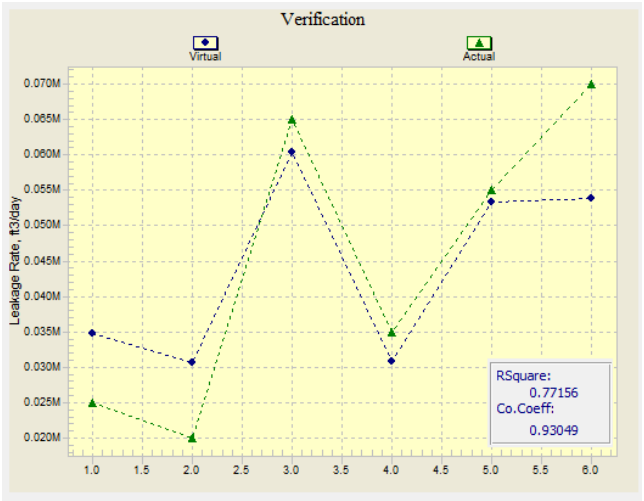

Figure 271. Verification results for leakage Rate(Y)-noisy data

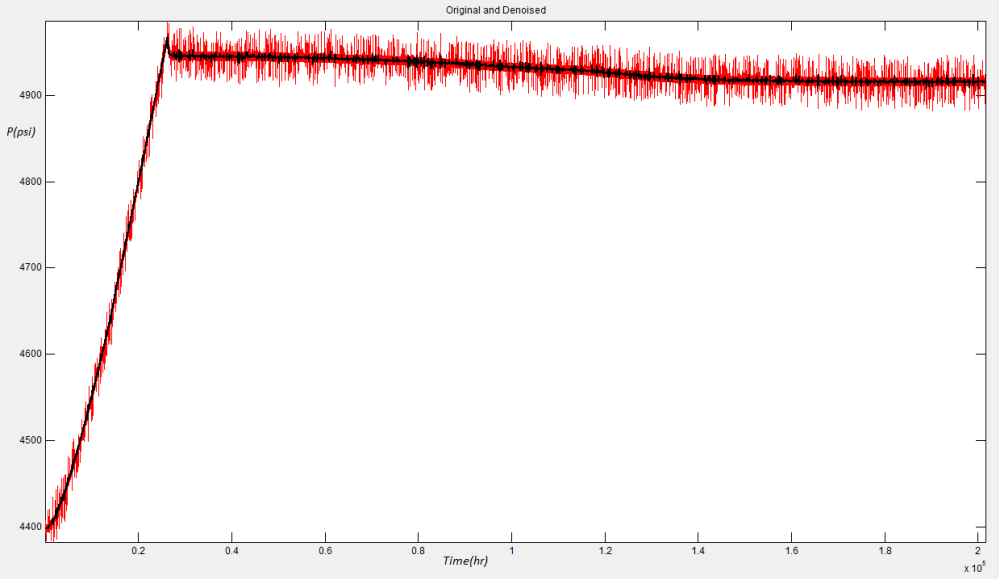

Figure 272. De-noising pressure data for leakage scenario#1 (red: noisy data, black: de- noised data)

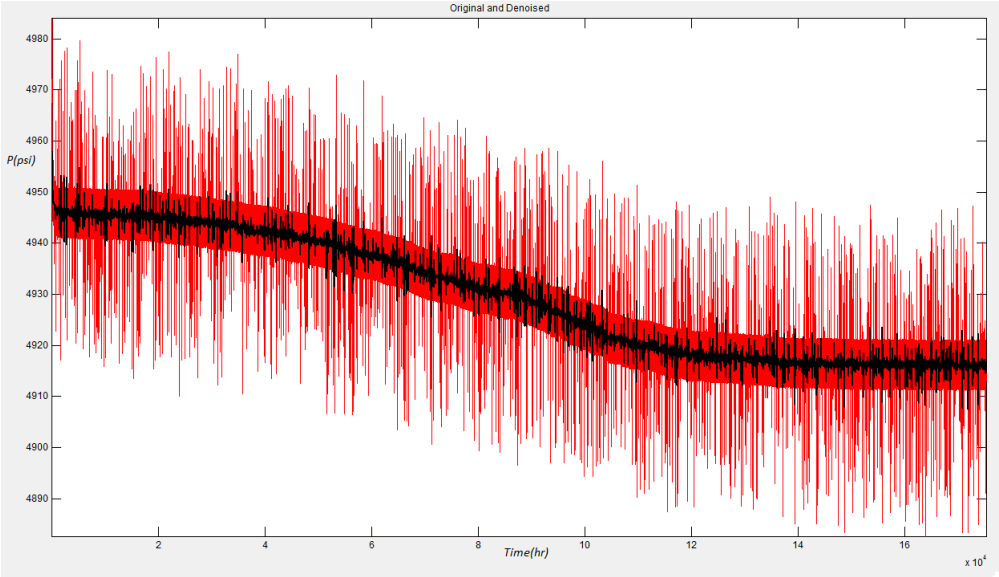

Figure 273. De-noising pressure data for scenario 1 during post injection (red: noisy data, black: de-noised data)

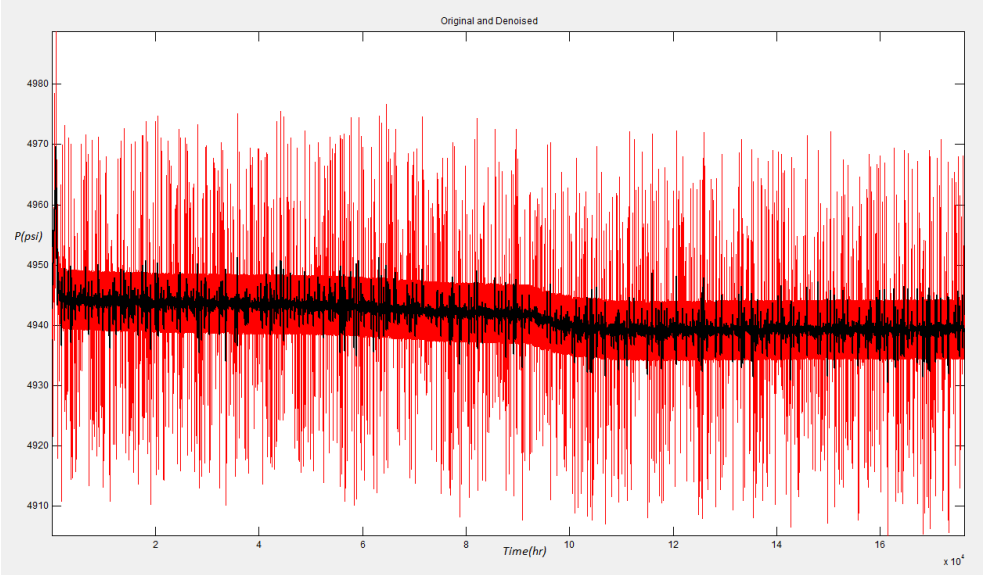

Figure 274. De-noising pressure data for scenario 2 during post injection (red: noisy data, black: de-noised data)

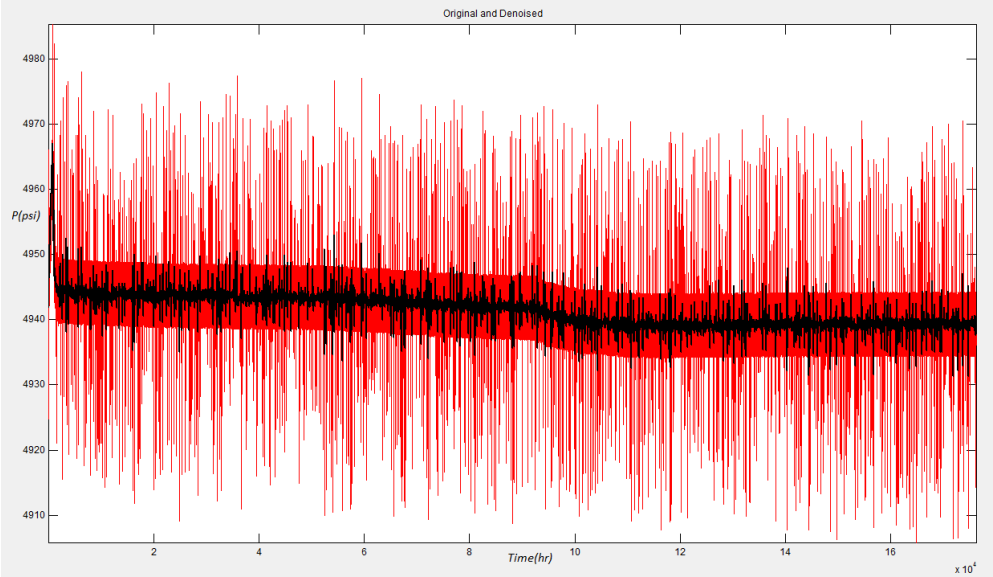

Figure 275. De-noising pressure data for scenario 3 during post injection (red: noisy data, black: de-noised data)

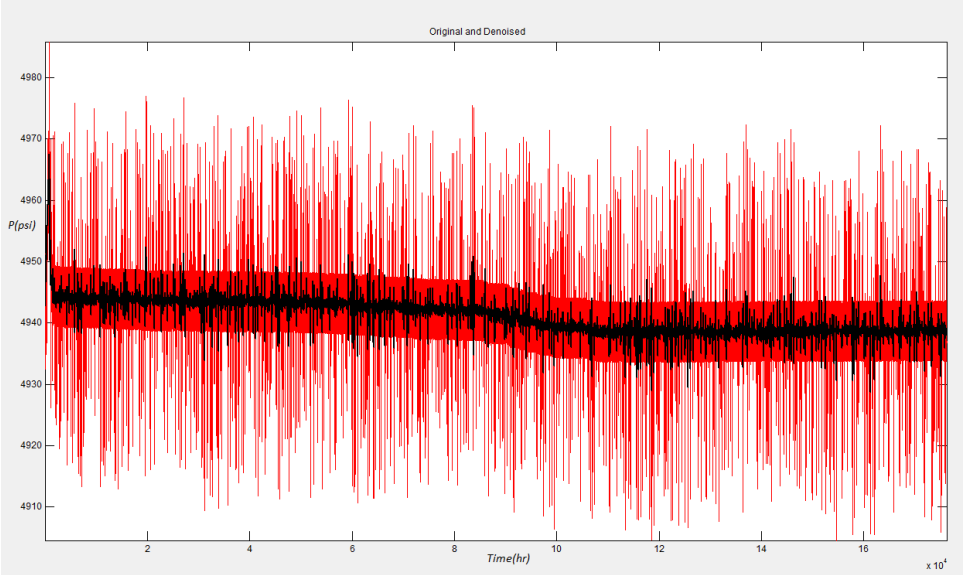

Figure 276. De-noising pressure data for scenario 4 during post injection (red: noisy data, black: de-noised data)

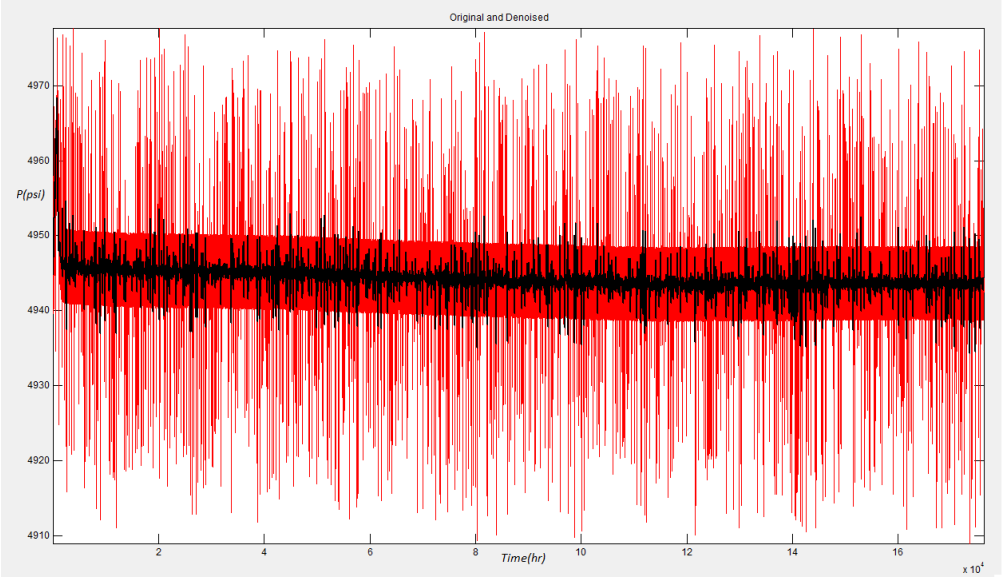

Figure 277. De-noising pressure data for scenario 5 during post injection (red: noisy data, black: de-noised data)

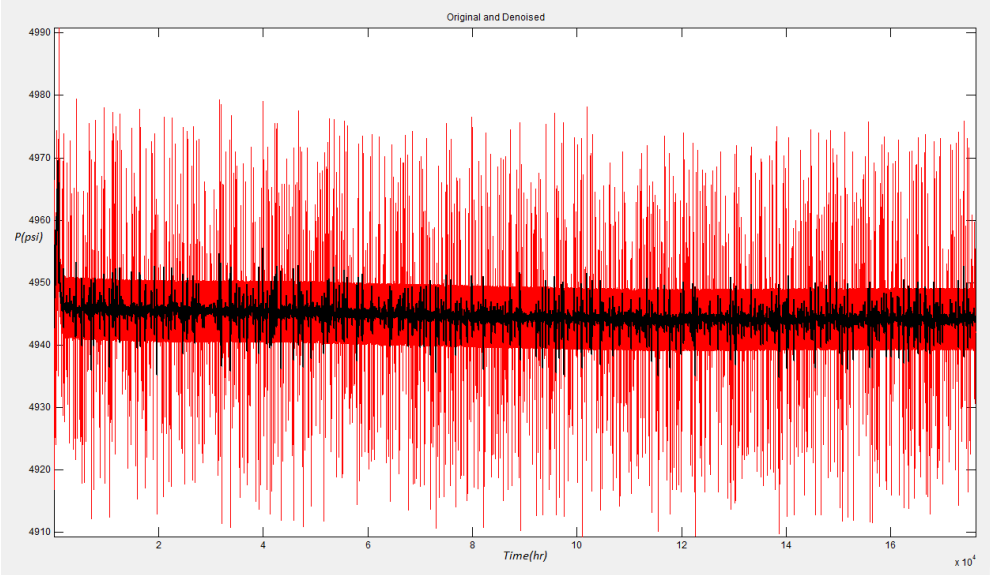

Figure 278. De-noising pressure data for scenario 6 during post injection (red: noisy data, black: de-noised data)

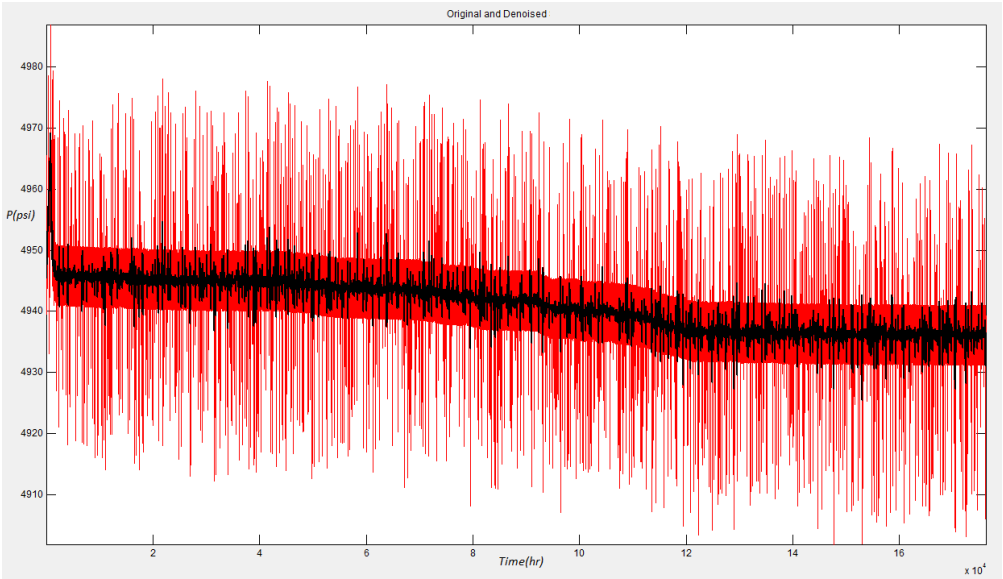

Figure 279. De-noising pressure data for scenario 7 during post injection (red: noisy data, black: de-noised data)

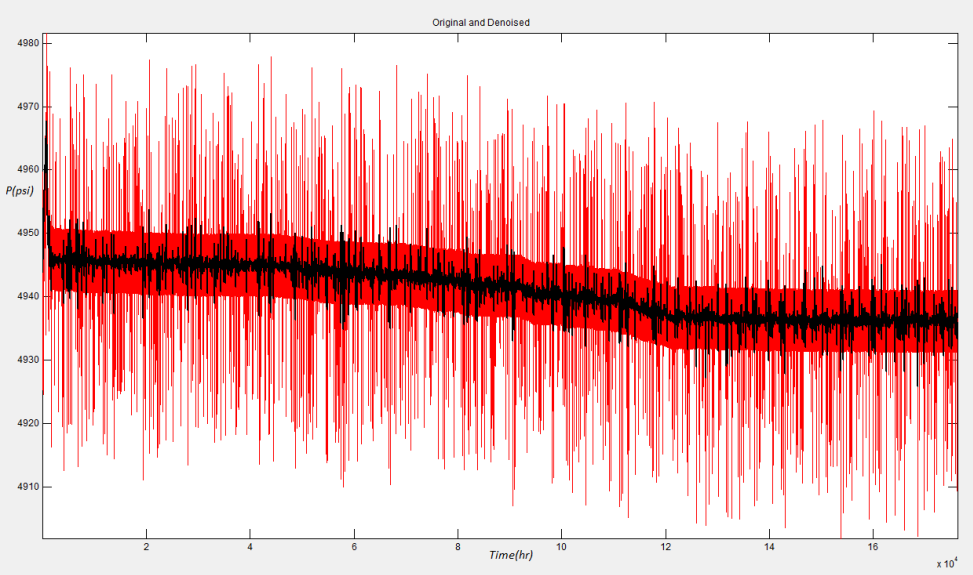

Figure 280. De-noising pressure data for scenario 8 during post injection (red: noisy data, black: de-noised data)

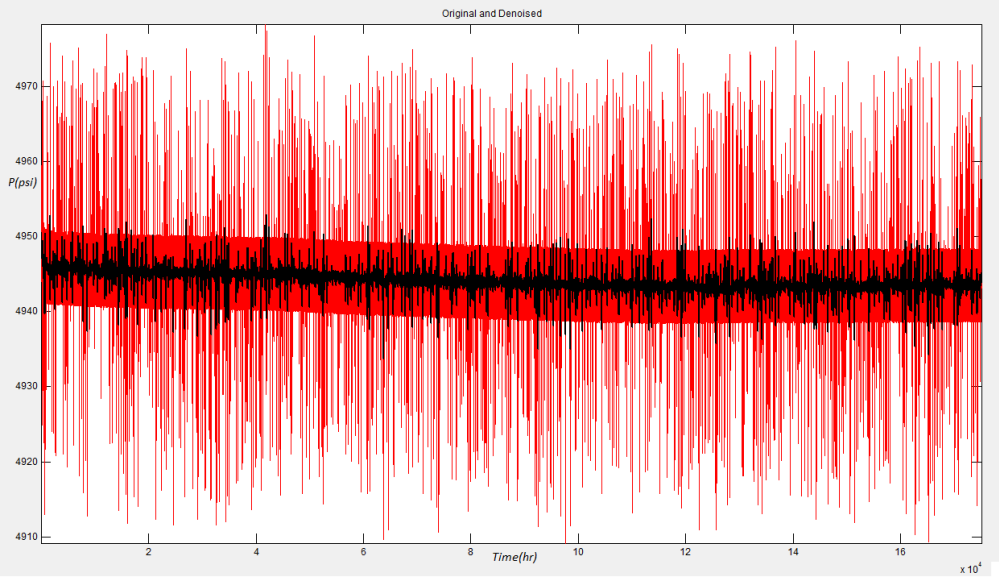

Figure 281. De-noising pressure data for scenario 9 during post injection (red: noisy data, black: de-noised data)

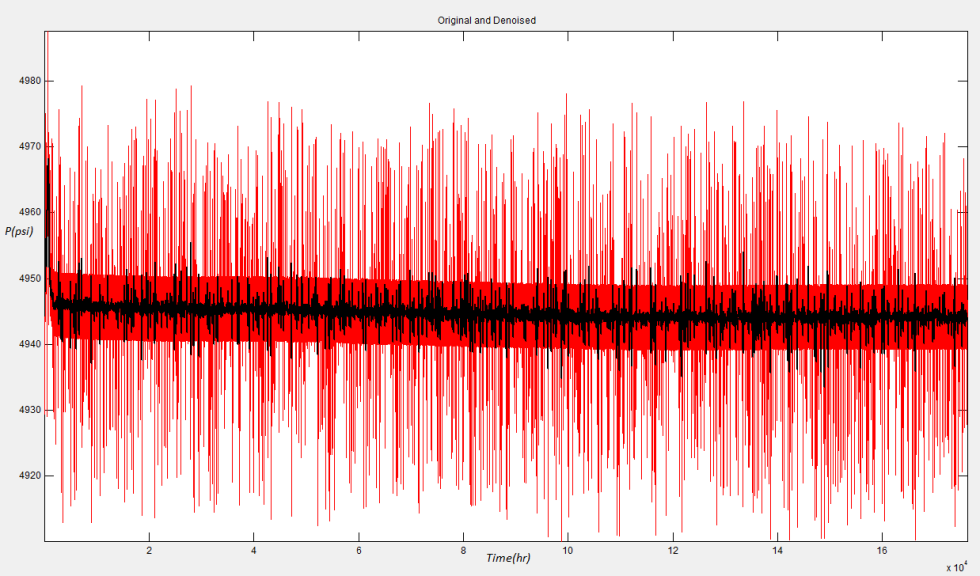

Figure 282. De-noising pressure data for scenario 10 during post injection (red: noisy data, black: de-noised data)

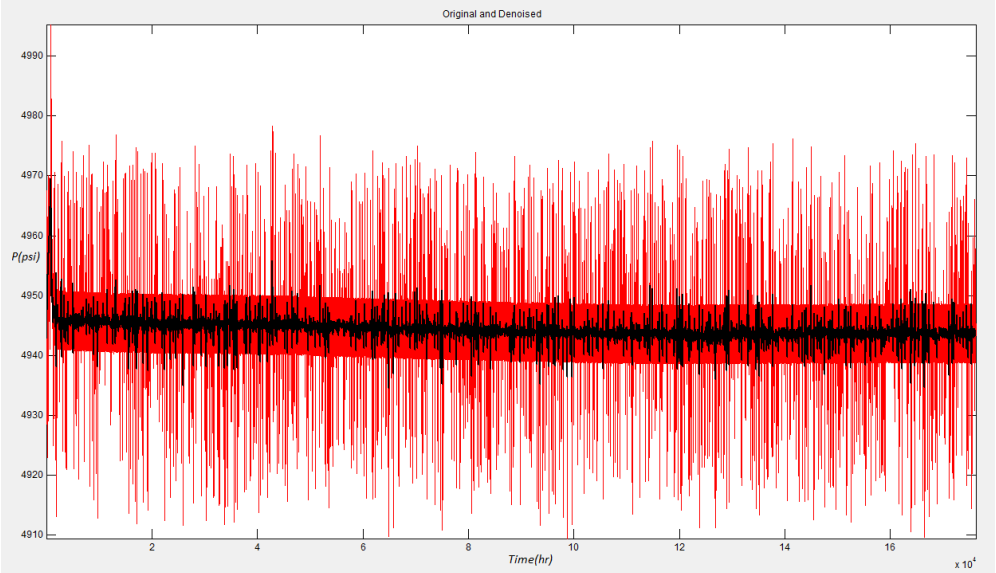

Figure 283. De-noising pressure data for scenario 11 during post injection (red: noisy data, black: de-noised data)

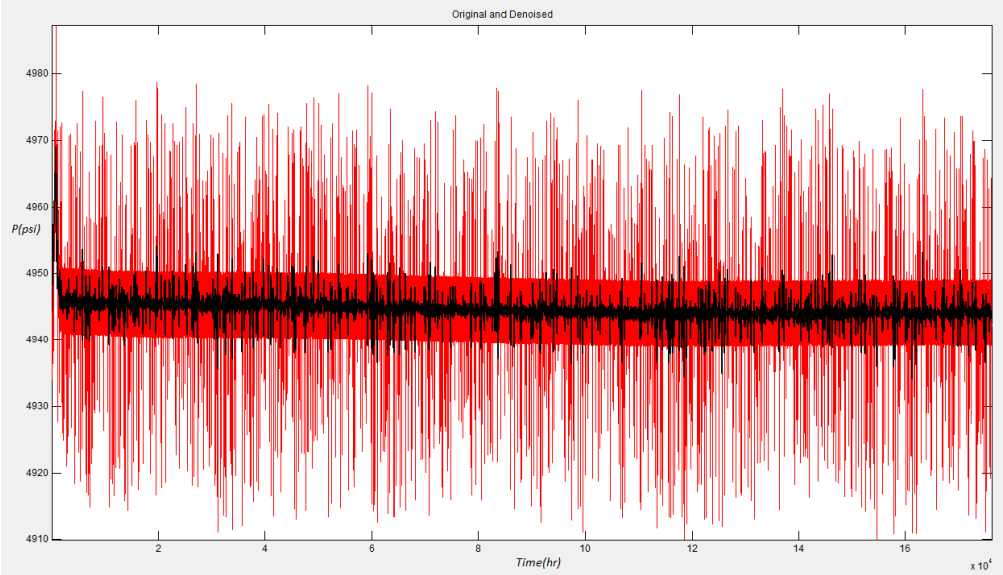

Figure 284:De-noising pressure data for scenario 12 during post injection (red: noisy data, black: de-noised data)

APPENDIX 3

THE HISTORY MATCHING PROCESS

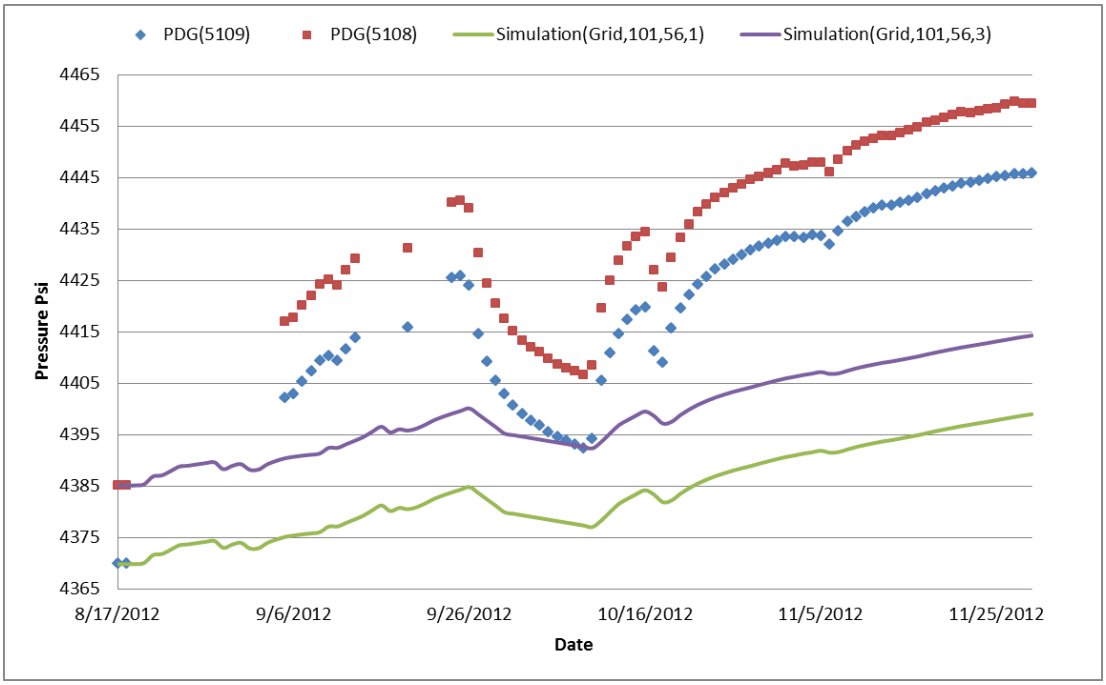

Figure 285. Comparison between actual PDG data and simulation results –Modified reservoir boundary (smaller boundary)

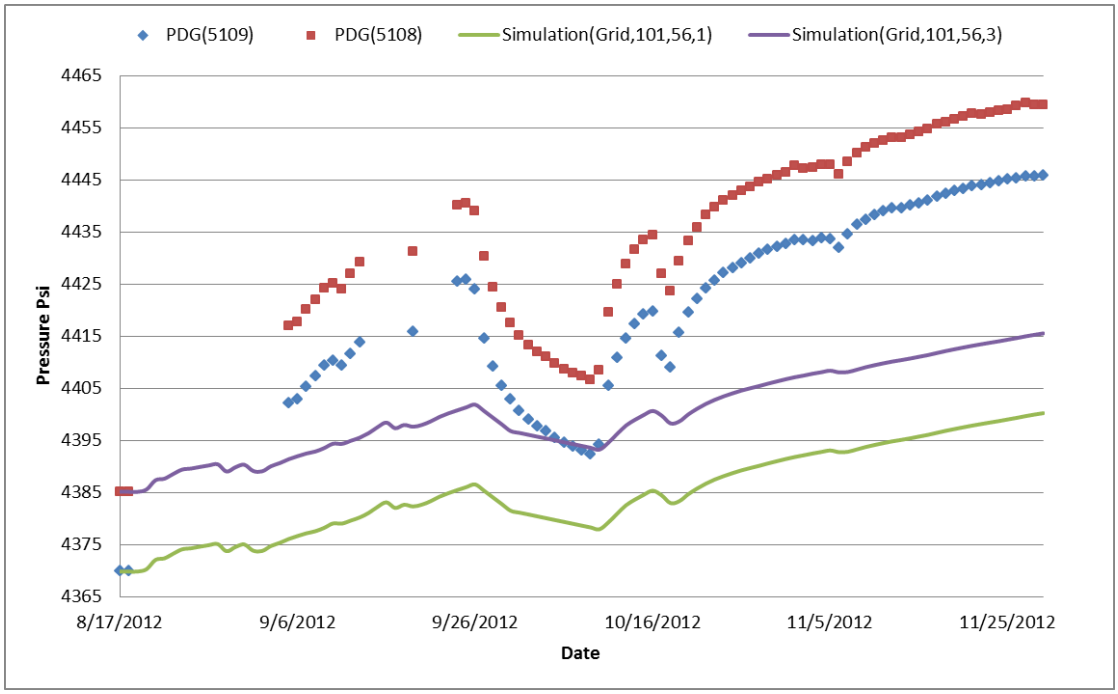

Figure 286. Comparison between actual PDG data and simulation results –Modified vertical permeability (K_v=.1*k_h)

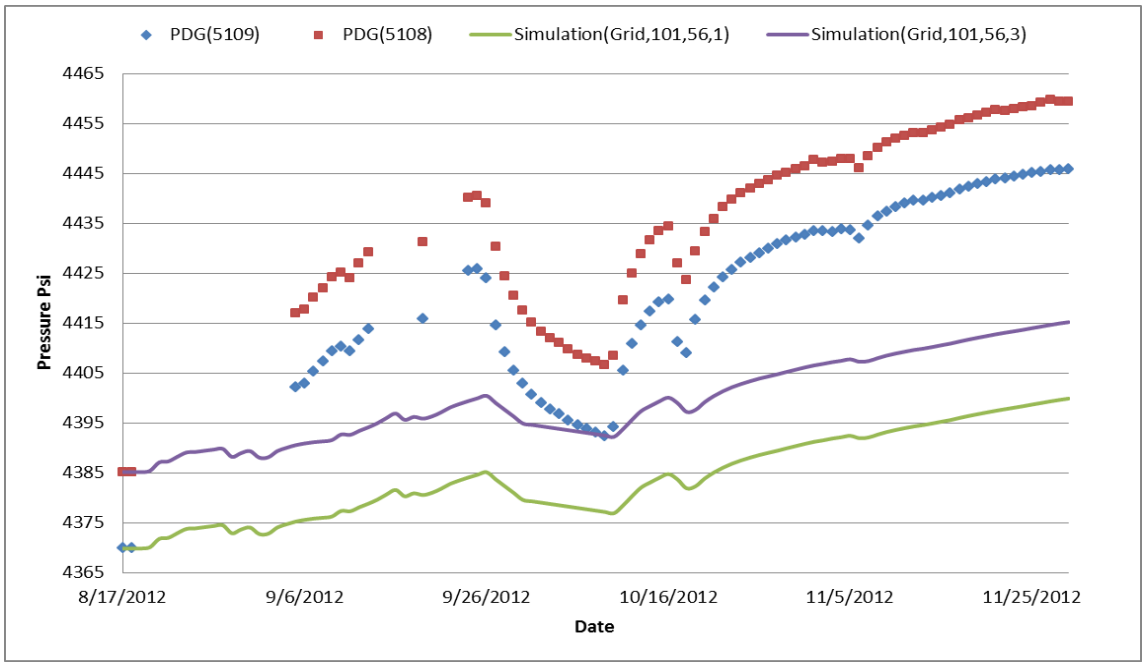

Figure 287. Comparison between actual PDG data and simulation results –Modified brine compressibility (Cbr=1e-6)

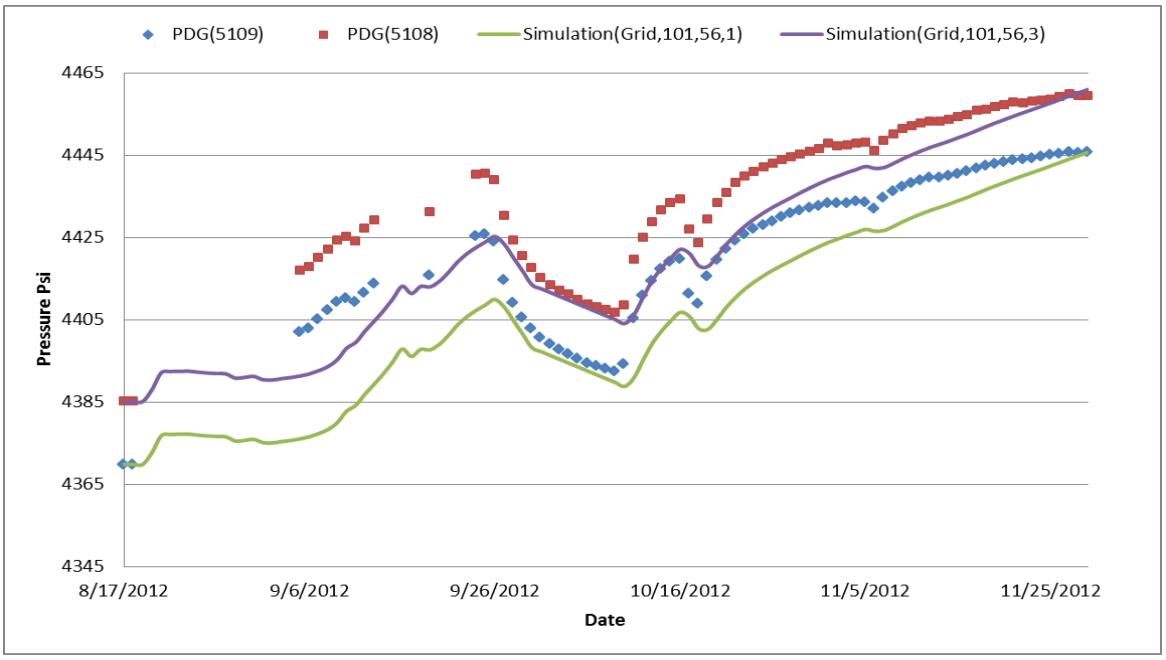

Figure 288. Comparison between actual PDG data and simulation results –Modified reservoir boundary (with updated reservoir parameters)

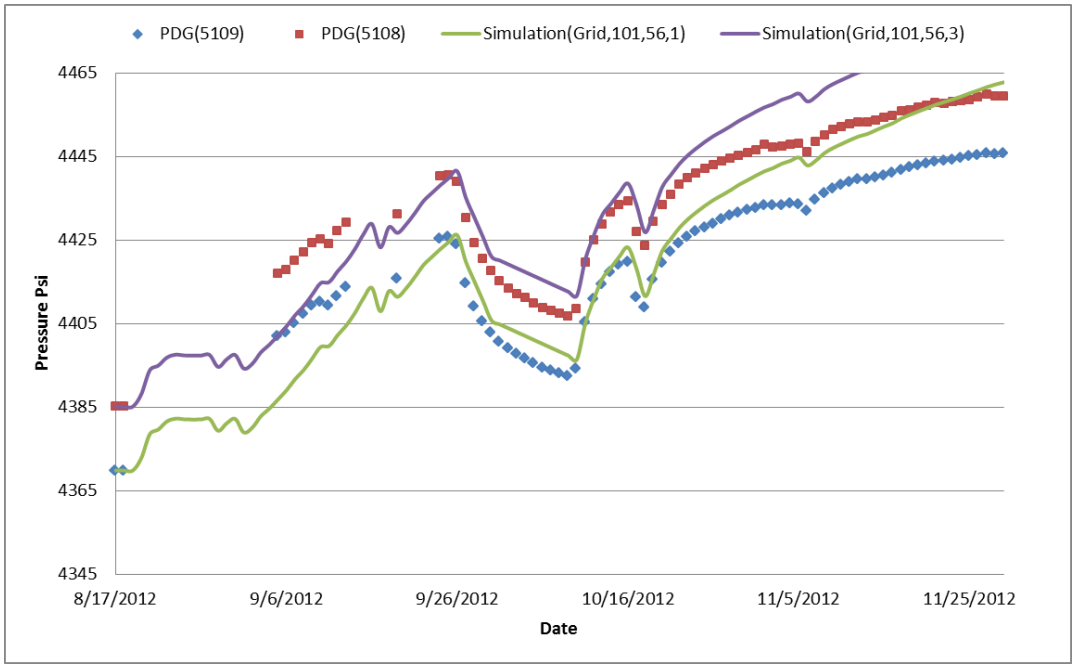

Figure 289. Comparison between actual PDG data and simulation results –Modified reservoir water relative permeability (with updated reservoir parameters)

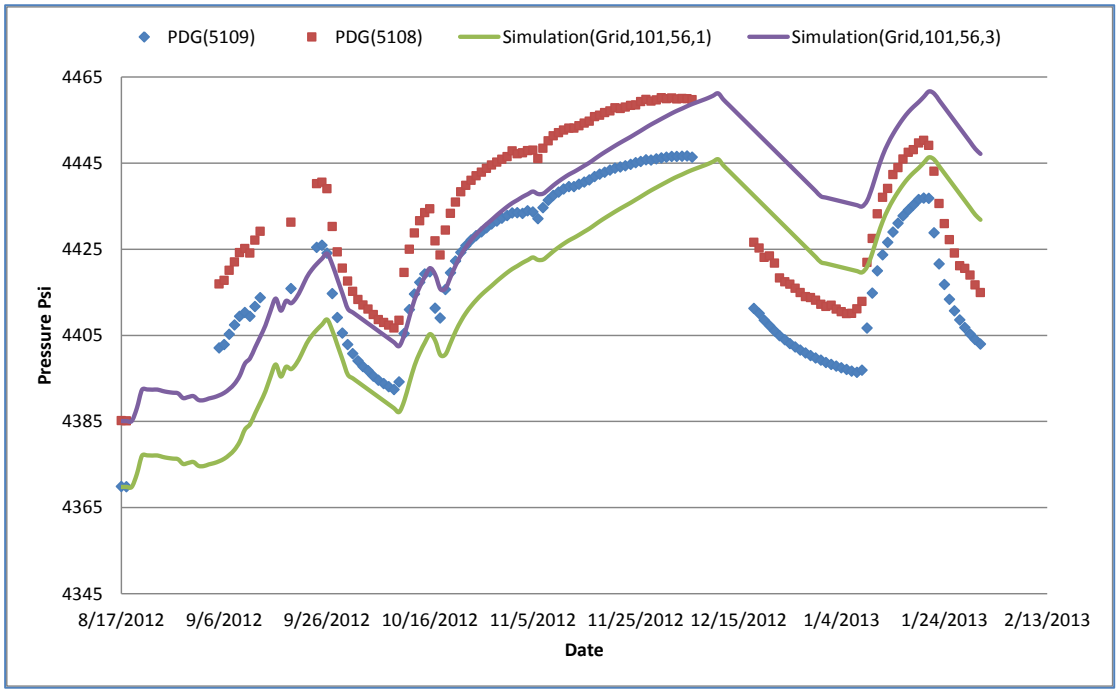

Figure 290. Comparison between actual PDG data and simulation results –Base Case

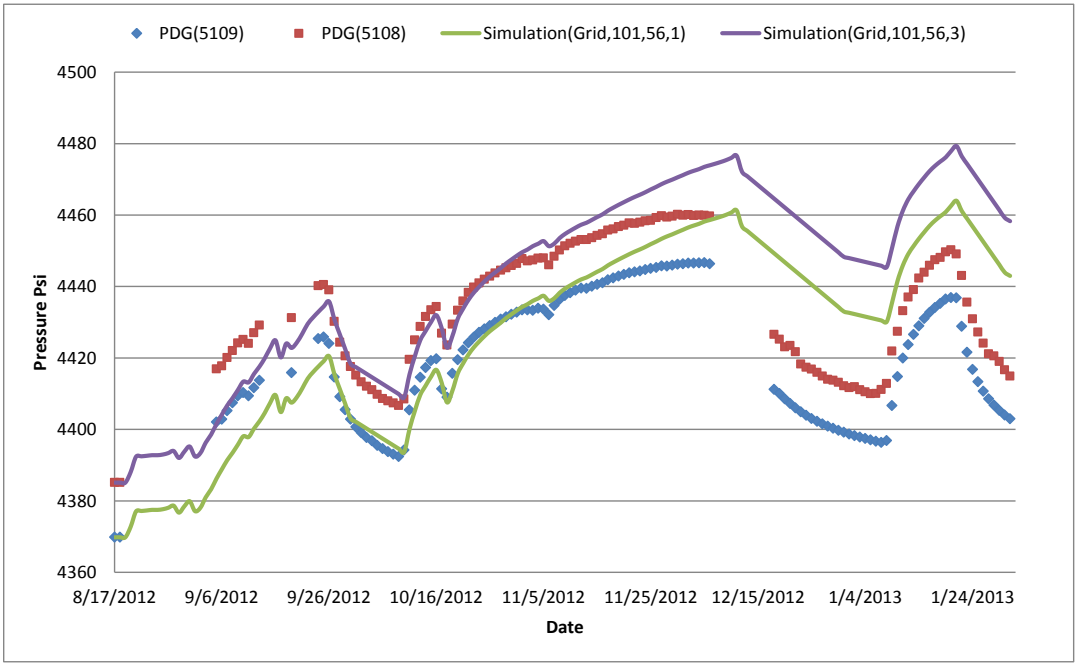

Figure 291. Comparison between actual PDG data and simulation results –K_{rg} high

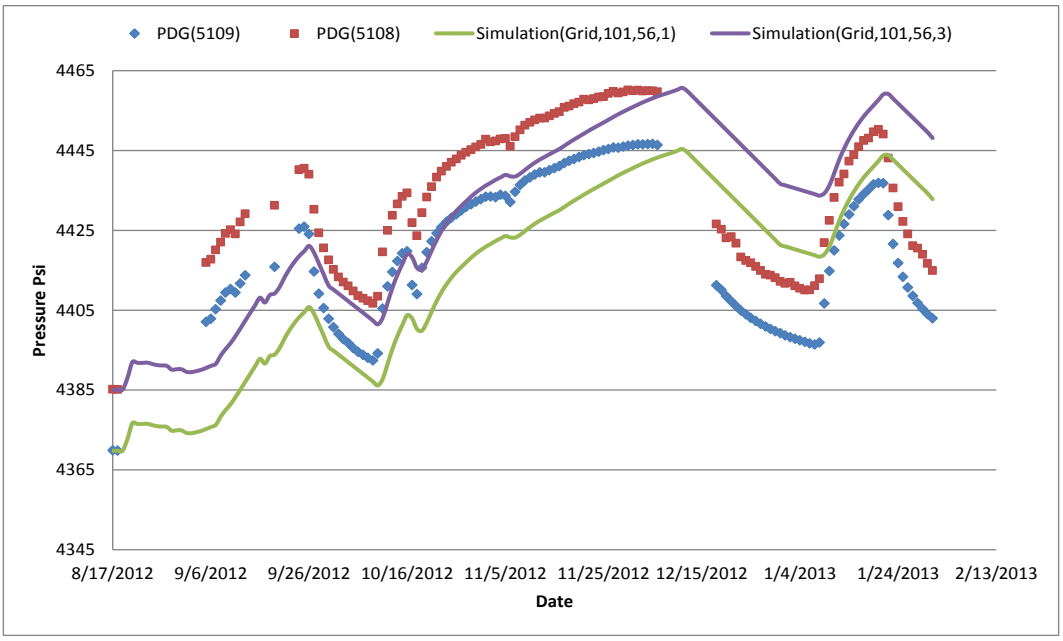

Figure 292. Comparison between actual PDG data and simulation results –K_{rg} low

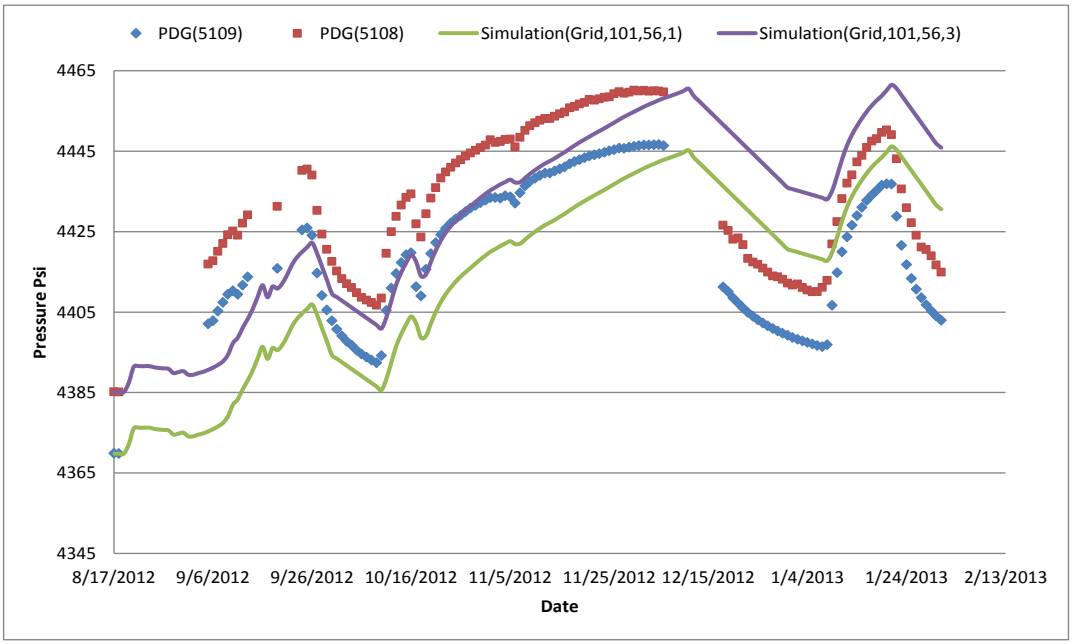

Figure 293. Comparison between actual PDG data and simulation results –K_v/K_h=.9

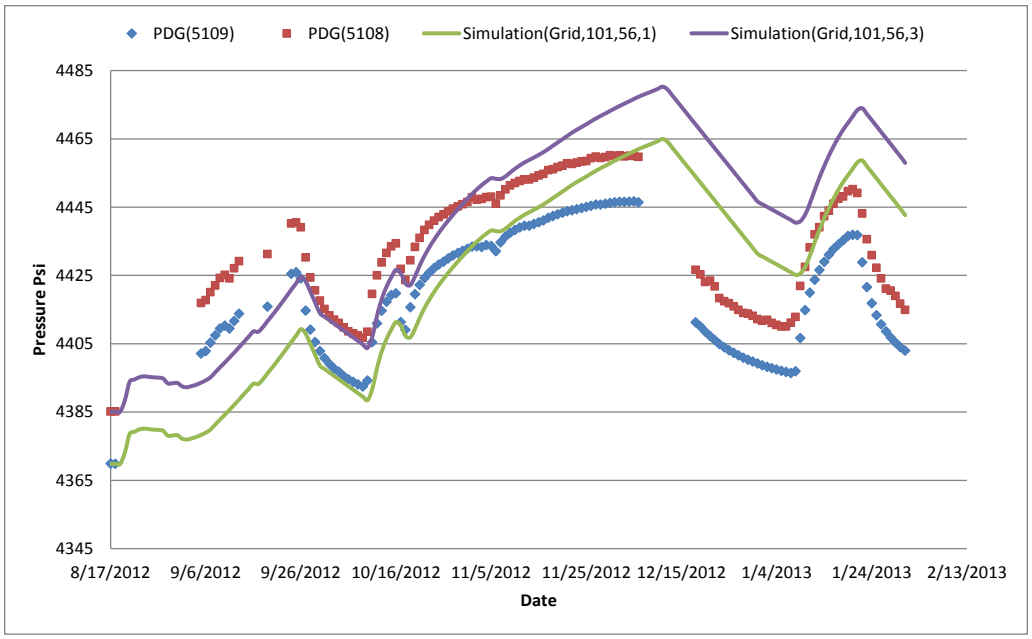

Figure 294. Comparison between actual PDG data and simulation results –K is half of the base case

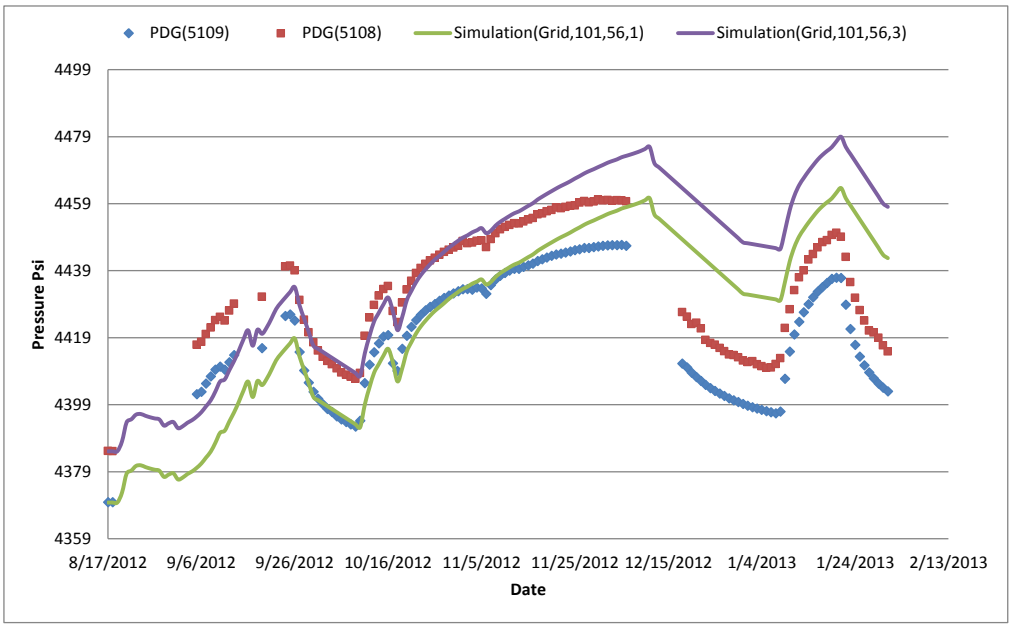

Figure 295. Comparison between actual PDG data and simulation results –K_{rw} high

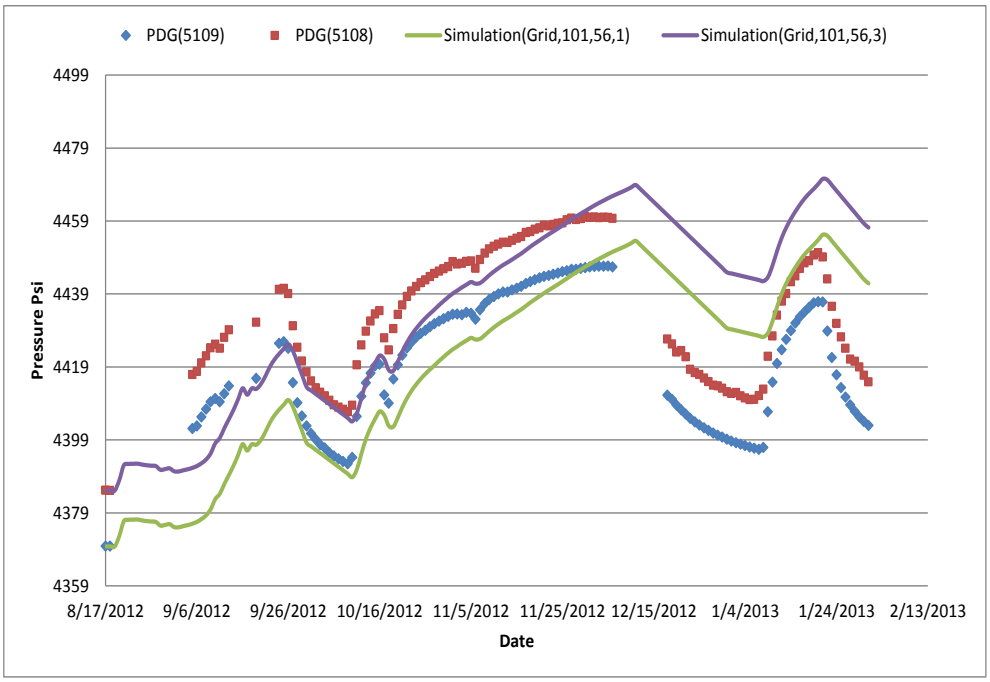

Figure 296. Comparison between actual PDG data and simulation results –reservoir with smaller boundary

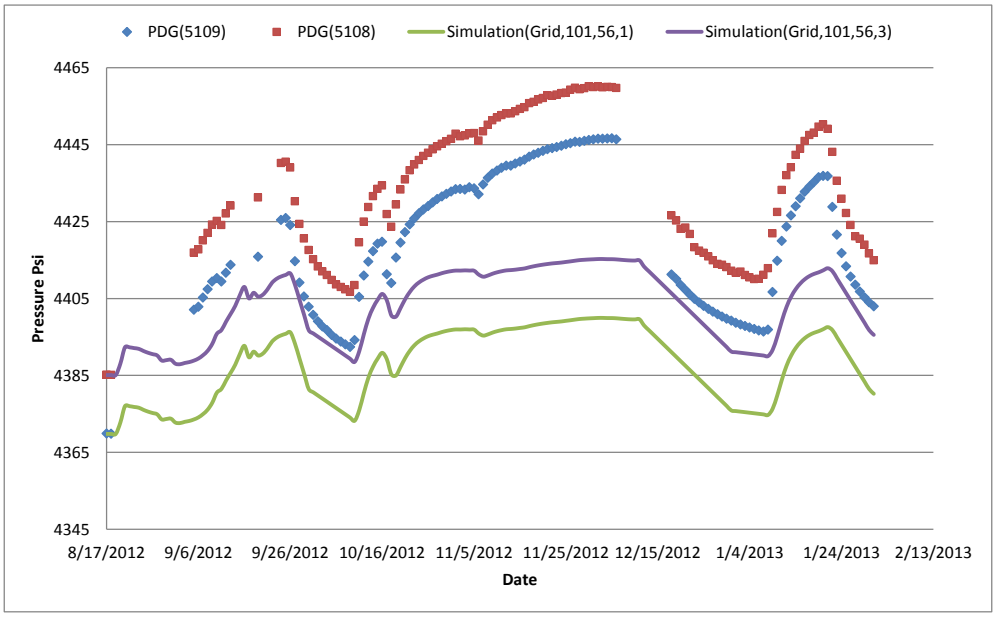

Figure 297. Comparison between actual PDG data and simulation results –reservoir with smaller boundary

APPENDIX 4

LEAKAGE RATES

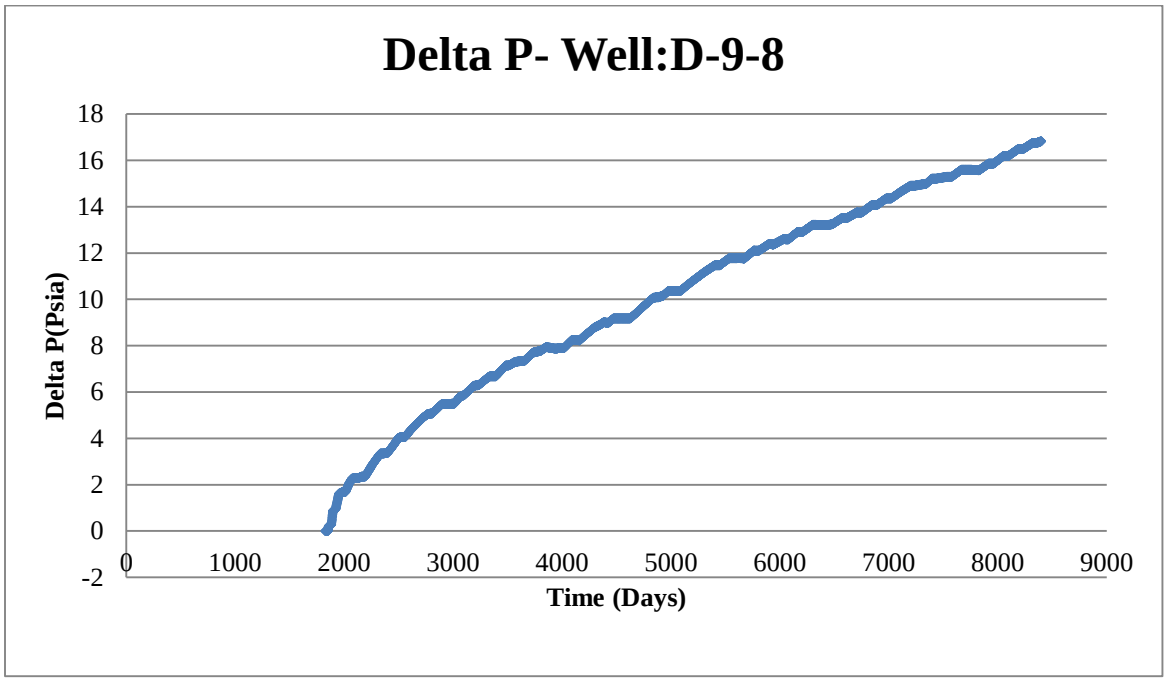

Figure 298. ΔP in well D-9-8 well in the case that well D-9-6 leakage rate is 99750ft^3/day

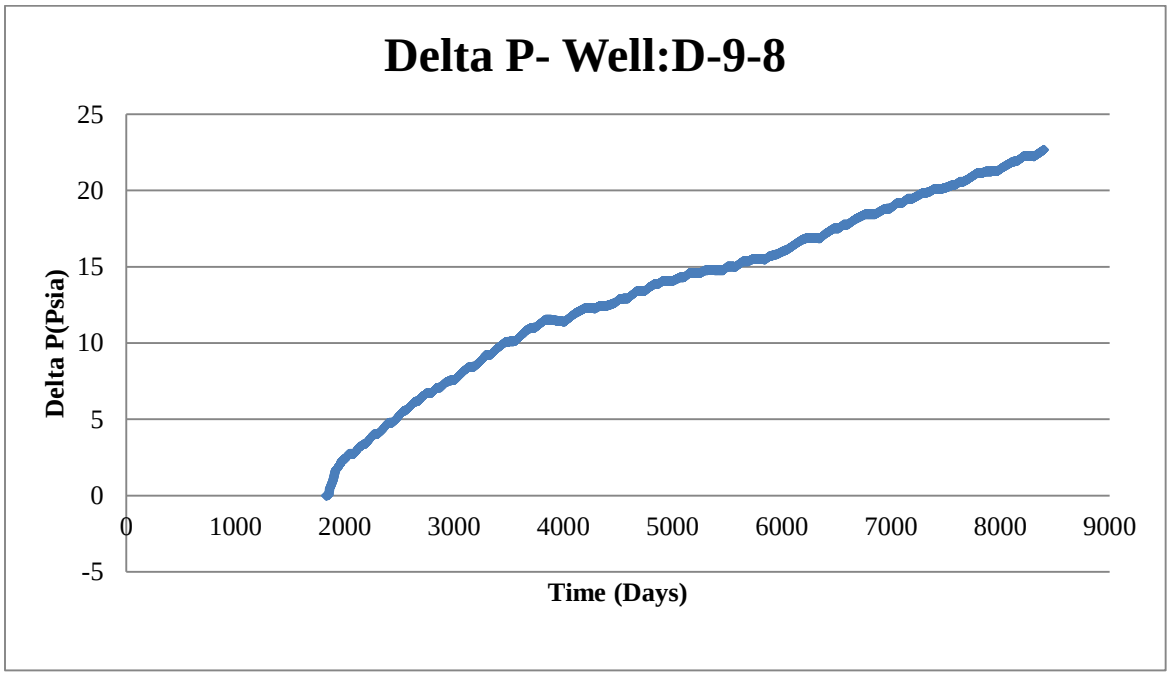

Figure 299. ΔP in well D-9-8 well in the case that well D-9-6 leakage rate is 120750ft^3/day.

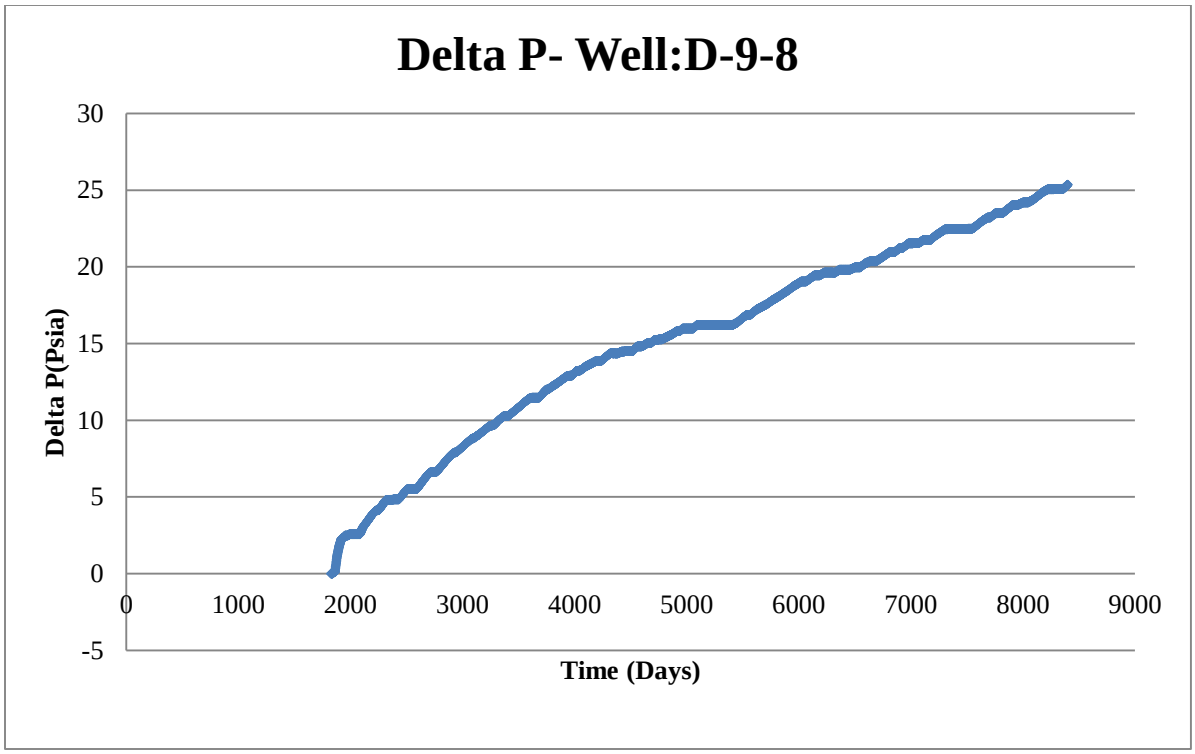

Figure 300. ΔP in well D-9-8 and Injection well in the case that well D-9-6 leakage rate is 131250ft3/day.

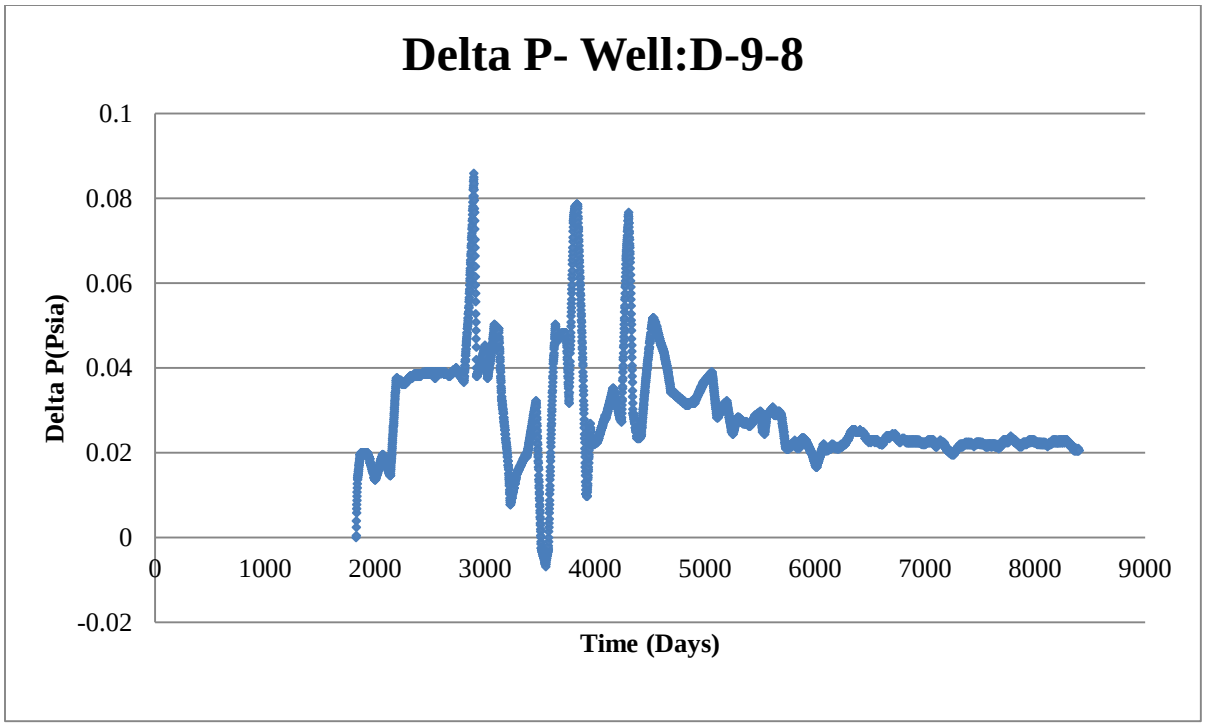

Figure 301. ΔP in well D-9-8 well in the case that well D-9-2 leakage rate is 1830ft^3/day.

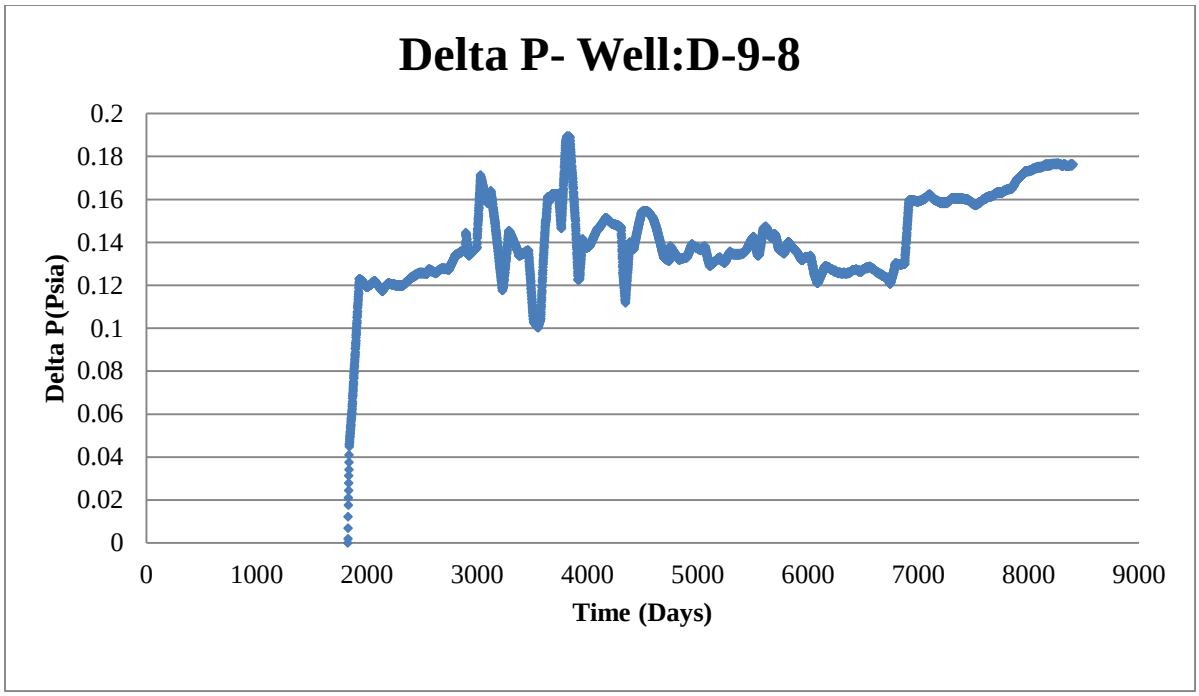

Figure 302. ΔP in well D-9-8 well in the case that well D-9-2 leakage rate is 5250ft^3/day.

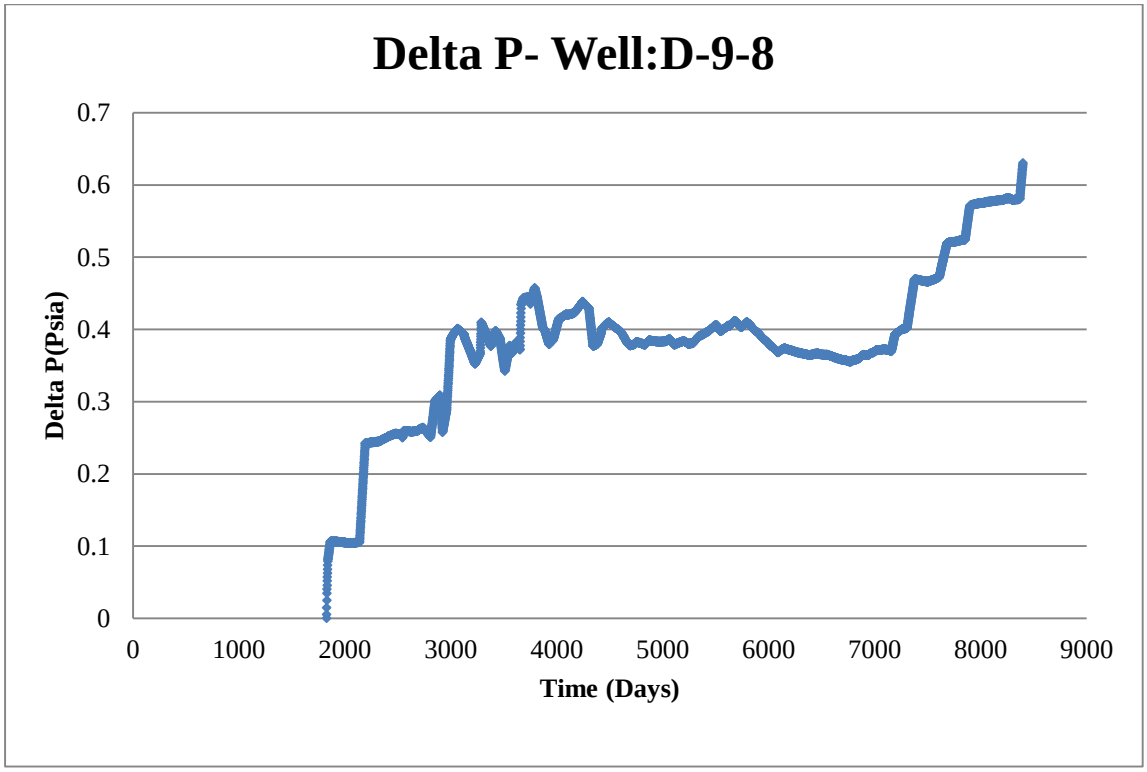

Figure 303. ΔP in well D-9-8 well in the case that well D-9-2 leakage rate is 11250ft3/day.

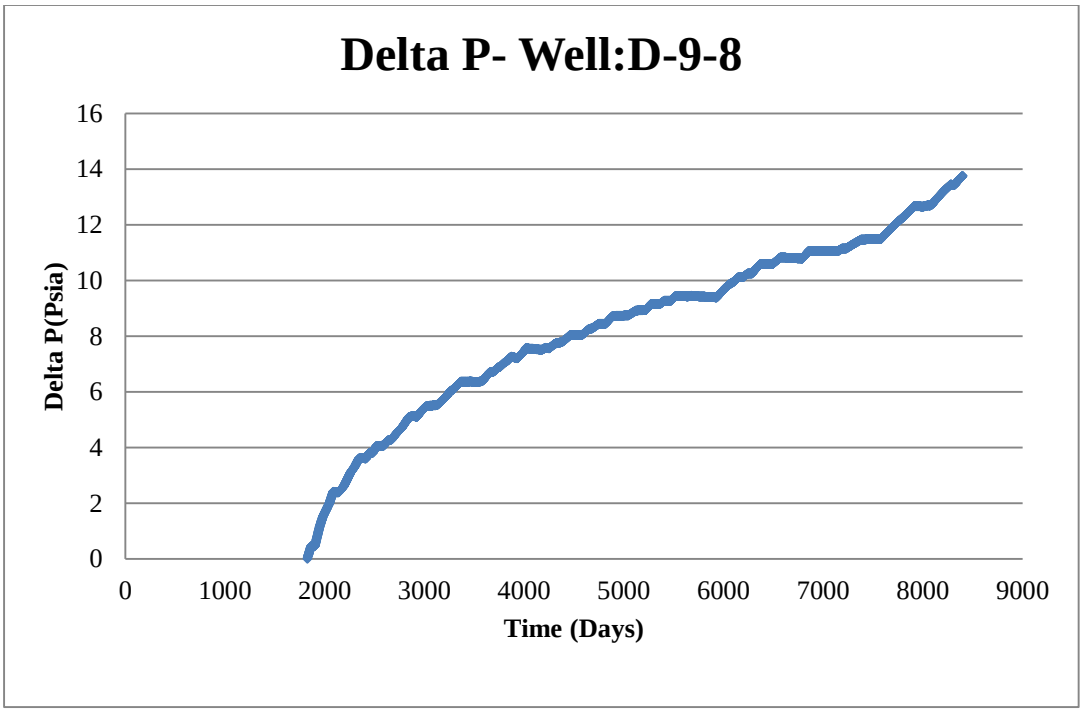

Figure 304. ΔP in well D-9-8 and Injection well in the case that well D-9-2 leakage rate is 42000ft^3/day

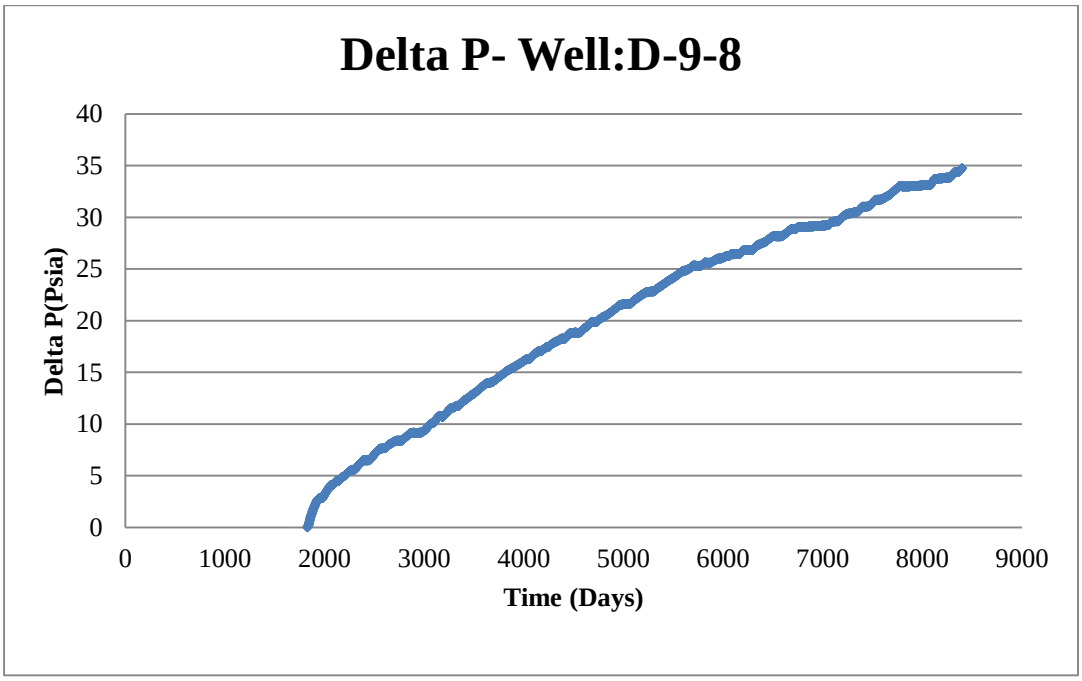

Figure 305. ΔP in well D-9-8 and Injection well in the case that well D-9-2 leakage rate is 73500ft^3/day.

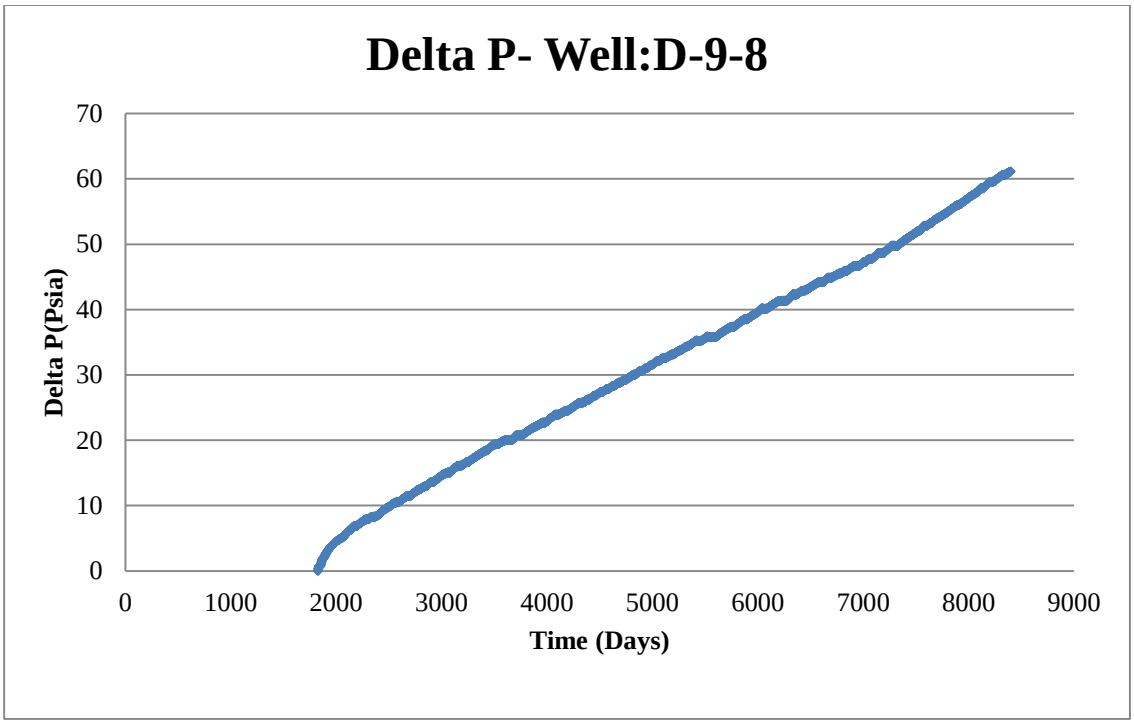

Figure 306. ΔP in well D-9-8 and Injection well in the case that well D-9-2 leakage rate is 99750ft3/day.

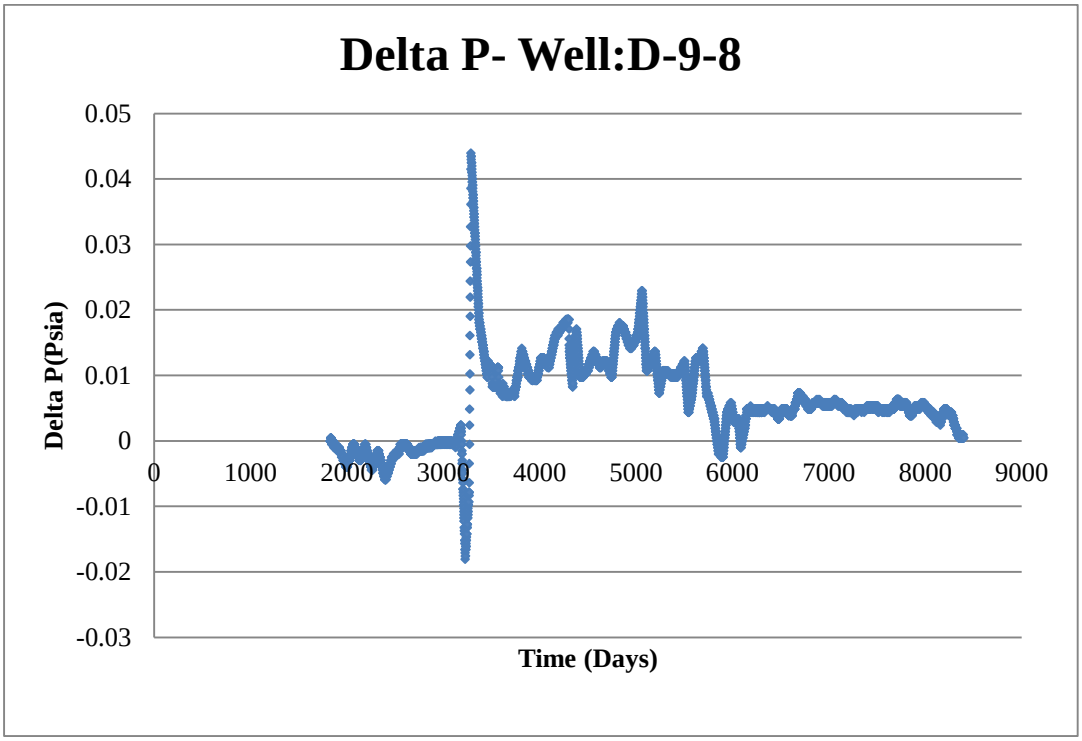

Figure 307. ΔP in well D-9-8 well in the case that well D-9-10 leakage rate is 1830ft3/day.

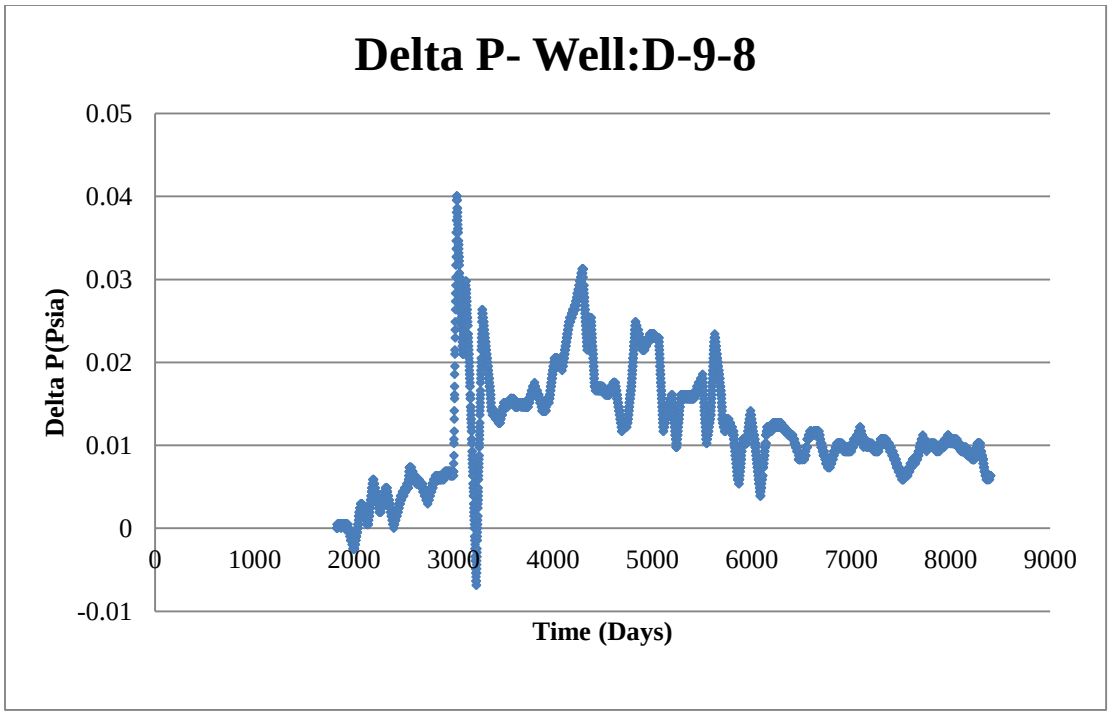

Figure 308. ΔP in well D-9-8 well in the case that well D-9-10 leakage rate is 5250ft3/day.

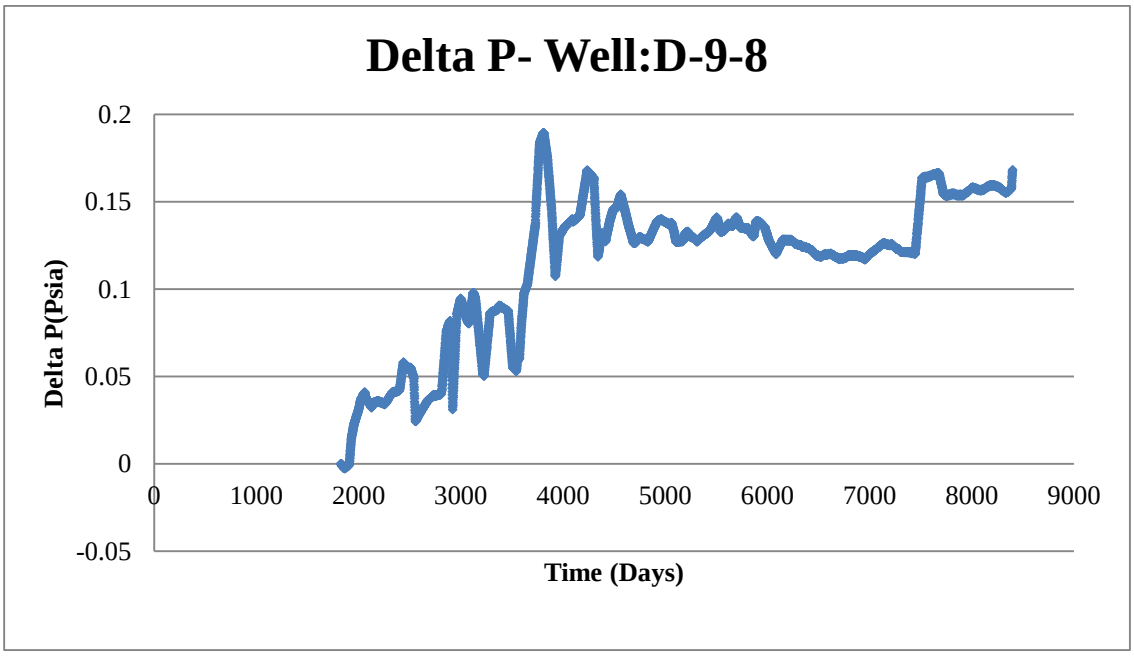

Figure 309. ΔP in well D-9-8 well in the case that well D-9-10 leakage rate is 11025ft^3/day.

APPENDIX 5

NEURAL NETWORK RESULTS

Results for the case that Neural Network training and calibration use hourly pressure data in one week after CO_2 leakage are shown below (Homogenous Model).

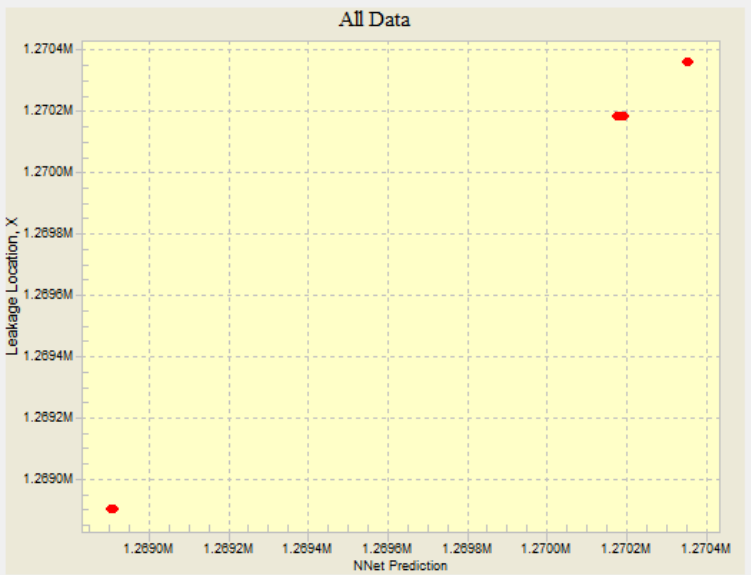

Figure 310.Actual Leakage Location(X) - Neural Network training results -1 week after leakage

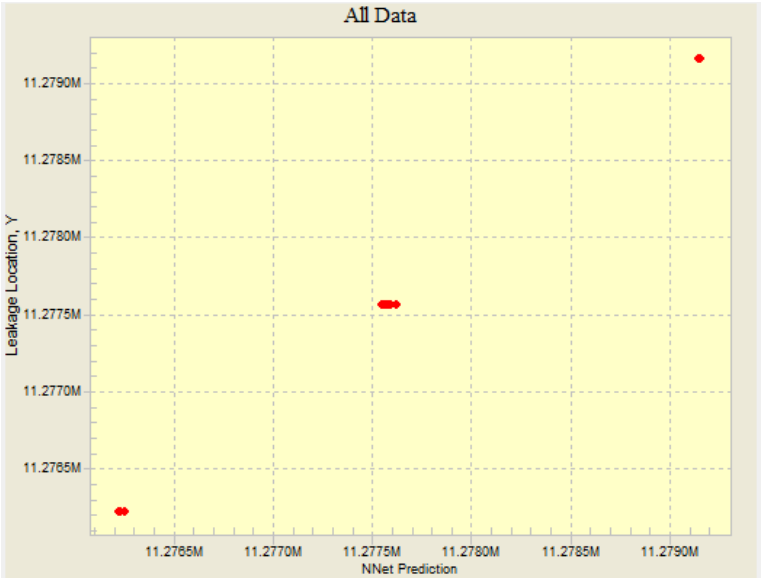

Figure 311. Actual Leakage Location(Y) - Neural Network training results -1 week after leakage

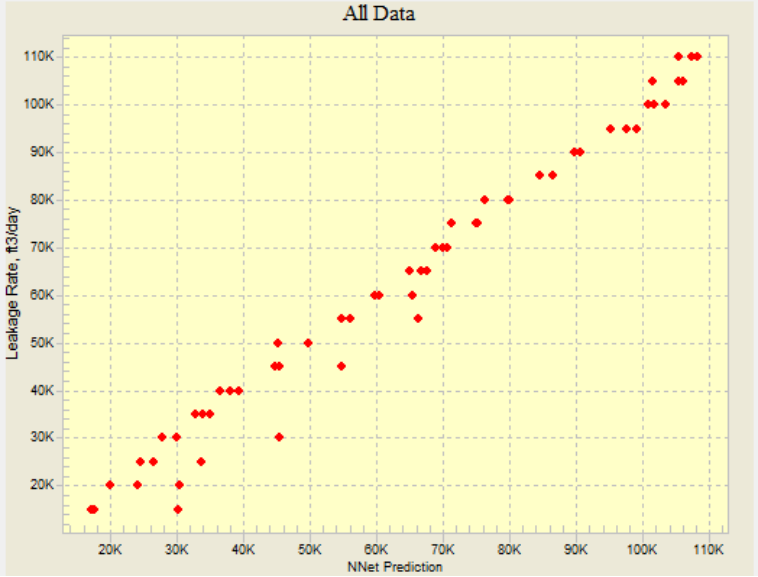

Figure 312. Actual Leakage Rate - Neural Network training results -1 week after leakage

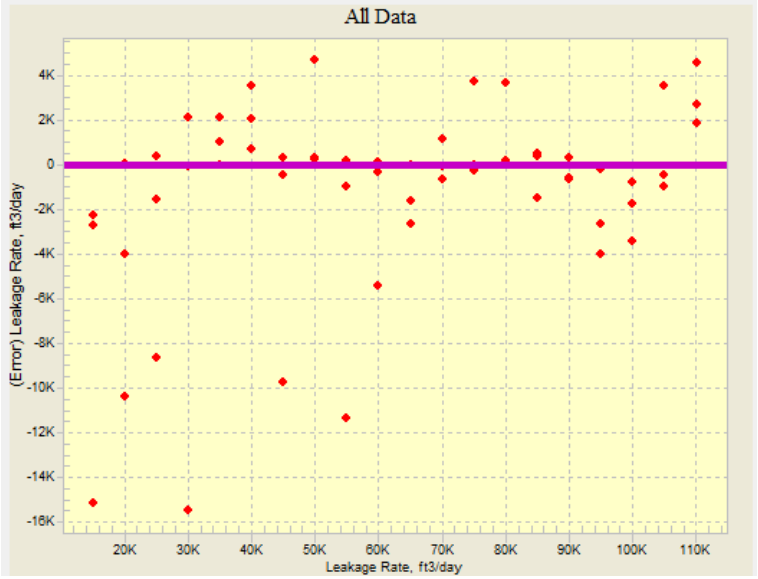

Figure 313. Errors in Leakage Rate (Neural Network training results) -1 week after leakage

Results for the case that Neural Network training and calibration use hourly pressure data in 5 weeks after CO_2 leakage are shown below.

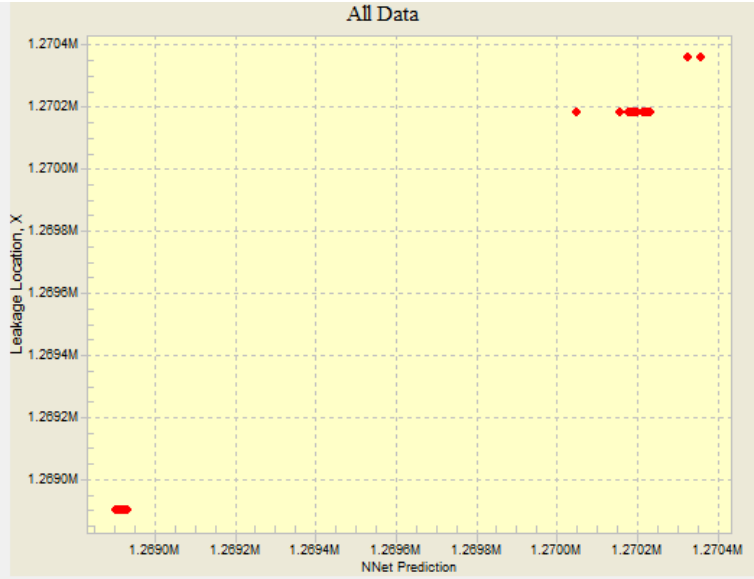

Figure 314. Actual Leakage Location(X) - Neural Network training results -5 weeks after leakage

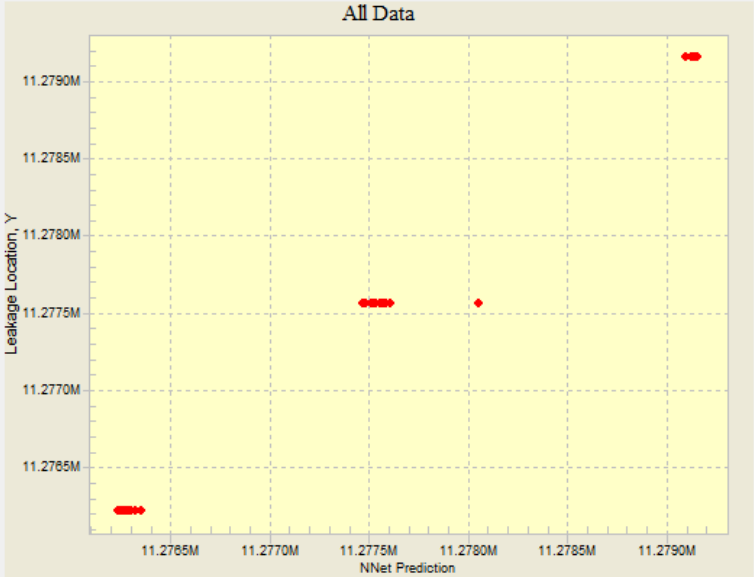

Figure 315. Actual Leakage Location(Y) - Neural Network training results -5 week after leakage

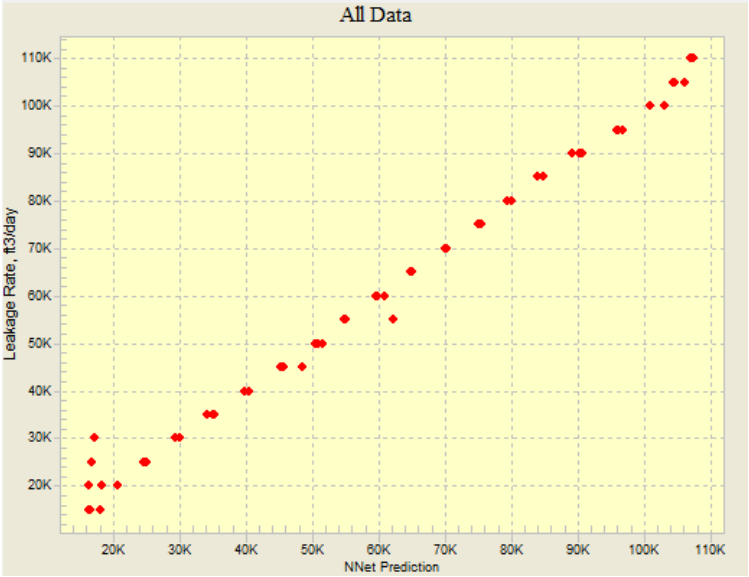

Figure 316. Actual Leakage Rate - Neural Network training results -5 weeks after leakage

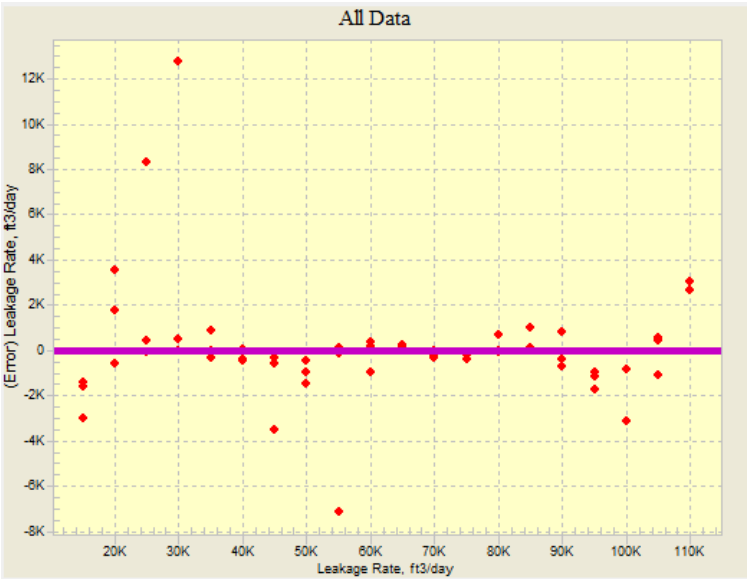

Figure 317. Errors in Leakage Rate (Neural Network training results) -5 weeks after leakage

Results for the case that Neural Network training and calibration use hourly pressure data in 8 weeks after CO_2 leakage are shown below.

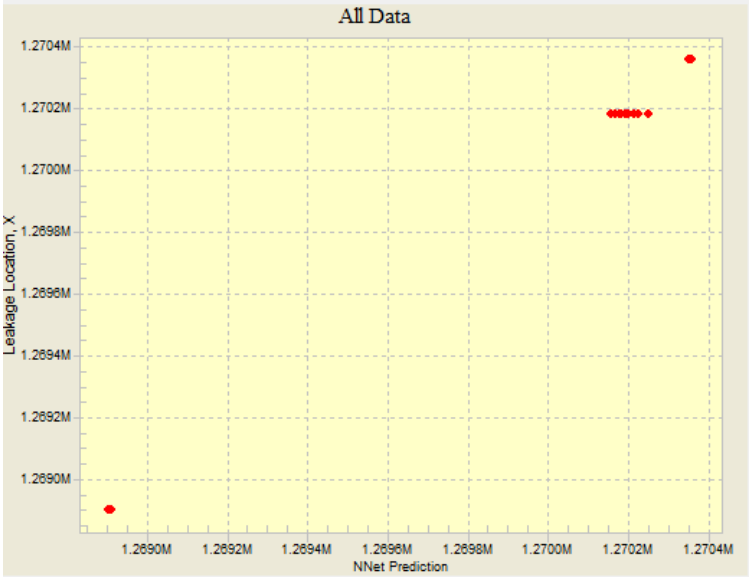

Figure 318. Actual Leakage Location(X) - Neural Network training results -8 weeks after leakage

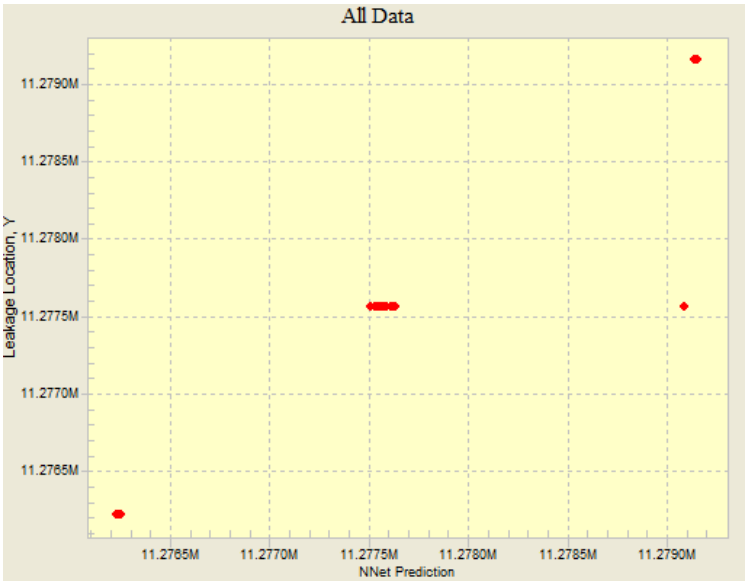

Figure 319. Actual Leakage Location(Y) - Neural Network training results -8 weeks after the leakage

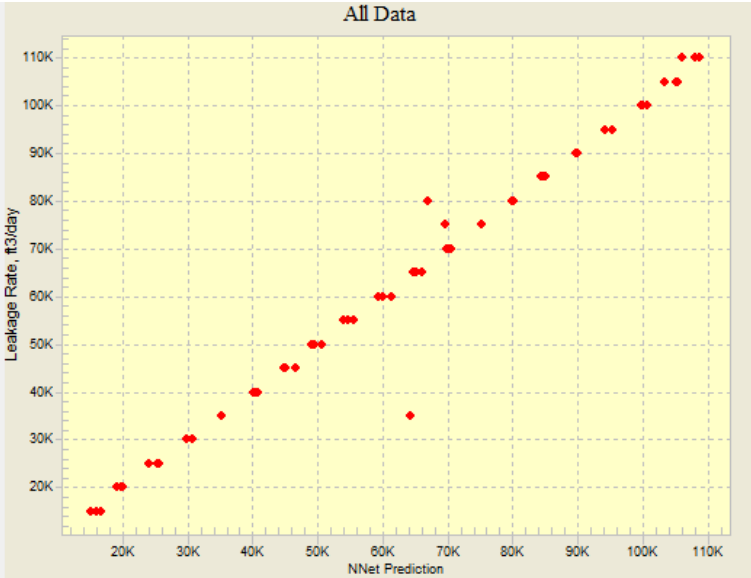

Figure 320. Actual Leakage Rate - Neural Network training results -8 weeks after leakage

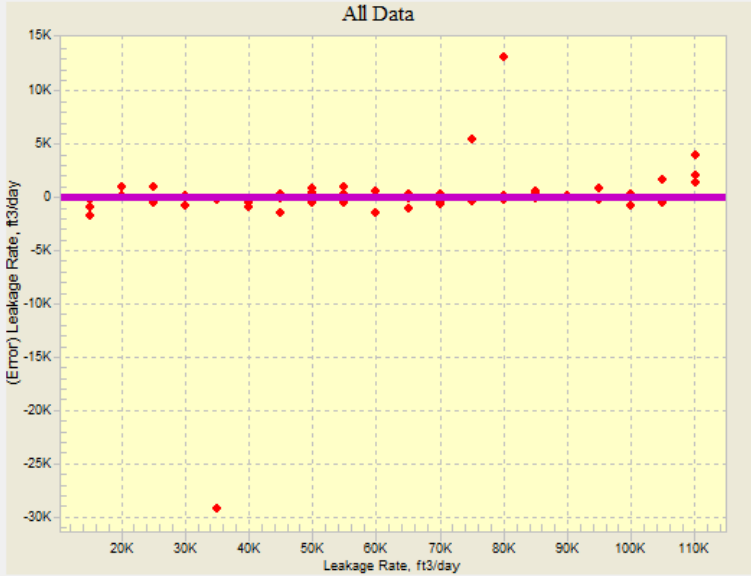

Figure 321. Errors in Leakage Rate (Neural Network training results) -8 weeks after leakage

Results for the case that Neural Network training and calibration use hourly pressure data in one week after CO_2 leakage are shown below (Heterogeneous Model).

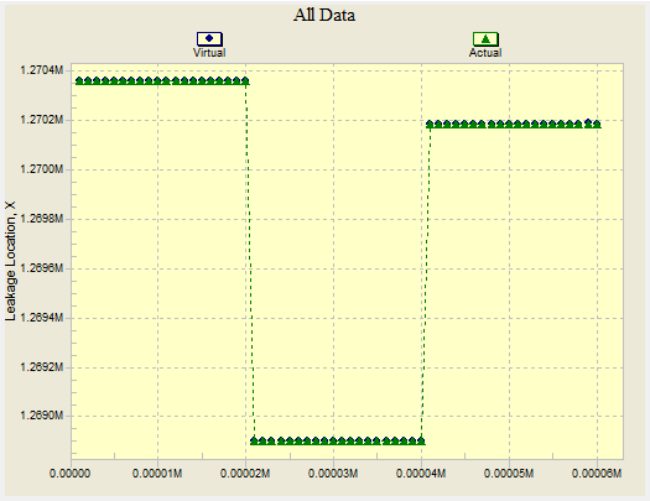

Figure 322. Leakage location(X) - Neural Network results for all steps (training, calibration and verification)-clean pressure data

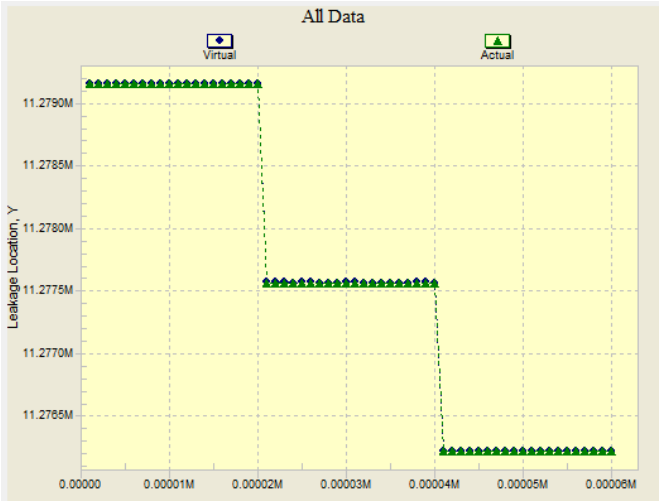

Figure 323. Leakage location(Y) - Neural Network results for all steps (training, calibration and verification)-clean pressure data

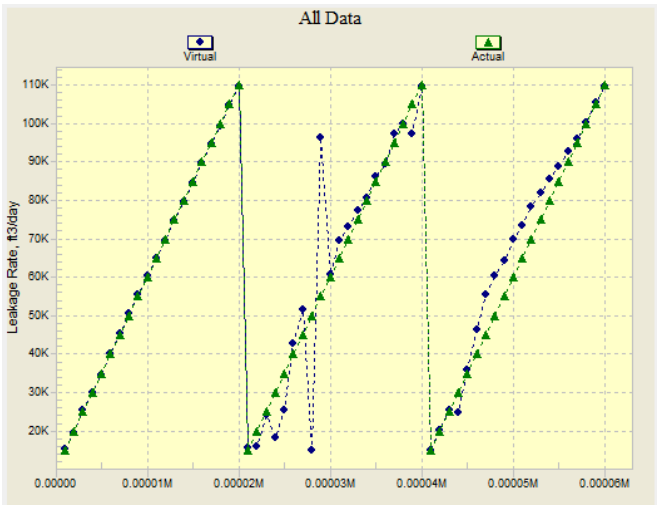

Figure 324. Leakage rate - Neural Network results for all steps (training, calibration and verification)-clean pressure data

Results of Neural Network training, calibration and verification, using Noisy pressure data

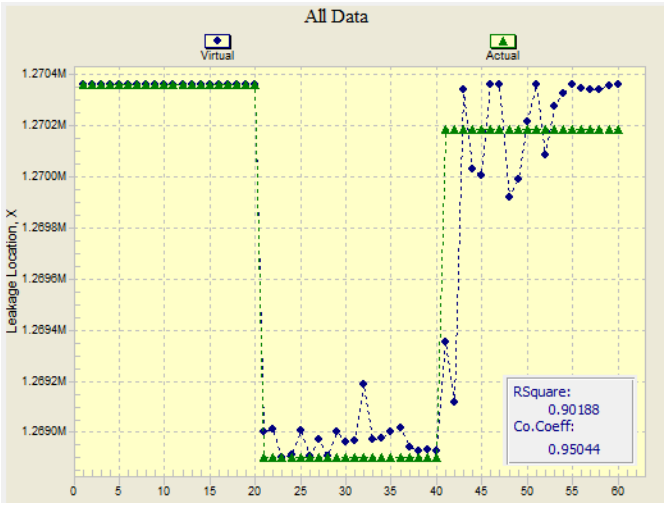

Figure 325. Leakage location(X)- Neural Network results for all steps (training, calibration and verification)-noisy pressure data

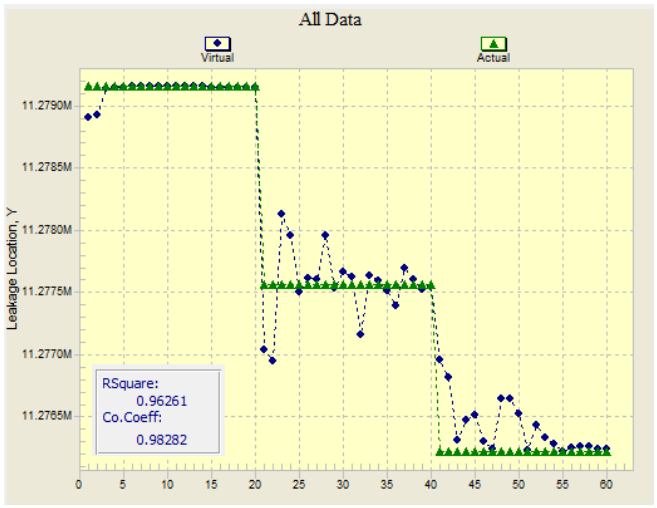

Figure 326. Leakage location(Y)- Neural Network results for all steps (training, calibration and verification)-noisy pressure data

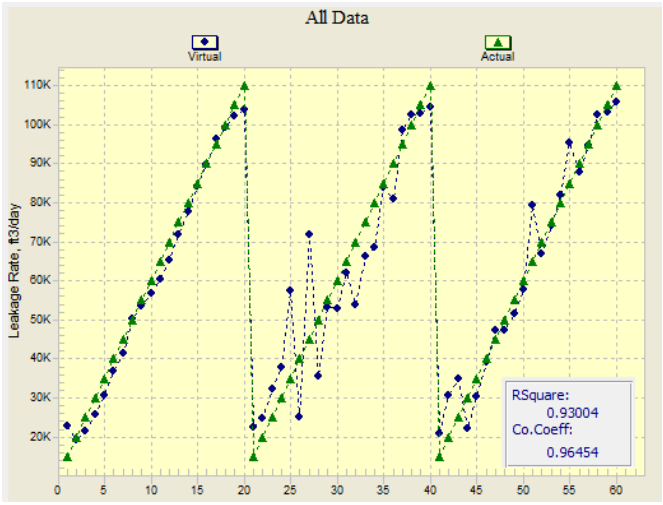

Figure 327. Leakage rate- Neural Network results for all steps (training, calibration and verification)-noisy pressure data

APPENDIX 6

INTELLIGENT LEAKAGE DETECTION SYSTEM (ILDS) RUNS

Blind run verification for RT-ILDS

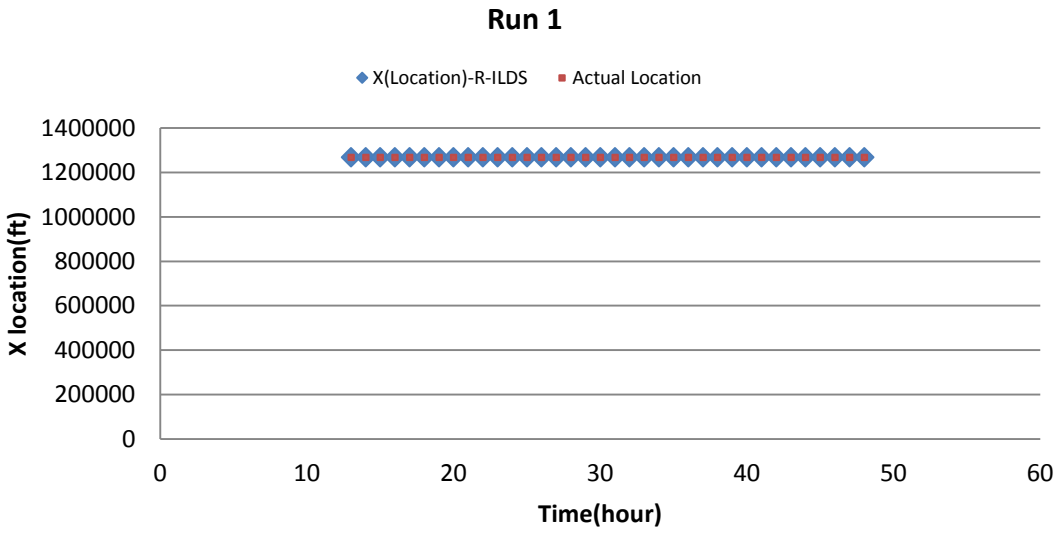

Figure 328. R-ILDS leakage location prediction, run1: well D-9-6 leaks 23 Mcf/day

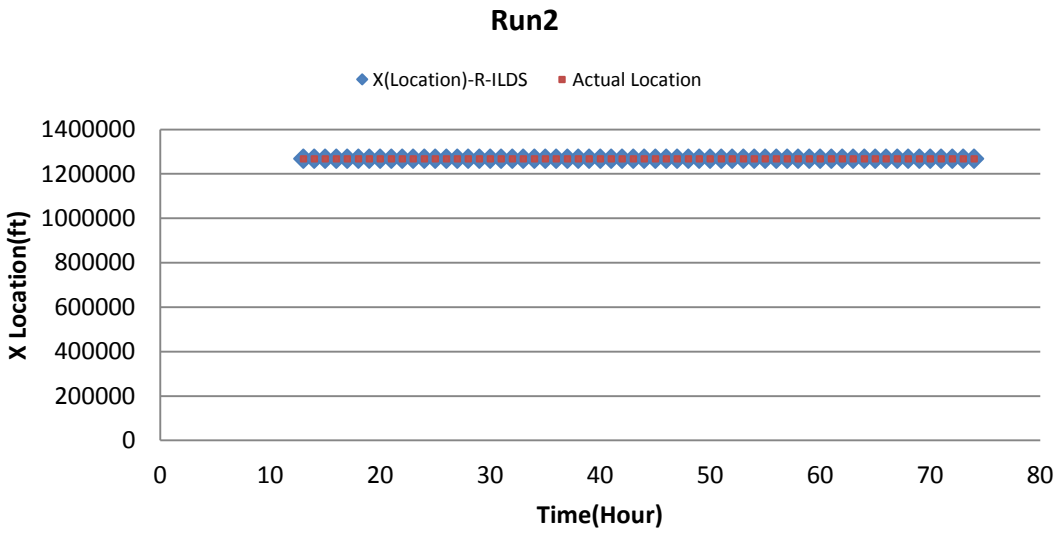

Figure 329. R-ILDS leakage location prediction, run2: well D-9-6 leaks 72 Mcf/day

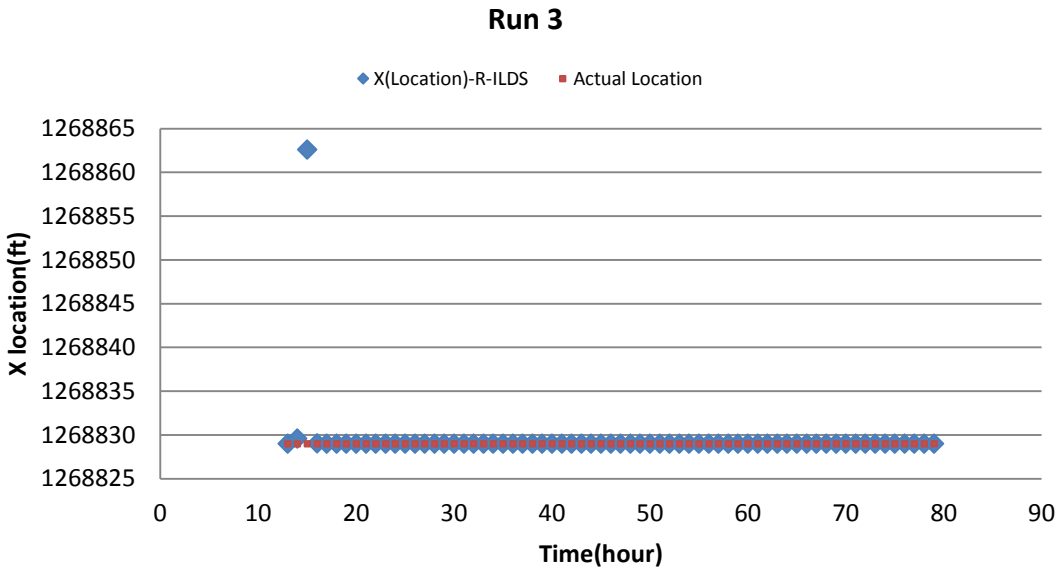

Figure 330. R-ILDS leakage location prediction, run3: well D-9-6 leaks 93 Mcf/day

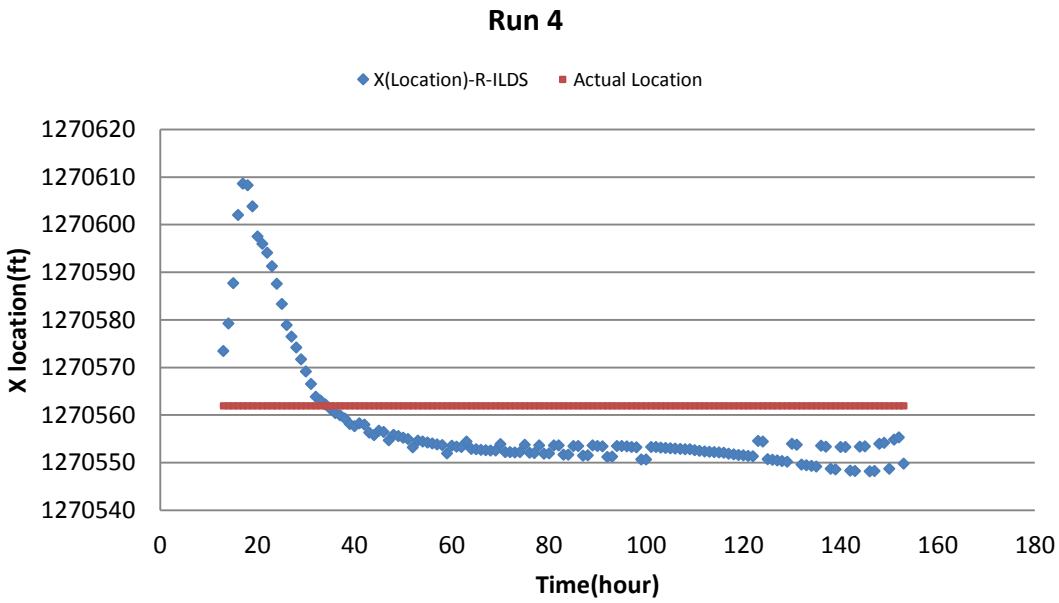

Figure 331. R-ILDS leakage location prediction, run4: well D-9-7 leaks 32 Mcf/day

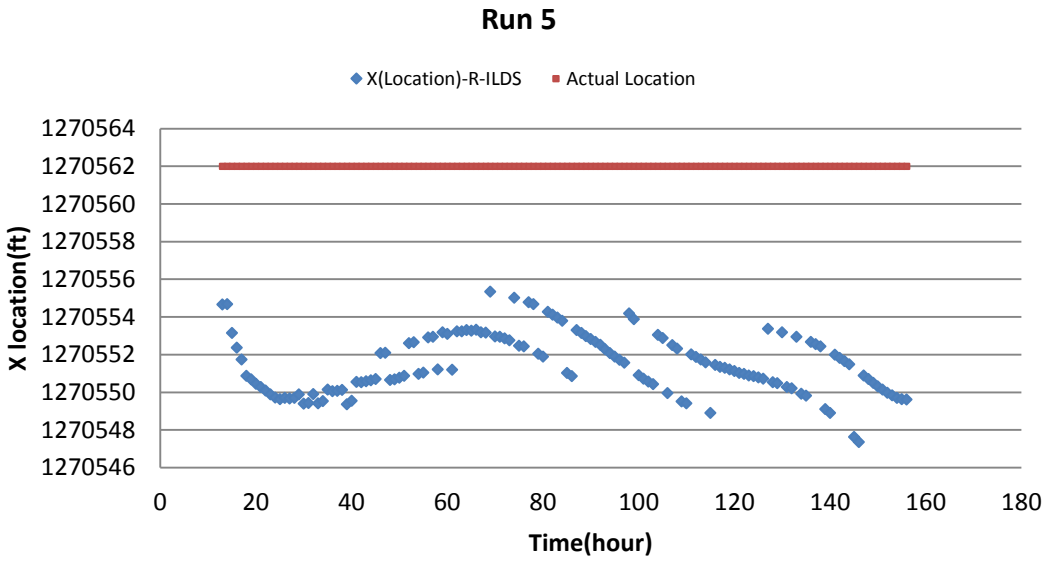

Figure 332. R-ILDS leakage location prediction, run5: well D-9-7 leaks 61 Mcf/day

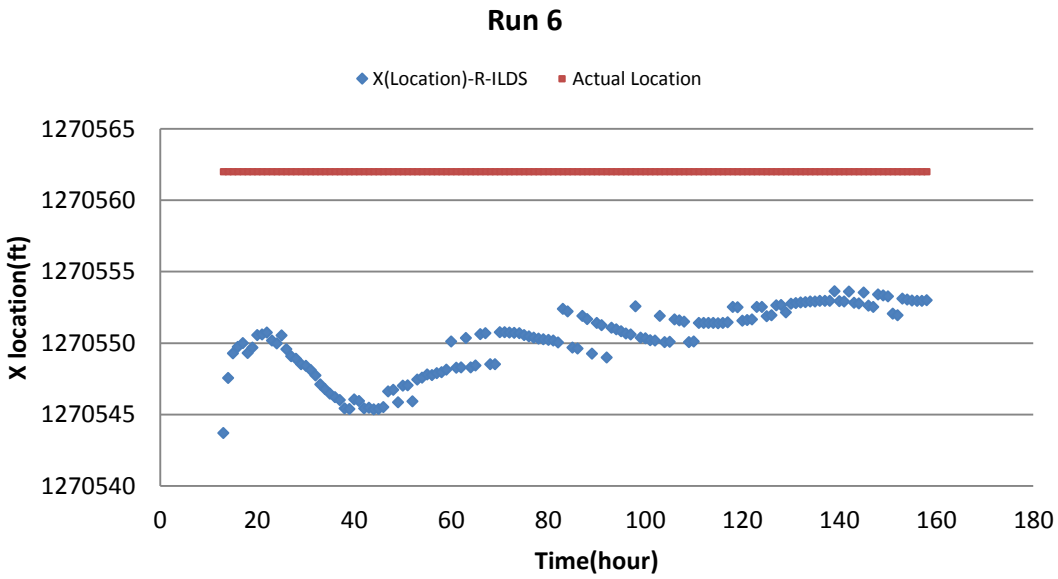

Figure 333. R-ILDS leakage location prediction, run6: well D-9-7 leaks 87 Mcf/day

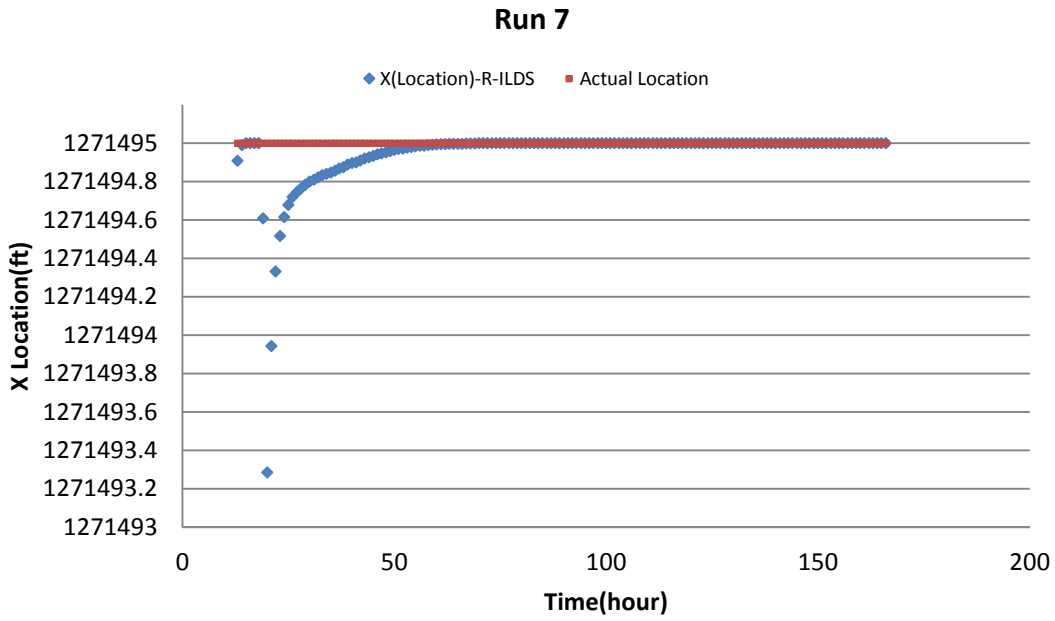

Figure 334. R-ILDS leakage location prediction, run7: well D-9-8 leaks 27 Mcf/day

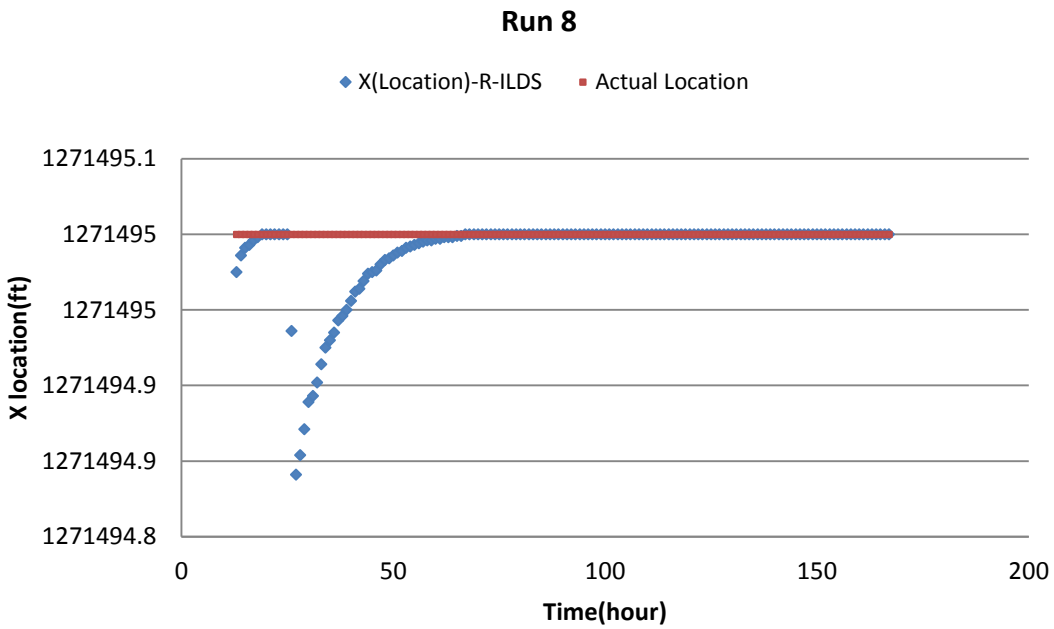

Figure 335. R-ILDS leakage location prediction, run9: well D-9-8 leaks 101 Mcf/day

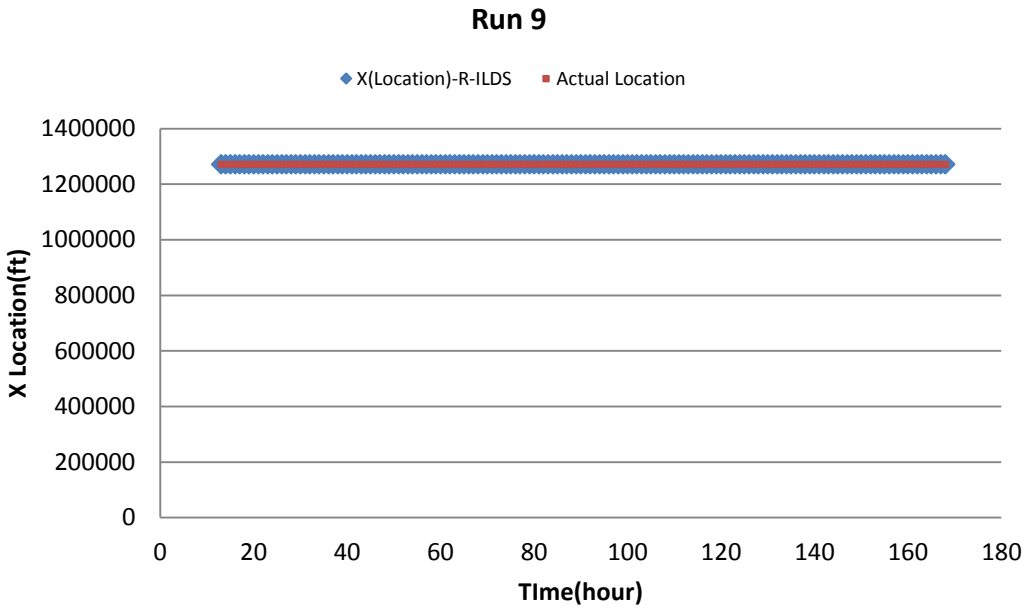

Figure 336. R-ILDS leakage location prediction, run9: well D-9-8 leaks 101 Mcf/day

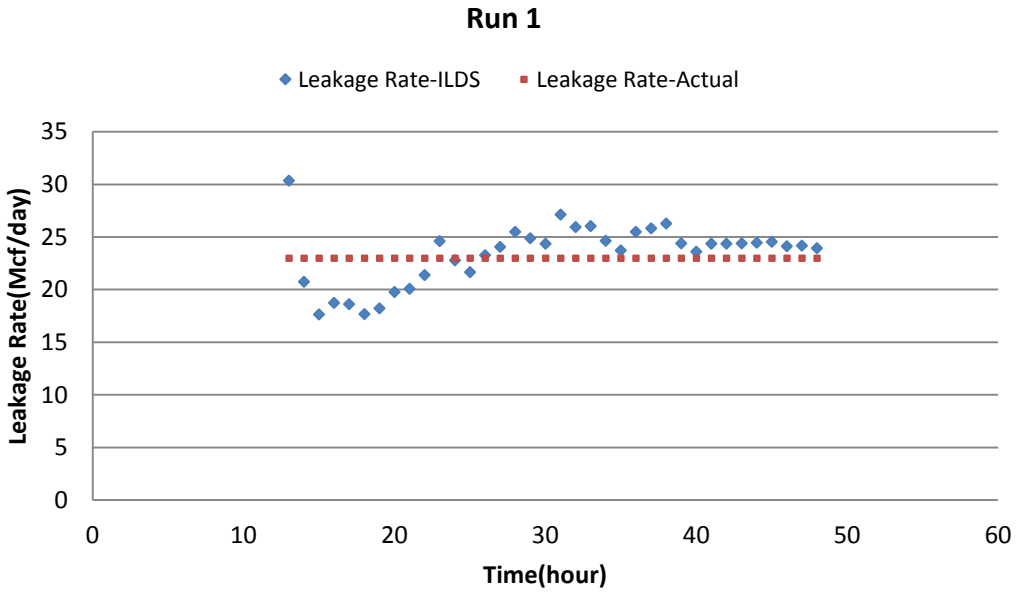

Figure 337. R-ILDS leakage rate prediction, run1: well D-9-6 leaks 23 Mcf/day

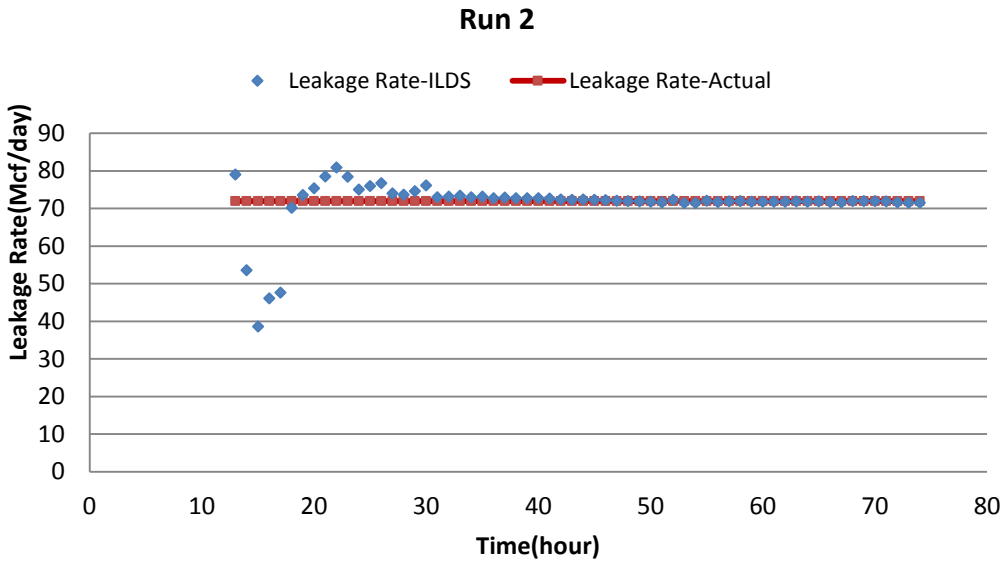

Figure 338. R-ILDS leakage rate prediction, run2: well D-9-6 leaks 72 Mcf/day

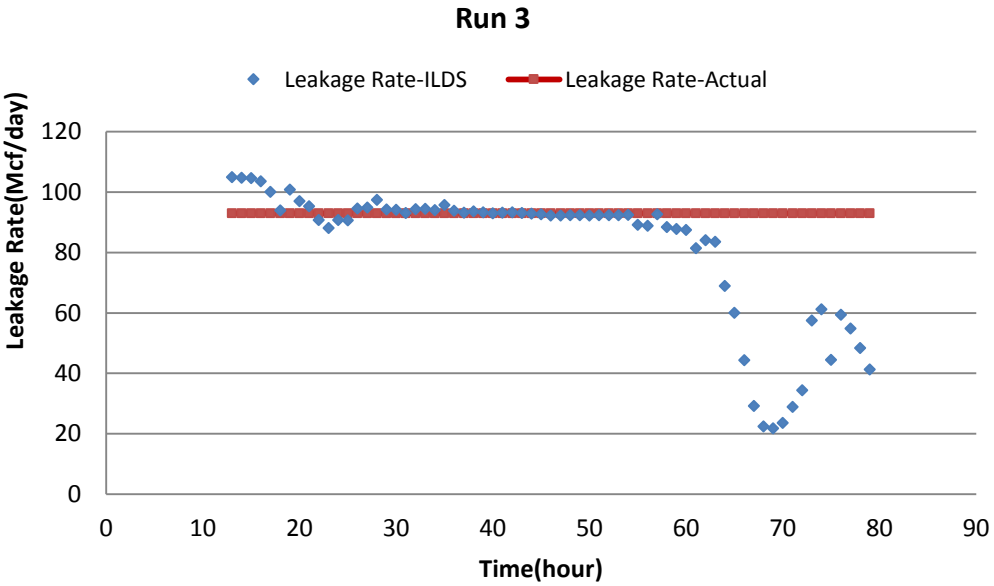

Figure 339. R-ILDS leakage rate prediction, run3: well D-9-6 leaks 93 Mcf/day

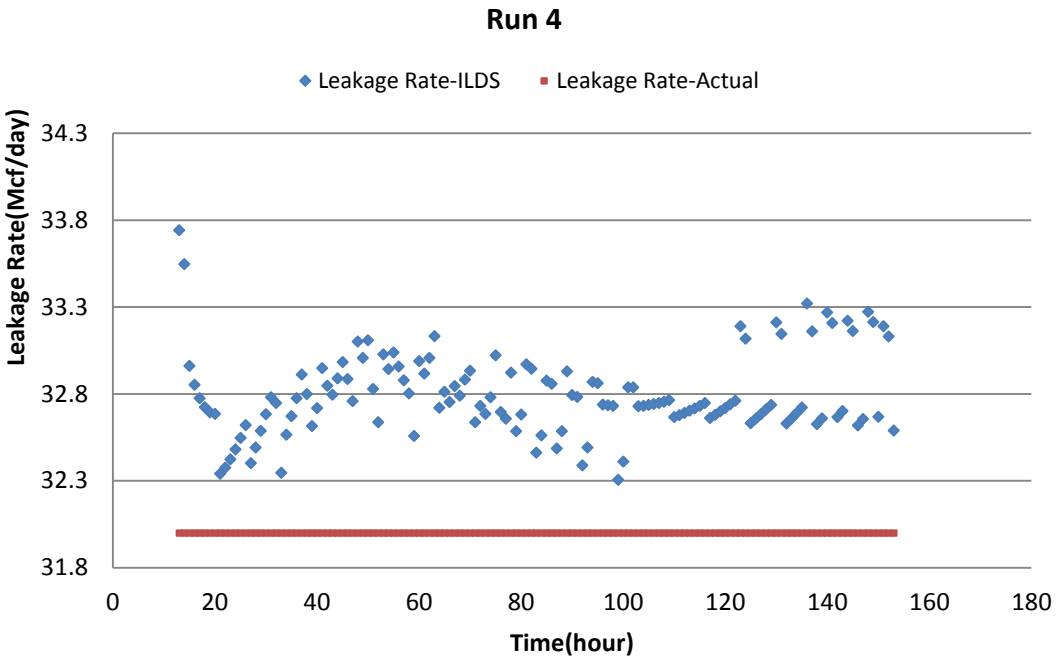

Figure 340. R-ILDS leakage rate prediction, run4: well D-9-7 leaks 32 Mcf/day

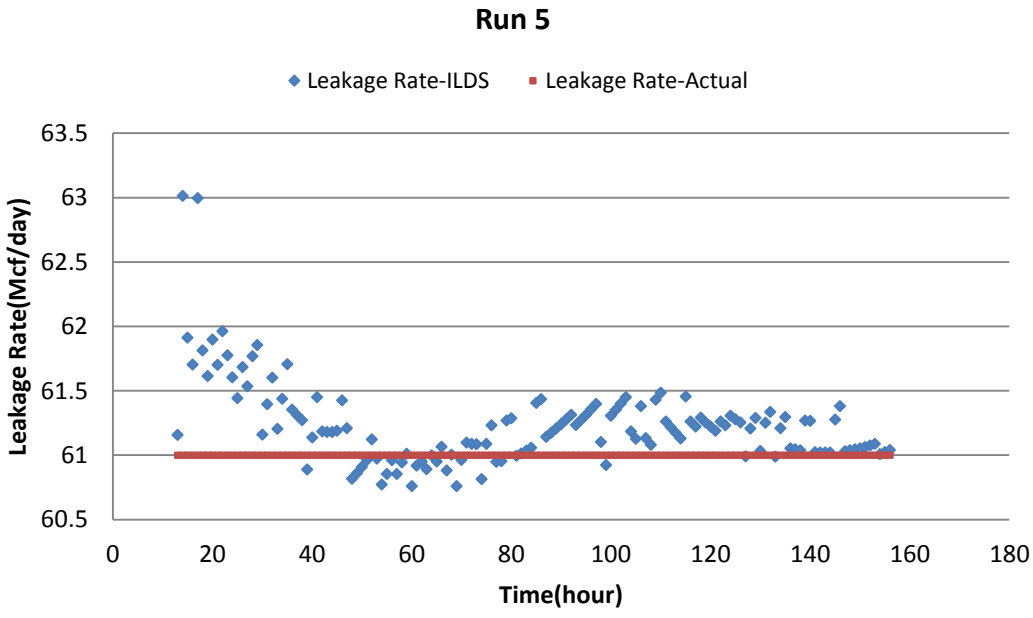

Figure 341. R-ILDS leakage rate prediction, run5: well D-9-7 leaks 61 Mcf/day

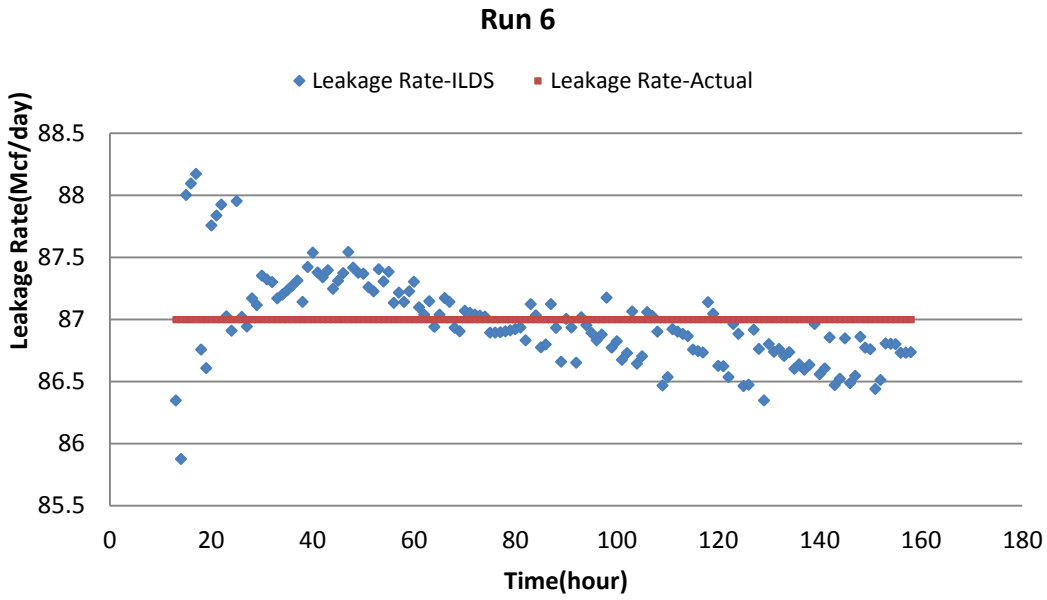

Figure 342. R-ILDS leakage rate prediction, run6: well D-9-7 leaks 87 Mcf/day

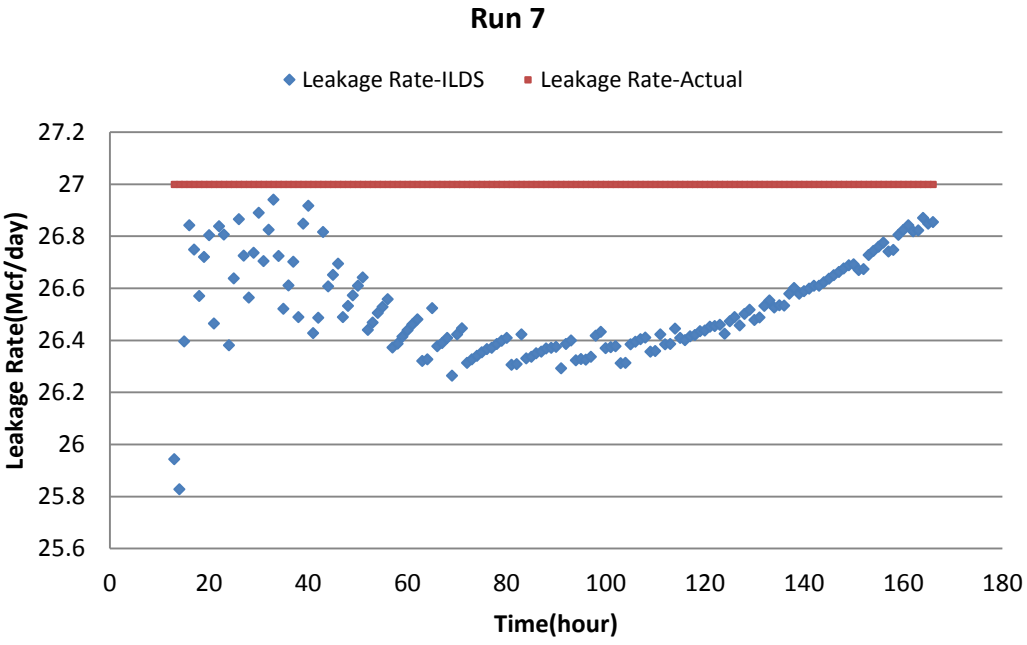

Figure 343. R-ILDS leakage rate prediction, run7: well D-9-8 leaks 27 Mcf/day

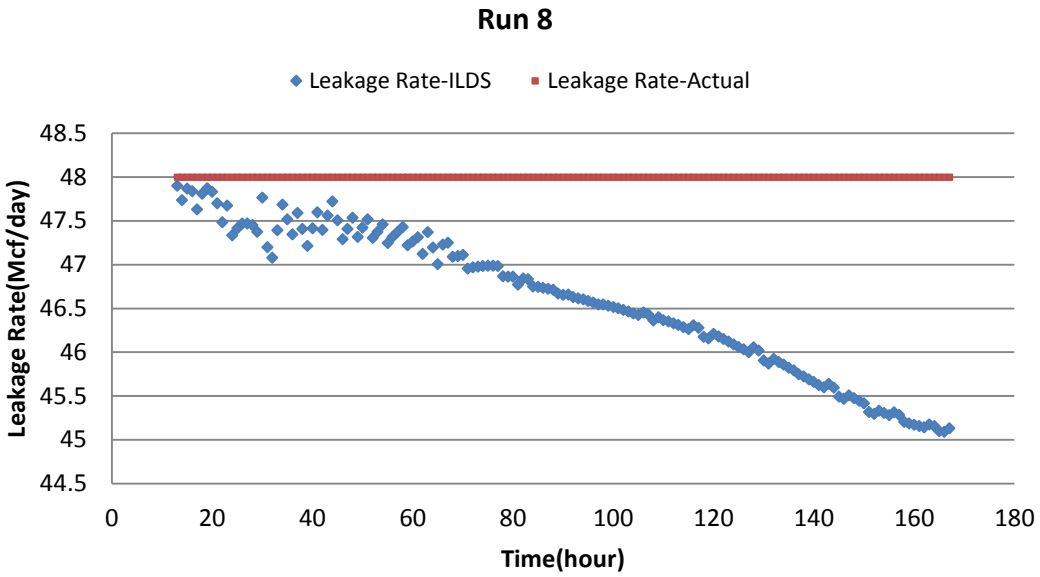

Figure 344. R-ILDS leakage rate prediction, run8:well D-9-8 leaks 48 Mcf/day

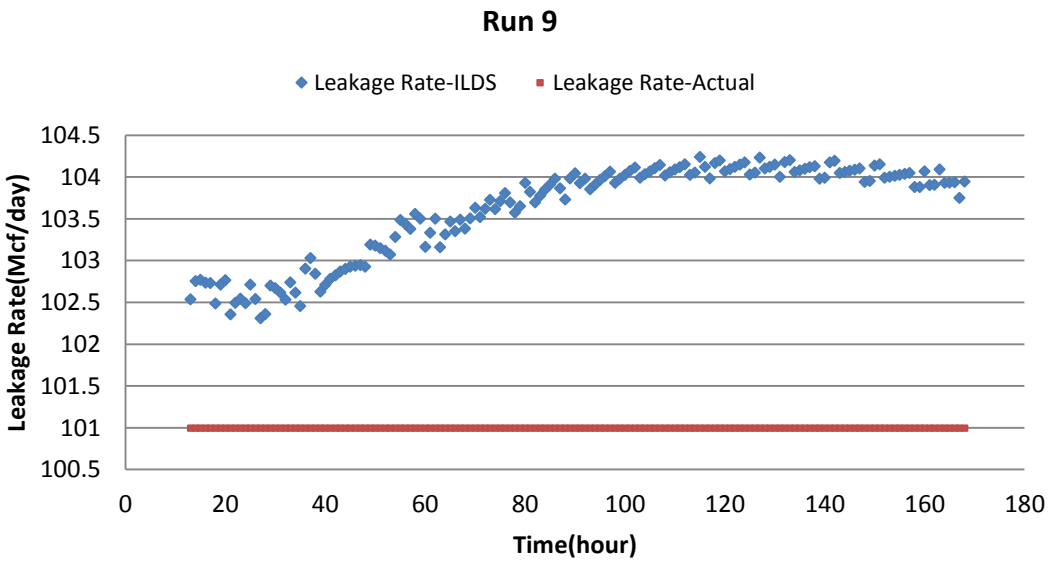

Figure 345. R-ILDS leakage rate prediction, run9: well D-9-8 leaks 101 Mcf/day

APPENDIX 7

ILDS SENSITIVITY ANALYSIS

Impact of reservoir parameters on R-ILDS Results (Section 6-3)

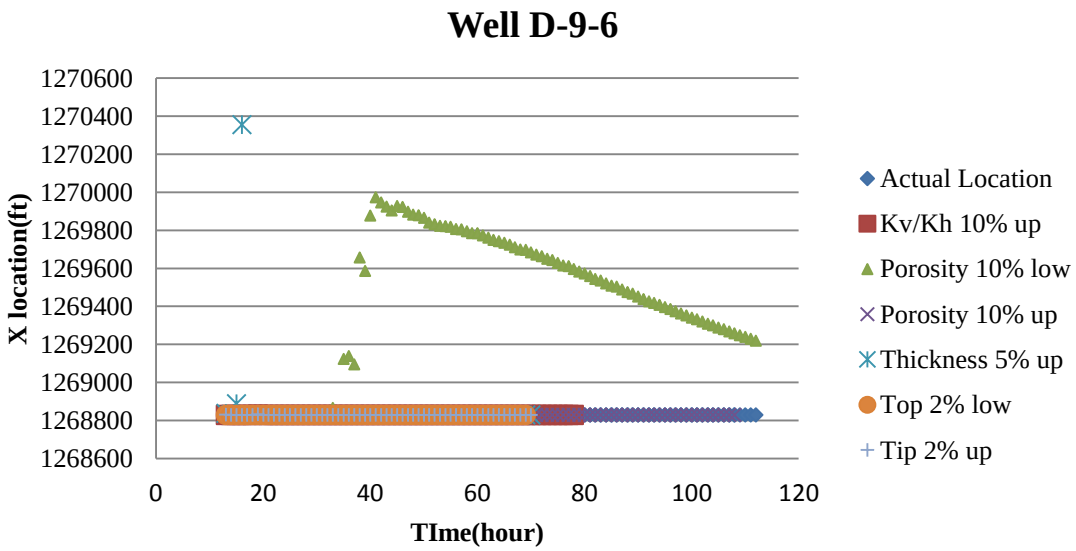

Figure 346. Sensitivity analysis of the reservoir parameters on R-ILDS leakage location prediction Well D-9-6

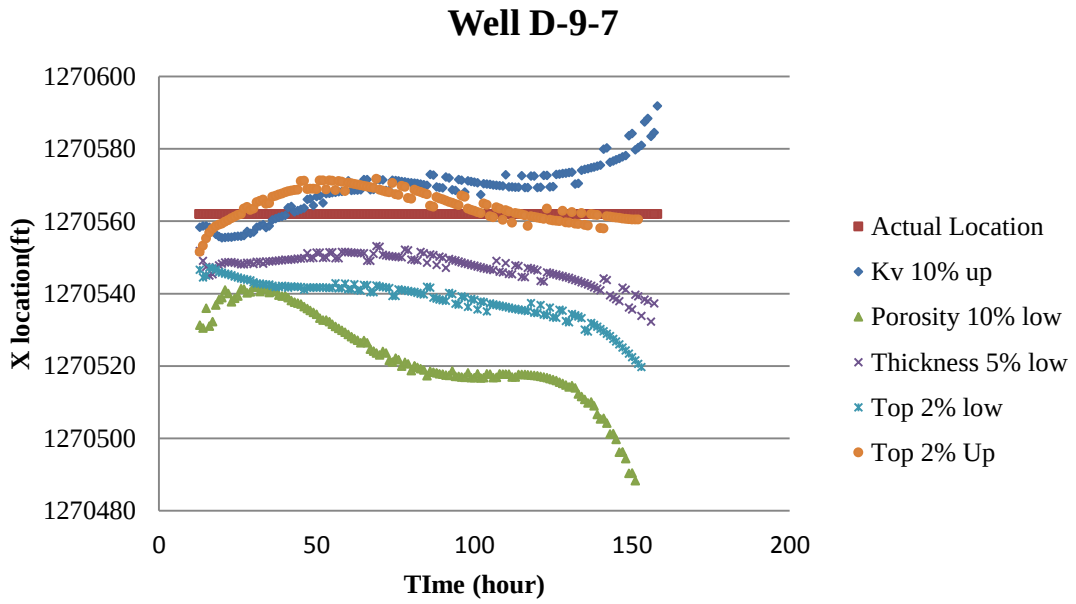

Figure 347. Sensitivity analysis of the reservoir parameters on R-ILDS leakage location prediction Well D-9-7

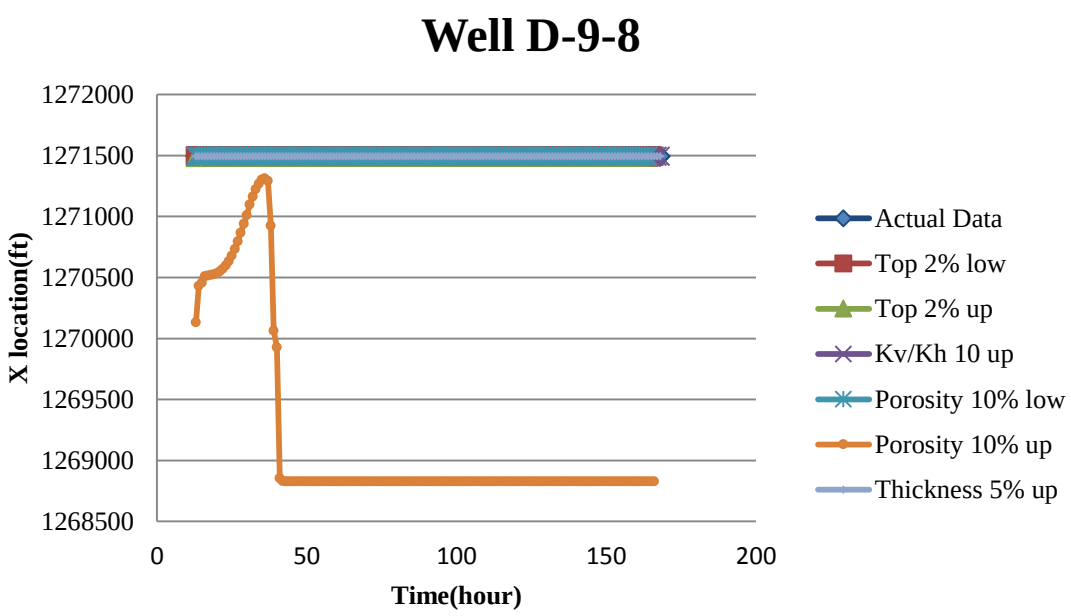

Figure 348. Sensitivity analysis of the reservoir parameters on R-ILDS leakage location prediction Well D-9-8

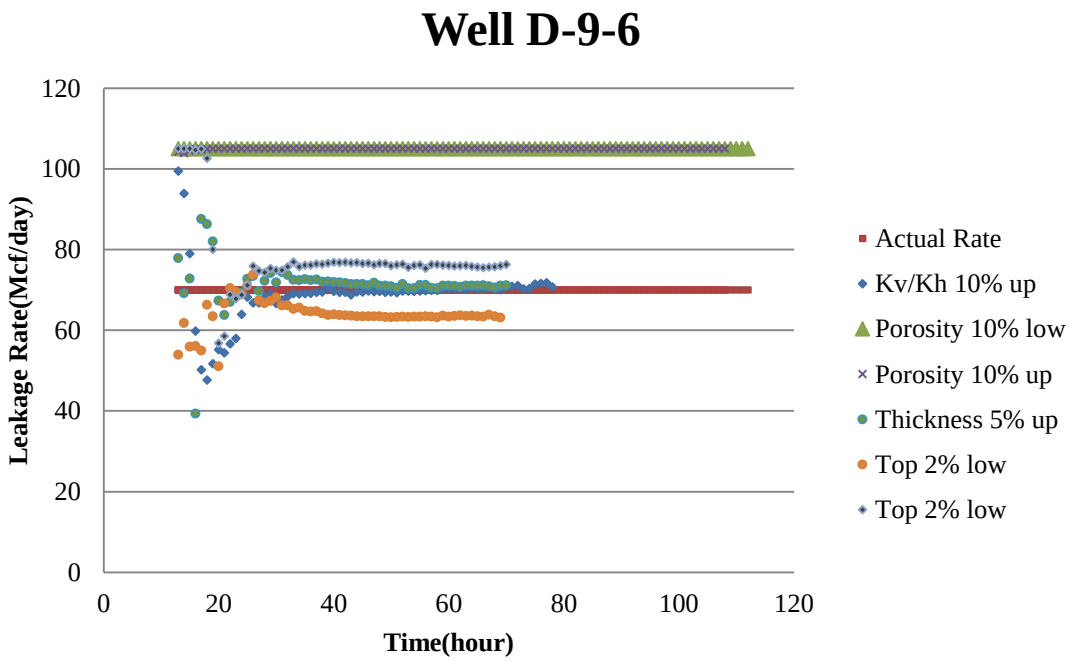

Figure 349. Sensitivity analysis of the reservoir parameters on R-ILDS leakage rate prediction Well D-9-6

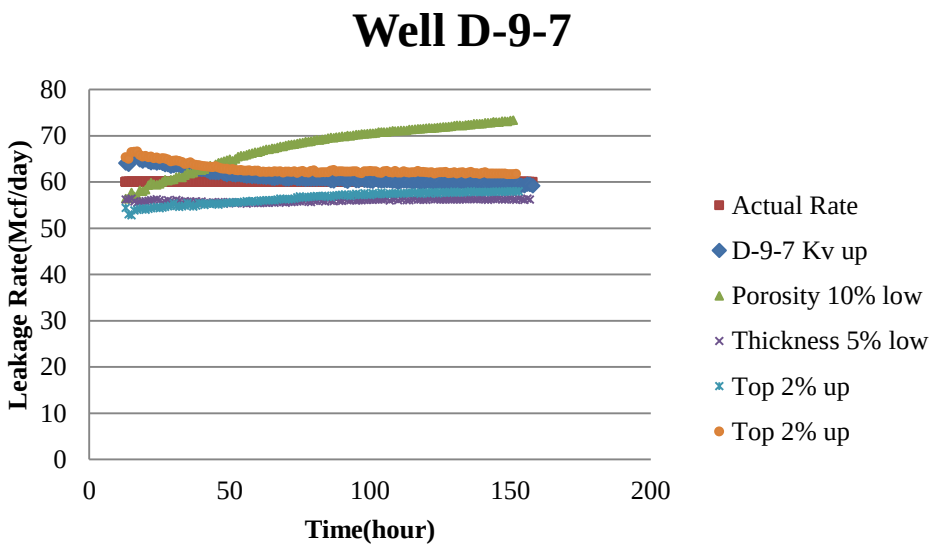

Figure 350. Sensitivity analysis of the reservoir parameters on R-ILDS leakage rate prediction Well D-9-7

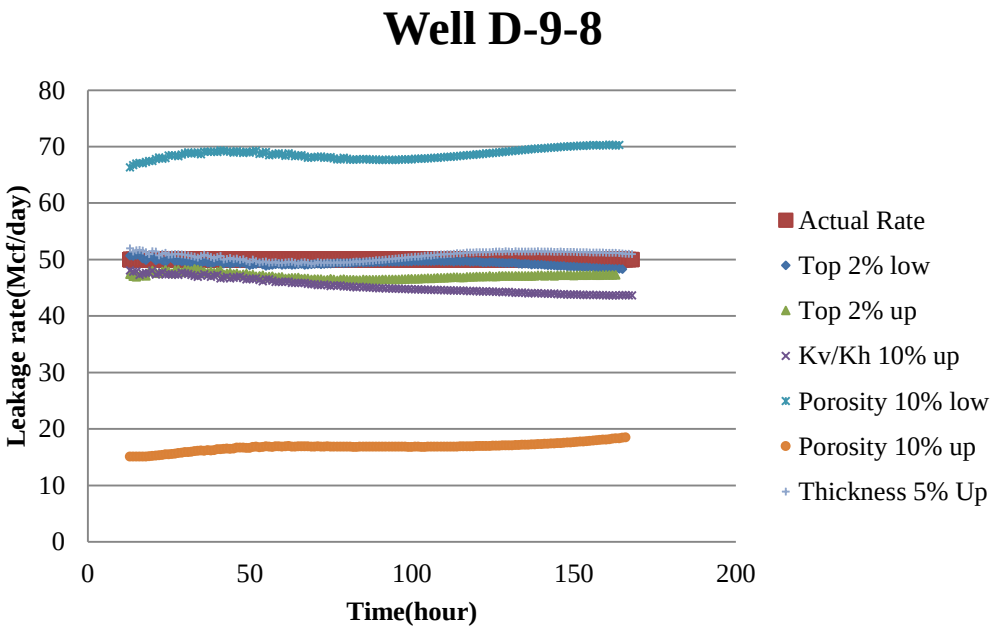

Figure 351: Sensitivity analysis of the reservoir parameters on R-ILDS leakage rate prediction Well D-9-7

APPENDIX 8

RT-ILDS RESULTS FOR VARIABLE RATES

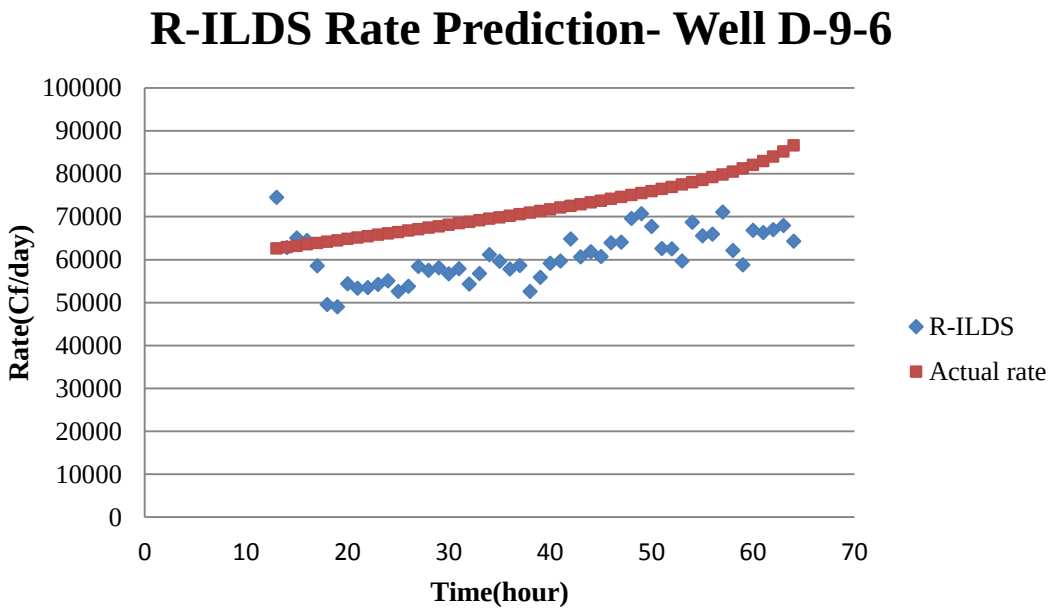

Figure 352. R-ILDS prediction for leakage rate in well D-9-6 (variable rate)

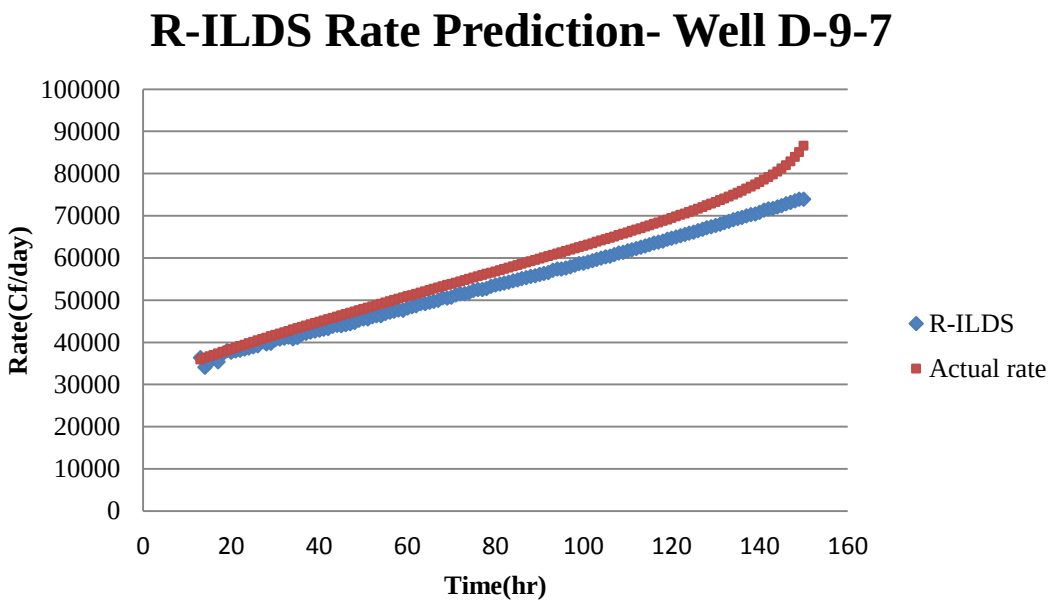

Figure 353. R-ILDS prediction for leakage rate in well D-9-7 (variable rate)

APPENDIX 9

NEURAL NETWORK BLIND RUNS

Results for RT-ILDS neural network and blind runs-PDG in injection well

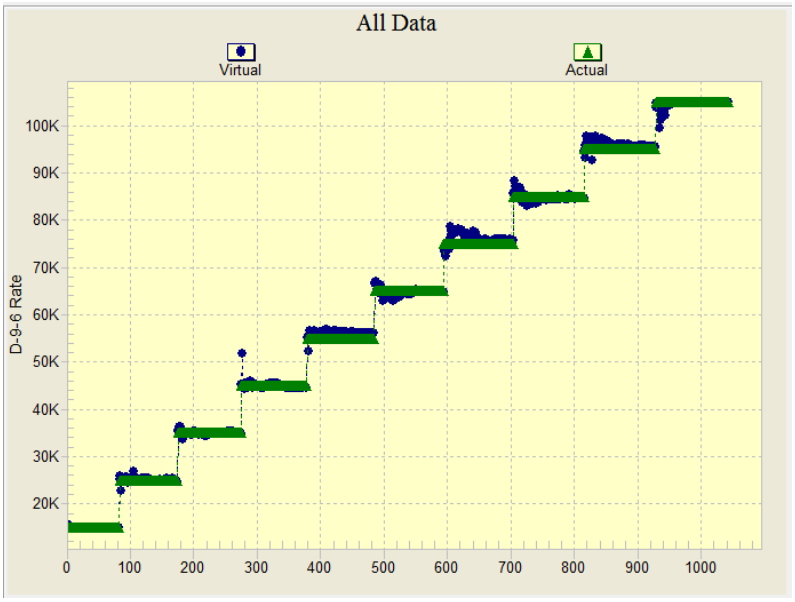

Figure 354. Neural network predictions for the leakage rate for the case that PDG is in Injection well, D-9-6 results

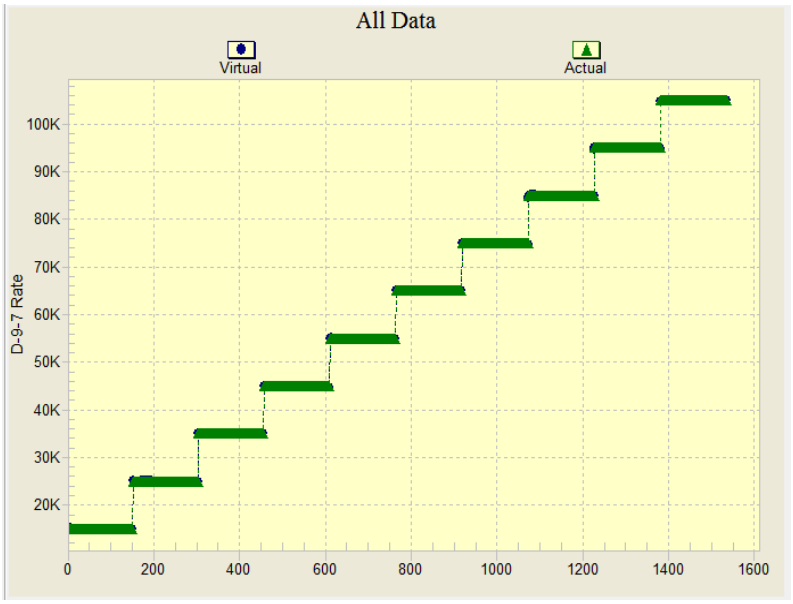

Figure 355. Neural network predictions for the leakage rate for the case that PDG is in Injection well, D-9-7 results

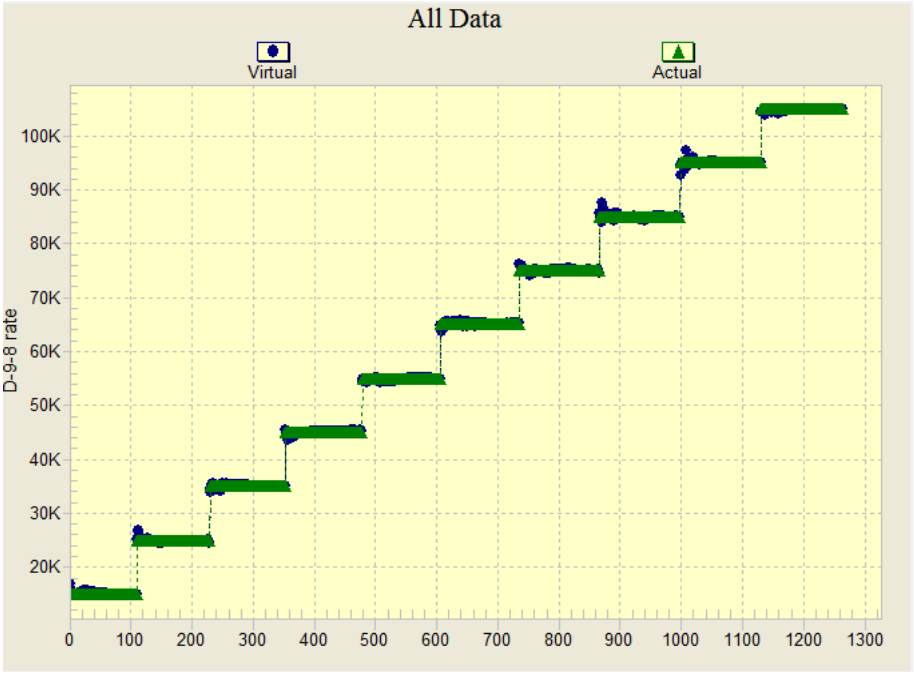

Figure 356. Neural network predictions for the leakage rate for the case that PDG is in Injection well, D-9-8 results

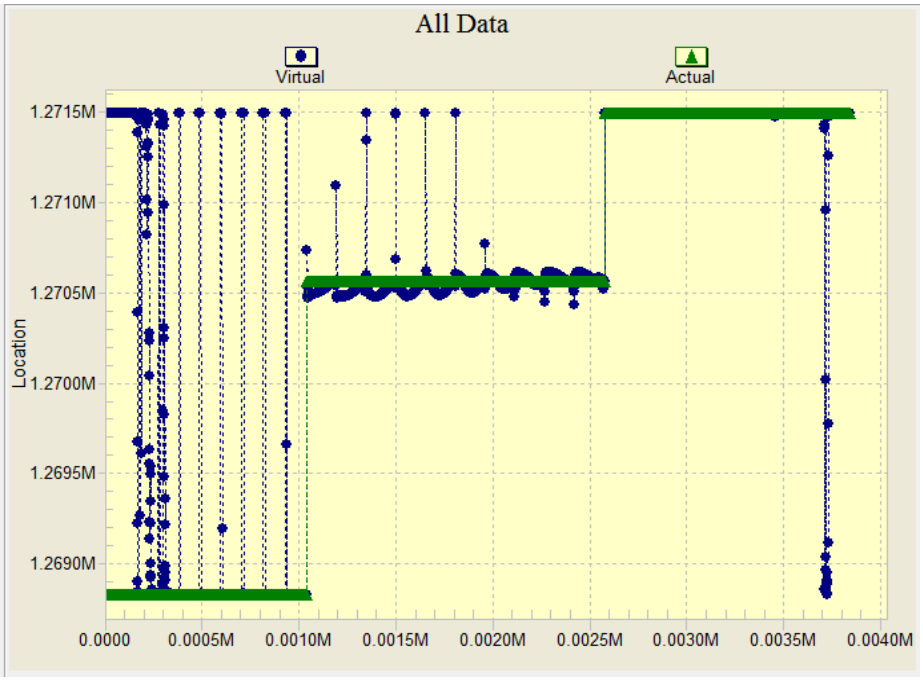

Figure 357. Neural network predictions for the leakage location for the case that PDG is in Injection well

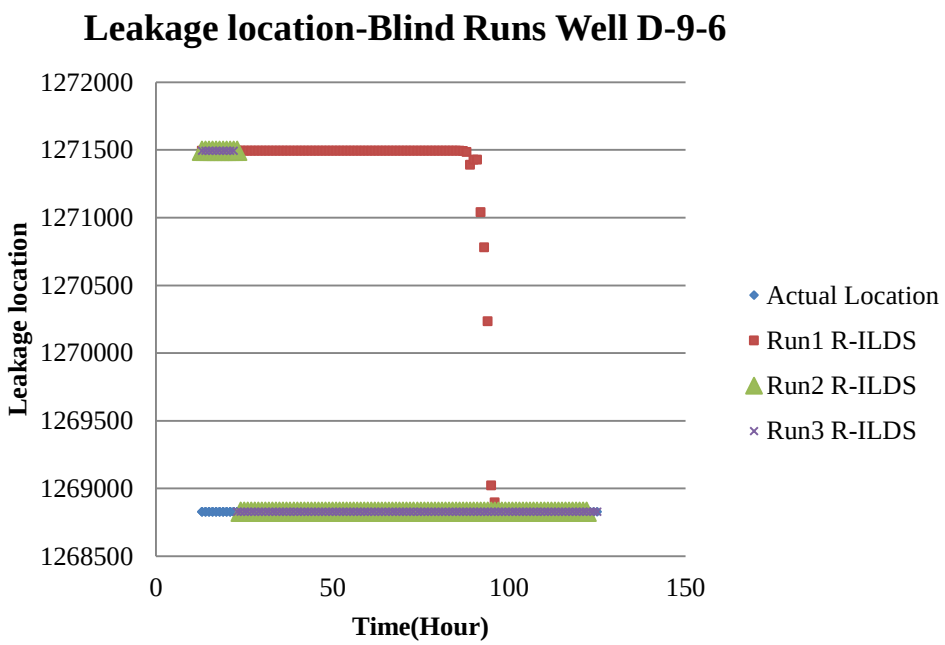

Figure 358. R-ILDS Leakage location prediction for well D-9-6, PDG in Injection well

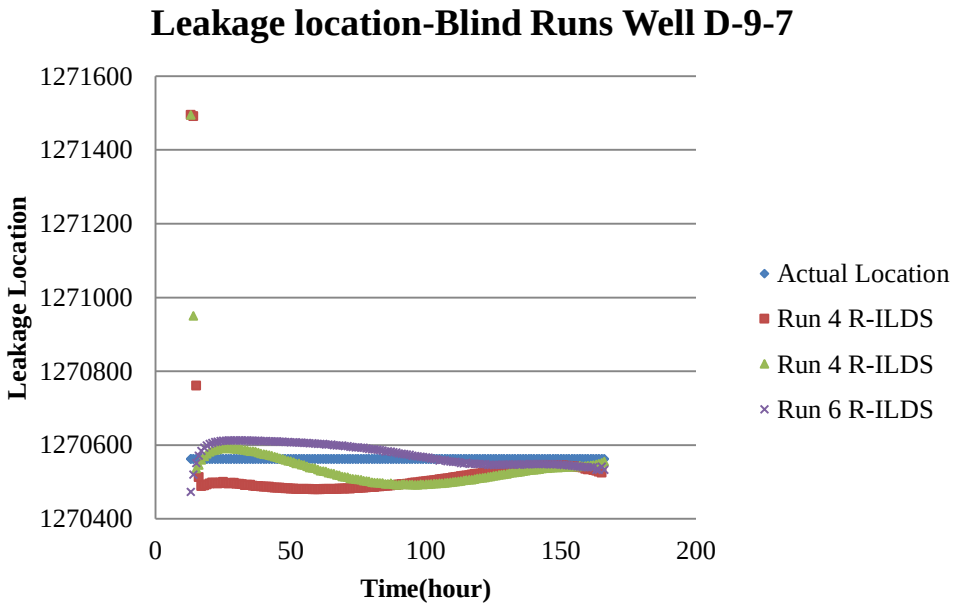

Figure 359. R-ILDS Leakage location prediction for well D-9-7, PDG in Injection well

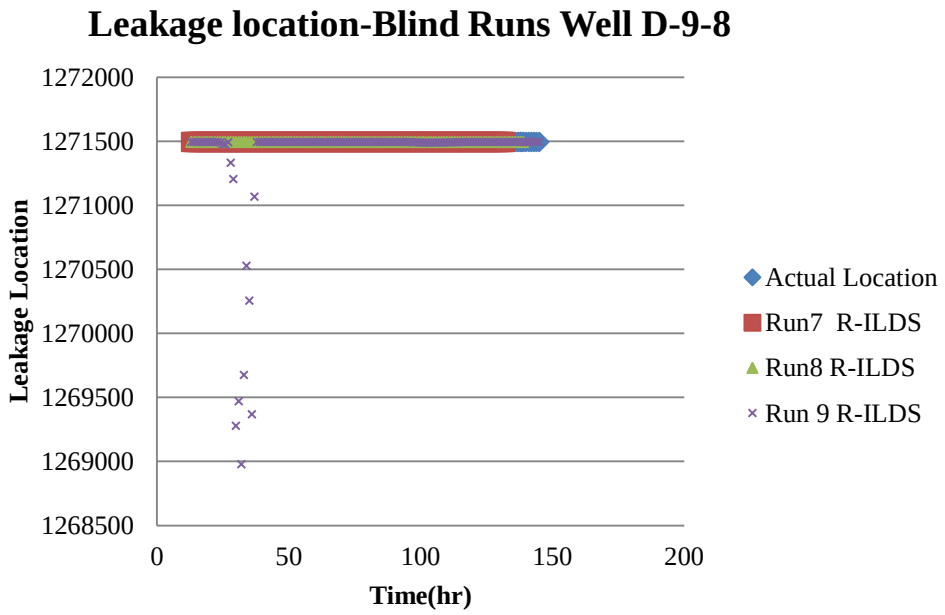

Figure 360. R-ILDS Leakage location prediction for well D-9-8, PDG in Injection well

APPENDIX 10

CAP-ROCK LEAKAGE RESULTS

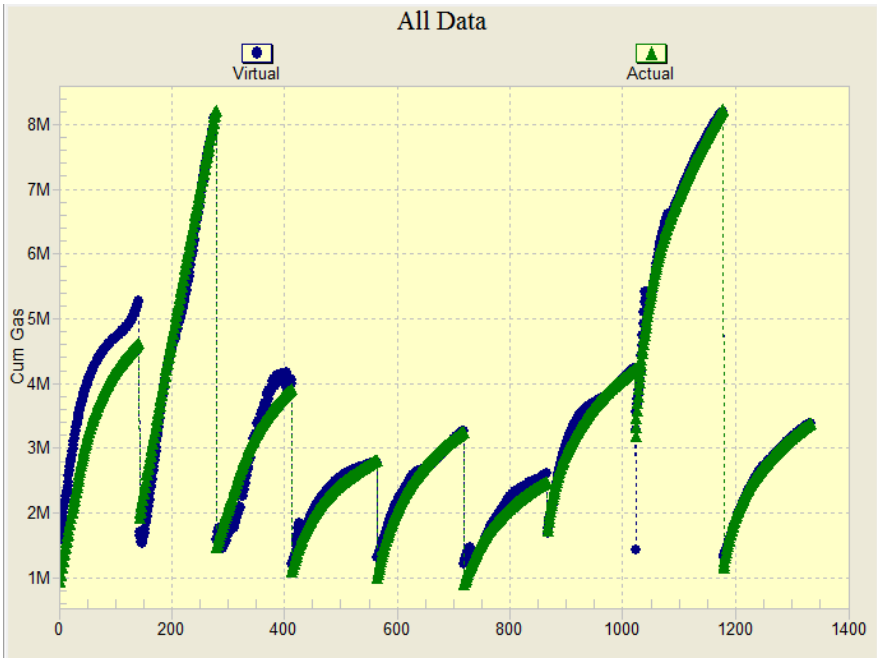

Figure 361. Neural network results for Cumulative leaked gas -cap-rock leakage

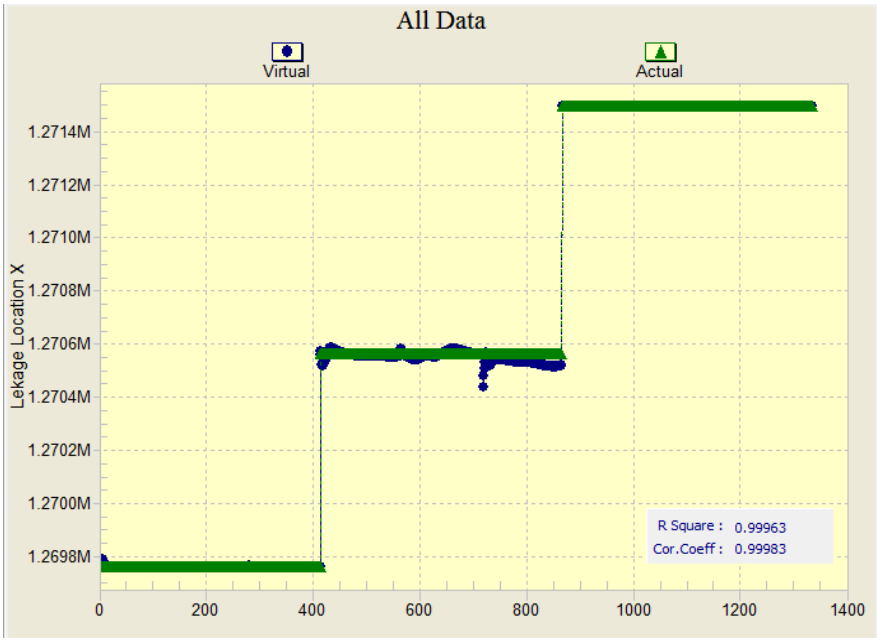

Figure 362. Neural network results for leakage location(X) -cap-rock leakage

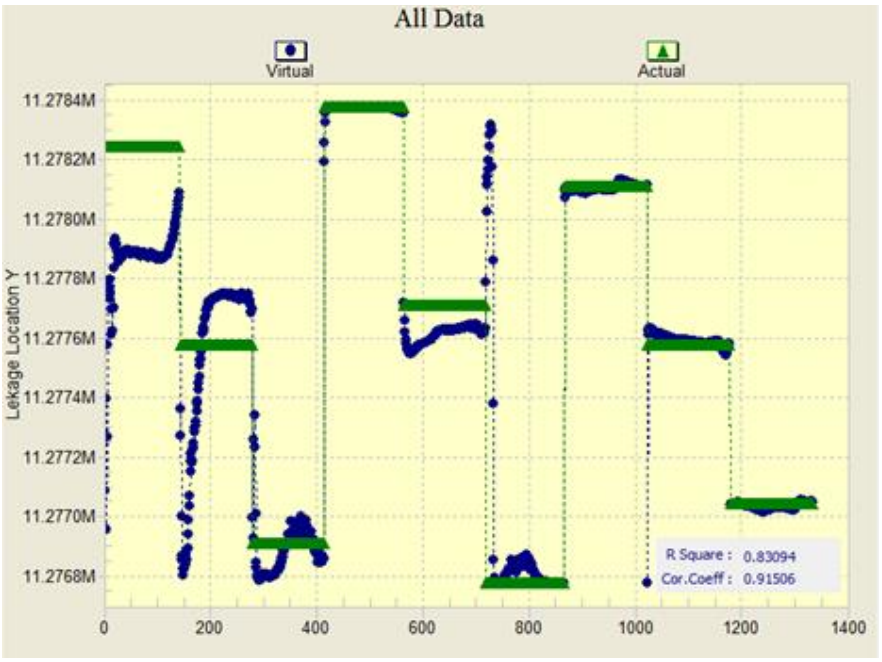

Figure 363. Neural network results for leakage location(Y) -cap-rock leakage

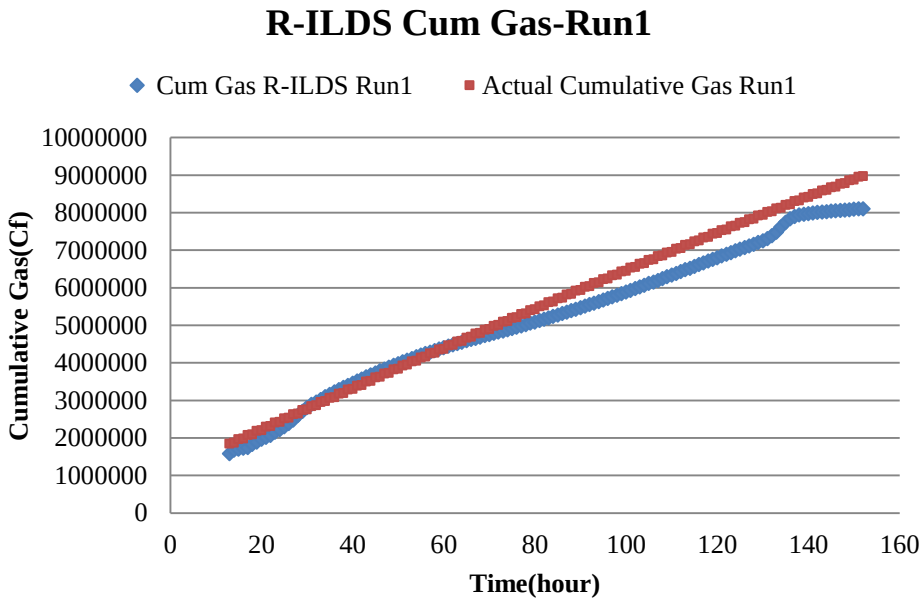

Figure 364. R-ILDS prediction for cumulative leaked gas, Blind Run 1(Cap-rock Leakage)

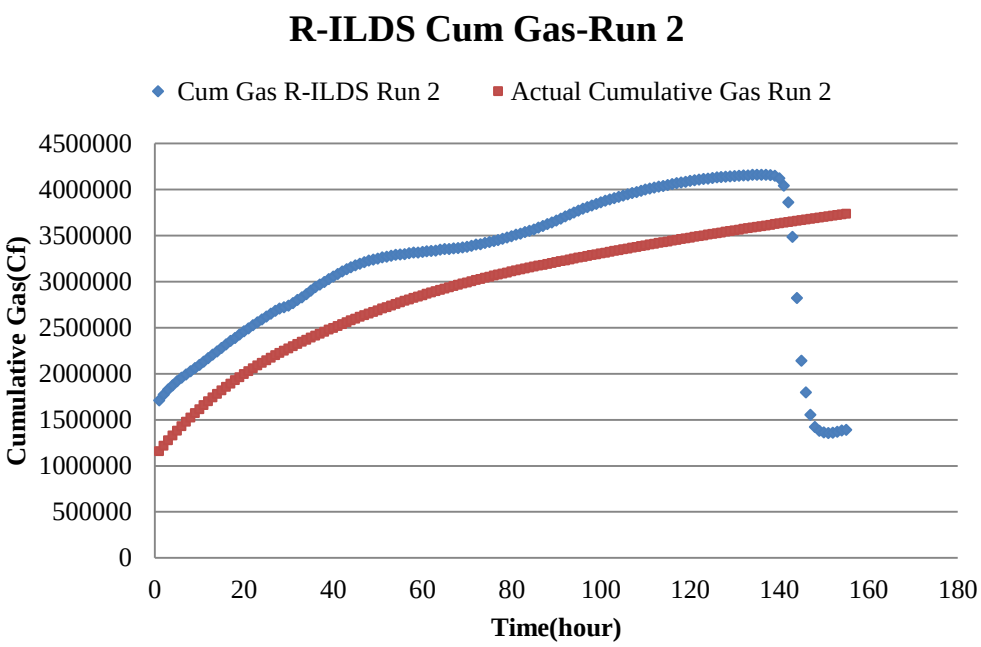

Figure 365. R-ILDS prediction for cumulative leaked gas, Blind Run 2(Cap-rock Leakage)

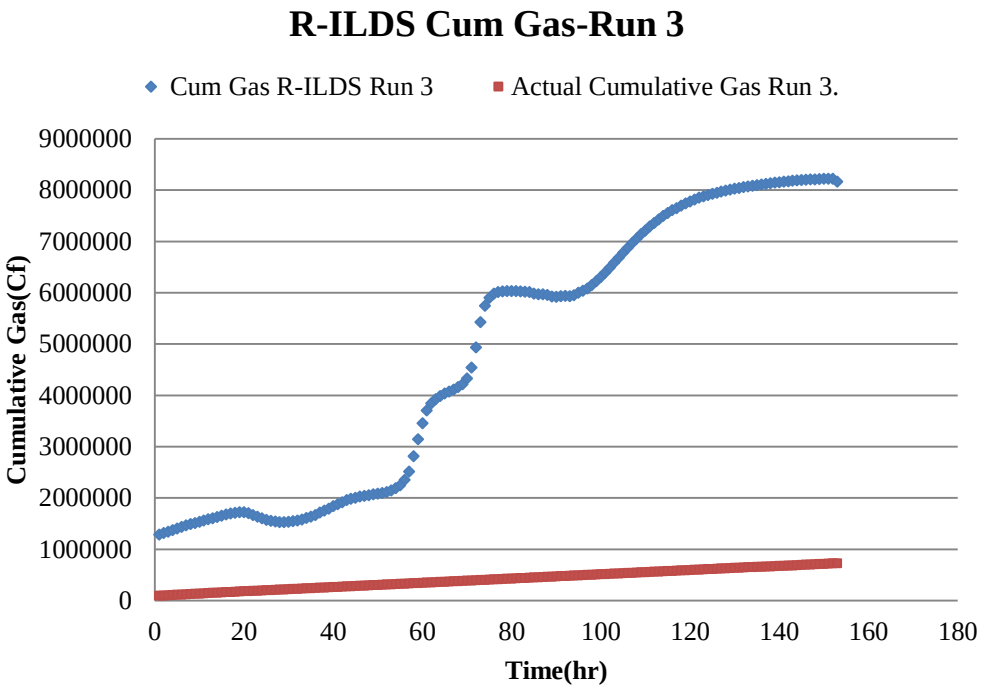

Figure 366. R-ILDS prediction for cumulative leaked gas, Blind Run 3 (Cap-rock Leakage)

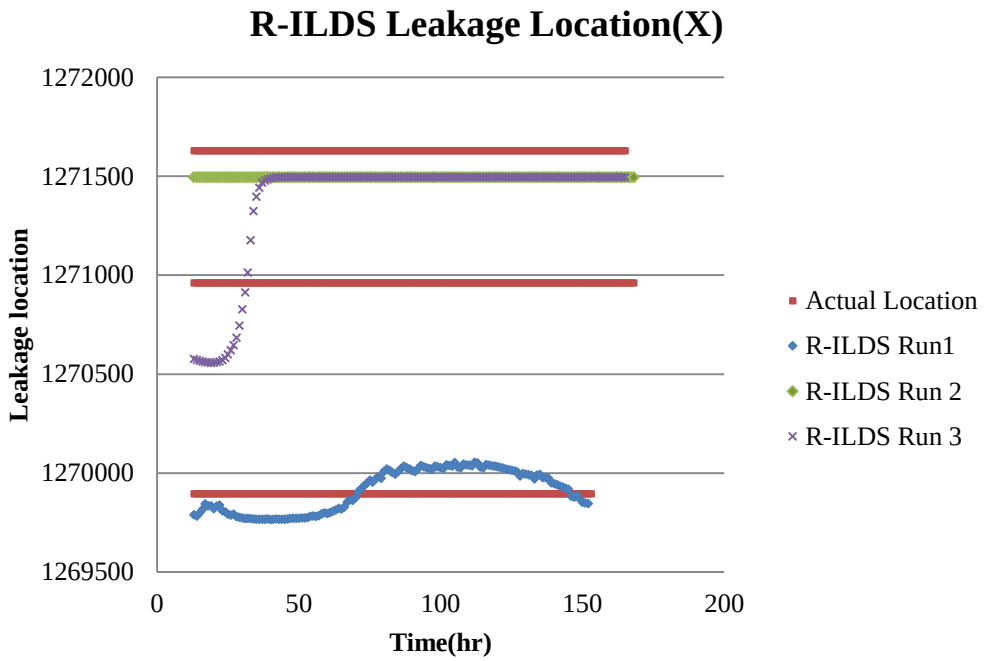

Figure 367: R-ILDS prediction for cumulative leaked gas, Blind Run 3 (Cap-rock Leakage)

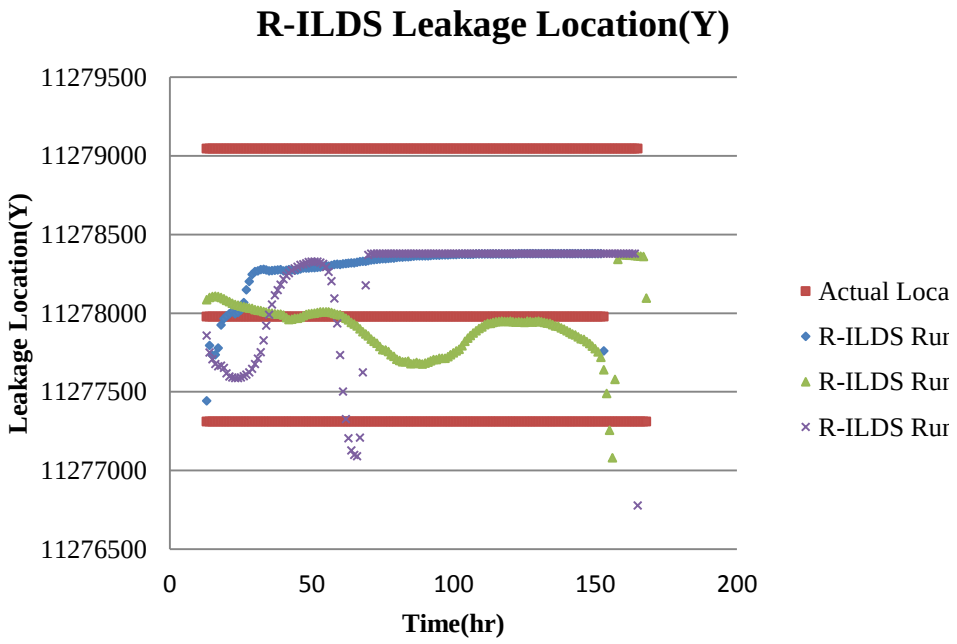

Figure 368: R-ILDS prediction for cumulative leaked gas, Blind Run 3 (Cap-rock Leakage)

APPENDIX 11

MULTI-WELL LEAKAGE RESULTS

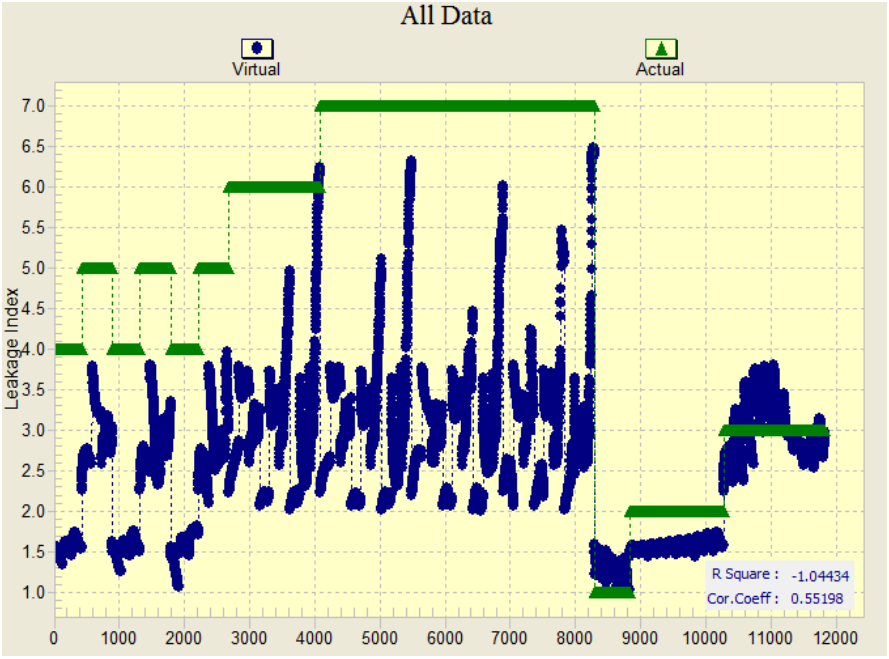

Figure 369. Neural network training results for Leakage Index (one, two and three-well leakage)

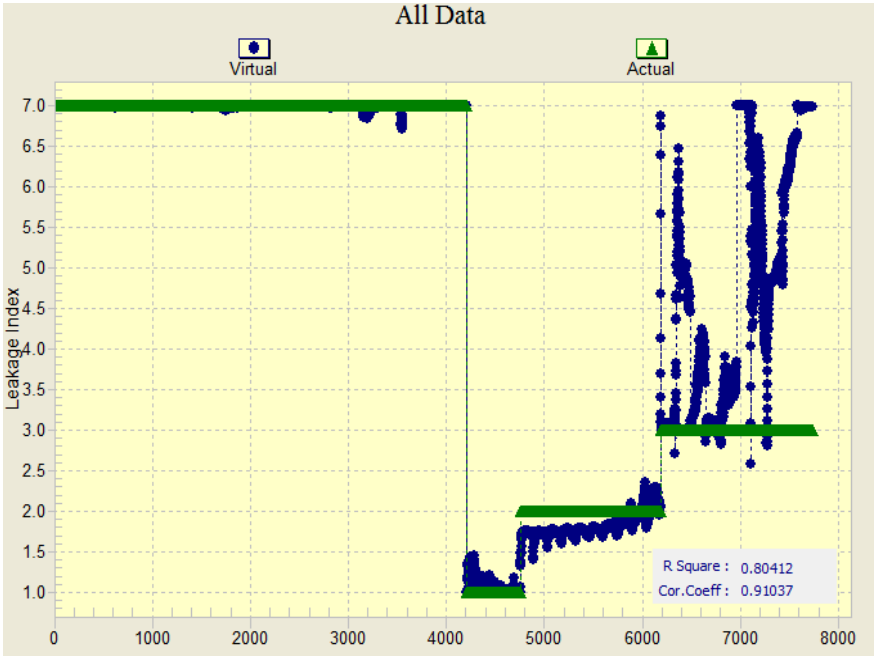

Figure 370. Neural network training results for Leakage Index (one and three-well leakage)

APPENDIX 12

THE SOFTWARE APPLICATION

INTELLIGENT LEAKAGE DETECTION SYSTEM (ILDS)

Installation instruction of the ILDS:

1. Run the Setup File
2. The Setup procedure will create a file called “ILDS.exe” in the following folder: “C:\Program Files (x86)\WVU\Intelligent Leakage Detection System”
3. Run the “ILDS.exe” as administrator by right clicking on the file and selecting “run as administrator”.

The Intelligent Leakage Detection System (ILDS) is a software application that has been developed as part of this project and is delivered according to the instructions provided by DOE. ILDS is designed such that it receives the pressure data from the permanent downhole gauges, processes them and connects the data to a series of trained neural networks for analysis. Upon receipt and process of the real-time data, the Software System (ILDS) will determine the possibility of a leak in the system. The ILDS will communicate its finding to the user through the following three conditions:

1. “All is well” or “No Leak is Being Detected”. Green Radar Screen
2. “There is the Possibility of a Leak in the System”. Orange Radar Screen (Transitional Phase)
3. “A Leak has been detected in the System”. Red Radar Screen

ILDS communicates its finding using a “radar” screen. A green moving radar screen on top of the map of the field, indicates that “All Is well” or “No Leak is Being Detected”. Alternatively, the system may detect the possibility of a leak. Since the system will not remain in this state for too long and will eventually converge into one of the other two states, this is called a “Transitional Phase”. In this “Transitional Phase” the radar screen will change to the orange color indicating that some unusual pressure activities have been detected in the system. ILDS continues its survey of the reservoir behavior in order to be able to make some conclusions regarding the nature of the unusual pressure behavior in the system. One of the two things may happen at this point:

a. The unusual behavior proves to be nothing (a drift in the gauge or some other nuances) in which case the radar screen will return to green indicating “No Leak is Being Detected”

b. The unusual behavior persists and eventually results in detection of a leak in the system. In this case the orange radar screen will turn red indicating “A Leak has been detected in the System”.

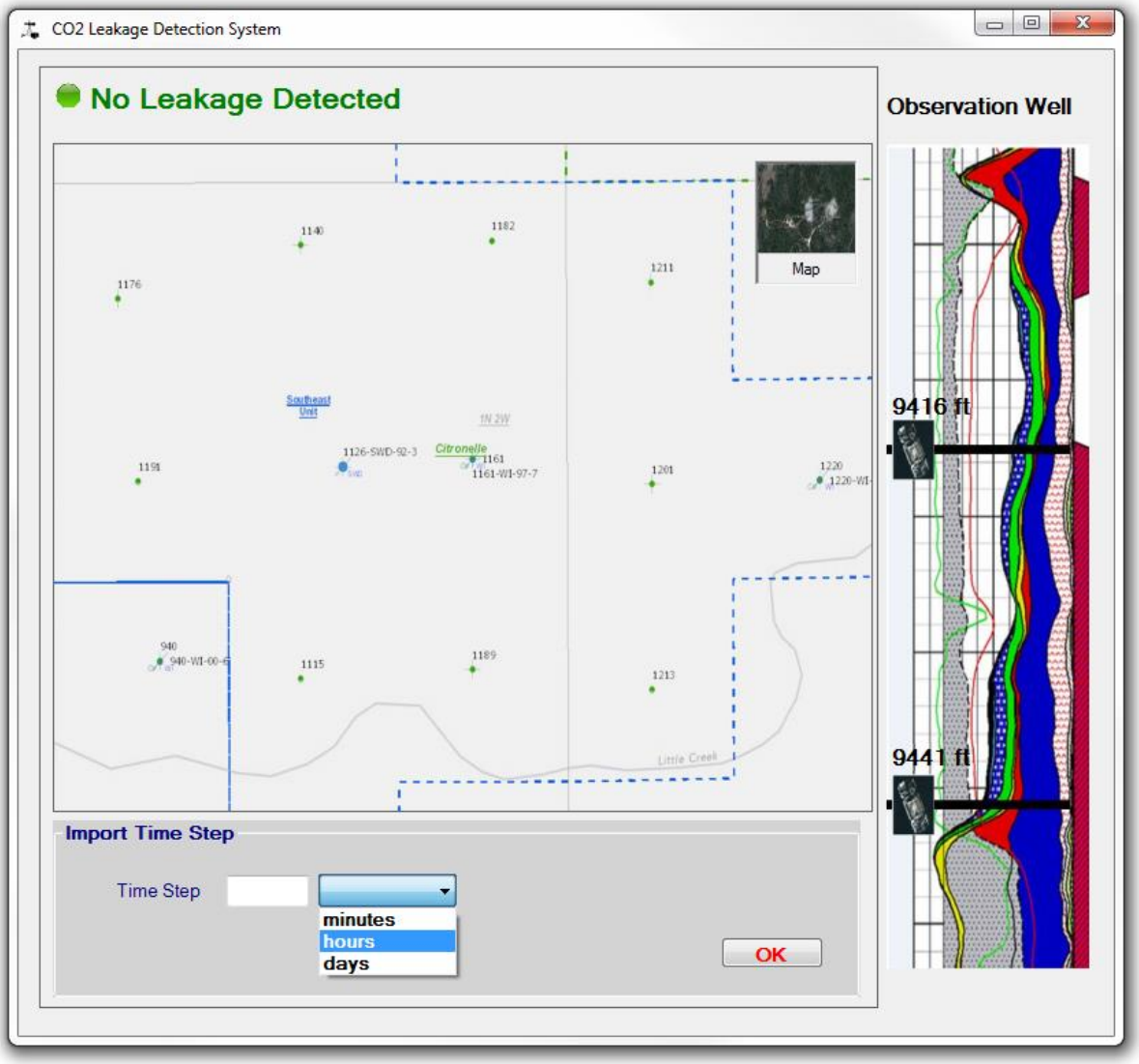

Figure 371. Identify the time step for pressure data.

And finally, if and once “A Leak has been Detected in the System”, the radar screen will turn red. Furthermore, once a leak is detected in the system, ILDS will provide two more pieces of information:

1. It estimates the location of the leak.
2. It estimates the amount of the leak.

For cap-rock leakage detection, cumulative leaked gas and coordinates of leakage locations are the output of the ILDS.

Figure 371 shows the main interface of the ILDS. The main ILDS interface includes three sections. The main section (top-left) includes the map of the field (the map of the Citronelle field for this project). The color and the caption of the button on top of this section identify the status of the leak detection. In Figure 371 the color is green and the caption reads “No Leakage Detected”. The color of the button and the caption will change accordingly during the transition phase or if a leak is detected in the system.

On the right hand side of the interface a figure identifies the locations of the permanent downhole pressure gauges in the observation well. In the observation well, two pressure downhole gauges were installed at depths of 9416 ft. and 9441 ft. below surface. And finally a panel on the bottom left provides means for identifying the time-step for the analysis. Upon identification of the time step, the information is communicated to “ILDS” by clicking on the “OK” button. This action will open a dialog box shown in Figure 372 where the user can identify the location of the file containing the real-time pressure data. Use of a data historian for the collection and preparation of the real-time data is covered in a separate section of this report.

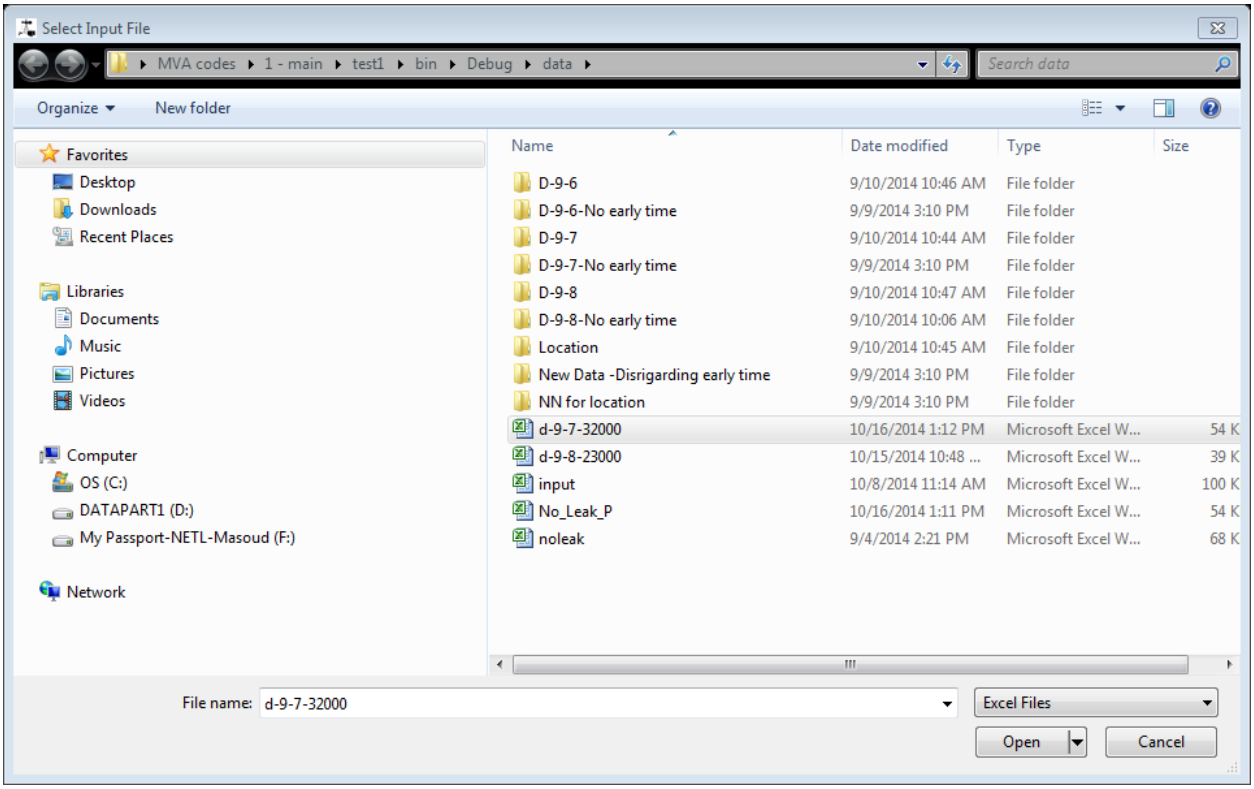

Figure 372. Dialog box for identification of the location of real-time pressure data.

Once the real-time pressure file is selected, IDLS connects to this file and continuously reads and then process the imported pressure data. The real-time pressure data from the permanent down-hole gauges is usually noisy, therefore in order to make the analysis more accurate the noisy data must first be de-noised. The de-noising process takes place in the background without any interaction from the user.

The clean (de-noised) data is forwarded to a module to calculate the change in pressure. If the change in pressure is above a certain threshold, the statistical module is invoked to calculate the required statistics of the data series. The complete data set is then introduced to a series of trained, intelligent systems to detect the leak.

At this point in time the system (ILDS) reacts by generating an “Orange” radar screen, while identifying whether an actual leak has been detected or not. If an actual leak is detected, the system will generate a “red” radar screen and estimates the location and the amount of the leak. The flow chard of the system described above is shown in Figure 373.

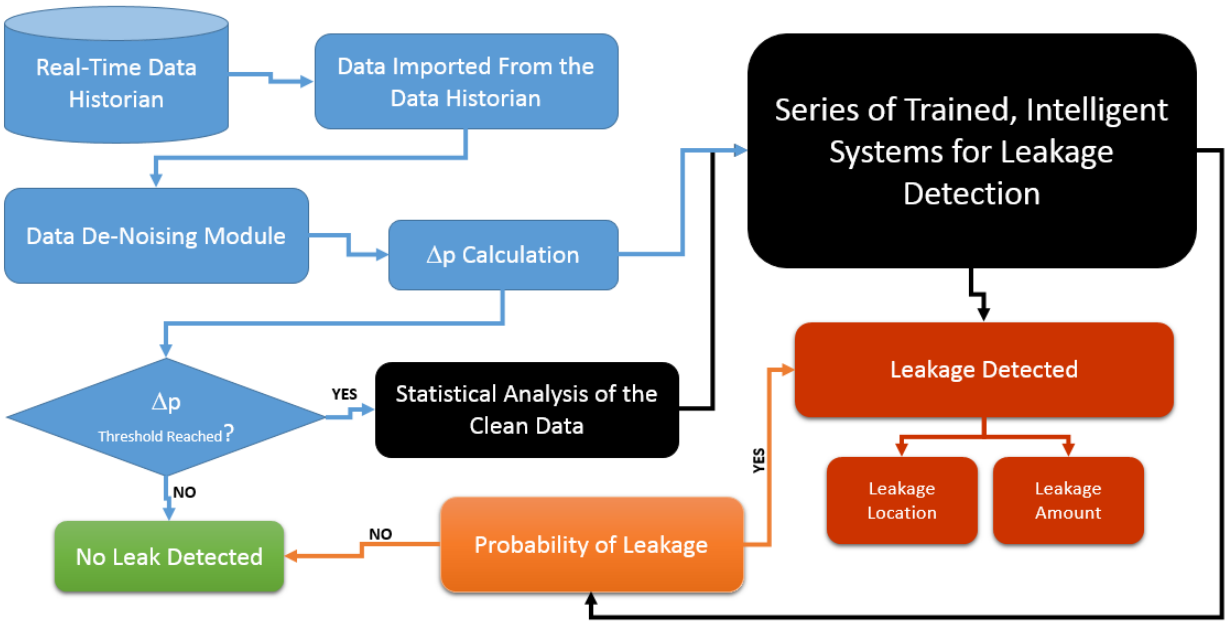

Figure 373. Flow Chart describing the Intelligent Leak Detection System.

Figure 374 shows the interface of ILDS when it is reading the pressure data. In the upper right hand corner of the interface the real-time pressure is displayed (represented by a line chart). This is to let the user observe (in real-time) the pressure behavior at the observation well. The value of Δp (change in pressure, delta pressure) is also calculated and plotted in this interface (located in the bottom right hand side).

The Δp chart shows the difference between pressure measurements at the observation well with the expected pressure values at this location when no leakage is expected (the reference pressure[9]). ILDS analyzes each new pressure data to determine the status of the leakage. A green moving radar screen on the map of the field indicates that “No Leak is Being Detected” (as shown in Figure 374).

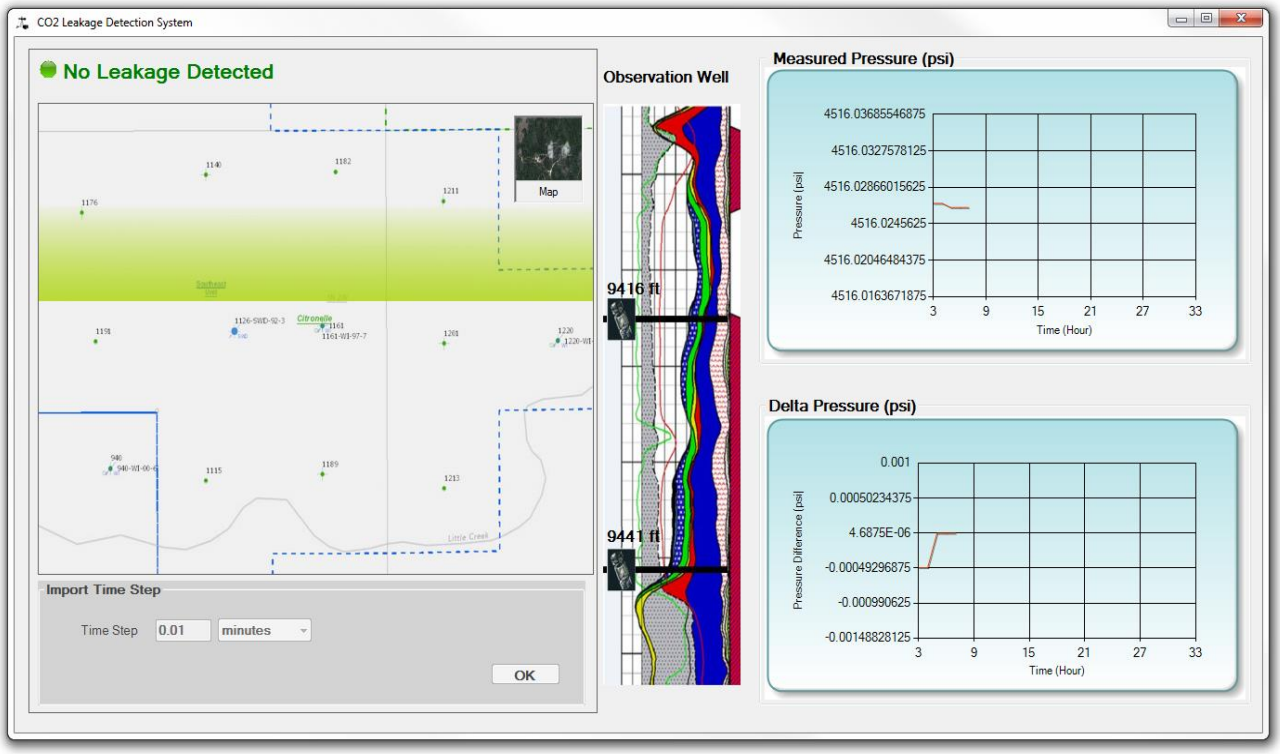

Figure 374. Software is reading pressure data. No leakage is detected.

Once the behavior of the pressure is calculated to be unusual (Δp passes a certain threshold), the information is passed to a statistics module so that certain statistics of the signals can be calculated. Upon calculation of the required statistics, values of Δp, pressure derivative, Δp average, Δp summation, Δp standard deviation, Δp skewness and kurtosis for each time step are organized and passed to the trained, intelligent systems for leakage detection. All these calculations are performed in the background and the process is completely hidden from the user.

In this stage, the status of the system changes to “Possibility of Leakage” and the color of the radar screen and the background color of the pressure charts are changed to orange in order to

[9] Please note that the values of the reference pressure can be modified if new information becomes available identifying what the reference pressure should be. Values of the reference pressure for this version of ILDS was calculated based on history matched model generated for this project.

attract the attention of the person in charge of this system[10]. Figure 375 shows the interface in "Transitional Phase". In this phase the system is trying to identify (estimate) the location of the leakage. Each time step a location is determined by ILDS and shown in the field map by a red circle (Figure 376). As time goes on, and more data is collected, and transmitted through the data historian to the ILDS, the estimation of the location becomes more accurate, until the estimated location will stop moving. This is the final estimated location of the leakage by the ILDS.

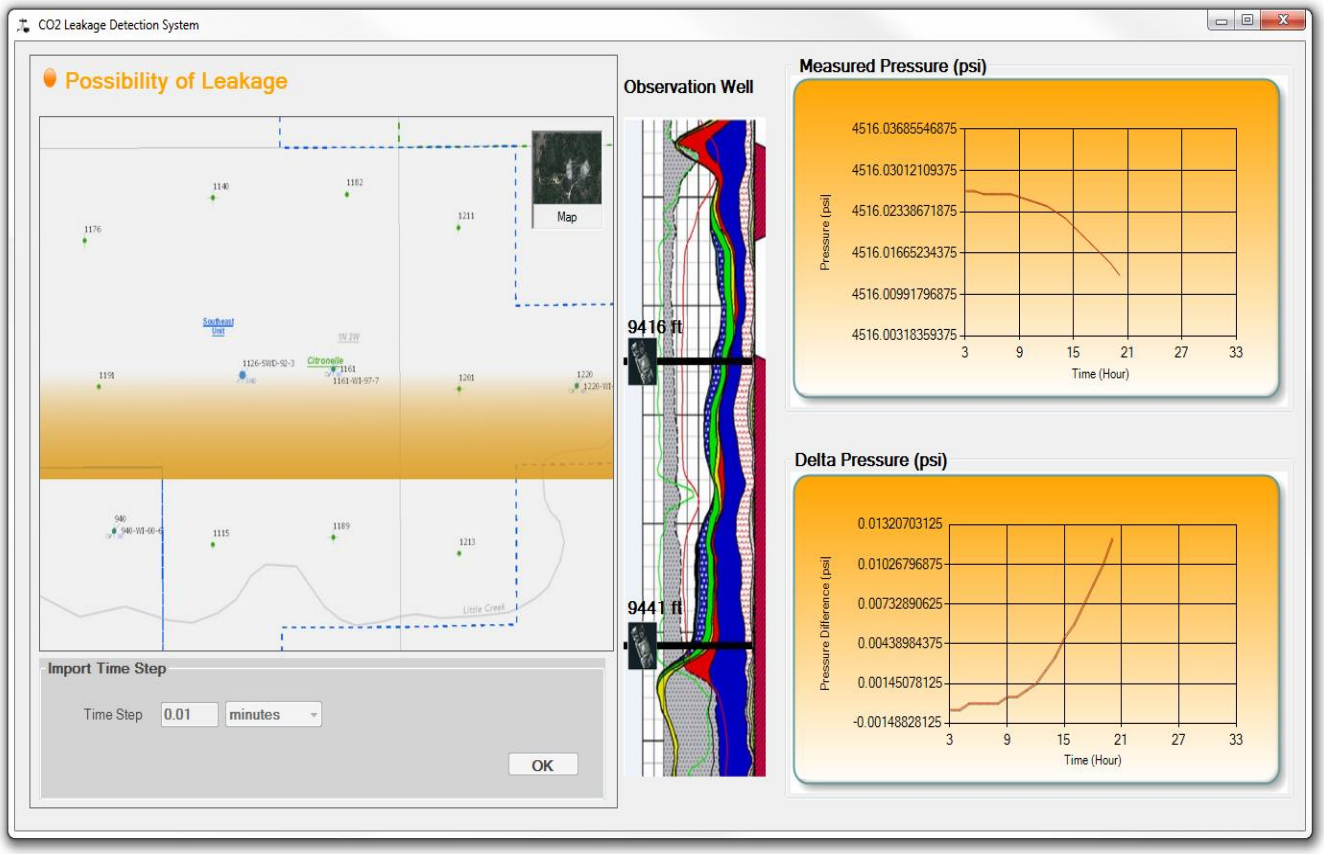

Figure 375. Pressure behavior is unusual and there is a possibility of leakage.

When ILDS has converged to the final leakage location, the status of the interface changes to "Leakage Has Been Detected" and the color of the radar screen and the background color of the pressure charts turn to the color "red". The system continues to process the data in order to estimate the amount of leakage. Once the amount of the leakage (that is a function of the severity of pressure change) is estimated, the location of the leakage, the amount of the leakage, as well

[10] Please note that an automatic system can be developed at this point to generate an alert in the form of Email or Text Message in order to alert the responsible parties. Development of such a facility eliminates the need of a person continuously attending to the leakage detection system.

as the amount of time that has passed from the start of the leakage is shown in bottom left of the interface (Figure 376).

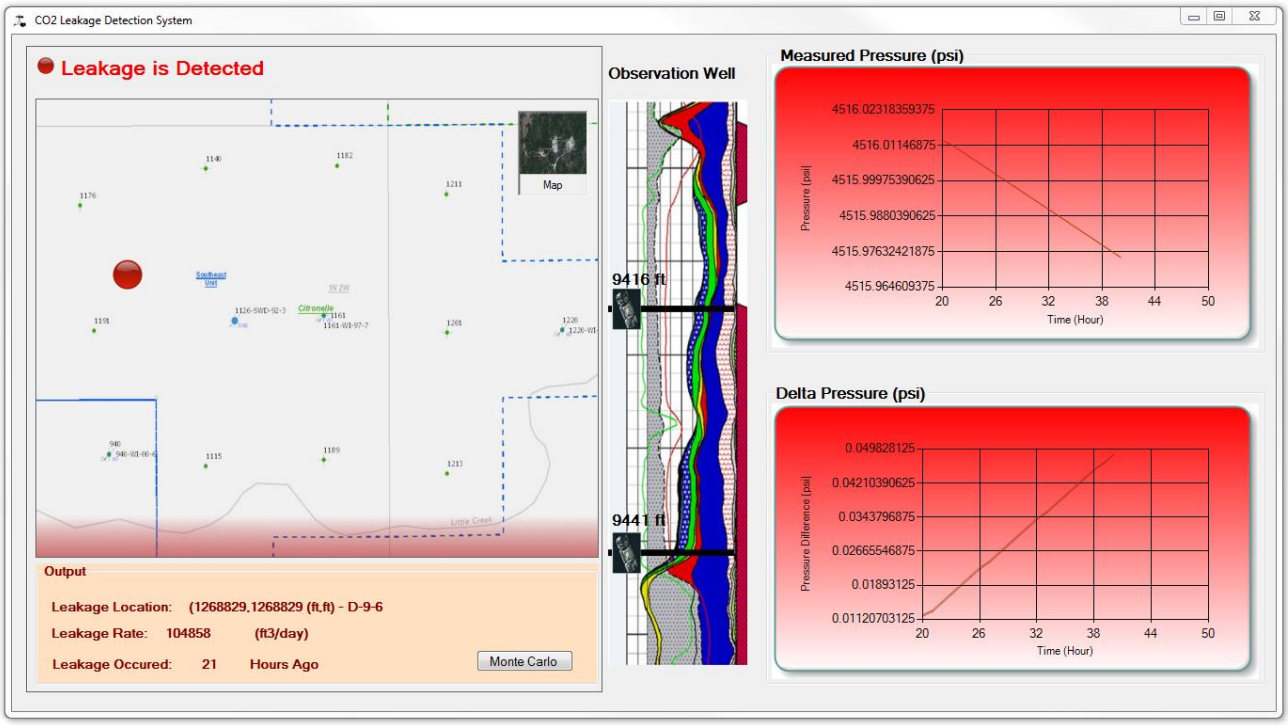

Figure 376. Leakage is detected. Leakage location and amount is shown in the form.

Connecting the ILDS to a Data Historian

The design of ILDS is such that it will read the real-time pressure data from an excel file. Therefore, in order for the real-time pressure data to be communicated to ILDS it must go through the following process: (Please note that this process is reasonably standard for recording real-time data from the instruments in the field)

1. Data is transmitted from the downhole pressure gauge to a data collection center on the surface.
2. The surface data collection center stores the transmitted data into a data historian.
3. The data historian is capable of reformatting the historical (real-time) data into the required format (This format of ILDS is CSV or any format recognizable by Excel).
4. The real-time pressure data in the form of a excel spreadsheet is continuously updated and made available to the ILDS.

Figure 377 shows a screen shot of the excel spreadsheet that include the real-time pressure data that is used as input to the ILDS. Please note that the data includes headers on the first row.

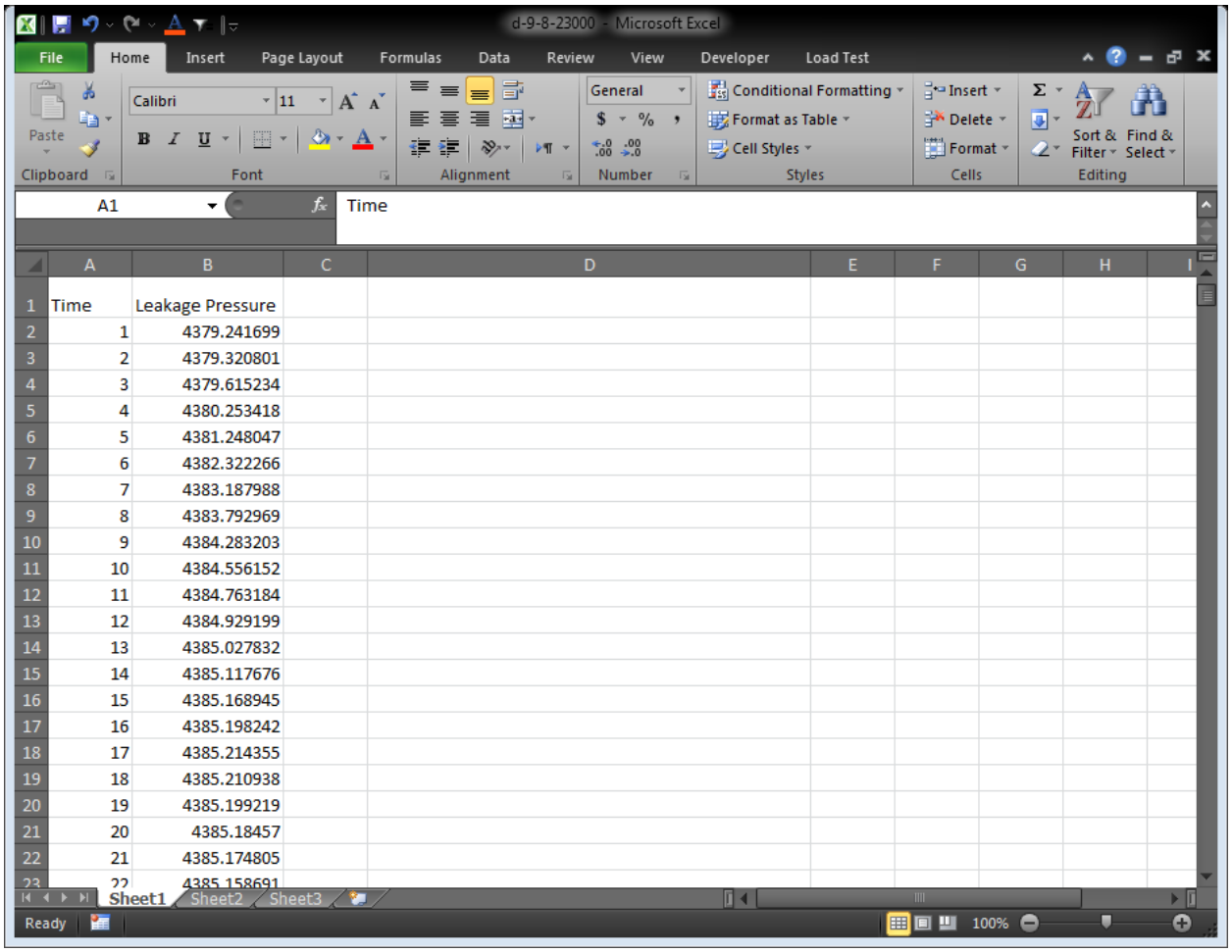

Figure 377. Input excel file format

APPENDIX 13

PUBLICATIONS RESULTED FROM THIS PROJECT

"Pressure History Matching for CO2 Storage in Saline Aquifers: Case Study for Citronelle Dome". Haghighat, S. A., Mohaghegh, S. D., Gholami, V., Shahkarami, A. Manuscript #P306522, 2013 Carbon Management Technology Conference. Alexandria, Virginia, 21-23 October, 2013.

"Using Big Data and Smart Field Technology for Detecting Leakage in a CO2 Storage Projects". Haghighat, A., Mohaghegh, S. D., Gholami, V., Shahkarami, A., Moreno, D. SPE 166137, SPE Annual Technical Conference and Exhibition. New Orleans, Louisiana, September 30 - October 2, 2013.

"Reservoir Simulation of CO2 Sequestration in Deep Saline Reservoir, Citronelle Dome, USA". Haghighat, S., Mohaghegh, S. D., Borzouie, N., Moreno, D. and Shahkarami, A. Twelfth Annual Conference on Carbon Capture, Utilization and Sequestration. Pittsburgh, PA, MAY 13-16, 2013.

REFERENCES

Charles R. Nelson, James M. Evans, Edward N. Steadman, John A. Harju, “Factors Affecting The Potential for CO2 Leakage from Geologic Sinks”, NETL Report, 2005

CMG software, Technical Manual

Cooper C.:” A Technical Basis for Carbon Dioxide Storage”, CO2 Capture Project, 2010

Denbury Resources, Incorporated, Plano, Texas,:” SECARB PHASE III ANTHROPOGENIC TEST Volume 1 of 2”, Prepared for: Alabama Department of Environmental Management, 2010

Jalali J, “Artificial Neural Networks for Reservoir Level Detection of CO2 Seepage Location Using Permanent Down-Hole Pressure Data”, PhD Dissertation, Petroleum and Natural gas Engineering Department, West Virginia University, 2010

Jansen J.D., SPE, Shell Intl. E&P (SIEP) and Delft University of Technology (DUT); Douma S.D., SPE, and Brouwer D.R, SPE, SIEP; and P.M.J. Van den Hof, O.H. Bosgra, and A.W. Heemink, DUT, “Closed Loop Reservoir Management, SPE Reservoir Simulation Symposium”, 2-4 February 2009, The Woodlands, Texas

Koperna G.J, Kuuskraa V.A.,Reistenberg D.E, Rhudy R., Trautz R., Hill G.,Esposito R.A,” The SECARB Anthropogenic Test: The First US Integrated Capture, Transportation, and Storage Test” Carbon Management Technology Conference, 7-9 February 2012, Orlando, Florida, USA

Krause M., Perrin J.C., Benson S. M., “Modeling Permeability Distributions in a Sandstone Core for History Matching Coreflood Experiments”, SPE International Conference on CO2 Capture, Storage, and Utilization, 2-4 November 2009, San Diego, California, USA

Kuuskraa V.A.,” Cost-Effective Remediation Strategies for Storing CO2 in Geologic formations”, SPE International Conference on CO2 Capture, Storage, and Utilization, 2-4 November 2009, San Diego, California, USA, 2009

Kuuskraa V.A., Koperna G.J., Schepers K.C., “CO2-Storage Engineering: Real Solutions to Real Problems”, SPE International Conference on CO2 Capture, Storage, and Utilization, 10-12 November 2010, New Orleans, Louisiana, USA

Liner C. L., Geng P., Zeng J., King H, Li J,” A CO2 Sequestration Simulation Case Study at the Dickman Field, Ness Co., Kansas”, SPE Annual Technical Conference and Exhibition, 30 October-2 November 2011, Denver, Colorado, USA

Lozzio M, SPE, Akemu O,SPE, James L,SPE, Desroches J,SPE,Sclumberger, Lombardi S, Lombardi S and Annunziatellis A., Universitá di Roma , “Quantifying the Risk of CO2 Leakage Through Wellbores”, SPE New Orleans ,Louisiana, USA ,November 2010

Mantilla C. A., Srinivasan S, Cross E. A, Bryant S. L, “Inexpensive Assessment of Plume Migration During CO2 Sequestration”, SPE International Conference on CO2 Capture, Storage, and Utilization, 2- 4 November 2009, San Diego, California, USA

Masoudi R., Jalil M.A.A, Press D., Lee K., Tan C.P, Anis L., Darman N., Othman M, “An Integrated Reservoir Simulation-Geomechanical Study on Feasibility of CO2 Storage in M4 Carbonate Reservoir, Malaysia”, International Petroleum Technology Conference, 7-9 February 2012, Bangkok, Thailand

Meckel T.A., Hovorka S.D., “Above-Zone Pressure Monitoring as a Surveillance Tool for Carbon-Sequestration Projects”, SPE International Conference on CO2 Capture, Storage, and Utilization, 10-12 November 2010, New Orleans, Louisiana, USA”

Mohaghegh S, WVU, Virtual-Intelligence Applications in Petroleum Engineering: Part 1—Artificial Neural Networks, Journal of Petroleum Technology

Petrusak R, SPE, Cyphers S., SPE, Bumgardner S, SPE, Advanced Resources International; Hills D, Pashin J., Geological Survey of Alabama; Esposito R, Southern Company, “Saline Reservoir Storage in an Active Oil Field: Extracting Maximum Value From Existing Data for Initial Site Characterization”; Southeast Regional Carbon Sequestration Partnership (SECARB) Phase III, SPE International Conference on CO2 Capture, Storage, and Utilization, 10-12 November 2010, New Orleans, Louisiana, USA

Riestenberg D.E, Koperna G.J, Kuuskraa V.A., Esposito R., Harisson K,Berry R.,Sparks j.,Rhudy R., ”CO2 Sequestration Permitting at the SECARB Mississippi Test Site”, SPE mericas E&P Environmental and Safety Conference, 23-25 March 2009, San Antonio, Texas

Roland N. Horne, SPE, Stanford University, Listening to the Reservoir, “Interpreting Data from Permanent Downhole Gauges”, Journal of Petroleum Technology, December 2007

Senel O., Nikita Chugunov N., “CO2 Injection in a Saline Formation: How Do Additional Data Change Uncertainties in Our Reservoir Simulation Predictions?” Carbon Management Technology Conference, 7- February 2012, Orlando, Florida, USA

Sifuentes W., Blunt M.J., SPE, Giddins M.A.,” Modeling CO2 Storage in Aquifers: Assessing the key contributors to uncertainty”, Offshore Europe, 8-11 September 2009, Aberdeen, UK

Tao Q., Bryant S.L, Meckel T.A, Luo Z, “Wellbore Leakage Model for Above-Zone Monitoring at Cranfield, MS”, Carbon Management Technology Conference, 7-9 February 2012, Orlando, Florida, USA

Theresa L. Watson, T.L. Watson & Associates, and Stefan Bachu, Alberta Energy Resources Conservation Board, “Evaluation of the Potential for Gas and CO2 Leakage Along Wellbores”, journal SPE Drilling & Completion, SPE 106817-PA

Torn A., Torabi F., Asghari K., Mohammadpoor M., “Effects of Aquifer Parameters on Long-Term Storage of Carbon Dioxide in Saline Aquifers”, Carbon Management Technology Conference, 7-9 February 2012, Orlando, Florida, USA

Wilson, T. and Wells, “Multi-frequency EM surveys help identify possible near-surface migration pathways in areas surrounding a CO2 injection well”, Environmental and Engineering

Geophysical Society, Fast Times, vol. 15, no. 3, p 43-53, 2010, San Juan Basin, New Mexico, USA,

Xiao C., Harris M.L., Wang F, Grigg R," Field Testing and Numerical Simulation of Combined CO2 Enhanced Oil Recovery and Storage in the SACROC Field", Canadian Unconventional Resources Conference, 15-17 November 2011, Alberta, Canada

Zeidouni M., Pooladi-Darvish M., University of Calgary,2010, "Characterization of Leakage through Cap-Rock with Application to CO2 Storage in Aquifers Single Injector and Single Monitoring Well" , Canadian Unconventional Resources and International Petroleum Conference, 19-21 October 2010, Calgary, Alberta, Canada, SPE 138178-MS

Zhou, Q.; Birkholzer, J.; Rutqvist, J.; Tsang, C-F,:" Sensitivity study of CO2 storage capacity in brine aquifers with closed boundaries: Dependence on hydrogeologic properties", DOE Technical Report Server (U.S. Department of Energy), 2008